

WESTERN SYDNEY
UNIVERSITY



Classification and Alignment of DRAGNs

Miranda Yew

A thesis submitted for the degree of
Doctor of Philosophy
at
Western Sydney University

Submitted
June 2022
Revised July 2023

Supervisors:
Dr Evan Crawford
Prof. Ray Norris
A/Prof. Laurence Park
Prof. Miroslav Filipović

Dedication

*Dedicated to my mother who is looking down on
me from above, and my father for your support.*

I hope I have made you proud...

老爸, 愛你永遠.

Acknowledgements

The work in this thesis could not have been made possible without the guidance and support of a great number of people.

First and foremost, I would like to acknowledge my wonderful supervisory team, consisting of **Evan Crawford, Ray Norris, Laurence Park and Miroslav Filipović**. Evan and Miroslav had made up my Masters supervisory panel so we already had an understanding of each other from there. But Ray and Laurence joined midway through my candidature when I had a huge shift in my project. I recall talking about wanting to do this project and asking many questions of Ray, who at that time, was not supervising me. He was also quite interested in the project and soon, I had another supervisor! Laurence too, turned up in one of our weekly supervisory meetings to talk about circular statistics, and soon became a regular! Despite the hurdles (that came mostly from a huge shift in project and unexpected results), they have guided and assisted me well throughout my candidature. I have learned a lot from them, especially since they all have different approaches to science, which has led to many an interesting discussion!

Evan and Miroslav, thank you both for your help and guidance over the course of both my Masters and PhD! It's been wonderful to work with you two again. In particular, Evan, as my primary supervisor, I hope I haven't been too much of a pain these last four years! We may have disagreed at times, but I've really enjoyed our fun discussions, whether about science or otherwise. I'm glad to have being your student and hope we will remain collaborators and good friends.

Ray and Laurence, you both may have come on quite late, but I honestly couldn't see this project finishing without either of you! Ray, it's been an honor and absolute pleasure to work with you. Your encyclopedic knowledge had me learning but also scratching my head at times! I hope this won't be the end of our collaboration, I mean you've even given me a new 'name' (Miranada/DRAGN-lady) ;)! Laurence, thank you for your support and for pointing things out that I wouldn't and couldn't have seen. I've enjoyed being your student and have learned so much from you.

I would like to give a shout-out to my office 'mates', for the fresh insights, care and jokes, oh and the occasional arranging of my desk! In no particular order: Kieran, Velibor, Peter, Devika, Pero, Rami. Keep being awesome, guys!

I would like to thank Aunty Juno and Uncle Sonny, for your constant prayers and care for me. You've

been like godparents to me from young and I'm ever grateful for your support in everything I do.

I would like to thank my family. It was a wish of my grandmother (奶奶) in Singapore to see me graduate. She might not be able to be here in person but I would like to still thank her for her love and prayers for me.

Finally, I need to thank my dad. Honestly, he's been more stressed out about my PhD than I've been! 老爸, I haven't been the best daughter and can drive you up the wall at times (okay maybe many times), but I wouldn't be where I am right now if not for you. You are my rock. You supported me in my passion, in everything I do, and you're there to pick me up when things fall apart for me. I don't tell you often how much you mean to me, as it's hard to describe in just a few words, but I love you, and thank God everyday for putting you in my life.

Now for the formal Acknowledgements:

This work uses data from the facilities below:

The Australian SKA Pathfinder is part of the Australia Telescope National Facility (<https://ror.org/05qajvd42>) which is managed by CSIRO. Operation of ASKAP is funded by the Australian Government with support from the National Collaborative Research Infrastructure Strategy. ASKAP uses the resources of the Pawsey Supercomputing Centre (<https://ror.org/04f2f0537>). Establishment of ASKAP, the Murchison Radio-astronomy Observatory and the Pawsey Supercomputing Centre are initiatives of the Australian Government, with support from the Government of Western Australia and the Science and Industry Endowment Fund. We acknowledge the Wajarri Yamatji people as the traditional owners of the Observatory site.

This work includes archived data obtained through the CSIRO ASKAP Science Data Archive, CASDA (<http://data.csiro.au>).

This publication makes use of data products from the Wide-field Infrared Survey Explorer, which is a joint project of the University of California, Los Angeles, and the Jet Propulsion Laboratory/California Institute of Technology, funded by the National Aeronautics and Space Administration.

I wish to acknowledge the Darug Nation whose land the University's Kingswood campus is located on.

The work presented in this thesis is, to the best of my knowledge and belief, original except as acknowledged in the text.

I hereby declare that I have not submitted this material, either in full or in part, for a degree at this or any other institution.

.....
Miranda Yew



.....
July 12, 2023

Contents

List of Tables	iv
List of Figures	v
Abstract	vii
List of Abbreviations	viii
1 Introduction	1
1.1 Active Galactic Nuclei	2
1.2 AGN Classification	5
1.3 Radio Galaxies	8
1.3.1 Radio Galaxy Structures	12
1.3.2 Hybrid morphology	17
1.3.3 Isotropy in Radio Galaxy Structures	19
1.4 Research Aims and Significance	20
1.5 Thesis Outline	21
2 Methodology and Data Sources	22
2.1 Units and Terminology	22
2.1.1 FR definition	23
2.2 Data	23
2.2.1 ASKAP Radio Data	23
2.2.1.1 G-23 Radio Data	24
2.2.1.2 EMU Pilot Survey	26
2.2.2 WISE IR Data	27
2.2.3 The GAMA G23 Region	30
2.2.3.1 KiDS Optical Data	30
2.2.4 EMU Pilot Survey	30



2.2.4.1	Optical Data	31
2.3	Morphological classification	31
2.4	Multi-wavelength Cross-identifications	32
2.4.1	G23 Data	32
2.4.2	EMU Pilot Survey	34
2.5	Estimating the luminosity function	36
2.6	Source Selection	39
2.7	Determining FR ratio	39
2.8	Parallel Transport	41
2.8.1	Angular Dispersion	44
2.8.2	Kolmogorov–Smirnov test	45
2.9	Circular Statistics	46
3	A Study of the Fanaroff-Riley dichotomy with the GAMA-23 Survey	48
3.1	Introduction	48
3.2	Results and Discussion	51
3.2.1	The FRI and FRII radio luminosity break	51
3.2.2	Redshift distribution	57
3.2.3	FRx sources	58
3.2.4	HyMoR sources	59
3.3	Conclusion	59
3.4	Source Catalogue	61
4	Continuation of the Fanaroff-Riley dichotomy with the EMU Pilot Survey	81
4.1	Results	81
4.1.1	Owen-Ledlow Diagram	82
4.1.2	Source Catalogue	86
5	Alignment of DRAGNs	168
5.1	Introduction	168
5.2	Determining Major Axis	169
5.3	Statistical methods	169
5.4	Results and Analysis	170
5.4.1	Two-dimensional analysis	171
5.4.2	Three-dimensional analysis	174
5.5	Comparison with previous studies	175

6	Summary and Future Work	186
6.1	Summary	186
6.1.1	A catalogue of DRAGNs	186
6.1.2	Fanaroff-Riley classification with ASKAP/EMU	186
6.1.3	Alignment of Radio Sources	187
6.2	Future Work	187
6.2.1	Radio	187
6.2.2	Multi-wavelength	188
6.2.3	Classification	188
6.2.4	Machine-Learning	189
6.2.5	Simulations	190
6.2.6	Alignment of DRAGNs	190
6.3	Epilogue	190
	References	191
A	A Second Epoch Chandra Observation of the Spiral Galaxy NGC 6744	212
B	New Optically Identified Supernova Remnants in the Large Magellanic Cloud	221
C	Discovery of a Pulsar-powered Bow Shock Nebula in the Small Magellanic Cloud	
	Supernova Remnant DEM S5	246
D	The ASKAP-EMU Early Science Project:	
	Radio Continuum Survey of the Small Magellanic Cloud	267

List of Tables

2.1	Cosmological parameters used throughout this work.	23
2.2	Observation details for the ASKAP G23 data. All dates and times are in Australian Eastern Standard Time (AEST; UTC+10).	26
2.3	EMU Pilot Observation details	27
2.4	EMU-PS value-added processing	38
3.1	G23 value-added processing	51
3.2	DRAGN Classification statistics for G23	51
3.3	G23 value-added catalogue	62
4.1	DRAGN Classification statistics for the EMU-PS	82
4.2	EMU-PS value-added catalogue	88
5.1	Flux bins	171
5.2	The parameters used to divide the selected sample of 1779 sources into three equal redshift z bins.	175
5.3	Comparison with previous work	176

List of Figures

1.1	AGN Structure	3
1.2	AGN Taxonomy	5
1.3	AGN Viewing Angle	8
1.4	Cygnus A	10
1.5	Centaurus A	11
1.6	Fanaroff-Riley Morphology	14
1.7	Owen-Ledlow diagram	16
1.8	Hybrid radio source example	18
2.1	Measurements to determine the FR ratio	24
2.2	ASKAP Field of View (FoV)	25
2.3	EMU-PS sensitivity	26
2.4	Merged EMU Pilot Mosaic	28
2.5	EMU Pilot Pointings	29
2.6	EMU Pilot Survey Map	31
2.7	FRx candidate example	33
2.8	G23 radio to CATWISE2020	34
2.9	G23 CATWISE2020 to KiDS	35
2.10	G23 CATWISE2020 to redshifts	35
2.11	EMU radio to CATWISE2020	36
2.12	EMU CATWISE2020 to DES	37
2.13	G23 CATWISE2020 to DESI	37
2.14	Ratio Algorithm good examples	40
2.15	Ratio Algorithm bad examples	40
2.16	Illustration of parallel transport	42
3.1	Owen Ledlow original plot	52
3.2	G23 O-L Plot	53



3.3	G23 O-L Plot Histogram	54
3.4	Similar to Figure 3.2, here I show only sources with a spectroscopic redshift.	55
3.5	Size vs luminosity for G23	56
3.6	Photometric vs Spectroscopic	57
3.7	G23 redshift plots	58
3.8	HyMoRS examples	60
4.1	Owen-Ledlow Diagram (All) for EMU-PS	83
4.2	Owen-Ledlow Diagram (FR) for EMU-PS	84
4.3	Size vs Luminosity for EMU-PS	85
4.4	EMU-PS redshift plots	86
5.1	Position Angle example	170
5.2	PA distribution	172
5.3	Median angular radius	173
5.4	Logarithm of significance level	178
5.5	Logarithm of SL with flux bins	179
5.6	Distribution of PAs per tile	180
5.7	Median angular radius per EMU-PS tile	181
5.8	Logarithm of SL per EMU-PS tile	182
5.9	Position angles of tile 9442	182
5.10	Maximum Dispersion Measure	183
5.11	PA distribution (redshift)	183
5.12	Logarithm of significance level (redshift)	184
5.13	Logarithm of SL with redshift bins	185

Abstract

The study of Active Galactic Nuclei formation and evolution is important in modern astronomy, as they represent an evolutionary stage in every galaxy, and thus are important to understand the formation and evolution of galaxies. However, there is not yet a full understanding of the physics and evolution of the population that emit brightly at radio wavelengths. In order to properly compare observations with theory, a large survey of radio-loud galaxies is required. In this project, I will be studying Double Radio sources Associated with Galactic Nuclei, as I wanted to learn more about them. I will be focusing on the Fanaroff-Riley types I and II in particular. I study their luminosities and find a large overlap between the two classes, more so than previous studies, with no obvious ‘break’. I also study their alignment in the sky, and find significant alignment up to 4 degrees. This is to test claims that the position angles of radio galaxies are aligned over cosmic distances. Such an alignment could only have arisen at the time of formation which would perhaps be able to provide some insight into early formation of supermassive black holes. I will be using data from the Evolutionary Map of the Universe pilot survey that was obtained with CSIRO’s Australian Square Kilometre Array Pathfinder, as well as GAMA-23 Early Science. A survey of this size will allow study of a large sample of sources that are free from selection effects and biases of previous and older studies and will be a valuable training set for my colleagues who are developing machine learning algorithms to find and classify radio sources.

List of Abbreviations

3C	Third Cambridge Catalogue of Radio Sources
AAT	Anglo-Australian Telescope
AGN	Active Galactic Nuclei
ASKAP	Australian Square Kilometre Array Pathfinder
CCD	Charge-coupled device
COSMOS	Cosmological Evolution Survey
CNN	Convolutional Neural Network
CRAFT	Commensal Real-time ASKAP Fast Transients survey
DES	Dark Energy Survey
DESI	Dark Energy Spectroscopic Instrument
DINGO	Deep Investigation of Neutral Gas Origins survey
DRAGN	Double Radio source Associated with Galactic Nucleus
EM	Electromagnetic
EMU	Evolutionary Map of the Universe
ESO	European Southern Observatory
FIR	Far Infrared
FIRST	Faint Images of the Radio Sky at Twenty-centimeters
FR	Fanaroff-Riley
FR0	Fanaroff-Riley Class 0
FRI	Fanaroff-Riley Class I
FRII	Fanaroff-Riley Class II
FSRQ	Flat-spectrum radio quasars
FWHM	Full width at half maximum

FoV	Field of View
GAMA	Galaxy And Mass Assembly
GLEAM	GaLactic and Extragalactic All-sky Murchison Widefield Array
GRG	Giant Radio Galaxy
HERG	High Excitation Radio Galaxy
H I	Atomic Hydrogen
H II	Ionised hydrogen
HyMoRS	HYbrid MOrphology Radio Sources
ICM	Intracluster Medium
IGM	Intergalactic Medium
ISM	Interstellar Medium
IR	Infrared
KDE	Kernel Density Estimation
K-S	Kolmogorov-Smirnov
KiDS	Kilo-Degree Survey
LERG	Low Excitation Radio Galaxy
LMC	Large Magellanic Cloud
LINER	Low Ionisation Nuclear Emission-line Region
LOFAR	Low-Frequency Array
LoG	Laplacian of the Gaussian
LoTSS	LOFAR Two-Metre Sky Survey
MIGHTEE	MeerKAT International GHz Tiered Extragalactic Exploration
ML	Machine Learning
NIR	Near Infrared
PA	Position Angle
PAF	Phased Array Feed
PCA	Principal Component Analysis
PINK	Parallelized rotation and flipping Invariant Kohonen
PSF	Point spread function
QSO	Quasi-stellar Object

RFI	Radio-frequency interference
RG	Radio Galaxy
RGZ	Radio Galaxy Zoo
RMS	Root Mean Square
SFG	Star forming galaxy
SKA	Square Kilometre Array
SL	Significance level
SMBH	Supermassive Black Hole
SNR	Supernova Remnant
M_{\odot}	Solar Mass
TGSS	TIFR GMRT Sky Survey
VLA	Very Large Array
VLASS	Very Large Array Sky Survey
VLBA	Very Long Baseline Array
VLT	Very Large Telescope
VST	VLT Survey Telescope
WISE	Wide-field Infrared Survey Explorer



Chapter 1

Introduction

The understanding we have of galaxy formation starts almost 14 billion years ago, shortly after the Big Bang. In this early stage of the Universe, expansion and cooling occurred in the first instants after the Big Bang (10^{-30} of a second), enabling charged particles (electrons and protons) to combine and form the first atoms of hydrogen and helium (e.g. [Avila-Reese, 2007](#)). Small quantum fluctuations in the matter density distribution grew over time which then gave rise to the structure of the present Universe. Active Galactic Nuclei (AGNs), being the luminous compact regions at the center of galaxies, represent an evolutionary stage and thus are important to understanding the formation and evolution of galaxies. In order to increase our understanding of galaxy formation and evolution, and the Universe as a whole, data from large astronomical surveys are used.

Recent deep, wide-field radio surveys such as the GaLactic and Extragalactic All-sky Murchison Widefield Array (GLEAM; [Hurley-Walker *et al.*, 2017](#)), Very Large Array Sky Survey (VLASS; [Villarreal Hernández and Andernach, 2018](#)) and LOFAR Two-Metre Sky Survey (LoTSS; [Shimwell *et al.*, 2019](#)) to name a few, are now starting to pry open the low surface-brightness and distant radio Universe. In doing so, they are providing an extensive look of the radio-loud AGN population, with markedly less restrictive selection effects than older studies and over a wider range in luminosity. To identify and catalogue the large samples of sources generated by modern radio surveys (e.g. [Crawford *et al.*, 2017](#); [Williams *et al.*, 2019](#)), and to categorize the resulting samples for scientific analysis (e.g. [Aniyan and Thorat, 2017](#); [Alhassan *et al.*, 2018](#); [Wu *et al.*, 2019](#); [Ma *et al.*, 2019](#)), automated approaches are required. Sensitive low frequency observations are, however, also simultaneously uncovering a more complex extended source population, such as hybrid Radio Galaxies (RGs; [Kapińska *et al.*, 2017](#)), and restarting and remnant RGs ([Mahatma *et al.*, 2018, 2019](#)). There is hence the risk of simple classification schemes concealing important physical distinctions. With large, new samples of extended radio sources being made available like the Evolutionary Map of the Universe (EMU; [Norris *et al.*, 2011](#)), I aim to revisit the applicability and usefulness of Double Radio sources Associated with Galactic Nuclei (DRAGNs), focusing on the

Fanaroff-Riley (FR) classification (Fanaroff and Riley, 1974) for new and upcoming radio survey populations. I will be using data obtained with the Australian Square Kilometre Array Pathfinder (ASKAP) for the EMU Pilot Survey and the Galaxy And Mass Assembly (GAMA)-23 field. These new, large samples will then hopefully advance understanding of AGNs, in particular, the physical evolution of RGs and the environmental impact.

A big part of this thesis is investigating the classification of RGs. Before introducing the problem, I will first describe how RGs like DRAGNs fit into the AGNs scheme, then investigate the types of RGs. At the end of the chapter, I will give an outline of the objectives of my study and a brief summary of the upcoming chapters.

1.1 Active Galactic Nuclei

A galaxy is an isolated system made up of stars, gas and dust, all bound by gravity (Hubble, 1922, 1926). A majority of galaxies shine, primarily at optical wavelengths, due to the effect of stellar and interstellar gas emission. The spectra of these normal galaxies are characterized by stellar absorption lines and emission lines emanating from Ionised hydrogen (H II) regions. Galaxies populate the Universe, often residing in clusters and groups and often contain an accreting SMBH which have masses typically in the range of $10^6 - 10^{10} M_{\odot}$. These quiet and invisible black holes are impossible to observe directly as no light can escape. However, during the times when matter accretes onto the black hole, the material will spiral inward and form a disk due to the angular momentum of gas and stars. This accretion disk heats up due to gravitational and frictional forces, and can outshine the rest of the galaxy. These bright cores are known as AGNs, and provide the strongest evidence for the existence of SMBHs (e.g. Kormendy and Richstone, 1995; Magorrian *et al.*, 1998; Richstone *et al.*, 1998). However, AGN are found only within a small percentage of galaxies with SMBHs. The energy that is output from AGN are mostly of a non-thermal nature (i.e. the emission profile does not match that of a gas at a certain temperature) with many strongly emitting other types of radiation in the Electromagnetic (EM) spectrum.

In recognizing that all AGN types are most likely driven by accreting SMBHs, this will help to provide a more complete picture of these objects. A clearer understanding can be obtained if the variations of AGN classifications are reduced by showing that two or more ‘types’ are intrinsically the same despite different appearances. Such a unifying scenario was first developed for Seyfert galaxies (Osterbrock, 1977; Koski, 1978), which have two distinct subclasses (Type 1 and Type 2) distinguished by the presence of absence of narrow or broadened (or both) optical spectral emission lines. It may also hold broader ramifications for AGNs in general as a similar explanation may also be applicable to other classifications.

Seyfert galaxies were first identified in 1943 by Carl K. Seyfert (Seyfert, 1943). He identified a class of spiral galaxies with high surface brightness ‘star-like’ cores that featured strong and broad emission

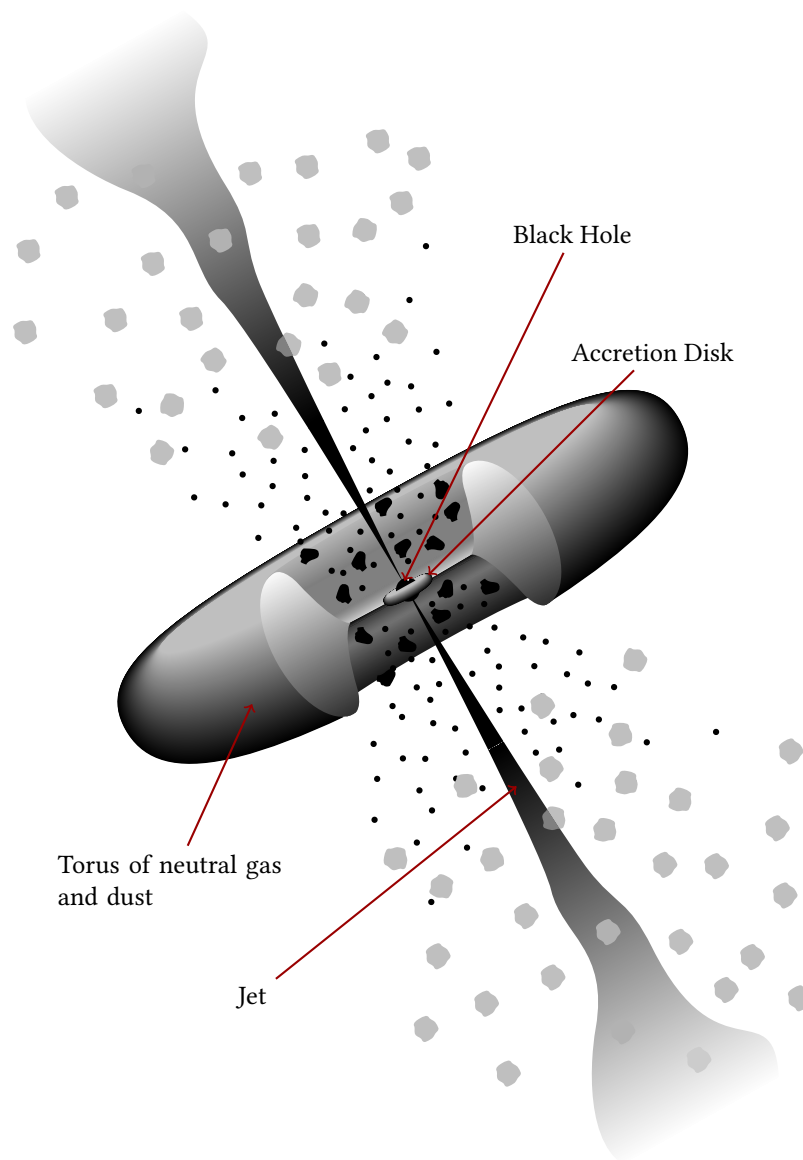


Figure 1.1: An artist rendition showing the different features of an AGN; namely the black hole, accretion disk and torus of gas and dust. The extreme brightness of an AGN is powered by accretion onto a Supermassive Black Hole (SMBH). Additionally, not all AGN have jets. Adapted from: *Urry and Padovani (1995)*.

lines in their spectra, which are often absent in normal galaxies. The Doppler widths of these emission lines corresponded to gas velocities of several thousand kilometres per second. These galaxies are now known as ‘Seyfert galaxies’ and are categorized into two distinct classes depending on the presence or absence of emission lines (Khachikian and Weedman, 1974).

Current evidence now shows that the cores of Seyfert 2 galaxies house Seyfert 1 engines. In the 1980s, broad Atomic Hydrogen (H I) emission lines were identified from polarized light by Antonucci and Miller (1985) from the Seyfert 2 galaxy NGC 1068. Their proposed explanation was that the core engine of NGC 1068 was similar to those reported in Seyfert 1 galaxies. The difference came from the observer’s line of sight to the engine, which was being impeded by a geometrically and optically thick torus. Direct observation of the engine’s not possible, but the light reflected from exposed areas of the galaxy not obstructed by the torus could be observed. This explanation lays the groundwork for what has evolved into the unified AGN model.

In the original Unified Model (Antonucci, 1993; Urry and Padovani, 1995; Urry, 2003), AGNs are modelled to include a giant torus of cold gas and dust, with an accretion disk feeding the central SMBH. Broadened and strong doppler lines are observed in their optical spectra, which originate from ionized gas that’s highly excited under the influence of the continuum emission from the disk as well as the gravitational field at different distances from the nucleus. Broader emission lines result from the high-velocity of gas clouds near the torus. The torus obscures the central parts at greater distances, causing the low-velocity dispersion clouds of gas to produce narrow emission lines instead. In some cases, narrow beams of energetic particles (jets) are produced from the black hole and accretion disk which eject outward in opposite directions away from the disk (see Figure 1.1). These relativistic jets become a powerful source of radio emission. The factors that determine an AGN are:

- the mass of the central SMBH,
- the accretion rate of material falling onto the SMBH,
- whether the black hole has a powerful jet,
- the spin of the SMBH,
- the angle at which the galaxy is viewed.

The study of the formation and evolution of AGN is a vigorously studied area in modern astronomy. A possible scenario for the formation of young AGN is that they arise from the collision of two or more galaxies, during the process of merging (e.g. Kauffmann and Haehnelt, 2000; Volonteri *et al.*, 2003; Wyithe and Loeb, 2003). Our own galaxy, the Milky Way, is proposed to have consumed another galaxy in the past, causing a SMBH (known as Sagittarius A*) to form at its centre (Ghez *et al.*, 2005). However, there is not yet full understanding behind the physics and evolution of the AGN population that emit strongly

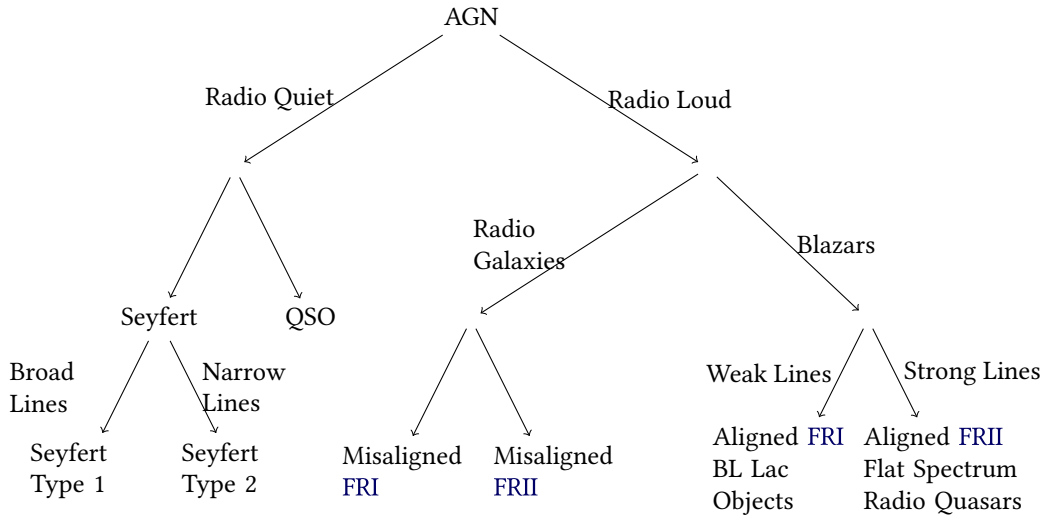


Figure 1.2: Classification of **AGN** based on the radio emission and excitation lines in their spectra. *Credit: Dermer and Giebels (2016)*

at radio wavelengths (known as radio-loud). In order to properly compare observations with theory, and to improve theories of the evolution of galaxies, a large survey of radio galaxies is required.

1.2 AGN Classification

There are many types of **AGNs**, which can be distinguished depending on their morphological properties, frequency, spectral features, and the orientation of the jet relative to the observer’s line of sight. This results in a fairly rich taxonomy (see Figure 1.2). Some classifications can also be attributed to the radiation patterns of **AGNs** being strongly anisotropic.

In the 1960s, radio interferometers had the capability to provide positional accuracies of a few arc-seconds. This was crucial in identifying the optical component of multiple radio sources, which were found to be low redshift galaxies (e.g. [Minkowski, 1960](#)).

In 1963, the first Quasi-stellar Object (**QSO**) or quasar, **3C 273** from the Third Cambridge Catalogue of Radio Sources, was discovered by Maarten Schmidt ([Schmidt, 1963](#)), by identifying the wavelengths of the radio radiation emitted. This gave rise to the theory that these **QSOs** may be among the most distant and oldest objects ever observed. Quasars or **QSOs** are the most luminous non-transient objects in the Universe, usually outshining their host galaxy. The brightness of their cores is due to the large accumulation of material onto the **SMBH**, which causes the material to spiral around with immense amounts of energy. This energy can be released and observed as **EM** radiation.

In the 1970s, another subclass of **AGN** was discovered in massive elliptical galaxies – the BL Lac objects ([Hoffmeister, 1929](#)), coined after the prototype BL Lacertae in the Lacerta constellation. These are extremely variable ‘star-like’ objects characterized by a strong non-thermal spectrum showing very

weak or no emission lines. They form part of the blazar class (Angel and Stockman, 1980), which are a class of AGN with relativistic jets directed towards an observer. This class includes both BL Lac objects and Flat-spectrum radio quasars (FSRQ) quasars. Relativistic beaming makes blazars seem much brighter than they would be if their jets were directed away from the Earth. Blazars emit strong emission across the EM spectrum and are confirmed to be transmitters of high-energy gamma ray photons. They are highly variable AGN often undergoing rapid and dramatic fluctuations in brightness on short timescales (hours to days; Ulrich *et al.*, 1997), and have no emission lines in their spectra.

Kellermann *et al.* (1989) found that quasars fell in two categories based on arcsecond-scale observations from the Palomar Bright Quasar Survey (BQS). A majority had a radio flux density close to the optical flux density; these were called ‘radio-quiet’, while 15–20% were ‘radio-loud’ i.e., they emitted more strongly at radio wavelengths than at other wavelengths. A ‘radio-loud’ AGN is thus defined as an object with $S_{5\text{GHz}}/S_{\text{B-band}} \geq 10$, S_ν being the flux density at frequency ν (Kellermann *et al.*, 1989).

Following this definition, AGN are typically divided into the two classes of ‘radio-quiet’ and ‘radio-loud’ nuclei (Wilson and Colbert, 1995). The radio-loud AGN describes sources with a radio flux density that is an order of magnitude or greater than the flux density at optical wavelengths. Examples of ‘radio-loud’ AGN include RGs, BL Lac objects and radio-loud quasars. These AGN can have powerful jets that extend well beyond the extent of their host galaxies, stretching hundreds of kiloparsecs and even a megaparsec in length. The radio emission from AGNs is typically regarded as disorderly synchrotron radiation coming from a non-thermal distribution of relativistic electrons (e.g. Jones *et al.*, 1974). Radio-quiet AGN are simpler, in that any radio emission from the jet is typically comparable in brightness to the radio emission from star formation activity in the host galaxy.

Fanaroff and Riley (1974) were the first to classify the extended morphologies of radio-loud sources. Such early observations were relatively insensitive and thus only detected the brightest objects, which were nearly all double or triple in structure, with very few compact sources. Now in modern radio surveys, a large proportion (~90%) of sources are compact in nature (Shabala *et al.*, 2008; Sadler *et al.*, 2014; Norris *et al.*, 2021), and about half are Star forming galaxies (SFGs).

Fanaroff and Riley discovered that the total radio power and morphology of RGs are grouped into two distinct subclasses based on 57 sources from the Third Cambridge Catalogue of Radio Sources (3C)R sample (Mackay, 1971): the low-power class, Fanaroff-Riley Class I (FRI), showed extended diffuse plumes with no distinct jet termination, while the high-power class, Fanaroff-Riley Class II (FRII), displayed narrow, well-collimated jets with distinct end points called ‘hot spots’. Fanaroff and Riley specifically excluded any central source from this comparison.

There are names given to several types of RGs based on their structure in the radio wavelength:

1. Double Radio sources Associated with Galactic Nuclei (DRAGNs) were proposed independently in the 70s for the first time by (Scheuer, 1974) and (Blandford and Rees, 1974). Later in the 1980s, the

underlying physical mechanism was broadly confirmed by numerical fluid dynamics. A DRAGN is defined as a radio source that contains at least one of the following types of extended, synchrotron-emitting structures: jets, lobes, and/or hotspot complexes. To differentiate them from starburst and normal galaxies, the latter of which may contain compact sources that can also be construed as a 'hotspot', an addition to the definition is as follows: if a DRAGN is identified solely on the basis of containing hotspots, there should be no more than two. Although some DRAGNs have only one type of extended structure, the vast majority have lobes as well as hotspots or jets (or both).

DRAGNs were previously referred to as extragalactic radio sources. This term unfortunately also has another more literal meaning, namely referring to an extragalactic object discovered in a radio survey of some region of the sky. The confusion arose because almost all extragalactic sources were DRAGNs in early radio surveys. However, in modern deep radio surveys, the majority of sources are thought to be SFGs, rather than DRAGNs.

2. Bent-tail (BT) RGs lean more towards standard FRI structure than FR II, with their lobes bending in the same direction (e.g. Wing and Blanton, 2011). The bent morphology is presumed to be caused by the experience of high ram pressure. Ram pressure exerted on the lobes will distort the morphology when the ambient gas density is high and the relative velocity is large between the ambient gas and the RG. These two conditions are easily met within the Intracluster Medium (ICM), which consists of high-density regions filled with plasma of galaxy clusters.
3. Fat double or relaxed sources are galaxies that have neither jets nor hotspots but diffuse lobes. Some of these extended galaxies may be radio relics or halos with energy supplies that have been permanently or temporarily shut off. Radio relics are huge diffuse synchrotron sources powered in cluster edges by merger shocks, whereas radio halos appear projected on the center of galaxy clusters.
4. Giant Radio Galaxies (GRGs; Willis *et al.* 1974; Ishwara-Chandra and Saikia 1999; Tang *et al.* 2020) are RGs with jet lengths > 0.7 megaparsecs. This rare subclass of RGs includes the largest-scale structures known in the Universe along with cluster radio relics (Bagchi *et al.*, 2006; Rottgering *et al.*, 1997; van Weeren *et al.*, 2011). They constitute the extreme tail of the RG population. Giant Radio Galaxies (GRGs) are thought to be the endpoint of RG evolution because they have grown to such enormous sizes. They extend way beyond the confines of their host galaxy and serve as direct probes of the Intergalactic Medium (IGM).

The subclass of radio-quiet galaxies include radio-quiet quasars, Seyfert galaxies and Low Ionisation Nuclear Emission-line Regions (LINERs; Heckman, 1980). Different orientations with respect to the accretion disk and black hole give rise to the apparent differences between the types of AGN (see Figure 1.3).

This thesis focuses solely on the radio galaxy class of AGNs, which will be examined in detail in the following section.

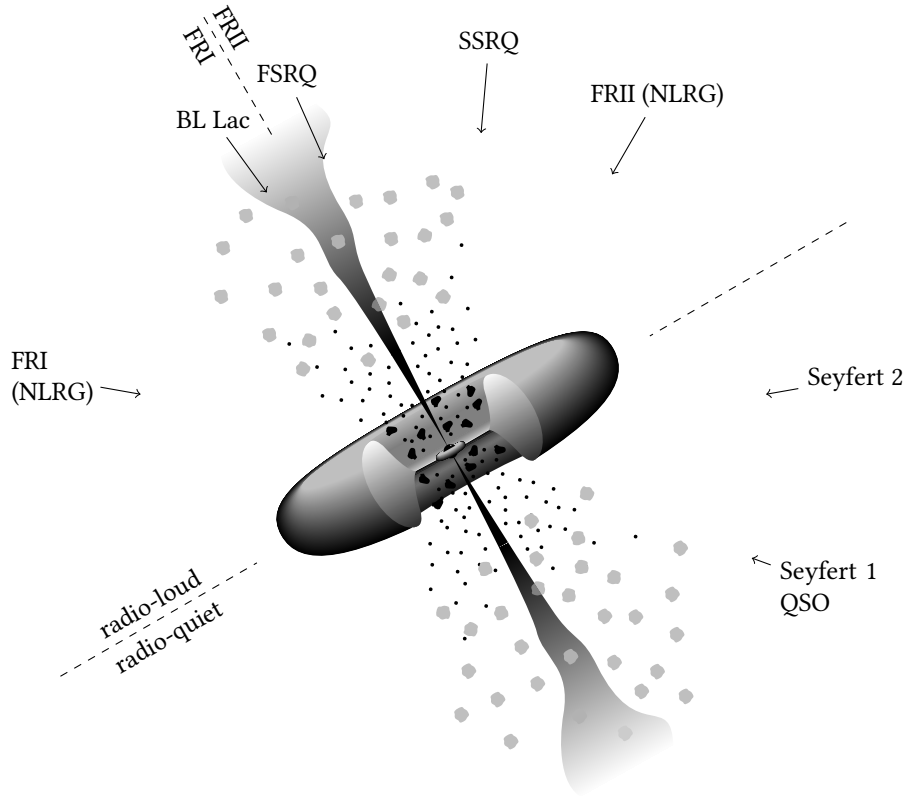


Figure 1.3: An extension of Fig. 1.1 showing the apparent differences between the different types of AGN due to having different angles with respect to the line of sight. If an observer were to look at an AGN along the edge of its accretion disk, they would see a great deal of intense radio energy – a RG. If the observer was viewing from a slight angle, they would see a stream of visible light from the superheated accretion disk – a quasar. Finally if they viewed an AGN down the jet barrel, they would see the very intense energy source of a BL Lac object. Classifications above the dotted line are for radio-loud AGN while classifications below the line are for radio-quiet AGN (Verschuur *et al.*, 1988). Credit: Urry and Padovani (1995)

1.3 Radio Galaxies

Radio Galaxies (RGs) as their name implies, strongly emit large amounts of radio emission. The radio emission is non-thermal, producing synchrotron emission due to relativistic ($E > m_e c^2$) electrons spiraling in magnetic fields, which can cover a very large range in frequency. RGs are all AGNs and should not be confused with SFGs.

RGs differ from SFGs in that the emission from SFGs is non-thermal synchrotron radio emission of relativistic electrons accelerated by shock fronts in Supernova Remnants (SNRs), which confines the radio emission to the inner few kiloparsecs of a galaxy (Condon, 1992a; Seymour *et al.*, 2008). SFGs display relatively weak radio emission, which is strongly correlated with the Far Infrared (FIR) flux

(Helou *et al.*, 1985; Yun *et al.*, 2001), and is typically detected from galaxies in the local Universe, with an average redshift $z < 0.5$.

In comparison, AGNs are strong emitters of synchrotron radio emission. The source of the emission, however, originates from the lobes and jets of relativistic electrons accelerated from the surroundings of the SMBH. The emission can be observed as a single, double, or triple component, or in some cases, as a complex structure with visible jets. Additionally, the strong radio emission can be detected up to very high redshifts.

RGs were discovered accidentally by wartime radar engineers in the 1940s (Bolton *et al.*, 1949). However, it was a decade later before they were properly studied by the then new science of radio astronomy (e.g. Jennison and Das Gupta, 1953; Baade and Minkowski, 1954); Cygnus A being the first discovered (see Fig. 1.4; Jennison and Das Gupta, 1953). Following the development of large radio interferometers in the 1970s, which allowed detailed mapping of the extended radio emitting structures, the classification of radio AGN really started. Extragalactic radio sources were found to generally have a dual structure; with lobes that radiate synchrotron emission and had the possibility of containing compact high luminosity concentrations (hot spots), which were connected by thin jets perpendicular to the accretion disk to radio sources in the center of the galaxies (e.g. Miley, 1980). Later, the term DRAGN (Double Radio source Associated with Galactic Nucleus) was coined (Leahy, 1993) for these strong radio sources of double structure. The structures extend on scales that are often greater than the host galaxies (~50 kiloparsecs to 1 megaparsec). However, not all AGNs produce large and powerful radio jets. Most AGN jets are barely resolved or unresolved, making it hard to surmise the substructure within. The jets are very well-collimated beams, with small opening angles of only a few degrees. These structures are often linear over their entire length, but can show gradual or sharp bends which change the direction yet do not disrupt the jet otherwise. The jets are powerful enough to transport material far beyond the host galaxy, sometimes several hundred thousand or million light years away, which then often turn into large extended radio lobes when they collide with the IGM and cause the material to be illuminated in the radio-continuum. An example of this is Centaurus A (see Figure 1.5; Feain *et al.*, 2011).

In stronger RGs, the jets end in a hot spot at the outer edges of the radio lobes. If the jet is a supersonic flow, the hot spot's location might potentially be where it meets the ambient medium and decelerates through a shock transition. The radio lobes will then be the reverse shocked jet material. In weaker RGs, the jets widen and brighten (either suddenly or gradually) before touching the lobes. The surface brightness of the lobes then decreases away from the galaxy, opposite to what happens in high-powered sources. If the jet is a transonic (close to speed of sound) or subsonic (less than speed of sound) flow, the broadening and brightening may be indication of deceleration and turbulence. Since the analyzed data in my thesis is primarily from the radio-continuum, RGs are of particular interest.

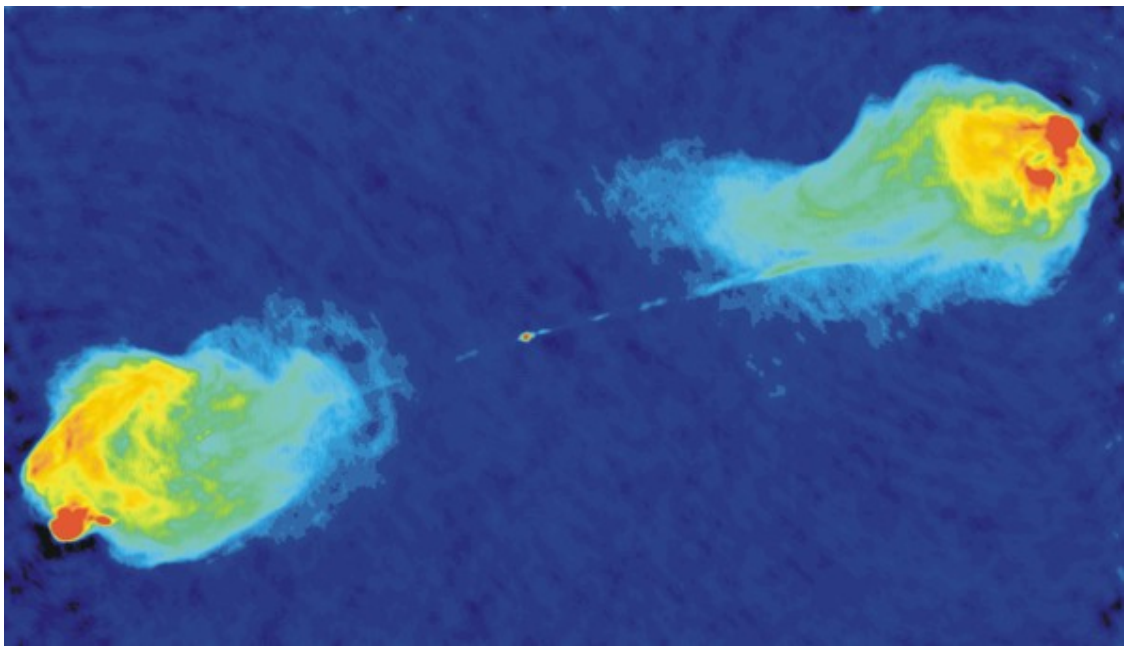


Figure 1.4: An image showing the RG Cygnus A. The galaxy consists of a double-lobed structure, with two bright lobes on either side of a compact nucleus connected by faint, narrow jets, and hot spots at the ends. The nucleus is believed to be a giant elliptical galaxy ~ 240 Mpc away. *Credit: NRAO/AUI; R. Perley, C. Carilli and J. Dreher*

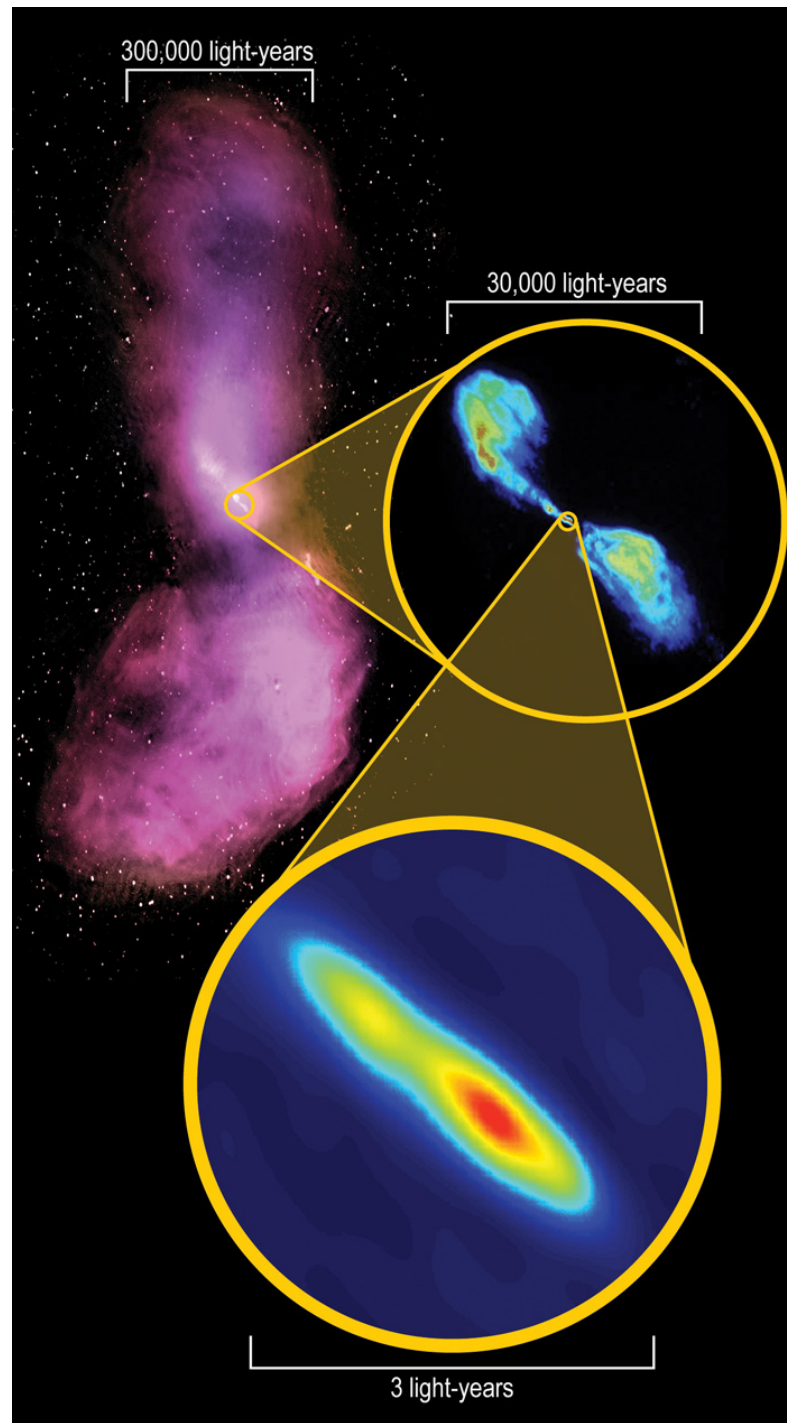


Figure 1.5: A composite image of Centaurus A, one of the largest and nearest RGs in the sky. The asymmetric jets and radio lobes can be seen in pink, extending more than 10 degrees in the sky, on either side of the central AGN. *Credit: Whole galaxy: I. Feain, T. Cornwell and R. Ekers (CSIRO/ATNF); ATCA northern middle lobe pointing courtesy R. Morganti (ASTRON); Parkes data courtesy N. Junkes (MPIfR). Inner radio lobes: NRAO / AUI / NSF. Core: S. Tingay (ICRAR) / ICRAR, CSIRO and AUT.*

1.3.1 Radio Galaxy Structures

By looking at radio morphology and spectral index, astronomers can determine whether the observed radio emission in low-redshift radio sources is dominated by AGNs or star formation. Evidence for AGN-dominated emission would be provided by the presence of a jet or jets, and double or triple-radio structures. At higher redshifts, radio and Infrared (IR) observations can be more effective at distinguishing between AGN and emission dominated by star formation (e.g. Seymour *et al.*, 2008, 2009).

To determine the physical properties of galaxies, an important step is to measure the distance of radio sources via redshifts associated with the identification of the radio emission host galaxies. The difficulty in cross-identification can be illustrated by a linear alignment of three radio sources (e.g. Norris *et al.*, 2006), which can be either:

1. a chance alignment of radio emission from three separate galaxies;
2. three radio components consisting of a single radio-loud AGN with two extended lobes; or
3. the chance alignment of a DRAGN and a compact radio source.

The Fanaroff-Riley correlation has withstood the test of time (Miley, 1980; Antonucci, 1993; Saripalli, 2012), though the transition is not as sharp at higher frequencies (Urry and Padovani, 1995). The distinction of the two types was based originally on the morphology of the large-scale radio emission. Formally, it's determined by the ratio of the distance between the regions of maximum radio emission on opposite ends of the nucleus to the total extent of the source: FRI sources tended to be brightest towards the centre (known as edge-darkened), while FRII sources were brightest at the edges (known as edge-brightened) as shown in Figure 1.6.

The distinction between FRIs and FRIIs is not limited to just morphology. A distinct sharp divide in luminosity at $\sim 10^{25} \text{ W Hz}^{-1}$ at 1.4 GHz was also observed between the two classes, although this dividing luminosity was later found to depend on optical brightness by Ledlow and Owen (1996), with FRIs at lower luminosity than FRIIs.

Much debate still remains about the relationship between jet morphology and accretion mode (e.g. Hardcastle *et al.*, 2007a, 2009; Best and Heckman, 2012; Gendre *et al.*, 2013; Mingo *et al.*, 2014; Ineson *et al.*, 2015; Tadhunter, 2016; Hardcastle, 2018a). With more detailed radio observations, it is revealed that the morphology reflects the radio source's mode of energy transport. The two FR radio structures are thought to result from the different environmental interactions that low and high power jets have (Scheuer, 1974; Bicknell, 1986). FRIIs appear to be capable of efficiently transporting energy via high power jets to the ends of the lobes, whereas FRI jets are inefficient and low power, radiating a large amount of energy away as they travel. It can be assumed that the FRI/FRII dichotomy is dependent on the environment of the host galaxy, as the transition between FRI and FRII occurs in more massive galaxies at higher luminosities. Since it is known that FRI jets decelerate in the regions of strongest radio

emission, the FRI/FRII transition then reflects whether a jet or beam of particles can propagate through the host galaxy without being delayed by interaction with the IGM.

However, the fundamental question of whether the two source types were the same intrinsically or different remains unanswered: could FRIs and FRIIs be the result of very different central engines and host galaxies, or the result of different environmental interactions? At high redshifts and at radio wavelengths, they stand out due to their high luminosities. This means they can shed light into the early Universe, specifically the environments of highest density and probing the evolution of the most massive galaxies (McCarthy, 1993; Miley and De Breuck, 2008). The discovery of a hybrid morphology in some RGs by Gopal-Krishna and Wiita (2000), where one lobe showed FRI edge-brightened structure and the another was edge-darkened FRII, bolstered the theory that the environment surrounding jets was ultimately responsible for large scale structure development.

There were also earlier claims that this structural difference came about due to the interaction of jet power and the environmental density of the host galaxy. Jets of equal power in a rich environment will disrupt (and thus become FRI) more effectively than compared to a poor environment (Bicknell, 1995; Kaiser and Best, 2007). The discovery that the FR luminosity break is dependent on the optical magnitude of the host galaxy (Ledlow and Owen, 1996) would lend credence to this explanation. FRIs were observed to have higher radio luminosities in more luminous host galaxies, where the Interstellar Medium (ISM) is assumed to be of higher density. Such a result, however, was founded on samples that were highly flux-limited, with different environments and redshift distributions for the two FR types. Because of the serious selection effects, it is debatable whether this relationship applies across the entire RG population (Best, 2009; Lin *et al.*, 2010; Wing and Blanton, 2011; Singal and Rajpurohit, 2014; Capetti *et al.*, 2017b; Shabala, 2018).

The weak correlation between radio luminosity and jet power complicates testing physical models with radio observational data for jet dynamics and the FR break. Specifically, a difference is assumed to exist in the efficiency of emitting radio luminosity for a given jet power between the two FRI types (Croston *et al.*, 2018). This difference could be explained by the correlation of FRIs and FRIIs with lobe particle content. Croston *et al.* (2018) have suggested that the jets of FRII RGs consist mainly of an electron-positron plasma, while FRI RGs are loaded by significant amounts of baryonic material. The impact of entrainment of the surrounding material in disrupting FRI jets as they decelerate may best explain this situation, while undisrupted FRII jets remain unaffected. There are some significant caveats to using radio luminosity as a proxy for jet power. These include a combination of effects from environment, radiative losses, and differences in particle content (e.g. Croston *et al.*, 2018; Hardcastle, 2018b). This makes estimating the energy output of radio sources and feedback processes challenging (e.g. Sabater *et al.*, 2019; Hardcastle *et al.*, 2019). Therefore, the relevance of morphology to the conjecture of environmental impact from discovered AGN jets in radio surveys is strong impetus to gain a deeper physical

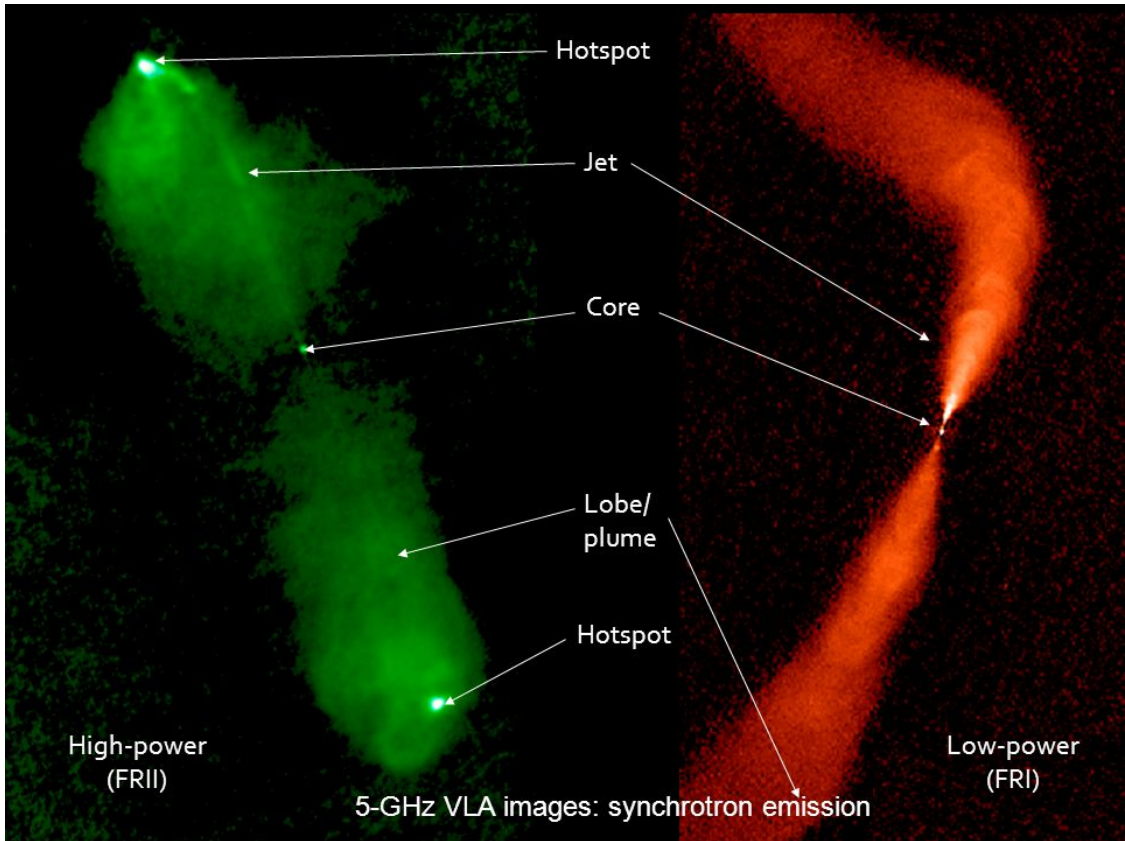


Figure 1.6: A pseudo-colour image showing the large-scale radio structure of two RGs in the 3C sample; FRII 3C98 (left) and FRI 3C31. Lobes, jets, plumes and hotspots are clearly labelled. *Credit: VLA; Daniel Evans (Harvard), Julia Lee (Harvard), Martin Hardcastle (U. Herts), Ralph Kraft (SAO), Jane Turner (UM-BC/GSFC)*

understanding of the canonical FRI/FRII break, as well as of the full diversity of the morphology of the DRAGN population.

The brighter FRIIs are commonly the focus of studies of jet evolution and interaction with the environment of the host galaxy (e.g. Kaiser and Alexander, 1997; Kaiser and Cotter, 2002; Kaiser and Best, 2007; An and Baan, 2012). However, by modelling the more morphologically complex FRIs, the physical properties of the jet (e.g., thermodynamics, kinematics, and radiation) surrounding the ISM and the process of accretion have been investigated.

In 1994, Laing *et al.* (1994) defined Low Excitation Radio Galaxies (LERGs) and High Excitation Radio Galaxies (HERGs) based on the optical emission line ratios. The method was similar to that used to differentiate Seyferts and LINERs in radio quiet AGN (Kewley *et al.*, 2006). All FRIs with a reliable classification are LERGs, but FRIIs can contain both LERGs and HERGs (e.g. Buttiglione *et al.*, 2010).

The SMBHs that drive powerful jets are associated with giant elliptical galaxies at low redshifts (Matthews *et al.*, 1964), with only a few found in spiral galaxies (Hota *et al.*, 2011; Bagchi *et al.*, 2014). There are several possible explanations for this preference towards elliptical galaxies. One possible reason is that elliptical galaxies are theorized to generally contain SMBHs (Begelman *et al.*, 1984), which

means they are capable of powering AGN. Another possible explanation is that elliptical galaxies are claimed to reside in richer environments (Einasto *et al.*, 2008) which would provide a large-scale IGM to restrict the source. The preference towards elliptical galaxies could also be due to the fact that greater pockets of cold gas in spiral galaxies disrupt or suppresses a forming jet. One more possibility is that radio-loud AGNs are only found to be associated with the most massive SMBHs, which are associated with the most massive halos. Massive halos are primarily associated with elliptical galaxies at low redshift (e.g. Rees *et al.*, 2016).

A variety of other properties, both on large and small scale, also play a role in the divide of the two radio morphologies. This indicates that there are deeper underlying fundamental processes that have a significant impact on the type of structures formed. Following this classification scheme, many studies to comprehend how these two basic DRAGN morphologies came about have been made. Expanding on the basic models of Blandford and Rees (1974); Scheuer (1974); Falle (1991), newer models have been constructed that are capable of reproducing the data collected on FRI/FRII populations with fair consistency (e.g. Kaiser *et al.*, 1997; Blundell *et al.*, 1999). To explain these morphological differences, two types of models have been proposed in the literature. Extrinsic models were based solely on the jet interaction with the environment. These models focused on the environmental differences found between FRIs and FRIIs (e.g. Prestage and Peacock, 1988), and on their apparently distinct host galaxies (Owen and Ledlow, 1994). The differentiating factor is postulated to be the IGM density, where jets of sources experience differing degrees of resistance depending on the density of their surrounding mediums. This in turn yields sources with either FRI or FRII structures. Intrinsic models were postulated based on fundamental differences observed between FRIs and FRIIs, such as the properties of their emission lines (Zirbel and Baum, 1995). These models proposed that the dichotomy was caused by differences in the properties of the central SMBH (e.g. Baum *et al.*, 1995; Ghisellini and Celotti, 2001). The main underlying theme of any model aiming to simulate the large-scale radio structures is the interplay between the jet and the ambient medium through which it propagates. Weak jets produced by low accretion flow rates primarily exhibit FRI structure, whereas the stronger FRIIs are produced by higher accretion flow rates. In 2015, a new class of compact RGs with sizes <5 kiloparsecs was observed by Baldi *et al.* (2015), and referred to as Fanaroff-Riley Class 0's (FR0s). Although additional morphological types have been discovered, they have typically been understood within the context of the two main FR types.

FRIs and FRIIs also compare interestingly in terms of their environments. While FRIs are often found at nearby redshifts ($z < 0.5$) in dense galaxy clusters (Saripalli, 2012), FRIIs are usually observed to be hosted by field galaxies. However, at higher redshifts, both FRIs and FRIIs can be found in rich environments (Prestage and Peacock, 1988; Hill and Lilly, 1991). The host elliptical galaxies of FRI and FRII structures were also found in literature to exhibit differences. Broad band imaging of the host galaxies of the latter were found to be bluer than the former and frequently gave indication of merger

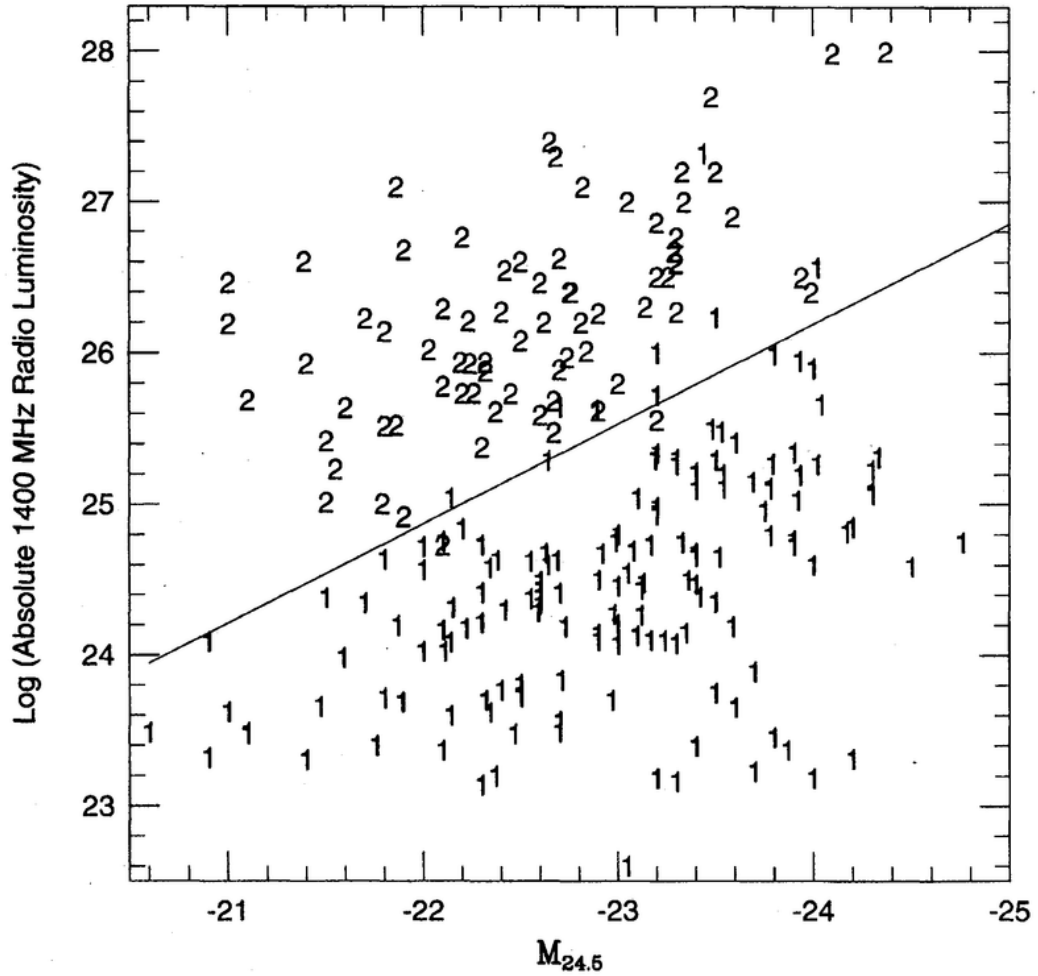


Figure 1.7: FRI and FRII radio galaxies delineated by sharp division in optical/radio luminosity plane. Credit: (Ledlow and Owen, 1996)

activity (Heckman *et al.*, 1986; Smith and Heckman, 1989; Baldi and Capetti, 2008; Ramos Almeida *et al.*, 2012). On the other hand, the host galaxies of FRIs were discovered to be more massive than those of the FRIIs (Owen and Laing, 1989; Govoni *et al.*, 2000). The FRII sample studied by Capetti *et al.* (2017b) revealed a low-radio powered population at least two orders of magnitude lower than those obtained at high radio flux thresholds. This conclusion correlates with previous results by Best (2009); Wing and Blanton (2011); Lin *et al.* (2010) that a radio source formed by a weak jet can be either edge-darkened or edge-brightened, and the outcome is independent of the optical properties of the host galaxy. The same team conducted a similar study with FRIs (Capetti *et al.*, 2017a) and discovered that the link between host galaxy properties and radio morphology is still conserved. The defined threshold above which edge-darkened structures do not form has a strong positive dependence on the host galaxy luminosity.

The Owen-Ledlow diagram (see Figure 1.7), which shows the relation between total radio power and absolute optical magnitude (Owen, 1993; Owen and Ledlow, 1994; Ledlow and Owen, 1996), has contributed to a major development in this field. The diagram shows a clear divide between the two

FR types about a line with slope of ~ 1.8 . The dividing power was thought to be fixed by Fanaroff and Riley, but it was found to be increasing with the host galaxy's luminosity instead. If the effect of jets by entrainment, instabilities and turbulence gave rise to FRI structures, then this increase could be explained as jets having difficulty remaining collimated and supersonic due to an increasingly denser medium (Bicknell, 1995). This FR dividing power dependence on the absolute isophotal magnitude of the host galaxy put the focus on the role of environment in producing the two distinct radio morphologies.

Recently, Mingo *et al.* (2019) carried out a morphological investigation of radio-loud AGN using the Low-Frequency Array (LOFAR; van Haarlem *et al.*, 2013) LOFAR Two-Metre Sky Survey (LoTSS; Shimwell *et al.*, 2017) Data Release 1 (DR1; Shimwell *et al.* 2019) catalogue (Williams *et al.*, 2019). They found 1256 FRI and 423 FRIIs spanning the redshift range $z \sim 0.8$. Contrary to the clear luminosity break in Fanaroff and Riley (1974) and Owen (1993); Owen and Ledlow (1994), Mingo *et al.* (2019) found that sources of FRI and FRII morphologies in LoTSS could be found over a wide range of radio luminosities. A subset of their FRIIs showed luminosities three orders of magnitude lower than the recognized FR break. These sources are most likely comprised of older FRIIs that are decreasing in luminosity, as well as being hosted by low-mass galaxies allowing their jets to stay unperturbed. As for why these low luminosity FRIIs were not detected in previous flux-limited studies like the 3CRR (Laing *et al.*, 1983), it is most likely due to them being a heterogeneous population in the nearby Universe, and these earlier surveys having higher flux limits. To date, Mingo *et al.* (2019)'s study is the largest and most comprehensive dataset of RG morphological information available.

1.3.2 Hybrid morphology

The existence of HYbrid MORphology Radio Sources (HyMoRS) was first pointed out by Gopal-Krishna and Wiita (2000), and they have since been invoked in the debate over the origins of morphological distinctions in RGs. The claim of the study was that HyMoRS make up a different class of AGN along with the large-scale RGs of FRI and FRII types. These HyMoRS have varying FR morphologies on either side of the nucleus (see Figure 1.8). However, it is most likely that they are FRII sources with bent morphology viewed at a specific orientation, with lobes that appear to differ due to the observer's line of sight (Smith and Donohoe, 2019; Harwood *et al.*, 2020).

The mixed FR morphology of HyMoRS suggests that probably these are the missing link between FRI and FRII RGs. FRI and FRII were originally defined by the R_{FR} ratio of the distance between the peaks of brightest emission on either side of the nucleus to the overall extent of the source. If $R_{FR} < 0.5$, the radio source would be classed as an FRI, otherwise it was classified as an FRII. The understanding of RGs has evolved since the establishment of the FR classification, both observationally and theoretically. It is now known that FRIIs display strongly collimated and highly stable, primarily one-sided jets that terminate and form the distinguished features of hotspots. Strong shocks at these end points re-accelerate

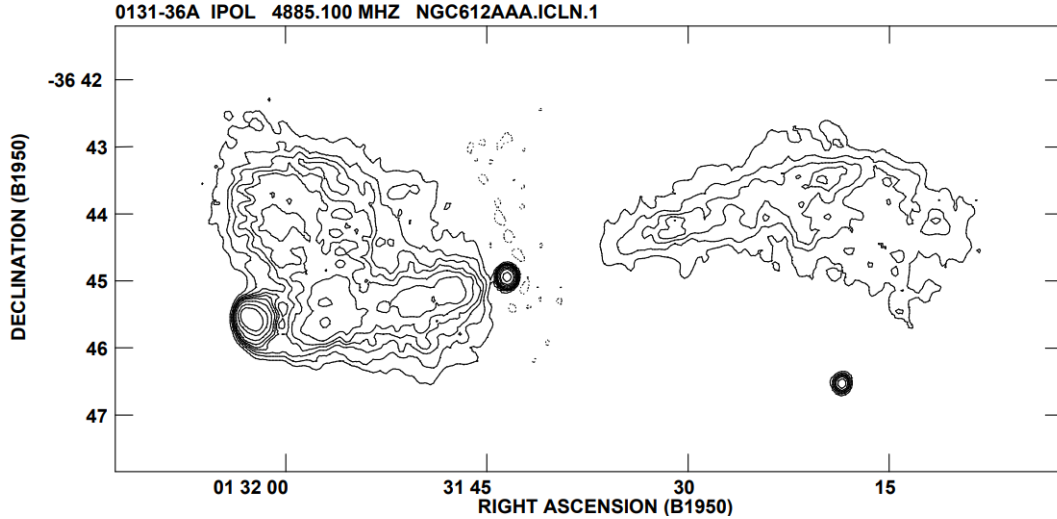


Figure 1.8: An example of hybrid radio morphology, with the left side displaying FRII structure while the right side shows FRI structure. *Credit: Gopal-Krishna and Wiita (2000)*

relativistic particles, which are then carried away via the backflow of material to form a cocoon encompassing the radio source (Blandford and Rees, 1974; Scheuer, 1974). In comparison, FRIs appear to have heavily turbulent, not well collimated jets. After interacting strongly with the external medium shortly after ejection, these jets decelerate (Komissarov, 1988; Laing and Bridle, 2014).

For more than twenty years, scientists have debated the physical origin of the FR dichotomy in RG populations (e.g. Baum *et al.*, 1992, 1995; De Young, 1993; Reynolds *et al.*, 1996a; Meier *et al.*, 1997; Rawlings, 2002; Kaiser and Best, 2007; Kawakatu *et al.*, 2009; Saripalli, 2012; Gendre *et al.*, 2013, to name a few). Theoretical works (e.g. Bicknell, 1994, 1995; Kaiser and Best, 2007; Kawakatu *et al.*, 2009) describe the FR dichotomy in terms of the power of the relativistic outflows, as well as jet deceleration and interaction with their environment. A plethora of observational studies back up this interpretation (e.g. Hill and Lilly, 1991; Zirbel, 1997; Laing *et al.*, 2011; Gendre *et al.*, 2013; Thorat *et al.*, 2013; Laing and Bridle, 2014). Analytical solutions for the transition of FRIIs into FRIs have also been devised (Wang *et al.*, 2011; Turner and Shabala, 2015). Some authors, however, prefer to interpret the FR dichotomy as the product of fundamental differences in their central engines (e.g. Meier *et al.*, 1997; Rawlings, 2002). For example, spectroscopic analysis of emission nebulae associated with RGs revealed that the accretion disk's angular momentum could play a role in the formation of extragalactic radio source morphologies (Baum *et al.*, 1992, 1995). Furthermore, it has been proposed that the AGN in FRI RGs are fed at low accretion rates and may have low black hole spins, whereas those in FRII RGs are likely to have higher rates of accretion and possibly higher black hole spins. The variations in jet particle composition have also been taken into account (e.g. Celotti and Fabian, 1993; Reynolds *et al.*, 1996a; Laing and Bridle, 2002).

The prevailing view is that the FR radio source morphology is most probably the result of a combination of the environment and jet power (e.g. Best, 2009; Saripalli, 2012). Simply put, HyMoRSs display FRI

morphology on one side of the core and FRII morphology on the other, and appear to be a class of object that could aid in disentangling the two effects. HyMoRSs, however, are a rare type of RG, occurring possibly as low as an estimated $< 1\%$ of all extended RGs (Gawroński *et al.*, 2006). They offer the chance to investigate two distinct morphologies yielded by a single central engine, providing a potential unique insight into the origins of the FR dichotomy.

Despite the potential wealth of data of HyMoRS, survey searches (e.g. Banfield *et al.*, 2015; Kapińska *et al.*, 2017) and milliarcsecond-scale investigations using VLBI (VLBI; Cegłowski *et al.*, 2013) have been the only methods used until recently. The studies that used arcsecond resolution data (e.g. Gawroński *et al.*, 2006) were archival, narrowband observations in a single array configuration. This means that due to the absence of uv-coverage on short spacings, the diffuse lobes are resolved out. The morphology and mechanisms that gave rise to the formation of HyMoRS thus remain largely unexplored, and the role of non-intrinsic effects such as orientation, cannot be excluded (Harwood *et al.*, 2020; Kumari and Pal, 2021)

1.3.3 Isotropy in Radio Galaxy Structures

Several studies have been conducted to look for evidence of non-uniformity in the orientation of galaxies following Hawley and Peebles (1975). If such an observation is found, the presence of any alignment and specific preferential orientations can provide insight on the origin and evolution of galaxies, the formations of SMBHs and the link to large-scale cosmic structure. The alignment could have been caused by large-scale environmental influences during the formation or evolution of galaxies. Hutsemekers (1998); Hutsemekers and Lamy (2001); Hutsemekers *et al.* (2005, 2011) provided evidence that quasar polarisation vectors have very large-scale orientations. The study looked at galaxies around the North and South galactic poles and observed large-scale coherence in the polarisation Position Angles (PAs) of the galaxies. There was a preference for the axes of double-lobed radio quasars to be aligned with the vectors of optical polarisation in AGN and this was observed by Stockman *et al.* (1979). In 1990, a study by Rusk (1990) showed a relation between the optical polarisation and the structural axis of a galaxy. It has also been noted that FRIs often have their radio jets aligned with the optical minor axes of their host galaxies (Andernach, 1995; Battye and Browne, 2009; Saripalli, 2012; Kaviraj *et al.*, 2015). This suggests that the jets have been left relatively undisturbed for a prolonged period of time to have their black holes realign with the minor axes. The PAs of AGN jets can thus be used as a measure for the orientation of the host galaxy's major axis. In addition, Taylor and Jagannathan (2016); Contigiani *et al.* (2017); Panwar *et al.* (2020) have claimed that FRIs seemed to be aligned over cosmic distances.

The Universe has a structure, composed of galaxies and gas – the cosmic web. The cosmic web is stretched out across the Universe, composed of clustered galaxies and gas within interconnecting filaments, separated by giant voids. A few studies (e.g. Taylor and Jagannathan, 2016; Contigiani *et al.*,

2017; Osinga *et al.*, 2020) have found a small but significant deviation from isotropy of a sample of radio galaxies, showing that radio galaxies tend to have their radio jet directions aligned with those of nearby neighbours.

Taylor and Jagannathan (2016) found that FRIs were observed to be aligned with those of other radio galaxies up to a separation of one degree along a filament of the cosmic web. The direction of RG jets is determined by the angular momentum axis of the host galaxy's SMBH that drives the AGN activity. Thus, the jet alignment that Taylor and Jagannathan (2016) observed implies an alignment of the angular momentum axes of SMBHs on scales of several tens of megaparsecs or greater. An alignment like this could only have occurred at the time of formation. If the spin of the SMBH or orientation of the accretion disk emitting the jets is really related to mergers, a preferred direction of the merging along the large-scale structure filaments could result in jet alignment. This would perhaps be able to provide some insight into the formation of SMBHs. However, FRIIs may not have the same conditions, preventing the SMBH from realigning with the minor axis. Contigiani *et al.* (2017) conducted a study using two surveys, Faint Images of the Radio Sky at Twenty-centimeters (FIRST) and TIFR GMRT Sky Survey (TGSS). The radio sources in their samples were identified via the Radio Galaxy Zoo (RGZ) project and found a local alignment of galaxies separated by up to 2.5 degrees for FIRST and 1.5 degrees for TGSS. Panwar *et al.* (2020) also conducted a similar study using FIRST data. They found a strong significant effect for angular distances less than 1 degree. Using LOFAR data, Osinga *et al.* (2020) tested the claim that the PAs of RGs are oriented randomly in the sky. They found a significant deviation from uniformity of about four degrees at angular scales.

1.4 Research Aims and Significance

The major science goals for this project are as follows:

- To survey and catalogue all FRI and FRII galaxies in the GAMA-23 and EMU Pilot Survey ASKAP observations,
- To conduct a study of DRAGNs, focusing primarily on FRIs and FRIIs using this catalog, and
- To study the alignment of radio sources using this catalog.

There is still much to be investigated about the physics, characteristics, and evolution of RGs, specifically the FR classes I and II. Some key questions in the field include:

1. How does the evolution of the host galaxy play a role in determining the number of FRI and FRII RGs?
2. Recent studies have shown a large overlap in terms of luminosities between the two classes. What does this mean and why does this happen?

3. It has been observed that neighbouring FRIs have been seen in literature to be aligned with each other perhaps due to the underlying structure of the cosmic web whereas FRIIs do not exhibit such behavior. This project aims to test if the effect is real with the selected dataset. If they do align, what does this mean? If they don't, what have I done differently to previous studies to warrant a different result? Is it because of the different observation fields?

For the purpose of this project, I will focus on a comparison of the properties of FRIs and FRIIs, and on the claim that the jets of nearby radio sources tend to be aligned with each other. I will produce a comparable dataset to the one done by Mingo *et al.* (2019) but obtained at a higher frequency and sensitivity, which will enable a comprehensive assessment of the models proposed.

1.5 Thesis Outline

In this thesis, I study the alignment and classification of DRAGNs, focusing on the FR classes. I chose to study DRAGNs after finding extended radio sources and wanting to learn more about them. This thesis is organised into the following chapters and sections.

In Chapter 2, I present a summary of the general analysis techniques and multi-wavelength observations used throughout this work. For Chapter 3, I present original work that will be submitted to the peer reviewed journal Monthly Notices of the Royal Astronomical Society (MNRAS). The work will make use of ASKAP early science data on the GAMA-23 field, to study the FR types of radio sources, and compare with other studies. The G23 field was chosen to test and prepare for the EMU Pilot Survey. I have reformatted the chapter for consistency with the rest of the thesis. In Chapter 4, I apply the techniques used for the G23 on the EMU pilot survey. I give a comprehensive analysis of these results and discuss their implications. In Chapter 5, I study the alignment of the radio sources presented in the thesis. I also compare my results to previous studies. Finally, in Chapter 6 I conclude with a brief summary of the results from the work I present in this thesis and discuss future work, describing how this study can be carried forward.

Additionally, I present other work that has been published and done over the course of my candidature in the Appendix. These include an X-ray follow-up study to the work from my masters project, Yew *et al.* (2018, Appendix A) and a study of SNRs in the Large Magellanic Cloud (LMC) (Yew *et al.*, 2021, Appendix B). I have also contributed to observations and writing for Alsaberi *et al.* (2019, Appendix C) and Joseph *et al.* (2019, Appendix D).

Chapter 2

Methodology and Data Sources

Context

In this chapter, I give a general overview of the analysis techniques applied to G23 and EMU-PS products that helped in building the catalog, as well as describe the multi-wavelength datasets used. In Sections 2.2.1 and 2.2.2, I briefly describe the general radio and infrared observations used. Section 2.6 describes the source finding process to classify Double Radio sources Associated with Galactic Nuclei (DRAGNs), in particular Fanaroff-Riley (FR) types of sources from the associated data products. I describe the algorithm used to calculate the ratio that determines an Fanaroff-Riley Class I (FRI) and Fanaroff-Riley Class II (FRII) in 2.7. Finally in Section 2.9, I discuss statistics for data measured on a circle, which is relevant for looking at alignment of sources.

2.1 Units and Terminology

Consistent with the recommendations of Norris *et al.* (2021) for Evolutionary Map of the Universe (EMU) publications, I adopt a flat Λ CDM model, with parameter values taken from the mean posterior of the Planck 2018 cosmology, as described in Paper VI (Planck Collaboration IV, 2020), these are shown in Table 2.1.

For numerical results, I use the International System of Units (SI) unless stated otherwise.

For spectral indices, I adopt the power law convention that:

$$S_\nu \propto \nu^{+\alpha} \tag{2.1}$$

where S_ν is flux density, ν is frequency, and α is the spectral index.

Table 2.1: Cosmological parameters used throughout this work, taken from Table 2 in Norris *et al.* (2021).

Description	Parameter	Value
Hubble Constant	H_0	67.36
Matter density	Ω_m	0.3153
Cosmological constant density	Ω_Λ	0.6847
Optical depth to reionization	τ	0.0544
Physical baryon density	$\Omega_b h^2$	0.02237
Physical Cold Dark Matter density	$\Omega_{\text{CDM}} h^2$	0.1200
Physical Neutrino density	$\Omega_\nu h^2$	0.000694
Neutrino hierarchy	1 massive, two massless	
Primordial spectral index of scalar fluctuations	n_s	0.9649
Amplitude of scalar fluctuations	A_s	2.055×10^{-9}

2.1.1 FR definition

Throughout this work, I adopt the traditional definition given by Fanaroff and Riley (1974). Given a two component radio source and ignoring any central source, if the ratio $R_{FR} = a/b$ of the separation between the points of peak intensity on opposite sides of the core (host galaxy, labelled a in Figure 2.1) is lower than 0.5 (i.e. $R_{FR} = a/b < 0.5$) relative to the total extent of the source (labelled b in Figure 2.1), then it is classed as an **FRI**; if $R_{FR} = a/b > 0.5$, it is an **FRII**. For sources that are on the ratio's borderline, I refer to them as FRx.

2.2 Data

2.2.1 ASKAP Radio Data

The project will focus primarily on the **FR** classes I and II using data obtained by the Australian Square Kilometre Array Pathfinder (**ASKAP**; Hotan *et al.*, 2021).

In the centimetre wavelength regime, the primary components that a sensitive radio telescope require are: wide bandwidth, a large collecting area, low receiver noise, good polarisation characteristics, and immunity to Radio-frequency interference (**RFI**). Additionally, a wide Field of View (**FoV**) is required to quickly survey large portions of sky, and a large diameter, or long baselines are required for the ability to resolve fine details. With the recent advances in Phased Array Feed (**PAF**) technology, the traditional horn-like radio telescope feed is no longer the sole receptor of choice.

The **ASKAP** is an interferometric array of 36 dish antennas, each 12-m in diameter. It's designed for all-sky surveys and is equipped with Chequerboard Phased-Array Feeds (**PAFs**; Hay and O'Sullivan, 2008) consisting of a 6×6 array of beams (up to a maximum of 72 beams), which produces an instantaneous 30 deg^2 **FoV** as seen in Figure 2.2 to a Root Mean Square (**RMS**) noise of $\sim 10 \mu\text{Jy}/\text{beam}$. Using the **PAF** receivers, **ASKAP** is able to survey the sky significantly faster than previous telescopes. Generally, the raw data collected with a radio telescope is processed by individual observers after data collection, how-

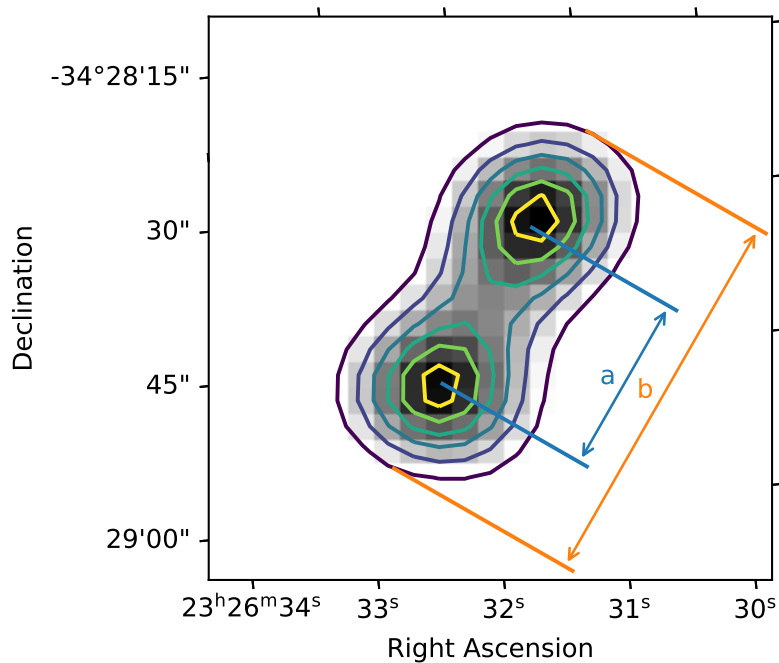


Figure 2.1: Measurements to determine the FR ratio, where a is the separation between the points of peak intensity on opposite sides of the core and b is the total extent of the source.

ever, this is not feasible for *ASKAP* due to the large data volumes¹ e.g. $\sim 2.5\text{GBs}^{-1}/\sim 75\text{PByr}^{-1}$. Instead, *ASKAP* data is processed by the telescope operations team using an automated custom-built processing pipeline, *ASKAPsoft* (Guzman *et al.*, 2019)². In the first five years of operation, 75% of time on *ASKAP* will be dedicated to large survey projects³ which includes: the Evolutionary Map of the Universe (EMU, a radio continuum survey), the Widefield *ASKAP* L-Band Legacy All-Sky Blind Survey (WALLABY, a shallow all-sky Atomic Hydrogen (*H I*) spectral line survey), the First Large Absorption Survey in *H I* (FLASH, a blind *H I* absorption survey), an *ASKAP* survey for Variables and Slow Transients (VAST), the Galactic *ASKAP* Spectral Line Survey (GASKAP, a *H I* and OH spectral line survey of the Milky Way and Large/Small Magellanic Clouds), a Polarisation Sky Survey of the Universe’s Magnetism (POSSUM, a widefield survey of magnetic fields), the Commensal Real-time *ASKAP* Fast Transients survey (*CRAFT*), and Deep Investigations of Neutral Gas Origins (DINGO, a deep *H I* spectral line survey of smaller areas on the sky). A full description of *ASKAP* may be found in Hotan *et al.* (2021).

2.2.1.1 G-23 Radio Data

The first dataset I make use of in this project are the observations of the 23 hr field of the Galaxy And Mass Assembly (*GAMA*; Liske *et al.*, 2015)⁴, a 50 deg^2 area of the southern sky, centred at the right

¹<https://www.atnf.csiro.au/projects/askap/computing.html>

²<https://researchdata.edu.au/askap-science-data-version-0233/1377805>

³The full list and further details can be found at <https://www.atnf.csiro.au/projects/askap/science.html>

⁴<http://www.gama-survey.org/>

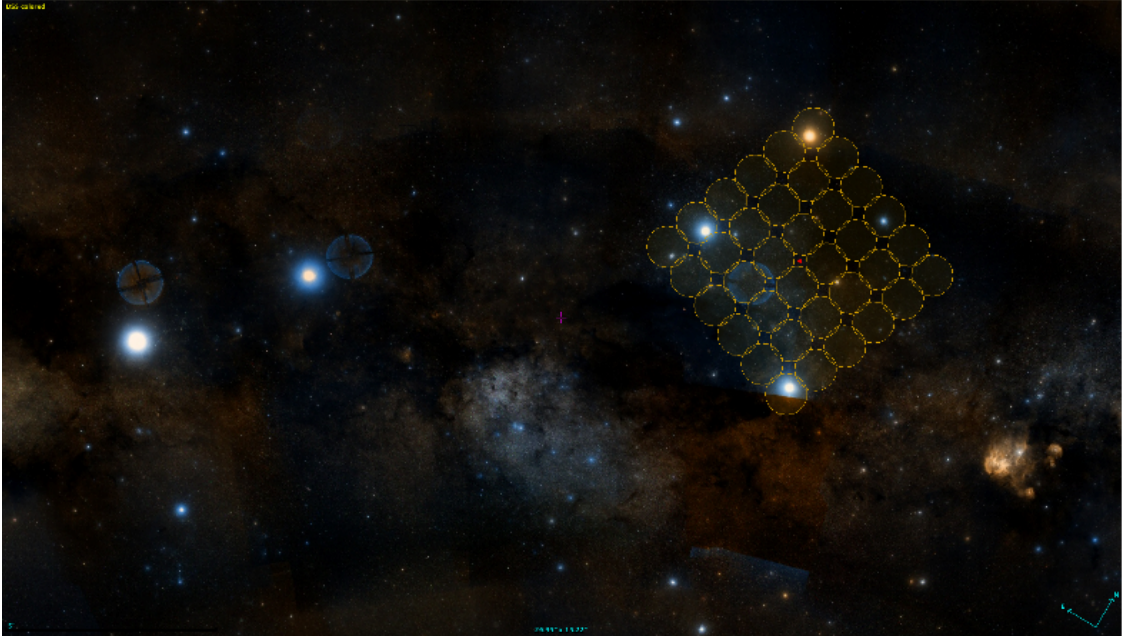


Figure 2.2: ASKAP’s FoV is depicted on a DSS2 image showing the 36 beams as individual circles. In comparison, the FoV of a traditional telescope would be a single slightly smaller circle. The diameter of the moon is half that of one of these circles. *Credit: Australia Telescope National Facility, <https://www.atnf.csiro.au/projects/askap/index.html>*

ascension $\alpha_{J2000}=23^h$ and the declination $\delta_{J2000}=-32^\circ$. *GAMA* contains spectroscopic information for galaxies at low to moderate redshift ($z \lesssim 1$) complete down to 19.8 mag in the r band and 19.2 mag in the i-band, covering a total area of $\sim 286 \text{ deg}^2$. Its multi-wavelength coverage spans the optical (VST KiDS; Kilo-Degree Survey), Near Infrared (NIR) (VIKING; VISTA Kilo-degree Infrared Galaxy Survey) and Far Infrared (FIR) (Herschel). Because EMU has access to the *GAMA* regions of the sky, this makes *GAMA* ideal for providing optical data on the galaxies observed by EMU.

The *GAMA* 23^h field or G23 (Leahy *et al.*, 2019) was originally observed at 888 MHz with ASKAP as part of the EMU Early Science Program and the Deep Investigation of Neutral Gas Origins survey (DINGO). These early observations used ASKAP-12, a sub-array of ASKAP that had between 12 and 16 operational antennas and a bandwidth between 192 and 240 MHz. Here, I use more recent observations after ASKAP reached its full complement of 36 antennas. For multi-wavelength cross-matching, I make use of the optical wide-field imaging survey photometry from Kilo-Degree Survey (KiDS; de Jong *et al.*, 2013)⁵, and the CATWISE2020 catalogue (Marocco *et al.*, 2020) for Infrared (IR).

For these observations the beam footprint square 6×6 with a pitch of 0.9° was used with ASKAP, with no interleaving. An array of 35 antennas were used, with antenna 11 being offline. The G23 region was covered by two overlapping tiles (with a separation of 0.9°), and their corresponding bandpass observations are detailed in Table 2.2. The survey was carried out at 887.5 MHz.

The data was processed with the ASKAPsoft pipeline (Whiting *et al.*, 2017; Whiting, 2020) version

⁵<https://kids.strw.leidenuniv.nl/>

Table 2.2: Observation details for the ASKAP G23 data. All dates and times are in Australian Eastern Standard Time (AEST; UTC+10).

SBID	Start Date	Start Time	Duration	Purpose
8131	7 Mar 2019	22:16:11	2:12:28	Bandpass
8132	8 Mar 2019	00:28:40	9:01:16	Science
8136	8 Mar 2019	21:31:41	2:12:55	Bandpass
8137	8 Mar 2019	23:44:37	10:01:08	Science

0.24.0. First a bandpass was derived from observations of the primary flux calibrator (PKS1934–683), setting the flux scale to that of Reynolds (1994). This bandpass was then applied to the science observations, and two rounds of phase self-calibration were performed. The final image was formed with a multi-scale clean algorithm with scales of 0 (corresponding to a point source), $37''.5$ and $75''$, and a Briggs (1995) robustness of -0.5 . Each beam within the observation was processed separately, and the resulting images were mosaicked together (via `linmos`) while weighting the images for the primary beam shape. The final image has a pixel size of $2''.5$ and a restoring beam of $10''.0 \times 8''.5$ and Position Angle (PA) 83.7° . The surface brightness sensitivity is similar to that of the EMU Pilot Survey (see Figure 2.3).

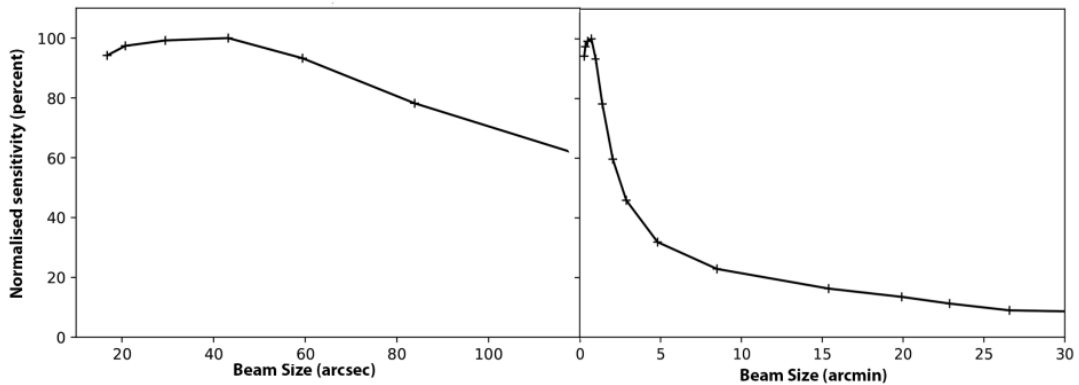


Figure 2.3: Two plots showing the sensitivity of EMU-PS as a function of spatial scale. The plots show the same result, just over different spatial scale range. Credit: (Norris et al., 2021)

Since source extractors such as *Selavy* and *pybdsf* are relatively insensitive to extended structures, no automated source extraction was performed. Instead, the sources were identified by visual inspection, as described in Section 2.3.

2.2.1.2 EMU Pilot Survey

The EMU pilot survey was observed using ASKAP from 15 July to 24 November 2019. In all Pilot Survey observations, as many of the 36 antennas were used as possible. However, due to maintenance or hardware issues, some antennas may not be included in an observation. The actual number of antennas used in the observations is shown in Table 2.3. The 36 beams cover an area of about 30 square degrees on the sky, which I refer to as a ‘tile’.

Table 2.3: EMU Pilot Observation details, including the ASKAP observing block number for the target and calibrator observations.

Date	Field name	RA (J2000)	Dec. (J2000)	Target SBID	Number of antennas
15 Jul 2019	EMU_2059-51	21:00:00.00	-51:07:6.4	9287	36
17 Jul 2019	EMU_2034-60	20:34:17.14	-60:19:18.2	9325	35
18 Jul 2019	EMU_2042-55	20:42:00.00	-55:43:29.4	9351	35
24 Jul 2019	EMU_2115-60	21:15:25.71	-60:19:18.2	9410	35
25 Jul 2019	EMU_2132-51	21:32:43.64	-51:07:6.4	9434	34
26 Jul 2019	EMU_2027-51	20:27:16.36	-51:07:6.4	9437	36
27 Jul 2019	EMU_2118-55	21:18:00.00	-55:43:29.4	9442	36
02 Aug 2019	EMU_2156-60	21:56:34.29	-60:19:18.2	9501	36
03 Oct 2019	EMU_2154-55	21:54:00.00	-55:43:29.4	10083	35
24 Nov 2019	EMU_2205-51	22:05:27.27	-51:07:6.4	10635	34

The publicly available survey data consists of ten overlapping tiles, each with its own source catalogue. When these catalogues are merged, a huge number of duplicate sources are created, which must be rectified to assure the integrity and consistency of the information. This method also does not take full advantage of the additional information available where tiles overlap, such as increased sensitivity. The survey involves observing each of the ten tiles for ten hours.

To address these issues, the ten tiles were merged in the image plane using the *linmos* task in *ASKAPsoft*, which takes a weighted average of the data in overlapping regions. I show the final merged dataset in Figure 2.4. This image with a spatial resolution of 11-13'' is called the ‘native resolution image’. A full description of the EMU Pilot Survey can be found in Norris *et al.* (2021).

The location of the survey area in the sky is shown in Figure 2.6, and the details of the pointing centres are shown in Figure 2.5.

2.2.2 WISE IR Data

After compiling the radio sample, I need to determine the likely central host by visual inspection of the Wide-field Infrared Survey Explorer (WISE; Wright *et al.*, 2010)⁶ IR image, searching for an IR source close to the expected host position. This included sectioning the full radio image into smaller areas to simplify the process, before manually going through and determining the IR hosts of each radio source, with the IR image overlaid on top. To confirm the IR host, I take the following into account:

- For FRIs, the IR host should centre on, or be the closest IR source to the given radio source, or lie on the radio emission ridge line, in case of asymmetric jets.
- For FRIIs, any sources with IR emission in the lobes/hotspots are discarded from my catalog as they are not likely to be really DRAGNs. Instead, I look for any obvious IR emission between the lobes.

⁶https://www.nasa.gov/mission_pages/WISE/main/index.html

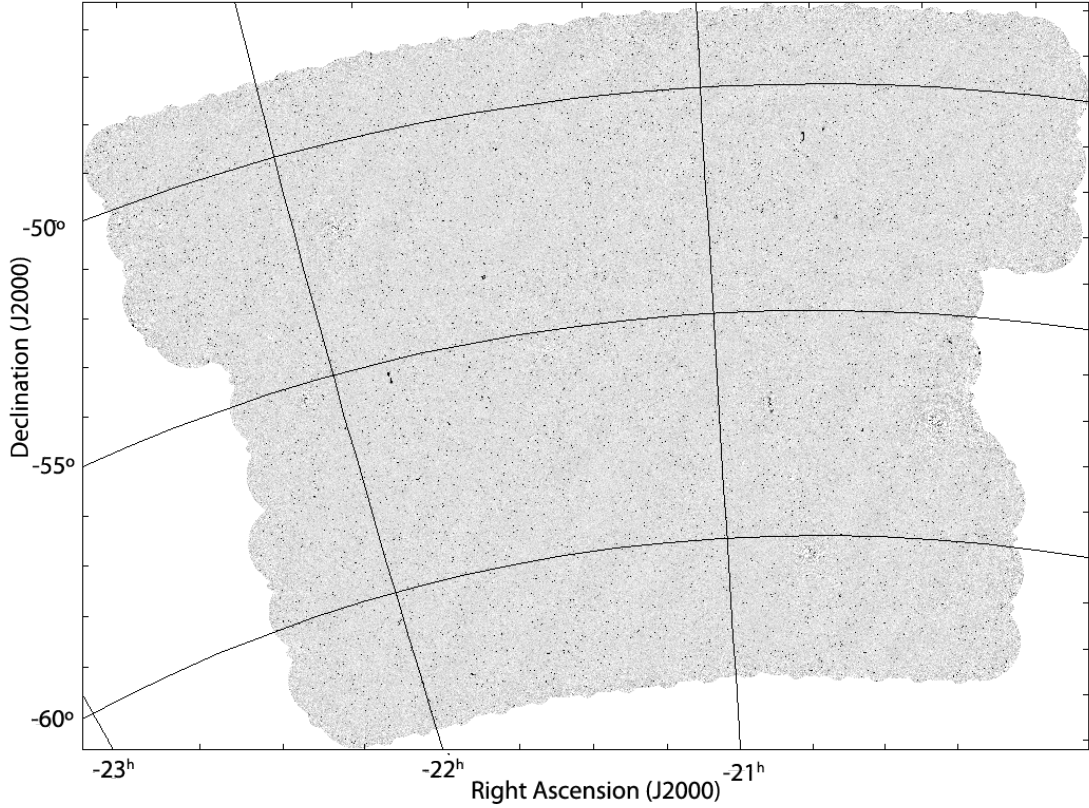


Figure 2.4: The native resolution ($13'' \times 11''$) resulting image of the 270 square degrees EMU Pilot Survey, containing about 220,000 radio sources.

Similar to FRIs, I pick the IR host as close to the centre of the radio source if possible. Additionally, the IR host should lie on the major axis of the source (or emission ridge).

To determine the IR hosts of the sample, I cross-matched the radio image with WISE images. Specifically, I used the unWISE (Lang, 2014; Meisner *et al.*, 2017b,a; Schlafly *et al.*, 2019) reprocessing of the WISE (Wright *et al.*, 2010) and NEOWISE (Mainzer *et al.*, 2014) data. I downloaded⁷ and combined the tiles that fully enclose the G23 region with the SWarp package (Bertin *et al.*, 2002), weighting the tiles with the inverse-variance maps provided by unWISE. AllWISE (Cutri *et al.*, 2013)⁸ combines data from the cryogenic and post-cryogenic phases of the WISE survey. The unWISE data is based on significantly deeper imaging, which increases the total exposure time by a factor of 5 relative to AllWISE. For WISE bands 1 and 2 at 3.4 and 4.6 μm frequencies (angular resolution of 6.1'' and 6.4'' respectively) I use the unWISE data release 6; for bands 3 and 4 at 12 and 22 μm (angular resolutions of 6.5'' and 12'' respectively) I use the AllWISE (Cutri *et al.*, 2021) release. In this study, I primarily use the W1 band image mosaic. For catalogue data, I use the CATWISE2020 catalogue, which is selected from WISE and NEOWISE survey data (Marocco *et al.*, 2021)⁹.

The Full width at half maximum (FWHM) of the WISE Point spread function (PSF) are 6.4 and 6.7

⁷<http://unwise.me>

⁸http://wise2.ipac.caltech.edu/docs/release/allwise/expsup/sec2_1a.html

⁹<https://catwise.github.io/>

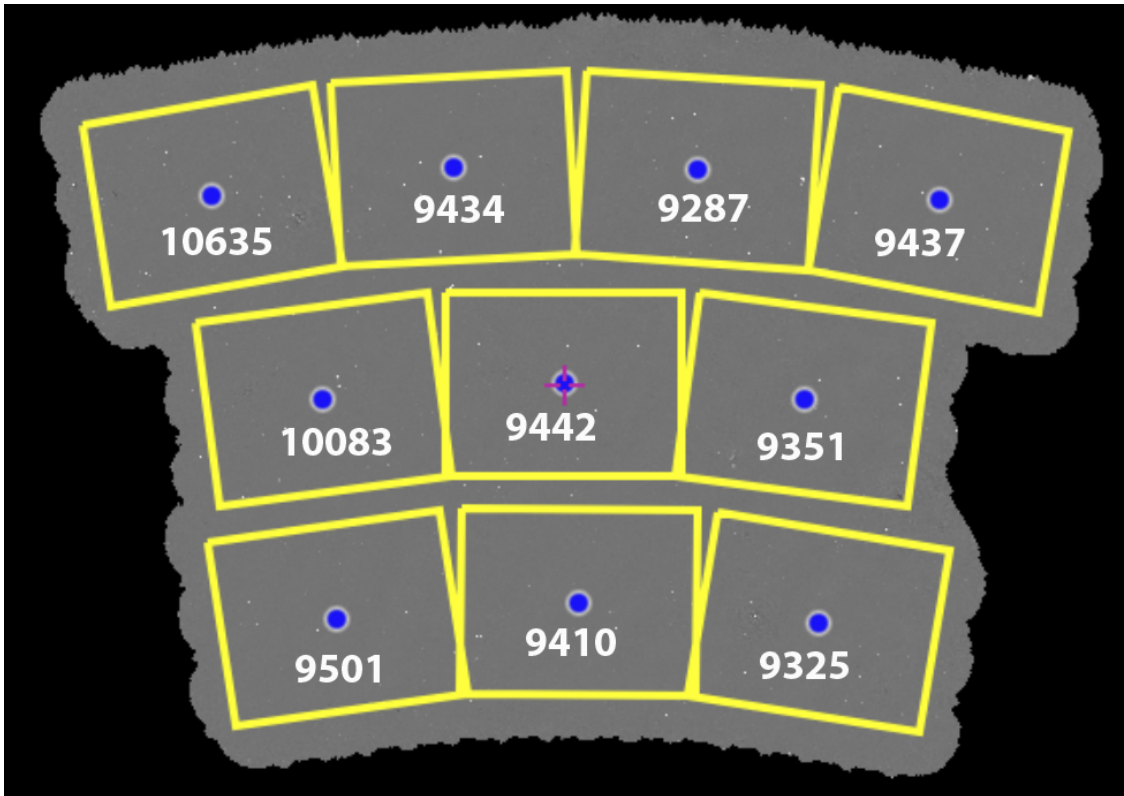


Figure 2.5: The ten individual ASKAP tiles as arranged on the sky for EMU Pilot Survey with their ASKAP schedule block identification (SBID) numbers.

arcseconds in the W1 and W2 bands respectively used for the NEOWISE¹⁰ program. Combined with the detection of large number of sources in the deep WISE imaging, this will mean a majority of the sources in the images will overlap with other sources. To obtain an accurate model of the photometry of these overlapped sources, the crowdsource analysis pipeline (Schlafly *et al.*, 2018) is used to simultaneously model all the sources and determine the fluxes and positions in the unWISE tiles.

The unWISE¹¹ catalogue covers the whole sky at 3.4 and 4.6 microns, and is a deep, comprehensive catalogue of sources derived from the unWISE coadds (Meisner *et al.*, 2019) of the WISE images. The unWISE coadds include images from the NEOWISE phase of the WISE mission, providing exposure time five times the factor of the initial WISE survey coadds. There are over two billion sources from these coadds in the unWISE catalogue.

The deeper imaging used in the unWISE catalogue compared to the first year of the WISE survey, combined with the crowded-region modelling, allows source detection for roughly three times the number of sources as were detected in the AllWISE catalogue. The AllWISE catalogue combines data from the WISE survey's cryogenic and post-cryogenic phases and its software is used in CatWISE. The CatWISE catalogue has four times the exposure of AllWISE.

¹⁰<https://neowise.ipac.caltech.edu/>

¹¹<https://catalog.unwise.me/>

2.2.3 The GAMA G23 Region

G23 is the largest of the two GAMA southern fields (G23, G02), located between right ascension from 339° to 351° , and declination from -35° to -30° . The size of the field is $\sim 50 \text{ deg}^2$, after taking into account area loss due to bright stars. The optical spectra were primarily obtained with the 2dF instrument, which is mounted on the 3.9-m Anglo-Australian Telescope (AAT) at Siding Spring Observatory (Australia) and feeds the AAOmega spectrograph. The spectroscopic redshifts used in this study were obtained from the GAMA project (e.g. Baldry *et al.*, 2010, 2018; Robotham *et al.*, 2010; Hopkins *et al.*, 2013; Gunawardhana *et al.*, 2013; Liske *et al.*, 2015) and were not publicly available at time of submission of this thesis. The redshifts are assigned a quality number from 0 to 4. A value of zero (0) indicates data reduction failure, 1 indicates that no redshift was found, and a value of 4 gives the highest certainty with an associated probability ≥ 0.95 (Driver *et al.*, 2011). For this study, I consider any source with a quality number equal to 3 or 4.

2.2.3.1 KiDS Optical Data

The KiDS (Kilo-Degree Survey) is a ≈ 1500 square degree optical survey (de Jong *et al.*, 2013; Bilicki *et al.*, 2018), carried out with the wide-field imager OmegaCAM (Kuijken, 2011) on the VLT Survey Telescope (VST; Capaccioli and Schipani, 2011). The combination of the two yields a PSF equal to the atmospheric seeing over the full FoV down to 0.6 arcseconds. KiDS was created as a cosmology survey to study the galaxy population out to redshift ~ 1 and, in particular, to measure the effect of weak gravitational lensing by structure along the line of sight on galaxy morphology.

The median redshift is about 0.7, and the observations are made in four filters/bands (u, g, r, i), with the deepest r band reaching a depth of 25.4 magnitude (AB system). The resolution of the images is subarcsecond, making it a valuable data set for visualizing fine details within galaxies that are typically not visible using IR WISE images. KiDS has a number of data releases, beginning with KiDS-ESO-DR1 and the release used in this study is KiDS-ESO-DR4 (see Kuijken *et al.*, 2019, for more details). This release also contains photometric redshifts, which I used for sources that did not have a spectroscopic redshift from GAMA.

2.2.4 EMU Pilot Survey

The second chosen dataset for this project is that of the 270 deg^2 Evolutionary Map of the Universe (EMU; Norris *et al.*, 2011) Australian Square Kilometre Array Pathfinder (ASKAP; Johnston *et al.*, 2007; DeBoer *et al.*, 2009) pilot survey field (Norris *et al.*, 2021). The EMU pilot survey maps about 270 deg^2 of sky in the Dark Energy Survey (DES; Abbott *et al.*, 2019) field (see Figure 2.6) down to a RMS of about $25 \mu\text{Jy}/\text{beam}$.

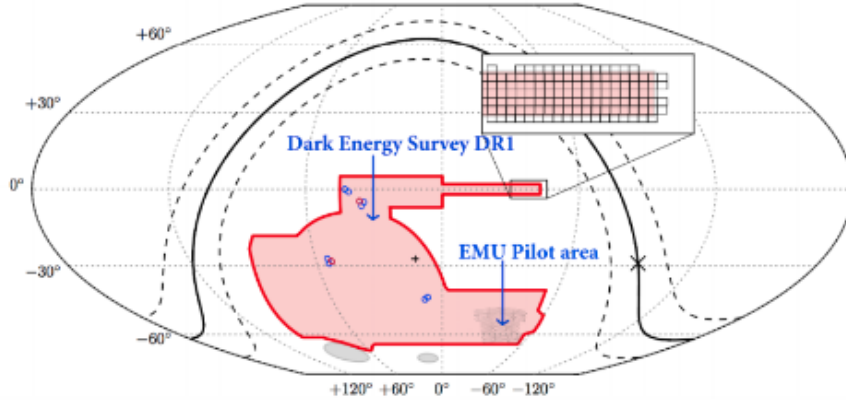


Figure 2.6: The location on the sky of the EMU Pilot Survey area within DES DR1, adapted from [Abbott *et al.* \(2018\)](#). EMU observed a field at a centre frequency of 944 MHz for about ~ 100 hours (10 hours per pointing) with an area of 270 deg^2 in the DES survey. *Credit: ASKAP EMU*

2.2.4.1 Optical Data

Photometry was taken from DES, which uses the Dark Energy Camera (DECam; [Honscheid and DePoy, 2008](#); [Flaugher *et al.*, 2015](#)), a 570 Megapixel camera with a 3 square degree FoV and 62 Charge-coupled devices (CCDs) mounted on the main focus of the Blanco 4 m telescope at the Cerro Tololo Inter-American Observatory (CTIO) in northern Chile. The DES Data Release (DR1) includes data products derived from wide-area survey observations taken in the first three years of science operations (Y1–Y3, from August 2013 to February 2016). The survey covered 5000 square degrees in *grizY* bandpasses to approximately 10 overlapping dithered exposures in each filter.

Photometric redshifts were taken from the Dark Energy Spectroscopic Instrument (DESI) Legacy Survey redshift catalogue ([Zou *et al.*, 2019, 2020](#))¹² Data Release 8 (DR8). Spectroscopic redshifts were not available at the time of submission.

2.3 Morphological classification

To perform morphological classification, I used a native (i.e. at the unconvolved resolution of $10''.0 \times 8''.5$) mosaic restored continuum image of the G23 field.

Part of the motivation for this project is to provide a ‘ground-truth’ data-set for developing automated source extraction and identification algorithms. Therefore, instead of using an automated method of classifying sources like [Mingo *et al.* \(2019\)](#) or [Gürkan *et al.* \(2022a\)](#), I carry out my morphological classification primarily via extensive visual inspection of a greyscale image. Using the criteria I’ve determined, I classify sources as FRI, FRII, or candidate hybrid HYbrid MORphology Radio Sources (HyMoRS) (FRI on one side, FRII on the other). I also identify a further class which I label FRx, which are sources

¹²<https://www.legacysurvey.org/>

where the classification changes depending on the choice of the lowest contour level, because the overall source size is comparable with the resolution. I show an example of an FRx candidate in Figure 2.7, denoting how the ratios would seem different with varying contours.

Another resolution-related issue is that changing resolution may change the location of the brightest pixel in the image (e.g. at low resolution a bright jet knot in an FRI might get ‘absorbed’ by much lower surface brightness lobe material) - and hence the FR classification may also change.

As the goal is to assemble a list of DRAGNs, I exclude any point sources, double-double sources or single fuzzy blobs from the sample.

In addition, I performed a number of spot checks, by re-inspecting a subset of the G23 field, blindly searching for complex sources. These checks are in broad agreement with the primary visual inspection, and did not find any significant number of additional sources. I am therefore confident that I have found most of the FRI and FRII sources in the field, down to $20''$ in size and a peak flux density of $6.5 \times 10^{-4} \text{ mJy beam}^{-1}$.

2.4 Multi-wavelength Cross-identifications

2.4.1 G23 Data

After identifying the WISE host, I cross-match it to other wavelengths, using the same procedure as Norris *et al.* (2006), who found that cross-matching radio with IR, and then cross-matching the IR with optical, gives a lower false-ID rate than matching radio with optical directly. I first match the manually determined WISE band-1 IR hosts of the radio sources against the CATWISE2020 catalogue. I then take the resulting CATWISE2020 coordinates of the sources and crossmatch with the KiDS optical catalogue. Finally, I take the CATWISE2020 coordinates again and cross-match with the GAMA table to get spectroscopic redshifts.

I measure the number of cross-matches between the manually determined WISE IR hosts and the CATWISE2020 catalogue as a function of search radius, and then estimated the false-ID rate by shifting the radio declination positions by $1'$ and then repeating the cross-match. I show the result in Figure 2.8. The choice of an optimum search radius depends on the application (i.e. is it better to maximise the number of cross-matches or minimise the number of false-IDs?). I therefore include all cross-matches up to a search radius of $10''$ in the catalogue, but for further work here I adopt a maximum search radius of $2.5''$. This is due to the fact that after increasing the search radius above $2.5''$, the number of sources slightly changes (as seen from Figure 2.8). Adopting this search radius, I get an estimated 1.4% false-ID rate and a 94% total cross-match rate. The resulting numbers of sources are listed in Table 3.1.

To cross-match the CATWISE2020 positions against KiDS r-band optical positions, I again explored the false-ID rate and the true-ID rate as a function of search radius, as shown in Figure 2.9. As a result,

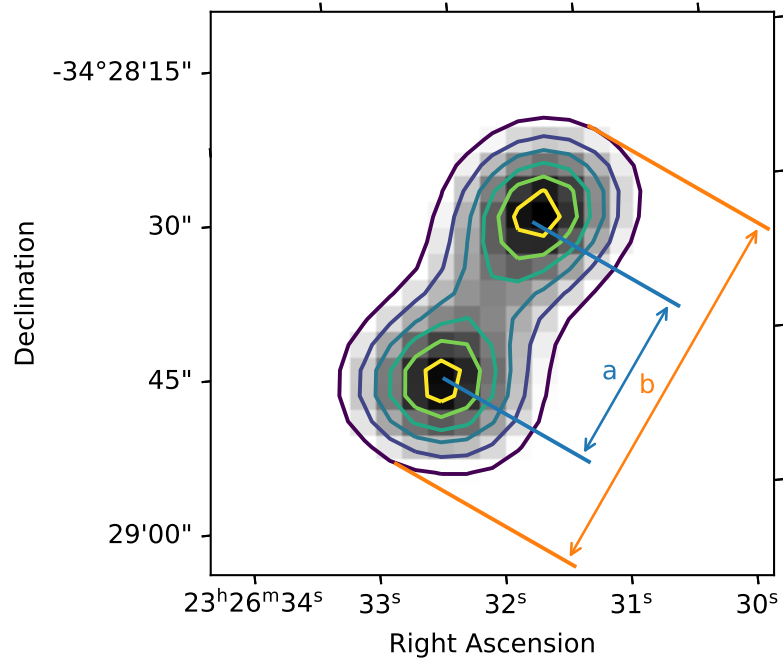
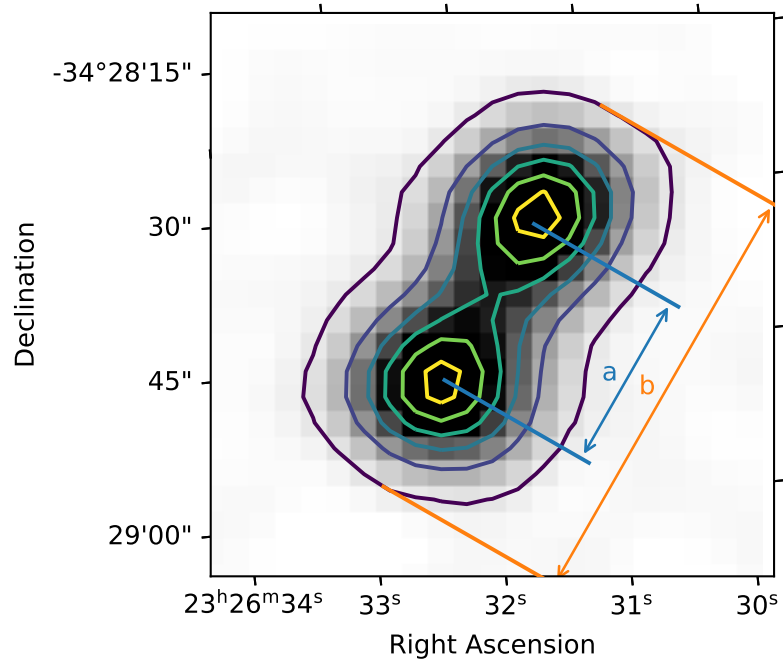


Figure 2.7: Source J232632–342839 as an example of an FRx candidate in the sample. The top image is the source initially seen in the radio image, which satisfies the FR II criterion ($R_{FR} = a/b > 0.5$). The bottom image shows the same source with different contours, which satisfies the FR I criterion ($R_{FR} = a/b < 0.5$). In both panels the contours are equally spaced from the chosen lowest contour to 90% of the peak.

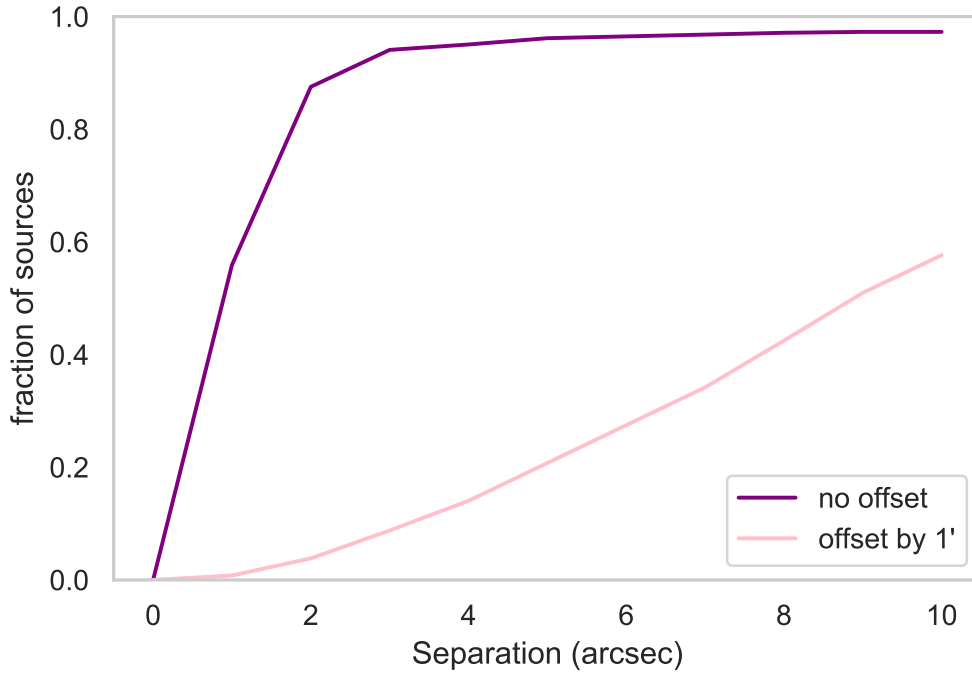


Figure 2.8: The fraction of radio sources cross-matched with the CATWISE2020 catalogue as a function of separation or difference between radio coordinates, using manually determined WISE IR host coordinates for the radio sources. This plot is for both unshifted data (dark solid line) and for data shifted by 1' in the radio declination coordinate (light solid line).

I adopt a search radius of 2.5''. Additionally, I cross-match the CATWISE2020 positions against GAMA redshifts, using the same technique, shown in Figure 2.10, and adopt a search radius of 2.5''.

To augment my redshift sample, I cross-match the G23 sample of sources that did not have a spectroscopic redshift with KiDS photometric redshifts. The resulting numbers of sources after each stage are listed in Table 3.1.

2.4.2 EMU Pilot Survey

Similar to what I did for the G23 data, I first manually pick out radio sources from the ASKAP image, then overlay the IR image on top to find the IR core. In total, I manually identify 4173 radio sources. With a list of determined WISE IR hosts, I then cross-match against the CATWISE2020 catalogue, followed by cross-matching the CATWISE2020 coordinates of the sources against the DES optical catalogue, before finally cross-matching the CATWISE2020 coordinates with the DESI photometric redshifts.

I measure the number of cross-matches as a function of separation between my manually selected WISE IR hosts and the CATWISE2020 catalogue, then I estimate the false-ID rate by shifting the radio declination positions by 1 arcminute and repeating the cross-match. This shift was chosen as a compromise between two factors. Some radio sources can be up to one arcminute in size, and so a distance of less than one arcminute would falsely identify with another part of the source. But a few rare sources (e.g.

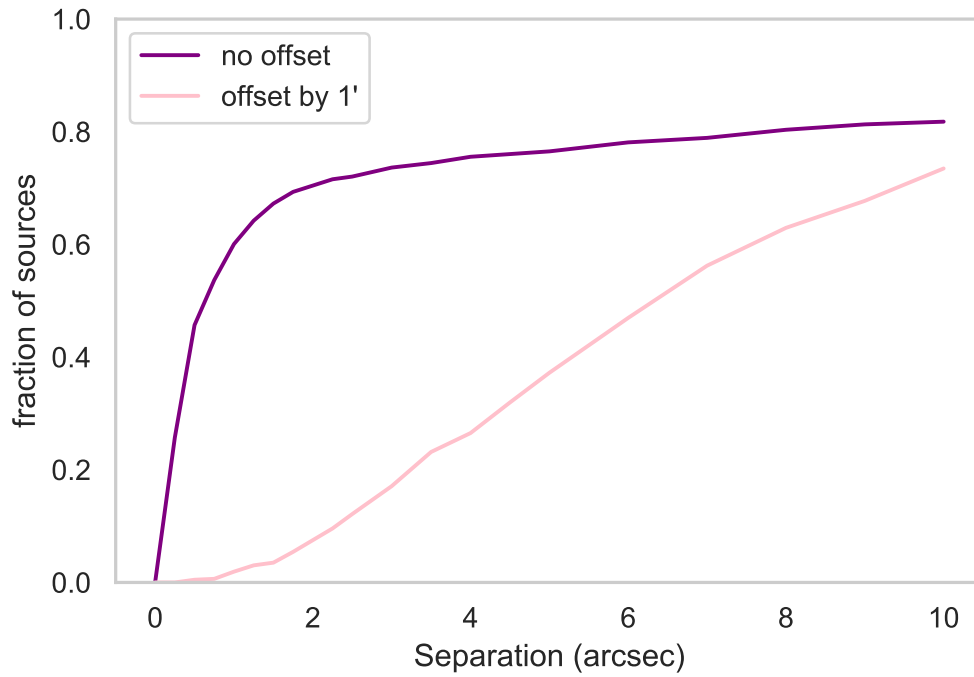


Figure 2.9: The fraction of radio sources cross-matched with the KiDS DR4 catalogue as a function of separation, using the CATWISE2020 catalogue coordinates for the radio sources. This plot is for both unshifted data (dark solid line) and for data shifted by 1' in the radio declination coordinate (light solid line).

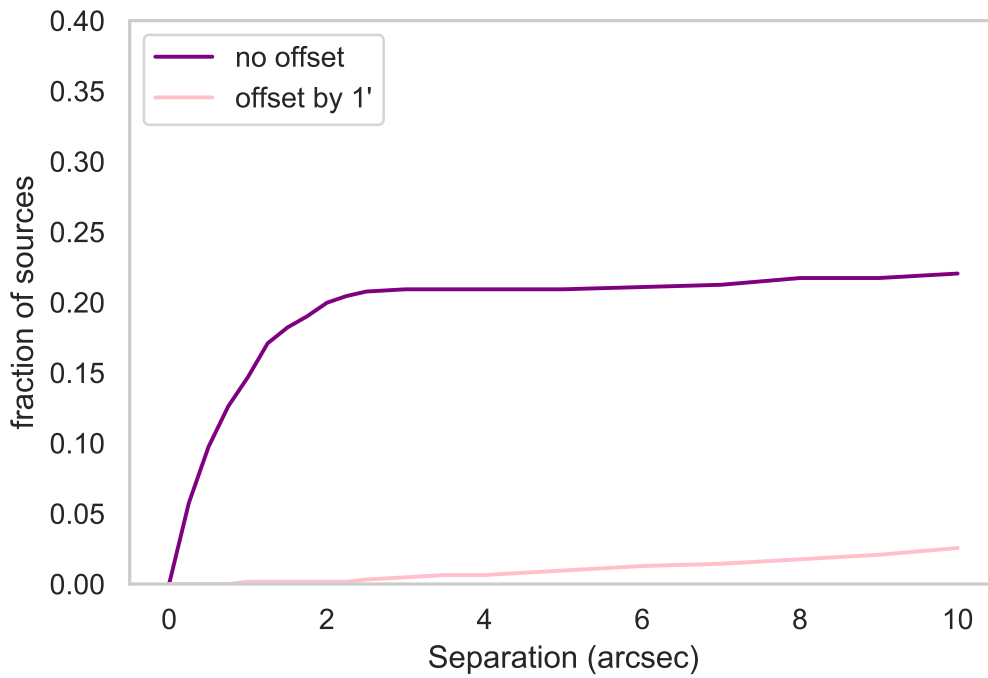


Figure 2.10: The fraction of radio sources cross-matched with the GAMA spectroscopic and KiDS photometric redshift catalogues as a function of separation, using the CATWISE2020 catalogue coordinates for the radio sources. This plot is for both unshifted data (dark solid line) and for data shifted by 1' in the radio declination coordinate (light solid line).

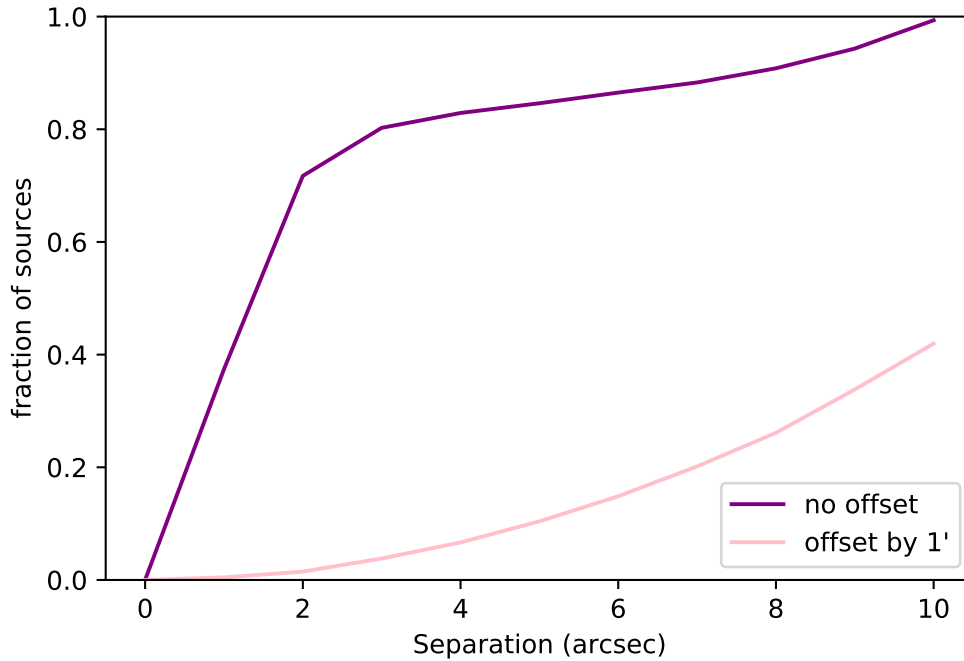


Figure 2.11: The fraction of radio sources cross-matched with the CATWISE2020 catalogue as a function of separation, using manually determined WISE IR host coordinates for the radio sources. This plot is for both unshifted data and for data shifted by one arcminute in the radio declination coordinate.

Giant Radio Galaxies (GRGs)) are even bigger, so one could argue that an even larger distance, such as 10 arcminutes might work here. However, the problem then arises that the Universe shows structure on that scale, so the source density at a point might be quite different from the source density 10 arcminutes away. So 1 arcminute has been found to be a good compromise between these two effects.

The result is shown in Figure 2.11. I therefore include all cross-matches up to a search radius of 10 arcseconds, but for further work here I adopt a maximum search radius of 2.2 arcseconds, at which I get a 1.4% false-ID rate and a 75% total cross-match rate. The resulting numbers of sources are listed in Table 2.4. To cross-match the CATWISE2020 positions against DES optical positions, I again explored the false-ID rate and the true-ID rate as a function of search radius, as shown in Figure 2.12. For the optical, I adopt a search radius of 2 arcseconds. Additionally, I cross-match the CATWISE2020 positions against DESI photometric redshifts, using the same technique, shown in Figure 2.13, and similarly adopt a search radius of 2 arcseconds.

2.5 Estimating the luminosity function

Throughout this work I assume that the radio spectrum exhibited by radio sources can be written as a simple power law $S_\nu \propto \nu^\alpha$, where S_ν is a monochromatic flux density at frequency ν and α is the spectral index. The observed fluxes were converted to monochromatic rest-frame (emitted) luminosities. This

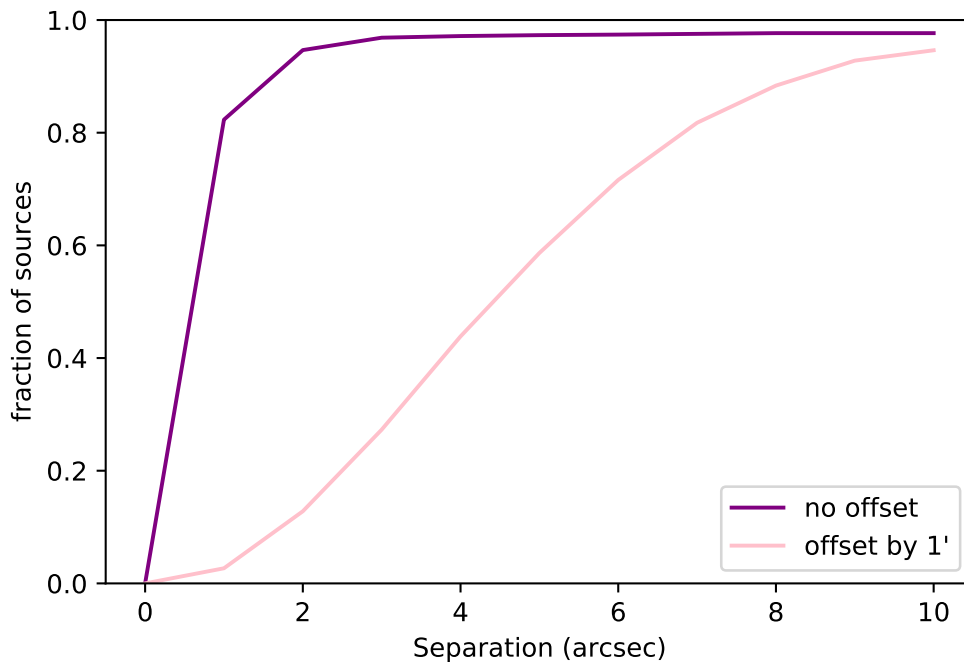


Figure 2.12: The fraction of radio sources cross-matched with the [DES](#) catalogue as a function of separation, using the CATWISE2020 catalogue coordinates for the radio sources. This plot is for both unshifted data and for data shifted by one arcminute in the radio declination coordinate.

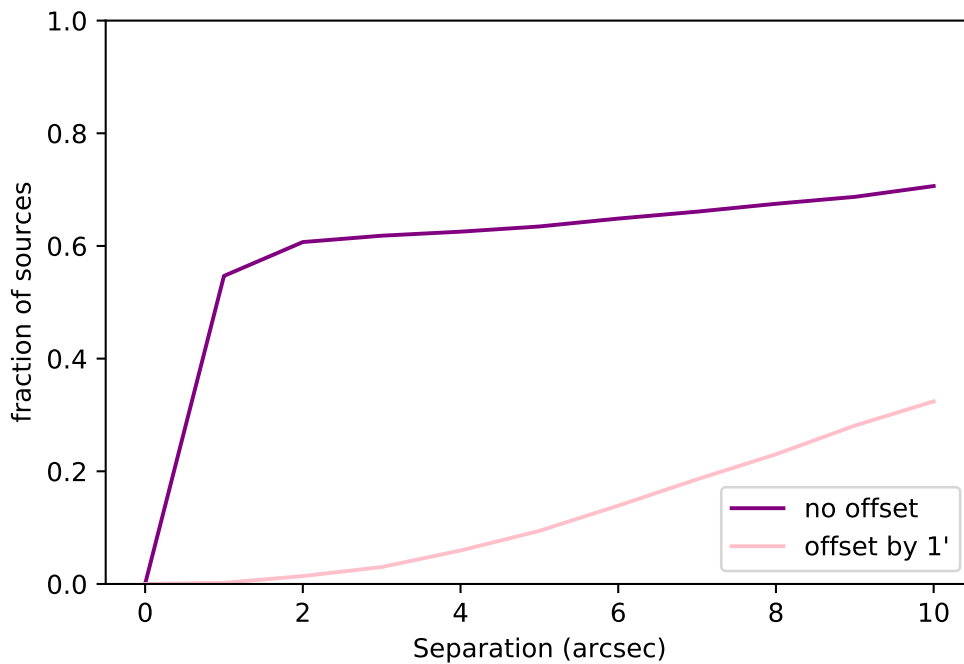


Figure 2.13: The fraction of radio sources cross-matched with the [DESI](#) photometric redshift catalogues as a function of separation, using the CATWISE2020 catalogue coordinates for the radio sources. This plot is for both unshifted data and for data shifted by one arcminute in the radio declination coordinate.

Table 2.4: The numbers of sources that remain after each stage of the value-added processing for the EMU-PS.

Criterion	# Sources	Percentage of source sample
Initial source extraction	4173	n/a
CATWISE2020 Crossmatch (10 arcsec)	4146	99
CATWISE2020 Crossmatch (2.2 arcsec)	3083	75
DES DR1 Crossmatch (2 arcsec)	2933	70
DESI photo z Crossmatch (2 arcsec)	1779	43

results in the standard radio k -correction of $K(z) = (1+z)^{-(1+\alpha)}$, which gives the rest-frame radio luminosity at frequency ν_1 as:

$$L_{\nu_1} = 4\pi D_L^2(z)K(z)S_{\nu_2} \quad (2.2)$$

where D_L is the cosmological luminosity distance (Hogg, 1999). The bolometric k -correction accounts for the spectrum shift relative to the receiver, and a further bandwidth correction $[1+z]^{-1}$, accounts for the spectrum stretching relative to the receiver's bandwidth. For the computation of this k -correction, $K(z)$, I assign a spectral slope of $\alpha = -0.72$ to all sources (Condon, 1992b; Coble *et al.*, 2007). To plot radio luminosity versus optical magnitude, I convert the r-band apparent magnitude from the KiDS catalogue into rest-frame absolute magnitude. This is done using the following equation:

$$M = m - 5\log_{10}\left(\frac{D_L}{10}\right) \quad (2.3)$$

where m is the apparent r-band apparent magnitude from the KiDS catalog.

The k -correction is a correction to an astronomical object's observed magnitude (or equivalently, flux) that converts an object's quantity of light at redshift z to an equivalent measurement in the object's respective rest frame. If a comparison of observations of objects in different bands is to be made, the k -corrections are also required.

I express all radio luminosities in terms of the 888 MHz luminosity. When making comparisons with earlier work, I applied a k -correction for the different frequencies used in the earlier work, assuming a spectral index of -0.72 . I have also corrected for the different Hubble constant used in those papers. Thus, to compare their luminosities with ours, the L_{178} luminosity used by Fanaroff and Riley (1974) should be multiplied by a factor of 0.18, and the L_{1400} luminosity used by Owen and Ledlow (1994) should be

multiplied by a factor of 0.77.

2.6 Source Selection

The first step in assembling my catalog consists of going through the radio images by eye using SAOImage DS9 (Joye and Mandel, 2003), searching for sources that looked like they were double lobed. I do three scans of the radio image in total. The first is a quick dirty scan, picking out any obvious, large DRAGNs and placing circular regions around each source that encompasses as much of the source as possible. I set the greyscale level so the 5-sigma peaks could just be seen, and due to screen size, I set the spatial scale so an area of 10×20 arcminute was on my screen. Following that, I do a visual raster scan through the emission of the entire radio image, starting from the top left corner, moving across and down in a zig-zag pattern to the bottom right, picking out and classifying sources. The whole process can take around six hours for one 30 square degree field on the sky. This second scan will have picked out a majority of sources but it is to be expected some might slip through the net. And so I do a final third scan, focusing on picking out any sources that might have been missed. A visual inspection would naturally yield much subjectivity in picking out the sources, but I stuck to the original definition as much as possible.

2.7 Determining FR ratio

As stated above, this work is based on the original definition by Fanaroff and Riley so the ratio plays a big part. Thus, after collecting a table of initial classifications, the final classification will be confirmed with calculating the a/b ratio of the sources. To do this, an algorithm is created to determine a , the distance between the peaks of emission, and b , the total extent of the source. The code is summarized below in text.

Firstly, the rms noise σ needs to be calculated. This is done by using the σ -clipping process on the entire radio image, where values that are 2.5 times the first σ are rejected (assuming the mean of the noise is zero).

With this, a cutout of the source based on the CATWISE2020 IR positions and angular size given is made.

To find the 5σ -contour in the image, I use the marching cubes algorithm (Lorenson and Cline, 1987), as implemented in `skimage.measure.find_contours()` (van der Walt *et al.*, 2014). Then I apply Principal Component Analysis (PCA) to find the orientated bounding box for the 5σ -contour. The length of the major axis of this box (in pixels) will thus be b , and the PA of the box is θ . Any pixels outside the bounding box are blanked. This is done multiscale, from the size of the restoring beam up to $b/2\sqrt{2}$ in order to make finding sources within (blob detection) smoother.

The process of blob detection will require the use of Laplacian of the Gaussian (LoG) filters, which will

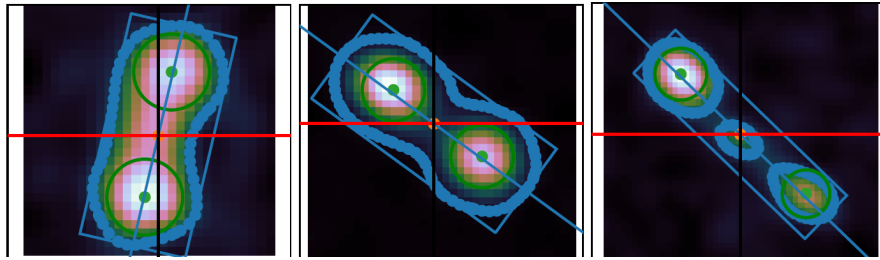


Figure 2.14: Some examples of where the ratio algorithm did a good job. The orange dot represents the geometric centre and the green dots signify the probable peaks.

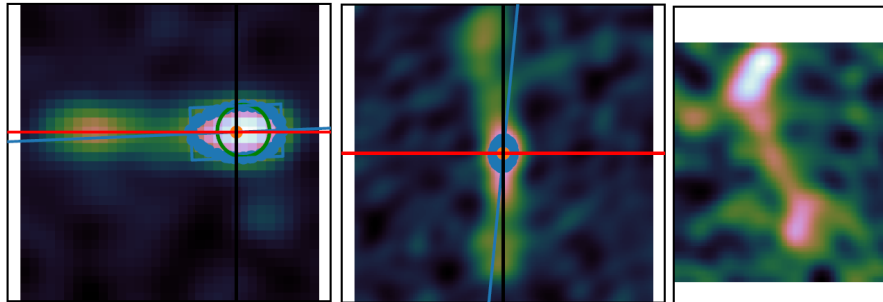


Figure 2.15: Some examples of where the ratio algorithm failed in blob detection.

pick out partially isolated maxima. Let's consider an input image $f(x, y)$. The input image is convolved by a Gaussian kernel to give a scale space representation $L(x, y; t) = g(x, y, t) * f(x, y)$ at a certain scale t . Then a second derivative or the Laplacian operator $\nabla^2 L = L_{xx} + L_{yy}$ is applied to the image. For low intensity (dark) blobs of radius $r = \sqrt{2t}$, this will yield strong positive responses and negative responses for bright blobs of similar size. This is done multiscale, from the size of the restoring beam up to $b/2\sqrt{2}$ in order to make finding sources within (blob detection) smoother.

If there are enough sources, the one furthest from the centre of the box is selected as the starting point, and the one furthest from that, on the other side, will be the end point. Then the distance between the two end points or maxima, will be a .

For around 80% of the sources, the algorithm does a good job in picking out the points of peak emission and the extent of the source (see Figure 2.14). The remaining 20% that the algorithm failed in either determining a or b or both, I manually measure it via the radio image. The failure might be due to the noise floor being too high, or the blobs of emission could not be detected (see Figure 2.15). The process in measuring a may also fail in some cases.

The algorithm helps especially well for borderline sources where $a/b \sim 0.5$, as it is difficult to determine whether they are FRI or FRII. I call these sources FRx.

For this, I need to determine the maximum and minimum values of b that are reasonable and consistent with the data. Assuming the difference between b_{\min} and b_{\max} scales with the beamsize, I then

define:

$$\begin{aligned} B_{\max} &= B + (\text{beamsize} \times C) \\ B_{\min} &= B - (\text{beamsize} \times C) \end{aligned} \tag{2.4}$$

where C is a parameter chosen subjectively to determine the best numerical difference that makes a source **FRI** or **FRII**. For both the G23 and EMU-PS, I assume a value of 10 arcseconds for the beamsize and $C = 0.5$.

With this, I'm able to calculate the **FR** ratio (a/b) of the sources and finalise the classifications. The final classifications take the following into account:

1. If $a/b_{\min} < 0.5$, the source is classified as **FRI**
2. If $a/b_{\max} > 0.5$, the source is classified as **FRII**
3. If $a/b_{\min} > 0.5 > a/b_{\max}$ the source is classified as **FRx**
4. Sources with one or no peaks determined are classed as 'single' or 'unknown' respectively
5. Sources (other than singles or unknowns) with $B < 40$ are classed as **FRx**, as at that size, the source is too small compared to the beamsize to yield a reliable classification
6. With the above, the classification of sources with $B < 50$ are to be considered weak

2.8 Parallel Transport

In the EMU-PS catalogue, the **PA** is defined as the angle of a source's major axis measured east of the local north direction. I adopt a similar method to (Osinga *et al.*, 2020). To keep the **PAs** consistent across all ten tiles/pointings, I translated the **PAs** of the sources to be measured east of the north celestial pole.

Since the **PA** is defined with respect to the local meridian, the vectors corresponding to the **PAs** at different points on the celestial sphere cease to be tangent and are unable to be directly compared. These vectors must be transported along the great circle that connect these points. I employ the parallel transport method, which allows the radio source 'vectors' to be transported to a different position on the celestial sphere following Jain *et al.* (2004); Contigiani *et al.* (2017). This method is described below for completeness.

Using spherical coordinates, I parametrize the celestial sphere (r, θ, ϕ), and define a natural orthonormal basis at each point dictated by the coordinate system. This set of local unit vectors (u_r, u_θ, u_ϕ) point respectively towards the centre of the sphere, northward along the local meridian and eastward. The aim is to compare the **PAs**, θ_{p1} and θ_{p2} , of two sources with positions, P_1 and P_2 , on the celestial sphere (see Figure 2.16).

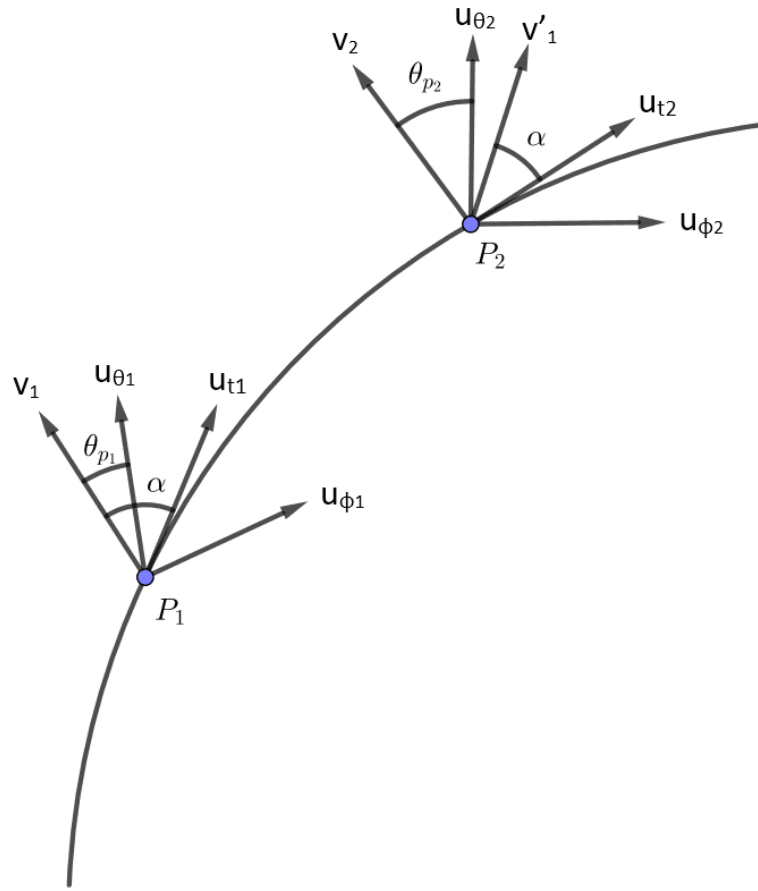


Figure 2.16: A 2D schematic illustration of parallel transport. The PA θ_{p1} corresponds to vector v_1 and PA θ_{p2} corresponds to vector v_2 . To compare the two vectors, v_1 must be translated along the great circle via parallel transport. This is shown by the arc extending from position P_1 to position P_2 . The transported vector is denoted by v'_1 and the local basis vectors are given by (u_θ, u_ϕ) . The angle α between the tangent vector u_r and the vector v remains constant in parallel transport. *Credit: Jain et al. (2004); Osinga et al. (2020)*

I consider a source at location P_1 with PA θ_{p1} , determined up to a rotation of π radians. The unit vector which can be used to identify it is given as:

$$v_1 = \cos \theta_{p1} u_{\theta1} + \sin \theta_{p1} u_{\phi1} \quad (2.5)$$

Parallel transport on a sphere enables a coordinate-invariant inner product to be defined between two vectors, by translating one of them along arcs of great circles connecting the two vectors. To do this, I consider two tangent vectors v_1 and v_2 with PAs θ_{p1} and θ_{p2} , defined respectively in $P_1 = (r_1, \theta_1, \phi_1)$ and $P_2 = (r_2, \theta_2, \phi_2)$. These two points are part of the same unit sphere ($r_1 = r_2 = 1$). To obtain vector, v'_1 , I transport the vector, v_1 , to the position, P_2 . This results in the translated vector v'_1 forming an angle, θ'_p , relative to the local north-pointing vector, $u_{\theta2}$. Next, I need to calculate θ'_p , the parallel transported angle. So let u_s be the unit vector perpendicular to the plane that contains the two radial vectors u_{r1} and

u_{r2} . Then u_s is found by:

$$u_s = \frac{u_{r1} \times u_{r2}}{|u_{r1} \times u_{r2}|} \quad (2.6)$$

I define the unit vectors u_{t1} and u_{t2} as tangent to the great circle at the points P_1 and P_2 . These vectors are given by:

$$\begin{aligned} u_{t1} &= u_s \times u_{r1} \\ u_{t2} &= u_s \times u_{r2} \end{aligned} \quad (2.7)$$

By parallel transporting v_1 to position P_2 along the great circle, the angle v_1 makes with respect to the tangent to the great circle remains unchanged. I then analyse the orientation of u_{t1} and u_{t2} relative to the local basis at the position of the two sources, to estimate the angle by which the vector has turned due to the transport. Let ζ_1 be the angle between u_{t1} and $u_{\phi1}$ and ζ_2 the angle between u_{t2} and $u_{\phi2}$. As per the definition of the inner product, these angles are given by:

$$\begin{aligned} \zeta_1 &= \arccos(u_{\phi1} \cdot u_{t1}) \\ \zeta_2 &= \arccos(u_{\phi2} \cdot u_{t2}) \end{aligned} \quad (2.8)$$

where the sign of the resulting angle ζ_1 or ζ_2 is equal to the sign of $u_{\theta1} \cdot u_{t1}$ or $-u_{\theta2} \cdot u_{t2}$ respectively. The transported vector v'_1 thus makes an angle $\theta'_{p1} = \theta_{p1} + (\zeta_2 - \zeta_1)$, which is defined relative to the local frame in P_2 . Thus the generalized dot product between v_1 and v_2 can now be defined as the dot product between the transported vectors v'_1 and v'_2 :

$$v_1 \odot v_2 = v_1 \cdot v_2 = \cos(\theta_{p1} - \theta_{p2} + \zeta_2 - \zeta_1) \quad (2.9)$$

This is the derivation of the practice for transporting PAs along a sphere which may be applied to any problem involving angles on a sphere. Since my dataset is purely directional, I have $v_1 \cdot v_2 = 1$. For the same reason and for comparing the difference between PAs, I redefine the generalized inner product using the following simplified notation:

$$(\theta_{p1}, \theta_{p2}) = \cos[2(\theta_{p1} - \theta_{p2} + \zeta_2 - \zeta_1)] \quad (2.10)$$

The factor two comes into play here to ensure that the cosine function spans the full $-\pi$ to $+\pi$ range, (Bietenholz, 1986). Since the PAs range from 0 to π , this expects values of -1 to $+1$, where $+1$ indicates perfect alignment (Jain *et al.*, 2004) between θ_{p1} and θ_{p2} and -1 implies perpendicular orientations.

2.8.1 Angular Dispersion

Here, I introduce dispersion, a measure of the variance in a set of angles, to examine the significance of PA alignment (Jain *et al.*, 2004; Contigiani *et al.*, 2017). This measure is determined solely by the differences between neighbouring PAs and is thus an appropriate choice when testing preferential alignment. Similar to Osinga *et al.* (2020) I will not investigate in which direction the preference lies but simply whether there is a preferred direction. Given the i -th source, I consider the n nearest neighbours, including the source itself. The dispersion as a function of their positions angles θ is defined as

$$d_{i,n}(\theta) = \frac{1}{n} \sum_{k=1}^n (\theta, \theta_k) \quad (2.11)$$

where θ_k is the PA of the respective neighbours of a source. The generalized inner product (θ, θ_k) is given in Equation 2.10.

The PA θ that maximizes the dispersion around source i is a measure of the centrality of the set of angles, and thus corresponds to the definition of the mean PA of source i and its $n-1$ nearest neighbours. The magnitude of $d_{i,n}|_{\max}$ then represents the dispersion around this mean. The dispersion of a set of angles has the domain $(0, 1]$, where a value of 1 indicates perfect alignment of all n nearest neighbours. I take the derivative of Equation 2.11 with respect to θ to find the value of θ that gives the maximum dispersion and get for $d_{i,n}|_{\max}$:

$$d_{i,n}|_{\max} = \frac{1}{n} \left[\left(\sum_{k=1}^n \cos \theta_k \right)^2 + \left(\sum_{k=1}^n \sin \theta_k \right)^2 \right]^{1/2} \quad (2.12)$$

By taking the derivative, I'm measuring the sensitivity of the dispersion to small changes in θ . Following Jain *et al.* (2004), this maximal value is regarded as the measure of the dispersion of the n sources and their mean direction as θ . The maximum value allowed for the dispersion is $d_{i,n}|_{\max} = 1$, which corresponds to perfect alignment of the sources. The inner product's coordinate-invariance (Equation 2.10) extends to the dispersion.

I assign a number of nearest neighbours n , for a sample of N sources. Then testing for the non-uniformity of alignment in this sample, the statistic is then defined as:

$$S_n = \frac{1}{N} \sum_{i=1}^N d_{i,n}|_{\max} \quad (2.13)$$

corresponding to the mean dispersion. Thus, S_n represents the strength of a local alignment signal in the full sample of N sources while taking into account the n nearest neighbors of every source.

As Jain *et al.* (2004) found, the standard error or deviation of the dispersion $d_{i,n}|_{\max}$ from its mean value is $\propto 1/\sqrt{n}$. This is mirrored by S_n

$$S_n \propto \frac{1}{\sqrt{n}} \quad (2.14)$$

When considering multiple values of n , I express the measurements of S_n as one-tailed significance levels (SL). The Significance level (SL) for rejecting the null hypothesis that a target sample of sources is randomly oriented is then determined by comparing the statistic, S_n , to the distribution of the statistic for shuffled simulated control samples. This removes any dependence of the orientation on position while still preserving other statistics and is expressed as:

$$SL = 1 - \Phi\left(\frac{S_n - \langle S_n|_{MC} \rangle}{\sigma_n}\right) \quad (2.15)$$

where Φ is the cumulative normal distribution function, $\langle S_n|_{MC} \rangle$ is the expected value for S_n in absence of alignment, and σ_n is the standard deviation found through Monte Carlo simulations. The simulations permute the set of sources about the set locations. Doing this attempts to preserve the statistics of the sources, but breaks any dependence of orientation with location. I then employ the following approximate scale: $\log_{10}SL < -3.5$, very strong alignment; $-2.5 > \log_{10}SL > -3.5$, strong alignment; $-1.5 > \log_{10}SL > -2.5$ weak alignment.

Jain *et al.* (2004) verified that S_n is normally distributed for randomly oriented samples of sources if $N \gg n \gg 1$. The SL at which the hypothesis of uniformity in the PAs should be rejected can be evaluated on a local scale using the dispersion measure and the resulting statistic, by considering varying numbers of nearest neighbors. The number of nearest neighbors is analogous to fixing apertures with angular radii extending to the n -th nearest neighbor around all sources. S_n can then be used to investigate the significance of alignment at various angular scales. Because the dispersion is an average of n neighbors, different measurements of S_n are not independent. Thus, the S_n statistic probes alignment to scales equivalent to n , and once a signal is observed for some n , a preferentially positive signal for greater n is expected. If the redshifts of the sources are known, this can be extended to probe nearest neighbors in three dimensions. This allows for the investigation into the dependence of a possible alignment effect and S_n as a function of physical scale.

2.8.2 Kolmogorov–Smirnov test

Throughout the work, I perform a two-sample Kolmogorov-Smirnov (K-S; Karson, 1968) test. The K-S test is used to determine whether a sample is drawn from a population with a specific distribution, and is based on the empirical distribution function (ECDF). The test is non-parametric, meaning the test statistic is not assumed to be following a given distribution. Another advantage of this test is that it is an exact test (e.g. a sufficient sample size is required for the chi-square goodness-of-fit test approximations to be valid). Despite such advantages, the K-S test is only applicable to continuous distributions, and requires that

the distribution be completely specified. In other words, if the parameters of shape, location, and scale are derived from the data, the critical region of the test becomes invalid. Generally, it must be inferred through simulation. Additionally, since the K-S test looks for deviations from the null hypothesis, it's most sensitive near the centre of the distribution than at the ends.

2.9 Circular Statistics

When considering the distribution of PAs of sources, one should consider if the data is grouped into one or more 'preferred' directions. Working under the assumption of null hypothesis statistical testing, this means testing that the distribution from which the sample is selected is uniformly spread around the entire circumference of the circle (i.e. the null hypothesis), with no implicit preference for one direction over another. In studies evaluating circular data, the null hypothesis of uniformity is usually tested in any statistical examination (Landler *et al.*, 2019), and it remains the norm. This is because most tests performed in circular statistics are only valid if the data is non-uniform (Mulder and Klugkist, 2020). To begin a test, the Null hypothesis, H_0 , and Alternative hypothesis, H_A are defined, where the Null is assumed to be true, until we gather enough evidence to reject it. In this project, I assume as my null hypothesis the PAs of radio sources jets are uniformly (randomly) distributed.

Circular distributions arise when measuring data that is cyclic, such as angles. They are fundamentally different from linear data or real data from the real domain due to their periodic nature; on the circle, measurements at 0 degrees and 360 degrees represent the same direction whereas on a linear scale in the real domain, they would be located at opposite ends of the circle. For this reason, circular data requires specific analytical statistics to suit the circular domain (Mardia, 1975). Because traditional statistical analysis methods do not work for circular variables, an entirely new field of circular statistics has been developed.

A fundamental hypothesis of interest is that of circular uniformity. To determine whether apparent alignments occur by chance, or reflect real spatial correlation in radio jet directions, I investigate the statistical probability of the alignments given an underlying random sample of jet directions. Conventional estimators such as the mean need to be redefined for analysis involving PAs on a circle. Fisher (1995) contains a concise collection of methods for dealing with circular statistics.

The Rayleigh Test of Uniformity (Rayleigh, 1880) also known as Rayleigh's z test, measures and assesses the significance of the mean resultant length of a single vector, \vec{r} , compared to a uniform distribution with a mean resultant length that is statistically null i.e. agreement with the null hypothesis. The mean resultant length or magnitude of the mean vector is a measure of the concentration of data points around a circle. The Rayleigh test assumes unimodal data, meaning that there is at most one major clustering of points around the circle. In cases where the data is multi-modal, the Rayleigh test performs

poorly which leads to the z statistic likely being small even if the data is not uniform (see [Batschelet, 1981](#)).

As a part of this project is to study the alignments of radio sources, circular statistics will play a huge part.

Chapter 3

A Study of the Fanaroff-Riley dichotomy with the GAMA-23 Survey

Context

An important task with any new telescope is commissioning early science. The work I present in this chapter uses early science observations taken with Australian Square Kilometre Array Pathfinder (*ASKAP*) on the Galaxy And Mass Assembly (*GAMA*)-23 (G23) field. These observations will be used by *ASKAP*'s Evolutionary Map of the Universe (*EMU*) survey science project to determine how close early predictions of *ASKAP*'s performance were to its current capabilities.

I explore the correlation between peak radio luminosity and Fanaroff & Riley (1974) classifications using the G23 field. The field covers an area of around 50 square degrees at 888 MHz from the *EMU* Early Science data, from which I have compiled a sample of 706 Double Radio sources Associated with Galactic Nuclei (*DRAGNs*). My analysis confirms previous findings that radio luminosity does not unambiguously define whether a source is Fanaroff-Riley Class I (*FRI*) or Fanaroff-Riley Class II (*FRII*). I also find no significant evidence for the redshift distributions of the two classes to differ, except for sensitivity effects. I also find populations that do not fit in the original *FRI* and *FRII* definition, including HYbrid MORphology Radio Sources (*HyMoRS*) and Fanaroff-Riley (*FR*)x sources.

3.1 Introduction

One of the most powerful phenomenological clues to the origin and physics of extragalactic radio sources has come from the *FR* classification. Fanaroff and Riley (1974) showed that radio-loud Active Galactic Nucleis (*AGNs*) can be categorized into two morphological types: *FRI* and *FRII*, based on the position of the brightness peaks of the radio emission. The two types of structures are thought to be the result

of various interactions with the environment between low and high power jets (Scheuer, 1974; Bicknell, 1986). The original FR definition classified sources according to the ratio R_{FR} of the distance between the regions of peak intensity on opposite sides of the central host galaxy, to the total extent of the source, as shown in Figure 2.7. Sources with $R_{\text{FR}} < 0.5$ are classified as Class I (i.e. the edge-darkened FRIs), while those with $R_{\text{FR}} > 0.5$ are classified as Class II (i.e. the edge-brightened FRIIs). Any central source was excluded from this classification. The sources in Fanaroff and Riley’s sample with 178 MHz luminosity fainter than $2 \times 10^{25} \text{ W Hz}^{-1} \text{ sr}^{-1}$ (for $H_0 = 50 \text{ km s}^{-1} \text{ Mpc}^{-1}$) were classified as FRI while the more luminous sources were all FRII. This was expanded upon with work by Owen and Ledlow (1994).

Over the past decade, some studies on the FR dichotomy have used a different definition. Rather than classify sources based on the ratio of the distance between intensity peaks to the full extent of the source, the classification is instead defined by whether the source is core-brightened or not (e.g. Grandi *et al.*, 2021; Baldi *et al.*, 2019). Because they adopt a different definition of the FR classification, (e.g. they classify core-dominated FRIIs as FRIs), their findings cannot be compared with other results, and so I do not discuss them any further.

Several physical interpretations of the FR classification have been proposed, which invoke either or both the interaction of the jet with the external medium, and the nuclear intrinsic properties of the accretion and jet formation processes. The previous models attribute the duality to the possible entrainment of a jet on small scales (Alexander, 2006; Bicknell, 1995; Gopal-Krishna and Wiita, 1988, 2001; Krause *et al.*, 2012; Perucho and Martí, 2007), whereas more recent models include the possibility of different jet plasma content (electron–positron pairs or normal electron–proton plasma), or the black hole spin (Reynolds *et al.*, 1996b; Baum *et al.*, 1995; Meier, 1999).

Despite the considerable debate over the relationship between jet morphology and accretion mode (e.g. Best and Heckman, 2012; Gendre *et al.*, 2013; Mingo *et al.*, 2014; Ineson *et al.*, 2015; Tadhunter, 2016; Hardcastle *et al.*, 2007a, 2009; Hardcastle, 2018a), the divide in FR morphology is generally explained as a difference in jet dynamics. The FRII edge-brightened type of Radio Galaxies (RGs) are assumed to have relativistic jets that terminate in hotspots, whereas the edge-darkened FRIs are considered to be disrupted on kiloparsec scales (e.g. Bicknell, 1995; Krause *et al.*, 2012; Laing and Bridle, 2002; Tchekhovskoy and Bromberg, 2016). A long-standing hypothesis is that this FR structural difference is caused by the interaction of jet power and environmental density of the host galaxy, so that equal-powered jets will be disrupted (and thus become FRI) more easily in a rich environment than in a poor one (Bicknell, 1995; Kaiser and Best, 2007). The result by Ledlow and Owen (1996) that the FR luminosity break is dependent on the magnitude of the host galaxy seems to support this explanation, where FRI RGs have higher radio luminosities in brighter host galaxies that are assumed to have a higher density Interstellar Medium (ISM).

The study, however, was based on highly flux-limited FRI and FRII samples with varying redshift

distributions and environments. Thus, the findings may not be applicable to the broader population of RGs (Best, 2009; Lin *et al.*, 2010; Capetti *et al.*, 2017b; Shabala, 2018; Singal and Rajpurohit, 2014; Wing and Blanton, 2011).

Additionally, Vardoulaki *et al.* (2021) show that at 0.75 arcseconds resolution and sensitivity of $2.3 \mu\text{Jy beam}^{-1}$ with the Cosmological Evolution Survey (COSMOS) field, one does not preferably find FRIs in denser environments than FRIIs.

Several surveys followed FR's study (e.g. Baldwin *et al.*, 1985; McGilchrist *et al.*, 1990; Hill and Rawlings, 2003), before large sky surveys came along. Obtaining a large and representative sample of RGs is critical for properly addressing several issues, including:

1. Building the luminosity functions of galaxies,
2. Investigating the properties of the galaxy hosts,
3. Studying environment and cosmic evolution of galaxies, to compare with those of other classes of sources like radio-quiet AGNs and Quiescent galaxies.

Large area surveys, like that of the G23 field in this chapter which consists of around 40 000 sources, provide the opportunity to look at several key issues and base conclusions on a solid statistical foundation. The radio, Infrared (IR) and optical observations made available by recent large-area surveys, in particular, allow for the identification of large numbers of radio sources, particularly DRAGNs, obtain spectroscopic redshifts and determine the properties of the host galaxies.

In this part of the project, I investigate the relationship between luminosity and radio morphology for FRI and FRII galaxies using the EMU (Norris *et al.*, 2011) Early Science data on the Galaxy And Mass Assembly (GAMA; Driver *et al.*, 2011; Leahy *et al.*, 2019)-23 field, from the Australian Square Kilometre Array Pathfinder (ASKAP; Johnston *et al.*, 2008; Hotan *et al.*, 2021). Whereas this study focuses on FRI and FRII sources, there is another study presenting the broader population of radio sources in the G23 field (Gürkan *et al.*, 2022b).

A similar but larger study has been performed by Mingo *et al.* (2019) using the LOFAR Two-Metre Sky Survey (LoTSS; Shimwell *et al.*, 2017). My study is complementary to theirs as I am probing the same class of galaxies at a higher frequency, and a similar parameter space. Therefore, I can test whether the differences between their results and earlier studies are simply due to their lower observing frequency. This survey probes to a lower flux density compared to theirs, although, after correcting for a canonical spectral index, I find the two surveys have an intrinsically comparable sensitivity.

Table 3.1: The numbers of sources that remain after each stage of the value-added processing for G23.

Criterion	# Sources	Percentage of source sample
Initial source extraction	757	n/a
CATWISE2020 Crossmatch (10'')	749	99
CATWISE2020 Crossmatch (2.5'')	706	94
KiDS DR4 Crossmatch (2.5'')	628	83
KiDS DR4 photo z Crossmatch (2.5'')	556	74
GAMA spec z Crossmatch (2.5'')	150	20

Table 3.2: Classification statistics of the G23 sample of DRAGNs. The last column shows the number of sources that have a redshift. The total number of sources is 706.

Morphology	# Sources	Full z range
FRI	195	134
FRII	429	360
HyMOR	30	28
FRx	52	44

3.2 Results and Discussion

The primary goal of my morphological research is to revisit the relationship between the FR class, radio luminosity, and host-galaxy properties, comparing my work to that primarily of [Ledlow and Owen \(1996\)](#) and [Mingo *et al.* \(2019\)](#). After following the methodology outline in Chapter 2, the resulting number of visually identified radio sources amount to 757 (see Table 3.1).

I list the number of sources for each classification in Table 3.2. Uncertain sources refer to those with obvious FRI/FRII morphologies but whose ratios sit on the borderline.

3.2.1 The FRI and FRII radio luminosity break

In the archetypal paper by [Fanaroff and Riley \(1974\)](#), a ‘sharp division’ in luminosity was observed between the two FR classes for low redshift sources. It was later found ([Owen and Ledlow, 1994](#); [Ledlow and Owen, 1996](#)) that this break varied with optical luminosity (see Figure 3.1).

Figures ?? show the same plot as in [Ledlow and Owen \(1996\)](#) but for the sample of G23 DRAGNs compiled in this thesis. While the overall trend is similar to that of Owen & Ledlow, I find a large overlap between FRI and FRII galaxies, and the break that they found (shown by the dashed line in Figures ??) is very much blurred in my data.

To test whether the broadening is due to my use of photometric redshifts, I plot a similar rendition of Figure 3.2 in Figure 3.4, using only sources with a spectroscopic redshift. That plot is in broad agree-

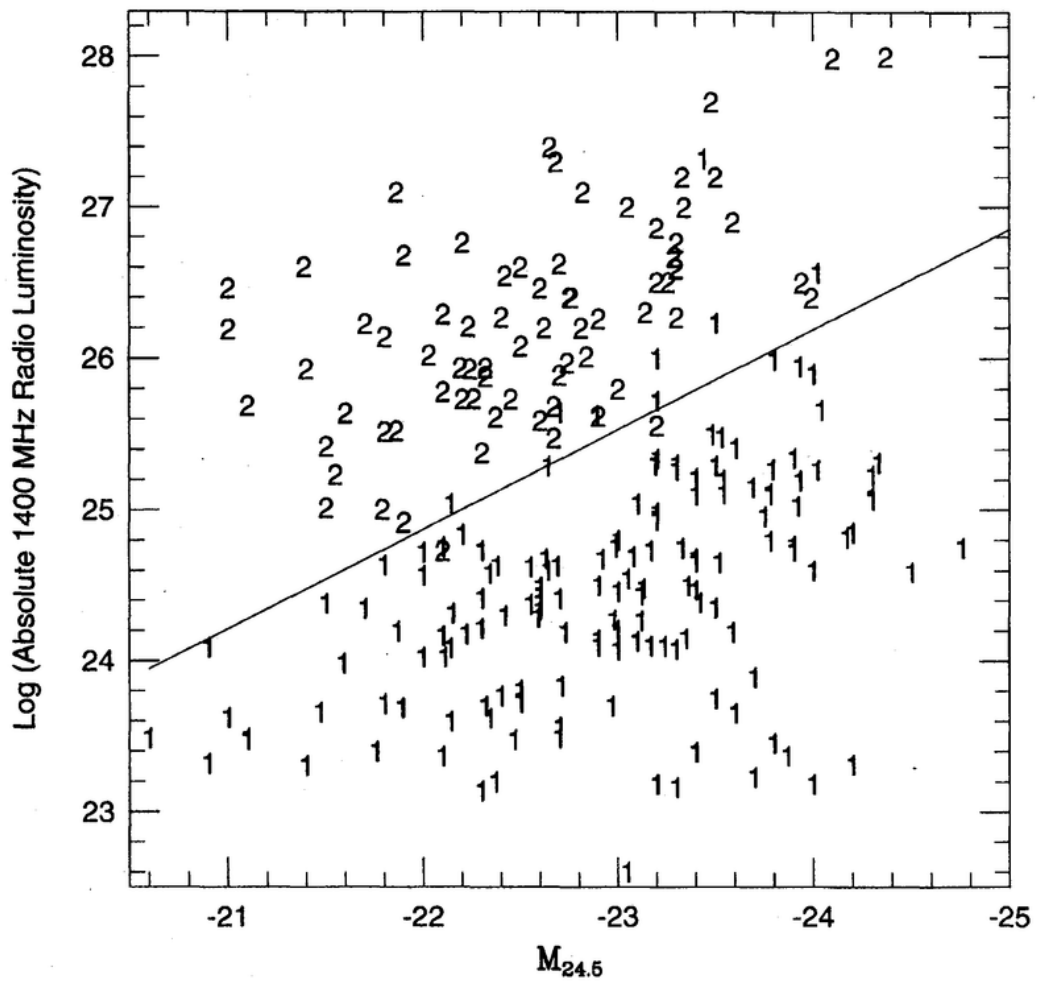


Figure 3.1: An example sample of FRI (1) and FRII (2) objects in the optical magnitude/radio luminosity plane. The line dividing the two classes is also shown in black. Reproduced from Ledlow and Owen (1996).

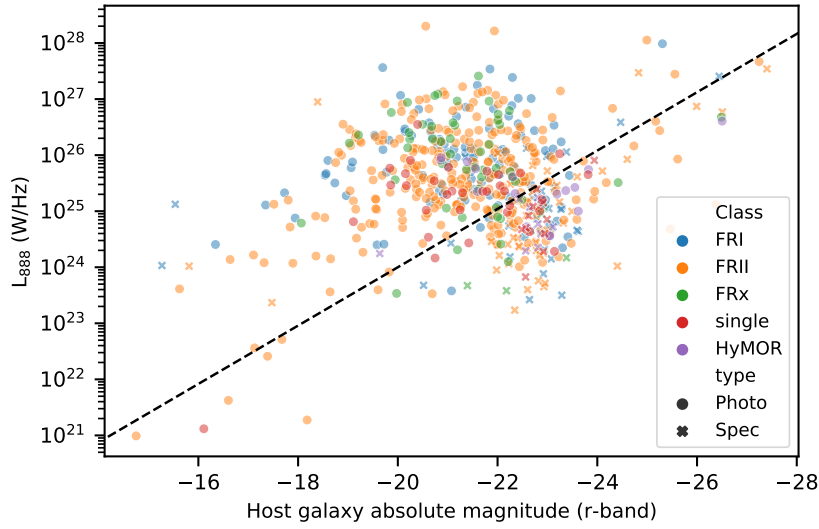


Figure 3.2: A plot showing the correlation between the 888 Mhz radio luminosity and host-galaxy r-band magnitude (an ‘Owen & Ledlow’ plot). This plot shows all the G23 FR populations consisting of 134 FRIs, 360 FRIIs, 44 FRx candidates, and 26 HyMoRS. This does not encapsulate the whole sample, as it only includes sources with both an optical counterpart and a measured redshift. The black dashed line shows the transition between FRI and FRII found by Owen & Ledlow, corrected for different frequency and Hubble constant. Sources that have a photometric redshift from the KiDS catalogue are marked with a cross, while sources with a spectroscopic redshift from the GAMA catalogue are marked with a circle. The bottom plot shows only FRIs and FRIIs, with histograms to show the distribution better.

ment with Figure 3.2, confirming that the broadening is not an artefact caused by photometric redshifts. However, there might be bias due to selection effects as the sample is significantly smaller.

This overlap is clearly different from the early results (Fanaroff and Riley, 1974; Owen and Ledlow, 1994; Ledlow and Owen, 1996) which used samples with much higher flux densities. However, this overlap has also been seen in other studies that probe to lower flux density limits (Best, 2009; Miraghaei and Best, 2017; Mingo *et al.*, 2019). The broadening has been shown by Best (2009) to be caused by a selection effect in the data used by Owen and Ledlow, in that their FRIs were at much lower z than FRIIs, which led to the spurious clean break in their data.

To explore the relationship with luminosity further, I plot 888 MHz luminosity (k -corrected) versus the physical size (in kiloparsecs) for the FRIs and FRIIs of the G23 sample (Figure 3.5). I also show a Kernel Density Estimation (KDE) (Parzen, 1962) plot to depict the probability density function of the sample. Histograms for both axes are included to better illustrate the source distributions. Analytical and numerical models of radio sources consistently show that source evolution in size-luminosity space is complex, and environment-dependent. The exact track a source follows is governed by a competition between the energy injected by the jets, and adiabatic, synchrotron and Inverse Compton losses. Following an initial increase in luminosity with size (Alexander, 2000), the luminosity plateaus and eventually begins to decline at the largest sizes, as the ambient pressure drops and the source expands rapidly (Shabala *et al.*, 2008; Turner and Shabala, 2015). For environments characteristic of galaxy groups and clusters,

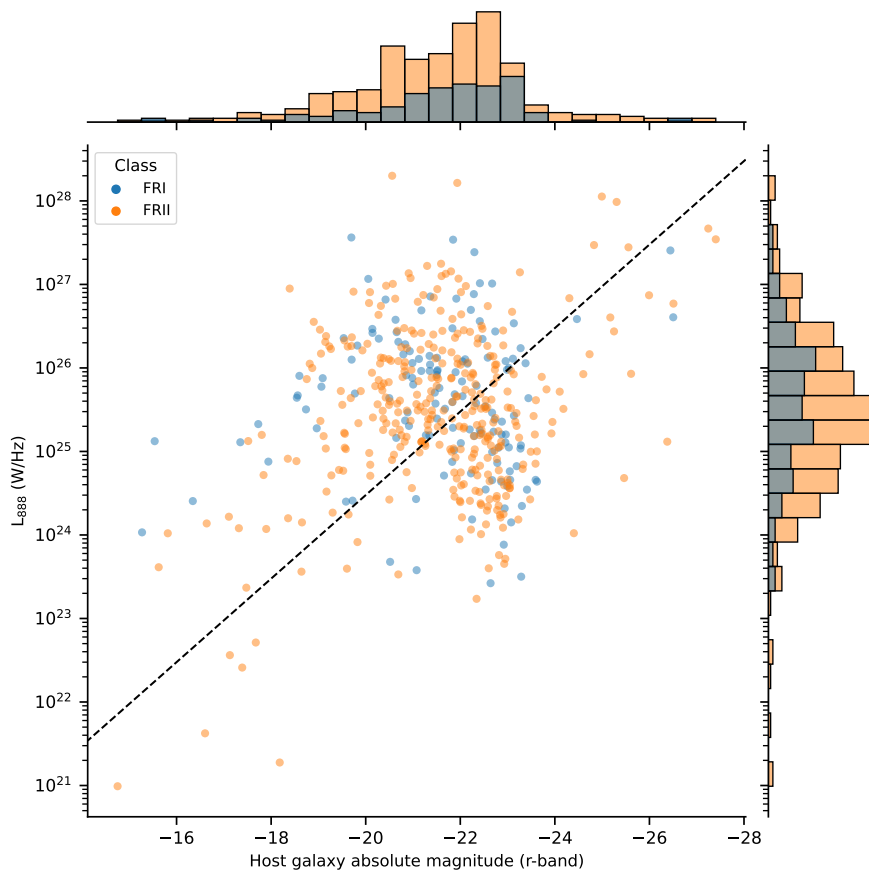


Figure 3.3: A plot showing the correlation between the 888 Mhz radio luminosity and host-galaxy r-band magnitude (an ‘Owen & Ledlow’ plot). This plot shows only the G23 FRI and FR II populations, with histograms to show the distribution better. This does not encapsulate my whole sample, as it only includes sources with both an optical counterpart and a measured redshift. The black dashed line shows the transition between FRI and FR II found by Owen & Ledlow, corrected for different frequency and Hubble constant.

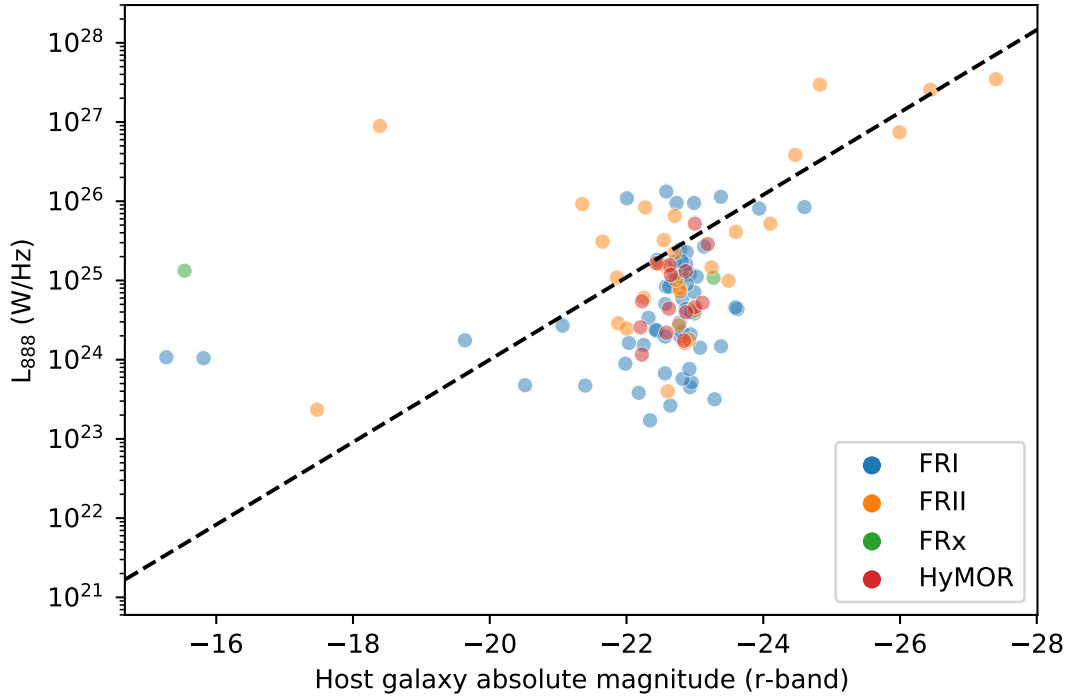


Figure 3.4: Similar to Figure 3.2, here I show only sources with a spectroscopic redshift.

this turnover in luminosity evolution happens on scales somewhat larger than the core radius, typically hundreds of kpc (Hardcastle and Krause, 2013; Yates *et al.*, 2018). I find the median luminosity of the FRIs in the G23 sample to be $5.87 \times 10^{24} \text{ W Hz}^{-1}$ while the FR IIs have a median of $3.20 \times 10^{25} \text{ W Hz}^{-1}$.

Like Mingo *et al.* (2019), I note the lower right corner and top left corner of Figure 3.5 are unoccupied. For the former, it could possibly be due to surface brightness limits, such that a significant population of physically large, low luminosity sources could exist, but is unobservable at present (see also the discussion in Turner and Shabala, 2015; Hardcastle *et al.*, 2019). However, my G23 observations, like the EMU Pilot Survey observations, have a high sensitivity to low surface brightness emission (see Figure 18 in Norris *et al.* (2021)). For the top left corner, it could be affected by radio resolution, so that very luminous (and thus often high redshift) sources of small physical size may not be distinguishable as FRIs and FR IIs galaxies, and so would not appear in this plot.

Despite these selection effects, both FRIs and FR IIs seem to increase in size as a function of luminosity. Furthermore, at a given luminosity, FRIs and FR IIs are of roughly the same physical size.

For FRI galaxies, this could be explained by a selection effect. For a given integrated luminosity of an extended source at a given redshift, larger sources have a lower surface brightness, and are therefore less likely to be detected. Assuming the brightness of an FRI decreases monotonically with radius from the nucleus, more luminous FRIs will have a detectable surface brightness to a larger radius, and so will be observed as being larger than their less luminous counterparts.

However, there are also physical effects which can result in a similar effect, such as the Inverse

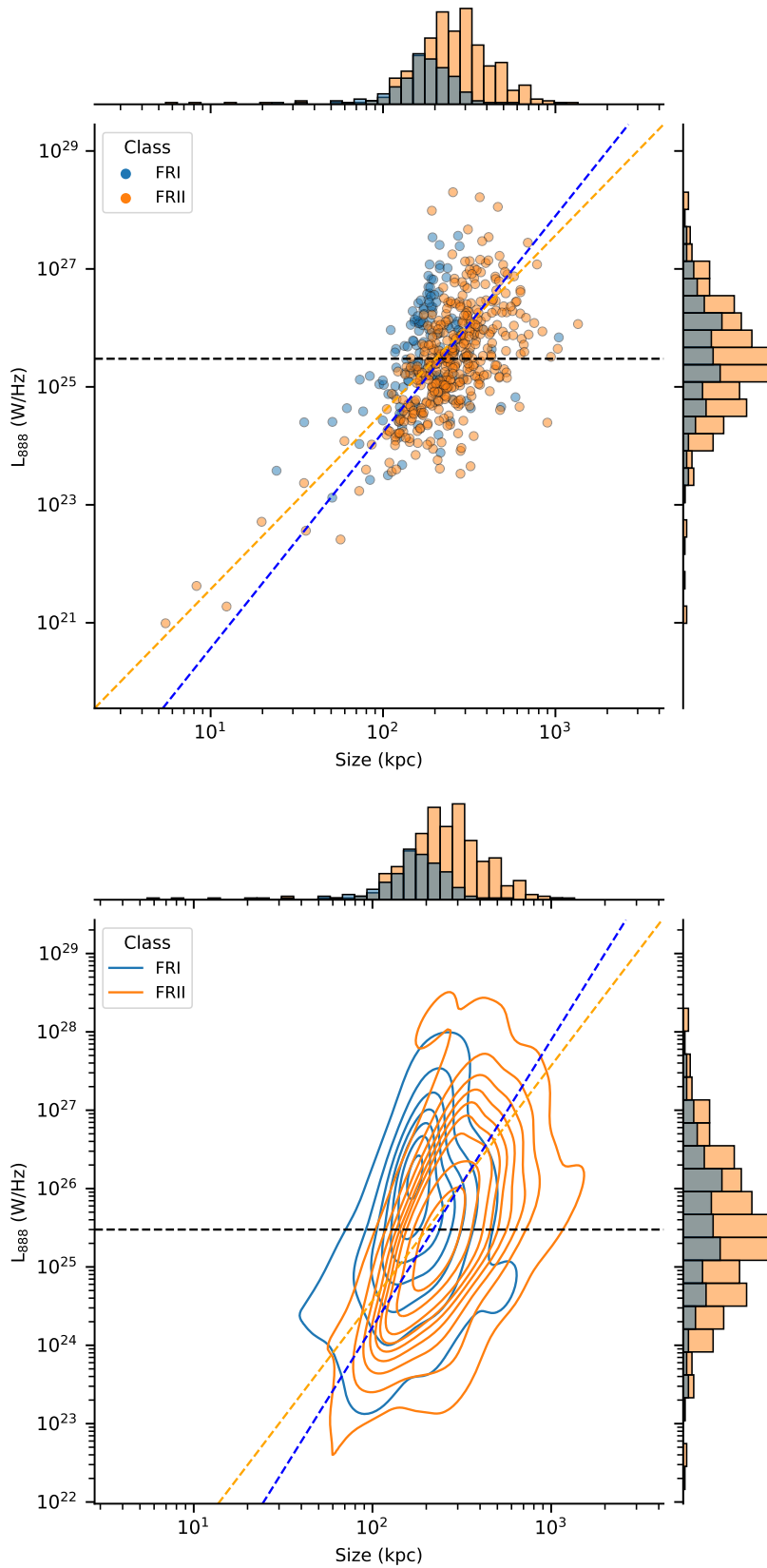


Figure 3.5: Two plots showing the 888 MHz luminosity versus physical size for the FRIs (blue) and FR IIs (orange) populations of my study. The traditional FR luminosity division between both populations is at $\sim 10^{25}$ W Hz $^{-1}$, indicated by the dashed black line. The bottom image is a KDE plot. The slopes of both the FRI (2.08) and FR II (1.82) populations are shown via the dashed blue and orange lines respectively

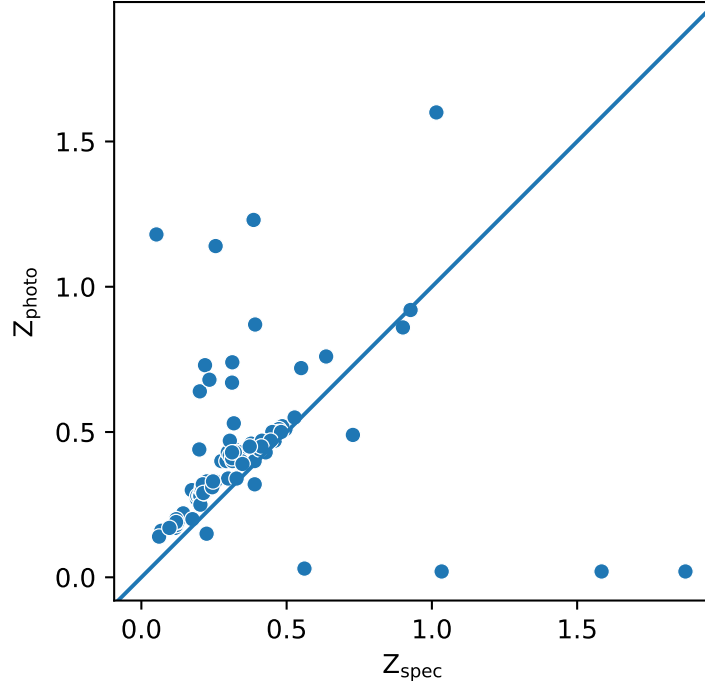


Figure 3.6: A scatter plot of the sources with photometric redshifts (from the KiDS catalogue) against the spectroscopic redshifts from the GAMA catalogue of the G23 sample. The diagonal line is a one-to-one line.

Compton cooling of the synchrotron-emitting electrons by the cosmic microwave background for high redshift sources, which will also reduce the size of less luminous sources.

Such effects do not apply to **FR II** type radio galaxies, where the emission is dominated by hot-spots where surface brightness sensitivity is not a major factor in their detectability. However, it could be argued that if the connecting jets fall below the surface brightness sensitivity limit, then the hotspots might not be recognised as components of a single **FR II**.

I conclude that while there is a clear relationship between the observed size of an **FRI** or **FR II** and its luminosity, it is currently unclear whether this is primarily due to intrinsic physical causes or to selection effects.

3.2.2 Redshift distribution

To study the redshift distribution of the G23 sample, I use both spectroscopic (from **GAMA**) and photometric redshifts (from Kilo-Degree Survey (**KiDS**)). To check the reliability of the photometric redshifts, I plot them against the spectroscopic redshifts from **GAMA**, in Figure 3.6. I find that 65% of redshifts agree within $\Delta z \leq 0.1$ so that trends that I observe based on photometric redshifts are in most cases reliable.

In Figure 3.7, I plot the redshift distribution of the G23 sample, confined to those sources with an optical **KiDS** counterpart. There is a rapid drop-off of both **FRI** and **FR II** beyond $z \sim 1.4$, with **FRI**s dropping

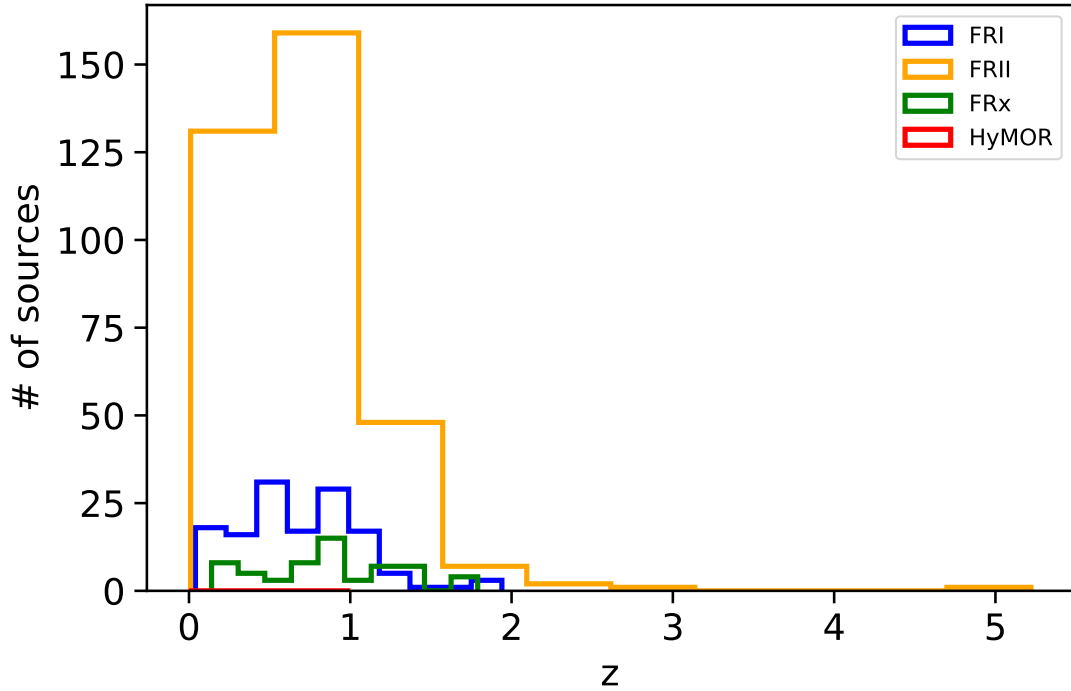


Figure 3.7: Plot showing the distribution of sources (150) with optical counterparts and linear bins in G23 as a function of redshift.

more precipitously than FR IIs.

One factor contributing to this drop-off may be the ‘redshift desert’ (Renzini and Daddi, 2009), where redshifts are hard to obtain at the interval between ~ 1.4 -3 redshift because $[\text{O II}]$ at 374 nanometre and the 400 nanometre break have moved out of the observed wavelength range. Nevertheless, I find that although both the FR populations have a median redshift around 0.5, the FR II sources extend up to a higher redshift compared to the FR I class, which cannot be caused by the ‘redshift desert’ effect.

Below $z = 1$, the redshift distributions are broadly similar, suggesting that FR I and FR II co-exist in the Universe, and that the ratio of FR I to FR II radio galaxies does not depend on the evolution of their host galaxies or host dark matter halos. However, a two-sample Kolmogorov-Smirnov (K-S) test for my FR I and FR II populations gives a p-value of 7.31×10^{-6} , so I can reject the null hypothesis that the FR I and FR II samples are drawn from the same parent population. The difference is probably caused by the lower luminosity of the FR Is, so that a smaller fraction are above the sensitivity limit, particularly at high redshift.

3.2.3 FRx sources

As discussed in Section 2.3, I find a small subset (52 sources; $\sim 6\%$) of the main sample that show either a FR II or FR I morphology, depending on the contour levels or grey-scale used, and we label these as FRx sources. These are sources in which the overall extent of the source is only a factor of ~ 2 larger than the

beam size (giving a R_{FR} ratio of < 0.5), and so in these cases the classical definition as given by Fanaroff and Riley (1974) is ambiguous. I stress that I attribute this to an observational selection effect, rather than to any physical cause. I presume this situation did not arise in the earlier work because earlier surveys are less sensitive, the sources are much stronger, have a larger angular scale. I have labelled such sources a separate class; FRx in the G23 sample. Presumably, higher resolution observations would identify these as either FRI or FRII.

3.2.4 HyMoR sources

HyMoRS were first identified by Gopal-Krishna and Wiita (2000), who argued that HyMoRS are a separate class of object alongside the large-scale RGs of FRI and FRII types and typically display FRI radio structures on one side of the nucleus and FRII on the other. These sources provide the opportunity to investigate two distinct morphologies that are a result of a single central engine, potentially providing a unique insight into the cause of the dichotomy between the two FR classes. Previous studies on HyMoRS have been limited to survey searches (e.g. Banfield *et al.*, 2015; Kapińska *et al.*, 2017), and milliarcsecond-scale investigations using Very Long Baseline Array (VLBA; Cegłowski *et al.*, 2013). Recent studies have since expanded this field using for example, the Faint Images of the Radio Sky at Twenty-centimeters (FIRST) survey and Very Large Array (VLA) observations (e.g. Harwood *et al.*, 2020; Kumari and Pal, 2021). The nature of these systems remains under debate, but they are likely a heterogeneous class.

In the G23 sample, a small subset of my sources (30 sources: $\sim 3\%$) were discovered to have this hybrid morphology. I plot them in Figure 3.2, and find my population of HyMoRS sit roughly in the region of overlap between the FRI and FRII populations. This supports the idea that HyMoRS may be an intermediate or evolutionary stage between FRI and FRII.

I show some examples of candidate HyMoRS in Figure 3.8. While I only identify a small fraction of hybrid candidates in the G23 sample, it does significantly increase the number of candidate HyMoRS. I note that Mingo *et al.* (2019) obtained a similar result to us, identifying $\sim 5\%$ with the LoTSS.

3.3 Conclusion

I have carried out a morphological investigation of 757 AGN with extended radio emission in the G23 field, leading to the following conclusions:

- I confirm the results of Mingo *et al.* (2019) that radio luminosity does not reliably predict whether a source is FRI and FRII morphology, and show that these results are also true at the higher frequencies and lower flux densities used here.

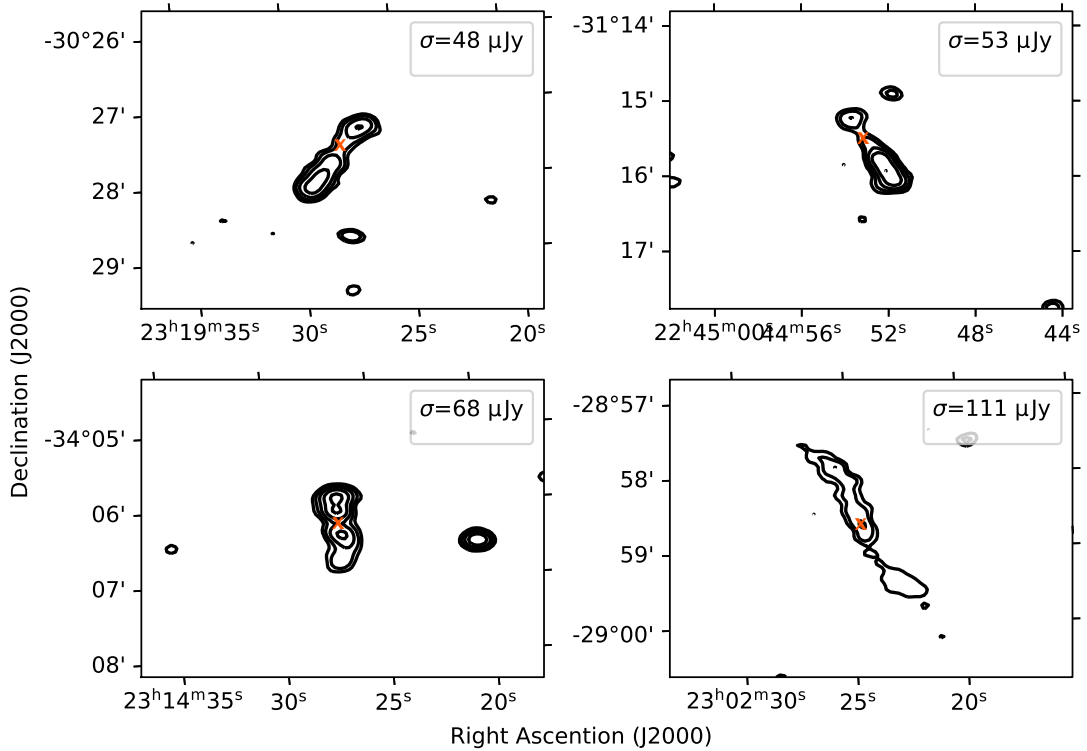


Figure 3.8: Examples of sources classified as HyMoRS in the G23 sample. The contour levels are: 3, 6, 12, 24, 48 σ (as indicated in each panel). The position of the nucleus is denoted with the orange dot. The coordinates refer to the G23 radio image.

- While **FRII** radio galaxies extend to higher redshifts than **FRI**s, I find their redshift distributions at low redshift are similar, although statistically different in terms of shape, median and luminosity. I speculate that the small difference is caused by sensitivity,
- **DRAGNs** can be found over a wide range of radio luminosity. While **FRII**s tend to be at higher luminosities than **FRI**s, as was the result by [Fanaroff and Riley \(1974\)](#), there is a significant luminosity overlap in between the two classes. This result is in agreement with the low-frequency study by [Mingo *et al.* \(2019\)](#).
- I find hybrid **FRI/FRII** galaxies (**HyMoRS**) to occupy an intermediate position in luminosity between the **FRI**s and **FRII**s classes. This is consistent with the hypothesis that they are a genuine class of hybrid morphology rather than some observational artefact.
- I find a small subset of small sources (52 sources; $\sim 6\%$) showed either a **FRII** or **FRI** morphology, depending on the contour levels or grey-scale used and I class these as **FRx**. Higher resolution observations would presumably identify them as either **FRI** or **FRII**. The percentage of these **FRx** sources are negligible and they have not been used for any derived conclusions, but have been plotted in presented figures in this chapter for comparison only.

3.4 Source Catalogue

The GAMA-23 radio source catalogue of FR, FRx and hybrid sources is presented here. There are a total of 706 sources distributed across ten tiles. This catalogue only includes sources that have a CATWISE counterpart (within 2.5 arcsec). The column names and descriptions are given below:

- Source Name: the name given to the source based on its coordinates
- RA: the right ascension of the source in hours, minutes and seconds (radio)
- DEC: the declination of the source, in degrees, arcminutes and arcseconds (radio)
- Flux Density: the integrated flux of sources given in Jansky
- Size: the size of the DS9 regions given in arcseconds
- a : the distance between peaks of emission as determined by the ratio algorithm
- b : the extent of the source as determined by the ratio algorithm
- PA: the position angles of the sources as outputted by the algorithm
- a/b_{\max} : calculation of a/b with maximum values of b that's reasonable for the data
- a/b_{\min} : calculation of a/b with minimum values of b that's reasonable for the data
- Class: the classification as determined by the ratios
- KiDS ID: the ID as given in the [KiDS DR4](#) catalogue
- MAG: the r-band magnitude as given in the [KiDS DR4](#) catalogue
- Z: the redshift as given from [GAMA](#) spectroscopic or [KiDS DR4](#) photometric

Table 3.3: The value-added catalogue of all found DRAGNs in the G23 field

Source Name	RA (J2000) (deg)	DEC (J2000) (deg)	Flux Density (Jy)	Size (")	a (")	b (")	PA ($^{\circ}$)	a/b_{\max}	a/b_{\min}	Class	KiDS ID	Mag (r-band)	Z
J224812.2-300437	342.05	-30.077	0.002	15.94	13.11	24.50	2.50	0.49	0.60	FRx	KiSDR4 J224812.283-300436.03	20.91	0.46
J224103.1-335818	340.26	-33.972	0.002	19.13	12.71	25.43	2.11	0.46	0.55	FRx	KiSDR4 J224103.126-335818.11	21.66	0.85
J223757.5-324602	339.49	-32.767	0.003	15.48	11.20	25.47	1.20	0.40	0.49	FRx	KiSDR4 J223757.224-324604.83	25.09	1.30
J230458.5-315049	346.24	-31.847	0.003	23.05	26.14	26.14	1.37			single	KiSDR4 J230458.488-315048.62	17.87	0.24
J224311.1-332250	340.80	-33.381	0.004	17.24	17.24	26.26	0.98			single	KiSDR4 J224311.068-332250.04	23.56	1.05
J232441.0-302349	351.17	-30.397	0.003	17.06	17.06	26.28	2.07			single	KiSDR4 J232440.995-302348.55	24.43	1.05
J223354.6-334940	338.48	-33.827	0.003	17.84	15.21	26.97	2.99	0.52	0.62	FRII	KiSDR4 J224909.143-315114.04	22.03	0.97
J224909.2-315114	342.29	-31.854	0.004	18.48	17.53	27.53	1.63			single			
J230025.2-344814	345.11	-34.803	0.004	21.51	27.64	27.64	0.43			single			
J224247.8-315340	340.70	-31.895	0.007	17.82	27.73	27.73	3.01			single	KiSDR4 J224247.888-315340.17	23.95	0.98
J223605.5-352055	339.02	-35.349	0.004	20.16	27.85	27.85	3.02			single	KiSDR4 J223605.517-352054.38	20.65	1.12
J224819.7-351131	342.08	-35.192	0.002	21.74	18.83	28.23	0.58	0.61	0.73	FRII	KiSDR4 J224819.749-351130.28	23.01	1.06
J224339.2-315232	340.91	-31.875	0.005	17.92	18.31	28.31	0.13			single	KiSDR4 J224339.133-315232.00	19.61	0.47
J224600.6-314437	341.50	-31.743	0.003	17.92	14.43	28.37	1.44			single	KiSDR4 J224600.630-314436.17	22.96	1.36
J230443.9-331856	346.18	-33.316	0.003	22.44	11.99	28.83	0.64	0.38	0.46	FRI	KiSDR4 J230443.919-331856.05	22.99	0.91
J230910.8-335900	347.30	-33.982	0.003	2	14.43	29.18	3.11	0.46	0.54	FRx	KiSDR4 J230910.759-335859.28	17.76	0.19
J232043.7-320458	350.18	-32.082	0.002	21.22	16.01	29.31	1.15	0.50	0.60	single	KiSDR4 J232043.649-320457.75	23.25	1.03
J232029.1-294705	350.12	-29.784	0.004	17.47	12.86	29.34	2.13	0.40	0.47	FRII	KiSDR4 J232029.245-294703.40	23.97	0.79
J225730.1-343102	344.38	-34.517	0.001	16.06	12.86	29.64		0.40	0.47	FRI	KiSDR4 J225730.131-343101.46	23.81	0.79
J232620.2-312610	351.58	-31.435	0.005	16.55	13.46	29.67	1.19	0.42	0.50	FRI	KiSDR4 J232619.588-312612.08	24.54	0.53
J224006.6-303250	340.03	-30.547	0.006	17.65	17.65	29.76	1.65			single	KiSDR4 J224006.711-303250.99	24.55	1.09
J231513.4-333148	348.81	-33.530	0.002	20.96	14.00	29.79	0.88	0.43	0.51	single	KiSDR4 J231513.409-333147.71	22.41	0.83
J231614.4-293043	349.06	-29.512	0.003	22.26	14.00	29.84	1.67	0.43	0.51	FRx	KiSDR4 J231614.340-293042.48	19.81	0.42
J231112.0-302441	347.80	-30.411	0.002	19.70	14.66	29.94	1.32	0.45	0.53	FRx			
J232126.6-343448	350.36	-34.580	0.006	17.94	17.94	29.99	0.69			single	KiSDR4 J232126.537-343446.82	18.74	0.39
J225309.0-320318	343.29	-32.055	0.005	17.90	30.06	30.06	2.82			single			
J224133.3-332420	340.39	-33.405	0.005	19.72	30.13	30.13	0.69			single	KiSDR4 J224133.274-332418.61	21.94	0.85
J232402.7-311928	351.01	-31.325	0.005	16.69	30.14	30.14	0.92			single	KiSDR4 J232402.664-311927.32	17.14	0.01
J230151.8-301927	345.47	-30.324	0.009	16.04	30.15	30.15	1.91			single	KiSDR4 J230151.762-301927.05	24.14	1.09
J230501.5-303620	346.25	-30.605	0.003	20.42	30.17	30.17	1.57			single	KiSDR4 J230501.496-303619.75	22.89	0.77
J224520.8-344608	341.34	-34.769	0.004	17.48	14.14	30.38	0.77	0.43	0.51	FRx	KiSDR4 J224520.820-344607.36	22.04	1.07
J224519.8-324432	341.33	-32.741	0.003	16.72	18.20	30.59	1.80	0.55	0.65	FRII	KiSDR4 J224519.711-324431.54	23.64	0.97
J231217.4-334809	348.07	-33.801	0.007	19.72	15.81	30.68	2.82	0.48	0.56	FRx	KiSDR4 J231217.435-334809.21	20.74	0.58
J224731.3-320316	341.88	-32.055	0.002	21.67	24.12	30.85	1.82	0.72	0.85	FRII	KiSDR4 J224731.227-320315.74	21.83	0.60
J223752.5-304047	339.47	-30.680	0.006	25.56	18.03	30.96	0.84	0.54	0.63	FRII	KiSDR4 J223752.557-304047.02	19.00	0.32
J231833.8-314120	349.64	-31.688	0.005	19.95	12.29	31.01	2.56	0.37	0.43	FRI	KiSDR4 J231833.823-314119.77	21.75	0.81
J231349.7-312208	348.46	-31.368	0.003	21.60	16.01	31.40	2.18	0.47	0.55	FRx			
J231746.8-314900	349.45	-31.817	0.007	19.95	12.70	31.64	0.47	0.37	0.44	FRI	KiSDR4 J231746.453-314859.46	24.98	0.22

Continued on next page

Table 3.3 – Continued from previous page

Source Name	RA (J2000) (deg)	DEC (J2000) (deg)	Flux Density (Jy)	Size (")	a (")	b (")	PA (°)	a/b_{\max}	a/b_{\min}	Class	KIDS ID	Mag (r-band)	Z
J225642.4-292443	344.18	-29.412	0.002	21.24	21.68	31.66	1.92	0.63	0.74	FR II	KIDS DR4 J225642.358-292442.98	24.05	0.82
J231112.9-350138	347.80	-35.028	0.003	23.30	19.94	31.75	0.39	0.58	0.68	FR II	KIDS DR4 J231112.932-350138.56	23.06	0.88
J231321.4-285223	348.34	-28.873	0.005	19.48	15.81	32.04	1.96	0.46	0.54	FR X	KIDS DR4 J231321.391-285223.03	22.72	1.22
J231116.6-293128	347.82	-29.523	0.005	17.89	18.20	32.14	2.74	0.53	0.61	FR II	KIDS DR4 J231116.633-293127.86	23.64	0.94
J224447.5-332528	341.20	-33.424	0.006	18.29	15.81	32.16	0.38	0.46	0.53	FR X	KIDS DR4 J224447.549-332527.89	19.20	0.14
J223840.1-295303	339.67	-29.884	0.008	18.72	13.47	32.18	1.30	0.39	0.45	FR I	KIDS DR4 J223840.111-295302.98	22.81	1.30
J223346.9-335642	338.44	-33.945	0.008	18.93	32.64	32.64	1.41			single	KIDS DR4 J223346.890-335641.88	21.03	0.69
J223414.5-293541	338.56	-29.594	0.023	17.27	14.14	32.70	0.78	0.40	0.47	FR I	KIDS DR4 J223414.136-293537.76	24.26	0.60
J224634.0-334135	341.64	-33.692	0.002	19.05	14.54	32.73	2.98	0.41	0.48	FR I	KIDS DR4 J224633.955-334134.59	19.99	0.54
J232758.1-320340	351.99	-32.061	0.006	19.53	18.03	32.83	2.20	0.51	0.59	FR II	KIDS DR4 J232757.889-320341.12	23.67	0.70
J230150.1-354532	345.46	-35.759	0.004	19.03	19.04	33.17	0.41	0.53	0.62	FR II			
J224622.7-293700	341.59	-29.616	0.003	18.49	14.41	33.17	1.18	0.40	0.47	FR I			
J231202.0-301313	348.01	-30.220	0.003	21.19	28.04	33.18	0.74	0.79	0.91	FR II	KIDS DR4 J224622.675-293658.20	21.45	0.77
J224346.3-324146	340.94	-32.695	0.005	42.28	24.89	33.19	0.15	0.70	0.81	FR II	KIDS DR4 J231201.987-301312.12	22.39	0.80
J224739.7-325200	341.92	-32.868	0.003	22.23	22.86	33.29	0.07	0.64	0.74	FR II	KIDS DR4 J224739.828-325158.49	23.45	0.62
J232402.4-345641	351.01	-34.945	0.013	18.29	13.08	33.34	0.76	0.36	0.42	FR I	KIDS DR4 J232402.336-345640.94	21.55	0.76
J225814.1-323640	344.56	-32.611	0.010	18.78	16.01	33.34	0.96	0.45	0.52	FR X	KIDS DR4 J225814.050-323639.57	21.92	0.81
J231003.1-343927	347.51	-34.658	0.003	17.71	13.19	33.40	2.48	0.37	0.43	FR I	KIDS DR4 J231003.552-343933.04	24.58	1.94
J230911.0-341245	347.29	-34.212	0.008	20.77	33.45	33.45	1.23			single	KIDS DR4 J230910.977-341245.48	19.06	0.37
J230950.8-300551	347.46	-30.097	0.006	21.66	33.53	33.53	0.79			single			
J223508.1-293923	338.78	-29.656	0.008	20.59	33.56	33.56	0.93			single	KIDS DR4 J223508.076-293921.66	21.53	0.94
J224454.3-323150	341.23	-32.531	0.019	19.24	11.90	33.57	2.39	0.33	0.38	FR I	KIDS DR4 J224453.902-323143.82	24.76	1.32
J232510.3-342318	351.29	-34.390	0.003	20.08	25.43	33.63	2.86	0.70	0.82	FR II	KIDS DR4 J232510.269-342317.82	20.51	0.54
J231830.5-311406	349.63	-31.235	0.004	19.79	19.04	33.90	2.73	0.52	0.61	FR II	KIDS DR4 J231830.604-311406.45	25.20	1.21
J224308.0-315807	340.78	-31.971	0.006	21.61	18.20	33.93	0.28	0.50	0.58	FR X	KIDS DR4 J224307.967-315807.43	22.90	1.11
J223351.6-330217	338.47	-33.038	0.004	20.02	19.04	34.01	1.23	0.52	0.60	FR II	KIDS DR4 J223351.595-330216.97	22.14	0.83
J22402.4-342741	351.01	-34.460	0.004	20.58	34.02	34.02	1.76			single	KIDS DR4 J232402.489-342739.37	22.17	0.90
J222224.5-340322	350.60	-34.055	0.007	19.17	18.20	34.48	1.40	0.49	0.57	FR X	KIDS DR4 J232224.443-340321.31	21.30	0.83
J224708.8-300824	341.79	-30.140	0.005	20.96	20.16	34.53	2.91	0.54	0.63	FR II	KIDS DR4 J224708.852-300822.88	19.95	0.49
J224544.7-340029	341.44	-34.008	0.002	24.70	28.13	34.55	2.42	0.76	0.88	FR II	KIDS DR4 J224544.501-340028.34	23.50	0.81
J223630.3-302234	339.13	-30.376	0.003	19.71	16.65	34.57	1.32	0.45	0.52	FR X	KIDS DR4 J223630.615-302235.38	24.91	0.64
J231958.7-293824	349.99	-29.640	0.012	17.76	16.77	34.68	2.09	0.45	0.52	FR X			
J223325.6-301336	338.36	-30.227	0.014	18.26	34.73	34.73	0.86			single	KIDS DR4 J223325.572-301335.18	19.38	0.49
J231245.6-335934	348.19	-33.993	0.009	19.72	18.20	34.75	1.87	0.49	0.56	FR X	KIDS DR4 J231245.666-335928.28	25.29	1.66
J224237.1-302111	340.65	-30.353	0.023	20.08	34.78	34.78	1.06			single	KIDS DR4 J224237.092-302110.69	19.40	0.47
J23135.9-330448	337.90	-33.080	0.007	19.48	35.19	35.19	0.54			single			
J231341.4-344102	348.42	-34.685	0.010	23.22	17.68	35.39	2.39	0.47	0.54	FR X			
J230713.0-311436	346.80	-31.244	0.005	22.43	19.04	35.53	0.33	0.50	0.58	FR II			
J232603.5-331744	351.51	-33.295	0.004	21.84	27.10	35.55	0.71	0.71	0.82	FR II	KIDS DR4 J232603.425-331741.76	17.96	0.32

Continued on next page

Table 3.3 – Continued from previous page

Source Name	RA (J2000) (deg)	DEC (J2000) (deg)	Flux Density (Jy)	Size (")	a (")	b (")	PA (°)	a/b_{\max}	a/b_{\min}	Class	KIDS ID	Mag (r-band)	Z
J225443.8-314850	343.68	-31.815	0.014	20.29	15.00	35.55	0.04	0.39	0.45	FRI	KiDSDR4 J231854.808-324220.65	20.43	0.61
J231854.8-324221	349.73	-32.704	0.009	23.21	15.81	35.64	0.06	0.41	0.48	FRI	KiDSDR4 J224003.022-344742.61	20.57	0.79
J224003.0-344743	340.01	-34.795	0.004	27.54	15.54	35.68	1.93	0.41	0.47	FRI	KiDSDR4 J223918.923-295919.19	20.53	0.54
J223918.9-295919	339.83	-29.989	0.005	21.12	17.68	35.81	1.41	0.46	0.53	FRx	KiDSDR4 J232033.390-304023.44	23.20	1.02
J232033.4-304024	350.14	-30.673	0.008	22.03	35.88	35.88	0.05	0.48	0.55	single	KiDSDR4 J224701.872-321746.82	22.56	0.89
J232112.0-292455	350.30	-29.416	0.001	18.01	18.39	35.93				FRx	KiDSDR4 J225707.439-303421.37	21.61	0.75
J224701.9-321747	341.76	-32.296	0.015	19.19	35.94	35.94	0.31	0.41	0.47	single	KiDSDR4 J232233.812-301013.00	18.90	0.38
J225707.4-303421	344.28	-30.575	0.013	20.47	15.81	35.97	2.72	0.41	0.47	FRI	KiDSDR4 J231311.107-290038.38	23.94	1.42
J232233.9-301011	350.64	-30.170	0.020	22.03	36.02	36.02	2.83	0.52	0.60	single	KiDSDR4 J225416.970-293431.29	21.81	0.77
J231311.1-290038	348.30	-29.010	0.009	19.87	20.16	36.03	2.62	0.52	0.60	FRx	KiDSDR4 J233500.951-330520.90	19.78	0.56
J225417.1-293433	343.57	-29.575	0.005	21.13	20.16	36.23	0.07	0.52	0.60	FRx	KiDSDR4 J231337.751-290850.98	23.26	0.99
J233500.9-330522	338.76	-33.089	0.014	23.38	36.34	36.34	2.67	0.64	0.73	single	KiDSDR4 J223339.318-293517.44	23.12	1.26
J231607.0-323735	349.03	-32.626	0.006	21.32	24.91	36.49	0.47	0.48	0.55	single	KiDSDR4 J23150.565-291046.95	21.35	0.84
J230446.1-335155	346.19	-33.866	0.004	23.37	36.71	36.78	1.09	0.48	0.55	FRx	KiDSDR4 J231807.175-334353.45	25.47	1.11
J231337.7-290851	348.41	-29.148	0.006	23.84	19.04	36.91	1.22	0.48	0.55	FRx	KiDSDR4 J232004.165-314501.61	18.31	0.34
J233339.3-293518	338.41	-29.588	0.008	22.31	12.75	36.98	2.97	0.32	0.37	FRI	KiDSDR4 J230406.098-303023.82	21.89	0.94
J230908.6-312601	347.29	-31.434	0.034	23.08	14.58	37.05	0.59	0.37	0.42	FRx	KiDSDR4 J231553.543-290538.98	24.34	1.15
J23150.7-291047	350.46	-29.179	0.013	19.00	12.75	37.06	0.85	0.42	0.48	FRx	KiDSDR4 J223110.727-345523.72	23.15	0.97
J231807.2-334354	349.53	-33.732	0.002	16.90	16.69	37.06	0.85	0.42	0.48	FRx	KiDSDR4 J224408.112-341442.93	18.55	0.35
J232004.1-314502	350.02	-31.751	0.016	21.29	22.50	37.14	0.03	0.57	0.65	single	KiDSDR4 J230010.643-301537.75	23.21	0.96
J230406.1-303024	346.03	-30.507	0.004	22.90	17.68	37.16	1.55	0.44	0.51	FRx	KiDSDR4 J223208.727-331532.31	23.24	0.92
J231553.6-290539	348.97	-29.094	0.012	21.75	17.68	37.30	0.21	0.44	0.51	FRx	KiDSDR4 J223207.769-295425.98	19.91	0.46
J223110.8-345524	337.79	-34.924	0.023	19.47	16.77	37.41	0.67	0.42	0.48	FRx	KiDSDR4 J231158.311-290437.58	22.78	1.05
J224408.1-341443	341.03	-34.245	0.003	24.35	27.35	37.51	0.50	0.68	0.78	FRx	KiDSDR4 J230943.273-293529.89	19.89	0.42
J230010.6-301538	345.04	-30.261	0.029	18.22	14.68	37.54	0.34	0.37	0.42	FRx	KiDSDR4 J231117.873-350551.89	21.60	0.89
J232207.8-295426	338.04	-33.261	0.032	20.18	17.87	37.59	2.96	0.45	0.51	FRx	KiDSDR4 J231003.719-344309.69	20.06	0.54
J231158.3-290438	347.99	-29.077	0.010	23.98	17.87	37.61	1.88	0.45	0.51	FRx	KiDSDR4 J223261.122-311639.65	22.17	0.87
J230943.3-293530	347.43	-29.592	0.016	22.42	13.62	37.65	1.70	0.34	0.39	FRx	KiDSDR4 J225021.005-333642.42	20.80	0.86
J231117.9-350552	347.82	-35.097	0.009	23.04	28.80	37.72	0.87	0.62	0.71	FRx	KiDSDR4 J225857.954-293235.35	24.44	0.49
J231003.8-344310	347.52	-34.720	0.015	22.11	20.89	38.11	2.20	0.51	0.59	FRx	KiDSDR4 J225736.887-303333.88	22.99	1.37
J232612.1-311640	351.55	-31.277	0.005	21.51	18.20	38.14	1.77	0.45	0.51	FRx	KiDSDR4 J225444.526-335445.66	15.90	0.49
J225021.0-333642	342.59	-33.611	0.003	17.67	14.84	38.34	0.82	0.36	0.41	FRx	KiDSDR4 J225349.090-340922.99	22.75	1.39
J223832.8-304711	339.64	-30.787	0.008	23.31	21.51	38.64	0.66	0.52	0.59	FRx			
J232719.7-322326	339.33	-32.391	0.034	18.93	14.14	38.69	0.90	0.34	0.39	FRx			
J225857.5-293235	344.74	-29.543	0.020	19.61	16.77	38.71	1.97	0.41	0.46	FRx			
J225736.9-303334	344.40	-30.559	0.031	24.94	18.20	38.83	2.78	0.44	0.50	FRx			
J225444.5-335446	343.69	-33.915	0.011	25.48	22.50	39.09	0.07	0.54	0.61	FRx			
J225348.9-340925	343.45	-34.157	0.042	21.18	17.50	39.12	0.42	0.42	0.48	FRx			

Continued on next page

Table 3.3 – Continued from previous page

Source Name	RA (J2000) (deg)	DEC (J2000) (deg)	Flux Density (Jy)	Size (")	a (")	b (")	PA (°)	a/b_{\max}	a/b_{\min}	Class	KIDS ID	Mag (r-band)	Z
J232110.0-310200	350.29	-31.033	0.007	23.81	39.13	1.07	1.07			single	KiDSDR4 J232109.987-310159.36	19.68	0.31
J225751.4-343040	344.47	-34.511	0.005	23.97	25.50	39.18	0.20	0.61	0.70	FR II	KiDSDR4 J225751.381-343039.45	20.96	0.71
J225557.4-292026	343.99	-29.343	0.002	21.27	24.57	39.37		0.59	0.67	FR II	KiDSDR4 J225557.353-292026.44	21.12	0.64
J222955.8-324424	337.48	-32.740	0.011	20.82	18.20	39.43	1.34	0.43	0.49	FR I			
J230100.3-303913	345.25	-30.657	0.013	24.13	29.17	39.45	3.14	0.70	0.79	FR II	KiDSDR4 J230100.272-303913.41	18.63	0.04
J230642.4-311820	346.68	-31.306	0.004	22.43	31.64	39.69	0.52	0.75	0.85	FR II			
J231915.3-320032	349.81	-32.009	0.035	21.06	39.70	1.97				single			
J232137.9-314947	350.41	-31.829	0.006	26.51	13.20	39.78	0.50	0.31	0.35	FR I	KiDSDR4 J231915.329-320031.98	24.07	1.12
J223623.2-331420	339.10	-33.239	0.035	20.02	17.50	39.96	3.03	0.41	0.47	FR I	KiDSDR4 J223623.157-331419.66	22.14	0.88
J224108.2-292131	340.28	-29.358	0.012	21.74	17.68	40.08	0.55	0.42	0.47	FR I	KiDSDR4 J224108.227-292130.41	22.20	0.86
J231518.2-290727	348.83	-29.124	0.018	23.41	18.20	40.08	0.28	0.43	0.48	FR I	KiDSDR4 J231518.072-290724.95	21.54	0.51
J232121.4-351645	350.34	-35.279	0.012	23.28	40.15	0.52				single	KiDSDR4 J232121.646-351642.35	21.67	0.59
J223103.1-344733	337.76	-34.792	0.006	21.58	20.62	40.23	1.39	0.48	0.55	FRx	KiDSDR4 J223103.332-344730.23	23.89	1.34
J223412.6-302009	338.55	-30.335	0.011	26.68	40.24	2.19				single	KiDSDR4 J223412.595-302009.84	19.28	0.20
J225148.5-354528	342.95	-35.758	0.010	23.21	18.03	40.30	2.54	0.42	0.48	FR I			
J232105.5-293740	350.27	-29.628	0.007	24.29	28.15	40.48	1.54	0.66	0.74	FR II	KiDSDR4 J232105.486-293740.02	15.74	0.21
J230922.9-343836	347.35	-34.643	0.004	32.95	28.49	40.50	1.76	0.66	0.75	FR II	KiDSDR4 J230922.876-343836.08	18.77	0.34
J231212.1-300641	348.05	-30.111	0.053	23.99	13.46	40.58	1.88	0.31	0.35	FR I	KiDSDR4 J231212.501-300644.18	23.32	0.26
J223628.9-331408	339.12	-33.236	0.019	21.31	20.16	40.65	2.93	0.47	0.53	FRx	KiDSDR4 J223628.859-331408.20	20.88	0.68
J224921.0-305048	342.34	-30.847	0.004	26.20	30.48	40.65	0.49	0.71	0.80	FR II	KiDSDR4 J224920.972-305048.30	22.91	0.82
J225344.4-351303	343.44	-35.217	0.052	20.09	14.58	40.70	1.13	0.34	0.38	FR I			
J224046.5-320339	340.19	-32.063	0.004	26.83	32.62	40.81	1.27	0.75	0.85	FR II			
J230051.7-352353	345.22	-35.398	0.002	21.51	26.12	40.86	1.36	0.60	0.68	FR II	KiDSDR4 J230051.651-352353.25	19.25	0.49
J230958.5-333746	347.49	-33.629	0.025	21.13	15.81	40.92	1.30	0.36	0.41	FR I	KiDSDR4 J230957.760-333745.45	23.95	0.65
J232051.4-291743	350.21	-29.295	0.008	23.29	23.58	40.93	0.62	0.54	0.61	FR II	KiDSDR4 J232051.437-291742.84	23.15	1.04
J232522.9-324422	351.35	-32.739	0.004	26.22	31.19	40.95	0.85	0.72	0.81	FR II	KiDSDR4 J232522.915-324422.00	18.85	0.41
J231221.7-291415	348.09	-29.237	0.004	24.44	30.46	41.11	0.56	0.70	0.79	FR II	KiDSDR4 J231221.700-291413.54	19.17	0.48
J225837.7-301315	344.66	-30.221	0.032	19.28	18.20	41.12	1.37	0.42	0.47	FR I	KiDSDR4 J225837.739-301314.57	24.12	1.04
J224921.7-315654	342.34	-31.948	0.025	21.21	17.68	41.13	0.88	0.41	0.46	FR I	KiDSDR4 J224921.701-315654.25	20.80	0.97
J230951.1-332540	347.46	-33.428	0.020	24.66	16.77	41.23	1.93	0.38	0.43	FR I	KiDSDR4 J230951.138-332538.04	24.37	0.77
J224113.3-323906	340.30	-32.652	0.046	22.22	16.01	41.26	0.69	0.37	0.41	FR I	KiDSDR4 J224113.259-323906.11	23.33	1.14
J230524.6-342020	346.35	-34.339	0.034	21.28	15.00	41.28	1.58	0.34	0.39	FR I	KiDSDR4 J230524.605-342020.35	23.25	0.92
J225452.1-331700	343.72	-33.283	0.010	38.38	16.77	41.29	2.84	0.38	0.43	FR I	KiDSDR4 J225452.104-331658.94	19.27	0.36
J231936.5-310038	349.90	-31.011	0.008	22.04	22.64	41.64	1.68	0.51	0.58	FR II	KiDSDR4 J231936.522-310039.02	23.24	0.86
J225541.1-344220	343.92	-34.705	0.002	20.44	19.27	41.70	1.13	0.44	0.49	FR I	KiDSDR4 J225541.014-344219.60	21.70	0.74
J231155.3-301543	347.98	-30.263	0.021	21.01	18.03	41.73	2.09	0.41	0.46	FR I	KiDSDR4 J231155.228-301542.36	19.81	0.53
J230747.8-292941	346.95	-29.495	0.003	26.57	31.62	41.73	2.08	0.71	0.81	FR II	KiDSDR4 J230747.812-292941.08	22.30	0.80
J231710.5-314529	349.29	-31.757	0.012	24.88	28.90	41.76	2.82	0.65	0.74	FR II	KiDSDR4 J231710.483-314528.79	24.24	1.16
J230950.0-301011	347.46	-30.169	0.001	21.66	41.82					single			0.29

Continued on next page

Table 3.3 – Continued from previous page

Source Name	RA (J2000) (deg)	DEC (J2000) (deg)	Flux Density (Jy)	Size (")	a (")	b (")	PA (°)	a/b_{\max}	a/b_{\min}	Class	KIDS ID	Mag (r-band)	Z
J230936.4-301837	347.40	-30.310	0.004	25.50	14.31	41.83	2.31	0.32	0.36	FRI			0.10
J230621.3-343211	346.59	-34.537	0.026	22.35	20.62	41.90	0.16	0.46	0.52	FRx	KIDS DR4 J230621.335-343211.39	22.92	1.33
J224120.5-310639	340.34	-31.110	0.004	42.11	39.35	41.95	0.51	0.89	1.00	FRII			0.22
J232038.0-330934	350.16	-33.159	0.007	26.53	25.52	42.00	1.90	0.57	0.65	FRII			0.39
J232215.9-291913	350.57	-29.320	0.076	22.11	14.77	42.10	1.82	0.33	0.37	FRI	KIDS DR4 J232215.834-291914.50	20.38	0.54
J230115.3-314745	345.31	-31.795	0.006	25.79	23.58	42.26	2.13	0.53	0.59	FRII	KIDS DR4 J230115.424-314745.31	18.48	0.33
J223926.6-335334	339.86	-33.893	0.023	20.61	18.20	42.26	1.86	0.41	0.46	FRI	KIDS DR4 J223926.623-335333.99	22.75	0.90
J225408.9-345525	343.54	-34.924	0.009	27.27	20.52	42.33	2.74	0.46	0.52	FRx	KIDS DR4 J225408.979-345527.63	16.84	0.22
J224733.7-310308	341.89	-31.055	0.005	39.22	24.75	42.45	0.80	0.55	0.62	FRII	KIDS DR4 J224733.699-310307.88	21.96	0.87
J225559.1-345207	344.00	-34.869	0.009	23.58	22.64	42.55	0.12	0.50	0.57	FRII	KIDS DR4 J225559.051-345206.76	21.93	1.22
J224857.5-290434	342.24	-29.076	0.023	22.54	18.20	42.69	1.36	0.40	0.45	FRI	KIDS DR4 J224857.563-290434.54	25.05	1.63
J223933.6-315632	339.89	-31.942	0.010	27.61	22.36	42.95	0.51	0.49	0.55	FRx			0.12
J224638.3-325514	341.66	-32.921	0.017	25.10	22.36	42.99	1.53	0.51	0.55	single	KIDS DR4 J224638.267-325513.85	18.74	0.34
J224943.0-343317	342.43	-34.556	0.016	22.80	23.05	43.04	0.37	0.51	0.57	FRII	KIDS DR4 J224943.022-343318.21	25.22	1.13
J225059.1-342136	342.75	-34.360	0.009	23.27	22.36	43.11	1.96	0.49	0.55	FRx	KIDS DR4 J225059.110-342136.30	22.56	0.92
J224200.6-301609	340.50	-30.270	0.008	23.33	25.00	43.12	2.17	0.55	0.62	FRII	KIDS DR4 J224200.633-301609.25	22.67	0.96
J224253.0-345622	340.72	-34.941	0.005	26.38	26.58	43.24	2.35	0.58	0.65	FRII	KIDS DR4 J224252.950-345620.53	24.65	1.00
J225054.1-323213	342.73	-32.538	0.002	21.00	23.67	43.24	1.80	0.52	0.58	FRII	KIDS DR4 J225054.190-323210.49	20.76	0.23
J231109.9-295556	347.79	-29.932	0.106	21.88	17.50	43.26	0.02	0.38	0.43	FRI			
J230048.8-322728	345.20	-32.452	0.006	24.02	33.11	43.36	2.52	0.72	0.81	FRII	KIDS DR4 J230049.190-322722.41	21.96	1.24
J230727.4-354538	346.86	-35.760	0.047	22.26	14.07	43.51	1.03	0.31	0.34	FRI			
J230845.2-292727	347.19	-29.454	0.003	26.41	29.15	43.52	2.57	0.63	0.71	FRII	KIDS DR4 J230845.229-292719.54	24.44	1.22
J232039.3-305013	350.16	-30.836	0.031	22.19	22.36	43.54	2.59	0.49	0.54	FRx	KIDS DR4 J232038.892-305014.36	25.27	1.63
J231659.8-333841	349.25	-33.645	0.026	21.99	18.03	43.59	2.52	0.39	0.44	FRI	KIDS DR4 J231659.772-333840.86	23.83	1.13
J225758.8-304249	344.50	-30.714	0.002	21.29	23.55	43.67	0.40	0.51	0.57	FRII	KIDS DR4 J225759.192-304247.14	23.10	0.40
J225040.5-295812	342.67	-29.970	0.002	23.64	28.01	43.86	0.53	0.60	0.68	FRII	KIDS DR4 J225040.586-295811.27	19.60	0.48
J225459.0-350056	343.75	-35.015	0.006	24.67	26.60	43.89	0.83	0.57	0.64	FRII	KIDS DR4 J225459.057-350057.07	20.33	0.78
J232541.9-320351	351.42	-32.065	0.062	24.65	20.16	43.92	3.03	0.43	0.49	FRI	KIDS DR4 J232541.848-320351.07	19.39	1.87
J232713.0-323928	351.81	-32.658	0.016	24.55	22.50	44.18	1.56	0.48	0.54	FRx	KIDS DR4 J232713.109-323927.78	22.74	0.82
J230049.8-293521	345.21	-29.590	0.010	27.47	13.46	44.27	3.03	0.29	0.32	FRI	KIDS DR4 J230049.449-293525.35	25.10	0.83
J230046.6-291741	345.19	-29.296	0.009	25.34	26.10	44.27	0.32	0.56	0.62	FRII	KIDS DR4 J230046.794-291741.88	22.98	0.68
J230522.3-312600	346.34	-31.433	0.014	23.47	26.10	44.29	1.24	0.56	0.62	single	KIDS DR4 J230522.314-312559.59	19.26	0.47
J231215.8-303212	348.07	-30.536	0.051	21.24	20.16	44.37	2.03	0.43	0.48	FRI	KIDS DR4 J231215.966-303209.89	22.66	0.13
J224824.5-341307	342.10	-34.218	0.007	26.39	24.62	44.38	1.18	0.53	0.59	FRII	KIDS DR4 J224824.482-341307.18	19.93	0.43
J230033.0-312451	345.14	-31.417	0.004	25.82	32.02	44.38	2.47	0.68	0.76	FRII	KIDS DR4 J230033.053-312450.63	18.50	0.01
J232631.8-342840	351.63	-34.478	0.040	23.51	11.18	44.53	2.58	0.24	0.27	FRI	KIDS DR4 J232631.904-342838.94	17.51	0.27
J232727.8-301602	351.87	-30.268	0.010	23.99	44.61	44.61	1.14	0.53	0.59	single	KIDS DR4 J232727.821-301601.84	18.62	0.33
J232624.5-310250	351.60	-31.049	0.013	23.24	25.00	44.79	0.70	0.53	0.59	FRII	KIDS DR4 J232624.560-310249.81	23.31	0.99
J230422.5-294248	346.09	-29.713	0.002	23.61	25.51	44.88	1.33	0.54	0.60	FRII	KIDS DR4 J230422.484-294248.49	21.56	0.76

Continued on next page

Table 3.3 – Continued from previous page

Source Name	RA (J2000) (deg)	DEC (J2000) (deg)	Flux Density (Jy)	Size (")	a (")	b (")	PA (°)	a/b _{max}	a/b _{min}	Class	KIDS ID	Mag (r-band)	Z
J222223.5-300446	350.60	-30.079	0.018	25.31	24.62	44.92	2.70	0.52	0.58	FR II	KIDS DR4 J232223.521-300445.96	20.19	0.59
J225718.1-314425	344.32	-31.739	0.019	24.07	24.75	44.93	2.33	0.52	0.58	FR II	KIDS DR4 J225718.136-314424.65	20.67	0.67
J223136.2-333433	337.90	-33.576	0.009	25.89	26.58	45.04	0.26	0.56	0.62	FR II			
J230415.5-300230	346.06	-30.042	0.020	26.17	22.50	45.16	1.53	0.47	0.53	FRx	KIDS DR4 J230415.644-300224.95	25.37	1.17
J224505.2-311745	341.27	-31.296	0.007	39.46	20.16	45.18	2.72	0.42	0.47	FR I	KIDS DR4 J224505.159-311744.94	22.64	0.79
J225555.0-321632	343.90	-32.275	0.050	20.80	20.16	45.18	2.10	0.42	0.47	FR I			
J225131.0-323043	342.88	-32.512	0.025	23.33		45.28	2.38			single	KIDS DR4 J225131.004-323043.52	19.37	0.73
J230113.5-320909	345.31	-32.152	0.054	22.34	18.03	45.29	1.02	0.38	0.42	FR I	KIDS DR4 J230113.452-320908.63	21.09	0.80
J232147.3-315245	350.45	-31.879	0.020	25.32	22.50	45.42	1.54	0.47	0.52	FRx	KIDS DR4 J232147.293-315245.45	22.35	1.01
J223309.0-335048	338.29	-33.847	0.003	24.62		45.51	2.99			single	KIDS DR4 J223309.172-335049.26	21.76	0.51
J230525.5-342516	346.36	-34.421	0.019	25.49	22.64	45.53	1.60	0.47	0.53	FRx	KIDS DR4 J230525.503-342515.58	24.28	1.35
J224803.9-352932	342.02	-35.492	0.015	26.13	23.58	45.76	2.48	0.49	0.55	FRx	KIDS DR4 J224803.329-352935.81	25.53	1.16
J232141.7-332437	350.42	-33.410	0.002	23.14		45.98	1.13			single	KIDS DR4 J232141.730-332436.78	24.32	0.76
J232009.9-284200	350.04	-28.700	0.046	22.36	22.64	46.03	3.11	0.47	0.52	FRx			
J224544.7-323141	341.44	-32.527	0.017	32.97	21.73	46.06	1.28	0.45	0.50	FR I	KIDS DR4 J224544.679-323141.53	21.07	1.01
J224226.4-302450	340.61	-30.414	0.016	29.39	20.54	46.11	1.92	0.42	0.47	FR I	KIDS DR4 J224226.402-302449.64	19.59	0.53
J230431.0-334249	346.13	-33.713	0.013	29.56	28.57	46.21	2.52	0.59	0.65	FR II	KIDS DR4 J230430.957-334247.77	18.43	0.30
J225248.3-304444	343.20	-30.747	0.048	23.65	21.51	46.31	2.12	0.44	0.44	FR I	KIDS DR4 J225248.326-304444.18	20.86	0.59
J224240.4-301809	340.67	-30.303	0.024	23.52	21.36	46.36	1.26	0.44	0.49	FR I	KIDS DR4 J224241.026-301810.13	24.36	1.01
J231057.6-323614	347.74	-32.603	0.016	24.81	22.36	46.38	1.94	0.46	0.51	FRx			0.47
J232227.3-303149	350.61	-30.529	0.002	24.47	25.05	46.38	2.38	0.51	0.57	FR II	KIDS DR4 J232227.288-303149.32	22.50	1.34
J224708.0-285938	341.78	-28.994	0.002	25.78	19.88	46.39	1.65	0.41	0.45	FR I	KIDS DR4 J224707.962-285938.30	23.29	0.92
J230419.3-324545	346.08	-32.762	0.011	25.74	28.50	46.47	0.96	0.58	0.65	FR II	KIDS DR4 J230419.357-324544.60	21.62	0.85
J232707.4-332602	351.78	-33.431	0.013	28.06	23.72	46.55	0.26	0.48	0.54	FRx	KIDS DR4 J232707.330-332601.12	18.68	0.67
J224155.0-332740	340.48	-33.462	0.033	24.45	22.36	46.56	1.98	0.46	0.51	FRx	KIDS DR4 J224155.015-332740.75	22.89	0.92
J224148.1-332002	340.45	-33.334	0.135	24.10	16.01	46.58	2.39	0.33	0.36	FR I	KIDS DR4 J224148.115-332001.65	21.84	0.86
J223528.2-351322	338.87	-35.223	0.003	31.33	39.06	46.62	2.68	0.80	0.89	FR II	KIDS DR4 J223528.177-351322.17	22.87	0.84
J23129.1-320536	337.87	-32.093	0.012	25.67	20.16	46.66	2.74	0.41	0.46	FR I	KIDS DR4 J223129.142-320536.30	23.19	0.96
J232415.2-323909	351.06	-32.652	0.085	24.90	16.01	46.73	1.98	0.33	0.36	FR I	KIDS DR4 J232415.151-323907.92	24.70	1.25
J224919.8-323628	342.33	-32.608	0.016	26.12	22.50	46.98	0.20	0.45	0.51	FRx	KIDS DR4 J224919.817-323628.43	18.92	0.42
J231519.5-342713	348.83	-34.453	0.041	24.35	21.36	47.02	1.86	0.43	0.48	FR I	KIDS DR4 J231519.498-342713.36	23.57	0.89
J224430.0-350908	341.13	-35.153	0.007	31.17	35.22	47.04	0.39	0.71	0.79	FR II	KIDS DR4 J224430.059-350907.79	17.46	0.23
J230949.5-311425	347.46	-31.241	0.020	23.61	22.36	47.17	0.48	0.45	0.50	FRx			
J224637.8-342554	341.66	-34.433	0.029	26.89	15.00	47.24	1.14	0.30	0.34	FR I	KIDS DR4 J224637.816-342552.86	18.92	0.45
J225336.7-314553	343.40	-31.765	0.384	23.91	18.03	47.25	2.92	0.36	0.40	FR I			
J231435.4-352724	348.65	-35.457	0.034	25.35		47.28	1.13			single	KIDS DR4 J231435.381-352723.18	20.04	0.72
J223334.8-312050	338.39	-31.348	0.010	30.79	32.88	47.28	0.06	0.66	0.73	FR II	KIDS DR4 J223334.704-312050.24	22.00	2.24
J231245.2-315130	348.19	-31.859	0.106	21.99	21.51	47.31	2.36	0.43	0.48	FR I			1.16
J225733.7-334538	344.39	-33.761	0.039	28.93	23.56	47.32	2.85	0.47	0.53	FRx	KIDS DR4 J225733.689-334537.54	17.73	0.25

Continued on next page

Table 3.3 – Continued from previous page

Source Name	RA (J2000) (deg)	DEC (J2000) (deg)	Flux Density (Jy)	Size (")	a (")	b (")	PA (°)	a/b_{\max}	a/b_{\min}	Class	KIDS ID	Mag (r-band)	Z
J231204.3-325053	348.02	-32.848	0.234	22.24	16.77	44.48	2.61	0.36	0.40	FR II	KIDS DR4 J231204.293-325052.90	20.54	1.88
J232217.5-343035	350.57	-34.512	0.005	26.71	30.52	47.50	0.98	0.61	0.68	FR II	KIDS DR4 J232217.463-343035.22	23.28	0.93
J223724.2-342801	339.34	-34.468	0.008	40.97	30.41	47.60	1.42	0.61	0.67	FR II	KIDS DR4 J223724.201-342801.35	19.33	0.04
J231959.0-285728	35	-28.958	0.034	23.40	21.51	47.61	2.29	0.43	0.48	FR I	KIDS DR4 J231959.024-285728.29	24.52	0.96
J231601.1-321137	349.00	-32.193	0.003	24.30	22.36	47.70	2.91	0.45	0.49	single	KIDS DR4 J231601.068-321136.38	21.22	0.77
J230105.0-334943	345.27	-33.828	0.019	24.40	22.36	47.73	1.98	0.45	0.49	FR I	KIDS DR4 J230105.064-334942.25	18.34	0.31
J225909.2-330706	344.79	-33.118	0.001	24.02	25.40	47.80	0.79	0.51	0.56	FR II	KIDS DR4 J225909.187-330705.82	23.35	0.91
J225721.5-303651	344.34	-30.616	0.015	26.98	30.10	47.89	0.79	0.60	0.66	FR II	KIDS DR4 J230155.834-302620.97	18.69	0.30
J230155.8-302621	345.48	-30.438	0.010	30.08	25.74	48.01	0.50	0.51	0.57	FR II	KIDS DR4 J225907.347-345209.01	18.52	0.32
J225907.2-345208	344.78	-34.868	0.024	27.16	17.68	48.02	0.50	0.35	0.39	FR I	KIDS DR4 J231714.166-345520.84	22.64	0.92
J231714.2-345521	349.31	-34.923	0.004	25.35	48.10	48.10	2.79	0.49	0.54	single			
J224000.7-312747	34	-31.462	0.001	22.40	24.70	48.10	0.44	0.40	0.44	FRx	KIDS DR4 J224933.897-292818.42	21.83	0.83
J224933.9-292819	342.39	-29.472	0.066	23.41	20.16	48.20	1.47	0.40	0.44	FR I	KIDS DR4 J232218.302-314408.37	19.93	0.62
J232218.3-314408	350.58	-31.735	0.057	23.36	21.51	48.24	1.05	0.42	0.47	FR I	KIDS DR4 J231549.884-353551.87	17.85	0.21
J231550.0-353552	348.96	-35.597	0.103	23.67	19.04	48.26	1.13	0.38	0.42	FR I	KIDS DR4 J231221.162-292555.88	18.13	1.20
J231221.2-292556	348.09	-29.433	0.033	24.76	21.21	48.31	0.83	0.42	0.46	FR I	KIDS DR4 J232552.668-300640.06	23.07	0.65
J232552.6-300641	351.47	-30.110	0.015	26.91	24.62	48.31	1.96	0.48	0.54	FRx	KIDS DR4 J225708.397-302040.58	21.34	0.80
J223708.4-302041	339.29	-30.344	0.120	23.73	21.36	48.35	0.39	0.42	0.47	FR I	KIDS DR4 J225934.908-304440.03	19.99	0.55
J225935.0-304441	344.89	-30.745	0.085	23.92	19.53	48.48	0.81	0.38	0.42	FR I	KIDS DR4 J230202.957-340932.47	23.50	1.20
J230203.0-340934	345.52	-34.159	0.028	24.75	25.12	48.58	1.69	0.49	0.55	FRx	KIDS DR4 J230344.921-302148.78	23.11	1.34
J230345.1-302148	345.94	-30.363	0.056	22.85	23.58	48.67	1.05	0.46	0.51	FRx	KIDS DR4 J231627.294-312228.53	21.11	0.55
J231627.3-312229	349.11	-31.375	0.033	23.69	20.62	48.68	1.75	0.40	0.45	FR I	KIDS DR4 J223303.812-300656.48	18.96	0.41
J233303.8-300656	338.26	-30.115	0.016	27.87	30.10	48.84	0.21	0.59	0.65	FR II	KIDS DR4 J223209.072-333247.25	23.01	0.90
J223209.0-333246	338.04	-33.546	0.016	24.97	23.72	49.20	2.74	0.46	0.51	FRx	KIDS DR4 J232601.471-303243.15	19.41	0.90
J232601.5-303243	351.51	-30.544	0.068	23.29	21.51	49.27	1.22	0.42	0.46	FR I			
J231032.5-311430	347.63	-31.243	0.057	26.72	25.00	49.64	0.76	0.48	0.53	FRx			
J225423.3-314135	343.60	-31.693	0.017	25.84	27.04	49.73	2.22	0.52	0.57	FR II	KIDS DR4 J230454.098-303049.11	22.64	0.30
J230454.1-303049	346.22	-30.513	0.017	34.25	22.44	49.75	0.85	0.43	0.48	FR I	KIDS DR4 J224922.201-344206.41	24.01	1.31
J224922.2-344207	342.34	-34.702	0.011	26.97	29.26	49.75	1.16	0.56	0.62	FR II	KIDS DR4 J224612.527-305629.45	20.62	0.50
J224612.5-305629	341.55	-30.942	0.045	28.73	23.72	49.77	0.12	0.45	0.50	FRx	KIDS DR4 J225653.137-290139.08	23.25	0.90
J225652.8-290139	344.22	-29.028	0.067	22.50	15.81	49.85	2.40	0.30	0.33	FR I			
J224208.1-342120	340.53	-34.358	0.003	28.79	39.53	49.86	2.54	0.75	0.83	FR II	KIDS DR4 J232254.084-345509.74	19.74	0.43
J232254.1-345510	350.73	-34.919	0.022	26.04	19.19	49.87	2.01	0.37	0.41	FR I			
J231441.8-304019	348.68	-30.672	0.028	27.32	25.00	49.87	0.83	0.48	0.53	FRx			
J224842.3-300952	342.18	-30.165	0.030	27.84	24.75	49.99	2.27	0.47	0.52	FRx	KIDS DR4 J224842.328-300952.26	23.05	0.91
J224018.0-334232	340.07	-33.708	0.064	24.79	20.16	5	1.84	0.38	0.42	FR I	KIDS DR4 J224017.974-334231.85	21.47	0.90
J225744.9-350554	344.44	-35.097	0.004	29.18	35.53	50.10	0.69	0.68	0.75	FR II	KIDS DR4 J225744.856-350553.81	21.99	0.71
J230015.9-302557	345.07	-30.432	0.002	24.52	31.63	50.15	1.18	0.60	0.66	FR II	KIDS DR4 J230015.878-302556.70	24.06	1.11
J231038.3-305434	347.65	-30.913	0.005	36.44	44.40	50.19	0.97	0.84	0.93	FR II			

Continued on next page

Table 3.3 – Continued from previous page

Source Name	RA (J2000) (deg)	DEC (J2000) (deg)	Flux Density (Jy)	Size (")	<i>a</i> (")	<i>b</i> (")	PA (°)	<i>a</i> / <i>b</i> _{max}	<i>a</i> / <i>b</i> _{min}	Class	KIDS ID	Mag (r-band)	Z
J22254.7-300838	350.73	-30.144	0.005	28.69	38.09	50.20	2.38	0.72	0.80	FR II	KIDS DR4 J232254.567-300838.35	18.16	0.30
J224810.7-285434	342.04	-28.908	0.014	26.70	27.61	50.29	0.05	0.52	0.58	FR II	KIDS DR4 J224810.683-285433.42	21.88	0.71
J223954.0-344438	339.97	-34.743	0.080	24.95	25.50	50.29	2.94	0.48	0.53	FR x			
J231103.7-315435	347.76	-31.910	0.007	31.28	23.05	50.30	2.14	0.44	0.48	FR I			
J231608.2-335514	349.03	-33.921	0.022	25.61	26.10	50.41	0.24	0.49	0.54	FR x	KIDS DR4 J231608.116-335509.19	24.43	1.33
J224630.5-302953	341.63	-30.498	0.010	27.51	35.53	50.42	2.39	0.67	0.74	FR II	KIDS DR4 J224630.470-302947.36	21.32	0.35
J231905.5-302026	349.77	-30.342	0.014	34.21	26.09	50.47	2.61	0.49	0.54	FR x	KIDS DR4 J231905.495-302025.63	20.91	0.70
J223521.4-305501	338.84	-30.916	0.018	25.74	26.93	50.52	1.97	0.51	0.56	FR II	KIDS DR4 J223521.307-305500.75	23.85	1.61
J230408.0-343306	346.03	-34.551	0.002	26.17	32.81	50.66	1.99	0.62	0.68	FR II	KIDS DR4 J230408.399-343306.92	23.78	0.66
J230303.3-340524	345.76	-34.089	0.036	27.55	21.43	50.69	2.58	0.40	0.44	FR I	KIDS DR4 J230303.304-340523.44	20.24	0.40
J231655.4-340349	349.23	-34.063	0.018	30.34	19.53	50.86	0.66	0.37	0.40	FR I	KIDS DR4 J231655.346-340348.58	23.44	1.03
J224032.6-332526	340.14	-34.630	0.042	26.89	25.00	50.90	0.93	0.47	0.52	FR x	KIDS DR4 J224032.561-343754.12	19.79	0.27
J223814.6-332526	339.57	-32.881	0.029	27.38	25.50	51.02	1.39	0.48	0.53	FR x	KIDS DR4 J223814.563-325255.97	23.81	0.96
J225428.9-332916	343.62	-33.487	0.067	25.95	18.20	51.05	0.34	0.34	0.37	FR I	KIDS DR4 J225428.929-332915.24	17.45	0.22
J231724.9-344138	349.35	-34.699	0.046	25.46	31.56	51.13	1.06	0.59	0.65	FR II	KIDS DR4 J231724.909-344137.73	20.28	0.65
J232713.8-342335	351.81	-34.392	0.024	25.01	29.15	51.14	2.10	0.54	0.60	FR II	KIDS DR4 J232713.559-342337.16	22.40	0.29
J224036.4-332342	340.15	-33.395	0.095	26.74	21.26	51.17	0.63	0.40	0.44	FR I	KIDS DR4 J224036.409-332342.22	16.03	0.12
J224839.1-293346	342.16	-29.562	0.021	27.58	23.58	51.19	2.22	0.44	0.48	FR I	KIDS DR4 J224839.049-293346.05	19.55	0.49
J224330.9-311812	340.88	-31.301	0.002	26.13	25.43	51.20	0.47	0.52	0.52	FR x	KIDS DR4 J224330.889-311811.77	19.66	0.42
J223449.5-350307	350.96	-35.052	0.016	28.94	31.62	51.30	0.33	0.59	0.65	FR II	KIDS DR4 J223449.524-350307.39	23.00	1.34
J230950.7-304225	347.46	-30.707	0.039	27.34	28.50	51.34	2.38	0.53	0.58	FR II			
J225603.4-300901	344.01	-30.150	0.038	34.92	20.16	51.55	2.80	0.37	0.41	FR I	KIDS DR4 J231740.338-324238.92	19.22	0.45
J231740.4-324239	349.42	-32.710	0.010	36.31	23.72	51.73	1.93	0.44	0.48	FR I	KIDS DR4 J223906.744-292847.53	19.18	0.46
J223906.8-292847	339.78	-29.480	0.004	27.55	34.61	51.82	2.68	0.64	0.70	FR II	KIDS DR4 J231556.032-314353.60	23.30	0.87
J231556.1-314354	348.98	-31.731	0.013	32.26	30.10	51.99	2.38	0.55	0.61	FR II	KIDS DR4 J223814.151-351011.68	22.87	0.77
J223813.5-351007	339.56	-35.169	0.002	29.29	36.94	52.01	2.63	0.68	0.75	FR II	KIDS DR4 J23174.211-291517.65	23.00	1.08
J23174.2-291518	349.31	-29.255	0.012	28.57	24.15	52.07	0.68	0.44	0.49	FR I	KIDS DR4 J230419.337-292853.74	22.92	0.53
J230419.2-292857	346.08	-29.482	0.008	30.16	43.22	52.11	2.78	0.79	0.87	FR II	KIDS DR4 J223213.996-334045.99	21.78	0.87
J223214.0-334047	338.06	-33.680	0.002	28.48	36.59	52.45	1.65	0.67	0.73	FR II	KIDS DR4 J225005.869-315932.77	24.85	0.83
J231728.4-291645	349.37	-29.281	0.025	28.78	28.50	52.61	2.17	0.52	0.57	FR II	KIDS DR4 J231728.626-291647.25	21.60	0.76
J231205.8-295714	348.03	-29.954	0.002	26.38	18.49	52.62	2.40	0.34	0.37	FR I	KIDS DR4 J231205.829-295713.71	18.66	0.25
J225005.9-315933	342.52	-31.992	0.013	31.72	28.50	52.79	2.33	0.52	0.57	FR II	KIDS DR4 J225005.869-315932.77	21.81	0.96
J225200.1-311301	343.00	-31.217	0.093	27.26	25.74	52.88	2.65	0.46	0.51	FR x	KIDS DR4 J225200.084-311300.45	20.80	0.49
J223214.8-291723	338.06	-29.290	0.032	26.21	20.16	53.05	2.37	0.36	0.40	FR I	KIDS DR4 J223214.818-291724.24	20.80	0.49
J230406.0-313809	346.02	-31.637	0.005	28.57	37.18	53.15	1.31	0.67	0.73	FR II	KIDS DR4 J230405.951-313809.34	19.69	0.49
J225616.0-344546	344.07	-34.763	0.015	29.06	31.82	53.16	2.28	0.57	0.63	FR II	KIDS DR4 J225616.037-344546.46	20.60	0.68
J224027.8-294954	340.11	-29.835	0.001	26.48	33.19	53.39	0.59	0.59	0.65	FR II	KIDS DR4 J224027.724-294950.69	24.20	0.85
J231458.1-295318	348.74	-29.885	0.028	28.20	32.88	53.42	0.16	0.59	0.65	FR II			
J225213.4-335521	343.06	-33.923	0.016	34.51	20.16	53.44	1.92	0.36	0.40	FR I	KIDS DR4 J225213.375-335521.48	21.16	0.70

Continued on next page

Table 3.3 – Continued from previous page

Source Name	RA (J2000) (deg)	DEC (J2000) (deg)	Flux Density (Jy)	Size (")	a (")	b (")	PA (°)	a/b_{\max}	a/b_{\min}	Class	KIDS ID	Mag (r-band)	Z
J225958.2-304219	344.99	-30.706	0.010	31.03	33.69	53.44	1.04	0.60	0.66	FR II	KIDS DR4 J225958.238-304219.35	22.77	1.00
J230721.2-345442	346.84	-34.912	0.004	31.11	41.63	53.46	2.57	0.74	0.82	FR II	KIDS DR4 J230721.011-345437.87	23.90	0.66
J230831.9-300415	347.13	-30.072	0.002	28.24	38.34	53.60	0.75	0.68	0.75	FR II			
J223543.2-350235	338.93	-35.043	0.020	26.52	33.63	53.60	0.73	0.60	0.66	FR II	KIDS DR4 J223543.192-350235.17	22.76	0.85
J225219.9-352035	343.08	-35.344	0.008	34.40	36.40	53.62	2.80	0.65	0.71	FR II	KIDS DR4 J225220.057-352035.51	18.29	0.34
J225651.6-321137	344.21	-32.193	0.009	33.08	41.83	53.65	2.98	0.74	0.82	FR II	KIDS DR4 J225651.585-321136.24	19.53	0.46
J231024.6-335916	347.60	-33.988	0.204	27.76	2	53.69	1.56	0.36	0.39	FR I	KIDS DR4 J231024.539-335914.86	23.74	0.15
J231303.6-330229	348.26	-33.042	0.027	32.38	21.51	53.82	0.57	0.38	0.42	FR I	KIDS DR4 J231303.754-330229.19	18.65	0.18
J232432.8-310211	351.14	-31.038	0.013	36.04	18.14	53.84	3.10	0.32	0.35	FR I	KIDS DR4 J232432.803-310211.77	18.71	0.44
J225509.3-304443	343.79	-30.742	0.003	33.90	46.01	53.85	1.07	0.82	0.90	FR II	KIDS DR4 J225509.304-304441.14	17.53	0.21
J230858.0-322522	347.24	-32.423	0.022	27.20	30.10	53.86	1.55	0.53	0.59	FR II	KIDS DR4 J230858.068-322522.34	23.48	0.87
J224118.9-295817	340.32	-29.974	0.003	32.39	44.13	53.90	1.18	0.78	0.86	FR II	KIDS DR4 J224118.901-295817.67	20.64	0.66
J224206.0-300228	340.53	-30.038	0.039	27.25	30.10	53.96	0.85	0.53	0.59	FR II	KIDS DR4 J224206.340-300231.74	21.79	1.03
J232444.8-291028	351.19	-29.173	0.073	25.05	27.61	54.13	1.56	0.49	0.53	FR x	KIDS DR4 J232444.770-291028.07	24.16	1.35
J232112.0-312749	350.30	-31.463	0.007	30.67	36.40	54.14	1.26	0.64	0.70	FR II	KIDS DR4 J232112.017-312748.97	24.31	0.94
J231931.5-295433	349.88	-29.910	0.014	69.54	34.73	54.19	2.75	0.61	0.67	FR II	KIDS DR4 J231931.440-295432.38	22.19	1.02
J224019.7-300911	340.08	-30.152	0.018	28.14	34.82	54.23	2.77	0.61	0.67	FR II	KIDS DR4 J224019.653-300910.81	23.64	0.99
J230141.7-341557	345.42	-34.265	0.007	33.84	45.25	54.27	0.32	0.80	0.87	FR II	KIDS DR4 J230141.739-341555.75	19.45	0.48
J230306.4-304054	345.78	-30.681	0.016	28.70	32.50	54.34	1.47	0.57	0.63	FR II	KIDS DR4 J230306.369-304053.16	21.62	1.06
J225700.6-332214	344.25	-33.371	0.023	32.65	27.61	54.44	3.11	0.48	0.53	FR x	KIDS DR4 J225700.578-332211.44	17.42	0.22
J231449.7-344254	348.71	-34.714	0.002	26.76	37.91	54.51	0.86	0.67	0.73	FR II	KIDS DR4 J231449.445-344247.67	25.34	0.84
J230039.7-315812	345.17	-31.970	0.032	29.57	31.32	54.54	0.53	0.55	0.60	FR II	KIDS DR4 J230039.728-315811.65	22.24	1.06
J232393.1-340418	339.88	-34.072	0.093	29.46	24.75	54.57	2.29	0.43	0.48	FR I	KIDS DR4 J232393.1344-340418.11	15.23	0.04
J230131.1-295131	345.38	-29.858	0.078	28.64	27.95	54.64	1.75	0.49	0.54	FR x	KIDS DR4 J230131.108-295129.70	24.01	1.73
J225635.5-301635	344.15	-30.277	0.003	35.35	46.81	54.74	2.48	0.82	0.90	FR II			
J224417.5-292312	341.07	-29.386	0.003	27.90	19.33	54.83	1.85	0.34	0.37	FR I	KIDS DR4 J224417.526-292311.46	18.57	0.42
J224806.9-302204	342.03	-30.367	0.004	32.68	46.37	54.86	1.41	0.81	0.89	FR II	KIDS DR4 J224806.922-302202.18	16.46	0.12
J231408.5-313443	348.54	-31.579	0.017	32.24	35.38	55.03	0.10	0.61	0.67	FR II			
J225717.3-303344	344.32	-30.563	0.016	30.04	34.01	55.10	0.64	0.59	0.65	FR II	KIDS DR4 J225717.284-303344.54	19.21	1.79
J224256.0-314120	340.73	-31.688	0.011	32.41	19.83	55.20	0.56	0.34	0.38	FR I	KIDS DR4 J224255.991-314119.66	18.54	0.32
J232238.5-334007	350.66	-33.669	0.104	28.55	25.74	55.25	1.98	0.45	0.49	FR I	KIDS DR4 J232238.554-334007.76	22.71	0.97
J230921.5-304929	347.34	-30.824	0.013	29.61	32.60	55.25	1.63	0.56	0.62	FR II			
J231446.9-351109	348.70	-35.190	0.008	30.48	37.50	55.29	2.48	0.65	0.71	FR II	KIDS DR4 J231447.090-351105.47	22.40	0.78
J230522.8-312325	346.34	-31.391	0.001	28.87	39.92	55.34		0.69	0.76	FR II	KIDS DR4 J230522.757-312325.23	22.94	0.97
J233447.5-315951	338.70	-31.997	0.002	28.19	36.63	55.40	3.04	0.63	0.69	FR II			
J224354.8-325120	340.97	-32.855	0.065	29.89	27.50	55.42	1.61	0.47	0.52	FR x	KIDS DR4 J224354.518-325127.57	22.80	0.91
J223724.8-301031	339.35	-30.175	0.087	27.41	23.05	55.58	0.07	0.40	0.43	FR I	KIDS DR4 J223724.819-301031.03	20.54	0.72
J230110.9-321801	345.30	-32.301	0.176	27.53	17.50	55.59	1.68	0.30	0.33	FR I	KIDS DR4 J230110.918-321800.59	19.67	0.60
J223648.6-350251	339.21	-35.045	0.059	30.95	30.52	55.65	0.97	0.52	0.57	FR II	KIDS DR4 J223648.305-350242.79	23.88	0.76

Continued on next page

Table 3.3 – Continued from previous page

Source Name	RA (J2000) (deg)	DEC (J2000) (deg)	Flux Density (Jy)	Size (")	a (")	b (")	PA (°)	a/b_{\max}	a/b_{\min}	Class	KIDS ID	Mag (r-band)	Z
J230337.0-332735	345.90	-33.460	0.225	27.28	22.36	55.78	1.30	0.38	0.42	FRI	KIDS DR4 J230336.989-332734.83	20.99	0.83
J224718.6-325525	341.83	-32.923	0.002	28.47	36.99	55.80	1.25	0.63	0.69	FRII	KIDS DR4 J224718.600-325525.02	19.14	0.43
J225704.8-294440	344.27	-29.745	0.074	29.02	24.75	55.83	0.78	0.42	0.46	FRI	KIDS DR4 J225704.831-294439.85	20.86	0.51
J232326.8-330355	350.65	-33.066	0.001	27.34	16.30	56.08		0.28	0.30	FRI	KIDS DR4 J232326.769-330355.14	20.61	0.31
J225524.9-314552	343.85	-31.764	0.164	27.05	25.74	56.08	2.01	0.44	0.48	FRI			
J225031.4-351536	342.63	-35.259	0.020	33.38	31.32	56.14	0.93	0.53	0.58	FRII	KIDS DR4 J225031.484-351535.39	21.69	0.59
J223946.8-340725	339.95	-34.126	0.016	51.60	31.32	56.42	2.76	0.53	0.58	FRII	KIDS DR4 J223946.869-340724.18	17.31	0.21
J232104.5-332706	350.28	-33.450	0.009	32.31	44.63	56.54	1.25	0.76	0.83	FRII	KIDS DR4 J232104.345-332706.85	22.94	1.54
J225141.5-321151	342.92	-32.198	0.087	34.50	18.20	56.57	3.11	0.31	0.34	FRI	KIDS DR4 J225141.418-321151.30	17.74	0.24
J225026.1-301331	342.61	-30.225	0.012	34.54	33.54	56.62	2.08	0.57	0.62	FRII	KIDS DR4 J225026.096-301330.65	21.25	0.55
J223307.1-311414	338.28	-31.236	0.338	22.99	15.21	45.98	2.98	0.31	0.35	FRI	KIDS DR4 J223307.112-311413.59	22.62	1.12
J225822.4-293626	344.59	-29.608	0.003	26.78	35.28	57.17	1.48	0.59	0.65	FRII	KIDS DR4 J225822.411-293623.37	22.66	0.75
J230857.8-300107	347.24	-30.018	0.002	25.94						single			0.38
J225925.9-315515	344.86	-31.922	0.013	34.44	32.88	57.93	1.48	0.54	0.59	FRII	KIDS DR4 J225925.926-315515.20	23.83	1.08
J225206.8-341221	343.03	-34.206	0.021	32.00	37.50	58.10	2.54	0.62	0.67	FRII	KIDS DR4 J225206.793-341220.67	21.71	0.70
J222926.0-325809	337.36	-32.970	0.036	29.87	23.72	58.19	2.88	0.39	0.43	FRI			
J230010.9-330549	345.04	-33.097	0.011	33.15	40.08	58.24	1.53	0.66	0.72	FRII	KIDS DR4 J230010.911-330548.80	21.89	0.68
J24320.5-311620	340.84	-31.272	0.003	35.23	20.65	58.31	1.32	0.48	0.53	FRx	KIDS DR4 J224320.542-311620.31	18.82	0.22
J224531.5-305210	341.38	-30.870	0.003	22.66	20.65	58.47	1.22	0.34	0.37	FRI	KIDS DR4 J224531.417-305209.88	18.93	0.42
J224843.9-330743	342.18	-33.128	0.003	32.14	39.11	58.82	0.66	0.64	0.69	FRII	KIDS DR4 J224843.898-330742.44	19.41	0.41
J225726.7-335648	344.36	-33.946	0.011	32.73	37.50	59.01	1.04	0.61	0.66	FRII	KIDS DR4 J225726.714-335647.93	21.66	0.81
J22259.6-313249	350.75	-31.548	0.007	26.63	35.87	59.10	1.81	0.58	0.63	FRII	KIDS DR4 J232259.668-313249.97	20.99	0.26
J230321.5-344746	345.84	-34.797	0.011	33.15	38.24	59.22	1.76	0.62	0.67	FRII			
J223228.2-315058	338.12	-31.849	0.163	29.23	25.12	59.32	1.35	0.41	0.44	FRI	KIDS DR4 J223228.323-315058.26	21.58	0.94
J225858.2-313631	344.74	-31.609	0.014	33.74	35.36	59.40	0.81	0.57	0.62	FRII	KIDS DR4 J225858.159-313631.30	23.31	0.84
J232211.4-351323	350.55	-35.223	0.032	38.05	17.50	59.46	0.16	0.28	0.31	FRI	KIDS DR4 J232211.352-351324.63	19.69	0.48
J224640.3-333853	341.67	-33.647	0.011	34.38	19.53	60.12	2.39	0.31	0.34	FRI	KIDS DR4 J224640.295-333853.40	21.56	0.75
J224301.5-294356	340.76	-29.733	0.056	32.76	25.00	60.17	0.82	0.40	0.43	FRI	KIDS DR4 J224301.462-294356.42	21.02	0.54
J230307.5-330538	345.78	-33.093	0.054	30.68	25.00	60.19	1.37	0.40	0.43	FRI	KIDS DR4 J230307.515-330538.36	18.54	0.23
J230015.8-335038	345.07	-33.844	0.127	31.62	27.95	60.44	0.55	0.44	0.48	FRI			
J225235.5-324017	343.15	-32.672	0.090	34.03	27.04	60.50	2.13	0.43	0.47	FRI	KIDS DR4 J225235.655-324016.65	15.84	0.12
J231327.8-302044	348.36	-30.346	0.002	31.04	40.30	60.58	2.06	0.64	0.69	FRII	KIDS DR4 J231327.757-302042.96	23.51	0.97
J223152.8-311107	337.97	-31.180	0.006	35.06	43.73	60.65	2.58	0.69	0.75	FRII	KIDS DR4 J223152.788-311106.14	24.04	1.09
J224250.5-300804	340.71	-30.135	0.063	32.93	25.00	60.79	0.99	0.40	0.43	FRI	KIDS DR4 J224250.857-300801.01	23.78	0.51
J223934.1-351803	339.89	-35.298	0.015	38.04	23.72	60.99	3.12	0.37	0.41	FRI	KIDS DR4 J223934.093-351803.09	23.22	1.02
J232555.3-313954	351.48	-31.666	0.015	35.73	33.54	61.04	0.49	0.53	0.57	FRII	KIDS DR4 J232555.265-313953.18	22.22	0.86
J222645.0-313613	351.69	-31.603	0.010	40.54	34.00	61.41	0.62	0.53	0.58	FRII	KIDS DR4 J222645.035-313612.53	22.91	1.15
J225126.8-293056	342.86	-29.516	0.007	35.12	43.66	61.56	1.33	0.68	0.74	FRII			
J225737.7-302823	344.41	-30.473	0.012	34.54	43.66	61.57	1.78	0.68	0.74	FRII	KIDS DR4 J225737.696-302822.61	23.09	1.23

Continued on next page

Table 3.3 – Continued from previous page

Source Name	RA (J2000) (deg)	DEC (J2000) (deg)	Flux Density (Jy)	Size (")	a (")	b (")	PA (°)	a/b_{\max}	a/b_{\min}	Class	KIDS ID	Mag (r-band)	Z	
J232534.5-345700	351.39	-34.951	0.019	34.71	28.28	61.92	0.86	0.44	0.48	FRI	KIDS DR4 J232534.388-345659.03	20.59	0.43	
J224207.9-295252	340.53	-29.882	0.003	30.54	43.42	62.10	2.54	0.67	0.73	FRII	KIDS DR4 J224207.890-295251.46	21.57	0.74	
J231308.6-332029	348.29	-33.342	0.152	37.11	45.28	62.28	2.25	0.70	0.76	FRII	KIDS DR4 J231308.599-332028.28	17.47	0.19	
J230455.6-343134	346.23	-34.525	1.750	30.01	35.41	62.30	0.82	0.55	0.59	FRII	KIDS DR4 J230455.659-343134.25	24.02	1.17	
J230256.9-332330	345.74	-33.392	0.062	34.09	35.79	62.38	3.02	0.55	0.60	FRII	KIDS DR4 J230256.845-332328.42	18.36	0.30	
J231554.3-285944	348.98	-28.997	0.004	30.49	43.14	62.42	2.69	0.66	0.72	FRII	KIDS DR4 J231554.280-285944.64	23.01	1.05	
J223454.9-295758	338.74	-29.963	0.002	33.34	41.38	62.42	1.13	0.64	0.69	FRII	KIDS DR4 J223454.792-295757.85	21.88	0.51	
J232415.5-295803	351.06	-29.967	0.007	35.63	44.51	62.50	0.65	0.68	0.74	FRII	KIDS DR4 J232414.920-295803.00	23.73	0.23	
J232232.0-305249	350.63	-30.881	0.011	36.06	41.23	62.57	1.81	0.63	0.69	FRII	KIDS DR4 J232231.949-305248.99	22.58	0.83	
J223426.4-325225	338.61	-32.874	0.002	31.73	42.76	62.71	0.66	0.66	0.71	FRII	KIDS DR4 J223426.172-325227.08	23.62	0.84	
J231904.8-321600	349.77	-32.270	0.010	43.13	44.15	62.78	0.07	0.68	0.73	FRII	KIDS DR4 J231904.677-321558.62	17.71	0.19	
J223943.1-330819	339.93	-33.140	0.005	27.01	31.62	62.81	2.35	0.48	0.52	FRx	KIDS DR4 J223943.089-330818.37	20.90	0.75	
J230846.9-334814	347.20	-33.803	0.119	33.43	31.32	63.00	2.00	0.48	0.52	FRx	KIDS DR4 J230846.831-334813.90	23.86	0.85	
J231708.4-341441	349.29	-34.244	0.530	29.73	27.95	63.30	0.83	0.42	0.46	FRI	KIDS DR4 J231708.425-341441.05	18.95	0.22	
J223533.3-330539	338.89	-33.094	0.013	34.61	43.01	63.35	0.97	0.65	0.71	FRII	KIDS DR4 J223533.373-330538.65	21.06	0.74	
J225303.0-323910	343.26	-32.654	0.005	31.50	27.85	63.53	2.57	0.42	0.46	FRI	KIDS DR4 J225303.042-323909.72	23.77	1.04	
J225019.7-303652	342.58	-30.614	0.034	33.32	29.53	63.88	1.86	0.60	0.64	FRII	KIDS DR4 J225019.762-303651.68	19.41	0.05	
J231536.0-322255	348.90	-32.379	0.015	39.19	37.61	63.99	1.13	0.42	0.45	FRI	KIDS DR4 J231535.940-322255.08	19.76	0.48	
J232107.1-342713	350.28	-34.453	0.100	35.60	34.82	64.05	0.46	0.52	0.57	FRII	KIDS DR4 J232107.037-342712.36	23.87	0.92	
J225918.9-331157	344.83	-33.200	0.010	41.46	45.96	64.08	2.43	0.69	0.75	FRII	KIDS DR4 J225918.901-331156.42	22.20	0.74	
J232303.5-313016	350.76	-31.508	0.008	36.66	48.29	64.18	0.38	0.72	0.78	FRII	KIDS DR4 J232303.512-313015.93	23.77	0.98	
J230700.3-301447	346.75	-30.247	0.002	31.28	43.91	64.25	0.95	0.66	0.71	FRII	KIDS DR4 J230700.276-301447.20	23.73	1.08	
J232552.1-315045	351.47	-31.846	0.013	36.07	43.66	64.30	2.83	0.65	0.71	FRII	KIDS DR4 J232552.029-315045.12	21.44	0.59	
J225251.1-341855	343.21	-34.318	0.027	33.62	38.47	64.42	0.19	0.57	0.62	FRII	KIDS DR4 J225251.281-341848.45	25.18	1.07	
J223735.2-310741	339.40	-31.132	0.015	36.47	46.73	64.52	2.89	0.70	0.75	FRII	KIDS DR4 J223735.300-310742.84	25.00	0.86	
J230904.6-302611	347.27	-30.437	0.011	36.84	49.61	64.55	1.07	0.74	0.80	FRII				
J224946.7-285121	342.45	-28.856	0.022	34.45	44.23	64.89	0.80	0.66	0.71	FRII	KIDS DR4 J224946.761-285142.93	22.02	0.79	
J223926.7-285143	339.86	-28.863	0.023	35.74	26.51	64.91	0.98	0.39	0.42	FRI	KIDS DR4 J230551.804-294927.71	18.58	0.54	
J230551.8-294928	346.47	-29.822	0.015	35.24	47.76	64.93	2.40	0.71	0.77	FRII				
J225457.4-321224	343.74	-32.207	0.054	34.61	41.25	65.05	0.19	0.61	0.66	FRII				
J230859.2-322857	347.25	-32.483	0.003	33.13	18.20	65.06	1.14	0.27	0.29	FRI	KIDS DR4 J230859.151-322856.53	22.42	0.84	
J224926.2-295327	342.36	-29.892	0.008	30.21	38.92	65.17	3.02	0.58	0.62	FRII	KIDS DR4 J224926.271-295326.41	18.76	0.51	
J224429.4-323301	341.12	-32.550	0.010	36.39	23.05	65.30	1.37	0.34	0.37	FRI	KIDS DR4 J224429.383-323259.35	16.99	0.20	
J225819.2-325340	344.58	-32.893	0.004	32.25	44.71	65.31	1.06	0.66	0.71	FRII	KIDS DR4 J225819.312-325338.99	24.98	0.95	
J230215.1-320938	345.57	-32.157	0.032	37.07	44.51	65.72	0.66	0.65	0.70	FRII	KIDS DR4 J230215.044-320938.27	22.78	1.02	
J231426.9-340607	348.61	-34.102	0.018	37.30	51.23	65.78	0.05	0.75	0.81	FRII	KIDS DR4 J231426.936-340606.62	20.29	0.60	
J230741.9-350725	346.92	-35.124	0.004	31.74	42.79	65.82	0.21	0.63	0.68	FRII	KIDS DR4 J230741.913-350725.27	18.40	0.29	
J224131.1-340725	340.38	-34.120	0.046	34.46	45.07	65.92	2.49	0.66	0.71	FRII	KIDS DR4 J224131.078-340724.51	22.31	0.92	
J225050.9-315756	342.71	-31.965	0.049	36.24	40.83	65.97	2.80	0.60	0.64	FRII	KIDS DR4 J225050.994-315755.08	18.25	0.30	

Continued on next page

Table 3.3 – Continued from previous page

Source Name	RA (J2000) (deg)	DEC (J2000) (deg)	Flux Density (Jy)	Size (")	a (")	b (")	PA (°)	a/b_{\max}	a/b_{\min}	Class	KIDS ID	Mag (r-band)	Z
J224125.9-324246	340.36	-32.713	0.012	36.28	51.54	65.98	2.46	0.75	0.81	FRII	KIDS DR4 J224125.922-324246.15	19.89	1.19
J225707.2-335931	344.28	-33.991	0.117	34.81	32.60	66.10	2.53	0.48	0.51	FRx	KIDS DR4 J225707.257-335930.34	21.20	0.71
J231428.4-305511	348.62	-30.920	0.055	35.52	41.91	66.14	0.26	0.61	0.66	FRII			
J225044.9-323443	342.69	-32.578	0.038	36.17	39.53	66.20	0.63	0.58	0.62	FRII			
J232616.9-320838	351.57	-32.143	0.007	37.61	50.31	66.25	1.13	0.73	0.79	FRII	KIDS DR4 J232616.814-320837.98	21.55	1.20
J232407.8-333244	351.03	-33.547	0.009	39.49	56.43	66.48	2.64	0.82	0.88	FRII	KIDS DR4 J232407.818-333244.09	23.21	0.90
J232816.9-344708	352.07	-34.783	0.018	91.74	45.89	66.50	2.42	0.67	0.72	FRII	KIDS DR4 J232816.941-344707.41	18.35	0.43
J224211.0-321822	340.54	-32.298	0.009	60.94	45.71	66.77	2.40	0.66	0.71	FRII		19.29	0.42
J223426.7-303330	338.61	-30.560	0.035	39.56	40.08	66.78	0.07	0.58	0.62	FRII	KIDS DR4 J223426.701-303330.56	20.91	0.36
J231550.5-341650	348.96	-34.281	0.357	36.29	33.35	67.15	1.49	0.48	0.52	FRx	KIDS DR4 J231550.421-341648.95	20.91	0.88
J224509.9-301242	341.29	-30.212	0.462	32.95	26.58	67.43	2.38	0.38	0.41	FRI	KIDS DR4 J224509.686-301239.94	21.90	0.67
J231710.5-345849	349.30	-34.974	0.005	38.60	48.09	67.57	1.08	0.69	0.74	FRII	KIDS DR4 J231710.446-345848.39	24.52	1.02
J232606.7-343102	351.53	-34.517	0.004	33.28	47.09	67.94	1.21	0.67	0.72	FRII	KIDS DR4 J232606.706-343101.43	21.53	0.67
J224452.4-311545	341.22	-31.264	0.010	36.63	51.81	68.02	0.47	0.73	0.79	FRII	KIDS DR4 J224452.407-311546.04	20.60	0.62
J231415.9-303718	348.57	-30.622	0.630	36.35	22.36	68.05	1.86	0.32	0.34	FRI	KIDS DR4 J231415.943-303717.73	20.49	0.61
J224100.6-325747	340.25	-32.963	0.012	38.95	50.99	68.13	2.97	0.72	0.78	FRII	KIDS DR4 J224100.601-325746.83	21.20	0.78
J225610.9-312436	344.04	-31.413	0.007	35.60	44.93	68.14	1.07	0.64	0.68	FRII	KIDS DR4 J225611.057-312434.75	23.69	0.93
J232041.4-303008	350.17	-30.502	0.081	37.11	42.50	68.29	0.49	0.60	0.65	FRII	KIDS DR4 J232040.869-303004.95	25.30	1.49
J223807.2-310514	339.53	-31.086	0.142	35.68	38.08	68.44	1.20	0.54	0.58	FRII	KIDS DR4 J223807.266-310514.92	24.73	0.82
J231552.8-335255	348.97	-33.882	0.010	37.92	47.76	68.62	2.33	0.67	0.72	FRII	KIDS DR4 J231553.467-335257.91	22.70	1.09
J225325.2-351607	343.36	-35.269	0.013	31.22	33.90	68.66	2.12	0.48	0.51	FRx	KIDS DR4 J225325.171-351606.63	19.23	1.79
J231647.1-344236	349.20	-34.709	0.388	34.50	30.10	69.34	1.56	0.42	0.45	FRI	KIDS DR4 J231647.051-344235.74	17.22	0.05
J233540.2-311909	338.92	-31.319	0.030	37.49	47.50	69.86	1.61	0.66	0.71	FRII	KIDS DR4 J233540.388-314447.55	22.83	0.89
J232037.8-334840	350.16	-33.811	0.026	37.75	40.31	70.35	0.08	0.55	0.59	FRII	KIDS DR4 J232037.769-334839.39	23.18	0.92
J224824.0-314408	342.10	-31.733	0.008	39.90	48.09	70.59	3.05	0.66	0.71	FRII	KIDS DR4 J224823.923-314407.17	20.02	0.49
J232321.5-290629	350.84	-29.108	0.014	36.50	48.09	70.59	3.05	0.66	0.71	FRII	KIDS DR4 J232321.508-290628.58	22.06	0.90
J224742.7-330642	341.93	-33.111	0.024	43.29	35.53	70.87	0.76	0.48	0.52	FRx	KIDS DR4 J224742.544-330641.63	17.60	0.24
J232322.1-300625	350.84	-30.100	0.011	38.49	50.56	70.99	2.99	0.69	0.74	FRII	KIDS DR4 J232322.029-300625.12	17.43	0.25
J224548.3-351827	341.45	-35.307	0.113	41.25	22.64	71.14	0.94	0.31	0.33	FRI	KIDS DR4 J224548.299-351827.11	24.08	1.02
J232721.7-322518	351.84	-32.422	0.005	29.12	37.11	71.17	1.62	0.50	0.54	FRII	KIDS DR4 J232721.623-322515.26	18.97	0.44
J22310.2-345608	350.80	-34.936	0.033	38.18	45.63	71.28	1.79	0.62	0.66	FRII	KIDS DR4 J22310.215-345607.28	18.84	0.42
J224317.2-315814	340.82	-31.972	0.007	44.95	57.39	71.38	2.59	0.78	0.83	FRII	KIDS DR4 J224317.200-315814.25	23.90	0.92
J225436.0-330539	343.65	-33.091	0.018	39.03	51.54	71.52	0.41	0.70	0.75	FRII	KIDS DR4 J225435.943-330538.75	21.60	1.21
J224449.9-334330	341.21	-33.725	0.144	38.00	40.70	71.61	0.22	0.55	0.59	FRII	KIDS DR4 J224449.899-334330.58	16.65	0.01
J233329.3-315900	338.38	-31.977	0.006	40.62	56.68	71.73	0.84	0.76	0.82	FRII		23.48	1.09
J230025.4-311012	345.11	-31.168	0.014	38.21	55.90	72.40	0.19	0.75	0.80	FRII	KIDS DR4 J230025.495-311009.59	22.80	0.19
J232133.4-343933	350.39	-34.660	0.044	38.44	49.62	72.83	2.46	0.66	0.71	FRII	KIDS DR4 J232133.346-343932.61	18.50	0.39
J223708.4-322744	339.29	-32.463	0.004	47.67	59.66	72.92	1.63	0.79	0.85	FRII			

Continued on next page

Table 3.3 – Continued from previous page

Source Name	RA (J2000) (deg)	DEC (J2000) (deg)	Flux Density (Jy)	Size (")	a (")	b (")	PA (°)	a/b _{max}	a/b _{min}	Class	KIDS ID	Mag (r-band)	Z	
J223955.2-304146	339.98	-30.696	0.012	29.39	28.54	73.01	0.73	0.38	0.40	FRI	KIDS DR4 J223321.348-312106.44	20.25	0.28	
J223321.3-312107	338.34	-31.351	0.010	40.80	52.75	73.01	1.66	0.70	0.75	FRII	KIDS DR4 J231928.706-302746.76	24.08	0.73	
J231928.3-302743	349.87	-30.463	0.154	41.11	51.48	73.04	2.61	0.68	0.73	FRII	KIDS DR4 J232413.688-335658.64	22.95	0.99	
J232413.7-335659	351.06	-33.948	0.036	39.42	45.62	73.11	2.97	0.60	0.65	FRII	KIDS DR4 J225416.281-351406.70	17.42	0.24	
J225416.3-351407	343.57	-35.239	0.029	78.00	19.53	73.17	0.58	0.26	0.28	FRI	KIDS DR4 J224338.638-344907.96	20.01	0.48	
J224338.7-344908	340.91	-34.818	0.246	38.76	45.07	73.29	0.65	0.59	0.64	FRII	KIDS DR4 J231326.784-331730.61	21.16	0.66	
J231326.9-331731	348.36	-33.288	0.003	44.73	65.34	73.30	0.19	0.86	0.92	FRII	KIDS DR4 J232245.562-330619.14	20.94	0.71	
J222445.6-330619	350.69	-33.105	0.004	37.82	48.11	73.53	1.94	0.63	0.68	FRII	KIDS DR4 J225518.199-330002.98	24.86	0.81	
J225518.0-330010	343.82	-33.002	0.007	38.06	23.75	73.71	3.10	0.31	0.33	FRI	KIDS DR4 J230022.810-320205.12	21.21	0.68	
J230022.8-320205	345.10	-32.035	0.002	37.66	55.19	74.29	0.97	0.72	0.77	FRII	KIDS DR4 J225036.083-290325.75	20.56	0.08	
J225036.2-290327	342.65	-29.056	0.069	38.24	45.07	74.39	0.97	0.59	0.63	FRII				
J225323.4-321732	343.35	-32.293	0.019	42.42	59.77	74.58	1.66	0.78	0.83	FRII				
J224542.8-354358	341.43	-35.732	0.381	33.21	26.34	74.94	0.55	0.34	0.36	FRI				
J223116.2-344941	337.82	-34.828	0.007	41.48	57.12	75.18	2.72	0.74	0.79	FRII	KIDS DR4 J223116.206-344940.31	23.96	1.26	
J232228.5-284439	350.62	-28.743	0.111	36.42	37.25	75.20	1.66	0.48	0.51	FRx	KIDS DR4 J232228.357-284438.63	23.74	1.13	
J223956.8-315547	339.99	-32.776	0.013	40.30	62.47	75.90	1.73	0.77	0.82	FRII				
J223908.8-324633	339.79	-32.776	0.034	39.71	52.74	76.08	1.03	0.67	0.72	FRII	KIDS DR4 J223908.818-324633.39	24.60	1.33	
J231229.8-353729	348.12	-35.622	0.019	38.24	53.85	76.27	1.98	0.68	0.73	FRII				
J231440.3-305246	348.67	-30.881	0.056	43.43	38.24	76.67	1.73	0.48	0.52	FRx				
J223113.7-315342	337.81	-31.896	0.005	49.42	62.26	76.69	2.36	0.79	0.84	FRII	KIDS DR4 J223113.703-315342.22	22.02	0.37	
J224321.9-294610	340.84	-29.770	0.009	35.06	21.09	76.95	0.32	0.27	0.28	FRII	KIDS DR4 J224321.790-294611.26	17.78	0.32	
J224313.9-290428	340.81	-29.075	0.008	40.22	18.00	77.16	2.04	0.23	0.24	FRI	KIDS DR4 J224313.944-290428.66	23.43	1.10	
J223458.5-325044	338.74	-32.846	0.073	40.90	53.69	77.23	0.49	0.67	0.72	FRII	KIDS DR4 J223458.526-325044.26	22.60	1.23	
J230303.9-323229	345.77	-32.540	0.009	46.63	53.06	77.35	2.51	0.66	0.71	FRII	KIDS DR4 J230303.901-323228.47	18.90	0.39	
J225330.0-315029	343.38	-31.840	0.028	36.43	58.59	77.40	0.37	0.73	0.78	FRII				
J224957.7-303923	342.49	-30.656	0.006	41.56	59.17	77.79	1.76	0.74	0.79	FRII	KIDS DR4 J224957.717-303922.79	22.39	0.87	
J224607.5-304305	341.53	-30.717	0.230	30.58	34.73	61.15	2.32	0.55	0.59	FRII	KIDS DR4 J224607.480-304303.75	22.59	1.01	
J223012.2-322219	337.55	-32.370	0.038	40.95	43.73	77.95	1.07	0.54	0.58	FRII	KIDS DR4 J223012.179-322218.72	19.56	0.48	
J223551.5-305741	338.97	-30.965	0.011	42.34	60.88	78.19	2.78	0.75	0.80	FRII	KIDS DR4 J223551.509-305740.87	24.73	1.59	
J232213.8-284657	350.56	-28.781	0.023	37.38	34.73	78.21	1.00	0.43	0.46	FRI	KIDS DR4 J232213.795-284656.12	22.17	0.69	
J223057.2-315542	350.23	-31.928	0.031	41.70	55.90	78.47	1.74	0.69	0.74	FRII	KIDS DR4 J223057.205-315542.62	19.87	0.14	
J230840.9-342545	347.17	-34.437	0.004	42.92	59.81	78.61	0.05	0.74	0.79	FRII	KIDS DR4 J230840.932-342544.70	19.40	0.41	
J232040.5-303539	350.17	-30.595	0.128	41.14	50.99	78.64	1.74	0.63	0.67	FRII	KIDS DR4 J232040.504-303538.48	19.41	0.39	
J224946.0-291610	342.44	-29.271	0.027	36.73	44.51	78.81	1.96	0.55	0.58	FRII	KIDS DR4 J224946.024-291610.11	23.35	0.85	
J222944.1-330920	337.43	-33.152	0.010	42.10	61.05	78.83	2.17	0.75	0.80	FRII				
J231251.3-323525	348.21	-32.590	0.092	41.82	52.74	78.93	0.11	0.65	0.69	FRII				
J232039.8-335105	350.17	-33.849	0.040	43.15	55.07	79.19	1.47	0.67	0.72	FRII				
J225916.2-341715	344.82	-34.287	0.014	45.81	64.64	79.36	1.12	0.79	0.84	FRII	KIDS DR4 J225916.197-341715.17	23.07	0.89	

Continued on next page

Table 3.3 – Continued from previous page

Source Name	RA (J2000) (deg)	DEC (J2000) (deg)	Flux Density (Jy)	Size (")	a (")	b (")	PA (°)	a/b_{\max}	a/b_{\min}	Class	KIDS ID	Mag (r-band)	Z
J224431.6-351242	341.13	-35.219	0.009	45.18	60.10	79.37	0.27	0.73	0.78	FRII	KIDS DR4 J224431.423-351241.46	24.96	0.53
J230215.1-343302	345.56	-34.551	0.003	39.18	58.40	79.37	0.68	0.71	0.76	FRII	KIDS DR4 J230215.117-343302.21	23.65	0.95
J230724.7-354604	346.85	-35.768	0.044	34.17	60.89	79.51	1.28	0.74	0.79	FRII			
J224036.2-333654	340.15	-33.615	0.004	40.31	59.40	79.62	1.47	0.72	0.77	FRII			
J230913.4-341410	347.31	-34.236	0.025	44.03	55.34	79.91	2.85	0.67	0.71	FRII	KIDS DR4 J224036.149-333654.53	24.77	1.21
J225620.7-294431	344.09	-29.744	0.004	44.78	62.86	80.16	0.42	0.76	0.81	FRII	KIDS DR4 J230913.365-341409.64	18.33	0.37
J225318.0-285409	343.33	-28.901	0.024	44.05	49.31	80.48	2.12	0.59	0.63	FRII	KIDS DR4 J225620.702-294433.85	24.39	0.78
J230551.9-295544	346.47	-29.927	0.010	48.48	66.53	80.80	1.43	0.80	0.85	FRII	KIDS DR4 J225318.025-285408.71	18.11	0.39
J231753.4-292939	349.47	-29.495	0.057	42.13	57.13	80.88	0.41	0.69	0.73	FRII	KIDS DR4 J230552.008-295543.29	19.85	0.51
J230827.9-341151	347.11	-34.186	0.008	58.29	70.60	81.23	3.10	0.84	0.90	FRII	KIDS DR4 J231753.345-292938.72	23.55	1.56
J225604.7-302337	344.02	-30.394	0.004	40.77	60.66	81.25	0.51	0.72	0.77	FRII	KIDS DR4 J230827.894-341150.69	15.07	0.01
J225229.2-290603	343.12	-29.101	0.384	42.21	55.51	81.51	2.60	0.66	0.70	FRII	KIDS DR4 J225604.632-302332.65	24.64	0.53
J223709.3-315255	339.29	-31.882	0.101	43.34	60.42	81.56	2.74	0.72	0.76	FRII	KIDS DR4 J225229.179-290602.65	23.94	1.90
J224954.6-352654	342.48	-35.447	0.017	43.20	67.09	81.56	2.89	0.80	0.85	FRII			
J232124.8-284528	350.35	-28.758	0.152	38.29	42.57	81.70	0.82	0.51	0.54	FRII	KIDS DR4 J224954.630-352653.96	22.17	0.83
J231939.4-325949	349.91	-32.997	0.023	41.78	60.47	81.80	0.51	0.72	0.76	FRII	KIDS DR4 J232124.818-284528.37	21.80	0.88
J230831.2-341925	345.88	-34.328	0.034	52.34	71.96	81.89	1.68	0.85	0.91	FRII	KIDS DR4 J231939.373-325949.04	25.20	1.07
J223710.4-353929	339.29	-35.659	0.043	41.67	58.36	81.91	0.90	0.69	0.73	FRII	KIDS DR4 J230831.201-341924.47	18.26	0.31
J224101.9-312759	340.26	-31.463	0.025	45.46	60.83	82.33	0.12	0.72	0.76	FRII			
J232601.7-330329	351.51	-33.056	0.024	50.15	52.02	82.55	1.92	0.61	0.65	FRII	KIDS DR4 J232601.693-350327.73	17.82	0.40
J232624.0-313741	351.60	-31.627	0.029	45.78	56.18	82.58	0.52	0.66	0.70	FRII	KIDS DR4 J232623.988-313740.89	19.25	0.44
J224822.6-304653	342.09	-30.782	0.119	38.39	46.70	82.81	1.17	0.55	0.58	FRII	KIDS DR4 J224822.636-304652.42	23.81	1.03
J224436.6-342913	341.15	-34.488	0.013	44.11	65.43	82.94	2.35	0.77	0.81	FRII	KIDS DR4 J224436.608-342912.94	23.49	0.84
J231525.7-320938	348.86	-32.160	0.025	46.44	62.50	83.20	0.91	0.73	0.77	FRII	KIDS DR4 J231525.636-320937.58	22.34	0.88
J225633.2-292619	344.13	-29.436	0.030	43.49	62.50	83.23	2.49	0.73	0.77	FRII	KIDS DR4 J225633.130-292619.19	20.09	0.33
J231001.1-342934	347.51	-34.492	0.021	44.23	58.31	83.27	2.62	0.68	0.72	FRII	KIDS DR4 J231000.601-342928.84	17.92	0.79
J231828.2-295547	349.62	-29.934	0.013	60.58	60.47	83.43	2.69	0.70	0.75	FRII	KIDS DR4 J231828.189-295547.18	21.98	0.97
J223601.1-291832	339.01	-29.316	0.160	41.88	57.50	83.68	3.11	0.67	0.71	FRII	KIDS DR4 J223601.125-291831.34	23.42	0.94
J224616.7-323543	341.57	-32.596	0.003	43.11	64.21	84.29		0.74	0.79	FRII	KIDS DR4 J224616.742-323543.33	18.98	0.29
J223520.2-334419	338.84	-33.743	0.024	42.71	55.74	84.69	2.31	0.64	0.68	FRII	KIDS DR4 J223519.946-334427.11	24.20	1.79
J231407.3-331057	348.53	-33.185	0.017	42.29	63.95	84.80	2.01	0.73	0.78	FRII	KIDS DR4 J231407.676-331100.77	25.30	1.15
J224714.0-290232	341.81	-29.041	0.080	45.76	60.52	85.17	2.38	0.69	0.73	FRII	KIDS DR4 J224714.026-290231.99	23.30	1.32
J223540.6-350423	338.92	-35.073	0.091	51.73	27.95	86.05	2.50	0.32	0.33	FRI	KIDS DR4 J223540.719-350421.60	17.45	0.23
J231303.5-330835	348.26	-33.148	0.050	44.73	67.27	86.35	0.73	0.76	0.80	FRII	KIDS DR4 J231303.495-330834.90	21.16	0.67
J225932.0-315856	344.87	-31.977	0.007	49.49	75.31	86.42	2.23	0.85	0.90	FRII	KIDS DR4 J225931.969-315856.48	21.26	5.22
J224150.0-333510	340.46	-33.587	0.006	48.14	71.63	86.44	0.71	0.81	0.85	FRII	KIDS DR4 J224150.119-333507.25	22.57	0.24
J230335.3-331512	345.90	-33.245	0.003	40.76	62.87	86.70	0.38	0.70	0.75	FRII	KIDS DR4 J230335.325-331512.31	20.44	0.60
J231857.0-324014	349.74	-32.671	0.018	50.03	67.33	86.71	1.92	0.75	0.80	FRII	KIDS DR4 J231857.015-324014.45	19.05	0.39
J230037.5-292737	345.16	-29.457	0.022	46.15	63.74	86.96	0.86	0.71	0.75	FRII	KIDS DR4 J230037.538-292737.06	20.93	0.61

Continued on next page

Table 3.3 – Continued from previous page

Source Name	RA (J2000) (deg)	DEC (J2000) (deg)	Flux Density (Jy)	Size (")	a (")	b (")	PA (°)	a/b_{\max}	a/b_{\min}	Class	KIDS ID	Mag (r-band)	Z
J224933.0-344959	342.38	-34.833	0.002	43.16	61.37	87.15	0.70	0.68	0.73	FRII	KIDS DR4 J224933.006-344938.11	23.19	0.96
J225456.4-330633	343.73	-33.107	0.039	44.85	64.03	87.16	2.23	0.71	0.76	FRII	KIDS DR4 J225457.053-330627.09	24.22	0.67
J230206.6-332201	345.53	-33.367	0.034	47.50	62.97	87.21	1.68	0.70	0.74	FRII	KIDS DR4 J230206.575-332200.46	21.85	1.06
J231630.8-313614	349.14	-31.601	0.040	45.32	64.08	87.70	1.22	0.71	0.75	FRII	KIDS DR4 J231630.835-313614.59	22.38	0.70
J231343.4-295306	348.43	-29.882	0.066	49.19	53.93	87.80	1.51	0.60	0.63	FRII	KIDS DR4 J231343.242-295307.29	17.64	0.32
J232212.0-351908	350.55	-35.319	0.110	41.67	53.50	87.92	2.52	0.59	0.63	FRII	KIDS DR4 J232212.040-351907.85	22.56	0.94
J224202.0-313614	340.51	-31.611	0.011	49.31	69.33	88.40	2.69	0.76	0.81	FRII			
J224137.4-295220	340.41	-29.871	0.006	51.84	71.09	88.47	1.49	0.78	0.83	FRII	KIDS DR4 J224137.398-295219.38	19.00	0.50
J224723.6-303644	341.86	-30.619	0.007	46.90	74.20	88.99	2.10	0.81	0.86	FRII	KIDS DR4 J224723.390-303640.47	20.36	0.13
J231707.2-292519	349.28	-29.421	0.012	48.51	72.91	89.24	0.86	0.79	0.84	FRII	KIDS DR4 J231707.235-292518.59	21.52	0.62
J225546.1-354437	343.94	-35.735	0.040	46.81	68.24	89.60	0.17	0.74	0.78	FRII			
J225104.5-334617	342.77	-33.768	0.006	45.31	66.39	90.41	2.55	0.71	0.76	FRII	KIDS DR4 J225104.488-334617.02	18.54	0.34
J230930.8-341327	347.38	-34.225	0.048	49.43	63.20	90.62	2.63	0.68	0.72	FRII	KIDS DR4 J230930.749-341327.06	19.22	0.48
J230940.6-335124	347.42	-33.857	0.003	74.00	30.33	91.77	1.71	0.32	0.34	FRI	KIDS DR4 J230940.573-335123.85	19.47	0.54
J225006.2-311817	342.53	-31.299	0.005	51.24	77.64	92.34	0.86	0.82	0.86	FRII	KIDS DR4 J225006.139-311816.95	20.95	0.74
J230046.3-330825	345.18	-33.137	0.010	49.49	77.90	92.93	2.02	0.82	0.86	FRII	KIDS DR4 J230046.442-330827.50	25.44	1.40
J230704.3-333331	346.78	-33.559	0.012	52.28	72.16	93.12	1.80	0.75	0.80	FRII	KIDS DR4 J230704.284-333330.47	21.53	0.63
J231612.0-285240	349.05	-28.877	0.086	48.69	64.52	93.23	0.94	0.67	0.71	FRII	KIDS DR4 J231612.267-285240.76	22.56	0.23
J225237.5-300333	343.16	-30.058	0.007	47.82	73.18	93.52	0.64	0.76	0.80	FRII	KIDS DR4 J225237.521-300332.16	19.77	0.45
J230259.0-294849	345.75	-29.814	0.048	41.15	44.83	93.55	1.06	0.47	0.49	FRI	KIDS DR4 J230259.567-294850.93	16.09	0.17
J224208.8-341715	340.54	-34.288	0.083	45.96	6	94.75	1.35	0.62	0.65	FRII			
J223210.9-345950	350.79	-34.998	0.100	47.67	66.19	95.14	1.37	0.68	0.71	FRII	KIDS DR4 J232310.914-345950.26	21.52	1.26
J224725.2-343613	341.86	-34.604	0.020	51.15	86.51	95.54	0.19	0.88	0.93	FRII	KIDS DR4 J224725.239-343615.55	17.59	0.29
J224741.3-300138	341.92	-30.028	0.298	55.79	39.14	96.63	1.37	0.39	0.42	FRI	KIDS DR4 J224741.286-300138.37	17.75	0.31
J230919.9-341950	347.33	-34.331	0.035	51.98	71.59	96.83	2.71	0.72	0.76	FRII	KIDS DR4 J230919.900-341949.94	24.47	1.42
J224638.6-341856	341.66	-34.318	0.485	46.55	59.28	97.15	2.74	0.59	0.63	FRII	KIDS DR4 J224638.605-341856.26	19.13	0.93
J225817.5-325836	344.57	-32.985	0.029	53.53	86.03	97.34	0.77	0.86	0.91	FRII	KIDS DR4 J225817.479-325839.43	25.41	1.11
J225338.3-344742	343.41	-34.796	0.064	53.68	51.54	97.47	0.83	0.52	0.54	FRII	KIDS DR4 J225338.246-344742.20	16.69	0.21
J230025.6-310356	345.11	-31.065	0.008	53.11	86.22	98.02	2.16	0.86	0.90	FRII	KIDS DR4 J230025.865-310400.55	24.20	0.20
J231223.9-313144	348.10	-31.526	0.031	58.92	44.73	98.68	0.47	0.44	0.47	FRI			
J232533.6-302549	351.39	-30.432	0.029	51.58	78.51	98.86	0.15	0.77	0.81	FRII	KIDS DR4 J232533.581-302548.65	19.40	1.58
J225625.8-354558	344.10	-35.759	0.089	53.18	68.39	99.00	2.34	0.67	0.71	FRII			
J225434.6-320928	343.64	-32.157	0.095	52.19	31.59	99.63	2.87	0.31	0.33	FRI	KIDS DR4 J232704.247-304159.86	18.81	0.19
J232704.2-304200	351.76	-30.703	0.023	52.66	67.70	99.94	1.37	0.66	0.69	FRII			
J223635.7-320003	339.15	-32.000	0.064	48.75	77.66	100.18	0.06	0.76	0.80	FRII			
J225543.8-344049	343.93	-34.680	0.059	55.31	72.54	100.22	1.53	0.71	0.74	FRII	KIDS DR4 J225543.753-344049.02	23.86	0.99
J230322.4-325406	345.84	-32.898	0.048	52.00	77.01	100.31	2.94	0.75	0.79	FRII			
J231915.1-285321	349.81	-28.893	0.032	74.83	49.24	100.40	1.42	0.48	0.50	FRx	KIDS DR4 J231915.076-285320.51	18.45	0.41
J230608.2-310336	346.53	-31.059	0.012	51.88	81.43	100.80	2.74	0.79	0.83	FRII	KIDS DR4 J230608.177-310336.30	20.17	0.69

Continued on next page

Table 3.3 – Continued from previous page

Source Name	RA (J2000) (deg)	DEC (J2000) (deg)	Flux Density (Jy)	Size (")	a (")	b (")	PA (°)	a/b_{\max}	a/b_{\min}	Class	KIDS ID	Mag (r-band)	Z
J231225.1-350454	348.10	-35.083	0.129	50.54	70.04	101.20	0.92	0.68	0.71	FR II	KIDS DR4 J231225.038-350454.20	21.02	0.81
J232429.2-300527	351.12	-30.092	0.007	6	73.82	101.48	2.67	0.71	0.75	FR II	KIDS DR4 J232429.250-300527.45	22.37	0.73
J231320.9-322509	348.34	-32.418	0.006	56.05	84.28	101.77	1.96	0.81	0.85	FR II			0.24
J231100.3-332016	347.75	-33.337	0.027	50.88	75.21	102.16	1.19	0.72	0.75	FR II	KIDS DR4 J231100.273-332015.70	18.40	0.31
J231221.6-294224	348.09	-29.707	0.013	50.18	74.32	103.12	1.28	0.70	0.74	FR II	KIDS DR4 J231221.555-294224.35	15.78	0.12
J231237.5-304048	348.16	-30.685	0.010	38.59	72.51	103.17	2.39	0.69	0.72	FR II			
J230617.8-321557	346.57	-32.267	0.004	6	77.74	103.26	1.68	0.74	0.77	FR II	KIDS DR4 J230617.800-321556.47	20.60	0.61
J231316.9-311816	348.32	-31.308	0.029	79.81	59.42	103.44	0.37	0.56	0.59	FR II			0.42
J230027.7-305453	345.12	-30.913	0.004	60.88	62.02	103.46	2.47	0.59	0.61	FR II	KIDS DR4 J230027.630-305451.61	17.21	0.20
J232502.8-350352	351.26	-35.065	0.171	58.40	62.50	104.07	1.03	0.59	0.62	FR II	KIDS DR4 J232502.723-350351.23	18.79	0.31
J223919.2-315652	339.83	-31.948	0.014	55.06	104.81	104.81	2.19			single			0.27
J225524.7-345308	343.85	-34.886	0.017	56.48	82.23	104.88	0.34	0.77	0.80	FR II	KIDS DR4 J225524.728-345307.82	22.08	0.95
J230713.0-344127	346.80	-34.693	0.038	54.63	81.39	105.50	0.74	0.75	0.79	FR II	KIDS DR4 J230713.294-344127.81	23.82	1.33
J231904.4-354135	349.77	-35.693	0.039	49.57	77.86	105.52	3.05	0.72	0.76	FR II			
J232507.8-343136	351.28	-34.526	0.044	53.19	82.80	107.42	2.07	0.75	0.79	FR II			0.97
J225119.8-342120	342.83	-34.355	0.160	56.90	55.90	107.45	0.08	0.51	0.53	FR II	KIDS DR4 J225119.733-342120.21	15.31	0.10
J231245.4-353947	348.19	-35.663	0.010	60.27	97.67	107.69	0.36	0.89	0.93	FR II			
J230734.1-333251	346.89	-33.548	0.235	57.89	72.67	108.34	2.46	0.66	0.69	FR II	KIDS DR4 J230734.138-333251.82	22.81	0.98
J231129.6-353325	347.87	-35.557	0.090	57.60	75.58	108.58	0.98	0.68	0.71	FR II	KIDS DR4 J231129.405-353331.93	22.31	0.72
J223656.4-325310	339.23	-32.886	0.022	59.06	80.16	108.59	1.63	0.72	0.76	FR II	KIDS DR4 J223656.352-325309.78	24.57	1.04
J230351.2-344728	345.95	-34.781	0.003	54.66	80.99	108.86		0.73	0.76	FR II	KIDS DR4 J230351.227-344727.77	21.94	0.95
J230652.6-295200	346.72	-29.870	0.200	63.76	66.17	109.01	2.77	0.59	0.62	FR II	KIDS DR4 J230652.623-295159.00	19.12	0.40
J231234.8-340420	348.15	-34.072	0.305	55.99	80.78	109.22	1.91	0.72	0.76	FR II	KIDS DR4 J231234.765-340419.97	16.44	0.20
J225212.0-353900	343.05	-35.649	0.464	55.44	78.46	109.87	2.18	0.70	0.73	FR II			
J230542.2-304314	346.42	-30.718	0.006	62.46	27.10	109.95	0.49	0.24	0.25	FR I	KIDS DR4 J230542.189-304311.80	17.15	0.20
J225713.4-343248	344.30	-34.544	0.105	58.69	85.51	110.28	2.60	0.76	0.79	FR II	KIDS DR4 J225713.428-343248.31	22.59	1.16
J230316.4-301754	345.82	-30.298	0.080	60.12	33.78	110.49	2.97	0.30	0.31	FR I	KIDS DR4 J230316.321-301752.96	19.32	0.50
J223706.6-315601	339.28	-31.934	0.007	56.05	84.87	110.57	0.68	0.75	0.79	FR II			
J225450.5-324239	343.71	-32.710	0.012	61.86	97.19	111.21	2.25	0.85	0.89	FR II	KIDS DR4 J225450.489-324238.53	17.81	0.23
J230221.4-295129	345.59	-29.859	0.042	70.19	28.11	111.48	0.25	0.25	0.26	FR I	KIDS DR4 J230221.353-295128.63	18.73	0.47
J231037.7-334518	347.66	-33.755	0.093	57.55	84.59	112.54	0.97	0.74	0.77	FR II	KIDS DR4 J231037.693-334518.45	21.88	2.78
J231813.3-321503	349.55	-32.252	0.008	65.39	95.69	112.81	1.25	0.83	0.87	FR II	KIDS DR4 J231813.301-321502.77	23.03	0.86
J231016.8-330106	347.57	-33.018	0.078	61.49	82.23	113.19	2.74	0.71	0.74	FR II	KIDS DR4 J231016.865-330107.17	19.52	0.32
J224036.1-335517	340.15	-33.922	0.042	61.32	93.68	113.48	1.92	0.81	0.84	FR II	KIDS DR4 J224036.112-335516.76	20.22	0.64
J224046.4-334907	340.20	-33.827	0.002	58.23	92.49	113.53		0.80	0.83	FR II	KIDS DR4 J224046.099-334911.49	24.64	0.22
J224959.9-331521	342.50	-33.255	0.052	63.18	80.09	114.15	0.26	0.69	0.72	FR II	KIDS DR4 J224959.853-331521.01	18.03	0.56
J223541.0-343957	338.92	-34.666	0.007	53.63	87.84	114.71	2.53	0.75	0.78	FR II	KIDS DR4 J223541.029-343956.68	18.56	0.30
J223120.7-314030	337.84	-31.669	0.424	49.42	70.78	116.32	0.71	0.60	0.62	FR II	KIDS DR4 J223120.674-314029.98	16.85	1.03
J230041.0-340422	345.17	-34.075	0.063	60.76	88.39	116.89	2.43	0.74	0.77	FR II	KIDS DR4 J230041.031-340422.06	20.92	0.72

Continued on next page

Table 3.3 – Continued from previous page

Source Name	RA (J2000) (deg)	DEC (J2000) (deg)	Flux Density (Jy)	Size (")	<i>a</i> (")	<i>b</i> (")	PA (°)	<i>a</i> / <i>b</i> _{max}	<i>a</i> / <i>b</i> _{min}	Class	KIDS ID	Mag (r-band)	Z
J223041.6-321920	337.67	-32.320	0.040	60.76	95.20	117.60	0.25	0.79	0.83	FR II	KiDS DR4 J223041.624-321920.26	25.04	1.44
J224006.4-294049	340.03	-29.680	0.036	65.02	100.78	119.00	2.78	0.83	0.87	FR II	KiDS DR4 J224006.447-294047.90	18.75	0.55
J231720.9-320733	349.34	-32.122	0.035	60.76	98.90	120.80	0.36	0.80	0.84	FR II	KiDS DR4 J231720.791-320732.86	22.72	1.16
J233329.7-321953	338.37	-32.331	0.071	63.93	89.23	122.24	2.63	0.72	0.75	FR II			
J230841.3-301514	347.17	-30.253	0.043	72.50	36.97	122.76	1.79	0.30	0.31	FR I			0.21
J231033.2-293206	347.64	-29.535	0.023	70.21	102.01	123.17	2.30	0.81	0.85	FR II	KiDS DR4 J231033.204-293206.07	18.60	0.35
J230224.6-285837	345.61	-28.966	0.016	79.69	109.80	123.41	0.12	0.87	0.91	FR II	KiDS DR4 J230224.513-285836.90	16.78	0.22
J223654.7-285145	339.23	-28.862	0.038	52.71	60.21	123.52	1.14	0.48	0.50	FR I	KiDS DR4 J223654.647-285145.18	19.78	0.46
J230631.7-335752	346.64	-33.957	0.071	68.69	98.65	124.27	0.06	0.78	0.81	FR II	KiDS DR4 J230631.748-335751.95	19.79	0.09
J231122.0-325625	347.85	-32.938	0.051	64.06	97.50	124.30	1.15	0.77	0.80	FR II	KiDS DR4 J231121.969-325624.48	23.96	0.83
J230052.3-325024	345.22	-32.840	0.005	66.10	111.50	125.20	1.20	0.87	0.91	FR II	KiDS DR4 J230052.305-325024.00	21.48	0.77
J225615.5-293047	344.06	-29.511	0.045	63.99	101.24	125.20	2.95	0.79	0.83	FR II	KiDS DR4 J225615.358-293044.89	18.76	0.25
J231259.7-343801	348.26	-34.620	0.015	65.17	103.50	125.44	0.66	0.81	0.84	FR II	KiDS DR4 J231259.709-343801.38	19.94	0.41
J224930.5-352609	342.37	-35.434	0.009	45.96	71.98	125.73	2.00	0.56	0.58	FR II	KiDS DR4 J224930.539-352609.51	23.13	1.34
J230141.8-344149	345.42	-34.696	0.011	68.11	47.87	127.10	1.74	0.37	0.38	FR I	KiDS DR4 J230141.796-344147.52	17.52	0.31
J225458.1-320734	343.74	-32.126	0.013	62.91	43.53	127.15	2.11	0.34	0.35	FR I			0.24
J230023.5-314148	345.10	-31.695	0.022	70.88	92.64	127.45	0.04	0.71	0.74	FR II	KiDS DR4 J230023.483-314147.89	19.36	0.41
J224043.1-314216	340.18	-31.704	0.144	72.20	91.00	130.49	1.91	0.68	0.71	FR II			
J231310.5-315753	348.29	-31.964	1.150	60.17	84.38	130.55	1.67	0.63	0.66	FR II			0.33
J225211.9-321558	343.05	-32.263	0.004	72.03	94.12	131.62	1.73	0.70	0.73	FR II			0.24
J223902.4-330507	339.77	-33.089	0.005	62.99	96.72	131.66	1.40	0.72	0.75	FR II			
J223651.2-334300	339.22	-33.717	0.010	72.57	112.75	132.51	1.51	0.84	0.87	FR II	KiDS DR4 J223651.200-334259.14	20.66	1.87
J230425.8-322602	346.10	-32.437	0.005	70.28	116.43	132.61	1.31	0.86	0.89	FR II			
J230246.7-290838	345.70	-29.145	0.094	71.57	11	133.09	3.06	0.81	0.84	FR II	KiDS DR4 J230246.724-290837.67	18.21	0.43
J232040.4-351434	350.17	-35.244	0.017	72.94	113.19	134.95	2.32	0.82	0.85	FR II	KiDS DR4 J232040.417-351434.36	21.82	0.82
J224038.2-321201	340.17	-32.189	0.065	71.28	111.02	135.74	0.63	0.80	0.83	FR II			
J230112.5-294440	345.30	-29.738	0.012	131.65	123.14	137.17	2.38	0.88	0.91	FR II	KiDS DR4 J230112.372-294440.16	18.24	0.31
J223821.4-302045	339.59	-30.346	0.014	83.48		137.21	1.45			single	KiDS DR4 J223821.475-302045.69	17.17	0.21
J230819.3-290550	347.08	-29.097	0.039	72.39	106.19	137.22	0.26	0.76	0.79	FR II	KiDS DR4 J230819.288-290549.89	19.69	0.44
J231111.4-333714	347.80	-33.622	0.006	62.99	111.05	137.52		0.79	0.82	FR II	KiDS DR4 J231111.343-333714.48	18.77	0.28
J230154.2-353541	345.49	-35.595	0.066	71.12	95.82	140.19	1.69	0.67	0.70	FR II	KiDS DR4 J230154.137-353541.18	20.60	0.69
J224436.2-335808	341.15	-33.970	0.025	78.98	42.81	140.57	0.10	0.30	0.31	FR I	KiDS DR4 J224436.214-335808.15	14.23	0.07
J223441.7-294855	351.17	-29.817	0.017	58.99	83.09	140.79	3.08	0.58	0.60	FR II	KiDS DR4 J223441.625-294856.42	20.15	0.48
J223711.7-342628	339.30	-34.436	0.060	67.70	77.20	140.98	2.46	0.54	0.56	FR II	KiDS DR4 J223711.836-342629.04	14.03	0.16
J223958.1-304041	339.99	-30.686	0.020	62.76	114.26	145.01	0.46	0.77	0.80	FR II			0.28
J232024.2-305736	350.10	-30.965	0.005	76.93	126.80	146.72	3.09	0.85	0.88	FR II	KiDS DR4 J232024.210-305735.35	23.59	0.97
J231327.7-344257	348.37	-34.725	0.200	75.38	125.10	147.12	3.08	0.84	0.86	FR II	KiDS DR4 J231327.720-344256.99	22.24	0.77
J224421.6-342935	341.09	-34.492	0.036	93.77	59.63	147.89	0.44	0.40	0.41	FR I	KiDS DR4 J224421.556-342936.96	16.56	0.12
J223508.8-333004	338.79	-33.502	0.068	77.08	125.22	148.21	2.01	0.83	0.86	FR II	KiDS DR4 J223508.807-333003.77	20.66	0.80

Continued on next page

Table 3.3 – Continued from previous page

Source Name	RA (J2000) (deg)	DEC (J2000) (deg)	Flux Density (Jy)	Size (")	a (")	b (")	PA (°)	a/b_{\max}	a/b_{\min}	Class	KIDS ID	Mag (r-band)	Z
J230039.3-311737	345.17	-31.294	0.098	78.88	115.68	148.79	1.46	0.76	0.79	FRII	KIDS DR4 J230039.293-311737.40	20.73	0.25
J231940.3-314624	349.92	-31.774	0.031	73.00	117.26	149.47	1.82	0.77	0.80	FRII	KIDS DR4 J231940.239-314623.34	22.78	1.27
J230635.2-315540	346.65	-31.928	0.027	69.08	37.53	149.97	1.27	0.25	0.25	FRI	KIDS DR4 J230635.171-315540.10	14.61	0.06
J232414.6-320153	351.06	-32.031	0.384	74.58	92.21	150.24	2.69	0.60	0.62	FRII	KIDS DR4 J232414.638-320153.15	16.14	0.12
J224452.7-292856	341.22	-29.482	0.564	81.85	104.43	151.09	1.65	0.68	0.70	FRII	KIDS DR4 J224452.653-292855.61	17.01	0.21
J231342.2-305429	348.42	-30.911	0.190	97.62	54.88	151.20	1.01	0.36	0.37	FRI			0.12
J224235.2-312655	340.65	-31.443	0.097	71.65	120.93	154.12	0.76	0.77	0.80	FRII			
J223917.6-311636	339.81	-31.285	0.012	80.21	137.30	154.32	0.99	0.88	0.90	FRII			
J224007.0-311011	340.03	-31.169	0.039	65.06	134.00	156.86	0.97	0.84	0.87	FRII			
J230540.9-304717	346.42	-30.785	0.054	94.69	124.20	158.12	2.44	0.77	0.80	FRII			
J225655.0-324213	344.23	-32.705	0.040	82.11	13	159.52	1.14	0.80	0.83	FRII	KIDS DR4 J225655.042-324212.47	20.79	2.27
J223329.0-312331	338.37	-31.378	0.011	86.59	147.58	162.86	3.13	0.89	0.92	FRII	KIDS DR4 J223329.056-312331.31	21.63	0.77
J224235.8-330444	340.65	-33.081	0.028	84.82	142.01	163.84	0.05	0.85	0.88	FRII	KIDS DR4 J224235.724-350444.55	24.76	0.88
J224201.2-285935	340.51	-28.996	0.179	86.56	135.58	167.72	1.86	0.80	0.82	FRII	KIDS DR4 J224201.186-285935.44	20.49	0.51
J225420.6-320518	343.59	-32.090	0.007	86.27	139.61	168.56	2.69	0.82	0.84	FRII			0.24
J225339.1-313122	343.42	-31.523	0.011	87.75	129.14	169.10	0.44	0.75	0.78	FRII	KIDS DR4 J225339.150-313118.58	18.37	0.03
J231609.9-292308	349.04	-29.370	0.008	93.70	155.50	171.73	0.09	0.89	0.92	FRII	KIDS DR4 J231609.895-292307.83	19.34	0.35
J231258.7-311736	348.24	-31.294	0.028	96.24	150.44	171.90	0.14	0.86	0.89	FRII			0.38
J223836.4-340435	339.65	-34.075	0.023	93.03	143.20	172.01	1.77	0.82	0.84	FRII	KIDS DR4 J223836.341-340435.09	21.14	0.74
J232036.8-335331	350.15	-33.892	1.350	93.13	115.43	175.80	1.35	0.65	0.67	FRII	KIDS DR4 J232037.492-335330.81	23.31	0.39
J232140.2-284948	350.42	-28.830	0.095	91.72	148.28	176.22	1.70	0.83	0.85	FRII	KIDS DR4 J232140.142-284948.62	23.72	1.21
J231604.3-320305	349.03	-32.055	0.037	98.31	152.80	176.28	1.00	0.85	0.88	FRII	KIDS DR4 J231604.200-320305.22	18.62	0.32
J230908.3-344047	347.28	-34.679	0.219	96.18	130.05	179.24	0.01	0.72	0.74	FRII	KIDS DR4 J230908.312-344046.47	20.66	0.44
J230753.6-305034	346.98	-30.843	0.129	97.76	148.24	184.54	2.93	0.79	0.81	FRII			0.37
J232511.8-323634	351.30	-32.612	0.310	100.24	153.89	187.89	2.43	0.81	0.83	FRII	KIDS DR4 J232511.777-323634.42	16.74	0.44
J233504.3-344031	338.77	-34.679	0.015	90.10	134.00	190.58	1.75	0.69	0.71	FRII			
J232720.1-343219	351.84	-34.564	0.012	104.23	165.02	191.59	2.73	0.85	0.87	FRII	KIDS DR4 J232720.055-343219.11	19.51	0.15
J233954.3-331726	339.98	-33.291	0.031	98.39	171.56	193.22	2.41	0.88	0.90	FRII	KIDS DR4 J233954.297-331726.08	22.81	0.78
J230615.9-333336	346.58	-33.576	0.009	127.41	80.09	199.51	3.01	0.40	0.41	FRI	KIDS DR4 J230615.932-333335.17	22.10	0.99
J225146.2-331958	342.93	-33.326	0.049	82.40	181.56	203.20	2.23	0.88	0.90	FRII	KIDS DR4 J225146.218-331957.68	21.99	0.76
J233450.7-314509	338.72	-31.747	0.029	110.31	179.34	204.32	0.63	0.87	0.89	FRII			
J223241.4-345009	338.17	-34.836	0.007	123.32	191.98	219.67	2.30	0.86	0.88	FRII	KIDS DR4 J223241.334-345009.27	16.31	0.14
J225116.7-334937	342.82	-33.829	0.036	117.77	213.23	230.03	0.09	0.92	0.94	FRII	KIDS DR4 J225116.672-334936.93	20.75	0.65
J225143.0-343908	342.89	-34.655	0.008	125.85	215.68	236.93	1.49	0.90	0.92	FRII	KIDS DR4 J225143.050-343907.89	18.12	0.12
J230653.8-343909	346.72	-34.652	0.081	120.83	215.36	239.78	3.04	0.89	0.91	FRII	KIDS DR4 J230653.828-343908.83	17.56	0.39
J230111.2-335601	345.29	-33.941	0.251	121.14	218.42	241.40	0.19	0.90	0.91	FRII	KIDS DR4 J230111.209-335559.91	17.28	0.09
J230406.5-334607	346.03	-33.775	0.056	107.24	128.30	255.23	0.40	0.50	0.51	FRx			
J225749.2-353156	344.46	-35.535	0.023	133.85	88.50	277.89	2.53	0.32	0.32	FRI	KIDS DR4 J225749.192-353155.68	17.66	0.28
J231136.3-285953	347.90	-28.989	0.353	142.23	203.53	289.88	1.94	0.70	0.71	FRII	KIDS DR4 J231136.252-285952.77	15.45	0.17

Continued on next page

Table 3.3 – Continued from previous page

Source Name	RA (J2000) (deg)	DEC (J2000) (deg)	Flux Density (Jy)	Size (")	a (")	b (")	PA (°)	a/b_{\max}	a/b_{\min}	Class	KIDS ID	Mag (r-band)	Z
J225918.7-311237	344.83	-31.208	0.042	166.32	310.58	325.93	2.10	0.95	0.96	FRII	KiDSDR4 J225918.701-311236.41	19.30	0.41
J223715.9-342342	339.32	-34.395	0.007	127.98	246.56	335.54	0.24	0.73	0.74	FRII	KiDSDR4 J223715.862-342341.36	23.51	0.92
J225336.0-345531	343.42	-34.921	0.433	178.89	371.69	375.67	1.13	0.98	1.00	FRII	KiDSDR4 J225336.009-345530.53	17.46	0.21
J223934.9-353058	339.91	-35.521	0.053	192.07	406.24	426.44	0.46	0.95	0.96	FRII	KiDSDR4 J223934.859-353058.42	20.77	0.63
J232124.6-313421	350.35	-31.573	0.013	233.40	425.21	443.33	0.68	0.95	0.96	FRII	KiDSDR4 J232124.534-313421.25	18.41	0.23

Chapter 4

Continuation of the Fanaroff-Riley dichotomy with the EMU Pilot Survey

Context

In this chapter, I describe the data products produced from the Evolutionary Map of the Universe (EMU) pilot survey, an overview of the analysis techniques applied to the products and the galaxy properties measurable from these analyses. I use the techniques developed for GAMA-23 (previous chapter) and apply them to the EMU pilot survey. Similarly, the science goals of studying Double Radio sources Associated with Galactic Nuclei (DRAGNs), focusing on the Fanaroff-Riley Class I (FRI) and Fanaroff-Riley Class II (FR II) source populations, remain the same.

Again, I explore the correlation between peak radio luminosity and Fanaroff and Riley (1974) classifications. This time, I am using a field covering an area of around 270 square degrees at 944 MHz, from which I have compiled a sample of 3083 DRAGNs. My analysis agrees with the results of Mingo *et al.* (2019) as well as my results in the previous chapter, however, it contrasts with that in the literature. This would be cause for future studies.

4.1 Results

The primary goal of this morphological investigation, as with the G23 data, is to revisit the relationship between Fanaroff-Riley (FR) class, radio luminosity, and host-galaxy properties. Having obtained the G23 results, I can now use the results of that dataset to compare with the EMU-PS. I list the number of

Table 4.1: Classification statistics of EMU pilot survey DRAGNs. The last column shows the number of sources that have a measured redshift.

Morphology	# Sources	Full z range
FRI	884	536
FRII	1156	615
HyMOR	88	56
FRx	252	126
single	703	446

sources for each classification in Table 4.1.

4.1.1 Owen-Ledlow Diagram

The apparent dependence of the FR break luminosity on optical-magnitude was first reported by Ledlow and Owen (1996). The study provided strong evidence for a jet deceleration and disruption origin of the FRI/FRII dichotomy (Bicknell, 1995; Kaiser and Best, 2007). If disruption of the jet is caused by interaction with environmental density, a jet in a denser environment is then likely to be disrupted if it's of similar power close to the FR break and become FRI. Thus, assuming that optical host galaxy magnitude is a good proxy for local density on the scale of jet disruption (a few kiloparsecs), the FR break luminosity should be observed to have a dependence. However, due to the potential influence of selection effects, the result by Ledlow and Owen (1996) has been disputed (e.g. Best, 2009; Lin *et al.*, 2010; Wing and Blanton, 2011; Singal and Rajpurohit, 2014; Capetti *et al.*, 2017b; Shabala, 2018). In both the Abell cluster samples examined in Ledlow and Owen (1996) and literature, the FR populations have redshift distributions that are significantly different and come from samples with highly limited flux. The large vertical scatter in the original plot of Ledlow and Owen (1996) is also significant, as highlighted by Saripalli (2012), because it shows that for a given type of host galaxy, both FRI and FRII structures are possible, likely due to distinctly different jet powers (or other environmental factors which are not as well correlated with optical magnitude).

There are several reasons why the substantial FRI/FRII luminosity overlap might be compatible with the jet disruption model for the FR break. For a given jet power, it's likely for scatter of at least an order of magnitude in radio luminosity to be present (e.g. Cavagnolo *et al.*, 2010; Croston *et al.*, 2018). This already accounts for some overlap in luminosity between the two types if an underlying FR break in jet power exists. Another effect that could be contributing to the overlap is that the synchrotron plasma is better confined in denser environments. This causes the plasma to lose less energy through adiabatic expansion, and making it appear brighter for a given jet power (e.g. Barthel and Arnaud, 1996). Thus, if FRI galaxies reside in rich environments causing their jets to disrupt, they will appear more luminous than low brightness FRIIs, further enhancing the overlap observed.

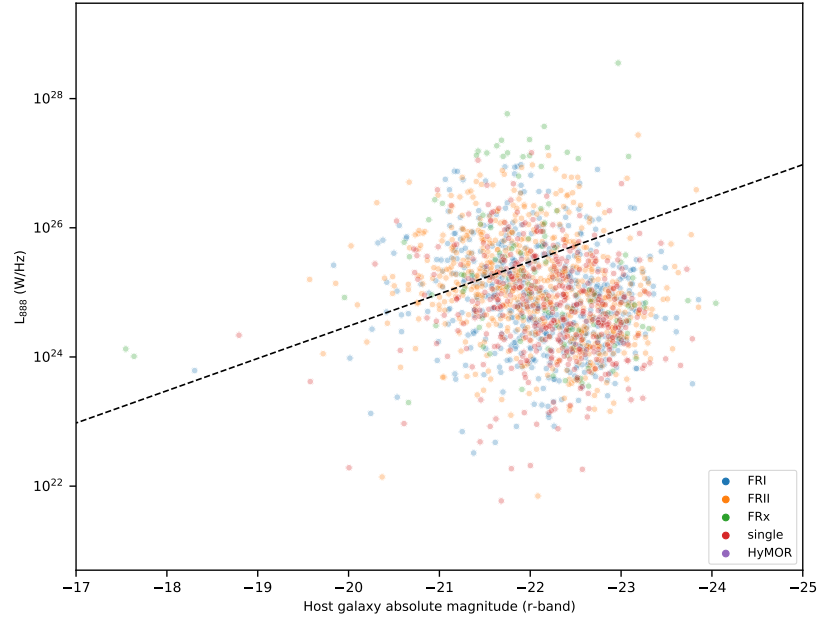


Figure 4.1: A plot of radio luminosity versus absolute host-galaxy r-band magnitude (an ‘Owen & Ledlow’ plot) for the EMU-PS populations. Histograms are displayed to show the distribution better. The plot does not encapsulate the whole sample, as it only includes sources with both an optical counterpart and a redshift. The black dashed line shows the transition between FRI and FR II found by Owen & Ledlow, corrected for different frequency and Hubble constant.

I wanted to revisit the result of Ledlow and Owen (1996) and investigate the FR break’s dependence on host galaxy properties within my sample. I plot the same plots as I did for the G23 data, now with the EMU-PS data. In Figure 4.2 I plot my EMU-PS data in the same way as Owen & Ledlow plotted theirs.

Similar to Mingo *et al.* (2019), I find there is no obvious distinction found between the FRI and FR II classes, in terms of optical luminosity of my study. When plotting radio luminosity as a function of absolute magnitude, the substantial overlap between the two populations remains, but both FR classes show an increasing trend of radio luminosity with optical magnitude. Compared to the G23 result (see Figure 3.2 in Chapter 3), the EMU-PS doesn’t show any discernible difference, and there is a larger scatter and overlapping of the radio sources. One possible reason for the substantial overlap is that the EMU-PS is going deeper than most surveys. Nevertheless, there may be an underlying dependence of the FR break on the magnitude of the host galaxy. However, given my sample statistics and the strong redshift dependencies present, the observed trend may be entirely due to selection effects, which may include a combination of radio surface brightness, volume effects and host-galaxy magnitude limits. Previous claims of host-galaxy dependence are likely to have been influenced by similar selection effects.

As I am following the original FR definition strictly, any sources that did not have two obvious peaks were classed as ‘single’. However, a majority of these sources would probably be classed as FRI just based on a visual inspection, and thus would cause the plot to show a similar trend to that of Owen & Ledlow.

To explore the relationship with luminosity further, I plot 888-MHz luminosity (k -corrected) versus

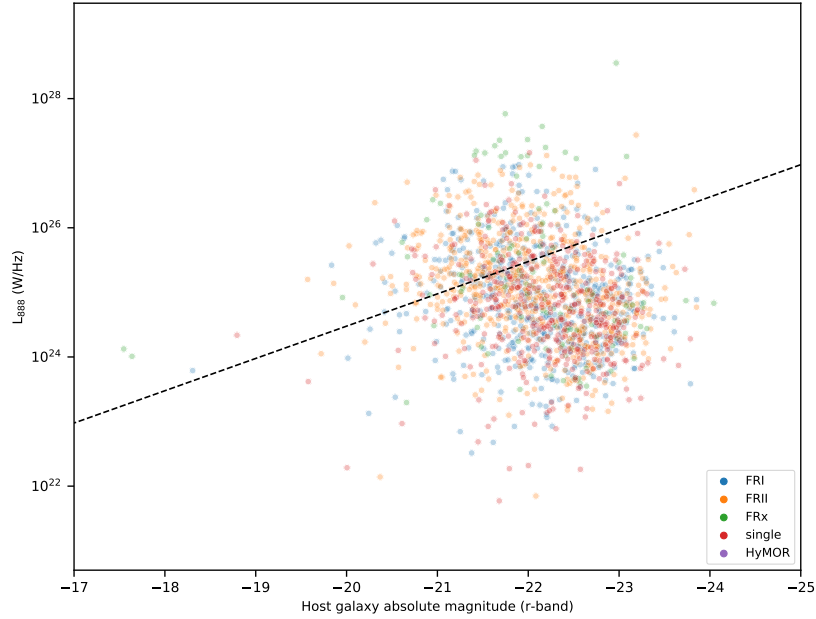


Figure 4.2: Two plots of radio luminosity versus absolute host-galaxy r-band magnitude (an ‘Owen & Ledlow’ plot) for the EMU-PS FR populations. Histograms are displayed to show the distribution better. The plot does not encapsulate the whole sample, as it only includes sources with both an optical counterpart and a redshift. The black dashed line shows the transition between FRI and FRII found by Owen & Ledlow, corrected for different frequency and Hubble constant.

the physical size (in kiloparsecs) for the FRIs and FRIIs of this sample (Figure 4.3). A Kernel Density Estimation (KDE) Plot is also shown along-side to depict the probability density function of the sample. To better illustrate the source distributions, histograms for both axes are included. I find the median luminosity of the FRIs in my sample to be $7.84 \times 10^{24} \text{ W Hz}^{-1}$, while the FRIIs have a median of $1.11 \times 10^{25} \text{ W Hz}^{-1}$.

Both FRIs and FRIIs seem to increase in size as a function of luminosity, as expected. However, comparing to the G23 result, there is a stronger veering off to either side for both Radio Galaxies (RGs) populations.

As EMU expands to larger regions of sky, building large samples spanning a wide luminosity range in narrow redshift bins at intermediate redshifts will be possible, and will eliminate the complications of redshift dependence for similar comparisons. Considering the large FR overlap and the numerous physical explanations for the lack of sharp transitions in the DRAGN population, it is possible that more focused in-depth comparisons of faint FRII hosts and environments with similarly luminous FRIs will be the best option to better physical insights into the origin of the FR dichotomy.

To study the redshift distribution, I use photometric redshifts from Dark Energy Spectroscopic Instrument (DESI) Legacy Imaging Surveys Data Release 8.

Figure 4.4 shows the redshift distribution of my sample, confined to those sources with an optical/Dark Energy Survey (DES) counterpart. Similar to G23, there’s a sharp drop-off at redshift 1. Again,

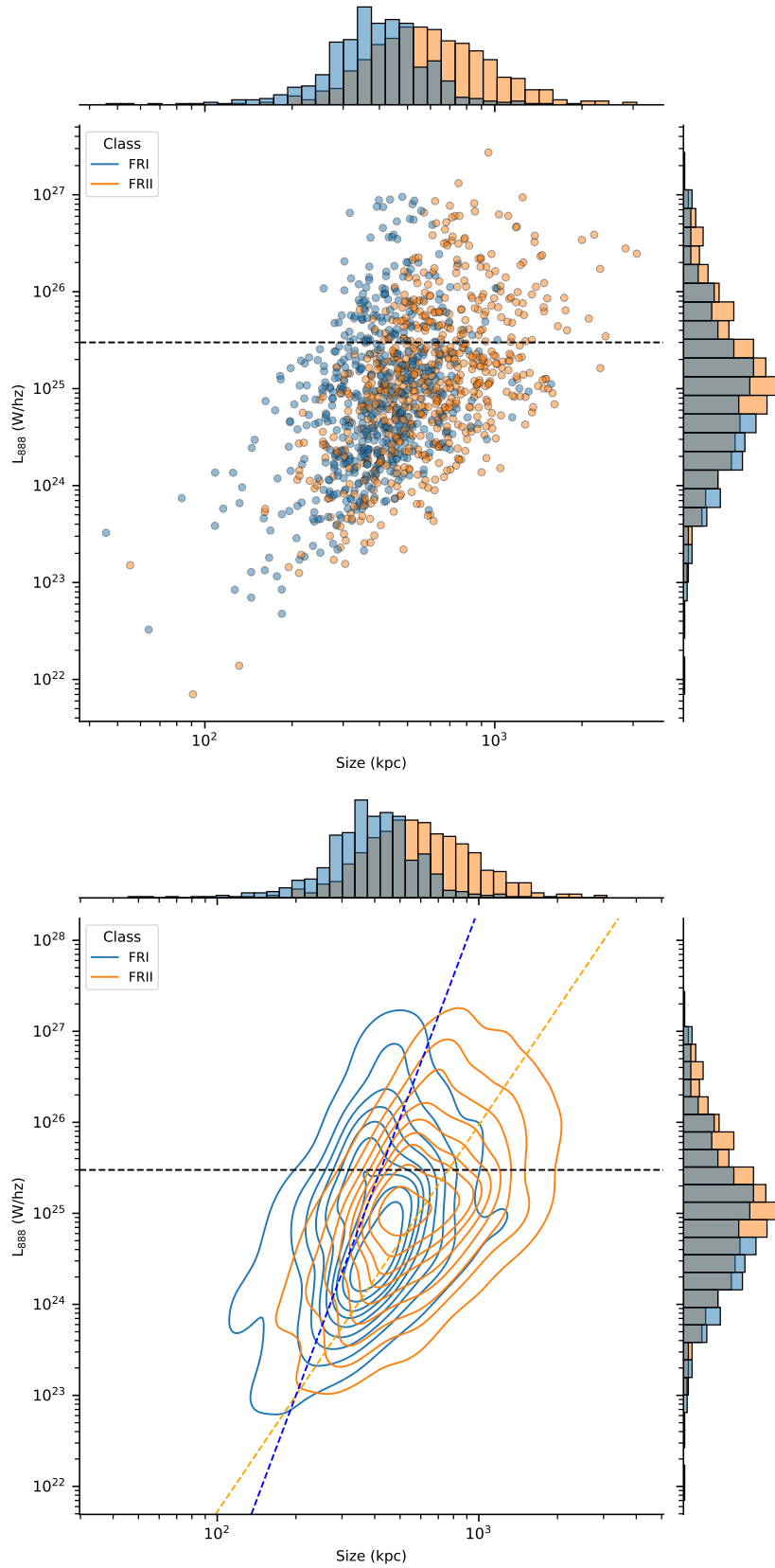


Figure 4.3: Two plots showing the 888 MHz luminosity as a function of physical size for the FRIs (blue) and FRIIs (orange) populations of the EMU-PS. The traditional FR luminosity division between both populations is at $\sim 10^{25}$ W Hz $^{-1}$, indicated by the dashed black line. The bottom image is a kernel density estimate plot. The slopes of both the FRI (2.11) and FRII (2.08) populations are shown via the dashed blue and orange lines respectively

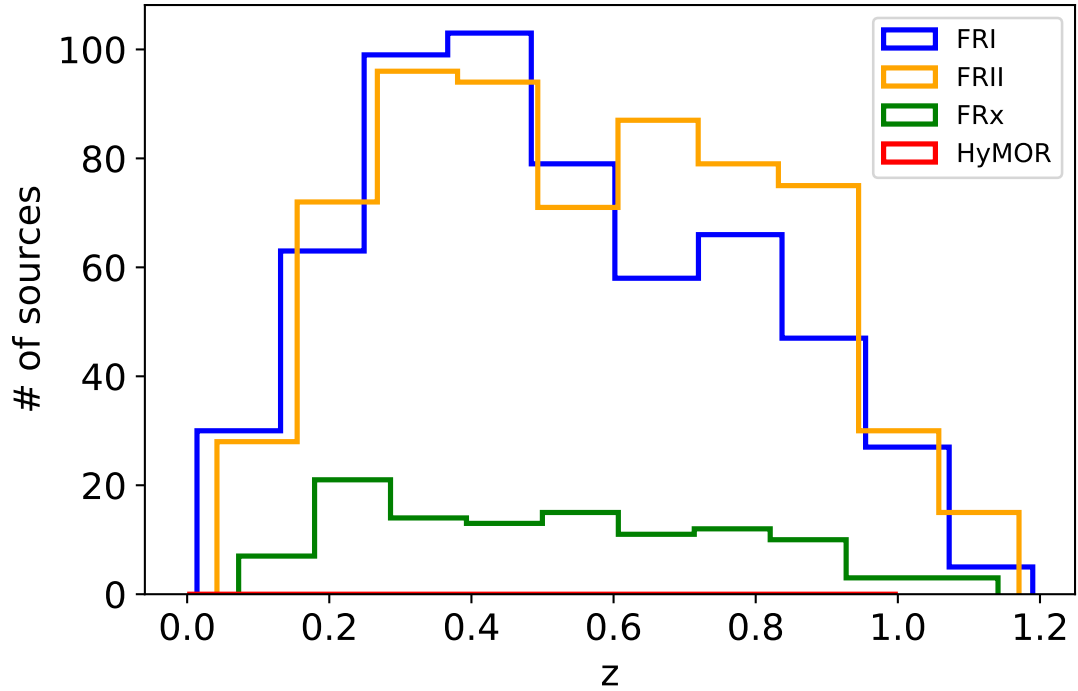


Figure 4.4: Plots showing the distribution of sources as a function of redshift. The top plot has linear bins while the bottom plot has bins in logspace.

the ‘redshift desert’ might be playing a role here. I also find no significant evidence for the redshift distributions of the two classes to differ, except for sensitivity effects.

Overall, the results in the EMU-PS seem to agree with what was obtained for the G23 field. Both show a larger overlap between FRI and FRII than has previously been seen, and the cause of this will need to be studied further. With large datasets coming from telescopes and ongoing radio surveys (e.g. Low-Frequency Array (LOFAR), MeerKAT, Very Large Array Sky Survey (VLASS), MeerKAT International GHz Tiered Extragalactic Exploration (MIGHTEE), EMU), and eventually Square Kilometre Array (SKA), studies of a similar nature will hopefully be able to probe into the physical complexity of the underlying source populations.

4.1.2 Source Catalogue

The EMU-PS radio source catalogue of FRI, FRII, FRx and HyMOR sources is presented here. There are a total of 3083 sources distributed across ten tiles. This catalogue only includes sources that have a CATWISE counterpart (within 2.2 arcsec). The column names and descriptions are given below:

- SBID: the scheduling block given during Australian Square Kilometre Array Pathfinder (ASKAP) observations
- Source Name: the name given to the source based on its coordinates

- RA: the J2000 right ascension of the source in hours, minutes and seconds (radio)
- DEC: the J2000 declination of the source in degrees, arcminutes and arcseconds (radio)
- Flux Density: the integrated flux density of sources given in Janskys
- Size: the size of the DS9 regions given in arcseconds
- a : the distance between peaks of emission as determined by the ratio algorithm
- b : the extent of the source as determined by the ratio algorithm
- PA: the position angles of the sources as outputted by the algorithm
- a/b_{\max} : calculation of a/b with maximum values of b that's reasonable for the data
- a/b_{\min} : calculation of a/b with minimum values of b that's reasonable for the data
- Class: the classification as determined by the ratios
- DESI ID: the ID given in the DESI DR 8 catalogue
- MAG: the r-band magnitude as given in the [DES](#) catalogue
- Z : the photometric redshift as given from [DESI DR8](#) catalogue

Table 4.2: The value-added catalogue of all found DRAGNS in the EMU-PS field

SBID	Source Name	RA (J2000) (deg)	DEC (J2000) (deg)	Flux Density (Jy)	Size (")	a (")	b (")	PA (°)	a/b _{max}	a/b _{min}	Class	Mag (r-band)	DESID	Z
9437	J200448-513536	301.2	-51.593	0.01	92.9	47.13	92.9		0.49	0.52	FRx	20.46	8000072638000860	0.52
9437	J200612-523239	301.55	-52.544	0.032	67.69	22.36	51.46	0.14	0.41	0.46	FRI	19.01	8000069073002370	
9325	J200628-614856	301.62	-61.816	0.017	111.72	84.34	106.39	1.75	0.77	0.81	FRII			
9437	J200633-512447	301.64	-51.413	0.021	75.09	16.97	57.04	2.39	0.29	0.31	FRI	22.21	8000072640005110	0.86
9325	J200640-603520	301.67	-60.589	0.007	66.36		66.36				single			
9437	J200643-500517	301.68	-50.088	0.008	103.61	60.14	82.28	1.74	0.71	0.75	FRII	21.05	8000078137000630	0.62
9437	J200652-533819	301.72	-53.639	0.007	38.62	16.12	38.62	1.74	0.39	0.45	FRI	17.22	8000064725004960	
9437	J200654-501758	301.73	-50.299	0.178	61.62		61.62				single	22.11		
9437	J200701-493303	301.76	-49.551	0.002	45.75	13.43	45.75	2.12	0.28	0.31	FRI			
9437	J200713-532344	301.81	-53.396	0.091	65.82	31.24	67.26	0.76	0.45	0.48	FRI			
9437	J200719-515252	301.83	-51.881	0.003	63.31	27.2	63.31	2.17	0.41	0.45	FRI	21.49	8000070848005900	0.86
9437	J200721-521334	301.84	-52.226	0.004	45.37		36.48	2.78			single	22.38		
9437	J200723-532427	301.85	-53.408	0.056	53.69		51.41	2.75			single	18.02	8000065585004540	0.28
9437	J200734-512321	301.89	-51.389	0.006	52.13	25.53	52.13	1.51	0.47	0.51	FRx	18.46	8000072640005670	0.37
9437	J200734-521242	301.89	-52.212	0.008	66.17		66.17	2.7			single	18.31	8000069958004130	0.32
9325	J200741-600739	301.92	-60.128	0.5	112.97	44.82	112.97		0.39	0.41	FRI	19.82		
9325	J200750-624026	301.96	-62.674	0.074	78.19	38.05	73	3.06	0.50	0.54	FRII			
9437	J200751-502318	301.97	-50.388	0.006	121.59	81.22	121.59	0.38	0.65	0.68	FRII	23.93		
9437	J200754-491650	301.98	-49.281	0.009	66.3		66.3				single			
9437	J200800-512318	302	-51.388	0.002	68.61	39.03	68.61	1.86	0.55	0.59	FRII	18.46	8000072641005410	0.36
9325	J200804-623745	302.02	-62.629	0.003	51.31	16.26	51.31	2.13	0.30	0.33	FRI			
9437	J200808-535056	302.04	-53.849	0.005	80.08		80.08				single	20.87	8000064726000510	0.63
9437	J200815-512721	302.07	-51.456	0.003	75.09		75.09	2.78			single	17.66	8000072641003770	0.27
9437	J200816-523113	302.07	-52.52	0.004	108.87	56.56	108.87	0.67	0.51	0.53	FRII	23.13	8000069074002920	0.82
9437	J200820-525505	302.09	-52.918	0.008	162.22	124.72	145.24	0.2	0.84	0.87	FRII	22.29		
9325	J200822-583357	302.1	-58.566	0.005	59.94	24.54	59.94		0.39	0.43	FRI	21.48	8000049378001350	0.76
9437	J200828-530013	302.12	-53.004	0.074	118.25	56.32	105.51	2.85	0.52	0.55	FRII	22.24	8000067320002820	0.7
9437	J200839-511044	302.16	-51.179	0.017	97.37	48.66	83.02	0.15	0.57	0.60	FRII	21.44	8000073544004610	0.7
9437	J200849-512803	302.21	-51.468	0.002	51.72		51.72	2.24			single	19.43	8000072641003560	0.39
9325	J200915-583602	302.31	-58.601	0.015	50.91	20.33	50.91	0.64	0.38	0.42	FRI	24.25		
9437	J200916-494033	302.32	-49.676	0.096	130.3	70.68	107.22	2.73	0.64	0.67	FRII	23.66		
9437	J200920-522401	302.34	-52.4	0.016	100.12	56.6	78.78	0.67	0.70	0.74	FRII	22.79		
9437	J200921-513806	302.34	-51.635	0.002	61.92		61.92	1.11			single	20.55	8000069075005610	0.6
9437	J200932-531012	302.39	-53.17	0.009	81.55	19.7	70.17	2.76	0.27	0.29	FRI	15.5		
9437	J200938-530946	302.41	-53.163	0.075	51.94	14.42	49.37	0.47	0.28	0.31	FRI	17.25	8000066451004420	0.25
9325	J200947-592800	302.45	-59.467	0.005	105.27	47.81	105.27	1.73	0.44	0.47	FRI	21.92		
9325	J200951-622213	302.47	-62.37	0.004	52.51		52.51	2.34			single			
9325	J200957-591630	302.49	-59.275	0.003	86.84		86.84	2.2			single	20.73	8000047129002710	0.66

Continued on next page

Table 4.2 – Continued from previous page

SBID	Source Name	RA (J2000) (deg)	DEC (J2000) (deg)	Flux Density (Jy)	Size (")	a (")	b (")	PA (°)	a/b _{max}	a/b _{min}	Class	Mag (r-band)	DESI ID	Z
9437	J201000-515245	302.5	-51.879	0.001	68	41.25	68	0.17	0.59	0.63	FRII	18.84	8000070849006210	0.35
9437	J201006-485949	302.53	-48.997	0.008	70.57	26.68	51.21	0.27	0.50	0.55	FRx			
9437	J201016-522910	302.57	-52.486	0.001	79.17	52.37	79.17		0.64	0.68	FRII	18.44	8000069075003670	0.24
9437	J201021-483024	302.59	-48.507	0.004	65.61		65.61				single			
9325	J201034-590606	302.65	-59.102	0.007	80.15	41.08	80.15	1.82	0.50	0.53	FRx	21.25	8000047875000530	0.65
9437	J201036-501644	302.65	-50.279	0.004	57.58		57.58	0.23	0.77	0.79	single	22.1	8000077210001700	0.84
9437	J201051-525836	302.71	-52.977	0.009	148.69	116	148.69	2.32	0.77	0.81	FRII	21.11		
9325	J201054-582054	302.73	-58.348	0.009	119.67	74.43	94.66	1.73	0.77	0.83	FRII	21.03	8000050140000440	0.72
9437	J201056-491930	302.74	-49.325	0.023	166.35	135.9	166.35	1.5	0.80	0.83	FRII			
9437	J201057-494813	302.74	-49.804	0.012	100.97	40.2	75.13	1.48	0.52	0.55	FRII	17.94		
9437	J201059-515210	302.75	-51.869	0.014	62.05	28.43	54.91	0.84	0.50	0.54	FRx	23.42		
9437	J201102-515706	302.76	-51.952	0.002	69.53	40.32	69.53	0.3	0.56	0.60	FRII	21.08	8000070850004220	0.56
9437	J201107-525702	302.78	-52.951	0.023	103.66	47.34	80.38	0.96	0.57	0.61	FRII	20.23	8000067321003550	0.35
9325	J201109-591550	302.79	-59.264	0.004	76.65	30.43	76.65	0.8	0.38	0.41	FRI	18.48	8000047130003030	
9437	J201112-505412	302.8	-50.903	0.001	70.87		70.87		0.46	0.50	single	21.15	8000074455004280	0.71
9325	J201114-604700	302.81	-60.783	0.025	77.49	28.43	59.29	2.51	0.46	0.50	FRx			
9437	J201120-531221	302.83	-53.206	0.002	56.4	20.36	56.4	1.28	0.35	0.38	FRI	15.54		
9325	J201122-575647	302.85	-57.947	0.017	260.84	186.71	260.84		0.71	0.72	FRII	19.54	8000050906004370	0.38
9437	J201125-502921	302.86	-50.489	0.001	56.38	32.04	56.38	1.28	0.54	0.59	FRII	23.16	8000076287002390	1.04
9437	J201126-533110	302.86	-53.519	0.013	92.98	49.48	76.33	0.22	0.63	0.67	FRII	22.61	8000065587002340	0.86
9437	J201127-534843	302.86	-53.812	0.015	51.93	20.4	47.95	0.17	0.40	0.45	FRI	23.7		
9437	J201129-515923	302.87	-51.99	0.01	75.09	39.95	62.08	2.23	0.62	0.67	FRII	23	8000070850003280	0.87
9437	J201143-514202	302.93	-51.701	0.042	44.13		44.53	2.76			single	23.96		
9437	J201144-494421	302.94	-49.739	0.003	124.15	83.17	124.15	2.19	0.66	0.68	FRII	21.73		
9325	J201148-593155	302.95	-59.532	0.002	85.89	44.88	85.89	0.54	0.51	0.54	FRII	22.41	8000046391001840	0.88
9437	J201152-503758	302.97	-50.633	0.002	108.57	81.14	108.57	0.2	0.73	0.76	FRII	20.31		
9325	J201155-585605	302.98	-58.935	0.017	93.23	39.85	75.63	1.26	0.51	0.54	FRII	23.55		
9325	J201208-575936	303.03	-57.993	0.007	100.22	42.37	100.22		0.41	0.43	FRI	20.42	8000050906003210	0.52
9437	J201214-530054	303.06	-53.015	0.007	104.31	45.68	72.52	2.62	0.61	0.65	FRII	22.98		
9437	J201217-514915	303.07	-51.821	0.005	64.61	27.2	64.61	2.28	0.41	0.44	FRI	23.03		
9437	J201218-534537	303.08	-53.76	0.023	75.73		75.73	2.02			single	19.73		
9437	J201221-483121	303.09	-48.523	0.003	57.42	18	36.49	1.64	0.46	0.53	FRx			
9437	J201233-514835	303.14	-51.81	0.003	62.82		62.82	0.79			single	20.36	8000071744001330	0.63
9325	J201235-580344	303.15	-58.062	0.003	79.48	47.83	79.48	1.45	0.58	0.62	FRII	17.28		
9437	J201243-553758	303.18	-53.633	0.009	67.83	30.53	53.37	2.09	0.55	0.60	FRII	20.82	8000064728004190	0.67
9325	J201247-620531	303.2	-62.092	0.002	53.04	17.09	32	0.37	0.50	0.58	FRx			
9437	J201252-495005	303.22	-49.835	0.001	72.89	26.28	72.89		0.35	0.37	FRI	18.96		
9325	J201254-593400	303.23	-59.567	0.008	59.81		59.81	3.04			single	22.87	8000046392001280	0.96
9437	J201256-505222	303.24	-50.873	0.023	299.02	184.77	299.02	3.12	0.61	0.62	FRII	18.01	8000074456005830	0.33

Continued on next page

Table 4.2 – Continued from previous page

SBID	Source Name	RA (J2000) (deg)	DEC (J2000) (deg)	Flux Density (Jy)	Size (")	a (")	b (")	PA (°)	a/b_{\max}	a/b_{\min}	Class	Mag (r-band)	DESI ID	Z
9437	J201259-530810	303.25	-53.136	0.011	54.87	16.41	44.27	1.54	0.35	0.39	FRI	21.06	8000066453004770	0.56
9437	J201302-504842	303.26	-50.812	0.005	70.87	70.87	70.87	2.69			single	20.38	8000075369001380	0.64
9437	J201304-485406	303.27	-48.902	0.05	148.55	100.33	131.64	3.05	0.75	0.78	FRII			
9325	J201305-603810	303.28	-60.636	0.004	132.49	71.99	86.56	0.31	0.81	0.86	FRII			
9437	J201310-511256	303.29	-51.216	0.002	108.08	83.56	108.08	1.59	0.76	0.79	FRII	23.42		
9325	J201311-593814	303.3	-59.637	0.043	86.27	34.06	68.63	2.33	0.48	0.51	FRx	21.54	8000045659003860	0.83
9437	J201312-512417	303.3	-51.405	0.013	95.27	48.17	77.63	2.46	0.60	0.64	FRII	18.54	8000072644004230	0.29
9437	J201315-534146	303.31	-53.696	0.022	43.17	18.87	46.85	2.55	0.38	0.43	FRI	24.93		
9325	J201325-600129	303.36	-60.025	0.195	71.93	30.53	66.9	2.22	0.44	0.47	FRI	21.93		
9325	J201328-603033	303.37	-60.509	0.004	84.89	30.51	84.89	0.99	0.35	0.37	FRI			
9325	J201337-604732	303.41	-60.792	0.007	94.57	62.1	82.89	0.26	0.73	0.77	FRII			
9437	J201345-534335	303.44	-53.726	0.006	91.55	47.93	91.55	1.17	0.51	0.54	FRII	18.73	8000064729002010	0.34
9325	J201349-591110	303.46	-59.186	0.007	103.89	67.53	88.31	1.63	0.74	0.79	FRII	25.22	8000047131004840	
9325	J201350-583122	303.46	-58.523	0.014	73.09	33.11	59.91	1.05	0.53	0.58	FRII	20.16	8000049381002250	0.57
9325	J201352-601441	303.47	-60.245	0.007	159.67	83.2	159.67	3.04	0.51	0.53	FRII	20.01		
9437	J201354-505640	303.48	-50.944	0.002	92.64	92.64	92.64	3.11			single	16.96	8000074457004140	0.14
9325	J201355-575802	303.48	-57.967	0.004	70.56	33.39	70.56	2.35	0.46	0.49	FRI	24.41	8000050907003370	
9437	J201359-483754	303.5	-48.632	0.002	81.66	42.28	81.66	3.04	0.50	0.53	FRII			
9325	J201402-622546	303.51	-62.429	0.009	101.19	59.23	81.23	1.78	0.71	0.75	FRII	17.86	8000037949003490	0.27
9325	J201412-615652	303.55	-61.948	0.025	94.16	40	81.26	3.02	0.48	0.51	FRx	22.16		
9437	J201414-502045	303.56	-50.346	0.052	101.34	52.35	84.44	2.39	0.60	0.64	FRII	22.98	8000077213000860	0.93
9325	J201416-613219	303.57	-61.539	0.007	52.27	12.73	36.91	2.18	0.32	0.37	FRI	21.93	8000040675001190	0.62
9325	J201419-575706	303.58	-57.952	0.012	45.97	40.49	40.49	0.85			single	20.92	8000050907003630	0.7
9437	J201420-482357	303.58	-48.399	0.002	65.61	27.64	65.61	2.99	0.41	0.44	FRI			
9325	J201421-622058	303.59	-62.349	0.02	64.57	20.88	52.93	0.83	0.38	0.41	FRI	18.84	8000038622000400	0.39
9437	J201423-495401	303.6	-49.9	0.014	87.87	50.94	87.87	2.44	0.56	0.60	FRII	22.83		
9437	J201424-482513	303.6	-48.42	0.001	68.97	44.08	68.97	0	0.62	0.66	FRII			
9437	J201435-484020	303.65	-48.672	0.007	67.77	35.97	67.77	1.87	0.51	0.55	FRII			
9437	J201441-511418	303.67	-51.238	0.007	69.48	69.48	69.48	2.63			single	20.89	8000073548003190	0.81
9325	J201444-623300	303.68	-62.55	0.004	56.64	17.62	56.64	2.33	0.30	0.33	FRI			
9437	J201446-501309	303.69	-50.219	0.001	53.72	53.72	53.72	0.18			single	20.46	8000077213003780	0.48
9325	J201447-585724	303.7	-58.957	0.031	193.74	142.4	193.74	1.69	0.73	0.74	FRII	16.49		
9325	J201453-482738	303.72	-48.461	0.113	113.07	68.82	101.01	0.59	0.66	0.70	FRII			
9437	J201454-490455	303.73	-49.082	0.003	93.09	42.65	93.09	1.72	0.45	0.47	FRI			
9437	J201458-505850	303.74	-50.981	0.008	81.28	42.77	66.7	1.77	0.62	0.67	FRII	18.01	8000074457003400	0.27
9437	J201459-524122	303.75	-52.689	0.001	52.96	23.27	52.96		0.42	0.46	FRI	18.87	8000068199003260	0.31
9325	J201500-611009	303.75	-61.169	0.008	58.12	16.46	58.12	3.13	0.27	0.30	FRI			
9437	J201506-503050	303.78	-50.514	0.015	61.38	24.17	50.27	0.34	0.46	0.51	FRx	23.6		
9325	J201506-584851	303.78	-58.814	0.038	50.91	20.4	48.35	2.07	0.40	0.44	FRI	22.73	8000048626001580	1.19

Continued on next page

Table 4.2 – Continued from previous page

SBID	Source Name	RA (J2000) (deg)	DEC (J2000) (deg)	Flux Density (Jy)	Size (")	a (")	b (")	PA (°)	a/b_{\max}	a/b_{\min}	Class	Mag (r-band)	DESI ID	Z
9325	J201507-575029	303.78	-57.841	0.032	95.1	50.17	81.72	2.73	0.60	0.63	FR II	23.78		
9325	J201507-592810	303.78	-59.469	0.014	59.81	14.28	59.81	3.1	0.23	0.25	FRI	21.22	8000046393003300	0.65
9437	J201517-491600	303.82	-49.267	0.007	87.14	55.85	87.14	1.66	0.62	0.66	FR II			
9437	J201519-491025	303.83	-49.174	0.001	56.57	56.57	56.57	0.77			single			
9325	J201530-614349	303.88	-61.73	0.003	117.38	83.32	117.38	2.98	0.70	0.73	FR II	21.1	8000039987002600	0.67
9437	J201532-530727	303.88	-53.124	0.008	56.51	17.09	41.3	1.92	0.39	0.44	FRI	23.55	8000066455004810	0.75
9437	J201537-491955	303.9	-49.332	0.003	93.09	30.71	93.09	2.41	0.32	0.34	FRI			
9325	J201539-594536	303.92	-59.76	0.007	48.51	16.12	37.51	2.09	0.40	0.46	FRI	25.63		
9437	J201540-484200	303.92	-48.7	0.023	65.61	28.64	52.79	0.31	0.52	0.57	FR II			
9437	J201541-493008	303.92	-49.502	0.029	77.88	28.43	55.58	0.61	0.49	0.54	FRx			
9437	J201543-482853	303.93	-48.481	0.003	100.07	49.32	100.07	0.13	0.48	0.51	FRx			
9437	J201547-505530	303.95	-50.925	0.005	97.37	64.03	82.09	2.48	0.76	0.80	FR II	25.99		
9325	J201547-592958	303.95	-59.499	0.003	51	51	51	2.02			single	21.9	8000046393002540	0.9
9325	J201551-585900	303.96	-58.983	0.006	84.95	50.12	67.82	2.67	0.71	0.77	FR II	24.7		
9325	J201553-583702	303.97	-58.617	0.078	142.13	76.78	139.6	2.44	0.54	0.56	FR II	17.72		
9437	J201559-524427	304	-52.741	0.056	91.78	48.41	77.39	2.45	0.61	0.65	FR II	20.1	8000068199002320	
9325	J201603-584613	304.01	-58.77	0.018	67.36	26.31	55.86	2.97	0.45	0.49	FRI	23.5		
9437	J201612-500455	304.05	-50.082	0.016	107.98	59.41	82.94	2.34	0.70	0.74	FR II	25.12		
9325	J201613-620409	304.06	-62.069	0.004	65.1	31.24	51.03	2.46	0.58	0.64	FR II	23.3		
9437	J201623-505646	304.1	-50.946	0.016	141.28	97.66	141.28	1.72	0.68	0.70	FR II			
9325	J201623-610556	304.1	-61.099	0.01	82.67	48.37	68.53	1.05	0.68	0.73	FR II	23.7	8000042073000550	
9325	J201630-613219	304.13	-61.539	0.008	208.93	167.09	208.93	0.31	0.79	0.81	FR II	19.36	8000040676001640	0.47
9325	J201633-502926	304.14	-50.491	0.073	219.73	181.11	210.67	1.04	0.85	0.87	FR II	20.41	8000076291003080	0.55
9437	J201636-533453	304.15	-53.581	0.004	193.47	150.95	193.47	0.09	0.77	0.79	FR II	17.33	8000065590000780	0.18
9437	J201638-494124	304.16	-49.69	0.016	67.08	31.62	57	1.27	0.53	0.58	FR II	16.58	8000079077003810	
9325	J201645-604326	304.19	-60.724	0.006	84.89	47.57	84.89	2.3	0.54	0.58	FR II	20.85	8000042780002420	0.77
9325	J201646-574440	304.2	-57.744	0.001	51.95	24.34	51.95	1.91	0.45	0.49	FRI	18.4		
9325	J201648-614955	304.2	-61.832	0.015	173	125.63	173	1.96	0.72	0.74	FR II	21.27	8000039987000560	0.47
9437	J201650-503948	304.21	-50.663	0.03	138.5	97.7	124.61	0.4	0.77	0.80	FR II	20.54	8000075372005010	0.63
9351	J201653-574707	304.22	-57.785	0.011	217.66	187.83	217.66	0.6	0.85	0.87	FR II	19.5		
9325	J201658-625719	304.25	-62.955	0.01	81.77	43.68	65.87	0.28	0.64	0.69	FR II	19.13		
9437	J201659-531527	304.25	-53.258	0.059	64.24	24.33	56.45	0.19	0.41	0.45	FRI	20.85		
9437	J201711-512732	304.3	-51.459	0.004	84.83	36.09	84.83	1.77	0.41	0.44	FRI	19.34	8000072646003950	0.37
9437	J201720-495231	304.34	-49.875	0.007	55.49	25.3	46.39	1.21	0.52	0.58	FR II	25.25	8000078144005790	
9437	J201722-531319	304.34	-53.222	0.006	87.03	46.04	67.4	1.53	0.66	0.71	FR II	24.66		
9325	J201723-610212	304.35	-61.037	0.005	123.98	76.45	123.98	2.88	0.60	0.63	FR II	20.24	8000042073001650	0.62
9437	J201723-505341	304.35	-50.895	0.032	67.64	28.64	60.02	0.16	0.46	0.50	FRI	17.5		
9325	J201726-594442	304.36	-59.745	0.003	81.19	44.38	81.19	2.92	0.53	0.56	FR II	22.4	8000045661002790	0.7
9325	J201728-592509	304.37	-59.419	0.002	59.74	22.69	59.74	1.42	0.36	0.40	FRI	20.09	8000046394004170	0.55

Continued on next page

Table 4.2 – Continued from previous page

SBID	Source Name	RA (J2000) (deg)	DEC (J2000) (deg)	Flux Density (Jy)	Size (")	a (")	b (")	PA (°)	a/b _{max}	a/b _{min}	Class	Mag (r-band)	DESI ID	Z
9325	J201732-630010	304.39	-63.003	0.075	96.57	56.57	86.3	1.42	0.64	0.68	FR II	22.45	8000036620003120	0.81
9437	J201735-535715	304.4	-53.954	0.022	198.19	154.09	198.19		0.77	0.79	FR II	21.7	8000063876003070	0.78
9437	J201738-503717	304.41	-50.621	0.003	92.87	43.64	92.87	0.21	0.46	0.48	FRI	20.34	8000076291000080	0.61
9325	J201739-591627	304.42	-59.274	0.019	80.81	39.65	69.9	1.88	0.55	0.59	FR II	21.01	8000047133002100	0.53
9325	J201742-591352	304.43	-59.231	0.005	125.38	108.08	125.38	1	0.85	0.88	FR II	21.23	8000047133002950	0.64
9437	J201743-502634	304.43	-50.443	0.004	80.22	52.04	80.22	1.59	0.63	0.67	FR II	22.92		
9325	J201745-631217	304.44	-63.205	0.019	199.36	148.63	199.36		0.74	0.76	FR II	15.73	8000035963004070	0.08
9437	J201745-531950	304.44	-53.331	0.003	74.83		74.83	2.36			single	20.49	8000066456000770	
9437	J201745-485426	304.44	-48.907	0.002	100.07	31.11	55.45	2.32	0.54	0.59	FR II			
9437	J201746-484511	304.44	-48.753	0.01	93.55	53.01	93.55	1.39	0.55	0.58	FR II			
9351	J201747-555957	304.45	-55.999	0.031	86.07		86.07				single	17.12	8000057227002810	0.23
9437	J201748-531327	304.45	-53.224	0.001	55.59	26.76	55.59	1.53	0.46	0.50	FRx	20.12	8000066456002920	0.66
9437	J201752-503116	304.47	-50.521	0.003	54.79		54.79	2.39			single	18.06	8000076292002710	0.29
9325	J201758-603746	304.5	-60.629	0.022	81.29	19.7	66.49	1.87	0.29	0.31	FR II	20.74	8000042780003980	0.57
9437	J201800-482444	304.5	-48.412	0.015	113.07	60.83	87.93	2.04	0.67	0.71	FR II	18.79		
9437	J201800-494013	304.5	-49.67	0.002	77.88	34.91	77.88	3.12	0.43	0.46	FRI	21.67		
9325	J201803-594816	304.51	-59.804	0.056	68.63	33.29	60.4	0.92	0.53	0.57	FR II	17.08	8000047879002830	0.38
9325	J201807-585944	304.53	-58.996	0.002	118.21	82.8	118.21	2.94	0.69	0.72	FR II	20.88		
9437	J201808-504339	304.53	-50.728	0.092	120.07	59.46	105.36	2.16	0.55	0.58	FR II	23.76		
9325	J201809-610725	304.54	-61.124	0.015	70.44	26.08	55.51	0.12	0.45	0.49	FRI	22.45	8000077215005170	0.88
9437	J201810-500225	304.54	-50.04	0.015	80.68	42.05	69.62	2.98	0.58	0.63	single	19.11	8000037951003130	0.3
9437	J201812-501000	304.55	-50.167	0.003	54.24		54.24	2.51			FR II	22.04	8000057227002410	0.89
9325	J201814-622933	304.56	-62.493	0.011	94.21	54.73	77.97	2.5	0.68	0.73	FRI	18.15	8000069080000780	0.25
9351	J201814-560141	304.56	-56.028	0.015	71.03	33.36	71.03	1.04	0.45	0.49	FR II	22.65	8000071748000380	0.9
9437	J201814-523525	304.56	-52.59	0.007	75.4	26.95	75.4	1.32	0.35	0.37	FR II	22	8000069080004480	1.05
9437	J201814-483340	304.56	-48.561	0.055	77.88	45.25	75.97	0.81	0.58	0.62	FR II	18.62	8000042074001530	0.36
9437	J201821-515051	304.59	-51.848	0.008	64.22	15.98	64.22	1.54	0.24	0.26	FRI	19.88	8000043492002270	0.53
9437	J201828-522409	304.62	-52.403	0.04	97.37	58.03	85.42	1.52	0.66	0.70	FR II	22.15	8000049383002420	0.76
9325	J201829-610316	304.62	-61.054	0.018	133.74	85.44	118.57	1.73	0.71	0.74	FR II	17.86	8000077215004790	0.25
9325	J201830-603016	304.63	-60.504	0.002	60.55	28.41	60.55	3.02	0.45	0.49	single	15.32	8000068201003140	0.05
9325	J201831-583122	304.63	-58.523	0.001	55.62		55.62	0.65			FR II	14.53		
9351	J201835-572440	304.65	-57.411	0.024	134.49	65.29	134.49	2.92	0.48	0.49	FR II	24.07		
9437	J201837-501045	304.66	-50.179	0.033	71.7	32.98	61.17	1.35	0.52	0.56	FR II	21.72	8000046395000270	0.76
9437	J201838-513733	304.66	-51.626	0.005	106.9	76.95	106.9	2.01	0.70	0.74	FR II	20.7		
9437	J201848-524234	304.7	-52.709	0.057	47.71	16.12	47.71	0.53	0.32	0.36	FRI	17.86	8000068201003140	0.05
9437	J201849-483726	304.71	-48.624	0.006	62.44	32.56	54.44	0.18	0.57	0.63	FR II	14.53		
9325	J201852-593639	304.72	-59.611	0.002	75.18		75.18	0.63			single	21.72		
9437	J201853-514823	304.72	-51.806	0.147	44.45		44.78	2.41			single	20.7		
9437	J201854-525448	304.73	-52.913	0.099	202.75	82.94	202.75	2.41	0.40	0.41	FRI	14.07	8000067326004000	0.04

Continued on next page

Table 4.2 – Continued from previous page

SBID	Source Name	RA (J2000) (deg)	DEC (J2000) (deg)	Flux Density (Jy)	Size (")	a (")	b (")	PA (°)	a/b _{max}	a/b _{min}	Class	Mag (r-band)	DESI ID	Z
9437	J201859-480947	304.75	-48.163	0.007	101.67	68.44	101.67		0.66	0.69	FRII			
9351	J201859-544147	304.75	-54.696	0.014	42.67		42.67	2.2			single	19.3	8000061346003370	0.33
9437	J201904-520139	304.77	-52.028	0.314	63.24	63.24		2.45			single	18.21		
9437	J201910-502425	304.8	-50.407	0.002	115.81	81.13	115.81		0.69	0.72	FRII	20.62	8000076292005590	0.59
9325	J201912-583702	304.81	-58.617	0.038	46.83	42.84		2.81			single	21.56		
9437	J201917-513106	304.82	-51.518	0.012	65.62	40.79	64.18	1.38	0.61	0.66	FRII	23.46		
9437	J201919-485621	304.83	-48.939	0.007	49.73		49.73	0.08			single			
9437	J201921-530406	304.84	-53.068	0.015	44.96		44.96	2.5			single	21.81	8000067326001130	0.73
9325	J201923-582411	304.85	-58.403	0.002	116.57	81.66	116.57	2.26	0.69	0.72	FRII			
9351	J201923-565141	304.85	-56.861	0.025	180.03	61.03	162.76	2.75	0.37	0.38	FR I			
9325	J201926-611425	304.86	-61.24	0.301	78.11	28	71.68	3.05	0.38	0.40	FR I	20.38	8000041373003140	0.68
9325	J201926-591832	304.86	-59.309	0.033	94.15	44.97	94.15	1.22	0.47	0.49	FR I	19.05	8000047134001270	0.36
9351	J201934-565658	304.89	-56.949	0.064	101.48	58.86	97.71	2.98	0.59	0.62	FRII			
9325	J201934-591122	304.89	-59.189	0.051	113.1	55.6	113.1	2.56	0.48	0.50	FRx	18.63	8000047134003940	0.29
9437	J201936-503628	304.9	-50.608	0.015	59.4		59.4	0.41			single	17.71	8000076293000330	0.29
9325	J201936-603226	304.9	-60.541	0.035	88.9	41.25	75.97	2.81	0.53	0.56	FRII	18.22		
9437	J201938-501524	304.91	-50.257	0.014	113.23	76.43	113.23	0.81	0.66	0.69	FRII	20.66	8000077216003070	0.59
9325	J201942-590535	304.93	-59.093	0.003	88.16	43.59	88.16	0.67	0.48	0.51	FRx	20.58	8000047879000660	0.72
9437	J201947-494629	304.95	-49.775	0.037	76.08		76.08	0.3			single	19.59		
9437	J201950-491800	304.96	-49.3	0.003	59.85	22.65	59.85	1.99	0.36	0.39	FR I			
9437	J201950-483726	304.96	-48.624	0.004	93.09	58.03	73.14	0.02	0.77	0.82	FRII	20.83	8000083815000020	0.74
9351	J201954-560325	304.98	-56.057	0.008	58.36	24.86	58.36	0.43	0.41	0.45	FR I	21.72	8000057228001410	
9351	J201957-555304	304.99	-55.884	0.013	96.36	40.05	76.15	0.05	0.51	0.54	FRII	18.32	8000057228005090	0.23
9437	J201957-533326	304.99	-53.557	0.004	75.47	28.8	75.47	1.69	0.37	0.39	FR I	20.56	8000065592001420	0.75
9325	J201959-590353	305	-59.065	0.355	70.04	24	68.38	0.05	0.34	0.36	FR I	22.32	8000047880001230	0.94
9437	J202006-511146	305.03	-51.196	0.004	63	25.46	46.16	0.81	0.52	0.58	FRII	20.99	8000073551003910	0.6
9437	J202010-484429	305.04	-48.741	0.002	93.09	59.48	93.09	2.38	0.62	0.66	FRII	19.04	8000082858002590	0.39
9351	J202011-550241	305.05	-55.045	0.004	65.05		65.05	2.54			single	18.9		
9437	J202013-515740	305.06	-51.961	0.005	97.69	65.26	97.69	0.59	0.65	0.69	FRII	22.62	8000070856002750	0.9
9351	J202015-551757	305.07	-55.299	0.036	79.04	38.05	79.04	0.05	0.47	0.50	FR I	23.58		
9437	J202016-522925	305.07	-52.49	0.004	108.15	54.28	108.15	2.86	0.49	0.51	FRx	19.21	8000069081002450	0.43
9437	J202018-501945	305.08	-50.329	0.013	52.43		52.43	2.15			single	20.78	8000077217001090	0.66
9437	J202020-513207	305.09	-51.535	0.013	95.11	50.89	95.11	0.19	0.52	0.55	FRII	19.31	8000072648001660	0.28
9325	J202022-581703	305.09	-58.284	0.007	174.96	112.13	174.96	2.7	0.63	0.65	FRII	17.79	8000050145002020	0.25
9437	J202032-485652	305.14	-48.948	0.009	54.36	21.54	45.11	2.74	0.45	0.51	FRx	19.1		
9351	J202033-541858	305.14	-54.316	0.008	53.44		53.44	1.37			single	21.88	8000063029001090	0.9
9351	J202037-565627	305.16	-56.941	0.008	55.9	28.64	50.59	1.34	0.54	0.60	FRII			
9351	J202037-551446	305.16	-55.246	0.022	72.51	30	61.68	2.51	0.47	0.51	FRx	23.27		
9437	J202048-494919	305.2	-49.822	0.11	63.37	30.59	59.26	2.03	0.50	0.54	FRx	23.16		

Continued on next page

Table 4.2 – Continued from previous page

SBID	Source Name	RA (J2000) (deg)	DEC (J2000) (deg)	Flux Density (Jy)	Size (")	a (")	b (")	PA (°)	a/b _{max}	a/b _{min}	Class	Mag (r-band)	DESI ID	Z
9351	J202049-544050	305.2	-54.681	0.014	66.76	66.76	1				single	21.13		
9351	J202051-552757	305.21	-55.466	0.006	179.44	106.28	179.44	2.07	0.58	0.60	FRII	19.15	8000058861003600	
9437	J202053-522632	305.22	-52.442	0.023	81.41	41.23	71.69	2.94	0.56	0.60	FRII	21.94	8000069082003200	0.75
9437	J202058-480632	305.24	-48.109	0.04	121.73	46.71	121.73		0.38	0.39	FRI			
9437	J202100-494948	305.25	-49.83	0.005	47.75		47.75	0.35			single	24.38		
9437	J202103-493632	305.26	-49.609	0.002	68.37		68.37	1.6			single	18.72		
9437	J202110-524513	305.3	-52.754	0.084	78.63		78.63	2.99			single	15.67	8000068202001980	0.11
9437	J202128-505312	305.37	-50.887	0.004	99.38	65.6	99.38	2.49	0.64	0.68	FRII	24.45	8000074461005290	
9351	J202131-543038	305.38	-54.511	0.005	63.61	32.56	63.61	0.2	0.49	0.53	FRx	16.35		
9325	J202147-592948	305.45	-59.497	0.009	239.78	164.86	239.78	0.62	0.68	0.69	FRII	17.82	8000046396002560	0.14
9325	J202149-614125	305.46	-61.69	0.002	65.12	35.8	65.12	1.38	0.53	0.57	FRII	20.53	8000039990004750	0.4
9437	J202149-525814	305.46	-52.971	0.105	149.68	75.63	149.68	2.26	0.50	0.51	FRx	20.93	8000067328003070	0.37
9351	J202149-560838	305.46	-56.144	0.007	71.65	28.64	54.4	2.85	0.50	0.52	FRII			
9351	J202153-541728	305.47	-54.291	0.004	92.97	47.31	92.97	0	0.50	0.50	FRx	16.89	8000063030001480	0.16
9351	J202156-540507	305.48	-54.085	0.003	60.67	31.62	60.67	2.52	0.50	0.54	FRII	20.64	8000063879000690	0.58
9351	J202201-562709	305.51	-56.453	0.009	105.84		105.84	0.47			single			
9437	J202204-503550	305.52	-50.597	0.015	75.94		75.94	3.1	0.73	0.76	single	18.94	8000076294000600	0.33
9325	J202206-561934	305.53	-56.326	0.025	152.01	106.17	142.19	3.1	0.73	0.78	FRII			
9325	J202208-590027	305.53	-59.008	0.019	140.3	96.21	126.39	2.82	0.75	0.78	FRII	22.14		
9351	J202216-533910	305.57	-53.653	0.015	47.62	17.2	43.22	2.54	0.38	0.42	FRI	22.84		
9351	J202216-544543	305.57	-54.762	0.027	46.33		46.33	2.43			single	25.45		
9351	J202218-544247	305.58	-54.713	0.004	37.68	22.09	37.69	1.56	0.55	0.63	FRII	18.45	8000061347002500	0.41
9325	J202219-592821	305.58	-59.473	0.001	57.9		57.9	2.08			single			
9351	J202221-564841	305.59	-56.811	0.01	73.98	44.96	73.98	2.5	0.59	0.63	FRII			
9325	J202224-603352	305.6	-60.564	0.015	100.27	68.82	92.14	2.49	0.73	0.77	FRII	16.52		
9437	J202224-523417	305.6	-52.571	0.001	52.67		52.67	0.14			single	17.99	8000069083000820	0.08
9351	J202226-550903	305.61	-55.151	0.025	49.45	15.59	49.53	2.48	0.30	0.33	FRI	22.69	8000059685005110	0.66
9351	J202227-554136	305.62	-55.693	0.006	52.31	14.83	36.07	0.85	0.38	0.44	FRI	22.33	8000058043004350	0.81
9437	J202230-504645	305.63	-50.779	0.011	47.14	20.1	43.84	0.07	0.43	0.49	FRI	21.47	8000075375001910	0.87
9325	J202240-625604	305.67	-62.934	0.002	76.2	27.84	76.2	1.77	0.35	0.38	FRI	20.09	8000036622004870	0.49
9437	J202243-525156	305.68	-52.866	0.006	50.54	18.44	37.29	0.73	0.46	0.53	FRx	19.78		
9325	J202248-594611	305.7	-59.77	0.011	89.59	40.1	65.92	2.5	0.59	0.63	FRII	19.01		
9325	J202251-571243	305.71	-57.212	0.006	95.04	59.34	95.04	1.94	0.61	0.64	FRII			
9325	J202252-620022	305.72	-62.006	0.005	76.2	29.78	51.04	2.27	0.56	0.61	FRII	18.54	8000039305002860	0.36
9437	J202254-491904	305.73	-49.318	0.002	60.75	12.94	60.75	1.05	0.20	0.22	FRI	18.82	8000080961001370	0.38
9437	J202257-515538	305.74	-51.927	0.004	107.04	73.57	91.95	1.26	0.78	0.82	FRII	23.55		
9437	J202257-493236	305.74	-49.543	0.007	79.6	29.68	66.23	2.3	0.43	0.47	FRI	17.89	8000080018001800	0.28
9325	J202258-612508	305.74	-61.419	0.007	124.87	90.08	124.87	3.02	0.71	0.74	FRII	20.61	8000040680005770	0.65
9325	J202302-595830	305.76	-59.975	0.024	51.85		51.85	3			single	21.78	8000044934003530	0.84

Continued on next page

Table 4.2 – Continued from previous page

SBID	Source Name	RA (J2000) (deg)	DEC (J2000) (deg)	Flux Density (Jy)	Size (")	a (")	b (")	PA (°)	a/b _{max}	a/b _{min}	Class	Mag (r-band)	DESI ID	Z
9351	J202305-552740	305.77	-55.461	0.002	89.98	64.17	89.98	0.15	0.69	0.73	FRII	20.91	8000080961005230	0.53
9437	J202305-490940	305.77	-49.161	0.006	65.7		65.7	3.07			single			
9325	J202308-603840	305.79	-60.644	0.003	163.83	119.56	163.83	2.35	0.72	0.74	FRII	18.58	8000058862000080	
9351	J202311-553643	305.8	-55.612	0.006	74.96		74.96	0.07			single	24.78		
9325	J202311-604651	305.8	-60.781	0.113	61.97	22	59.85	0.03	0.35	0.38	FRI	21.65	8000057230005430	0.71
9351	J202312-555326	305.8	-55.891	0.004	117.91	60.96	117.91	2.02	0.51	0.53	FRII	20.13		
9351	J202315-540030	305.81	-54.008	0.055	52.22	19.7	49.86	2.67	0.38	0.42	FRI	17.2	8000067329001930	0.08
9437	J202322-530116	305.84	-53.021	0.006	68.34		68.34	2.48			single	17.52	8000071751002620	0.26
9437	J202326-514441	305.86	-51.745	0.026	162	123.55	162	2.23	0.75	0.77	FRII	21.6		
9351	J202327-533912	305.87	-53.653	0.009	63.47	31.64	56.79	2.84	0.53	0.58	FRII	20.99	8000080018002430	0.58
9437	J202327-493136	305.87	-49.527	0.001	96.78	74.57	96.78	2.97	0.75	0.79	FRII	19.5	8000080018000240	1.02
9437	J202331-493703	305.88	-49.618	0.004	55.57	26.08	43.77	2.13	0.56	0.63	FRII	23.55	8000038626003690	0.75
9437	J202331-521647	305.88	-52.28	0.347	128.35	85.6	115.1	1.55	0.73	0.76	FRI	20.79	8000052461000610	0.42
9325	J202332-621416	305.89	-62.238	0.001	43.67	19.02	43.67	0.42	0.41	0.46	FRI	17.13		
9351	J202337-532611	305.91	-53.436	0.014	79.44	40.73	79.44	1.3	0.50	0.53	FRx	18.74	8000046397002620	0.42
9325	J202338-573530	305.91	-57.592	0.004	113.05	51.24	97.71	2.94	0.51	0.54	FRII	23.87		
9437	J202338-482650	305.92	-48.447	0.434	57.08		62.26	1.87			single	20.86	8000046397000080	
9325	J202341-593030	305.92	-59.508	0.029	80.71	21.63	80.71	0.83	0.26	0.28	FRI	23.74		
9325	J202342-622151	305.93	-62.364	0.003	54.96	17.33	33.77	0.79	0.48	0.55	FRx	19.95	8000068204002880	0.47
9351	J202344-560744	305.94	-56.129	0.003	96.36	63.72	96.36	2.91	0.64	0.68	FRII	19.77		
9325	J202345-593717	305.94	-59.621	0.022	71.45	36.06	62.41	0.55	0.56	0.60	FRII	20.86	8000046397000080	
9437	J202349-514048	305.96	-51.68	0.004	96.02	68.96	86.17	1.87	0.78	0.82	FRII	23.74		
9437	J202351-524205	305.96	-52.701	0.002	68.49	31.95	68.49	0.04	0.45	0.48	FRI	19.95	8000068204002880	
9437	J202354-524802	305.98	-52.801	0.008	50.54		50.54	1.45			single	19.77	8000068204001090	0.47
9351	J202356-565311	305.99	-56.886	0.004	63.46	24.08	42.2	1.67	0.54	0.61	FRII	24.45		
9351	J202357-561023	305.99	-56.173	0.026	96.36	48.08	73.73	0.8	0.63	0.68	FRII	18.64	8000038627000240	0.28
9351	J202358-553211	305.99	-55.536	0.006	96.36	60.83	83.7	2.37	0.71	0.75	FRII	18.81	8000058044003500	0.39
9437	J202401-482009	306.01	-48.336	0.01	121.73	86.66	106.4	0.78	0.80	0.83	FRII	25.94	8000049386004160	0.43
9325	J202402-615511	306.01	-61.92	0.001	85.29	59.97	85.29	2.28	0.68	0.72	FRII	23.1		
9437	J202407-500316	306.03	-50.054	0.071	131.66	91.93	123.52	2.36	0.73	0.76	FRII	19.06	8000039991001460	0.31
9325	J202408-614904	306.04	-61.818	0.017	132.38	78	118.84	2.84	0.64	0.67	FRII	19.59		
9351	J202409-563345	306.04	-56.563	0.003	86.22	29.13	86.22	0.07	0.33	0.35	FRI	18.48	8000038627000240	0.28
9325	J202413-622153	306.06	-62.365	0.007	54.96		54.96	2.88			single	18.85	8000058044003500	0.39
9351	J202415-554230	306.06	-55.708	0.007	110.91	43.08	110.91	2.51	0.38	0.40	FRI	19.34	8000049386004160	0.43
9325	J202419-582435	306.08	-58.41	0.009	71.44		71.44	2.36			single	19.67		
9325	J202420-620313	306.09	-62.054	0.002	57.82	22.86	57.82	2.16	0.38	0.41	FRI	19.67		
9351	J202420-572338	306.09	-57.394	3.499	101.48	93.72	101.48	1.12	0.90	0.95	FRII	19.67	8000035966005220	
9325	J202429-630855	306.12	-63.149	0.003	76.2	32.84	76.2	0.68	0.42	0.45	FRI			

Continued on next page

Table 4.2 – Continued from previous page

SBID	Source Name	RA (J2000) (deg)	DEC (J2000) (deg)	Flux Density (Jy)	Size (")	a (")	b (")	PA (°)	a/b_{\max}	a/b_{\min}	Class	Mag (r-band)	DESI ID	Z
9325	J202431-575932	306.13	-57.992	0.003	58.28	28.3	58.28	1.58	0.47	0.51	FRx	18.91	8000077219001890	0.39
9437	J202431-501641	306.13	-50.278	0.011	58.04	58.04	58.04	1.06			single	19.65	8000041375000360	0.35
9325	J202433-612154	306.14	-61.365	0.002	84.14	22.66	84.14	2.77	0.26	0.28	FR I			
9437	J202433-535547	306.14	-53.93	0.008	169.49	136.29	169.49	1.66	0.79	0.82	FR II			
9351	J202436-544538	306.15	-54.761	0.004	60.4	60.4	60.4	0.48			single	21.94		
9325	J202440-591730	306.17	-59.292	0.002	64.7	24.92	64.7	0.49	0.37	0.40	FR I	21.98		
9437	J202441-514819	306.17	-51.805	0.016	95.26	66.48	90.05	1.71	0.72	0.76	FR II	21.62		
9351	J202443-553954	306.18	-55.665	0.06	52.08	20.88	45.06	2.35	0.44	0.49	FR I	17.45	8000058044004440	0.25
9437	J202443-484352	306.18	-48.731	0.02	44.39	10.94	40.52	0.2	0.25	0.29	FR I	21.85	8000082861003490	0.65
9351	J202442-525351	306.19	-52.898	0.041	51.81	51.81	51.81	0.17			single	19.86	8000067329004360	0.4
9325	J202446-615531	306.19	-61.925	0.003	153.21	121.98	153.21	0.22	0.78	0.81	FR II	21.04		
9351	J202447-561900	306.2	-56.317	0.032	60.61	27.2	60.2	2.55	0.43	0.47	FR I			
9437	J202452-502326	306.22	-50.391	0.004	112.72	55.68	112.72	2.88	0.48	0.51	FRx	17.54	8000076296004340	0.19
9437	J202456-494816	306.23	-49.804	0.015	157.89	131.85	153.75	1.41	0.84	0.87	FR II	17.43	8000079082001700	
9437	J202458-523910	306.24	-52.653	0.008	100.92	65.3	100.92	2.55	0.63	0.66	FR II	17.19	8000068205004070	0.24
9325	J202458-594211	306.25	-59.703	0.051	160.53	111.52	142.15	2.63	0.77	0.80	FR II	22.91	8000045664003520	1.08
9325	J202459-573722	306.25	-57.623	0.003	95.76	54.65	95.76	2.62	0.56	0.59	FR II	22.55	8000052461000070	0.81
9325	J202500-622100	306.25	-62.35	0.028	76.2	27.42	61.21	3.1	0.43	0.47	FR I	19.1		
9437	J202502-502738	306.26	-50.461	0.003	92.54	34.86	84.21	2.83	0.40	0.43	FR I	19.1	8000076296002820	0.37
9351	J202505-540405	306.27	-54.068	0.057	256.83	171.67	256.83	1.45	0.66	0.67	FR II	15.67	8000063881000740	0.11
9351	J202515-544339	306.32	-54.728	0.009	48.67	48.67	48.67	2.29			single	25.18	8000061349002420	
9325	J202526-611544	306.36	-61.262	0.146	75.91	71.64	71.64	2.58			single	15.18	8000041376002660	0.09
9351	J202531-571141	306.38	-57.195	0.003	80	43.05	62.42	3.12	0.66	0.72	FR II			
9437	J202533-521851	306.39	-52.314	0.002	99.43	62.43	99.43	2.36	0.61	0.64	FR II	17.47	8000069970001270	0.21
9437	J202537-522822	306.41	-52.473	0.001	61.9	32.82	71.3	0.23	0.44	0.48	FR I	18.95	8000069084002890	0.34
9437	J202538-523611	306.41	-52.603	0.004	48	48	48	3.13			single	20.48		
9325	J202539-594611	306.41	-59.77	0.001	49.14	49.14	49.14	1.47			single	22.09	8000045665002080	1.05
9351	J202539-563829	306.42	-56.641	0.021	86.22	37.58	71.66	1.12	0.51	0.54	FR II			
9325	J202540-581948	306.42	-58.33	0.007	170.54	127.6	170.54	2.22	0.74	0.76	FR II	18.36	8000050148000960	0.28
9437	J202540-483803	306.42	-48.634	0.013	61.03	14.24	46.23	1.42	0.29	0.33	FR I	18.69	8000082862006420	0.4
9351	J202542-530016	306.43	-53.004	0.002	85.79	52.08	85.79		0.59	0.63	FR II			
9437	J202546-513646	306.44	-51.613	0.016	67.69	34.06	58.4	0.86	0.56	0.61	FR II	24.59		
9325	J202551-573114	306.46	-57.521	0.003	55.27	16.78	55.27	0.8	0.29	0.32	FR I	23.95		
9437	J202553-511712	306.47	-51.287	0.017	124.74	124.74	124.74	1.47			single	17.54	8000073555001820	0.23
9437	J202558-511943	306.49	-51.329	0.014	99.06	99.06	99.06	1.28			single	22.37	8000073555000590	
9351	J202558-542940	306.5	-54.494	0.001	55.48	31.44	55.48		0.54	0.59	FR II	21.57	8000062189002360	0.66
9325	J202559-591731	306.5	-59.292	0.011	73.79	34.41	77.32	2.89	0.43	0.46	FR I	21.62	8000047138001840	1.07
9351	J202611-533227	306.55	-53.541	0.419	105.35	68.12	100.81	1.6	0.66	0.69	FR II	21.08	8000065596001420	0.72
9437	J202611-515806	306.55	-51.968	0.015	71.72	35.44	59.02	1.87	0.58	0.63	FR II	20.86	8000070859003150	0.74

Continued on next page

Table 4.2 – Continued from previous page

SBID	Source Name	RA (J2000) (deg)	DEC (J2000) (deg)	Flux Density (Jy)	Size (")	a (")	b (")	PA (°)	a/b _{max}	a/b _{min}	Class	Mag (r-band)	DESI ID	Z
9351	J202614-570302	306.56	-57.051	0.021	71.04	37.64	71.04	1.32	0.51	0.55	FRII			
9351	J202615-562749	306.56	-56.464	0.009	43.71	11.3	43.71	1.77	0.24	0.27	FRI			
9325	J202619-593426	306.58	-59.574	0.003	76.7	29.98	76.7	0.29	0.38	0.40	FRI	17.65	8000046399001060	0.23
9325	J202620-594500	306.58	-59.75	0.002	61.6	24.14	61.6	3.02	0.38	0.41	FRI	24.88	8000045665002460	
9351	J202621-544656	306.59	-54.782	0.021	167.16	111.09	156.41	2.74	0.70	0.72	FRII	19.42	8000061350001220	0.28
9351	J202622-543251	306.59	-54.548	0.005	39.37	9.47	39.37	2.46	0.23	0.26	FRI	20.43	8000062189001430	0.65
9437	J202633-525204	306.64	-52.868	0.059	86.36	38.47	79.77	2.7	0.47	0.50	FRI	22.65	8000068206000100	
9325	J202635-613119	306.65	-61.522	0.004	88.62	32.78	88.62	0.49	0.36	0.38	FRI			
9325	J202636-592151	306.65	-59.364	0.003	56.66	32.1	56.66	1.35	0.54	0.59	FRII	20.82	8000047138000280	0.66
9351	J202637-571315	306.66	-57.221	0.003	60.33	21.54	38	1.94	0.53	0.61	FRII			
9325	J202637-583540	306.66	-58.594	0.007	81.05	39.3	81.05	2.89	0.47	0.50	FRx	22.96		
9437	J202638-521619	306.66	-52.272	0.006	73.14	35.43	55.91	2.54	0.61	0.66	FRII	19.42	8000069970002080	0.41
9437	J202639-522347	306.67	-52.396	0.004	78.58	43.28	63.62	2.87	0.65	0.71	FRII	19.76	8000069085005200	0.42
9437	J202640-490351	306.67	-49.064	0.012	68.05	22.09	54.26	0.49	0.39	0.43	FRI	19.66	8000081911001260	0.5
9351	J202641-533800	306.67	-53.633	0.237	44.02		44.02	1.48			single	22.8	8000064737004140	
9325	J202641-590923	306.67	-59.156	0.02	73.76	32.56	59.61	0.83	0.52	0.57	FRII	22.88	8000047138004570	
9325	J202642-601331	306.68	-60.225	0.001	90.53	52.88	90.53	2.97	0.57	0.60	FRII	19.25	8000044213003380	0.27
9351	J202646-552223	306.69	-55.373	0.289	170.1	114.32	157.11	0.86	0.72	0.74	FRII	18.39	8000059687000040	0.24
9351	J202646-542049	306.69	-54.347	0.004	61.84		61.84	2.6			single	21.65	8000063033000480	0.79
9325	J202651-603941	306.71	-60.661	0.004	86	27.96	86	2.07	0.32	0.33	FRI	18.16	8000042785005460	0.27
9351	J202702-544321	306.76	-54.723	0.002	58.81	24.9	58.81	1.59	0.41	0.44	FRI	21.14		
9351	J202714-531419	306.81	-53.239	0.003	100.78	53.84	100.78	1.57	0.52	0.55	FRII	22.18	8000066462002640	0.96
9325	J202715-551740	306.81	-55.294	0.028	202.37	146.22	186.15	1.62	0.78	0.80	FRII	19.81	8000059688001500	
9325	J202715-584222	306.81	-58.706	0.002	70.41	28.45	70.41	0.99	0.39	0.42	FRI	20.98	8000048633003040	0.62
9325	J202725-582903	306.86	-58.484	0.009	124.24	87.36	110.01	1.84	0.78	0.81	FRII	26.13		
9437	J202728-524646	306.87	-52.779	0.01	97.43	29.72	64.7	2.18	0.44	0.48	FRI	22.45		
9437	J202729-483701	306.87	-48.617	0.004	58.28	22.36	44.22	2.5	0.48	0.54	FRx	20.32		
9325	J202729-592445	306.87	-59.413	0.015	68.59	36	56.64	1.54	0.61	0.66	FRII	18.71		
9437	J202735-522810	306.9	-52.469	0.038	59.11	20.88	52.1	2.88	0.38	0.42	FRI	24.03		
9351	J202736-561524	306.9	-56.257	0.003	60.61	11.56	60.61	0.58	0.18	0.20	FRI			
9325	J202736-580237	306.9	-58.044	0.005	73.91	38.21	58.99	2.35	0.62	0.68	FRII	20.91	8000050915001460	0.62
9351	J202737-573606	306.9	-57.602	0.006	52.41		52.41	0.99			single	19.99	8000052463000390	
9351	J202737-582800	306.91	-58.467	0.016	131.73	88.54	111.66	0.81	0.78	0.81	FRII	17.62		
9351	J202742-532043	306.93	-53.345	0.002	100.78	61.46	100.78	0.15	0.60	0.63	FRII			
9437	J202746-483925	306.94	-48.657	0.003	55.84	26.46	55.84	2.16	0.45	0.50	FRI	18.79	8000082863005320	0.41
9437	J202747-495531	306.95	-49.925	0.015	115.09	115.05	146.03	1.19	0.77	0.80	FRII	19.59		
9437	J202803-530212	307.02	-53.037	0.005	53.76	21.54	38.44	1.94	0.53	0.60	FRII	20.83		
9351	J202805-551746	307.02	-55.296	0.004	45.98		45.98	2.16			single			
9325	J202805-622115	307.02	-62.354	0.003	53.46	22.39	53.46	1.82	0.40	0.44	FRI	19.92	8000038628000490	0.58

Continued on next page

Table 4.2 – Continued from previous page

SBID	Source Name	RA (J2000) (deg)	DEC (J2000) (deg)	Flux Density (Jy)	Size (")	a (")	b (")	PA (°)	a/b _{max}	a/b _{min}	Class	Mag (r-band)	DESI ID	Z
9325	J202807-631018	307.03	-63.172	0.031	96.14	47.7	96.14		0.48	0.51	FRx	17.04	8000035968004770	
9325	J202808-604246	307.04	-60.713	0.013	54.41	16.12	45.73	2.95	0.33	0.37	FRI	21.21	8000042785004230	0.55
9351	J202810-553458	307.04	-55.583	0.008	222.84	138.85	222.84	2.27	0.62	0.63	FRII	18.78	8000058865001000	0.26
9437	J202811-492726	307.05	-49.457	0.039	52.73	15.17	44.25	1.19	0.32	0.36	FRI	21.71		
9351	J202811-565038	307.05	-56.844	0.032	107.93	60.2	104.29	0.92	0.56	0.59	FRII			
9437	J202813-513315	307.06	-51.554	0.013	99.84	33.53	81.76	0.27	0.40	0.42	FRI	22.21	8000072653001480	0.75
9351	J202816-565132	307.07	-56.859	0.013	68.91	28.68	54.54	1.94	0.50	0.55	FRII			
9437	J202816-491540	307.07	-49.261	0.003	51.54		51.54	2.93			single	25.21		
9325	J202816-600241	307.07	-60.045	0.008	90.53	48.33	73.57	2.73	0.64	0.68	FRII	22.9		
9437	J202818-492352	307.08	-49.398	0.032	338.09	67.79	338.09	1.36	0.20	0.20	FRI	18.39	8000080022005540	0.3
9437	J202821-505025	307.09	-50.84	0.115	103.86	52.61	90.99	3.01	0.56	0.59	FRII	24.1	8000075379000460	
9351	J202827-581952	307.11	-58.331	0.001	79.58	46.02	79.58	2.01	0.56	0.60	FRII	22.58	8000050150000870	0.95
9325	J202828-583219	307.12	-58.539	0.003	81.05	45.47	81.05	1.18	0.54	0.58	FRII	19.99	8000049388001740	0.52
9351	J202831-550014	307.13	-55.004	0.082	96.37	55.32	85.29	2.31	0.63	0.67	FRII	21.29		
9437	J202831-524952	307.13	-52.831	0.008	116.15	81.92	102.04	1.43	0.78	0.82	FRII	22.66	8000068207000720	0.89
9437	J202834-521920	307.14	-52.322	0.003	74.6	29.82	74.6	1.85	0.39	0.41	FRI	23.1		
9325	J202835-580423	307.15	-58.073	0.002	54.58	25.39	54.58	0.71	0.44	0.49	FRI	19.35	8000050915000950	0.17
9437	J202836-494116	307.15	-49.688	0.003	51.31	14.29	34.59	1.51	0.39	0.45	FRI	20.9	8000079084004440	0.55
9437	J202838-511358	307.16	-51.233	0.003	83.17	30.32	83.17	3.09	0.35	0.38	FRI	20.86	8000073557002500	0.6
9325	J202838-624022	307.16	-62.673	0.001	63.71	33.63	63.71	3.14	0.51	0.55	FRII	21.4	8000037288005010	0.65
9437	J202839-505206	307.17	-50.868	0.149	61.05		61.05	0.29			single	22.74	8000075379000090	1
9351	J202845-582939	307.19	-58.494	0.027	51.87	22.8	54.64	1.89	0.40	0.44	FRI	18.07	8000049389002480	0.32
9437	J202854-491210	307.23	-49.203	0.012	143.12	95.41	118.88	1.12	0.79	0.82	FRI	19.32	8000080965004660	0.4
9437	J202854-490407	307.23	-49.069	0.002	121.58	71.94	121.58	2.12	0.58	0.60	FRII			
9325	J202855-590853	307.23	-59.148	0.004	130.55	87.57	130.55	0.87	0.66	0.68	FRII	18.65	8000047139004830	0.2
9437	J202901-492348	307.26	-49.397	0.021	67.21	29.73	57.16	0.09	0.50	0.54	FRx	21.69		
9351	J202902-531232	307.26	-53.209	0.002	67.39	38.24	67.39	1.72	0.55	0.59	FRII	19.52	8000066463002980	0.46
9325	J202902-595358	307.26	-59.899	0.01	77.35	36.06	62.38	2.58	0.56	0.60	FRII	28.09		
9437	J202903-520114	307.27	-52.021	0.158	85.59	39.6	79.09	0.71	0.49	0.52	FRx	20.64	8000070861002110	0.46
9351	J202908-530940	307.29	-53.161	0.005	67.39	34.93	55.99	1.76	0.60	0.65	FRII	25.44		
9351	J202910-540950	307.3	-54.164	0.013	67.67		67.67	2.69			single	22.8		
9437	J202914-483237	307.31	-48.544	0.271	85.98	14.56	80.43	0.82	0.18	0.19	FRI	21.09	8000083821002010	0.82
9325	J202918-604519	307.33	-60.755	0.001	91.07	63.59	91.07	0.13	0.68	0.72	FRII	19.2	8000042786003100	0.25
9351	J202918-562512	307.33	-56.42	0.004	69.66	34.66	69.66	2.43	0.48	0.52	FRx			
9437	J202918-485044	307.33	-48.846	0.001	82.25	44.59	82.25	2.48	0.53	0.56	FRII	19.55	8000079085001670	0.15
9437	J202921-494451	307.34	-49.748	0.032	128.12	69.12	109.78	2.3	0.62	0.64	FRII	18.17	8000084783004380	0.39
9437	J202930-481141	307.38	-48.195	0.038	72.11	19.39	72.11		0.26	0.28	FRI	20.2	8000064738000130	0.63
9351	J202931-535201	307.38	-53.867	0.007	112.6	64.62	88.94	0.46	0.71	0.75	FRII	20.24		
9437	J202935-490324	307.4	-49.057	0.001	58.06	29.16	58.06		0.48	0.52	FRx	20.59		

Continued on next page

Table 4.2 – Continued from previous page

SBID	Source Name	RA (J2000) (deg)	DEC (J2000) (deg)	Flux Density (Jy)	Size (")	a (")	b (")	PA (°)	a/b _{max}	a/b _{min}	Class	Mag (r-band)	DESI ID	Z
9437	J202939-504148	307.42	-50.697	0.02	104.08	24.04	104.08	0.25	0.23	0.24	FRI	16.54	8000075380002470	0.16
9351	J202941-540540	307.42	-54.094	0.03	50.89	20	47.79	3.13	0.40	0.44	FRI	21.33	8000063883000530	0.66
9437	J202943-501557	307.43	-50.266	0.023	44.55	41.99	41.99	0.07			single	20.65		
9351	J202943-554341	307.43	-55.728	0.004	46.78	17.19	35.36	0.9	0.45	0.52	FRx	22.19	8000058047002680	0.86
9351	J202945-544933	307.44	-54.826	0.048	96.37	55.46	91.96	0.44	0.59	0.62	FRII	19.13	8000061352000800	0.39
9325	J202950-624050	307.46	-62.681	0.017	197	107.83	197	0.35	0.54	0.55	FRII	17.91	8000037289004390	0.28
9437	J202951-485544	307.46	-48.929	0.002	74.45	41.39	74.45	2.66	0.54	0.58	FRII	20.4	8000081913004690	0.51
9325	J202954-584358	307.48	-58.733	0.008	57.51	57.51	57.51	0.79	0.30	0.33	single	19.92		
9325	J202956-575719	307.49	-57.955	0.148	66.47	17.09	54.36	0.29	0.30	0.33	FRI	19.38	8000050916003360	
9437	J202959-492715	307.5	-49.454	0.001	49.16	19.55	49.16	2.7	0.38	0.42	FRI			
9437	J203000-513106	307.5	-51.518	0.001	57.54	19.13	57.54	0.04	0.32	0.35	FRI	22.34	8000072654002000	0.92
9325	J203003-574037	307.51	-57.677	0.063	58.3	20	54.24	0.79	0.35	0.39	FRx	19.87	8000051687003610	0.44
9437	J203005-515816	307.52	-51.971	0.005	73.49	35.67	73.49	1.22	0.47	0.50	FRx	19.85	8000070862002930	0.5
9325	J203009-602424	307.54	-60.407	0.014	51.62	18.11	42.94	0.07	0.40	0.45	FRI	17.08		
9351	J203011-544450	307.55	-54.747	0.008	47.36	47.36	47.36	2.88	0.49	0.54	single	19.78	8000061352002250	0.5
9437	J203013-521431	307.56	-52.242	0.058	100.85	51.92	88.53	1.24	0.57	0.60	FRII	14.51		
9437	J203016-483812	307.57	-48.637	0.037	83.71	57.32	77.72	0.5	0.71	0.76	FRII	23.75	8000082865005350	
9351	J203017-541947	307.57	-54.33	0.014	72.53	31.3	58.55	0.42	0.51	0.56	FRII	23.59	8000063035000780	
9437	J203026-492716	307.61	-49.454	0.003	118.8	53.57	118.8	0.32	0.44	0.46	FRI	19.03		
9325	J203034-590020	307.64	-59.006	0.002	64.05	64.05	64.05	0.19	0.49	0.54	single	21.49	8000047885002200	0.67
9325	J203037-584114	307.66	-58.687	0.001	57.51	29.67	57.51		0.52	0.58	FRx	23.7	8000048634003470	
9325	J203040-610106	307.67	-61.018	0.006	51.84	24.08	44.01	2.4	0.42	0.47	FRII	21.87	8000042079002560	0.66
9437	J203042-514207	307.68	-51.702	0.061	71.72	34.93	72.34	1.7	0.47	0.50	FRx	16.59	8000071756002850	0.19
9437	J203049-484707	307.71	-48.785	0.051	83.1	36.88	85.07	1.25	0.42	0.45	FRx	20.81	8000082865002050	0.7
9325	J203056-573651	307.74	-57.614	0.382	89.93	38.15	86.01	2.11	0.43	0.46	FRI	16.25	8000052465000120	0.31
9351	J203059-572621	307.75	-57.439	0.012	56.12	22.09	56.12	1.71	0.38	0.41	FRI	18.04	8000052465003120	0.16
9437	J203100-491955	307.75	-49.332	0.012	95.49	54.04	84.18	0.03	0.62	0.66	FRII	16.16	8000080966001010	0.16
9325	J203103-594407	307.76	-59.735	0.001	70.06	34.87	70.06	0.12	0.48	0.52	FRx	20.93	8000045668003150	0.52
9325	J203103-572455	307.76	-57.415	0.003	51.51	51.51	51.51	2.06			single	18.73	8000052465003530	
9351	J203104-533640	307.77	-53.611	0.002	45.32	16.12	45.32	1.41	0.34	0.38	FRI	23.5		
9437	J203114-513716	307.81	-51.621	0.026	130.09	50.64	130.09	3.11	0.38	0.40	FRI	22.09	8000072655000070	0.8
9351	J203114-554550	307.81	-55.764	0.003	62.98	34.23	50.49	0.13	0.65	0.71	FRII	23.98		
9351	J203115-534245	307.81	-53.713	0.048	56.67	23.32	57	0.68	0.39	0.43	FRI	16.28	8000064739002740	0.1
9325	J203124-613651	307.86	-58.894	0.012	47.64	47.64	47.64	0.01			single	23.61		
9325	J203126-623525	307.86	-62.59	0.174	110.47	67.08	102.26	1.72	0.64	0.67	FRII	21.55	8000037957000920	0.62
9437	J203126-521448	307.86	-52.247	0.002	100.85	66.39	100.85	2.02	0.64	0.68	FRII	25.24		
9351	J203132-554428	307.88	-55.741	0.014	112.42	29.62	112.42	0.27	0.26	0.27	FRI	17.96	8000058048002530	0.21
9325	J203133-592052	307.89	-59.348	0.002	60.76	60.76	60.76	0.24	0.52	0.57	single	21.96	8000047140000600	0.69
9437	J203134-521845	307.89	-52.313	0.001	56.77	30.87	56.77				FRII	22.08	8000069973001160	1.03

Continued on next page

Table 4.2 – Continued from previous page

SBID	Source Name	RA (J2000) (deg)	DEC (J2000) (deg)	Flux Density (Jy)	Size (")	a (")	b (")	PA (°)	a/b _{max}	a/b _{min}	Class	Mag (r-band)	DESI ID	Z
9325	J203134-605941	307.89	-60.995	0.283	65.85	24	58.68	1.27	0.39	0.43	FRI	22.96		
9351	J203134-543836	307.9	-54.643	0.001	87.66	54.28	87.66		0.60	0.64	FRII	20.97	8000061353003410	0.63
9437	J203138-525953	307.91	-52.998	0.005	65.75	28.64	53.22	2.71	0.51	0.56	FRII	18.94		
9351	J203139-572049	307.91	-57.347	0.181	55.36	22.36	53.34	2.19	0.40	0.44	FRI	22.37	8000053246000480	0.8
9325	J203140-574252	307.92	-57.714	0.01	79.85	41.04	64.43	2.29	0.61	0.66	FRII	25.18		
9325	J203140-610604	307.92	-61.101	0.009	65.85		65.85	1.83			single	18.02	8000042080000500	0.25
9325	J203141-604854	307.92	-60.815	0.019	91.07	45.37	74.81	0.84	0.59	0.63	FRII	21.05	8000042787001660	0.65
9351	J203141-555536	307.92	-55.927	0.006	51.59	16.12	37.51	1.09	0.40	0.46	FRI	21.79	8000057235004210	0.81
9351	J203143-551541	307.93	-55.261	0.002	60.08	27.58	60.08	0.03	0.44	0.48	FRI	18.2	8000059690002190	0.24
9437	J203143-490831	307.93	-49.142	0.004	58.06	26.46	58.06	1.42	0.44	0.48	FRI	20.16	8000080967004810	0.47
9437	J203149-522529	307.96	-52.425	0.017	141.69	75.29	115.05	2.42	0.64	0.67	FRII	18.82	8000069088003780	0.28
9325	J203150-594310	307.96	-59.719	0.009	85.41		85.41	0.35			single	17.47	8000045668003470	0.24
9437	J203153-520913	307.97	-52.154	0.002	54.7		54.7	2.83			single	24.62	8000069973004370	
9351	J203153-551339	307.97	-55.228	0.01	72.23	23.32	72.23	2.51	0.31	0.33	FRI	17.96	8000059690002730	0.24
9351	J203156-554647	307.99	-55.78	0.029	50.65	18.97	49.35	2.78	0.37	0.40	FRI	17.4		
9325	J203157-584451	307.99	-58.748	0.003	73.23	39.22	73.23	1.44	0.52	0.55	FRII	20.77		
9351	J203159-534202	308	-53.701	0.162	46.69	18.44	44.94	1.08	0.39	0.43	FRI	24.22		
9351	J203205-530930	308.02	-53.158	0.013	122.61	59.06	122.61	1.08	0.47	0.49	FRI	23.98		
9351	J203213-551904	308.06	-55.318	0.008	43.58		38.05	0.48			single	22.08	8000059691001020	0.61
9325	J203219-603148	308.08	-60.53	0.005	59.46		59.46	3.11			single	20.48		
9351	J203220-525924	308.09	-52.99	0.042	126.27	89.8	126.27	0.53	0.70	0.73	FRII	21.88	8000067334002760	0.76
9437	J203224-510351	308.1	-51.064	0.003	93.18	61.74	93.18	0.45	0.65	0.68	FRII	23.47		
9351	J203224-555649	308.1	-55.947	0.035	62.69	27.78	56.07	0.94	0.47	0.52	FRx	17.2	8000057235003700	0.23
9351	J203229-535521	308.12	-53.923	0.018	71.84	22.31	56.56	0.06	0.38	0.41	FRI	19.81	8000063885003590	0.37
9437	J203231-515256	308.13	-51.882	0.054	472.93	97.92	472.93	1.68	0.21	0.21	FRI	14.44	8000070863004580	0.06
9325	J203231-610105	308.13	-61.018	0.022	328.1	214.94	328.1	3.12	0.65	0.66	FRII	19.75	8000042080003270	0.32
9351	J203232-532822	308.13	-53.473	0.044	53.94		45.91	3.11			single	18.97	8000065600002600	0.52
9437	J203234-495134	308.14	-49.859	0.002	42.46	13.97	42.46	3.05	0.31	0.35	FRI	23.47		
9351	J203234-562810	308.14	-56.469	0.012	106.74	45.52	106.74	2.47	0.42	0.44	FRI	16.58	8000055625003050	0.15
9325	J203235-582635	308.15	-58.443	0.004	69.27		69.27	1.44	0.39	0.42	single	20.74	8000049591003650	0.48
9325	J203240-621041	308.17	-62.178	0.043	58.38	22.36	55.34	2.24	0.39	0.42	FRI	21.85	8000038630005050	0.77
9351	J203241-565137	308.17	-56.86	0.002	69.03		69.03	1.28			single	20.74	8000054827000310	0.6
9351	J203241-555147	308.17	-55.863	0.001	91.09	59.33	91.09		0.63	0.67	FRII	23.47		
9325	J203247-574928	308.2	-57.824	0.003	54.03	19.7	54.03	0.39	0.35	0.38	FRI	25.52		
9351	J203247-560123	308.2	-56.023	0.004	149.05	95.06	149.05	1	0.63	0.65	FRII	20.09	8000057235002090	0.54
9325	J203248-622757	308.2	-62.466	0.005	60.08		60.08	0.03			single	20.19	8000037957004190	
9351	J203251-572504	308.21	-57.418	0.007	82.24	20.4	82.24	0.27	0.24	0.26	FRI	24.13		
9351	J203253-555937	308.22	-55.994	0.034	89.79		89.79	0.91			single	19.63	8000057235002700	0.51
9351	J203255-532100	308.23	-53.35	0.001	53.94		52.94	0.14			single	22.13	8000066465000440	0.67

Continued on next page

Table 4.2 – Continued from previous page

SBID	Source Name	RA (J2000) (deg)	DEC (J2000) (deg)	Flux Density (Jy)	Size (")	a (")	b (")	PA (°)	a/b _{max}	a/b _{min}	Class	Mag (r-band)	DESID	Z
9437	J203256-532750	308.24	-53.464	0.085	71.02	28.28	62.58	2.53	0.43	0.47	FRI	22.64	800006560002800	1.12
9325	J203258-610107	308.24	-61.019	0.004	98.32	61.53	98.32	3.03	0.61	0.64	FRII	20.81		
9325	J203259-593822	308.25	-59.639	0.007	52.7	40.24	40.24	2.94	0.39	0.43	single	19.62	8000045669005320	0.46
9325	J203302-582031	308.26	-58.342	0.076	51.07	20.4	49.87	1.09	0.39	0.43	FRI	20.03	8000050152000780	0.94
9325	J203303-621624	308.26	-62.262	0.226	53.89	53.84	53.84	0.12			single	21.99	8000038631002760	0.94
9351	J203304-565930	308.27	-56.992	0.018	50.15	44.57	43.78	1.62	0.48	0.51	single	17.13		
9437	J203306-481614	308.28	-48.271	0.008	90.4	87.7	87.7	0.23	0.48	0.51	PRx	16.92	8000084785002490	0.16
9351	J203306-551944	308.28	-55.329	0.006	87.7	50.65	91.86	2.99	0.54	0.57	single	19.86	8000059691000790	0.6
9325	J203308-583704	308.29	-58.618	0.004	91.86	50.65	91.86	2.99	0.54	0.57	FRII	21.76		
9437	J203309-482744	308.29	-48.462	0.002	77.47	43.27	77.47	1.64	0.54	0.58	FRII	23.3		
9351	J203314-524425	308.31	-52.74	0.046	92.54	43.46	66.01	1.23	0.63	0.68	FRII	24.22		
9351	J203314-533839	308.31	-53.644	0.019	65.94	28.21	65.94	1.37	0.41	0.44	FRI	20.32		
9437	J203319-513328	308.33	-51.558	0.004	53.1	53.1	53.1	1.77	0.85	0.88	single	23.59	8000064741003260	0.6
9351	J203320-531546	308.34	-53.263	0.027	199.24	149.05	172.83	0.71	0.85	0.88	FRII	21.54	8000066465002200	1.05
9437	J203320-502006	308.34	-50.335	0.008	55.65	18.87	42.67	2.57	0.42	0.47	FRI	17.26	8000081915003380	0.2
9437	J203324-485643	308.35	-48.945	0.029	68.71	29.28	61.48	1.12	0.46	0.50	FRI	17.26		
9437	J203329-510525	308.37	-51.09	0.007	72.9	22.8	47.3	0.71	0.46	0.51	PRx	16.34		
9325	J203330-593553	308.38	-59.598	0.255	73.35	22.63	69.13	0.73	0.32	0.34	FRI	20.51	8000039310000850	0.26
9325	J203330-620605	308.38	-62.101	0.005	123.56	84.88	101.69	0.99	0.81	0.86	FRII	18.41	8000044940002390	0.33
9325	J203330-600206	308.38	-60.035	0.002	60.29	27.09	60.29	1.99	0.43	0.47	FRI	18.82	8000079088002960	0.33
9437	J203333-494123	308.39	-49.69	0.001	76.03	42.58	76.03		0.54	0.58	FRII	18.97		
9325	J203336-571852	308.4	-57.314	0.001	93.14	57.43	93.14	0.17	0.60	0.63	FRII	18.97	8000042788005110	0.41
9437	J203337-604142	308.41	-60.695	0.001	50.77	31.62	50.77		0.59	0.65	FRII	23.69		
9437	J203345-492827	308.44	-49.474	0.002	47.29	14.14	33.2	2.33	0.40	0.46	FRI	27.76		
9437	J203345-514558	308.44	-51.766	0.012	46.95	13.04	39.94	2.71	0.31	0.35	FRI	18.11		
9437	J203354-492916	308.48	-49.488	0.013	134.83	103.32	126.8	0.83	0.80	0.83	FRII	20.44	8000066466000820	0.69
9437	J203354-513256	308.48	-51.549	0.006	118.34	39.09	118.34	1.96	0.32	0.34	FRI	20.79	8000067335004640	0.15
9351	J203358-570630	308.49	-57.108	0.001	70.36	44.54	70.36	0.95	0.61	0.66	FRII	16.23	8000078155004200	1.02
9351	J203402-531933	308.51	-53.326	0.008	162.82	89.1	147.14	0.19	0.60	0.62	FRII	19.61	8000039310002730	0.4
9351	J203408-525342	308.53	-52.895	0.007	148.78	93.56	117.58	1.76	0.78	0.81	FRII	21.94	8000058049001530	0.71
9437	J203408-495231	308.54	-49.875	0.009	62.83	18.94	47.64	0.51	0.38	0.42	FRI	26.54		
9437	J203409-490211	308.54	-49.036	0.004	60.15	36.83	60.15	1.53	0.59	0.64	FRII	18.74	8000053248005000	0.4
9325	J203409-620100	308.54	-62.017	0.004	111.49	40.41	111.49	2.21	0.35	0.37	FRI	19.99	8000068210003690	0.56
9351	J203411-554622	308.55	-55.773	0.024	131.61	72.96	131.61	3.12	0.54	0.57	FRII	17.05		
9437	J203415-520712	308.57	-52.12	0.056	114.8	67.23	99.45	2.67	0.66	0.69	FRII	18.19		
9351	J203416-570809	308.57	-57.136	0.007	49.3	15.38	35.43	1.39	0.41	0.47	FRI	17.05		
9437	J203419-524141	308.58	-52.695	0.002	54.11	54.11	54.11	1.28	0.40	0.43	single	17.05		
9351	J203421-554653	308.59	-55.781	0.007	66.52	27.59	66.52	0.73	0.40	0.43	single	17.05		
9325	J203428-574614	308.62	-57.771	0.005	38.41	34.94	34.94	0.43	0.40	0.43	single	17.05		

Continued on next page

Table 4.2 – Continued from previous page

SBID	Source Name	RA (J2000) (deg)	DEC (J2000) (deg)	Flux Density (Jy)	Size (")	a (")	b (")	PA (°)	a/b _{max}	a/b _{min}	Class	Mag (r-band)	DESI ID	Z
9437	J203438-521341	308.66	-52.228	0.016	86.37	50.64	76	3.1	0.65	0.69	FR II	25.21	8000069975003240	
9437	J203442-491607	308.68	-49.269	0.004	52.07	17.89	35.87	1.07	0.47	0.54	FRx	26.16	8000080969002120	
9325	J203443-602425	308.68	-60.407	0.025	91.98	64.9	86.81	2.17	0.73	0.77	FR II	24.14		
9351	J203452-543110	308.72	-54.519	0.001	57.18	25.3	57.18		0.42	0.46	FRI	22.77	8000062194001560	
9351	J203458-573840	308.74	-57.644	0.015	63.87	30.53	53.93	2.15	0.54	0.59	FR II	23.05		
9351	J203459-555737	308.75	-55.96	0.041	65.4	28.64	61.4	0.85	0.45	0.49	FRI	16.89	8000057236003010	0.11
9437	J203459-484455	308.75	-48.749	0.004	130.9	85.35	130.9	1.19	0.64	0.66	FR II	24.34		
9325	J203501-594003	308.76	-59.668	0.017	86.8	57.65	86.8	2.83	0.65	0.68	FR II	16.4		
9351	J203502-560332	308.76	-56.059	0.255	49.78	17.2	49.78	0.43	0.33	0.36	FRI	21.88	8000057236001130	0.97
9325	J203503-623457	308.76	-62.583	0.46	273.79	206.12	268.56	3.11	0.76	0.77	FR II	17.16	8000037958001030	
9325	J203503-574504	308.77	-57.751	0.002	55.28	21.8	55.28	0.74	0.38	0.41	FRI	17.14		
9325	J203505-612232	308.77	-61.376	0.012	88.32	37.11	88.32	1.16	0.41	0.43	FRI	19.94	8000041380000130	
9325	J203511-544344	308.8	-54.729	0.002	67.31	24.33	67.31		0.35	0.38	FRI	23.57		
9325	J203513-605123	308.81	-60.856	0.001	49.17	19.78	49.17	0.09	0.38	0.42	FRI	22.14	8000042789000440	0.79
9437	J203513-524442	308.81	-52.745	0.018	72.91	30.47	72.91	0.91	0.40	0.43	FRI	22.72		
9325	J203518-620149	308.83	-62.03	0.004	75.89	33.46	75.89	2.95	0.43	0.46	FRI	22.22	8000039311002410	0.67
9437	J203528-494223	308.87	-49.706	0.026	50.38	14.14	40.44	1.47	0.33	0.37	FRI	23.61		
9437	J203530-521336	308.88	-52.227	0.016	68.11	15.13	54	1.71	0.27	0.29	FRI	21.41	8000069976002870	0.52
9351	J203531-575019	308.88	-57.839	0.009	128.68	84.69	111.28	0.17	0.74	0.78	FR II	18.76		
9437	J203538-524255	308.91	-52.715	0.002	66.53	31.15	66.53	0.87	0.45	0.49	FRI	20.37	8000068211003800	0.52
9351	J203538-530235	308.91	-53.043	0.01	61.76		61.76	1.36			single	22.36	8000067336001770	1.05
9325	J203543-582858	308.93	-58.483	0.002	88.61	35.93	88.61	1.59	0.39	0.42	FRI	21.54	8000049392002430	0.73
9325	J203545-570852	308.94	-57.148	0.067	107.31	71.55	104.63	2.07	0.67	0.70	FR II	22.27	8000053249004820	0.82
9325	J203545-624611	308.94	-62.77	0.002	63.59	26.7	63.59	2.45	0.40	0.44	FRI	22.42	8000037291002560	0.92
9351	J203545-555953	308.94	-55.998	0.022	49.78	46.09	46.09	1.73	0.53	0.57	single	17.57	8000057237002360	0.23
9325	J203546-584939	308.94	-58.828	0.001	71.37	39.3	71.37		0.53	0.57	FR II	24.4	8000048637000820	0.24
9325	J203551-612319	308.97	-61.389	0.039	61.55	26.31	56.28	1.5	0.45	0.49	FRI	17.47	8000040686006410	0.66
9437	J203553-521030	308.97	-52.175	0.006	59.69	59.69	59.69	1.52	0.45	0.49	single	23.79	8000069976003860	0.51
9325	J203554-590702	308.98	-59.117	0.005	68.58	32.1	68.58	2.92	0.45	0.49	FRI	20.33	8000047888000130	0.66
9437	J203557-500929	308.99	-50.158	0.087	110.46	25	110.46	0.42	0.22	0.23	FRI	20.47	8000077227003850	0.51
9325	J203558-592030	308.99	-59.342	0.003	55.49	36.04	36.04	1.04	0.42	0.46	single	23.51		
9351	J203558-580946	309	-58.163	0.028	213.49	109.48	213.49	0.81	0.51	0.52	FR II	15.92	8000050154003620	0.09
9325	J203559-614156	309	-61.699	0.003	48.25	20.92	48.25	1.79	0.41	0.46	FRI	21.69	8000039996004590	0.82
9437	J203601-513050	309.01	-51.514	0.013	40.54	39.75	39.75	0.7			single	21.15	8000072658001730	0.41
9351	J203608-573649	309.03	-57.614	0.004	69.14	68.41	69.14	0.13	0.63	0.67	single	19.01	8000052467000240	0.41
9351	J203609-544623	309.04	-54.773	0.011	105.31	68.41	105.31	1.08	0.63	0.67	FR II	22.53	8000061355001530	0.94
9437	J203611-501045	309.05	-50.179	0.043	60.18	27.2	58.63	2.31	0.44	0.48	FRI	21.94	8000077227003580	0.55
9437	J203613-505729	309.06	-50.958	0.01	210.88	170.64	210.88	0.59	0.80	0.82	FRI	21.24	8000074471002660	0.83
9351	J203614-542105	309.06	-54.351	0.006	125.26	88.81	107.77	2.23	0.81	0.84	FR II	23.74		

Continued on next page

Table 4.2 – Continued from previous page

SBID	Source Name	RA (J2000) (deg)	DEC (J2000) (deg)	Flux Density (Jy)	Size (")	a (")	b (")	PA (°)	a/b _{max}	a/b _{min}	Class	Mag (r-band)	DESI ID	Z
9351	J203617-571229	309.07	-57.208	0.01	146.13	100.44	126.22	0.66	0.78	0.81	FR II	20.56	8000053249003360	0.63
9351	J203620-564142	309.08	-56.695	0.109	143.55	77.85	143.55	1.01	0.53	0.55	FR II	16.34	8000054829003980	0.14
9351	J203622-565855	309.1	-56.982	0.021	47.93	17.93	48.35	2.69	0.35	0.39	FR I			
9351	J203634-573855	309.14	-57.649	0.193	42.06	15.35	42.06	1.34	0.34	0.39	FR I			
9437	J203635-514204	309.15	-51.701	0.008	134.62	98.06	134.62	0.39	0.72	0.74	FR II	18.31	8000071759002060	0.34
9351	J203646-535248	309.19	-53.88	0.017	110.67	66.49	102.25	3.01	0.63	0.67	FR II	18.79	8000063888003680	0.36
9325	J203650-594734	309.21	-59.793	0.006	77.75	32.56	54.7	2.42	0.57	0.62	FR II	17.11	8000045671001880	0.23
9437	J203653-481049	309.22	-48.18	0.013	250.72	214.06	250.72		0.85	0.86	FR II	21.57	8000084788004350	0.45
9351	J203654-553844	309.23	-55.646	0.005	60.01	25.06	45.48	2.7	0.52	0.58	FR II	19.13	8000058051003570	0.41
9351	J203700-525300	309.25	-52.883	0.004	61.76	18.41	61.76	2.99	0.29	0.31	FR I	19.79	8000067337005050	0.33
9325	J203701-613311	309.25	-61.553	0.067	95.11	38.05	71.94	3.04	0.51	0.55	FR II	24.53		
9351	J203705-562817	309.27	-56.471	0.009	62.29		62.29	2.68			single	20.05	8000055627003190	0.53
9437	J203705-484606	309.27	-48.768	0.033	92.87	41.23	92.87	2.56	0.43	0.46	FR I	21.38	8000082869002230	0.91
9325	J203709-615813	309.29	-61.97	0.008	112.33	70.01	112.33	1.34	0.61	0.64	FR II	20.75	8000039312003050	0.4
9437	J203712-505012	309.3	-50.837	0.064	51.84	13.72	49.5	1.58	0.26	0.29	FR I	22.13		
9351	J203716-560811	309.32	-56.136	0.005	80.87	26.33	80.87	0.44	0.32	0.34	FR I	17.32	8000056430005080	
9325	J203717-612931	309.32	-61.492	0.007	108.79	45.4	108.79	2.87	0.41	0.43	FR I	21.5		
9437	J203719-502124	309.33	-50.357	0.005	57.29		38.71	2.75			single	21.1	8000077227000400	
9351	J203728-530203	309.37	-53.034	0.009	61.76		43.75	1.37			single	19.64	8000067337001790	0.5
9351	J203729-543903	309.37	-54.651	0.006	78.13	34.93	64.68	2.03	0.52	0.56	FR II	25.19		
9287	J203729-523309	309.37	-52.553	0.103	55.6		45.14	0.45			single			
9325	J203733-571909	309.39	-57.319	0.02	53.26		46.27	1.72			single	22.91	8000053250001260	1.03
9437	J203733-485831	309.39	-48.975	0.097	68.01		68.01	2.65			single	20.75	8000081918003240	0.86
9325	J203734-620055	309.39	-62.015	0.009	186.13	141.89	159.64	1.26	0.88	0.90	FR II	22.4	8000039312002520	1.11
9325	J203741-580829	309.42	-58.141	0.002	111.45	75.44	111.45	0.26	0.66	0.69	FR II	22.26	8000050154004230	0.71
9325	J203752-592351	309.47	-59.398	0.005	55.19		35.96	0.44			single	19.49		
9351	J203753-575054	309.47	-57.848	0.032	111.27	57.2	94.92	0.63	0.59	0.62	FR II	20.83		
9325	J203805-624027	309.52	-62.674	0.011	84.92	50.16	72.89	0.43	0.67	0.71	FR II	23.36		
9437	J203807-520529	309.53	-52.091	0.003	58.81		58.81	0.36			single	18.97	8000070867000820	0.39
9437	J203807-501447	309.53	-50.246	0.012	95.49	64.56	91.17	2.84	0.69	0.73	FR II	21.92	8000077228002340	0.75
9325	J203808-605011	309.54	-60.836	0.003	62.81		62.81	3.03			single	22.26	8000042790001090	0.92
9287	J203810-495229	309.54	-49.875	0.087	99.84	40.79	82.96	1.47	0.48	0.51	FRx	16.29	8000078157004060	0.15
9351	J203811-552514	309.55	-55.421	0.003	43.38	14.21	31.07	1.05	0.42	0.50	FR I	25.11		
9437	J203820-502440	309.59	-50.411	0.002	56.32	14.74	56.32	2.78	0.25	0.27	FR I	20.29	8000069092003730	0.67
9437	J203822-522704	309.59	-52.451	0.007	72.89	38.47	59.33	1.73	0.62	0.68	FR II	21.22		
9437	J203827-493226	309.62	-49.541	0.013	243.88	96.77	243.88	0.15	0.39	0.40	FR I	15.67	8000048639001710	0.37
9325	J203828-584553	309.62	-58.765	0.026	113.74	51.03	113.74	0.45	0.44	0.46	FR I	19.07		
9437	J203831-523144	309.63	-52.529	0.034	108.63	64.08	98.61	2.93	0.63	0.67	FR II	19.47		
9351	J203834-575612	309.64	-57.937	0.004	109.63	59.08	109.63	1.49	0.53	0.55	FR II	16.63	8000050920002890	0.1

Continued on next page

Table 4.2 – Continued from previous page

SBID	Source Name	RA (J2000) (deg)	DEC (J2000) (deg)	Flux Density (Jy)	Size (")	a (")	b (")	PA (°)	a/b _{max}	a/b _{min}	Class	Mag (r-band)	DESI ID	Z
9287	J203840-505337	309.67	-50.894	0.002	53.58	318.93	53.58	0.92	0.83	0.84	single	20	8000074472004070	0.6
9325	J203841-604520	309.67	-60.756	0.026	382.33	318.93	382.33	1.49	0.83	0.84	FRII	19.87		
9325	J203843-604850	309.68	-60.814	0.002	50.31	31.31	31.31	1.97	0.61	0.64	single	23.02	8000042791001660	1.24
9351	J203847-552020	309.7	-55.339	0.125	97.1	58.14	92.66	2.07	0.76	0.76	FRII	16.9		
9351	J203848-562307	309.7	-56.385	0.022	589.77	448.52	589.77	2.73	0.76	0.76	FRII	20.83		
9325	J203852-581711	309.72	-58.286	0.003	66.47	20.84	66.47	2.41	0.30	0.33	FRI	22.82	8000050155001510	0.82
9437	J203853-484949	309.72	-48.831	0.008	311.43	250.51	260.84	1.58	0.95	0.97	FRII	22.09	8000082871001010	0.93
9325	J203855-612008	309.73	-61.336	0.003	151.84	116.83	151.84	0.41	0.76	0.78	FRII	21.73	8000041382001290	0.47
9437	J203857-502701	309.74	-50.45	0.029	71.41		57.19	1.82			single	18.14	8000076305003310	0.42
9351	J203857-560923	309.74	-56.156	0.009	55.4	25.8	55.4	0.97	0.45	0.49	FRI	19.39	8000056431004800	0.46
9351	J203901-561835	309.76	-56.31	0.002	52.57	21.08	52.57	1.3	0.38	0.42	FRI	20.86	8000056431001440	0.54
9287	J203901-514522	309.76	-51.756	0.009	58.36	19.6	51.65	2.56	0.36	0.40	FRI	21.95	8000071761001860	0.82
9351	J203902-571244	309.76	-57.212	0.008	59.27	27.86	49.14	1.19	0.54	0.60	FRII	24.95		
9325	J203905-611025	309.77	-61.174	0.023	79.81	36.33	68.02	2.67	0.52	0.55	FRII	19.6	8000041382005060	0.75
9351	J203905-564413	309.77	-56.737	0.006	42.47		35.53	1.17			single	18	8000054831002750	0.27
9351	J203906-561139	309.78	-56.194	0.016	161.36	122.93	161.36	0.77	0.75	0.77	FRII	20.37	8000056431004440	
9351	J203907-545440	309.78	-54.911	0.034	56.53	24.08	54.26	0.71	0.42	0.47	FRI	23.18		
9437	J203907-511806	309.78	-51.302	0.002	110.43	63.65	110.43		0.56	0.59	FRII	22.36	8000073563001240	0.88
9351	J203918-554951	309.83	-55.831	0.291	81.08	36.71	76.56	2.19	0.46	0.50	FRI	22.26	8000058052000630	0.83
9325	J203922-594247	309.84	-59.713	0.009	279.98	220.69	279.98	2.31	0.78	0.80	FRII	21.14	8000045672002800	0.42
9325	J203923-591039	309.85	-59.178	0.003	63.11		63.11	0.67			single	19.98	8000047144003940	0.55
9287	J203925-494316	309.86	-49.721	0.007	74.92	20.59	50.64	2.69	0.39	0.43	FRI	21.86	8000079091002620	0.8
9351	J203928-533607	309.87	-53.602	0.114	153.17	55.46	153.17	1.52	0.36	0.37	FRI	15.92	8000065604000440	0.14
9351	J203930-563646	309.88	-56.613	0.002	68	20.05	68	1.44	0.28	0.31	FRI	19.46	8000055628000290	0.32
9351	J203933-563514	309.89	-56.587	0.002	57.87		57.87	1.66			single	18.74	8000055628000740	0.38
9351	J203935-543448	309.9	-54.58	0.004	79.89	44.53	79.89	1.32	0.54	0.58	FRx	19.38	8000053251000660	0.46
9325	J203937-572035	309.91	-57.343	0.002	53.26	26.52	53.26	1.47	0.48	0.52	single	17.71	8000037961004270	0.26
9325	J203938-622734	309.91	-62.459	0.003	113.65		113.65	2.32			single	17.88	8000047145001810	0.26
9325	J203938-591623	309.91	-59.273	0.004	93.08	49.18	93.08	1.63	0.51	0.54	FRII	19.09	8000037293004870	0.39
9325	J203939-624126	309.91	-62.691	0.003	96.17	54.63	71.88	0.42	0.73	0.79	FRII	19.16	8000064744000160	0.39
9351	J203940-535203	309.92	-53.868	0.01	53.44		41.98	0.33			single	19.47	8000038634000350	0.33
9325	J203942-622126	309.93	-62.357	0.011	73.65	35.78	64.12	2.65	0.54	0.58	FRII	18.49		
9287	J203943-530505	309.93	-50.885	0.002	52.19		52.19	2.72			single	18.49		
9351	J203945-581834	309.94	-58.309	0.006	110.74	63.95	110.74	2.27	0.56	0.59	FRII	22.23	8000050156001060	0.98
9325	J203948-592947	309.95	-59.496	0.001	59.75		59.75	0.11			single	18.05	8000046405002380	0.25
9287	J203948-500111	309.95	-50.02	0.403	96.1	42.52	113.28	2.19	0.37	0.38	FRI	17.33	8000078158002220	0.2
9351	J203949-562411	309.96	-56.403	0.002	64.3	29.46	64.3	2.39	0.44	0.48	FRI	22.18	8000055629004060	0.72
9437	J203950-503616	309.96	-50.604	0.007	233.41	178.61	233.41	0.39	0.76	0.77	FRII	18.14		
9325	J203953-625052	309.97	-62.848	0.013	97.93	57.27	82.48	1.37	0.67	0.72	FRII	19.38	8000037293000670	

Continued on next page

Table 4.2 – Continued from previous page

SBID	Source Name	RA (J2000) (deg)	DEC (J2000) (deg)	Flux Density (Jy)	Size (")	a (")	b (")	PA (°)	a/b _{max}	a/b _{min}	Class	Mag (r-band)	DESI ID	Z
9351	J203955-540909	309.98	-54.153	0.001	59.05	28.35	59.05	0.49	0.46	0.50	FRx			
9287	J204004-505551	310.02	-50.931	0.007	72.17	27.24	72.17	1.75	0.36	0.39	FRI	15.12	8000074473003660	0.04
9437	J204010-485005	310.04	-48.835	0.009	91.35	56.85	77.88	0.7	0.71	0.75	FRII	20.85		
9287	J204012-491713	310.05	-49.287	0.069	49.73	49.09	49.09	2.81			single			
9325	J204013-582818	310.06	-58.472	0.006	148.74	113.62	148.74	1.6	0.75	0.78	FRII	18.87	8000049395002480	0.4
9287	J204019-515412	310.08	-51.903	0.001	58.36	58.36	58.36	0.4			single	21.05	8000070868004530	0.71
9351	J204023-543841	310.1	-54.645	0.013	128.84	95.44	128.84	1.47	0.73	0.76	FRII	22.65	8000061358003430	1.16
9325	J204024-543203	310.1	-54.534	0.002	68.31	68.31	68.31	0.22			single	18.05	8000062197001440	0.34
9325	J204025-613625	310.1	-61.607	0.002	55.24	22.45	55.24	0.16	0.39	0.43	FRI	21.63	8000040688000710	0.79
9325	J204026-621333	310.11	-62.226	0.006	196.06	156.84	196.06	3.03	0.79	0.81	FRII	16.85		
9351	J204027-535401	310.11	-53.9	0.027	92.54	37.84	83.79	2.46	0.44	0.47	FRI	25.03		
9325	J204029-553912	310.12	-55.653	0.008	71.47	37.71	71.47	2.4	0.51	0.55	FRII	19.51	8000058053003110	0.51
9437	J204030-492625	310.13	-49.44	0.015	70.98	29.15	59.11	0.55	0.47	0.51	FRx	17.06	8000080030003410	0.23
9351	J204035-550655	310.15	-55.115	0.029	71.1	30.53	57.93	0.56	0.51	0.55	FRII	18.45	8000060525000250	
9351	J204041-543329	310.17	-54.558	0.003	83.83	55.55	83.83	0.19	0.64	0.68	FRII	25.76		
9325	J204042-610253	310.18	-61.048	0.368	79.41	60.08	74.83	1.62	0.78	0.83	FRII	23.24	8000042084002010	
9325	J204049-595319	310.21	-59.889	0.001	63.15	30.6	63.15		0.47	0.50	FRx			
9325	J204053-564418	310.22	-56.738	0.003	63.46	63.46	63.46	0.3			single	17.85	8000054832002350	0.27
9351	J204102-560206	310.26	-56.035	0.053	91.64	25.06	91.64	1.33	0.27	0.28	FRI	17.22	8000057240001910	0.2
9351	J204102-544548	310.26	-54.763	0.004	45.66	18	37.29	0	0.45	0.52	FRx	22.51	8000061358001650	0.86
9325	J204103-591947	310.26	-59.33	0.002	103.25	45.49	103.25	2.77	0.43	0.45	FRI	20.18	8000047145000920	0.54
9325	J204104-595142	310.27	-59.862	0.048	52.66	44.94	50.83	1.2	0.58	0.62	single	20.74	8000045673000290	0.64
9351	J204111-535929	310.3	-53.991	0.025	83	44.94	74.67	0.15	0.58	0.62	FRII	22.19		
9437	J204112-525118	310.3	-52.855	0.009	60.64	47.19	47.19	0.64			single	18.88	8000068215000290	0.33
9325	J204112-613948	310.3	-61.663	0.036	77.28	77.28	77.28	2.44	0.31	0.31	single	18.54	8000039999005350	0.04
9351	J204112-525740	310.3	-52.961	0.116	343.12	121.43	388.75	2.23	0.31	0.31	FRI	14.09	8000067339003560	0.04
9437	J204113-510720	310.3	-51.122	0.002	59.48	59.48	59.48	0.68			single	19.24	8000074474000060	0.43
9351	J204113-540015	310.31	-54.004	0.008	58.32	58.32	58.32	1.36			single	18.16	8000063890001920	0.31
9351	J204115-535055	310.31	-53.849	0.012	46.35	39.52	39.52	1.74			single	22.48	8000064745000420	1.01
9351	J204115-571821	310.32	-57.306	0.114	86.4	32.56	80.74	0.63	0.39	0.42	FRI	19.67	8000053252001350	0.34
9325	J204120-620822	310.33	-62.139	0.005	88.54	88.54	88.54	1.15			single	18.14	8000038635005530	0.28
9437	J204120-535457	310.34	-53.916	0.001	75.39	75.39	75.39				single	24.29		
9325	J204120-621415	310.34	-62.238	0.031	109.56	109.56	109.56	3			single	16	8000038635002870	0.13
9437	J204122-523827	310.35	-52.641	0.007	86.65	51.88	79.24	2.59	0.63	0.68	FRII	22.7		
9325	J204126-615111	310.36	-61.853	0.02	95.48	43.27	77.71	2.28	0.54	0.58	FRII	24.32		
9351	J204126-571630	310.36	-57.275	0.022	39.48	13.81	39.48	2.35	0.33	0.37	FRI	24.76		
9351	J204128-532526	310.37	-53.424	0.017	105.59	47.61	105.59	1.94	0.44	0.46	FRI	17.09	8000065605004110	0.2
9325	J204128-572855	310.37	-57.482	0.022	41.47	40.02	40.02	0.45	0.44	0.46	single	21.39	8000052470002830	1.04
9325	J204134-591218	310.39	-59.205	0.007	110.45	77.9	99.94	2.61	0.76	0.80	FRII			

Continued on next page

Table 4.2 – Continued from previous page

SBID	Source Name	RA (J2000) (deg)	DEC (J2000) (deg)	Flux Density (Jy)	Size (")	a (")	b (")	PA (°)	a/b _{max}	a/b _{min}	Class	Mag (r-band)	DESI ID	Z
9351	J204135-534133	310.4	-53.693	0.071	151.16	106.47	142.05	1.12	0.74	0.76	FRII	20.62	8000064746003290	0.4
9287	J204137-493330	310.41	-49.558	0.006	65.55	46.94	46.94	0.76			single	20.28	8000080030001160	0.63
9351	J204142-542843	310.43	-54.479	0.006	83.21	51.74	83.21	0.25	0.60	0.64	FRII	21.99	8000062198002320	1.08
9437	J204145-515257	310.44	-51.883	0.007	54.8	13.77	41.25	0.75	0.31	0.36	FRI	22.77	8000070869005130	0.86
9351	J204146-544141	310.45	-54.695	0.012	69.1	40	65.14	2.21	0.59	0.64	FRII	23.63	8000061359002860	
9287	J204148-514512	310.45	-51.753	0.003	66.48	33.33	63.06	0.69	0.51	0.55	FRII	25.27		
9287	J204148-522600	310.45	-52.433	0.001	55.6	25.48	55.6		0.44	0.48	FRI	21.94		
9351	J204150-534814	310.46	-53.804	0.009	127.96	84.12	104.18	2.06	0.79	0.83	FRII	20.24		
9325	J204153-574526	310.47	-57.757	0.007	97.88	30.49	97.88	1.55	0.30	0.32	FRI	21.77	8000051693002430	0.81
9351	J204157-545125	310.49	-54.857	0.002	47.94	67.05	46.85	2.75	0.67	0.70	single	21.8	8000061359000330	0.77
9325	J204158-584352	310.5	-58.731	0.06	104.48	22	97.63	1.9	0.42	0.47	FRII	21.44	8000048640002070	0.91
9437	J204200-500049	310.5	-50.014	0.032	57.09	22	49.28	1.6	0.42	0.47	FRI	19.04	8000078160001990	0.3
9325	J204205-625052	310.52	-62.848	0.012	193.67	163.08	193.67	0.07	0.83	0.85	FRII	18.92		
9325	J204207-573411	310.53	-57.57	0.001	72.8		72.8	1.85			single	19.09	8000052471001070	0.4
9351	J204207-575001	310.53	-57.834	0.025	98.44	50.36	80.53	0.11	0.61	0.65	FRII	18.03		
9325	J204209-600021	310.54	-60.006	0.052	56.22	24.74	55.07	1.96	0.43	0.47	FRI	24.53	8000044944002840	
9351	J204220-540452	310.59	-54.081	0.004	84.14	47.75	84.14	1.54	0.55	0.58	FRII	18.46	8000063891000750	0.3
9325	J204221-591116	310.59	-59.188	0.003	61.86		61.86	3.03	0.40	0.43	single	18.77	8000047146003260	0.32
9351	J204221-540704	310.59	-54.118	0.013	75.7	31.62	75.7	0.63	0.73	0.75	FRII	20.7	8000063891000060	0.74
9437	J204222-480148	310.59	-48.03	0.044	160.55	118.65	160.55		0.48	0.52	FRx	21.8	8000085757002010	0.83
9325	J204222-612035	310.6	-61.343	0.002	56.59	28.27	56.59	1.26	0.39	0.42	FRI	20.73		
9287	J204226-495309	310.61	-49.886	0.002	75.28	30.23	75.28	2.29	0.29	0.31	FRI	21.02	8000078160004330	0.67
9351	J204233-554809	310.64	-55.803	0.001	60.5	18.22	60.5		0.29	0.31	FRI	23.2		
9351	J204235-575900	310.65	-57.983	0.016	61.69	19.71	51.29	1.67	0.37	0.40	FRI	22.19	8000050922002360	0.92
9325	J204236-594634	310.65	-59.776	0.001	47.36	26.24	47.36		0.53	0.58	FRII	22.97	8000045673002140	
9287	J204241-500216	310.67	-50.038	0.002	84.41	34	84.41	0.66	0.39	0.42	FRI	18.78	8000078160001600	0.33
9351	J204244-550100	310.69	-55.017	0.002	65.27	27.94	65.27	3.09	0.41	0.45	FRI	19.61	8000060526001800	0.46
9437	J204245-504912	310.69	-50.82	0.013	82.13	42.82	82.13	0.94	0.51	0.54	FRII	22.48		
9325	J204247-603104	310.7	-60.518	0.001	67.68		67.68	2.71			single	17.75	8000043504002960	0.23
9325	J204249-590354	310.71	-59.065	0.002	61.86		61.86	2.96	0.27	0.28	single	23.56		
9325	J204250-610414	310.71	-61.071	0.003	50.95		32.56	1.05	0.54	0.57	single	23.93		
9351	J204254-534843	310.73	-53.812	0.002	54.22		54.22	0.36	0.36	0.40	single	20.1	8000064746001010	0.53
9437	J204255-521106	310.73	-52.185	0.015	142.34	38.78	142.34		0.27	0.28	single	17.88	8000069980004040	0.22
9325	J204256-602701	310.73	-60.45	0.002	79.88	44.27	79.88	1.57	0.54	0.57	FRII	22.94	8000050923000600	0.8
9325	J204259-580500	310.75	-58.083	0.017	53.5	17.89	47.15	2.73	0.36	0.40	FRI	20.43	8000077231003090	0.56
9287	J204302-501333	310.76	-50.226	0.005	72.87	34.23	54.27	3.04	0.60	0.66	FRII	21.26	8000043504001110	0.57
9325	J204302-603505	310.76	-60.585	0.001	67.68	24.92	67.68	2.17	0.36	0.38	FRI	22.37	8000063042003240	1.02
9351	J204304-541139	310.77	-54.194	0.112	59.26	19.8	52.59	0.82	0.36	0.40	FRI	14.27	8000074475002670	0.06
9437	J204308-505906	310.79	-50.985	0.271	254.17	79.46	213.06	1.44	0.37	0.38	FRI			

Continued on next page

Table 4.2 – Continued from previous page

SBID	Source Name	RA (J2000) (deg)	DEC (J2000) (deg)	Flux Density (Jy)	Size (")	a (")	b (")	PA (°)	a/b _{max}	a/b _{min}	Class	Mag (r-band)	DESI ID	Z
9325	J204309-614239	310.79	-61.711	0.009	81.67	38.83	81.67	2.9	0.46	0.49	FRI	18.52	8000040000004350	0.23
9351	J204317-555009	310.82	-55.836	0.008	44.31	36.28	36.28	1.34			single	23.62	8000058054000610	
9437	J204321-481716	310.84	-48.288	0.004	52.95	14.56	52.95	0.25	0.26	0.29	FRI	23.63		
9351	J204321-542627	310.84	-54.441	0.004	72.14	26.64	72.14	2.85	0.36	0.38	FRI	20.93		
9437	J204324-493615	310.85	-49.604	0.009	105.4	50.75	105.4	0.81	0.47	0.49	FRI	16.77	8000080031000340	0.1
9325	J204330-601114	310.88	-60.187	0.002	94.18	33.41	94.18	2.67	0.35	0.36	FRI	23.5		
9287	J204334-520048	310.9	-52.013	0.002	48.16	43.48	43.48	1.61			single	22.07		
9325	J204336-605133	310.9	-60.859	0.022	145.3	72.85	145.3	0.31	0.49	0.51	FRx	17.51	8000042793000420	0.27
9351	J204340-545424	310.92	-54.907	0.002	63.03	63.03	63.03	2.37			single	21.07	8000060526003690	0.67
9325	J204341-613634	310.92	-61.609	0.002	73.28	36.21	73.28	1.95	0.48	0.51	FRx	24.22		
9325	J204342-615314	310.93	-61.887	0.054	73.75	34.93	68.98	2.9	0.49	0.53	FRx	24.12		
9351	J204343-544920	310.93	-54.822	0.013	47.94	42.36	42.36	2.89			single	18.88	8000061360000790	0.34
9351	J204347-532755	310.95	-53.465	0.095	84.02	45.69	79.36	2.02	0.56	0.59	FRx	21.71	8000065606003030	0.79
9437	J204354-490521	310.98	-49.089	0.011	68.74	51.79	51.79	3.04			single	22.74		
9287	J204400-502124	311	-50.357	0.002	70.39	70.39	70.39	1.38			single	17.48	8000077232000360	0.15
9325	J204403-621640	311.01	-62.278	0.009	70.75	26.16	56.99	2.3	0.44	0.48	FRI	22.89	8000038636002480	
9351	J204412-571547	311.05	-57.263	0.02	40.25	39.97	39.97	0.58			single	21.54	8000053253002360	0.82
9287	J204414-523101	311.06	-52.517	0.031	63.77	63.77	63.77	0.37	0.62	0.65	single	17.3	8000069096001940	0.18
9437	J204416-520449	311.07	-52.08	0.003	98.73	62.4	98.73	0.95	0.62	0.65	FRx	20.87	8000070871000910	0.66
9325	J204424-585026	311.1	-58.841	0.013	82.69	37.36	82.69	2.61	0.44	0.47	FRI	23.2	8000048642000530	0.88
9287	J204425-521608	311.11	-52.269	0.022	47.64	42	42	0.68			single	16.52		
9437	J204431-482744	311.13	-48.462	0.01	52.93	20.1	42.78	1.64	0.44	0.50	FRI	20.64	8000083831003280	0.56
9287	J204436-505749	311.15	-50.964	0.006	206.73	146.86	206.73	1.34	0.70	0.72	FRx	22.97	8000074476003320	1.17
9351	J204441-533952	311.17	-53.664	0.034	276.58	232.01	261.04	0.01	0.88	0.90	FRx	22.46		
9287	J204441-535410	311.17	-53.903	0.003	66.27	66.27	66.27	0.22	0.52	0.54	single	22.03	8000063892004770	0.83
9437	J204447-481932	311.2	-48.326	0.024	108.64	57.66	108.64	2.09	0.52	0.54	FRx	22.68	8000084793001440	0.77
9351	J204448-544420	311.2	-54.739	0.007	237.34	185.81	237.34	0.45	0.77	0.79	FRx	23.31		
9287	J204449-500040	311.21	-50.011	0.003	81.1	32.68	81.1	0.23	0.39	0.42	FRI	23.54		
9325	J204452-614813	311.22	-61.804	0.19	67.05	61.73	61.73	1.47	0.32	0.34	single	18.02	8000078161002350	0.25
9351	J204455-545602	311.23	-54.934	1.128	63.03	26.68	80.06	0.75	0.32	0.34	FRI	17.25	8000040001002110	0.23
9287	J204457-502214	311.24	-50.371	0.003	62.41	62.41	62.41	2.78			single	17.1	8000077232000020	0.15
9325	J204457-603824	311.24	-60.64	0.001	54	54	54	0.98			single	23.14		
9325	J204458-574248	311.24	-57.713	0.015	56.74	42.66	42.66	1.77	0.31	0.34	single	21.1	8000051695002530	0.88
9287	J204513-535512	311.3	-53.92	0.004	65.46	21.1	65.46	0.16	0.31	0.34	FRI	19.44	8000063893004230	0.41
9437	J204513-522933	311.31	-52.493	0.013	129.34	93.93	118.66	0.57	0.78	0.81	FRx	21.89	8000069096002690	0.84
9351	J204520-571157	311.33	-57.199	0.07	90.46	44.72	85.37	2.98	0.51	0.54	FRx	19.45		
9351	J204520-562600	311.34	-56.433	0.003	58.62	42.8	39.53	0.72	0.54	0.62	FRx	21.23	8000055632003000	0.77
9325	J204520-601900	311.34	-60.317	3.33	85.78	23.6	85.78	2.68	0.49	0.52	FRx	21.54	800004422001810	1.14
9325	J204521-623144	311.34	-62.529	0.005	82.91	45.69	63.3	1.19	0.69	0.75	FRx	24.57		

Continued on next page

Table 4.2 – Continued from previous page

SBID	Source Name	RA (J2000) (deg)	DEC (J2000) (deg)	Flux Density (Jy)	Size (")	a (")	b (")	PA (°)	a/b _{max}	a/b _{min}	Class	Mag (r-band)	DESI ID	Z
9351	J204524-550230	311.35	-55.042	0.014	55.41	54.59	47.5	3.03	0.49	0.51	single	20.97	8000052472001820	0.37
9351	J204532-573029	311.39	-57.508	0.021	109.63	18.44	109.63	0.04	0.36	0.40	FRx	19.54	8000066473002660	0.65
9351	J204533-551843	311.39	-55.312	0.046	55.41	18.44	48.22	0.66	0.36	0.40	FRx	20.59	8000066473004720	0.63
9437	J204534-531424	311.39	-53.24	0.001	51.14	18.44	48.93	0.9	0.36	0.40	single	20.6	8000040690000180	0.69
9351	J204534-530737	311.4	-53.127	0.014	50.25	24.63	42.72	0.35	0.35	0.37	single	19.96	8000083832002680	0.63
9325	J204536-613715	311.4	-61.621	0.005	68.41	18.44	68.41	1.76	0.69	0.73	FRx	20.75	8000040001001730	0.73
9437	J204537-483038	311.4	-48.511	0.034	84.61	51.44	72.53	1.8	0.81	0.83	FRx	20.52	8000079095005040	0.32
9325	J204539-614819	311.41	-61.805	0.117	195.71	150.97	183.91	0.64	0.81	0.83	FRx	20.98	8000058056002600	0.45
9351	J204540-544900	311.42	-54.817	0.002	49.11	19.23	49.11	0.66	0.37	0.41	FRx	23.47	8000063044003850	0.42
9287	J204542-493747	311.43	-49.63	0.011	42.42	8.9	39.44	2.83	0.21	0.24	FRx	23.43	8000063893004420	0.61
9325	J204544-580852	311.44	-58.148	0.002	91.4	26.85	91.4	2.69	0.29	0.30	FRx	18.86	8000044223004430	0.88
9325	J204545-613300	311.44	-61.55	1.063	113.33	65.79	108.32	0.16	0.56	0.58	FRx	17.28	8000045675004030	0.76
9351	J204547-571324	311.45	-57.223	0.002	115.5	31.62	115.5	0.62	0.44	0.48	FRx	20.64	8000062200000180	0.94
9351	J204548-554123	311.45	-55.69	0.015	68.69	31.62	68.69	0.62	0.44	0.48	FRx	23.3	8000037296001830	0.98
9287	J204550-530108	311.46	-53.019	0.005	68.26	27.07	68.26	3.09	0.38	0.41	FRx	20.87	8000058056002600	0.45
9287	J204552-491938	311.47	-49.327	0.003	102.63	31.23	102.63	1.61	0.30	0.31	FRx	18.29	8000043506000030	0.18
9351	J204553-541140	311.47	-54.194	0.013	102	69.1	89.87	1.95	0.75	0.79	FRx	19.17	8000062201002550	0.44
9287	J204558-555424	311.49	-53.907	0.005	121.79	88.31	121.79	2.45	0.71	0.74	FRx	22.85	8000037296001830	0.98
9325	J204601-601121	311.51	-60.189	0.004	115.42	72.32	115.42	2.88	0.61	0.64	FRx	20.1	8000058056000230	0.15
9325	J204604-591739	311.52	-59.294	0.002	81.44	33.53	81.44	2.1	0.40	0.42	FRx	16.73	8000038637003340	0.47
9325	J204605-594044	311.52	-59.679	0.009	81.74	38.4	81.74	0.88	0.46	0.48	FRx	19.21	8000042794003770	1.01
9351	J204607-551650	311.53	-55.281	0.019	61.62	67.08	61.62	2.51	0.51	0.56	single	22.31	8000072665000760	0.32
9351	J204611-543648	311.55	-54.613	0.004	91.32	42.45	83.51	1.39	0.78	0.83	FRx	19.6	8000066473000410	0.53
9351	J204619-564007	311.58	-56.669	0.009	47.06	20.88	43.05	1.31	0.46	0.51	FRx	21.87	8000052473000710	0.41
9325	J204619-600138	311.58	-60.027	0.024	102.99	58.31	102.99	0.77	0.55	0.58	FRx	20.76	8000052473000710	0.41
9325	J204624-592218	311.6	-59.372	0.02	65.54	31.3	58.89	0.46	0.51	0.56	FRx	23.2	8000052473000710	0.41
9325	J204626-603716	311.61	-60.621	0.009	87.96	31.3	62.98	0.66	0.51	0.56	FRx	19.1	8000052473000710	0.41
9351	J204629-542953	311.62	-54.498	0.036	69.44	50.99	55.46	0.5	0.56	0.59	single	16.27	8000043506000030	0.18
9325	J204630-624839	311.63	-62.811	0.086	91.57	42.45	89	2.44	0.31	0.32	FRx	18.8	8000062201002550	0.44
9351	J204631-555130	311.63	-55.858	0.003	134.72	17.43	134.72	1.47	0.31	0.32	FRx	22.85	8000037296001830	0.98
9410	J204633-621411	311.64	-62.236	0.003	59.78	17.43	59.78	2.9	0.28	0.30	FRx	16.73	8000058056000230	0.15
9351	J204634-555509	311.64	-55.919	0.014	73.88	38.47	64.5	0.52	0.57	0.62	FRx	20.1	8000038637003340	0.47
9325	J204635-604343	311.65	-60.729	0.012	120.68	86.56	110.6	0.69	0.77	0.80	FRx	19.21	8000042794003770	1.01
9325	J204636-575936	311.65	-57.993	0.006	52.43	18.87	40.63	2.59	0.44	0.49	FRx	22.93	8000042794003770	1.01
9287	J204638-513525	311.66	-51.59	0.003	55.77	18.94	55.77	2.21	0.33	0.36	FRx	23.51	8000072665000760	0.32
9287	J204641-532241	311.67	-53.378	0.166	79.96	28.64	73.98	0.95	0.37	0.40	FRx	19.6	8000066473000410	0.53
9351	J204643-531027	311.68	-53.174	0.005	91.29	56.32	91.29	1.19	0.60	0.63	FRx	20.76	8000066473000410	0.53
9325	J204645-584832	311.69	-58.809	0.001	55.3	34.31	55.3	0.59	0.59	0.65	FRx	23.2	8000052473000710	0.41
9325	J204646-573440	311.69	-57.578	0.004	105.38	30.68	105.38	2.89	0.28	0.30	FRx	19.1	8000052473000710	0.41

Continued on next page

Table 4.2 – Continued from previous page

SBID	Source Name	RA (J2000) (deg)	DEC (J2000) (deg)	Flux Density (Jy)	Size (")	a (")	b (")	PA (°)	a/b _{max}	a/b _{min}	Class	Mag (r-band)	DESI ID	Z
9325	J204648-590704	311.7	-59.118	0.005	107.84	67.09	107.84	1.28	0.61	0.64	FR II	19.3		
9325	J204649-613903	311.71	-61.651	0.009	126.48	87.68	108.87	0.8	0.79	0.82	FR II	20.5	8000040001006320	0.44
9287	J204650-531716	311.71	-53.288	0.006	81.06	41.18	81.06	0.5	0.49	0.52	FRx	21.14	8000066473001690	0.62
9351	J204652-551940	311.72	-55.328	0.014	80.04	36	80.04	1.59	0.44	0.46	FRI	20.92	8000059699000750	0.48
9351	J204700-541245	311.75	-54.213	0.067	75.99	39.43	75.99	1.16	0.50	0.54	FR II	19.35	8000063044003470	
9351	J204710-561204	311.79	-56.201	0.009	77.77	32.25	77.77	2.64	0.40	0.43	FRI	19.71	8000056436002900	0.39
9325	J204712-572706	311.8	-57.452	0.013	58.3	27.29	58.3	2.37	0.45	0.49	FRI	26.95		
9351	J204713-534747	311.81	-53.796	0.003	82.1		82.1	2.15			single	19.45	8000064749001420	0.41
9325	J204714-585415	311.81	-58.904	0.002	55.3		55.3	2.08			single	19.69		
9287	J204714-512649	311.81	-51.447	0.031	92.87	50.36	92.87	3.07	0.53	0.56	FR II	22.52	8000072665003740	0.87
9287	J204715-491754	311.81	-49.298	0.002	86.2	35	86.2		0.39	0.42	FRI	23.34	8000080977001670	
9325	J204715-615310	311.82	-61.886	0.012	96.06	48.02	96.06	2.98	0.49	0.51	FRx	16.53	8000039316005800	0.12
9325	J204718-592324	311.83	-59.39	0.032	57.96	25.46	52.35	2.41	0.46	0.51	FRx	22.97	8000046409004270	
9325	J204718-592236	311.83	-59.377	0.002	73.1	26.69	73.1	1.24	0.35	0.38	FRI	16.83	8000046409004500	0.13
9351	J204718-570009	311.83	-57.003	0.024	189.98	149.04	176.21	2.43	0.83	0.86	FR II	22.66		
9351	J204731-553453	311.88	-55.581	0.01	187.58	136.39	187.58	1.16	0.72	0.74	FR II	20.92	8000058876000250	0.51
9287	J204736-521538	311.9	-52.261	0.002	74.81	34.54	74.81	0.32	0.45	0.48	FRI	17.44	8000069983002320	0.23
9410	J204736-613820	311.9	-61.639	0.012	111.33	60.5	111.33	0.25	0.53	0.56	FR II	17.76	8000040002006450	0.3
9287	J204736-505855	311.9	-50.982	0.002	62.07	23.83	62.07	0.28	0.37	0.40	FRI	25.85	8000074478003340	
9351	J204745-524526	311.94	-52.757	0.004	52.11		52.11	1.08	0.66	0.70	single	21.38	8000068219001700	0.76
9325	J204756-610336	311.99	-61.06	0.003	100.34	68.01	100.34	2.74	0.66	0.70	FR II	22.96	8000042088001540	0.76
9287	J204756-503052	311.99	-50.514	0.005	127.94	86.19	127.94	2.97	0.66	0.69	FR II	20.12		
9410	J204756-603647	311.99	-60.613	0.021	70.49		70.49	2.66			single	18.05	8000043507000010	0.26
9287	J204800-493414	312	-49.571	0.004	63.28	26.31	63.28	0.18	0.40	0.43	FRI	22.04		
9325	J204806-572542	312.03	-57.428	0.015	48.85		37.08	0.72	0.60	0.62	single	20.52		
9351	J204810-562002	312.05	-56.334	0.004	115.64	70.55	115.64	2.4	0.60	0.62	FR II	21.32	8000056436000920	0.7
9410	J204812-590441	312.05	-59.078	0.001	44.1		44.1				single			
9325	J204813-572330	312.06	-57.392	0.005	127.09	62.72	127.09	2.54	0.48	0.50	FRx	18.03	8000052474003390	0.24
9325	J204824-573811	312.1	-57.637	0.004	44.11		35.79	2.57			single	23.27	8000051697003270	
9410	J204825-610303	312.11	-61.051	0.008	87.93		81.21	2.47			single	18.85	8000042088001730	0.29
9410	J204827-592606	312.11	-59.435	0.523	56.11		56.91	2.61			single	20.03		
9325	J204836-583537	312.15	-58.594	0.126	59.55	24.33	57.15	1.44	0.41	0.45	FRI	22.14	8000049399000440	
9287	J204837-491009	312.15	-49.169	0.041	328.72	174.24	328.72	1.66	0.53	0.53	FR II	15.96	8000080978003860	0.11
9351	J204837-544802	312.16	-54.801	0.01	75.38	28.64	61.78	2.58	0.45	0.48	FRI	19.26	8000061363001200	0.41
9325	J204842-610553	312.18	-61.098	0.005	109.2	56.95	78.26	1.88	0.71	0.75	FR II	20.69	8000042088000670	0.53
9410	J204842-592014	312.18	-59.337	0.002	60.29		60.29	2.64			single	19.79	8000047149000910	0.42
9325	J204845-614000	312.19	-61.667	0.005	69.29		69.29	2.15			single	21.21	8000040002005860	0.68
9351	J204848-551104	312.21	-55.184	0.004	55.41	20.4	40.86	2.94	0.47	0.53	FRx	20.6	8000059700002930	0.45
9287	J204854-502700	312.23	-50.45	0.104	86.93	42.19	86.93	3.08	0.47	0.50	FRI	20.5		

Continued on next page

Table 4.2 – Continued from previous page

SBID	Source Name	RA (J2000) (deg)	DEC (J2000) (deg)	Flux Density (Jy)	Size (")	a (")	b (")	PA (°)	a/b_{\max}	a/b_{\min}	Class	Mag (r-band)	DESI ID	Z
9325	J204855-603403	312.23	-60.568	0.087	137.93	92.2	126.09	2.44	0.72	0.75	FR II	21.74	8000043507001100	0.98
9287	J204857-524445	312.24	-52.746	0.004	87.77	28.41	87.77	0.08	0.31	0.33	FR I	17.4	8000068219001940	
9410	J204909-584548	312.29	-58.763	0.004	57.77	57.77	57.77	0.48			single	18.99		
9325	J204910-582529	312.29	-58.425	0.001	55.88	26.88	55.88	2.43	0.46	0.50	FRx	18.89	8000049399002870	0.27
9410	J204911-621839	312.3	-62.311	0.004	62.89	28.41	62.89	0.16	0.43	0.47	FR I	18.79	8000038638001610	0.35
9287	J204919-511853	312.33	-51.315	0.008	50.25	43.45	43.45	0.92			single	24.23	8000073570001230	
9351	J204921-543419	312.34	-54.572	0.008	60.59	25.06	60.59	0.67	0.40	0.43	FR I	19.96	8000062202001180	0.56
9351	J204921-543144	312.34	-54.529	0.005	156.99	80.08	149.11	0.49	0.53	0.55	FR II	15.61	8000054836003000	0.14
9410	J204923-613021	312.35	-61.506	0.006	43.3	35.3	35.3	2.22			single	17.94	8000040692003620	0.24
9325	J204923-580524	312.35	-58.09	0.007	65.76	43.18	43.18	2.58			single	19.74	8000050926000520	0.42
9410	J204929-623446	312.37	-62.579	0.213	52.41	18	56.1	2.06	0.31	0.34	FR I	22.7	8000037965001130	0.99
9325	J204932-574618	312.39	-57.772	0.025	42.96	13.9	40.24	1.49	0.33	0.37	FR I	18.2	8000066475000980	0.3
9351	J204933-533243	312.39	-53.545	0.002	69.63	29.84	69.63	0.42	0.41	0.44	FR I	18.57	8000065610001330	0.56
9410	J204934-620821	312.4	-62.139	0.002	66.81	28.8	66.81	1.75	0.42	0.45	FR I	20.18	8000038638005960	0.23
9410	J204935-621132	312.4	-62.192	0.011	115.63	73.78	95.07	2.54	0.76	0.80	FR II	18.7	8000038638004860	1.05
9287	J204937-492551	312.4	-49.431	0.002	44.89	18.96	44.89	0.5	0.40	0.45	FR I	21.78	8000080035004380	0.37
9287	J204937-501151	312.41	-50.198	0.004	133.41	41.01	133.41	0.82	0.30	0.31	FR I	18.84	800007235004180	0.37
9351	J204940-550731	312.42	-55.125	0.009	62.92	20.73	47.95	2.64	0.41	0.46	FR I	20.87	8000059701004380	0.36
9325	J204940-601052	312.42	-60.181	0.002	56.83	22.09	56.83	0.07	0.37	0.41	FR I	23.53		
9351	J204941-543243	312.43	-54.545	0.002	60.59	60.59	60.59	0.44			single	19.17	8000062202001640	0.35
9410	J204945-612137	312.44	-61.36	0.001	53.58	53.58	53.58	1.26			single	19.06		
9351	J204946-530520	312.44	-53.089	0.004	52.25	52.25	52.25	1.04			single	19.21	8000041388000490	0.39
9410	J204956-605951	312.49	-60.998	0.008	60.73	17.4	60.73	2.88	0.28	0.30	FR I	23.95		
9351	J204957-571638	312.49	-57.277	0.003	54.36	25.06	48.65	2.64	0.49	0.54	FRx	23.31		
9287	J204959-482219	312.5	-48.372	0.011	63.41	31.19	63.41	1.65	0.47	0.51	FRx	18.4	8000053256001500	0.34
9325	J205003-623210	312.52	-62.536	0.003	106.27	69.31	96.67	0.75	0.70	0.74	FR II	19.86		
9287	J205004-503932	312.52	-50.659	0.054	47.9	47.9	47.9	1.89			single	21.85	8000037965002250	0.74
9287	J205005-513504	312.52	-51.584	0.002	55.43	50.59	50.59	0			single	23.92	800007593004250	0.46
9325	J205010-583952	312.54	-58.664	0.02	64.98	64.98	64.98	0.55			single	19.6	8000072667000850	0.77
9325	J205013-580928	312.55	-58.664	0.002	81.18	64.8	64.8	0.63			single	21.92	8000048645003200	
9287	J205013-522207	312.56	-52.369	0.004	65.76	65.76	65.76	2.28	0.70	0.72	FR II	20.63		
9410	J205015-624128	312.57	-62.691	0.01	193.41	136.56	193.41	0.65	0.41	0.43	FR I	24.73	8000037298004770	0.47
9287	J205015-523724	312.57	-52.623	0.022	99.6	41.87	99.6	0.06	0.41	0.43	FR I	19.55	8000069100000130	0.71
9287	J205018-523350	312.58	-52.564	0.003	53.75	13.37	47.92	1.28	0.27	0.29	FR I	22.01	80000691000001400	0.26
9351	J205022-541950	312.59	-54.331	0.017	53.75	53.75	53.75	0.64			single	17.46	8000063046000770	0.38
9287	J205024-524913	312.6	-52.82	0.002	70.92	70.92	70.92	2.12			single	19.41	8000068220000770	0.38

Continued on next page

Table 4.2 – Continued from previous page

SBID	Source Name	RA (J2000) (deg)	DEC (J2000) (deg)	Flux Density (Jy)	Size (")	a (")	b (")	PA (°)	a/b _{max}	a/b _{min}	Class	Mag (r-band)	DESI ID	Z
9410	J205025-605832	312.6	-60.976	0.056	121.45	80.11	115.69	0.72	0.68	0.71	FR II	17.71	8000042089003510	0.33
9287	J205026-515358	312.61	-51.899	0.03	66.75	25.3	53.91	1.81	0.45	0.49	FR I	23.95		
9287	J205027-495341	312.61	-49.895	0.007	129.68	70.67	129.68	0.94	0.53	0.56	FR II	20.51		
9410	J205028-615646	312.62	-61.946	0.026	73.96	29.73	62.24	1.43	0.46	0.50	FR I	22.4	8000039318004670	0.92
9287	J205029-522300	312.62	-52.383	0.028	61.47		50.73	0.42			single	23.1	8000069100004910	1.03
9351	J205034-541920	312.64	-54.322	0.003	78.14	23.41	78.14		0.29	0.31	FR I	20.37	8000063046000950	0.48
9287	J205043-502103	312.68	-50.351	0.008	138.66	98.85	138.66	1.36	0.70	0.73	FR II	23.8		
9351	J205048-563216	312.7	-56.538	0.015	67.16	26.83	51.84	1.99	0.49	0.54	FRx	21.27	8000055635001250	0.75
9410	J205049-594554	312.7	-59.765	0.008	149.52	100.51	131.88	2.08	0.75	0.78	FR II	16.89		
9325	J205050-594856	312.71	-59.816	0.002	59.43		59.43	2.7	0.46	0.53	single	17.2	8000045678001390	0.15
9351	J205051-554914	312.72	-55.821	0.004	44.01	18	36.52	1.62	0.46	0.44	FRx	22.81	8000058059000740	0.59
9287	J205054-523152	312.73	-52.531	0.011	53.75	22.8	53.75	2.69	0.41	0.44	FR I	17.24	8000069100002160	0.21
9325	J205058-594736	312.74	-59.793	0.006	59.43		59.43	1.9			single	17.33	8000045678001890	0.42
9410	J205106-600421	312.78	-60.073	0.01	45.79		39.33	0.01			single	19.71	8000044949001280	0.46
9287	J205109-502657	312.79	-50.449	0.01	218.17	81.72	218.17	2.53	0.37	0.38	FR I	18.98	8000076313003540	0.46
9287	J205110-505049	312.8	-50.847	0.024	53.27	23.41	52.17	2.94	0.43	0.47	FR I	23.14		
9287	J205112-523700	312.8	-52.617	0.009	71.18	32	71.18	0.07	0.43	0.40	FR I	17.05		
9351	J205116-534146	312.82	-53.696	0.323	60.06		56.85	1.53	0.37	0.40	FR I	22.12	8000064751002780	0.82
9351	J205121-534331	312.84	-53.725	0.049	174.26	98.53	174.26	1.17	0.56	0.57	FR II	15.78		
9351	J205124-571023	312.85	-57.173	0.013	132.35	75.43	97.05	2.75	0.76	0.80	FR II	21.84	8000053257003430	0.86
9287	J205126-485430	312.86	-48.908	0.003	91.3	52.48	91.3	3.14	0.56	0.59	FR II	18.29	8000081927004730	0.34
9287	J205127-515157	312.86	-51.866	0.002	62.66	25.31	62.66	0.83	0.39	0.42	FR I	20.42		
9410	J205128-610050	312.87	-61.014	0.003	105.12	78.25	105.12	0.03	0.73	0.76	FR II	24.23	80000420900002910	0.87
9410	J205131-592223	312.88	-59.373	0.065	47.2		45.9	0.14			single	22.96	8000047151000070	0.92
9351	J205132-582200	312.88	-58.367	0.002	80.24	34.41	80.24	2.54	0.42	0.44	FR I	19.77	8000050162000190	0.42
9410	J205133-585628	312.89	-58.941	0.005	57.77	21.58	57.77	1.42	0.36	0.39	FR I	22.03		
9287	J205133-491553	312.89	-49.265	0.002	66.73	19.68	66.73	1.59	0.28	0.31	FR I	20.34		
9351	J205133-575154	312.89	-57.865	0.009	179.83	130.75	179.83	1.21	0.72	0.74	FR II	20.78	8000050927003520	0.47
9287	J205141-485656	312.92	-48.949	0.238	62.3	26.08	61.75	1.35	0.41	0.44	FR I	19.17	8000081928003900	0.33
9325	J205141-580535	312.92	-58.093	0.005	71.94		71.94	0.47			single	20.22	8000050927000420	0.77
9351	J205145-535255	312.94	-53.882	0.048	52.07	18.44	48.39	0.74	0.36	0.40	FR I	22.37	8000063896004120	0.52
9351	J205146-532324	312.94	-53.39	0.01	73.24	31.3	73.24	0.46	0.41	0.44	FR I	19.68	8000065611004350	0.52
9325	J205154-622522	312.97	-62.423	0.004	120.83	82.15	120.83	3.02	0.67	0.69	FR II	23.35		
9287	J205155-524357	312.98	-52.733	0.164	310.44	176.09	310.44	1.35	0.56	0.57	FR II	13.76	8000068221001900	0.04
9287	J205200-504924	313	-50.823	0.005	50.3	18	36.92	1.55	0.46	0.52	FRx	21.76	8000075394000960	0.63
9410	J205201-620310	313.01	-62.053	0.005	104.32	53.5	104.32	2.06	0.50	0.53	FR II	21.14	8000039319001870	0.78
9351	J205203-551219	313.02	-55.205	0.005	57.63	26.31	57.63	2.94	0.44	0.48	FR I	22	8000059702002730	0.78
9410	J205207-605600	313.03	-60.933	0.005	167.85	135.88	167.85	1.04	0.80	0.82	FR II	23.51		
9410	J205209-620943	313.04	-62.162	0.004	67.88	32.61	67.88	2.06	0.46	0.50	FR I	19.84	8000038640005430	0.47

Continued on next page

Table 4.2 – Continued from previous page

SBID	Source Name	RA (J2000) (deg)	DEC (J2000) (deg)	Flux Density (Jy)	Size (")	a (")	b (")	PA (°)	a/b_{\max}	a/b_{\min}	Class	Mag (r-band)	DESIID	Z
9287	J205209-514223	313.04	-51.706	0.034	107.49	62.31	94.86	2.36	0.64	0.67	FRII	16.07	8000071769003200	0.12
9410	J205212-603509	313.05	-60.586	0.014	58.41	26	50.03	1.52	0.49	0.55	FRx	22.56	8000043509000940	0.99
9325	J205212-623158	313.05	-62.533	0.012	103.83	52.84	93.24	2.06	0.55	0.58	FRII	22.04	8000037966002770	0.38
9287	J205217-481316	313.07	-48.221	0.064	329.57	269.91	329.57		0.81	0.83	FRII	19.67	8000084798003790	0.38
9325	J205217-574626	313.07	-57.774	0.01	66.22	28.64	55.79	0.44	0.49	0.54	FRx	26.48		
9351	J205217-564257	313.07	-56.716	0.009	46.58	40.62	40.62	1.91	0.34	0.39	single	18.58	8000054838002050	0.35
9325	J205219-600533	313.08	-60.093	0.009	45.99	14.14	38.66	1.66	0.34	0.39	FRI	23.98		
9351	J205222-532652	313.09	-53.448	0.017	45.56	40.44	40.44	0.08	0.41	0.44	single	23.48	8000065611003160	
9351	J205223-540703	313.1	-54.118	0.002	64.07	27.03	64.07	0.14	0.41	0.44	FRI	22.04	8000063897000150	0.91
9410	J205226-584311	313.11	-58.72	0.002	54.58	26.03	54.58	2.85	0.46	0.50	FRI	21.45	8000048646002450	0.73
9351	J205230-555525	313.13	-55.924	0.003	104.81	104.81	104.81	2.81	0.31	0.33	single	14.26	8000057246002510	0.05
9351	J205232-551329	313.13	-55.862	0.028	93.15	26.31	82.04	1.8	0.31	0.33	FRI	18.05	8000058060000210	0.27
9351	J205232-551329	313.14	-55.225	0.009	81.95	46.18	71.48	2.83	0.62	0.67	FRII	21.47	8000059702002440	0.93
9287	J205237-491847	313.16	-49.313	0.003	62.14	20.11	62.14	1.12	0.31	0.34	FRI	23.78		
9351	J205241-550604	313.17	-55.101	0.001	47.64	43.19	43.19	1.92	0.61	0.64	single	22.69	8000060532000430	0.9
9325	J205243-611704	313.18	-61.284	0.141	118	65.6	104.34	2.5	0.61	0.64	FRII	18.77	8000041389002550	0.3
9351	J205243-545334	313.18	-54.893	0.047	105.62	52.06	84.54	1.81	0.60	0.63	FRII	22.77	8000060532003620	0.94
9287	J205243-504225	313.18	-50.707	0.003	68.21	68.21	68.21	0.51	0.45	0.48	single	20.69		
9351	J205243-524106	313.18	-52.685	0.004	92.9	92.9	92.9	0.65	0.45	0.48	single	14.65	8000068222003330	0.04
9351	J205244-565739	313.19	-56.961	0.043	69.86	28.84	62.25	0.93	0.45	0.48	FRI	16.71	8000054045002370	0.55
9325	J205249-620255	313.21	-62.049	0.015	76.06	51.59	51.59	1.97	0.49	0.52	single	20.54	8000039319002020	0.33
9287	J205252-514737	313.22	-51.794	0.092	123.77	50.99	100.99	0.69	0.49	0.52	FRx	19.39	8000071769001470	0.54
9287	J205253-511652	313.22	-51.281	0.052	210.63	159.7	191.38	1.17	0.82	0.85	FRII	21.21	8000073572001620	0.79
9410	J205253-620446	313.22	-62.079	0.032	52.12	43.58	43.58	2.39	0.45	0.48	single	23	8000039319001200	0.79
9442	J205255-572435	313.23	-57.41	0.003	75.05	75.05	75.05	3.12	0.53	0.58	single	23.86	8000052476003210	
9351	J205302-562918	313.26	-56.488	0.017	55.1	28.43	51.29	2.4	0.53	0.58	FRII	25.61		
9410	J205303-591828	313.26	-59.308	0.002	78.84	28.5	78.84	1.5	0.35	0.37	FRI	19.67	8000047151001330	0.41
9410	J205304-623632	313.27	-62.609	0.005	97.07	46.78	97.07	0.73	0.47	0.49	FRI	18.5	8000037967000240	0.13
9351	J205306-552450	313.28	-55.414	0.015	99.43	46.97	99.43	0.61	0.46	0.48	FRI	20.68	8000058879003350	0.52
9325	J205308-612349	313.29	-61.397	0.154	89.13	45.69	87.66	0.38	0.51	0.54	FRII	19.12		
9287	J205309-513106	313.29	-51.518	0.007	87.35	33.11	87.35	1.09	0.37	0.39	FRI	20.95	8000072669001880	0.73
9287	J205310-505213	313.29	-50.87	0.083	59.82	26.83	60.4	2.52	0.43	0.46	FRI	19.53	8000075395000110	0.39
9442	J205312-571042	313.3	-57.179	0.001	56.68	29.85	56.68	1.99	0.50	0.55	FRII	23	8000053258003340	0.86
9287	J205312-514341	313.3	-51.728	0.041	238.7	196.32	238.7	0.26	0.81	0.83	FRII	23.02	8000042798006630	1.04
9410	J205318-603822	313.33	-60.639	0.011	39.57	16.12	42.26	1.92	0.36	0.41	FRI	22.26		
9287	J205325-533313	313.36	-53.554	0.02	56.21	43.93	43.93	0.56	0.70	0.74	single	20		
9287	J205331-485007	313.38	-48.835	0.018	108.12	65.12	90.41	1.37	0.70	0.74	FRII	19.99	8000080038003840	0.49
9410	J205331-621346	313.38	-62.229	0.044	85.45	50.48	80.37	0.96	0.61	0.65	FRII			
9287	J205332-492728	313.39	-49.458	0.016	178.03	102.73	178.03	0.58	0.57	0.59	FRII			

Continued on next page

Table 4.2 – Continued from previous page

SBID	Source Name	RA (J2000) (deg)	DEC (J2000) (deg)	Flux Density (Jy)	Size (")	a (")	b (")	PA (°)	a/b _{max}	a/b _{min}	Class	Mag (r-band)	DESI ID	Z
9325	J205333-574022	313.39	-57.673	0.006	252.32	201.47	252.32	1.95	0.79	0.81	FR II	18.38	8000051700002790	
9442	J205335-555426	313.4	-55.907	0.003	44.02		32.8	2.76			single	22.56		
9410	J205337-621529	313.41	-62.258	0.027	52.7		52.7	1.43			single	15.62		
9287	J205338-502722	313.41	-50.456	0.01	113.67	62.1	92.91	2.71	0.65	0.69	FR II	23.93		
9287	J205339-504105	313.42	-50.685	0.011	104.66	64.14	88.72	1.6	0.70	0.74	FR II	20.36	8000075395003340	0.62
9287	J205344-501042	313.43	-50.178	0.006	53.84		40.86	0.89			single	26.09		
9410	J205344-621517	313.43	-62.255	0.033	99.76	59.27	99.76	2.83	0.58	0.61	FR II	17.57	8000038640002820	0.31
9287	J205344-500552	313.44	-50.098	0.011	64.31		64.31	1.93			single	23.14		
9442	J205346-575219	313.44	-57.872	0.051	161.15	107.7	140.81	2.59	0.75	0.78	FR II	20.4	8000051700000140	0.34
9410	J205350-585323	313.46	-58.89	0.001	71.08	42.78	71.08	2.63	0.58	0.62	FR II	20.23	8000047897003290	0.33
9325	J205351-585025	313.47	-58.84	0.02	267.48	207.12	234.67	0.17	0.87	0.89	FR II	18.91	8000048646000730	0.41
9287	J205357-492830	313.49	-49.475	0.003	59.88		59.88	0.22			single	21.81	8000080038003410	0.65
9351	J205358-544507	313.49	-54.752	0.004	71.18		43.48	1.08			single	17.71	8000061366001690	0.17
9287	J205359-502758	313.5	-50.466	0.002	56.92		56.92	0.44			single	24.06	8000076315002780	
9287	J205400-500155	313.5	-50.032	0.009	90.09	49.59	90.09	2.5	0.54	0.57	FR II	19.1	8000078167002030	0.32
9351	J205402-565450	313.51	-56.914	0.048	74.14	28	65.4	0.03	0.41	0.45	FRI	21.8	8000054046003180	0.71
9287	J205416-494638	313.57	-49.777	0.003	78.02	38.72	78.02	1.79	0.48	0.51	FRx	20.48	8000079101002020	0.57
9287	J205418-495836	313.58	-49.977	0.004	94.11	37.28	94.11	0.77	0.39	0.41	FRI	19.06	8000078168002950	0.3
9442	J205421-572908	313.59	-57.486	0.005	66.63	35.06	66.63	0.07	0.51	0.55	FR II	18.14		
9442	J205422-573608	313.6	-57.602	0.001	39.44	16.1	39.44		0.38	0.44	FRI	22.68	8000052477000360	0.97
9287	J205428-503227	313.62	-50.541	0.005	241.33	194.01	241.33	0.34	0.80	0.81	FR II	24.93		
9287	J205428-521823	313.62	-52.306	0.015	205.26	161.62	183.43	2.29	0.87	0.89	FR II	23.36		
9325	J205431-601046	313.63	-60.179	0.021	66.57	22.09	55.13	3.03	0.38	0.42	FRI	20.79	8000044227004870	0.53
9351	J205431-550841	313.63	-55.145	0.004	73.8	28.54	73.8	2.35	0.37	0.40	FRI	21.85	8000059703003600	0.79
9442	J205433-570606	313.64	-57.102	0.004	46.13	15.62	35.16	2.21	0.41	0.48	FRI			
9287	J205436-490451	313.65	-49.081	0.009	119.76	82.61	104.89	1.68	0.77	0.81	FR II	28.11		
9325	J205437-592947	313.65	-59.496	0.011	59.43		59.43	1.19			single	19.3		
9410	J205444-603414	313.69	-60.571	0.01	78.79	51.99	78.79	1.15	0.64	0.68	FR II	19.66	8000043510001510	0.43
9442	J205447-580122	313.7	-58.023	0.006	97.87	48.17	97.87	1.9	0.48	0.51	FRx	20.24		
9442	J205450-543935	313.71	-54.66	0.372	63.27		59.07	0.18			single	18.75		
9410	J205450-623511	313.71	-62.586	0.002	52.41		52.41	1.64			single	19.26	8000037968000810	0.3
9351	J205453-530220	313.72	-53.039	0.017	63.87		47.22	0.84			single	19.54	8000067348001560	0.51
9351	J205455-572344	313.73	-57.396	0.006	78.51		78.51	1.38			single	21.84	8000052478003070	0.83
9325	J205458-604815	313.74	-60.804	0.003	147.99	109.39	147.99	0.33	0.73	0.75	FR II	19.43	8000042799002180	
9287	J205500-511029	313.75	-51.175	0.002	90.2	53.21	90.2	0.25	0.57	0.61	FR II	21.08	8000073573003360	0.72
9325	J205503-621918	313.76	-62.322	0.017	64	24.74	52.17	2.33	0.45	0.50	FRI	22.07	8000038641001460	0.91
9325	J205513-601310	313.81	-60.219	0.006	56.52	22.99	56.52	2.36	0.39	0.43	FRI	20.57	8000044227003880	0.9
9325	J205520-584420	313.84	-58.739	0.007	38.44		35.59	2.3			single			
9287	J205521-495134	313.84	-49.859	0.001	55.19	15.2	55.19	3.13	0.26	0.29	FRI	20.75	8000079102000340	0.4

Continued on next page

Table 4.2 – Continued from previous page

SBID	Source Name	RA (J2000) (deg)	DEC (J2000) (deg)	Flux Density (Jy)	Size (")	a (")	b (")	PA (°)	a/b_{\max}	a/b_{\min}	Class	Mag (r-band)	DESID	Z
9442	J205526-580517	313.86	-58.088	0.017	65.41	27.2	57.32	0.27	0.45	0.50	FRI	18.91	8000050929000560	0.3
9325	J205530-620453	313.88	-62.081	0.006	117.27	80.62	117.27	1.32	0.67	0.70	FRII	19.97	8000039320001080	0.38
9442	J205532-562321	313.89	-56.389	0.007	44.05	37.77	37.77	2.63	0.67	0.69	single	22.32		
9351	J205548-545621	313.95	-54.939	0.161	253.11	172.36	254.09	0.43	0.67	0.69	FRII	17.02	8000060533002480	0.13
9351	J205549-582735	313.95	-58.46	0.174	110.74	46.77	100.63	2.01	0.45	0.48	FRI	18.79	8000049403002500	0.29
9287	J205552-492933	313.97	-49.493	0.005	179.58	125.59	179.58	0.76	0.69	0.71	FRII	24.3		
9325	J205553-591325	313.97	-59.224	0.004	62.27	62.27	62.27	0.74	0.45	0.49	single	20.95	8000047153003100	0.72
9325	J205557-601310	313.99	-60.219	0.006	71.2	26.31	56.02	1.45	0.45	0.49	FRI	22.75	8000044228004050	0.98
9442	J205558-552650	313.99	-55.447	0.069	58.55	27.2	56.1	2	0.46	0.51	FRx	18.74		
9325	J205605-621839	314.02	-62.311	0.064	93.89	40.5	93.89	0.72	0.42	0.44	FRI	18.27	8000038641001660	0.39
9287	J205610-513537	314.04	-51.594	0.009	105.28	45.7	85.21	0.45	0.52	0.55	FRII	20.94		
9442	J205616-570251	314.07	-57.048	0.024	64.96	34.06	59.99	2.29	0.55	0.59	FRII	24.06		
9351	J205617-565200	314.07	-56.867	0.004	104.88	58.5	78.72	0.43	0.72	0.77	FRII	22.84	8000054840000130	0.94
9351	J205619-524215	314.08	-52.704	0.008	62.99	41.32	41.32	2.56	0.62	0.68	single	20.26	8000068224003240	0.39
9325	J205622-601811	314.09	-60.303	0.005	78.24	36.51	56.18	2.5	0.62	0.68	FRII	21.15	8000044228002000	0.72
9287	J205623-513229	314.1	-51.541	0.012	157.85	119.28	140.32	2.55	0.84	0.87	FRII	24.12		
9325	J205624-591724	314.1	-59.29	0.005	72.77	72.77	72.77	2.81			single			
9287	J205626-500834	314.11	-50.143	0.001	61.84	61.84	61.84				single	20.75	8000077240003890	0.61
9410	J205630-630444	314.13	-63.079	0.057	75.44	28.07	71.59	1.44	0.38	0.41	FRI	17.64	8000036638000880	0.23
9287	J205631-482151	314.13	-48.364	0.035	463.03	400.3	463.03	0.07	0.86	0.87	FRII	19.04	8000084801000340	0.34
9442	J205634-533606	314.14	-53.602	0.075	55.07	57.81	57.81	2.48	0.51	0.54	single	22.2	8000065614000430	0.95
9351	J205634-530944	314.14	-53.162	0.065	88.62	42.07	80.25	2.43	0.51	0.54	FRII	18.36	8000066479003730	0.3
9287	J205640-522926	314.17	-52.491	0.013	68.02	47.71	47.71	1.67	0.37	0.40	single	22.89		
9351	J205644-532733	314.18	-53.459	0.003	54.92	21.16	54.92	2.27	0.37	0.40	FRI	22.48	8000065614002830	0.86
9351	J205646-534809	314.19	-53.803	0.002	74.25	38.39	74.25	2.6	0.50	0.54	FRII	17.48		
9287	J205648-492907	314.2	-49.485	0.006	64.55	22.8	64.55	0.62	0.34	0.37	FRI	22.73		
9351	J205649-551407	314.21	-55.235	0.007	71.18	40.06	61.37	0.71	0.63	0.68	FRII	20.81	8000059705001910	0.69
9410	J205652-595229	314.22	-59.875	0.003	97.33	97.33	97.33	1.02	0.63	0.68	single	20.16	8000045681000030	0.43
9287	J205656-484629	314.24	-48.775	0.021	180.12	130.77	158.96	2.04	0.81	0.84	FRII			
9410	J205657-620523	314.24	-62.09	0.003	76.07	76.07	76.07	3.11	0.46	0.50	single	19.94	8000039321000820	0.57
9325	J205704-605804	314.27	-60.968	0.109	82.42	34.23	71.55	1.48	0.46	0.50	FRI	18.33		
9410	J205706-622712	314.28	-62.453	0.039	92.36	50.99	79.21	1.36	0.62	0.66	FRII	24.03		
9287	J205714-481418	314.31	-48.238	0.011	88.14	88.14	88.14				single			
9287	J205726-521814	314.36	-52.304	0.14	84.18	24.21	75.45	0.92	0.31	0.33	FRI	19.58		
9287	J205728-491644	314.37	-49.279	0.014	104.34	66.57	89.31	2.11	0.73	0.77	FRII	26.28		
9410	J205728-590514	314.37	-59.087	0.025	195.63	147	173.71	0.59	0.83	0.86	FRII	23	8000047899000650	1.1
9351	J205730-523742	314.38	-52.645	0.028	87.08	34.93	87.08	0.08	0.39	0.41	FRI	20.67	8000068224004250	0.7
9410	J205734-602937	314.39	-60.494	0.002	101.55	101.55	101.55	0.2	0.77	0.80	single	19.73	8000043511004120	0.45
9287	J205734-532523	314.39	-53.39	0.015	141.5	95.47	122.26	0.9	0.77	0.80	FRII	20.3		

Continued on next page

Table 4.2 – Continued from previous page

SBID	Source Name	RA (J2000) (deg)	DEC (J2000) (deg)	Flux Density (Jy)	Size (")	a (")	b (")	PA (°)	a/b _{max}	a/b _{min}	Class	Mag (r-band)	DESI ID	Z
9287	J205735-505309	314.4	-50.886	0.079	130.7	85.44	117.49	1.87	0.71	0.74	FRII	23.24		
9287	J205737-515911	314.41	-51.986	0.017	67.53		46.23	0.99			single	17.58	8000070879002530	0.25
9442	J205737-552453	314.41	-55.415	0.007	65.07		65.07	1.68			single	20.5		
9442	J205737-571556	314.41	-57.266	0.004	57.19	21.63	57.19	2.18	0.36	0.40	FR I	23.66		
9442	J205741-551447	314.42	-55.246	0.002	55.09	22.63	55.09	1.52	0.39	0.43	FR I	19.76	8000059705001770	0.46
9287	J205746-481552	314.44	-48.264	0.387	88.14	20.33	88.14		0.22	0.24	FR I	23.02	8000084802002560	
9410	J205746-612701	314.45	-61.45	0.005	52.85	22	52.85	3.13	0.40	0.44	FR I	26.54		
9410	J205755-592308	314.48	-59.386	0.002	50.42		45.45	0.59			single	23.18		
9287	J205758-492558	314.5	-49.433	0.001	86.94	47.55	86.94	0.67	0.53	0.56	FR II	19.69	8000080041004480	0.39
9287	J205803-491407	314.51	-49.235	0.005	89.63	42.19	68.62	3.08	0.59	0.64	FR II	22.39	8000080984003300	1.04
9442	J205807-583529	314.53	-58.591	0.001	64.41		64.41	2.48			single	18.52	8000049404000400	0.35
9287	J205807-512052	314.53	-51.348	0.002	74.3	31.01	74.3	1.18	0.40	0.43	FR I	21.59	8000073575000400	0.81
9287	J205810-483749	314.54	-48.63	0.103	630.68	87.86	630.68	2.22	0.14	0.14	FR I	12.35	8000082883004900	0.01
9287	J205814-514220	314.56	-51.706	0.006	81.24	42.8	64.71	0.66	0.64	0.69	FR II	19.56		
9325	J205814-581014	314.56	-58.171	0.002	57.86	22.16	57.86	3.05	0.37	0.40	FR I	25.65		
9442	J205814-542836	314.56	-54.477	0.003	51.96		51.96	3.13			single	22.85	8000062207002050	0.38
9410	J205823-615408	314.6	-61.902	0.009	59.7	32.18	59.7	1.13	0.52	0.56	FR II	20.17		
9287	J205825-490521	314.61	-49.089	0.763	100.22	41.23	91.37	0.88	0.44	0.46	FR I	18.18		
9442	J205825-542247	314.61	-54.38	0.002	45.22		50.44	0.21			single	20.24		
9442	J205826-555021	314.61	-55.839	0.004	86.97	33.22	86.97	0.37	0.37	0.39	FR I	17.49		
9351	J205827-525205	314.62	-52.868	0.005	50.61	20	50.61	1.47	0.38	0.42	FR I	24.12		
9325	J205829-621015	314.62	-62.171	0.145	52.71	22.63	55.78	2.34	0.39	0.42	FR I	22.06	8000038643005240	1.12
9287	J205833-490247	314.64	-49.046	0.122	54.69		54.49	0.62			single	18.05	8000081932002100	0.26
9410	J205833-623110	314.64	-62.519	0.003	179.28	122.37	179.28	1.72	0.67	0.69	FR II	16.76		
9442	J205834-545605	314.64	-54.935	0.096	125.41	90.7	123.11	2.3	0.72	0.75	FR II	23.22		
9351	J205838-565523	314.66	-56.923	0.003	88.07	46.55	88.07	0.42	0.51	0.54	FR II	20.54		
9442	J205839-540942	314.66	-54.162	0.01	113.74	42.85	113.74	1.67	0.37	0.39	FR I	20.37		
9287	J205839-511127	314.67	-51.191	0.034	62.17	22.63	59.44	0.68	0.37	0.40	FR I	19.83	8000073576002500	0.51
9442	J205847-552226	314.7	-55.374	0.003	77.29		77.29	1.48			single	17.6	8000059706000000	0.24
9442	J205848-555648	314.7	-55.947	0.008	63.67		63.67	0.84			single	20.32	8000057250002430	0.33
9442	J205848-573613	314.7	-57.604	0.008	169.92	99.23	169.92	2.88	0.58	0.59	FR II	18.95	8000052480000280	0.33
9351	J205849-533306	314.7	-53.552	0.015	106.53	61.19	89.51	1.78	0.67	0.70	FR II	24.07		
9351	J205852-572312	314.72	-57.387	0.005	143.84	108.07	125.93	0.9	0.84	0.88	FR II	15.93		
9287	J205852-532502	314.72	-53.417	0.006	63.29	26	63.29	1.57	0.40	0.43	FR I	19.18	8000065615003590	0.37
9287	J205855-523208	314.73	-52.536	0.067	93.35	27.78	84.62	0.54	0.32	0.34	FR I	21.69	8000069105001780	0.76
9287	J205858-500315	314.74	-50.054	0.008	68.9		68.9	0.32			single	18.99	8000078171001440	0.34
9410	J205900-580901	314.75	-58.15	0.004	157.84	75.8	157.84	1.42	0.47	0.49	FR I	18.97	8000048649001380	0.43
9410	J205900-584732	314.75	-58.792	0.013	99.24	42.5	74.52	1.28	0.55	0.59	FR II	20.14	8000060535001230	0.23
9442	J205905-550235	314.77	-55.043	0.012	87.65	54.59	79.47	2.04	0.67	0.71	FR II	17.21		

Continued on next page

Table 4.2 – Continued from previous page

SBID	Source Name	RA (J2000) (deg)	DEC (J2000) (deg)	Flux Density (Jy)	Size (")	a (")	b (")	PA (°)	a/b_{\max}	a/b_{\min}	Class	Mag (r-band)	DESI ID	Z
9410	J205907-623537	314.78	-62.594	0.043	89.39	22.09	67.19	0.04	0.32	0.34	FRI	19.86	8000037970000900	0.51
9442	J205908-582647	314.79	-58.446	0.002	64.41	29.34	64.41	0.06	0.44	0.47	FRI	20.66	8000049405003310	0.57
9287	J205911-485403	314.8	-48.901	0.018	73.15	35.78	63.8	1.08	0.54	0.58	FRII	20.92		
9287	J205914-491534	314.81	-49.259	0.003	59.47	24.08	59.47	0.04	0.39	0.42	FRI	21.85	8000080985003050	0.85
9287	J205919-494750	314.83	-49.797	0.006	84.7	39.8	84.7	2.37	0.46	0.48	FRI	20.23	8000079104001560	0.45
9325	J205921-601010	314.84	-60.169	0.052	70.75	24.41	55.91	0.61	0.42	0.46	FRI	24.63	800004229005570	
9351	J205923-564347	314.85	-56.73	0.153	74.14	24.74	61.68	0.19	0.39	0.42	FRI	22.3		
9442	J205923-552803	314.85	-55.468	0.011	59.59	59.59	59.59	0.1	0.71	0.74	single	20.75	8000058883001770	0.69
9442	J205927-573428	314.87	-57.574	0.025	131.92	88.77	122.85	0.39	0.71	0.74	FRII	23.4		
9410	J205930-615252	314.88	-61.881	0.007	37.43	31.77	31.77	2.16	0.47	0.51	single	21.97	8000039522005840	0.78
9410	J205934-610628	314.89	-61.108	0.05	67.88	27.2	55.34	0.24	0.47	0.51	FRx	25.42		
9287	J205934-484453	314.9	-48.748	0.006	67.29	14.71	67.29	2.11	0.21	0.23	FRI	19.42	8000082884003250	0.39
9410	J205935-615706	314.9	-61.952	0.002	97.38	52.58	97.38		0.53	0.55	FRII	21.81	8000039522004260	0.84
9442	J205942-532933	314.93	-53.493	0.001	75.17	75.17	75.17	1.5	0.38	0.42	single	19.38	8000065616002030	
9410	J205943-623829	314.93	-62.641	0.033	76.85	26.08	50.45	2.62	0.49	0.54	FRx	25.38		
9442	J205950-574353	314.96	-57.731	0.001	150.75	123.85	150.75	0.72	0.81	0.84	FRII	19.87		
9325	J205950-612351	314.96	-61.398	0.003	57.48	27.78	44.43	2.13	0.59	0.66	FRII	25.87	8000040697006030	0.81
9410	J205952-595142	314.97	-59.862	0.007	45.64	18.11	45.64	1.98	0.38	0.42	FRI	21.99	8000045682000370	
9287	J205952-484346	314.97	-48.729	0.01	117.83	77.67	104.4	0.94	0.73	0.76	FRII	23.74		
9410	J205956-600256	314.98	-60.049	0.014	238.41	192.11	214.26	0.87	0.89	0.91	FRII	21.94	8000044953001980	0.94
9325	J205956-613942	314.98	-61.662	0.01	68.94	24.74	53.15	2.85	0.44	0.49	FRI	24.31		
9325	J210002-594843	315.01	-59.812	0.104	433.4	352.46	433.4	2.21	0.81	0.82	FRII	20.53	8000045682001330	0.65
9442	J210002-574804	315.01	-57.801	0.009	80.73	40.65	65.95	2.8	0.59	0.64	FRII	18.04	8000051703001120	0.24
9410	J210004-604101	315.02	-60.684	0.021	39.29	38.52	38.52	0.21	0.59	0.64	single	20.3	8000042801005740	
9410	J210008-611548	315.03	-61.263	0.011	42.88	35.28	35.28	1.18	0.53	0.56	single	20.56	8000041393003050	
9287	J210008-520133	315.03	-52.026	0.001	80.65	43.85	80.65	0.46	0.53	0.56	FRII	17.54		
9325	J210009-601416	315.04	-60.238	0.002	74.4	32.57	74.4	0.48	0.42	0.45	FRI	19.29	8000044230003590	0.45
9442	J210009-551558	315.04	-55.266	0.013	192.58	144.13	144.13	3.02	0.76	0.79	FRII	17.79	8000059707001370	0.23
9287	J210013-482816	315.06	-48.471	0.01	79.7	37.58	61.17	2.67	0.59	0.64	FRII	24.08	8000083842003790	
9287	J210020-503538	315.08	-50.594	0.012	95.34	54.04	79.47	1.56	0.66	0.70	FRII	18.01	8000076319000450	0.32
9410	J210022-603926	315.09	-60.657	0.004	39.29	32.68	32.68	0.81	0.66	0.70	single	21.1	8000042801006470	0.67
9287	J210023-525019	315.1	-52.839	0.005	141.5	79.42	141.5	1.86	0.55	0.57	FRII	17.36	8000068226000490	0.25
9442	J210023-555408	315.1	-55.902	0.006	99.77	59.75	84.07	2.53	0.69	0.73	FRII	23		
9410	J210028-593628	315.12	-59.608	0.021	104.23	50.18	78.87	0.45	0.62	0.66	FRII	15.09		
9287	J210037-494555	315.15	-49.765	0.023	101.13	56.04	85.55	1.51	0.64	0.67	FRII	20.62	8000079105002360	0.67
9442	J210038-571023	315.16	-57.173	0.02	68.8	19.25	55.5	2.65	0.33	0.36	FRI	22.18	8000053262002950	0.8
9410	J210039-603930	315.16	-60.658	0.059	79.93	34.18	73.31	1.19	0.45	0.48	FRI	21.73	8000042801006430	1.04
9442	J210053-56334	315.22	-56.559	0.004	66.01	66.01	66.01	1.68	0.62	0.65	single	19.48		
9442	J210054-544534	315.23	-54.759	0.006	99.39	63.22	99.39	1.59	0.62	0.65	FRII	17.33		

Continued on next page

Table 4.2 – Continued from previous page

SBID	Source Name	RA (J2000) (deg)	DEC (J2000) (deg)	Flux Density (Jy)	Size (")	a (")	b (")	PA (°)	a/b _{max}	a/b _{min}	Class	Mag (r-band)	DESI ID	Z
9442	J210101-571705	315.26	-57.285	0.078	117.32	56.89	89.88	1.4	0.62	0.65	FR II			
9410	J210102-624642	315.26	-62.778	0.021	67.88	39.29	66.02	1.84	0.57	0.62	FR II	23.44		
9442	J210102-561533	315.26	-56.259	0.002	47.06		32.79	2.59			single	16.75		
9287	J210106-483734	315.28	-48.626	0.165	72.33	40.25	74.15	2.07	0.53	0.56	FR II	22.08	8000082885006010	0.79
9325	J210108-610622	315.28	-61.106	0.014	193.13	157.32	193.13	2.5	0.80	0.83	FR II	24.38	8000042094000550	
9442	J210115-553702	315.32	-55.617	0.005	88.17	48.88	76.57	1.56	0.62	0.66	FR II	23.48		
9287	J210118-505448	315.33	-50.913	0.005	72.99	33.52	55.94	0.45	0.57	0.63	FR II	23.57		
9287	J210119-482837	315.33	-48.477	0.01	103.71		103.71	1.73			single	19.86	8000083843003640	0.59
9442	J210119-564811	315.33	-56.803	0.089	174.81	131.59	165.98	2.33	0.78	0.80	FR II	17.27		
9287	J210122-482109	315.34	-48.353	0.035	99.69	51.04	93.6	0.7	0.53	0.56	FR II	23.17	8000084804000670	1.13
9410	J210135-591535	315.4	-59.26	0.005	44.93	17.45	44.93	2.64	0.37	0.41	FR I	22.85	8000047156002260	0.96
9442	J210136-561252	315.4	-56.214	0.003	62.76	26.32	62.76	2.99	0.40	0.44	FR I	22.34	8000056444002240	1
9410	J210140-601545	315.42	-60.263	0.002	50.34	20.24	50.34	2.91	0.38	0.42	FR I	21.14	8000044231003190	
9442	J210141-562931	315.42	-56.492	0.006	58.47	22.8	46.35	2.58	0.47	0.52	FRx	17.09		
9442	J210145-544614	315.44	-54.771	0.016	74.01		74.01	1.46			single	20.17	8000061370001360	0.54
9410	J210148-621457	315.45	-62.249	0.005	63.41	27.39	63.41	2.22	0.42	0.45	FR I	17.43	8000038644003150	
9442	J210148-553721	315.45	-55.623	0.028	61.05	15.95	53.84	2.63	0.28	0.31	FR I	18.18		
9287	J210150-493612	315.46	-49.603	0.013	100.06	31.14	100.06	0.09	0.30	0.32	FR I	20.45		
9442	J210152-562719	315.47	-56.455	0.032	174.81	97.53	152.54	0.31	0.63	0.65	FR II	22.28	8000055641002420	0.91
9287	J210154-522349	315.48	-52.397	0.01	62.44	23.41	50.38	1.16	0.44	0.49	FR I	20.45	8000069107004020	0.44
9287	J210154-504046	315.48	-50.679	0.004	111.94	70.94	91.23	0.87	0.76	0.80	FR II	23.97		
9287	J210156-512817	315.49	-51.471	0.001	55.62	13.95	55.62	2.26	0.24	0.26	FR I	19.98	8000072674002100	0.47
9287	J210210-521630	315.54	-52.275	0.01	77.38	40.48	62.08	2.26	0.63	0.68	FR II	23.38	8000069992001980	
9442	J210211-543949	315.55	-54.664	0.018	138.53	88.57	126.37	3.06	0.69	0.72	FR II	21.92	8000061371002200	0.85
9287	J210211-485854	315.55	-48.982	0.049	60.69	24.74	57.58	1.22	0.41	0.45	FR I	20.04		
9410	J210214-612403	315.56	-61.401	0.003	46.92	19.8	35.92	2.4	0.52	0.59	FR II	22.7	8000040698006000	0.87
9287	J210215-494835	315.56	-49.81	0.005	125.23	88.09	105.58	1.8	0.81	0.85	FR II	20.96	8000079106001460	0.65
9410	J210215-593202	315.57	-59.534	0.011	104.23	64.56	89.33	1.32	0.70	0.74	FR II	22.84	8000046417002060	0.82
9442	J210218-542357	315.58	-54.399	0.043	122.31	63.69	107.27	0.88	0.58	0.61	FR II	17.59	8000062210002380	0.22
9287	J210220-484426	315.59	-48.741	0.057	91.08	44.51	91.08	0.94	0.48	0.50	FRx	18.65	8000082886003050	0.39
9442	J210221-543525	315.59	-54.59	0.025	192.58	137.8	192.58	2.47	0.71	0.72	FR II	14.01		
9442	J210222-543237	315.6	-54.544	0.006	117.66	59.09	95.07	2.72	0.61	0.64	FR II	22.5	8000062210001000	0.78
9442	J210228-525834	315.62	-52.976	0.037	94.34	46.17	78.93	1.45	0.57	0.60	FR II	21.61	8000067352002370	0.81
9442	J210230-563236	315.63	-56.543	0.002	58.47	14.14	58.47	3.01	0.23	0.25	FR I	25.61		
9351	J210232-555041	315.63	-55.845	0.005	78.05	32.56	52.15	2.94	0.60	0.66	FR II	19.41	8000058065000350	0.2
9442	J210238-564629	315.66	-56.775	0.044	46.67		46.67	0.86			single	17.75	8000054844001230	0.41
9442	J210242-554504	315.68	-55.751	0.014	63.08	21.09	52.24	1.52	0.39	0.42	FR I	19.65	8000058065001670	0.41
9287	J210244-503514	315.68	-50.587	0.008	84.72	43.88	64.96	2	0.65	0.70	FR II	19.63	8000076320000520	0.53
9442	J210251-555236	315.71	-55.877	0.01	114.06	50.39	114.06	2.85	0.43	0.45	FR I	19.55		

Continued on next page

Table 4.2 – Continued from previous page

SBID	Source Name	RA (J2000) (deg)	DEC (J2000) (deg)	Flux Density (Jy)	Size (")	a (")	b (")	PA (°)	a/b _{max}	a/b _{min}	Class	Mag (r-band)	DESI ID	Z
9287	J210253-502740	315.72	-50.461	0.002	105.19	56.23	105.19	0.23	0.52	0.55	FR II	20.36	8000076520002280	0.54
9287	J210253-530501	315.72	-53.084	0.03	112.35	69.66	104.28	0.9	0.65	0.68	FR II	21.15	8000067352000790	0.77
9410	J210257-602214	315.74	-60.37	0.007	57.11		57.11	0.25	0.72	0.75	single	22.34	8000044231000310	0.88
9287	J210302-514945	315.76	-51.829	0.016	161.73	103.48	140.93	2.45	0.38	0.39	FR I	22.34	8000071776000870	0.12
9287	J210303-481824	315.77	-48.307	0.014	149.09	57.84	149.09	3.09	0.80	0.82	FR I	16.55	8000084805001570	0.74
9442	J210304-551435	315.77	-55.243	0.016	200.47	136.85	169.64	1.02	0.57	0.62	FR II	23.1		0.2
9410	J210306-614928	315.78	-61.824	0.01	84.12	38.47	64.84	0.48	0.36	0.38	FR II	22.2	8000040009001370	0.32
9442	J210307-533437	315.78	-53.577	0.013	82.93	30.52	82.93	1.57	0.66	0.69	FR I	17.23	8000065618000720	0.45
9442	J210311-551850	315.8	-55.314	0.016	110.82	62.48	92.58	0.68	0.44	0.48	FR II	19.27	8000059708000730	0.48
9442	J210313-573811	315.8	-57.636	0.009	58.77	27.06	58.77	0.51	0.39	0.42	FR I	25.63		0.48
9442	J210322-532922	315.85	-53.489	0.003	49.75		35.65	3.09	0.39	0.39	single	19.88	8000065618002220	0.45
9287	J210326-481121	315.86	-48.189	0.059	83.84	34.07	83.84		0.63	0.63	FR I	22.13		1.05
9287	J210333-523230	315.89	-52.542	0.008	73.7		73.7	0.63	0.44	0.48	single	24.63	8000043514003870	0.29
9410	J210334-603010	315.89	-60.503	0.013	58.15	22.63	49.22	2.3	0.47	0.49	FR I	23.74	8000066483000870	0.77
9287	J210336-531917	315.9	-53.321	0.004	125.04	60.39	125.04	2.61	0.51	0.55	FR I	18.09		0.48
9287	J210337-522526	315.91	-52.424	0.074	81.39	42.19	79.83	0.98	0.62	0.65	FR II	22.71		0.44
9410	J210337-604101	315.91	-60.684	0.002	52.44		52.44	1.28	0.32	0.33	single	21.78	8000042803005230	0.02
9442	J210338-530839	315.91	-53.144	0.074	62.05		53.2	0.42	0.44	0.48	single	19.03	8000066483004070	0.39
9442	J210342-542534	315.93	-54.426	0.052	224.41	180.8	220.99	2.65	0.81	0.83	FR II	20.03	8000062211001900	0.48
9287	J210343-493450	315.93	-49.581	0.002	96.56	61.32	96.56	0.98	0.62	0.65	FR II	19.76	8000080045001100	0.3
9442	J210343-554309	315.93	-55.719	0.013	110.31	64.52	110.31	0.98	0.57	0.60	FR II	19.12	8000058066002090	0.44
9287	J210345-490202	315.94	-49.034	0.103	504.71	154.34	477.33	1.06	0.32	0.33	FR I	12.32	8000081935001990	0.44
9442	J210346-553418	315.94	-55.572	0.084	55.09	26	56.52	2.22	0.44	0.48	FR I	25.7		0.02
9287	J210349-515304	315.96	-51.884	0.002	63.59		63.59	0.62	0.44	0.48	single	19.3	8000070883003580	0.39
9287	J210350-495941	315.96	-49.995	0.007	48.82		37.12	0.74	0.50	0.54	single	22.8		0.23
9442	J210355-545840	315.98	-54.978	0.002	70.35	36.53	70.35	0.76	0.69	0.73	FR II	17.67	8000060538001710	0.31
9410	J210401-583754	316	-58.632	0.009	105.6	62.81	88.22	1.4	0.57	0.60	FR II	25.09		0.89
9287	J210403-494344	316.01	-49.729	0.003	131.3	76.71	131.3	1.47	0.61	0.64	FR II	18.56	8000079107003230	0.31
9287	J210403-515338	316.02	-51.894	0.016	63.59		47.01	0.8	0.41	0.45	single			
9287	J210406-532050	316.03	-53.347	0.004	66.76	23.46	66.76	2.4	0.34	0.37	FR I			
9351	J210406-564704	316.03	-56.784	0.01	62.55	22.36	47.89	1.07	0.44	0.49	FR I	22.05	8000054845001250	0.89
9287	J210406-531300	316.03	-53.217	0.003	116.06	72.34	116.06	0.69	0.61	0.64	FR II			
9410	J210406-600417	316.03	-60.071	0.018	80.78	26.6	61.65	0.04	0.41	0.45	FR I	18.43	8000044955001230	0.95
9442	J210407-25448	316.03	-52.913	0.004	60.07		60.07	0.22	0.66	0.72	single	22.2	8000067353003980	0.31
9410	J210411-602953	316.05	-60.498	0.004	78.34	40.2	58.59	0.11	0.66	0.72	FR II	24.8	8000043515003660	0.64
9410	J210415-595649	316.06	-59.947	0.001	55.06	23.65	55.06	0.87	0.41	0.45	FR I	24.74		0.64
9287	J210418-532006	316.08	-53.335	0.011	112.95	58.74	94.92	2.52	0.60	0.64	FR II	20.51	8000066484000700	0.64
9287	J210418-480918	316.08	-48.155	0.009	121.47	78.37	121.47		0.63	0.66	FR II	21.12		0.64
9410	J210419-604146	316.08	-60.696	0.004	52.44	16.54	52.44	1.6	0.30	0.33	FR I	23.13		0.64

Continued on next page

Table 4.2 – Continued from previous page

SBID	Source Name	RA (J2000) (deg)	DEC (J2000) (deg)	Flux Density (Jy)	Size (")	a (")	b (")	PA (°)	a/b _{max}	a/b _{min}	Class	Mag (r-band)	DESI ID	Z
9410	J210421-602841	316.09	-60.478	0.069	78.34	37.2	67.01	1.94	0.54	0.58	FR II	20.46		
9287	J210425-493222	316.11	-49.539	0.027	48.81	13.53	43.26	2.61	0.30	0.33	FRI	18.49	8000080045002180	0.25
9442	J210429-533242	316.12	-53.545	0.006	156.18	111.32	126.92	1.88	0.86	0.89	FR II	23.31	8000065619000900	
9442	J210434-532234	316.14	-53.376	0.008	49.75	15.63	38.44	2.65	0.38	0.43	FRI	25.46		
9410	J210436-621620	316.15	-62.272	0.011	63.68	29.73	58.19	0.73	0.49	0.53	FRx	17.54	8000038645002550	0.27
9287	J210437-483956	316.16	-48.666	0.015	47.26	43.67	43.67	0.82	0.53	0.56	single	22.13	8000082888004660	0.65
9442	J210437-580730	316.16	-58.125	0.027	103.59	50.34	91.64	0.73	0.53	0.56	FR II	17.03	8000050934000000	0.2
9287	J210440-532526	316.17	-53.424	0.008	114.27	70.68	96.68	1.12	0.71	0.75	FR II	21.4	80000656190003120	0.66
9410	J210443-573958	316.18	-57.666	0.003	68.22	31.59	68.22	2.23	0.45	0.48	FRI	24.05	8000051706003580	
9287	J210450-504550	316.21	-50.764	0.002	55.63	55.63	55.63	0.2	0.49	0.52	single	16.43	8000075402001260	0.17
9410	J210457-612634	316.24	-61.443	0.78	69.13	34.93	69.13	1.01	0.49	0.52	FRx	22.41	8000040700004800	1
9410	J210457-611147	316.24	-61.196	0.001	50.83	46.42	46.42	0.31			single	22.1		
9410	J210500-591207	316.25	-59.202	0.01	60.96	47.87	47.87	1.18			single	21.37	8000047158002530	0.76
9410	J210500-590349	316.25	-59.064	0.024	82.25	38.83	66.52	0.21	0.56	0.61	FR II	20.61		
9410	J210501-585349	316.25	-58.897	0.011	110.87	78.59	101.81	1.83	0.75	0.79	FR II	21.23	8000047903003230	0.58
9287	J210501-484846	316.26	-48.813	1.308	65.21	65.21	65.21	0.68			single	17.31		
9410	J210505-580510	316.27	-58.086	0.007	50.6	18.44	41.22	0.89	0.42	0.48	FRI	23.28		
9287	J210507-522504	316.28	-52.418	0.246	64.98	14.72	61.19	0.23	0.23	0.25	FRI	20.71	8000069109003500	0.87
9442	J210507-582454	316.28	-58.415	0.006	42.54	34.49	34.49	2.45			single	23.35		
9287	J210512-480657	316.3	-48.116	0.014	61.68	23.21	61.68	0.36	0.36	0.39	FRI			
9442	J210513-560238	316.31	-56.044	0.01	43.22	36.47	36.47	1.11			single	22.05		
9410	J210515-620357	316.31	-62.066	0.002	58.39	58.39	58.39	1.01			single	21.38	8000039325001570	0.67
9442	J210517-581401	316.32	-58.234	0.003	93.82	59.58	93.82	1.4	0.62	0.65	FR II	18.6		
9287	J210524-484343	316.35	-48.729	0.024	145.06	80.62	126.03	2.73	0.63	0.65	FR II	20.78	8000082888003230	0.5
9287	J210525-493354	316.36	-49.565	0.001	48.81	56.3	56.3	0.28	0.72	0.75	single	19.87	8000080046001410	0.41
9287	J210526-524932	316.36	-52.826	0.038	143.11	102.51	139.97	0.65	0.85	0.86	FR II	20.96	8000068229000600	0.54
9442	J210526-535250	316.36	-53.881	0.043	418.93	358.08	418.93	2.81	0.85	0.86	FR II	19.06	8000063905004430	0.43
9287	J210527-510700	316.37	-51.117	0.081	182.32	49.96	159.39	1.02	0.31	0.32	FRI	19.99	8000074489000150	0.52
9442	J210532-525717	316.39	-52.955	0.003	49.75	34.01	34.01	1.27			single	24.93	8000067354002800	
9442	J210533-560718	316.39	-56.122	0.033	110.24	60.03	91.58	0.02	0.64	0.67	FR II	20.63	8000057254000080	0.43
9442	J210537-533701	316.41	-53.617	0.002	109.05	64.12	79.37	1.49	0.78	0.83	FR II	18.36	8000065619000090	0.25
9442	J210537-554053	316.41	-55.681	0.003	55.09	15.83	55.09	0.22	0.27	0.30	FRI	21.8	8000058067002610	0.79
9410	J210542-571912	316.43	-57.32	0.102	150.82	39.93	136.19	2.6	0.29	0.30	FR I	16.34	8000053265000960	0.15
9410	J210545-585158	316.44	-58.866	0.035	48.2	15.23	44.02	0.36	0.33	0.37	FRI	23.82		
9287	J210549-494100	316.46	-49.683	0.011	76.9	31.3	63.6	1.92	0.47	0.51	FRx	22.55	8000071777000360	0.9
9287	J210550-515105	316.46	-51.852	0.006	104.42	37.07	104.42	0.77	0.35	0.36	FRI	19.39	8000074489002260	0.3
9287	J210550-505700	316.46	-50.95	0.034	126.7	68.04	126.7	0.07	0.53	0.55	FR II	20.82	8000051706001460	0.72
9442	J210552-574725	316.47	-57.979	0.016	51.15	41.32	41.32	1.24			single	20.32		
9442	J210553-571321	316.47	-57.223	0.029	168.54	62.75	143.72	1.99	0.43	0.44	FRI	20.93		

Continued on next page

Table 4.2 – Continued from previous page

SBID	Source Name	RA (J2000) (deg)	DEC (J2000) (deg)	Flux Density (Jy)	Size (")	a (")	b (")	PA (°)	a/b _{max}	a/b _{min}	Class	Mag (r-band)	DESI ID	Z
9410	J210556-602641	316.49	-60.445	0.007	39.22	28.17	31.99	2.22	0.32	0.34	single	23.13	8000043515005020	0.9
9287	J210558-515007	316.49	-51.835	0.006	84.22	69.26	84.22	2.63	0.63	0.66	FRI	19.2	800007177000660	0.41
9410	J210600-624844	316.51	-62.812	0.064	122.57	107.83	107.83	1.95	0.63	0.66	FRII	20.89	8000037305001400	0.7
9410	J210600-614900	316.51	-61.817	0.002	79.58	34.45	79.58	1.13	0.42	0.45	FRI	20.01	8000040011001380	0.41
9287	J210602-505145	316.51	-50.863	0.008	98.78	39.79	81.3	2.15	0.47	0.50	FRx	18.7	8000075403000140	0.37
9410	J210604-584428	316.52	-58.741	0.006	104.77		104.77	0.1			single	21.32	8000048653002120	0.92
9410	J210606-605556	316.53	-60.932	0.047	68.36		59.93	0.84			single	18.5	8000042097005090	0.24
9287	J210607-523433	316.53	-52.576	0.003	71.67	16.65	71.67	2.35	0.22	0.24	FRI	19.7	8000069109000780	0.44
9287	J210607-504450	316.53	-50.747	0.009	104.34	67.45	104.34	1.77	0.63	0.66	FRII	19.71	8000075403001450	0.38
9410	J210613-601211	316.56	-60.203	0.136	54.62	18.87	51.6	2.17	0.35	0.38	FRI	19.01		
9410	J210617-625309	316.57	-62.886	0.005	62.13	28.64	50.15	0.2	0.54	0.60	FRII	16.35		
9442	J210618-531050	316.58	-53.181	0.009	67.58	32.06	58.28	0.12	0.53	0.57	FRII	22.24		
9442	J210618-561449	316.58	-56.247	0.008	93.93	58	83.07	1.57	0.68	0.72	FRII	19.98		
9410	J210620-611221	316.59	-61.206	0.003	67.88	31.81	51.73	2.54	0.59	0.65	FRII	23.9		
9442	J210623-562851	316.6	-56.481	0.007	160.57	125.41	160.57	1.17	0.77	0.79	FRII	21.24		1
9410	J210627-602421	316.61	-60.406	0.005	56.6	25.7	56.6	0.23	0.43	0.48	FRI	21.02		
9287	J210630-514201	316.63	-51.7	0.044	65.7	20	55.59	0.86	0.34	0.38	FRI			
9410	J210647-594902	316.7	-59.817	0.003	87.38	28.63	87.38	2.45	0.32	0.34	FRI	20.09	8000045686001110	0.44
9287	J210647-520057	316.7	-52.016	0.017	145.27	107.42	130	2.08	0.81	0.84	FRII	22.8	8000070884001630	0.92
9287	J210650-482331	316.71	-48.392	0.008	145.21	93.42	145.21	1.87	0.63	0.65	FRII	19.07	8000083846005270	0.29
9410	J210655-603431	316.73	-60.575	0.03	95.69		95.69	0.08			single	16.39	8000043516001270	0.15
9410	J210657-584656	316.74	-58.782	0.003	62.05	45.34	62.05	2.27	0.63	0.68	single	17.95	8000057254003390	
9442	J210658-555524	316.74	-55.923	0.004	71.21	52.5	69.65	2.44	0.55	0.58	FRII	22.16	8000076323001000	0.33
9287	J210702-503253	316.76	-50.548	0.012	92.4	92.4	92.4	1.51	0.55	0.58	FRII	17.96	8000076323001000	0.33
9410	J210704-621044	316.77	-62.179	0.012	46.1		42.9	0.18			single	20.42	8000038647005300	0.58
9410	J210705-615108	316.77	-61.852	0.005	79.58	41.04	62.2	2.37	0.63	0.69	FRII	25.52	8000040011000530	
9442	J210707-545145	316.78	-54.863	0.065	282.36	194.18	231.68	2.76	0.83	0.85	FRII	16.55	8000061373000110	0.18
9287	J210710-492804	316.79	-49.468	0.005	82.03	31.71	82.03	0.86	0.38	0.40	FRI	20.01	8000080047003300	0.52
9410	J210710-624645	316.8	-62.779	0.017	68.94	31.24	59.23	2.29	0.51	0.55	FRII			
9410	J210718-584926	316.83	-58.824	0.003	82.32	51.1	82.32	0.81	0.60	0.64	FRII	19.55	8000048654000840	0.5
9410	J210721-605307	316.84	-60.885	0.001	50.98		48.28	0.26			single	19.53	8000042097006370	0.42
9442	J210722-541544	316.84	-54.262	0.002	110.84	78.95	110.84	1.15	0.70	0.73	FRII	22.33	8000063056001780	0.84
9410	J210725-585140	316.86	-58.861	0.001	44.61	29.18	44.61	1.91	0.62	0.69	FRII	21.38	8000048654000230	1.13
9442	J210727-570322	316.86	-57.056	0.005	117.15	70.87	117.15	1.52	0.59	0.62	FRII	17.11	8000054053001110	0.26
9287	J210729-481537	316.87	-48.26	0.015	68.54	31.24	68.54	0.73	0.44	0.47	FRI	17.99	8000084808002430	0.29
9287	J210731-493212	316.88	-49.537	0.112	64.28	28.28	58.03	1.45	0.47	0.51	FRx	21.72	8000080047001910	
9442	J210733-552513	316.89	-55.42	0.005	66.4	31.05	53.25	1.3	0.56	0.61	FRII	21.41	8000058887003170	0.76
9287	J210737-491121	316.91	-49.189	0.022	89.11	38.9	89.11	3.07	0.42	0.45	FRI	19.4	8000080991004080	0.5
9287	J210738-500048	316.91	-50.013	0.005	84.79		84.79	2.69			single	18	8000078176002370	0.28

Continued on next page

Table 4.2 – Continued from previous page

SBID	Source Name	RA (J2000) (deg)	DEC (J2000) (deg)	Flux Density (Jy)	Size (")	a (")	b (")	PA (°)	a/b _{max}	a/b _{min}	Class	Mag (r-band)	DESID	Z
9410	J210757-62-1607	316.99	-62.269	0.093	63.64	60.82	60.82	0.58	0.53	0.56	single	19.34	8000038647002700	0.3
9410	J210802-630128	317.01	-63.024	0.003	85.48	85.48	85.48	1.33	0.53	0.56	FRII	19.65	8000036643002790	0.67
9442	J210802-582305	317.01	-58.385	0.002	63.27	27.74	63.27	1.02	0.42	0.46	FR I	22.45	8000049409004310	0.67
9442	J210803-561108	317.01	-56.186	0.009	46.86	41.45	41.45	0.59	0.59	0.58	single	23.64	8000056447002890	0.67
9442	J210805-575232	317.02	-57.876	0.004	74.19	41.62	74.19	0.58	0.54	0.58	FRII	23.2		
9442	J210809-535656	317.04	-53.949	0.002	59.9	26.01	59.9	0.55	0.42	0.45	FR I	19.76	8000063906003180	0.46
9287	J210813-521202	317.05	-52.201	0.005	53.97	18.97	43.19	0.36	0.42	0.47	FR I	22.33	8000069996002640	0.79
9287	J210814-533701	317.06	-53.617	0.006	78.95	26.51	78.95	2.95	0.33	0.35	FR I	22.4	8000065621000200	0.87
9442	J210815-573941	317.06	-57.661	0.003	105.31	73	105.14	0.34	0.68	0.71	FRII	16.84	8000051707003180	0.15
9287	J210819-483325	317.08	-48.557	0.007	63.84	30.59	63.84	2.96	0.46	0.50	FR I	15.7	8000083847001590	0.15
9287	J210821-501315	317.09	-50.221	0.002	56.82	17.87	56.82	0.96	0.30	0.33	FR I			
9287	J210821-503453	317.09	-50.581	0.002	72.27	35.6	72.27	0.63	0.48	0.51	FRx	15.91		
9442	J210822-552421	317.09	-55.406	0.005	71.21	50.44	50.44	0.37	0.48	0.51	single	21.63	8000058888003620	0.76
9410	J210823-581204	317.1	-58.201	0.003	131.05	98.82	131.05	1.73	0.74	0.77	FRII	16.21	8000050171002670	0.13
9287	J210825-521409	317.11	-52.236	0.003	125.79	87.88	125.79	1.99	0.69	0.71	FRII	19.24	8000069996002030	0.31
9410	J210830-623404	317.13	-62.568	0.054	48.34	45.93	45.93	0.17	0.17	0.17	single	21.7	8000037974001480	0.9
9287	J210830-494557	317.13	-49.766	0.003	90.56	51.67	90.56	0.95	0.56	0.59	FRII	21.78	8000079110002580	0.63
9442	J210838-581456	317.16	-58.249	0.003	76.54	33.73	76.54	2.56	0.43	0.46	FR I	18.15	8000050171002060	0.26
9410	J210840-621240	317.17	-62.211	0.007	49.97	38.59	38.59	3.03	0.48	0.50	single	20.82	8000038647004380	0.68
9442	J210842-551830	317.18	-55.308	0.006	140.18	55.32	113.46	2.88	0.48	0.50	FR I	22.11	8000059711001000	0.81
9287	J210844-513418	317.18	-51.572	0.061	112.03	64.03	98.5	2.89	0.63	0.67	FRII	24.04		
9442	J210849-564417	317.21	-56.738	0.009	61.99	25.02	53.9	1.72	0.44	0.49	FR I			
9287	J210852-540446	317.22	-54.079	0.004	71.74	27.67	71.74	0.52	0.37	0.40	FR I	22.34	8000063906000990	0.84
9442	J210852-530516	317.22	-53.088	0.01	52.62	94.85	52.62	0.58	0.72	0.75	single	22.93	8000067356000690	0.83
9287	J210854-515257	317.23	-51.883	0.033	145.27	94.85	129.02	0.44	0.44	0.47	FRII	23.57		
9442	J210854-542314	317.23	-54.387	0.005	47.87	39.5	39.5	0.87	0.87	0.87	single	19.92	8000062214003890	0.6
9287	J210858-494132	317.25	-49.692	0.195	90.95	41.42	90.08	1.05	0.45	0.47	FR I	19.75	8000079111003860	0.47
9410	J210859-602805	317.25	-60.468	0.002	66.25	66.25	66.25	3.06	0.45	0.47	single	15.32		
9410	J210900-604142	317.25	-60.695	0.007	97.63	70.52	97.63	0.54	0.70	0.74	FRII	25.27	8000042805004330	0.19
9410	J210902-604927	317.26	-60.824	0.045	89.06	43.91	80.48	0.51	0.53	0.56	FRII	18.23		
9442	J210907-550628	317.28	-55.108	0.002	67.86	22.95	67.86	0.86	0.33	0.35	FR I	17.84	8000067356000620	0.63
9287	J210909-505710	317.29	-50.953	0.02	52.87	18.11	49.01	0.2	0.35	0.39	FR I	20.71	8000074492002580	0.19
9442	J210909-571627	317.29	-57.274	0.138	70.36	26.68	65.71	2.99	0.39	0.42	FR I	17.1	8000053267001590	0.13
9442	J210910-580804	317.3	-58.134	0.01	51.45	47.98	40.64	2.12	0.40	0.42	single	22.98	8000050171004090	0.84
9410	J210915-591422	317.31	-59.239	0.007	117.38	47.98	117.38	0.93	0.40	0.42	FR I	17.73	8000047160002030	0.27
9287	J210917-530533	317.32	-53.093	0.007	60.16	44	44	1.63	0.40	0.42	single	20.56	8000067356000620	0.63
9287	J210918-502641	317.33	-50.445	0.002	70.82	24.46	70.82	2.81	0.33	0.36	FR I	17.87	8000076324002730	0.28
9410	J210920-623103	317.34	-62.518	0.016	164.69	95.74	148.31	2.89	0.63	0.66	FRII	15.83	8000037974003040	0.28
9410	J210923-621634	317.35	-62.276	0.002	56.78	56.78	56.78	1.85	0.63	0.66	single	21.47	8000038648002480	0.74

Continued on next page

Table 4.2 – Continued from previous page

SBID	Source Name	RA (J2000) (deg)	DEC (J2000) (deg)	Flux Density (Jy)	Size (")	a (")	b (")	PA (°)	a/b _{max}	a/b _{min}	Class	Mag (r-band)	DESI ID	Z
9287	J210926-513530	317.36	-51.592	0.003	64.99	21.52	64.99	1.02	0.32	0.34	FRI	21.62	8000072679000470	0.75
9442	J210930-533402	317.38	-53.567	0.007	69.74	35.44	57.88	1.23	0.59	0.64	FRII	18.38		
9442	J210934-555005	317.39	-55.835	0.002	56.7		56.7	0.28	0.71		single	19.38	8000058069000680	0.41
9287	J210936-521834	317.4	-52.309	0.002	120.25	87.38	120.25	0.84	0.71	0.74	FRII	16.62	800006997000950	0.05
9442	J210936-532640	317.4	-53.444	0.082	58.08		49.55	0.05			single	21.55	8000065622002920	0.73
9287	J210942-514834	317.43	-51.809	0.014	85.52	41.76	66.29	2.84	0.61	0.65	FRII	21.7	8000071780000880	0.74
9442	J210947-574528	317.45	-57.758	0.006	70.09		70.09	0.24			single	20.54	8000051708001930	0.64
9287	J210947-520647	317.45	-52.113	0.036	73.83	41.04	65.9	2.28	0.60	0.65	FRII	20.84	8000070886000220	0.78
9442	J210954-531001	317.48	-53.167	0.669	120.3	52.35	104.08	0.08	0.49	0.52	FRx	21.16	8000066487003320	0.63
9442	J210957-583454	317.49	-58.582	0.007	58.88	18.8	47.44	2.01	0.38	0.42	FRI	22.03	8000049410000590	0.84
9442	J210959-571746	317.5	-57.296	0.001	60.65	23.02	60.65		0.36	0.40	FRI	17.91	8000053267001280	0.21
9442	J210959-582056	317.5	-58.349	0.002	58.38		58.38	2.97	0.42	0.45	single	21.93	8000050172000450	0.73
9442	J210959-535758	317.5	-53.966	0.002	71.55	30.84	71.55	0.46	0.42	0.45	FRI	19.34	8000063907002950	
9410	J211001-595515	317.51	-59.921	0.006	42.44	10.04	34.48	1.1	0.27	0.31	FRI	23.88		
9442	J211008-541817	317.54	-54.305	0.009	123.22	83.74	110.71	0.87	0.74	0.77	FRII	19.27		
9287	J211012-522227	317.55	-52.374	0.027	110.58	72.47	97.82	2.07	0.72	0.76	FRII	23.73	800006997000160	0.2
9410	J211012-602803	317.55	-60.468	0.008	99.89	31.05	99.89	0.63	0.30	0.32	FRI	17.87	8000043518003810	0.2
9287	J211013-504235	317.56	-50.71	0.007	68.55		46.87	0.98			single	20.45	8000075406002790	0.58
9287	J211015-525229	317.56	-52.875	0.008	65.35		65.35	2.12			single	24.78		
9410	J211026-625003	317.61	-62.834	0.002	55.59	10.7	55.59	1.09	0.18	0.20	FRI	19.64		
9410	J211027-585804	317.61	-58.968	0.004	51.42		51.42	3.1			single	20.79	8000047906002440	0.59
9442	J211028-542343	317.62	-54.395	0.015	60.13		54.42	2.89			single	21.82	8000062215003870	0.91
9410	J211029-590506	317.62	-59.085	0.027	61.22		56.64	1.85			single			
9287	J211030-584232	317.63	-58.709	0.066	86.52	39.46	86.52	3.07	0.44	0.47	FRI	19.95	8000048655002520	
9442	J211037-491212	317.65	-49.203	0.068	192.02	165.92	192.02		0.85	0.88	FRII	17.01		
9442	J211038-563338	317.66	-56.561	0.01	89.49	42.94	89.49	1.06	0.47	0.49	FRI	20.26		
9410	J211041-585427	317.67	-58.908	0.005	96.46		96.46	0.14			single	18.31	8000047906003250	0.33
9442	J211043-561144	317.68	-56.196	0.001	84.95	43.66	84.95	3.11	0.50	0.53	FRx	19.84	8000056449003040	0.5
9442	J211045-554434	317.69	-55.743	0.01	92.82	58.63	79.29	2.51	0.72	0.76	FRII	22.63	8000058070002450	
9442	J211047-553310	317.7	-55.553	0.032	61.28		51.18	1.44			single	19.19	8000058889001140	0.28
9442	J211048-570207	317.7	-57.035	0.002	53.75		53.75	0.79			single	24.63		
9442	J211051-581257	317.72	-58.216	0.002	65.97	29.11	65.97	1.52	0.43	0.46	FRI	21.49	8000050172002460	0.86
9442	J211056-561138	317.73	-56.194	0.016	46.86		43.94	0.8			single	25.2	8000056449003090	
9287	J211058-512619	317.74	-51.439	0.019	214.81	70.71	214.81	1.36	0.33	0.33	FRI	18.62	8000072680002980	0.38
9442	J211100-554303	317.75	-55.718	0.002	63.57		63.57	0.08			single	20.35	8000058070002810	0.54
9410	J211102-624835	317.76	-62.81	0.012	76.43	37.58	61.26	2.91	0.59	0.64	FRII	19	8000037308001550	0.35
9410	J211103-594305	317.76	-59.718	0.017	297.09	229.6	297.09	1.91	0.77	0.78	FRII	18.38	8000045688002360	0.29
9434	J211103-513522	317.76	-51.589	0.006	53.75		41.64	0.79			single	25.33		
9442	J211106-570217	317.78	-57.038	0.002	53.75		53.75	0.53			single	20.31	8000054055001110	

Continued on next page

Table 4.2 – Continued from previous page

SBID	Source Name	RA (J2000) (deg)	DEC (J2000) (deg)	Flux Density (Jy)	Size (")	a (")	b (")	PA (°)	a/b _{max}	a/b _{min}	Class	Mag (r-band)	DESI ID	Z
9287	J211109-500248	317.79	-50.047	0.004	124.73	77.96	124.73	1.4	0.61	0.64	FR II	19.21		
9410	J211111-615032	317.8	-61.842	0.002	69.34	36.17	69.34	2.8	0.50	0.54	FR II	17.87	8000040013000700	0.24
9442	J211112-551142	317.8	-55.195	0.005	90.1	48.92	90.1	0.22	0.53	0.56	FR II	18.64	8000059713002830	0.34
9442	J211117-581923	317.82	-58.323	0.012	161.61	92.11	134.65	0.6	0.67	0.70	FR II	21.81	8000050172000920	0.83
9410	J211119-580518	317.83	-58.088	0.004	117.07	84.18	117.07	2.31	0.70	0.73	FR II	19.9		
9410	J211123-591517	317.85	-59.255	0.003	66.1	31.71	66.1	0.74	0.46	0.50	FR I	19.65	8000047161001870	0.6
9410	J211125-592427	317.86	-59.408	0.044	88.18	19.77	64.4	3.04	0.30	0.32	FR I	18.62	8000046422003150	0.41
9434	J211128-533317	317.87	-53.555	0.003	59.45	18.75	59.45	2.33	0.30	0.33	FR I			
9287	J211129-530407	317.87	-53.069	0.063	97.52	41.62	82.76	2.65	0.49	0.52	FRx	22.78		
9434	J211129-520802	317.87	-52.134	0.002	55.78	19.26	55.78	2.89	0.23	0.25	single	20.35	8000069998003220	0.6
9442	J211135-584222	317.9	-58.706	0.006	79.79	19.26	79.79	0.15	0.23	0.25	FR I	20.01	8000048656002180	0.6
9410	J211137-631442	317.91	-63.245	0.129	102.55	55.24	102.55		0.53	0.55	FR II	18.79		
9442	J211137-573657	317.91	-57.616	0.006	161.15	115.86	161.15	1.24	0.71	0.73	FR II	21.53	8000052487000090	0.86
9434	J211141-524108	317.92	-52.686	0.003	57.82	20.72	57.82	0.91	0.34	0.37	FR I	23.36		
9410	J211142-611735	317.93	-61.293	0.011	201.32	123.81	201.32	0.26	0.61	0.62	FR II	19.27		
9410	J211146-580539	317.94	-58.094	0.003	161.28	124.38	161.28	2.4	0.76	0.78	FR II	21.26		
9410	J211147-624447	317.95	-62.746	0.001	63.85	35.11	63.85	0.93	0.53	0.57	FR II	22.11	8000037308003260	0.75
9442	J211150-581733	317.96	-58.293	0.159	79.48	41.62	78.09	1.66	0.52	0.55	single	21.93	8000050173001330	0.88
9442	J211151-550937	317.96	-55.16	0.003	54.89	19.26	54.89	1.66	0.87	0.88	FR II	21.55	8000059713003450	0.64
9442	J211152-542049	317.97	-54.347	0.143	282.42	229	261.72	2.06	0.87	0.80	FR II	18.62	8000079112001290	0.26
9287	J211153-494713	317.97	-49.787	0.032	277.86	220.62	277.86	2.31	0.79	0.80	FR II	21.88	8000051709003030	0.85
9410	J211153-574115	317.97	-57.688	0.006	54.46	23.37	54.46	1.47	0.34	0.36	single	99	8000079113005750	
9434	J211158-493837	317.99	-49.644	0.002	67.22	37.22	67.22	0.77	0.34	0.36	FR I			
9442	J211159-544458	318	-54.749	0.012	52.62	25.61	48.58	2.14	0.50	0.56	FR II	23.62	8000061376001380	0.83
9442	J211159-583038	318	-58.511	0.001	58.88	25.02	58.88		0.41	0.44	FR I	19.77	8000049411001690	0.43
9287	J211214-515413	318.06	-51.904	0.102	62.22	24.08	54.47	2.54	0.42	0.46	FR I	31.17		
9287	J211217-490053	318.07	-49.015	0.006	53.94	24.08	54.47	2.54	0.42	0.46	single	18.89	8000081941003040	0.42
9442	J211218-581744	318.08	-58.296	0.015	104.04	58.32	84.36	1.51	0.67	0.71	FR II	18.73	8000050173001260	0.43
9434	J211221-513918	318.09	-51.655	0.008	47.48	19.26	47.48	1.04	0.31	0.33	single	17.23		
9442	J211223-564712	318.1	-56.787	0.005	99.95	31.98	99.95	1.81	0.31	0.33	FR I	19.2	8000054849001710	0.42
9287	J212225-503435	318.1	-50.576	0.006	84.47	37.19	84.47	0.43	0.43	0.45	FR I	21.13	8000076226001030	0.66
9410	J211225-602608	318.11	-60.436	0.003	69.17	20	69.17	2.74	0.46	0.52	single	16.1	8000043519003990	0.1
9442	J211226-554031	318.11	-55.675	0.005	49.49	20	41.18	0.07	0.46	0.52	FRx	20.75	8000058071003120	0.59
9287	J211226-505157	318.11	-50.866	0.052	100.15	47.07	87.45	2.97	0.52	0.55	FR II	18.1	8000075407000210	
9287	J211227-522807	318.11	-52.469	0.004	100.09	66.45	85.51	1.43	0.76	0.80	FR II	23.9	8000069113002030	0.39
9434	J211228-494028	318.12	-49.674	0.004	117.45	67.58	117.45	0.31	0.56	0.59	FR II	19.12	8000079113004830	
9442	J211231-582424	318.13	-58.407	0.004	61.81	32.31	48.1	1.18	0.64	0.71	FR II	23.54	8000049412003380	
9410	J211231-603608	318.13	-60.602	0.013	57.76	22.8	50.07	2.89	0.43	0.48	FR I	19.1	8000043519000500	0.4
9434	J211232-511925	318.13	-51.324	0.005	58.34	22.8	58.34	0.16	0.43	0.48	single	17.36	8000073584000570	0.24

Continued on next page

Table 4.2 – Continued from previous page

SBID	Source Name	RA (J2000) (deg)	DEC (J2000) (deg)	Flux Density (Jy)	Size (")	a (")	b (")	PA (°)	a/b _{max}	a/b _{min}	Class	Mag (r-band)	DESI ID	Z
9442	J211233-561654	318.14	-56.282	0.01	55.88		55.88	2.16			single	20.98	8000056450001680	0.65
9442	J211233-561456	318.14	-56.249	0.02	84.76		84.76	0.23			single	19.92		
9442	J211239-562340	318.17	-56.394	0.006	96.47	60.11	96.47	2.67	0.61	0.64	FRII	21.07		
9434	J211242-510137	318.18	-51.027	0.003	52.17		52.17	0.49			single	20.88	8000074494001680	0.69
9442	J211242-573031	318.18	-57.509	0.013	165.26	72.25	142.95	0.12	0.50	0.51	FRx	19.45	8000052487003280	0.38
9287	J211246-501537	318.19	-50.26	0.05	111.98	69.05	100.99	2.99	0.67	0.70	FRII	25.09		
9442	J211246-551458	318.2	-55.249	0.007	55.21	24.41	55.21	2.27	0.42	0.46	FR I	21.6	8000059714002070	0.67
9287	J211248-483403	318.2	-48.568	0.001	64.6	27.73	64.6	1.03	0.41	0.45	FR I	21.32	8000083850001520	0.65
9410	J211249-600405	318.21	-60.068	0.004	72.94	27.58	72.94	1.53	0.37	0.39	FR I	19.88	8000044959001290	0.41
9410	J211253-574325	318.22	-57.724	0.01	54.46		42.51	2.78			single	21.74	8000051710002560	0.76
9287	J211254-484708	318.23	-48.786	0.002	58.69	25.63	58.69	0.63	0.42	0.46	FR I	22.51		
9442	J211254-565308	318.23	-56.886	0.003	62.44		62.44	0.15			single	22.03	8000054056003750	0.85
9442	J211257-545906	318.24	-54.985	0.027	93.75	36.06	73.46	0.63	0.47	0.51	FRx	22.85	8000060543001870	0.85
9442	J211258-561456	318.24	-56.249	0.337	176.28	122.07	170.75	2.95	0.70	0.73	FRII	21.15	8000056450002390	0.69
9410	J211259-584710	318.25	-58.786	0.014	67.83	32.56	59.26	2.9	0.53	0.57	FRII	22.9	8000048657001030	
9442	J211300-550246	318.25	-55.046	0.016	71.61	35.39	71.61	2.45	0.48	0.51	FRx	13.53		
9434	J211303-505019	318.26	-50.839	0.002	75.59	21.14	75.59	2.52	0.27	0.29	FR I	17.96	8000075408000650	0.92
9410	J211304-621947	318.27	-62.33	0.007	92.94	46.68	67.42	0.08	0.67	0.72	FRII	21.7	8000038649000970	
9410	J211305-612007	318.27	-61.335	0.005	213.25	164.32	213.25	0.12	0.76	0.78	FRII	20.95		
9434	J211306-521335	318.28	-52.226	0.003	74.87	26.31	74.87	0.71	0.34	0.36	FR I	22.67		
9434	J211308-495117	318.29	-49.855	0.001	49.07	13.85	49.07		0.27	0.30	FR I	19.66	8000079113000430	0.39
9287	J211310-534516	318.29	-53.754	0.023	80.05	26.91	61.48	0.89	0.42	0.46	FR I	22.25	8000064764002020	0.76
9410	J211313-590021	318.31	-59.006	0.036	112.49	63.53	94.29	2.57	0.66	0.69	FRII	17.89	8000047907001310	0.36
9442	J211316-573358	318.32	-57.566	0.004	107.67	64.6	107.67	1.52	0.59	0.61	FRII	19.33		
9434	J211326-532721	318.36	-53.456	0.009	168.66	95.2	168.66	2.77	0.56	0.57	FRII	23.54		
9410	J211329-604959	318.37	-60.833	0.012	44.77	14.84	39.31	0.54	0.35	0.40	FR I	23.98		
9410	J211330-614001	318.38	-61.667	0.097	108.19	66.27	100.39	0.99	0.64	0.68	FRII	20.91	8000040014004030	0.73
9434	J211333-525244	318.39	-52.879	0.01	79.84	42.05	68.03	1.51	0.60	0.64	FRII	23.09		
9442	J211335-582658	318.4	-58.449	0.011	92.75	43.91	80.11	2.11	0.53	0.57	FRII	16.92	8000049412002700	0.18
9442	J211335-582030	318.4	-58.342	0.008	156.84	107.5	156.84	0.17	0.67	0.70	FRII	20.32	8000050173000550	0.67
9442	J211335-571649	318.4	-57.28	0.002	77.51		77.51	1.28			single	19.84	8000053269001370	0.43
9442	J211341-560514	318.42	-56.087	0.007	61.57		64.57	1.76			single	20.61	8000057258000740	0.65
9434	J211341-493203	318.42	-49.534	0.011	90.83	43.86	76.1	0.7	0.56	0.60	FRII	23.69		
9287	J211342-484806	318.43	-48.802	0.071	53.94	20.4	50.61	1.88	0.38	0.42	FR I	20.85	8000082894001910	0.57
9434	J211342-512952	318.43	-51.498	0.01	101.1	56.04	82.01	0.94	0.66	0.70	FRII	22.24	8000072682001940	0.93
9410	J211346-602310	318.44	-60.386	0.014	76.81	28.62	62.1	1.98	0.44	0.48	FR I	18.63	8000043519004740	0.37
9410	J211348-591758	318.45	-59.299	0.033	76.04	36.38	76.04	0.93	0.46	0.49	FR I	21.01	8000047162000130	0.82
9410	J211349-625229	318.46	-62.875	0.015	165.77	35.56	165.77	1.07	0.21	0.22	FR I	15.58	8000037309000110	0.1
9442	J211349-572038	318.46	-57.344	0.005	87.81	24.9	87.81	1.68	0.28	0.29	FR I	21.43	8000053269000480	0.65

Continued on next page

Table 4.2 – Continued from previous page

SBID	Source Name	RA (J2000) (deg)	DEC (J2000) (deg)	Flux Density (Jy)	Size (")	a (")	b (")	PA (°)	a/b _{max}	a/b _{min}	Class	Mag (r-band)	DESI ID	Z
9434	J211352-530655	318.47	-53.115	0.013	46.9	41.25	41.25	0.71			single	18.77		
9410	J211402-611743	318.51	-61.295	0.003	42.99	33.72	33.72	0.19			single	22.12	8000041399001750	0.91
9442	J211402-535309	318.51	-53.886	0.006	90.82	82.49	82.49	1.76	0.54	0.57	FRII	23.23	8000063910004220	
9434	J211403-494500	318.51	-49.75	0.097	102.4	47.32	102.4	0.19	0.45	0.47	FRI	16.92	8000079114002880	
9410	J211403-591928	318.52	-59.324	0.003	49.34	19.7	49.34	2.06	0.38	0.42	FRI	20.57	8000047162000970	0.37
9442	J211404-561938	318.52	-56.327	0.007	184.97	141.18	184.97	0.28	0.75	0.77	FRII	20.8	8000056451000890	0.42
9434	J211406-494517	318.53	-49.755	0.019	38.76	12.51	38.87	1.29	0.30	0.34	FRI	21.38	8000079114002730	0.99
9434	J211407-521027	318.53	-52.174	0.024	146.73	93.74	125.46	1.07	0.73	0.76	FRII	19.83	800006999002610	0.41
9442	J211408-540739	318.53	-54.128	0.209	87.1	40.5	79.3	2.2	0.50	0.53	FRx	21.47	8000063060004680	0.81
9410	J211412-612252	318.55	-61.381	0.009	66.61	66.61	66.61	1.63	0.62	0.66	single	17.85		
9434	J211412-510812	318.55	-51.137	0.015	114.93	63.25	98.9	0.33	0.62	0.66	FRII			
9410	J211414-623126	318.56	-62.524	0.014	50.34	38.27	38.27	0.39	0.62	0.66	single	22.79	8000037977002500	1.07
9287	J211415-534506	318.57	-53.752	0.024	64.02	24.08	53.1	1.43	0.43	0.48	FRI	20.07	8000064765002040	0.53
9442	J211416-540840	318.57	-54.144	0.009	126.64	96.54	118.56	2.45	0.80	0.83	FRII	17.87		
9434	J211419-514514	318.58	-51.754	0.01	147.38	44.72	122.4	2.63	0.36	0.37	FRI	19.3	8000071783001450	0.45
9410	J211421-610429	318.59	-61.075	0.014	42.99	38.96	38.96	1.27	0.36	0.37	single	22.84	8000042101000920	
9410	J211427-630157	318.61	-63.033	0.017	53.07	44.57	44.57	2.31	0.49	0.52	single	17.53	8000036646001980	0.23
9410	J211428-630319	318.62	-63.055	0.064	81.18	36.88	72.85	0.48	0.49	0.52	FRx	19.58	8000036646001580	0.28
9434	J211432-520311	318.64	-52.053	0.001	45.59						single	24.31		
9410	J211433-600315	318.64	-60.054	0.015	62.71	26.91	52.87	0.73	0.49	0.53	FRx	25.01		
9442	J211434-574048	318.64	-57.68	0.05	53.19	34.61	50.39	1.39	0.65	0.72	FRII	20.44		
9434	J211441-495645	318.67	-49.946	0.103	62.06	28.28	59.5	1.84	0.46	0.50	FRI	18.69		
9442	J211442-561449	318.68	-56.247	0.01	66.86	28.59	66.86	2.24	0.41	0.44	FRI	17.95	8000056451001460	0.25
9410	J211446-601012	318.7	-60.17	0.044	88.9	41.76	82.27	2.85	0.49	0.52	FRx	18	8000044237003380	0.31
9442	J211448-535911	318.7	-53.986	0.012	71.44	29.53	57.8	0.98	0.49	0.53	FRx	21.13		
9442	J211448-574701	318.7	-57.784	0.003	53.19		53.19	1.07			single	20.78	8000051711001450	0.67
9442	J211457-571849	318.74	-57.314	0.03	118.43	83.49	118.43	0.38	0.69	0.72	FRII	18.79		
9410	J211503-601040	318.77	-60.178	0.005	80.01	44.31	80.01	0.51	0.54	0.57	FRII	18.1	8000044237003590	0.3
9434	J211505-510003	318.77	-51.001	0.15	144.59	91.67	131.22	0.8	0.69	0.71	FRII	18.91		
9442	J211508-571818	318.79	-57.305	0.002	76.48	41.1	76.48	1.9	0.52	0.56	FRII	20.82	8000053270001230	0.55
9442	J211509-542241	318.79	-54.378	0.01	57.79	22	49.42	1.53	0.42	0.47	FRI	18.99	8000062217004760	0.32
9434	J211513-500428	318.81	-50.074	0.019	95.73	48.7	82.4	0.35	0.57	0.61	FRII	19.18	8000078181001100	0.43
9410	J211516-625240	318.82	-62.878	0.01	54.15	22.63	48.06	2.36	0.45	0.50	FRI	21.68	8000036646006680	0.48
9442	J211520-562100	318.83	-56.35	0.024	78.55	56.07	56.07	2.1	0.45	0.50	single	19.22	8000056452000360	0.43
9434	J211524-531121	318.85	-53.189	0.007	143.76	93.72	143.76	2.66	0.64	0.66	FRII	16.99	8000066491002750	0.18
9434	J211531-523856	318.88	-52.649	0.009	143.76	80.01	143.76	2.22	0.55	0.57	FRII	21.9	8000068235002870	0.89
9442	J211531-583834	318.88	-58.643	0.009	55.83	20.59	43.01	2.07	0.45	0.51	FRx	20.9		
9442	J211532-562815	318.89	-56.471	0.005	74.23	29.12	51.93	0.26	0.54	0.59	FRII	18.3	8000055648002630	0.25
9434	J211535-513053	318.9	-51.515	0.001	41.66	19.92	41.66	1.62	0.45	0.51	FRx	25.11	8000072683002090	

Continued on next page

Table 4.2 – Continued from previous page

SBID	Source Name	RA (J2000) (deg)	DEC (J2000) (deg)	Flux Density (Jy)	Size (")	a (")	b (")	PA (°)	a/b _{max}	a/b _{min}	Class	Mag (r-band)	DESI ID	Z
9410	J211538-602241	318.91	-60.378	0.02	52.93	17.2	43.08	2.43	0.38	0.42	FRI	23.76		
9442	J211540-554616	318.92	-55.771	0.002	61.44	26.21	61.44	1.03	0.41	0.44	FRI	18.61	8000058073001650	0.28
9442	J211541-565446	318.92	-56.913	0.004	51.45		36.48	0.95			single	21.3	8000054058003200	0.68
9442	J211548-551747	318.95	-55.297	0.015	51.91		47.55	0.33			single	16.39		
9442	J211551-553200	318.97	-55.533	0.016	51.51		47.14	0.62			single	22.2	8000058892001620	0.99
9410	J211555-624827	318.98	-62.808	0.006	65.63		65.63	0.47	0.37	0.40	single	20.1	8000037310001270	0.58
9442	J211555-564702	318.98	-56.784	0.002	75.09	28.71	75.09		0.36	0.40	FRI	21.94	8000054851001550	0.91
9434	J211558-510527	319	-51.091	0.116	52.17	18.44	48.38	2.02			FRI	19.93	8000074496000600	
9442	J211603-544045	319.01	-54.679	0.001	50.29						single	22.23		
9434	J211606-490724	319.03	-49.123	0.002	67.45		67.45	1.4	0.54	0.57	single	17.73	8000081944000070	0.24
9434	J211614-512125	319.06	-51.357	0.045	100.09	48.41	87.81	2.16	0.26	0.27	FRII	21.36	8000073587000270	0.69
9410	J211619-595428	319.08	-59.908	0.066	174.29	46.59	174.29	2.18	0.26	0.27	FRI	18.16		
9410	J211626-604900	319.11	-60.817	0.012	155.82	94.34	128.39	2.45	0.72	0.75	FRII	22.61	8000042809001290	0.9
9434	J211632-530008	319.13	-53.002	0.008	173.94	114.7	173.94	1.67	0.65	0.67	FRII	19.29		
9410	J211634-630118	319.14	-63.022	0.024	192.02	149.91	183.28	1.74	0.81	0.83	FRII	17.42	8000036647002850	0.24
9410	J211634-584528	319.15	-58.758	0.016	38.1		33.68	1.58			single	20.62		
9442	J211637-573429	319.16	-57.575	0.002	53.19		53.19	0.88	0.40	0.42	single	21.56	8000052489000760	0.8
9434	J211639-505639	319.16	-50.944	0.002	90.93	36.97	90.93	0.09	0.40	0.42	FRI	20.64	8000074496003110	0.63
9410	J211640-594556	319.17	-59.766	0.004	60.87	28.28	46.38	1.42	0.58	0.64	FRII	18.83	8000045691002130	0.4
9434	J211641-531745	319.17	-53.296	0.003	57.46	16.4	57.46	3.09	0.27	0.30	FRI	24.72		
9410	J211643-610834	319.18	-61.143	0.004	56.86	26	56.86	2.75	0.44	0.48	FRI	23.87	8000041401004260	0.5
9410	J211647-625841	319.2	-62.978	0.011	188.91	97.2	188.91	2.54	0.51	0.52	FRII	21.12	80000366470004160	0.83
9442	J211651-562829	319.21	-56.475	0.006	67.1	23.59	51.9	0.12	0.43	0.48	FRI	21.67	8000055649002660	0.26
9442	J211651-580446	319.22	-58.079	0.018	259.1	198.06	231.67	2.18	0.85	0.86	FRII	17.36	8000050941000470	0.26
9410	J211653-593034	319.22	-59.509	0.04	62.64		50.52	1.65			single	13.64	8000046424001690	0.04
9434	J211655-515955	319.23	-51.999	0.036	152.51	49.4	152.51	2.21	0.32	0.33	FRI	19.67		
9434	J211656-515214	319.24	-51.871	0.041	203.66	57.3	203.66	2.1	0.28	0.28	FRI	14.44		
9434	J211656-524806	319.24	-52.802	0.006	46.23		37.01	2.98			single	17.14		
9434	J211700-511340	319.25	-51.228	0.009	63.57	32.56	57.43	0.84	0.54	0.59	FRII	15.87		
9442	J211705-541804	319.27	-54.301	0.002	58.97		58.97	0.03			single	22	8000063062001270	0.61
9434	J211706-520750	319.28	-52.131	0.007	86.47	42.79	86.47	0.99	0.48	0.51	FRX	20.9		
9442	J211709-555702	319.29	-55.951	0.007	165.04	101.36	165.04	2.01	0.61	0.62	FRII	18.35	8000057260002850	0.33
9410	J211710-594249	319.3	-59.714	0.173	116.48	62.29	100	0.76	0.61	0.64	FRII	20.95	8000045691003130	0.75
9434	J211713-502544	319.31	-50.429	0.048	58.04	22.8	50.26	2.19	0.43	0.48	FRI	21.47		
9442	J211714-551216	319.31	-55.204	0.018	70.82	26	58.85	1.51	0.42	0.46	FRI	19.2	8000059716002670	0.5
9434	J211715-522340	319.32	-52.394	0.1	120.36	50.16	88.55	1.09	0.55	0.58	FRII	24.98		
9410	J211715-605000	319.32	-60.833	0.006	54.73		54.73	2.64	0.58	0.61	single	19.04		
9434	J211716-490108	319.32	-49.019	0.002	100.34	59.41	100.34		0.45	0.48	FRII	23.92		
9442	J211717-545303	319.32	-54.884	0.129	94.94	42.05	89.97	1.07			FRI	22.98		

Continued on next page

Table 4.2 – Continued from previous page

SBID	Source Name	RA (J2000) (deg)	DEC (J2000) (deg)	Flux Density (Jy)	Size (")	a (")	b (")	PA (°)	a/b _{max}	a/b _{min}	Class	Mag (r-band)	DESI ID	Z
9287	J211718-533826	319.33	-53.641	0.04	160.45	74.64	160.45	2.6	0.46	0.47	FRI	17.55	8000064767003070	0.18
9410	J211719-600535	319.33	-60.093	0.003	53.17	16.85	53.17	0.41	0.30	0.33	FRI	19.84	8000044962000540	0.4
9434	J211721-523434	319.34	-52.576	0.01	94.85	57.29	79.53	1.17	0.70	0.74	FRII	19.7	8000069116000700	0.46
9442	J211722-551624	319.34	-55.273	0.002	94.86	57.59	94.86	0.87	0.59	0.62	FRII	22.76	8000059716001540	1.01
9434	J211725-503424	319.36	-50.573	0.028	164.58	130	153.99	1.31	0.83	0.86	FRII	23.48		
9434	J211731-484244	319.38	-48.712	0.022	100.43	54.92	85.4	0.17	0.62	0.66	FRII	22.09		
9442	J211745-545544	319.44	-54.929	0.007	81.02	42.38	65.99	1.22	0.62	0.67	FRII	20.71	8000060546002960	0.62
9410	J211748-623807	319.45	-62.635	0.003	111.18	62.82	111.18	0.04	0.55	0.58	FRII	18.53	8000037311005140	0.38
9434	J211749-532216	319.46	-53.371	0.001	67.8		67.8	0.96			single	19.06	8000066492000060	0.36
9434	J211801-522328	319.51	-52.391	0.461	57.44	17.05	60.64	0.89	0.27	0.29	FRI	17.61		
9410	J211804-613836	319.52	-61.643	0.003	73.92	41.05	73.92	1.23	0.54	0.57	FRII	22.96	8000040016004390	0.82
9442	J211806-554328	319.53	-55.724	0.005	63.4	27.31	63.4	1.05	0.41	0.45	FRI	23.22	8000058074002310	
9410	J211807-592150	319.53	-59.364	0.074	51.36	16.12	51.36	0.61	0.30	0.33	FRI	19.95		
9410	J211808-630440	319.54	-63.078	0.004	88.48	48.02	88.48	0.63	0.53	0.56	FRII	20.9	8000036648001360	0.65
9410	J211811-582052	319.55	-58.348	0.005	140.5	95.71	140.5	0.69	0.67	0.69	FRII	23.22	8000050176000250	
9442	J211813-533405	319.56	-53.568	0.024	76.56	46.06	70.16	1.59	0.63	0.68	FRII	22.18	8000065627000860	0.95
9442	J211815-552400	319.56	-55.4	0.007	86.25	50	75.05	1.55	0.64	0.69	FRII	21.41	8000058893003630	0.64
9434	J211817-534344	319.57	-53.729	0.001	72.09		72.09	0.05	0.56	0.60	single	22.71	8000064767001850	0.91
9442	J211821-570253	319.57	-57.618	0.002	78.82	45.6	78.82	0.54	0.56	0.60	FRII	23.15	8000052490000030	
9434	J211824-501554	319.6	-50.265	0.005	51.45		39.9	1.79			single	19	8000054059000940	0.4
9287	J211827-492501	319.61	-49.417	0.002	58.04		58.04	2.96			single	20.39	8000077254002180	0.5
9434	J211829-482303	319.62	-48.384	0.001	76.4	46.01	76.4	0.28	0.58	0.62	FRII	20.85	8000080054005340	
9434	J211831-531205	319.63	-53.201	0.149	68.23	30.91	68.23	0.39	0.44	0.47	FRI	20.93		
9287	J211833-483107	319.64	-48.519	0.032	217.27	154.29	184.18	0.22	0.83	0.85	FRII	18.15	8000066492002310	0.11
9287	J211838-504145	319.66	-50.696	0.013	97.88	44.72	84.07	2.99	0.52	0.55	FRII	17.53	8000083854002750	0.25
9434	J211841-501725	319.67	-50.29	0.027	71.23	37.2	62.71	2.2	0.57	0.62	FRII	20.19	8000075411003620	0.43
9410	J211843-602714	319.68	-60.454	0.027	52.93		52.93	1.72			single	22.28	8000077254001770	1.02
9410	J211854-603855	319.73	-60.649	0.01	64.61	25.09	61.14	1.78	0.39	0.43	FRI	17.9	8000043522003440	0.29
9434	J211854-522230	319.73	-52.375	0.022	142.64	79.4	112.7	0.66	0.69	0.72	FRII	18.1	8000042810004330	0.31
9434	J211855-533125	319.73	-53.524	0.004	45.16	18.97	36.09	2.86	0.49	0.56	FRx	22.61	8000069117003290	1.03
9434	J211856-531305	319.74	-53.218	0.012	57.31	26.68	50.04	1.32	0.51	0.56	FRII	23.11		
9442	J211859-561826	319.75	-56.307	0.027	55.89	18.44	52.68	0.69	0.33	0.37	FRI	22		
9434	J211900-483344	319.75	-48.562	0.052	114.13	62.9	94.7	1.08	0.65	0.68	FRII	25.32	8000056454001020	
9442	J211902-540304	319.76	-54.051	0.002	79.37		79.37	1.32			single	10.49		
9434	J211903-494423	319.77	-49.74	0.086	49.51		49.71	0.69			single	22.36	8000063912000990	0.92
9434	J211904-505541	319.77	-50.928	0.033	90.93	28.28	80.3	0.05	0.34	0.36	single	22.29	8000079117003160	0.88
9442	J211909-543329	319.79	-54.558	0.126	63.96		58.83	0.41			FRI	23.24		
9434	J211916-481723	319.82	-48.29	0.068	78.83		78.83	0.9			single	19.74	8000084816002380	0.42

Continued on next page

Table 4.2 – Continued from previous page

SBID	Source Name	RA (J2000) (deg)	DEC (J2000) (deg)	Flux Density (Jy)	Size (")	a (")	b (")	PA (°)	a/b _{max}	a/b _{min}	Class	Mag (r-band)	DESI ID	Z
9434	J211917-503937	319.82	-50.66	0.066	43.1	122.46	47.83	0.7	0.67	0.69	single	20.08		
9410	J211919-622257	319.83	-62.383	0.009	180.31	180.31	180.31	1.54	0.67	0.69	FRII	23.1	8000038652000030	0.99
9410	J211924-621508	319.85	-62.252	0.009	168.79	111.12	168.79	2.41	0.65	0.67	FRII	18.89	8000038652002520	0.41
9434	J211926-481303	319.86	-48.218	0.033	88.88		88.88				single	23.49		
9442	J211928-571450	319.87	-57.247	0.014	136.6	60.13	88.56	2.93	0.66	0.70	FRII	19.5	8000053272001720	0.38
9434	J211936-515448	319.9	-51.913	0.003	58.68		58.68	1.07			single	19.77	8000070892002990	0.4
9434	J211937-510756	319.91	-51.132	0.016	42.91		37.75	0.78			single	23.41	8000073589004180	
9287	J211943-484952	319.93	-48.831	0.042	58.81	28.64	55.73	2.01	0.49	0.54	FRx	24.51		
9410	J211944-593337	319.94	-59.56	0.002	62.64		62.64	2.34			single	20.54	8000046426001190	0.68
9410	J211945-602343	319.94	-60.395	0.026	100.27	62.1	89.66	0.25	0.67	0.71	FRII	24.9	8000043522004690	
9442	J211948-552524	319.95	-55.423	0.271	78.64	23.9	77.5	1.32	0.30	0.32	FRI	21.24	8000058894003230	0.66
9410	J211948-630316	319.95	-63.088	0.015	55.9		47.13	2.26			single	19.08		
9434	J211951-530347	319.97	-53.063	0.02	204.47	148.42	182.8	2.59	0.80	0.82	FRII	15.52	8000067363000820	0.08
9287	J211953-514710	319.97	-51.786	0.006	48.5	20	42.55	0.6	0.44	0.50	FRI	22.31		
9434	J211955-511331	319.98	-51.225	0.009	58.84	29.53	52.59	0.54	0.54	0.59	FRII	22.99		
9442	J211957-564520	319.99	-56.756	0.096	147.24	108.68	137.38	1.84	0.78	0.81	FRII	21.47	8000054853001460	0.94
9287	J211958-482244	319.99	-48.378	0.001	51.07	27.35	51.07	1.42	0.51	0.56	FRII	21.07	8000083855006250	0.54
9287	J212001-520216	320	-52.038	0.002	65.56		65.56	1.28			single	19.67		
9434	J212005-481114	320.02	-48.187	0.008	75.3	29.32	75.3		0.38	0.40	FRII	23.97		
9442	J212010-553728	320.04	-55.624	0.003	81.46	28.82	77.08	2.45	0.36	0.39	FRI	19.75	8000058894000050	0.33
9287	J212013-492542	320.05	-49.428	0.001	61.65	20	61.65	0.59	0.31	0.34	FRI	19.37	8000080055005120	0.44
9434	J212015-493253	320.06	-49.548	0.005	122.95	84.05	122.95	2.1	0.67	0.70	FRII	23.4		
9434	J212015-531023	320.06	-53.173	0.138	75.55	31.62	73.64	1.09	0.42	0.44	FRI	19.53	8000066493002840	0.42
9442	J212021-551336	320.09	-55.227	0.004	56.1	20.05	56.1	1.88	0.34	0.37	FRI	26.7		
9442	J212024-545920	320.1	-54.989	0.063	172.99	79.62	170.18	0.54	0.46	0.47	FRI	18.17	8000060548002000	0.32
9442	J212024-534752	320.1	-53.798	0.031	101.59	54.33	90.25	1.36	0.59	0.62	FRII	19.67		
9434	J212024-525945	320.1	-52.996	0.011	101.88	62.31	101.88	2.44	0.60	0.63	FRII	17.83	8000067363001780	0.25
9434	J212029-505126	320.12	-50.857	0.001	50.04	26.47	50.04	1.23	0.50	0.56	FRII	22.28	8000075412000310	0.78
9410	J212031-595137	320.13	-59.86	0.006	160.04	69.38	160.04	2.95	0.43	0.44	FRI	19.15	8000045693000260	0.39
9442	J212032-560655	320.13	-56.115	0.001	66.23	32.25	66.23		0.47	0.51	FRx	19.83	8000057262000110	0.48
9442	J212032-543802	320.14	-54.634	0.44	57.07		58.51	0.31			single	18.9		
9434	J212034-513439	320.14	-51.578	0.017	44.8	14.04	39.33	2.03	0.34	0.38	FRI	22.29	8000072686000680	0.75
9410	J212034-610405	320.14	-61.068	0.016	69.25	22.36	69.25	2.11	0.31	0.34	FRI	16.6		
9434	J212040-503226	320.17	-50.541	0.143	96.57	61.87	90.88	2.14	0.66	0.70	FRII	20.72	8000076332001830	0.71
9442	J212042-563307	320.18	-56.552	0.036	103.25	67.68	100.35	0.58	0.66	0.69	FRII	22.19		
9410	J212045-624854	320.19	-62.815	0.005	63.09	20.21	63.09	1.18	0.31	0.33	FRI	20.6	8000037312001290	0.57
9434	J212046-493858	320.19	-49.649	0.004	84.28	49.42	84.28	0.55	0.57	0.60	FRII	18.21	8000079118005420	0.36
9442	J212055-552209	320.23	-55.369	0.006	81.46	52.61	81.46	1.42	0.63	0.67	FRII	20.61	8000059718000110	0.28
9410	J212056-611045	320.24	-61.179	0.004	102.65	70.26	102.65	1.3	0.67	0.70	FRII	24.13	8000041403004190	

Continued on next page

Table 4.2 – Continued from previous page

SBID	Source Name	RA (J2000) (deg)	DEC (J2000) (deg)	Flux Density (Jy)	Size (")	a (")	b (")	PA (°)	a/b _{max}	a/b _{min}	Class	Mag (r-band)	DESI ID	Z
9434	J212058-485844	320.25	-48.979	0.008	90.71	48.37	90.71	1.4	0.52	0.55	FR II	17.68	8000081947003620	0.25
9442	J212102-564138	320.26	-56.694	0.014	189.36	48.43	189.36	1.97	0.25	0.26	FRI	17.36	8000054854002070	0.28
9434	J212108-490331	320.28	-49.059	0.002	71.41	28.23	71.41	2.01	0.38	0.41	FRI	19.64	8000081947001740	0.49
9410	J212111-593930	320.3	-59.658	0.009	108.06	60.42	108.06	2	0.55	0.57	FR II	20.1	8000045693003900	0.43
9410	J212113-603958	320.31	-60.666	0.002	57.21	28.31	57.21	1.79	0.47	0.52	FRx	19.57	8000042811004990	0.4
9410	J212121-582730	320.34	-58.458	0.004	86.68	51.72	86.68	0.75	0.58	0.61	FR II	23.38		
9434	J212123-501425	320.35	-50.24	0.004	40.82		50.41	2.47			single	19.8	8000077256002870	0.45
9410	J212127-614011	320.37	-61.67	0.008	104.11	51.32	104.11	2.86	0.48	0.51	FRx	19.91		
9410	J212128-611413	320.37	-61.237	0.002	102.65	69.21	102.65	2.73	0.66	0.69	FR II	23.6		
9410	J212129-604547	320.37	-60.763	0.172	63.98	28.28	61.89	1.74	0.44	0.48	FRI	22.45	8000042812002590	1
9442	J212138-560927	320.41	-56.158	0.006	145.43	89	145.43	1.91	0.60	0.62	FR II	19.8	8000056455002990	0.52
9434	J212142-500147	320.43	-50.03	0.004	46.39		32.39	2.56			single	19.1	8000078185001940	0.24
9434	J212142-491121	320.43	-49.189	0.002	100.43	52.15	88.99	3.1	0.57	0.60	FR II	18.68	800008100004660	0.43
9410	J212148-622524	320.45	-62.423	0.013	52.93		46.07	1.82			single	18.61	8000037980004260	0.35
9434	J212154-501520	320.48	-50.256	0.002	40.82		44	0.61			single	21.85	8000077256002500	0.77
9410	J212155-614904	320.48	-61.818	0.049	55.17	22.8	51.45	0.84	0.42	0.47	FRI	20.12	8000040018001320	0.27
9442	J212156-561244	320.48	-56.212	0.002	78.55	30.58	78.55	1.17	0.38	0.40	FRI	18.05	8000056455002160	0.27
9434	J212156-522701	320.48	-52.45	0.003	95.13	55.03	95.13	0.08	0.56	0.59	FR II	21.3		
9442	J212159-580334	320.5	-58.059	0.002	60.25		60.25	0.77			single	22.89	8000050943000650	1.02
9442	J212204-555503	320.52	-55.918	0.003	35.64	13.06	37.25	1.75	0.33	0.38	FRI	23.23		
9442	J212206-550039	320.53	-55.011	0.028	43.16		42.24	2.14			single	21.68	8000060548001580	0.84
9434	J212208-494055	320.54	-49.682	0.002	54.81	25.98	54.81	2.77	0.45	0.50	FRI	23.04	8000079119004310	0.89
9434	J212210-522119	320.54	-52.355	0.007	97.73	44.14	97.73	2.27	0.44	0.46	FRI	23.34	8000070004000240	0.89
9442	J212214-570653	320.56	-57.115	0.034	62.41		51.25	1.17			single	17.58		
9410	J212215-615600	320.56	-61.933	0.001	55.17	26.13	55.17	1.72	0.45	0.50	FRI	18.65	8000039333004040	0.29
9434	J212219-510453	320.58	-51.081	0.01	41.95	16.12	34.59	1.5	0.43	0.50	FRx			
9410	J212222-614629	320.6	-61.775	0.031	222.92	93.23	222.92	2.66	0.41	0.42	FRI	17.36	8000040018002140	0.18
9434	J212225-494452	320.61	-49.748	0.139	67.51	25.61	58.8	0.64	0.42	0.45	FRI	22.17	8000079119002810	0.97
9434	J212225-484123	320.61	-48.69	0.007	80.94	35.38	60.53	2.36	0.56	0.61	FR II	23.37	8000082899004940	
9434	J212226-533119	320.61	-53.522	0.005	83.93	44.53	83.93	1.82	0.52	0.55	FR II	19.99		
9442	J212228-560055	320.62	-56.015	0.079	216.99		204.34	0.88			single	19.84		
9434	J212233-513814	320.64	-51.637	0.006	89.89	44.24	89.89	2.01	0.48	0.51	FRx	21.49	8000071788002960	0.79
9442	J212235-583810	320.65	-58.636	0.002	51.85		52.73	1.1			single	23.06		
9434	J212239-485904	320.67	-48.984	0.002	38.06	16.45	38.06	1.48	0.41	0.46	FRI	22.78	8000081948003560	0.88
9434	J212240-531648	320.67	-53.28	0.004	94.75	52.98	94.75	1.38	0.54	0.57	FR II	21.8	8000066495001530	0.82
9442	J212244-582634	320.68	-58.443	0.07	70.84		58.07	2.08			single	19.19		
9410	J212253-584619	320.72	-58.772	0.011	85.29	59.46	82.65	2.4	0.70	0.74	FRI	23.87		
9442	J212255-552647	320.73	-55.446	0.015	69.93	18.91	54.94	1.69	0.33	0.36	FR II			
9434	J212304-505355	320.77	-50.899	0.021	41.95		40.09	2.8			single	19.88	8000074500003330	0.55

Continued on next page

Table 4.2 – Continued from previous page

SBID	Source Name	RA (J2000) (deg)	DEC (J2000) (deg)	Flux Density (Jy)	Size (")	a (")	b (")	PA (°)	a/b _{max}	a/b _{min}	Class	Mag (r-band)	DESID	Z
9442	J212308-555442	320.79	-55.912	0.045	53.81	21.54	51.97	2.83	0.40	0.44	FRI	22.26		
9434	J212308-494319	320.79	-49.722	0.065	61.13	24.17	57.51	0.3	0.40	0.44	FRI	23.35		
9410	J212309-591842	320.79	-59.312	0.02	44.68		41.18	2			single	23.3	8000047167001120	
9442	J212315-582718	320.82	-58.455	0.028	288.08	240.15	269.27	1.79	0.88	0.90	FRII	21.26		
9434	J212316-520905	320.82	-52.151	0.017	40.72		36.92	1.67			single			
9410	J212323-602351	320.85	-60.398	0.07	128.97	87.81	128.97	2.46	0.67	0.69	FRII	23.08	8000043524005100	0.75
9434	J212325-532253	320.86	-53.381	0.049	53.07	16.12	48	3.04	0.32	0.35	FRI	24.31		
9434	J212325-531346	320.86	-53.229	0.012	71.23		51.85	1.55			single	22.12		
9410	J212326-590113	320.86	-59.02	0.01	135.13	95.35	113.39	1.43	0.82	0.86	FRII	20.26	8000047912001270	0.48
9442	J212330-555534	320.88	-55.926	0.004	49.06		35.63	0.39			single	21.69	8000057264002470	0.82
9434	J212331-522644	320.88	-52.446	0.004	52.05		40.11	1.75			single	19.99	8000069120002050	0.59
9434	J212332-494509	320.89	-49.753	0.001	40.92	17.52	40.92	1.17	0.40	0.46	FRI	21.5	8000079120003260	0.73
9442	J212337-554957	320.91	-55.833	0.032	54.22		49.18	1.61			single	22.58	8000058077000470	0.98
9442	J212339-583835	320.92	-58.643	0.002	81.61		81.61	1.29			single	22.34	8000048662002540	0.94
9410	J212340-595531	320.92	-59.925	0.013	44.47		39.68	1.21			single	23.39		
9442	J212345-552642	320.94	-55.445	0.001	44.22	20.27	44.22	0.4	0.43	0.49	FRI	16.86		
9434	J212347-522805	320.95	-52.468	0.11	49.18	17.89	49.76	0.78	0.34	0.38	FRI	21.4	8000069120001790	0.73
9410	J212347-605442	320.95	-60.912	0.002	48.11	15.3	48.11	3.09	0.30	0.34	FRI	22.32	8000042105004030	0.55
9434	J212348-534953	320.95	-53.831	0.012	182.1	136.05	182.1	2.12	0.74	0.76	FRII	21.57	8000064771000580	
9434	J212401-492450	321	-49.414	0.008	47.98	20.1	41.3	1.47	0.46	0.52	FRx	18.51	8000080058005200	0.29
9410	J212405-594135	321.02	-59.693	0.009	55.15	22.8	46.06	2.19	0.47	0.52	FRx	23.09		
9442	J212407-583953	321.03	-58.665	0.005	62.43	26	45.76	0.4	0.54	0.60	FRII	20.31	8000048662002290	0.58
9434	J212408-493242	321.03	-49.545	0.001	52.62		52.62	1.71			single	19.53	8000080058001890	0.46
9442	J212409-582304	321.04	-58.384	0.018	62.19	28.43	53.38	2.31	0.51	0.56	FRII	23.93		
9410	J212410-623127	321.04	-62.524	0.068	71.61		63.28	2.5			single	17.37	8000037981002010	0.22
9410	J212414-605755	321.06	-60.965	0.011	48.11		44.9	0.22			single	17	8000042106003600	0.2
9442	J212418-543629	321.08	-54.608	0.009	125.8	94.23	125.8	0.49	0.73	0.76	FRII	23.66		
9434	J212424-494929	321.1	-49.825	0.005	69.02	28.32	69.02	1.14	0.40	0.43	FRI	21.02	8000079121001330	0.77
9410	J212428-600922	321.12	-60.156	0.004	101.18	34	73.27	0.56	0.45	0.48	FRI	23.33		
9442	J212429-562815	321.12	-56.471	0.006	60.26	28.99	60.26	2	0.46	0.50	FRx	23.21	8000055653001720	0.9
9410	J212431-621049	321.13	-62.18	0.054	80.62	38.21	76.83	2.34	0.48	0.51	FRx	19.33	8000038655004760	0.36
9442	J212432-551822	321.14	-55.306	0.003	62.25	30	62.25	0.91	0.46	0.50	FRx	22.74	8000059721001130	0.98
9442	J212433-561858	321.14	-56.316	0.085	92.78		92.17	1.89			single	20.67	8000056457000860	0.29
9442	J212437-553136	321.16	-55.527	0.004	58.82	26	58.82	3.11	0.42	0.46	FRI	22.35	8000058897001290	0.9
9434	J212441-494230	321.17	-49.708	0.023	44.03		37.5	0.85			single	19.61	8000079121004240	0.45
9434	J212448-532724	321.2	-53.457	0.002	62.24	26.83	62.24	0.04	0.41	0.45	FRI	23.48		
9442	J212453-553549	321.22	-55.597	0.028	54.09	21.54	56.04	0.55	0.37	0.40	FRI	23.56		
9434	J212456-492636	321.24	-49.443	0.005	47.98		34.52	0.14			single	21.85	8000080058004350	0.81
9410	J212457-631112	321.24	-63.187	0.01	95.49		95.49				single	21.38	8000035993004200	0.76

Continued on next page

Table 4.2 – Continued from previous page

SBID	Source Name	RA (J2000) (deg)	DEC (J2000) (deg)	Flux Density (Jy)	Size (")	a (")	b (")	PA (°)	a/b_{\max}	a/b_{\min}	Class	Mag (r-band)	DESI ID	Z
9434	J212457-512618	321.24	-51.438	0.008	62.3	16.03	47.61	2.93	0.32	0.36	FRI	19.4	8000072689002620	0.43
9410	J212457-622050	321.24	-62.347	0.006	69.84	37.2	57.5	0.91	0.62	0.68	FRII	23.42		
9410	J212457-615650	321.24	-61.947	0.062	55.17	20.1	55.28	1.78	0.35	0.38	FRI	22.88	8000039334003870	0.94
9410	J212501-583530	321.26	-58.592	0.004	78.52	37.78	78.52	0.9	0.47	0.50	FRI	20.02	8000049418000330	0.46
9410	J212505-594103	321.27	-59.684	0.011	51.73	20	45.52	2.18	0.42	0.46	FRI	21.11	8000045695003340	0.6
9434	J212507-511241	321.28	-51.211	0.009	88.18	38.83	66.49	2.54	0.56	0.61	FRII	20.76	8000073592002450	0.54
9410	J212514-584424	321.31	-58.74	0.005	175.58	85.55	175.58	0.74	0.48	0.49	FRI	18.86	8000048663001630	0.38
9442	J212522-564911	321.34	-56.82	0.008	117.71	89.54	104.24	2.44	0.84	0.88	FRII	19.57	8000054856000620	
9434	J212524-484603	321.35	-48.768	0.012	80.94	41.62	70.21	0.65	0.57	0.61	FRII	19.4	8000082901002860	0.43
9410	J212526-580312	321.36	-58.053	0.012	96.26	49.48	73.03	1.83	0.66	0.70	FRII	20.33		
9410	J212530-602802	321.38	-60.467	0.002	54.07	23.67	54.07	2.81	0.30	0.32	single	19.91	8000043525003480	0.45
9442	J212533-541139	321.39	-54.194	0.032	75.44	32.8	74.57	0.61	0.43	0.46	FRI	19.72		
9434	J212536-533831	321.4	-53.642	0.273	74.34	29.12	69.67	0.43	0.40	0.43	FRI			
9410	J212537-621652	321.41	-62.281	0.01	196.49	162.88	180.01	0.86	0.89	0.92	FRII	21.99	8000038655001920	0.73
9410	J212539-585926	321.42	-58.991	0.008	86.68	40.05	67.15	1.54	0.58	0.62	FRII	21.9		
9434	J212542-525747	321.43	-52.963	0.041	64.68	25.61	55.76	2.24	0.44	0.48	FRI	24.96		
9410	J212542-583019	321.43	-58.505	0.001	66.85	27.46	66.85	0.40	0.40	0.43	FRI	25.66		
9434	J212543-480541	321.43	-48.095	0.031	75.87	23.67	75.87	2.81	0.30	0.32	FRI	22.44	8000085786000790	0.59
9434	J212548-492605	321.45	-49.435	0.002	51.69	53.23	53.23	2.81	0.30	0.32	single	20.99	8000080059005110	0.43
9410	J212551-574800	321.46	-57.8	0.006	80.16	40.5	61.11	0.35	0.64	0.69	FRII	20.01		
9410	J212554-602451	321.48	-60.414	0.008	138.77	54.86	138.77	2.04	0.39	0.40	FRI	15.65	8000043525004640	0.11
9434	J212556-524409	321.49	-52.736	0.002	67.13	34.27	67.13	0.17	0.49	0.53	FRx	20.37	8000068242001750	0.57
9434	J212557-494410	321.49	-49.736	0.001	65.64	32.08	65.64	0.59	0.47	0.51	FRx	20.83	8000079122003650	0.58
9442	J212600-570557	321.5	-57.099	0.003	78.16	29.84	78.16	0.59	0.37	0.39	FRI	23.74		
9434	J212601-523412	321.51	-52.57	0.056	68.86	33.11	65.37	2.78	0.49	0.53	FRx	22.79	8000069121000670	0.85
9434	J212606-484948	321.53	-48.83	0.004	92.85	52.96	72.17	2.57	0.71	0.76	FRII	22.99		
9434	J212610-531026	321.54	-53.174	0.006	89.98	33.77	70.54	2.21	0.46	0.50	FRI	20.5	8000066497003010	0.63
9442	J212613-545052	321.55	-54.848	0.003	139.23	104.72	139.23	0.32	0.74	0.77	FRII	24.1	8000061384000430	
9410	J212613-622355	321.56	-62.399	0.006	45.22	33.96	33.96	2.61	0.44	0.46	single	22.43	8000037982004970	0.24
9434	J212614-531002	321.56	-53.167	0.01	122.32	51.31	114.48	2.88	0.44	0.46	FRI	17.46	8000066497003230	
9442	J212614-552114	321.56	-55.354	2.16	64.25	28.64	64.25	0.57	0.43	0.46	FRI	17.96	8000059722000250	
9434	J212616-525240	321.57	-52.878	0.009	101.27	50.55	101.27	0.46	0.49	0.51	FRx	17.67	8000067367003840	0.27
9434	J212616-510332	321.57	-51.059	0.004	70.35	17.04	40.87	2.64	0.39	0.44	FRI	21.18	8000074502000720	0.68
9434	J212619-534825	321.58	-53.807	0.032	101.21	22.36	84.74	1.93	0.26	0.27	FRI	17.9	8000064772000930	
9442	J212621-551205	321.59	-55.201	0.01	97.37	54.59	80.79	0.51	0.66	0.70	FRII	23.7		
9434	J212622-512854	321.59	-51.482	0.072	176.57	112.17	154.59	2.27	0.71	0.74	FRII	23.7		
9410	J212625-582119	321.61	-58.355	0.006	113.74	72.26	98.61	1.07	0.71	0.75	FRII	22.26	8000050180000110	0.87
9442	J212628-532458	321.62	-53.416	0.005	73.11	23.54	53.5	1.48	0.42	0.46	FRI	22.98	8000065632003170	0.99
9442	J212630-544723	321.63	-54.79	0.002	74.36	40.85	74.36	1.39	0.53	0.57	FRII	20.94	8000061385001390	0.54

Continued on next page

Table 4.2 – Continued from previous page

SBID	Source Name	RA (J2000) (deg)	DEC (J2000) (deg)	Flux Density (Jy)	Size (")	a (")	b (")	PA (°)	a/b _{max}	a/b _{min}	Class	Mag (r-band)	DESI ID	Z
9442	J212633-553029	321.64	-55.508	0.019	55.57	47.61	0.91	0.91			single	23.64		
9434	J212633-520542	321.64	-52.095	0.022	101.71	51.25	84.69	0.94	0.59	0.62	FR II	20.06	8000070897000370	0.58
9442	J212641-543235	321.67	-54.543	0.004	94.81	29.49	94.81	0.2	0.30	0.32	FR I	26.81		
9410	J212641-591317	321.67	-59.221	0.03	94.64	53.85	84.49	2.98	0.62	0.66	FR II	19.35		
9442	J212645-555557	321.69	-55.933	0.001	86.62		86.62				single	20.56	8000057266002730	0.59
9410	J212645-600421	321.69	-60.073	0.01	113.4		113.4	1.99			single	17.85		
9434	J212646-531702	321.69	-53.284	0.057	54.11	20	53.11	2.56	0.36	0.40	FR I	21.91	8000066497001430	0.94
9434	J212647-523555	321.7	-52.599	0.004	34.6	38.05	34.6	1.33	0.63	0.69	single	24.22	8000069122000340	0.54
9434	J212648-492142	321.7	-49.362	0.006	73.61	57.6	57.6	0.06	0.63	0.66	FR II	21.55	8000081003000430	0.79
9434	J212650-520047	321.71	-52.013	0.006	88.18	47.77	69.69	1.45	0.66	0.71	FR II	20.87	8000070897001470	0.79
9410	J212650-591339	321.71	-59.228	0.014	70.57	54.17	54.17	1.64		0.64	single	20.4		
9434	J212651-503657	321.71	-50.616	0.005	61.32	28.07	46.37	1.64	0.57		FR II			
9434	J212651-505236	321.72	-50.877	0.002	51.26		51.26	0.45			single	22.05	8000074503003190	0.83
9442	J212652-571908	321.72	-57.319	0.01	100.22	41.53	100.22	1.03	0.40	0.43	FR I	20.23	8000053276000670	0.64
9442	J212653-543935	321.72	-54.66	0.459	58.69	16.54	60.93	0.64	0.26	0.28	FR I	24.51		
9434	J212656-514852	321.74	-51.814	0.004	78.96	43.27	61.55	0.6	0.68	0.73	FR II	23.68		
9434	J212657-492654	321.74	-49.448	0.007	75.49	39.57	61.87	0.96	0.61	0.67	FR II	21.84	8000080060004710	0.72
9434	J212709-491619	321.79	-49.272	0.005	56.7		56.7	0.91			single	17.33	8000081003002340	0.31
9442	J212709-550238	321.79	-55.044	0.004	60.33		60.33	0.74			single	21.38	8000060551001230	0.66
9410	J212709-625226	321.79	-62.874	0.002	71.61	68.98	85.6	2.29	0.78	0.83	FR II	23.49		
9434	J212711-493307	321.8	-49.552	0.012	102.43	60.17	102.43	0.12	0.57	0.60	FR II	21.98	8000080060002180	0.73
9434	J212719-522213	321.83	-52.37	0.005	53.93	22.36	53.93	0.15	0.40	0.43	FR I	20.49	8000070008000060	0.81
9442	J212720-571300	321.84	-57.217	0.012	140.58	97.05	127.55	1.07	0.75	0.78	FR I	23.58		
9410	J212724-603122	321.85	-60.523	0.001	55.31	30.35	55.31	0.15	0.52	0.57	FR II	24.63	8000043526002380	0.3
9434	J212725-482430	321.85	-48.408	0.012	203.96	159.78	203.96	1.69	0.77	0.79	FR II	17.91	8000083860005310	
9434	J212727-524114	321.86	-52.687	0.008	152.14	114.06	133.28	1.04	0.84	0.87	FR II	23.73		
9442	J212728-572220	321.87	-57.372	0.04	98.85	60.03	95.61	0.88	0.61	0.64	FR II	20.5		
9434	J212730-493719	321.88	-49.622	0.003	38.26	14.53	38.26	1.57	0.36	0.41	FR I	21.65	8000045696002950	0.46
9442	J212732-583744	321.88	-58.629	0.011	57.52	28.07	52.2	1.45	0.51	0.56	FR II	24.05		
9442	J212735-572542	321.9	-57.428	0.001	49.41		49.41	0.92			single	21.11		
9410	J212750-602626	321.96	-60.44	0.002	158.83	132.04	158.83	0.16	0.82	0.84	FR II	18	8000043526004360	0.17
9410	J212750-594312	321.96	-59.72	0.003	63.62	25.69	63.62	2.6	0.39	0.42	FR I	19.78	8000045696002950	0.46
9434	J212751-511935	321.97	-51.326	0.002	57.63		57.63	0.87			single			
9442	J212752-552208	321.97	-55.369	0.132	101.89	45.61	90.81	1.27	0.49	0.52	FRx	19.25	8000059722000100	0.29
9434	J212753-515021	321.97	-51.839	0.002	100.37	68.57	100.37	0.78	0.67	0.70	FR II	24.53		
9442	J212757-551700	321.99	-55.283	0.005	85.42	49.33	85.42	1.25	0.56	0.59	FR II	21.19	8000059723001520	0.71
9442	J212759-550340	322	-55.061	0.004	50.97		50.97	1.55			single	20.93	8000060552001250	0.71
9442	J212803-544643	322.01	-54.779	0.003	104.96	59.15	104.96	0.62	0.55	0.58	FR II	17.95	8000079123003640	0.21
9434	J212807-494422	322.03	-49.739	0.006	81.3		81.3	3			single			

Continued on next page

Table 4.2 – Continued from previous page

SBID	Source Name	RA (J2000) (deg)	DEC (J2000) (deg)	Flux Density (Jy)	Size (")	a (")	b (")	PA (°)	a/b _{max}	a/b _{min}	Class	Mag (r-band)	DESI ID	Z
9410	J212808-583601	322.03	-58.6	0.071	65.41	30	61.52	2.22	0.47	0.51	FRx	24.22		
9410	J212811-603340	322.05	-60.561	0.014	105.67	41.64	105.67	0.25	0.38	0.40	FRI	17.25	8000043526001470	0.28
9434	J212811-501338	322.05	-50.227	0.001	50.67		50.67	0.11			single	20.81	8000077260002950	0.64
9434	J212818-520636	322.08	-52.11	0.017	53.17	21.54	53.17	2.72	0.39	0.43	FRI	19.13	8000070898000200	0.14
10083	J212822-572115	322.09	-57.354	0.001	64.81		64.81	0.88			single	20.6		
9442	J212827-550543	322.12	-55.095	0.026	107.86	48.04	93.03	1.5	0.50	0.53	FRII	16.88		
10083	J212829-574307	322.12	-57.719	0.005	49.38		49.38	2.72			single	23.55	8000071791001780	0.84
9434	J212831-514508	322.13	-51.752	0.135	67.1	32.25	64.99	0.13	0.48	0.52	FRx	21.82		
9442	J212834-544626	322.14	-54.774	0.003	55.13	14.14	36.92	0.09	0.36	0.41	FRI	24.25		
9410	J212835-602213	322.15	-60.37	0.029	189.19	46.32	189.19	2.38	0.24	0.25	FRI	15.67	8000044244000040	0.1
9434	J212839-490035	322.16	-49.01	0.035	154.08	112.83	153.92	1.29	0.72	0.75	FRII	16.67	8000081952002750	0.17
9442	J212844-550152	322.19	-55.031	0.015	42.54		42.54	0.25			single	24.76		
9410	J212845-611608	322.19	-61.269	0.004	63.35	42.66	63.35	1.66	0.65	0.70	FRII	23.19	8000041406002860	
9410	J212850-605915	322.21	-60.988	0.007	81.54	46.69	68.84	0.73	0.65	0.70	FRII	23.62	8000042108003970	
9442	J212853-562810	322.22	-56.469	0.001	56.05		56.05	0.77			single	23.18	8000055656001930	
9434	J212902-530632	322.26	-53.109	0.002	115.39	86.48	115.39	1.32	0.73	0.77	FRII	22.74	8000067368000260	0.91
9442	J212902-580029	322.26	-58.008	0.019	223.95	169.2	223.95	1.65	0.75	0.76	FRII	19.83	8000050947001720	0.41
9434	J212908-520620	322.29	-52.106	0.001	55.22		55.22	0.17			single	17.68	8000070898000270	0.14
9501	J212909-621055	322.29	-62.182	0.011	73.05	38.42	63.17	0.62	0.59	0.63	FRII	24.31		
10083	J212829-555442	322.31	-55.912	0.011	42.47		40	1.13			single	20.39	8000057267003420	0.65
9434	J212917-512557	322.32	-51.433	0.003	109.48	62.09	109.48	1.86	0.55	0.58	FRII	20.28		
9434	J212918-505208	322.33	-50.869	0.315	232.64	40.66	166.98	0.7	0.24	0.25	FRI	14.92		
9434	J212920-494708	322.33	-49.786	0.023	121	79.22	106.1	0.34	0.73	0.76	FRII	23.24		
9434	J212920-515250	322.34	-51.881	0.001	73.58		73.58	0.16			single	18.57	8000079124002310	0.33
9410	J212922-571754	322.34	-57.298	0.011	96.26	48.17	76.92	1.45	0.61	0.65	FRII	17.59	8000053278001250	0.35
9442	J212923-565126	322.35	-56.857	0.005	191.47	134.14	191.47	1.23	0.69	0.71	FRII	19.03	8000054858000220	0.37
9434	J212924-484045	322.35	-48.679	0.07	92.85	48.83	86.26	2.54	0.55	0.58	FRII	20.63	8000082904005320	0.66
9434	J212925-481325	322.36	-48.224	0.033	115.54	58.51	115.54		0.50	0.52	FRx	18.16	8000084823003480	0.28
9442	J212925-555139	322.36	-55.861	0.302	80.42	32.8	68.48	2.53	0.46	0.50	FRI	22.19	8000058080000190	1.01
9434	J212928-534922	322.37	-53.823	0.116	68.47	22.8	60.56	2.96	0.36	0.39	FRI	18.01		
9434	J212933-534146	322.39	-53.696	0.035	400.26	349.69	400.26	2.83	0.87	0.88	FRII	24.17		
9410	J212948-590945	322.45	-59.163	0.001	36.31	10.28	36.31	0.22	0.26	0.30	FRI	24.56	8000047170002990	0.38
9434	J212949-494557	322.46	-49.766	0.013	46.11		42.74	1.37			single	18.68	8000079124002700	
9410	J212952-592716	322.47	-59.454	0.001	59.57	25.44	59.57	0.98	0.41	0.45	FRI	20.77		
9442	J212953-550438	322.47	-55.077	0.022	136.17	85.59	117.79	0.98	0.71	0.74	FRII	22.68	8000060553000840	0.79
10083	J212959-564027	322.5	-56.674	0.005	58		58	1.91			single	18.07	8000054859002140	0.29
9501	J213002-620501	322.51	-62.084	0.005	106.14	73.13	106.14	2.53	0.67	0.71	FRII	23.39		
9501	J213003-615158	322.51	-61.866	0.002	68.29	35.31	68.29	1.33	0.50	0.54	FRx	23.7	8000040022000220	1.16
9501	J213007-613847	322.53	-61.646	0.046	85.1	52.04	80.25	1.62	0.63	0.67	FRII	23.16	8000040022006040	1.16

Continued on next page

Table 4.2 – Continued from previous page

SBID	Source Name	RA (J2000) (deg)	DEC (J2000) (deg)	Flux Density (Jy)	Size (")	a (")	b (")	PA (°)	a/b_{\max}	a/b_{\min}	Class	Mag (r-band)	DESI ID	Z
9434	J213012-555551	322.55	-53.931	0.007	74.92	19.26	53.3	0.69	0.36	0.39	single	20.35	8000063919003340	0.42
10083	J213013-543824	322.56	-54.64	0.001	51.75	19.26	51.75	0.82	0.36	0.39	FRI	23.81		
9410	J213017-582504	322.57	-58.418	0.074	50.32	45.96	45.96	0.81	0.67	0.71	single	20.4	8000049421002990	0.42
9410	J213019-590058	322.58	-59.016	0.008	89.59	55.21	80.5	1.39	0.67	0.71	FRII	20.12	8000047916001220	0.41
9434	J213019-503932	322.58	-50.659	0.002	50.57	26	50.57	0.9	0.49	0.54	FRx	21.23	8000075418003490	0.57
9442	J213019-541749	322.58	-54.297	0.004	71.04	30.01	71.04	1.13	0.41	0.44	FRI	20.61	8000063070001250	0.56
9501	J213022-603238	322.59	-60.544	0.022	212.22	99.22	212.22	0.15	0.46	0.47	FRI	17.28	8000043528001770	0.18
9442	J213022-540748	322.59	-54.13	0.006	181.86	138.92	154.85	2.41	0.88	0.91	FRII	21.55	8000063070003880	0.85
9410	J213025-585042	322.61	-58.845	0.137	79.96	40.05	73.21	1.55	0.53	0.57	FRII	21.44		
9434	J213026-495314	322.61	-49.887	0.004	135.88	102.77	135.88	0.58	0.74	0.77	FRII	18.52	8000078191005620	
9434	J213026-503735	322.61	-50.626	0.005	74.76	30.27	53.88	3.02	0.54	0.59	FRII	21.02	8000075419004190	0.62
9442	J213027-545127	322.62	-54.858	0.366	125.34	72.8	120.39	0.64	0.59	0.62	FRII	20.66	8000061387000170	0.63
9434	J213027-501942	322.62	-50.328	0.005	92.04	61.54	92.04	1.23	0.65	0.69	FRII	20.5	8000077262001130	0.4
9434	J213028-482503	322.62	-48.418	0.014	103.39	74.94	92.01	0.79	0.79	0.84	FRII	18.22		
9410	J213034-610237	322.64	-61.044	0.015	92.19	54.33	79.7	1.67	0.66	0.70	FRII	19.63		
9434	J213036-515126	322.65	-51.857	0.001	41.86	15.43	41.86	2.55	0.35	0.39	FRI	19.91	8000071793000270	0.31
9410	J213040-622737	322.67	-62.46	0.007	39.31	33.95	33.95	2.46	0.36	0.40	single	20.45		
9434	J213043-500641	322.68	-50.111	0.003	50.67	19.15	50.67	0.73	0.36	0.40	FRI	17.58	8000078191000250	0.27
9410	J213044-630018	322.69	-63.005	0.008	74.16	33.53	56.56	0.33	0.57	0.62	FRII	22.52	8000036653003160	0.94
9442	J213048-542021	322.7	-54.339	0.196	53.89	40.79	48.27	0.01	0.48	0.51	single	22.7		
9434	J213050-533328	322.71	-53.558	0.035	83.09	40.79	83.09	1.23	0.48	0.51	FRx	18.54		
9434	J213054-485723	322.73	-48.956	0.144	102.85		97.61	0.7			single	18.44	8000081953004370	0.24
9434	J213055-515242	322.73	-51.878	0.004	68.87	39.24	68.87	0.43	0.35	0.37	single	19.84	8000070899003560	0.46
9434	J213058-514445	322.74	-51.746	0.006	134.76	108.58	108.58	1.64	0.35	0.37	single	17.91	8000071793001660	0.32
9434	J213103-483724	322.76	-48.623	0.006	59.47	30	52.41	0.85	0.55	0.60	FRII	18.65	8000082905006770	0.33
9434	J213106-493555	322.78	-49.599	0.013	70.32	39.7	63.9	0.72	0.60	0.65	FRII	18.65	8000080063000740	0.42
10083	J213107-550434	322.78	-55.076	0.002	40.46	9.52	40.46	1.56	0.22	0.25	FRI	23.6	8000060554000810	0.26
9434	J213112-523533	322.8	-52.593	0.014	75.98		75.98	0.23	0.39	0.43	single	18.35	8000069125000490	0.7
9410	J213114-581519	322.81	-58.255	0.001	46.11	18.72	46.11	0.36	0.39	0.43	FRI	22.61	8000050183002240	
9434	J213121-521058	322.84	-52.183	0.002	47.57	30.46	47.57	2.27	0.54	0.59	single	18.67	8000078192004840	
9434	J213122-495602	322.85	-49.934	0.008	74.56	30.46	54.12	2.74	0.54	0.59	FRII	25.83	8000062227001290	
10083	J213125-543203	322.86	-54.534	0.089	52.42	68.35	54.57	0.43	0.70	0.73	single	21.61		
9434	J213125-524814	322.86	-52.804	0.064	105.45	32.98	95.61	2.73	0.50	0.54	FRx	19.66		
9442	J213129-541025	322.87	-54.174	0.053	75.7	32.98	63.8	1.79	0.50	0.54	FRII	28.58		
10083	J213135-565224	322.9	-56.873	0.027	162.93	106.08	143.83	2.98	0.72	0.75	FRII	22.64		
9434	J213136-495020	322.9	-49.839	0.001	59.49	26.29	59.49	0.42	0.42	0.46	FRI	24.4		
9410	J213136-582248	322.9	-58.38	0.251	74.8	29.73	72.77	0.67	0.40	0.42	FRI	21.81	8000049422003970	0.87
9434	J213137-501600	322.91	-50.267	0.004	50.4	23.41	41.62	1.24	0.53	0.60	FRII	24.04		
9501	J213141-602932	322.92	-60.492	0.037	134.23	93.11	134.23	2.94	0.68	0.71	FRII	21.84		

Continued on next page

Table 4.2 – Continued from previous page

SBID	Source Name	RA (J2000) (deg)	DEC (J2000) (deg)	Flux Density (Jy)	Size (")	a (")	b (")	PA (°)	a/b _{max}	a/b _{min}	Class	Mag (r-band)	DESI ID	Z
9410	J213146-595318	322.94	-59.888	0.001	55.77	37.31	55.77	2.76	0.64	0.70	FR II	20.51		
10083	J213148-543943	322.95	-54.662	0.004	55.7	49.23	55.7	2.47	0.36	0.40	FR I	21.09	8000061388003100	0.7
9434	J213150-481043	322.96	-48.179	0.006	96.08	21.22	96.08		0.50	0.53	FR x	19.47	8000084825006330	0.41
9434	J213151-493346	322.96	-49.563	0.001	101.91	74.67	101.91	0.59	0.72	0.75	FR II	22.95	8000080063001680	0.9
9501	J213152-613029	322.97	-61.508	0.001	131.99	95.94	131.99		0.71	0.74	FR II	22.51	8000040713003780	0.72
9434	J213157-513829	322.99	-51.641	0.005	63.63	30.59	52.43	1.76	0.56	0.61	FR II	20.27	80000071794003380	0.61
9410	J213158-582400	322.99	-58.4	0.005	64.9	30.14	54.84	1.32	0.53	0.58	FR II	24.35		
9434	J213201-534812	323.01	-53.803	0.465	59.48	22.36	62.9	2.53	0.34	0.37	FR I	19.5	8000064776001030	0.25
9434	J213201-495513	323.01	-49.92	0.044	50.98	18.97	47.61	2.03	0.38	0.42	FR I	23.21	8000078192005240	
9434	J213202-483132	323.01	-48.526	0.015	42.68	10.31	38.37	1.33	0.25	0.29	FR I	17.81	8000083863002910	0.24
9442	J213202-582407	323.01	-58.402	0.014	38.08		38.2	2.08			single	21.29	8000049422003530	0.83
9442	J213204-571627	323.02	-57.274	0.013	146.95	98.8	123.67	1.2	0.78	0.82	FR II	18.92	8000053279001620	0.48
10083	J213204-541715	323.02	-54.288	0.004	63.55	21.84	63.55	0.98	0.33	0.36	FR I	19.9	8000063071001500	
9410	J213205-605857	323.02	-60.983	0.389	100.1	50.16	84.45	1.47	0.58	0.61	FR II	23.73		
10083	J213206-570350	323.03	-57.064	0.021	41.19	16.12	41.1	2.36	0.37	0.42	FR I	24.31		
10083	J213207-570521	323.03	-57.089	0.002	113.42	82.22	113.42	0.51	0.71	0.74	FR II	22.66	8000054067000580	1.08
9434	J213207-500521	323.03	-50.089	0.013	113.45	44.57	113.45	1.65	0.38	0.40	FR I	20.92	8000078192000830	0.52
9410	J213207-502615	323.03	-50.438	0.003	202.16	163.05	202.16	1.95	0.80	0.82	FR II	20.48	8000076339003560	0.5
9410	J213209-595351	323.04	-59.898	0.001	55.77		55.77	1.97			single	20.49	8000044969005110	0.46
9410	J213211-620403	323.05	-62.068	0.002	92	56.54	92	3.02	0.60	0.63	FR II	22.88	8000039338001910	0.9
9434	J213211-504438	323.05	-50.744	0.012	46.95	20.88	46.95	0.4	0.42	0.47	FR I	25.19		
9434	J213215-493646	323.06	-49.613	0.002	75.89	31.62	75.89	0.89	0.40	0.43	FR I	21.96	8000080063000430	0.66
10083	J213219-542005	323.08	-54.335	0.007	85.54	38.83	65.24	1.79	0.57	0.62	FR II	24.12		
9434	J213222-534817	323.09	-53.805	0.003	69.21	31.27	69.21	1.82	0.44	0.47	FR I	22.89	8000064776001000	
9501	J213226-584253	323.11	-58.715	0.003	63.23	18.44	63.23	2.85	0.28	0.30	FR I	19.86	8000048667002090	0.49
9501	J213229-622453	323.12	-62.415	0.019	93.7	52.17	84.68	1.46	0.60	0.63	FR II	15.44	8000037985006690	0.1
9434	J213232-491450	323.13	-49.247	0.009	175.27	111.83	175.27	1.29	0.63	0.65	FR II	17.9	8000081007003360	0.27
10083	J213234-554111	323.14	-55.686	0.032	153.34	25.12	118.61	1.15	0.21	0.22	FR I	15.85		
10083	J213238-554800	323.16	-55.8	0.004	57.95	21.05	57.95	1.13	0.35	0.38	FR I	19.75	8000058082001110	0.46
10083	J213242-571637	323.18	-57.277	0.006	137.81	50.64	137.81	0.12	0.36	0.37	FR I	19.52	8000053279001720	0.44
9434	J213245-493217	323.19	-49.538	0.036	92.16	33.29	75.42	1.06	0.43	0.46	FR I	19.82	8000080064002220	0.58
9410	J213246-601618	323.19	-60.272	0.05	47.28	42.39	42.39	0.68			single	24.19		
10083	J213250-561608	323.21	-56.269	0.029	64.75	26.68	59.35	1.21	0.43	0.47	FR I	24.2		
9442	J213250-575139	323.21	-57.861	0.011	81.75	39.45	70.08	2.64	0.54	0.58	FR II	23.48	8000051721000290	
9410	J213252-610017	323.22	-61.005	0.25	66.62	30.59	64.82	1.29	0.45	0.49	FR I	20.14		
9434	J213254-494218	323.23	-49.705	0.014	110.18	42.19	110.18	0.12	0.37	0.39	FR I	17	8000079126004590	
9442	J213254-542712	323.23	-54.453	0.017	115.66	67.48	94.75	1.36	0.69	0.73	FR II	16.61		
9501	J213254-601939	323.23	-60.328	0.002	44.52		44.55	2.72			single	23.21		
9434	J213259-520127	323.25	-52.024	0.007	44.62	23.32	43.63	2.16	0.51	0.57	FR II	22.28	8000070901001790	0.74

Continued on next page

Table 4.2 – Continued from previous page

SBID	Source Name	RA (J2000) (deg)	DEC (J2000) (deg)	Flux Density (Jy)	Size (")	a (")	b (")	PA (°)	a/b_{\max}	a/b_{\min}	Class	Mag (r-band)	DESI ID	Z
9410	J213300-573116	323.25	-57.521	0.005	96.26	58.87	76.16	0.64	0.75	0.80	FR II			
9501	J213302-622711	323.26	-62.453	0.023	112.35	70.68	107.97	1.99	0.64	0.67	FR II	23.1	8000037985005750	1.02
9442	J213302-561854	323.26	-56.315	0.005	98.72	56.41	75.42	2.76	0.72	0.77	FR II	17.16		
9434	J213305-483015	323.27	-48.504	0.446	53.63	17.45	53.63	2.37	0.31	0.34	FR I	19.27		
10083	J213305-570256	323.27	-57.049	0.001	52.97	21.55	52.97		0.39	0.43	FR I	17.27		
9501	J213305-613700	323.27	-61.617	0.013	57.38	25.06	48.67	1.08	0.49	0.54	FRx	24.84		
9434	J213307-535319	323.28	-53.889	0.005	133.13	35.76	133.13	1	0.26	0.27	FR I	18.13	8000063921004050	0.27
9501	J213307-612656	323.28	-61.449	0.057	108.27	67.47	97.25	1.3	0.68	0.71	FR II	21.09	8000040713005490	0.77
9434	J213308-493559	323.29	-49.6	0.016	50.18		39.65	0.53			single			
9501	J213312-614621	323.3	-61.773	0.006	43.48	18.44	37.72	1.57	0.46	0.52	FRx	24.87		
9434	J213312-493108	323.3	-49.519	0.004	59.7		59.7	1.58			single	25.35	8000080064002860	
9442	J213313-583215	323.31	-58.538	0.005	211.89	168.53	211.89	0.71	0.79	0.80	FR II	20.38	8000049422001200	0.52
9434	J213315-481836	323.32	-48.31	0.014	83.57	37.94	83.57	2.29	0.44	0.47	FR I	20.17	8000084825002200	0.56
9434	J213317-521958	323.32	-52.333	0.005	55.1		55.1	2.23			single	19.48		
10083	J213318-582428	323.33	-58.408	0.026	43.85	16	40.11	1.6	0.38	0.43	FR I	19.98		
10083	J213323-551940	323.35	-55.328	0.002	65.93	33.81	65.93	0.83	0.49	0.53	FRx	22.46	8000059726000890	0.85
10083	J213323-562617	323.35	-56.225	0.003	60.26	19.82	60.26	2	0.32	0.34	FR I	23.96		
10083	J213324-561331	323.35	-56.258	0.004	73.27		73.27	0.66			single	18.35	8000056462002250	0.27
10083	J213327-542822	323.36	-54.473	0.018	45.74	16.97	43.67	2.47	0.37	0.41	FR I	23.86		
9442	J213327-563707	323.37	-56.619	0.024	78.16	22.63	67.45	0.91	0.32	0.35	FR I	20.79	8000055658000080	0.74
9410	J213328-590909	323.37	-59.153	0.001	89.59	58.76	89.59		0.64	0.67	FR II	21.75	8000047172003730	0.66
9434	J213335-502930	323.4	-50.492	0.004	78.48	28.73	78.48	0.66	0.35	0.38	FR I	22.33	8000076340003190	0.95
9501	J213335-621454	323.4	-62.248	0.002	87.62	46.42	87.62	2.52	0.52	0.55	FR II	23.03		
9434	J213339-531804	323.42	-53.301	0.082	200.05	133.05	181.31	1.98	0.72	0.74	FR II	14.96	8000066501001020	0.07
10083	J213340-581347	323.42	-58.23	0.031	64.58	31.3	60.88	2.7	0.49	0.54	FRx	23.48	8000050184003010	0.81
9434	J213341-525146	323.43	-52.863	0.006	64.25	30.27	58.01	3.01	0.50	0.55	FR II	21.33	8000040713004390	0.81
9442	J213342-573653	323.43	-57.615	0.005	64.83	32.13	64.83	2.84	0.48	0.52	FRx	21.64	8000068246000160	0.53
9434	J213342-490530	323.43	-49.092	0.004	67.9	38.83	55.77	0.95	0.67	0.73	FR II	19.84	8000052498000180	0.54
9434	J213342-515912	323.43	-51.987	0.007	47.57	12.94	40.18	0.82	0.30	0.34	FR I	20.96	8000081955001010	0.92
9442	J213343-574443	323.43	-57.745	0.012	99.74	44.14	99.74	0.24	0.43	0.45	FR I	18.44		
9410	J213347-613211	323.45	-61.536	0.044	83.39	38.83	83.39	1.46	0.45	0.48	FR I	20.26	8000040713002830	
9442	J213348-575355	323.45	-57.899	0.001	57.24	25.38	57.24	1.28	0.42	0.46	FR I	21.38	8000050950004660	0.69
9434	J213349-503205	323.45	-50.535	0.004	52.95	12.49	34.2	3.01	0.34	0.39	FR I	16.02	8000076340002010	0.18
10083	J213355-563016	323.48	-56.504	0.099	56.1	24.08	55.9	2.52	0.41	0.45	FR I	23.25	8000055659001820	
10083	J213355-564748	323.48	-56.797	0.006	88.97	27.83	88.97	0.63	0.30	0.32	FR I	19.66	8000054861001070	0.5
9434	J213358-503407	323.49	-50.569	0.038	176.57	139.63	166.06	2.48	0.83	0.85	FR II	20.53	8000076340001010	0.67
10083	J213406-561348	323.53	-56.23	0.002	56.31	20.11	56.31	1.06	0.34	0.37	FR I	20.76	8000056462002190	0.6
9434	J213407-515339	323.53	-51.894	0.024	47.57	16.12	42.71	1.13	0.36	0.40	FR I	21.51		

Continued on next page

Table 4.2 – Continued from previous page

SBID	Source Name	RA (J2000) (deg)	DEC (J2000) (deg)	Flux Density (Jy)	Size (")	a (")	b (")	PA (°)	a/b _{max}	a/b _{min}	Class	Mag (r-band)	DESI ID	Z
9410	J213413-603540	323.55	-60.594	0.001	56.44	30.03	56.44		0.51	0.56	FR II	21.06	8000043529000770	0.66
9410	J213414-621400	323.56	-62.233	0.004	142.85	77.58	142.85	2.56	0.53	0.55	FR II	22.59	8000038659004990	0.85
9434	J213420-521855	323.58	-52.315	0.002	69.37	36.79	69.37	0.54	0.51	0.55	FR II	22.13	8000070012001000	0.92
9501	J213427-611547	323.62	-61.263	0.003	81.68	47.99	81.68	1.63	0.57	0.61	FR II	21.45	8000041409003100	
9501	J213431-623322	323.63	-62.556	0.011	84.4	30.83	61.78	1.57	0.48	0.52	FRx	21.78	8000037986002550	0.8
9442	J213433-563053	323.64	-56.515	0.026	60.5	29.73	61.1	0.44	0.47	0.51	FRx	19.05		
9434	J213434-501456	323.64	-50.249	0.001	52.54	14.28	52.54	1.5	0.26	0.29	FR I	21.29	8000077264002880	0.57
9434	J213435-493400	323.65	-49.567	0.007	57.49	42.39	42.39	1.88			single	22.26	8000080065000960	
9501	J213438-600347	323.66	-60.063	0.004	80.36	45	80.36	1.62	0.54	0.58	FR II	22.16	8000044970001460	0.8
9434	J213439-494711	323.67	-49.786	0.001	67.58		67.58	0.91			single	21.32	8000079127002400	0.29
9442	J213445-574341	323.69	-57.728	0.035	40.54	11.19	40.38	1.16	0.26	0.30	FR I	23.31		
9501	J213445-602247	323.69	-60.38	0.008	148.39	105.17	148.39	0.1	0.70	0.72	FR II	18.52	8000043530006970	0.53
9501	J213447-630213	323.71	-63.037	0.004	83.12	31.39	83.12	0.93	0.37	0.39	FR I	19.72	8000036655002440	0.31
9434	J213449-491940	323.71	-49.328	0.001	53.57	23.06	53.57		0.41	0.45	FR I	19.72		
9442	J213450-560834	323.71	-56.143	0.001	58.36	14.77	58.36		0.24	0.26	FR I	19.84	8000056462003500	0.39
9501	J213454-621848	323.73	-62.313	0.169	108.07	57.27	106.06	0.21	0.53	0.55	FR II	20.09	8000038660002090	0.4
9442	J213457-541426	323.74	-54.241	0.003	115.66	85.3	115.66	1.26	0.72	0.75	FR II	22.01	8000063072001970	0.88
9442	J213500-574529	323.75	-57.758	0.107	110.19	71.02	105.45	1.36	0.66	0.69	FR II	22.27	8000051722002660	0.94
9434	J213503-525956	323.76	-52.999	0.007	126.69	61.95	126.67	2.91	0.48	0.50	FR I	18.1	8000067372001910	
9410	J213504-582432	323.77	-58.409	0.009	142.74	66.07	142.74	1.72	0.45	0.47	FR I	20.05	8000049423003430	0.32
9434	J213504-525007	323.77	-52.835	0.081	286.22	54.23	286.03	1.99	0.19	0.19	FR I	17.6		
10083	J213508-541256	323.78	-54.216	0.007	90.63	43.86	71.28	2.72	0.59	0.64	FR II	21.83	8000063073002490	0.69
9434	J213508-494322	323.79	-49.723	0.005	158.17	119.68	158.17	1.68	0.74	0.77	FR II	22.65	8000079128003330	0.84
9501	J213517-620415	323.82	-62.071	0.117	228.54	122	222.31	0.44	0.54	0.56	FR II	17.23	8000039339000980	0.38
9442	J213518-581019	323.83	-58.172	0.011	51.06	41.41	41.41	2.43			single	19.49	8000050185003970	0.38
9501	J213521-624525	323.84	-62.757	0.001	50.83		50.83	3.14			single	20.19	8000037319003660	0.46
9410	J213523-631207	323.84	-63.202	0.069	186.87	36.83	186.87		0.19	0.20	FR I	24.46		
9442	J213523-565405	323.85	-56.901	0.012	84.37	41.62	67.71	2.19	0.59	0.64	FR II	19.52	8000054068003360	0.42
9442	J213523-524542	323.85	-52.762	0.006	119.8	53.74	119.8	1.45	0.44	0.46	FR I	18.98	8000068248002000	0.46
9501	J213526-614100	323.86	-61.683	0.004	55.86		55.86	1.99			single	22	8000040025006320	0.81
9442	J213532-580042	323.89	-58.012	0.002	47.99	47.99	47.99	2.53	0.65	0.67	single	20.76	8000050951002570	0.62
9434	J213536-481410	323.89	-48.236	0.002	153.99	101.01	153.99		0.37	0.40	FR II	17.27	8000084827004320	0.19
9434	J213537-514555	323.91	-51.765	0.002	71.6	27.58	71.6	0.59	0.37	0.40	FR I	23.31		
9434	J213543-484356	323.93	-48.732	0.004	55.26		55.26	0.59			single	20.22	8000082908004050	0.48
9442	J213545-580243	323.94	-58.045	0.015	58.98		44.67	1.17			single	20.21	8000050951001520	
9501	J213548-594009	323.95	-59.669	0.031	62.52	26.83	57.79	0.41	0.45	0.49	FR I	20.23	8000045700004230	0.42
10083	J213557-561011	323.99	-56.17	0.001	37.65	12.83	36.75	1.6	0.33	0.37	FR I	21.58	8000056463002880	0.79
10083	J213558-571136	323.99	-57.193	0.001	61.08	32.87	61.08	1.47	0.52	0.56	FR II	21.62	8000053281003910	0.79
10083	J21300-561436	324	-56.243	0.001	71.55	44.39	71.55		0.60	0.64	FR II	15.28	8000056463001880	0.06

Continued on next page

Table 4.2 – Continued from previous page

SBID	Source Name	RA (J2000) (deg)	DEC (J2000) (deg)	Flux Density (Jy)	Size (")	a (")	b (")	PA (°)	a/b _{max}	a/b _{min}	Class	Mag (r-band)	DESI ID	Z
10083	J213601-555304	324.01	-53.884	0.003	146.34	96.97	146.34	0.91	0.65	0.67	FR II	18.42	8000063923003220	0.27
10083	J213603-562402	324.01	-56.401	0.003	73.27	25.38	73.27	1.43	0.33	0.36	FR I	21.38	8000055660002810	0.65
9410	J213606-612836	324.03	-61.477	0.004	81.15	45.8	81.15	2.14	0.55	0.58	FR II	18.49	8000040715004580	0.31
10083	J213607-574848	324.03	-57.813	0.009	64.61	29.06	64.61	3.09	0.43	0.47	FR I	18.1	8000051722001350	0.3
9501	J213609-613336	324.04	-61.56	0.011	100.56	59.47	86.13	0.84	0.67	0.71	FR II	17.32	8000040715002040	0.19
9442	J213609-551344	324.04	-55.229	0.641	201.81	134.24	196.04	1.01	0.68	0.69	FR II	19.86	8000059727002550	0.3
9442	J213614-534418	324.06	-53.738	0.003	81.88	37.52	81.88	0.81	0.44	0.47	FR I	19.04	8000064778001940	0.45
9501	J213614-584909	324.06	-58.819	0.019	296.09	157.78	296.09	2.87	0.53	0.54	FR II	18.82	8000048669000680	0.36
9501	J213616-574557	324.07	-57.766	0.18	59.53	22.8	62.67	0.73	0.35	0.38	FR I	22.48		
9410	J213618-600910	324.08	-60.153	0.001	58.69	25.45	58.69	1.15	0.42	0.45	FR I	20.92	8000044248006030	0.59
9501	J213623-602836	324.1	-60.477	0.001	61.77	34.87	61.77	1.15	0.54	0.59	FR II			
9434	J213623-480630	324.1	-48.108	0.002	91.06	45.29	91.06	0.48	0.48	0.51	FRx	21.44		
10083	J213624-554724	324.1	-55.79	0.006	69.09	28.69	69.09	0.05	0.40	0.43	FR I	17.27	8000058084001400	0.24
9442	J213624-571730	324.1	-57.292	0.014	96.65	20.59	96.65	2.59	0.21	0.22	FR I	18.28	8000053282001920	0.35
9442	J213626-572714	324.11	-57.454	0.005	165.43	109.45	165.43	0.89	0.65	0.67	FR II	18.19	8000052500003700	0.29
9501	J213630-605933	324.13	-60.993	0.007	117.19	78.8	103	1.09	0.75	0.78	FR II	19.76	8000042112003620	0.57
9434	J213637-512919	324.15	-51.489	0.017	50.12	18.97	45.98	1.93	0.39	0.44	FR I	17.92	8000072696002360	0.27
9501	J213637-624409	324.16	-62.736	0.044	210.42	153.99	198.57	2.79	0.77	0.79	FR II	17.31	8000037319004340	0.25
9501	J213638-583541	324.16	-58.595	0.002	58.18		58.18	2.27			single	19.87		
10083	J213640-544244	324.17	-54.712	0.002	63.41		63.41				single	21.7	8000061390002700	0.67
9434	J213641-523136	324.17	-52.527	0.001	56.68		56.68				single	21.3	8000069128001670	0.65
10083	J213641-561018	324.17	-56.172	0.023	71.55	38.21	68	0.86	0.54	0.58	FR II	24.48		
9501	J213642-575642	324.18	-57.945	0.01	81.98	37.95	81.98	2.43	0.45	0.48	FR I	22.15	8000050951004090	0.81
10083	J213643-561505	324.18	-56.251	0.003	57.67		57.67	0.97			single	17.48	8000056464001660	0.27
9434	J213646-520623	324.2	-52.106	0.006	63.07	32.31	54.71	0.41	0.56	0.62	FR II	22.81	8000070903000280	0.7
9434	J213648-493500	324.2	-49.583	0.005	47.01		47.01	2.48			single	19.55	8000080066001080	0.33
9501	J213649-624022	324.21	-62.673	0.194	80.96	21.73	80.96	2.94	0.26	0.28	FR I	17.9	8000037320005470	0.24
10083	J213654-561629	324.23	-56.275	0.001	53.91		53.91				single	20.28	8000056464001490	0.48
9501	J213655-574309	324.23	-57.719	0.002	51.44		51.44	1.97			single	19.32	8000051723003730	0.39
9501	J213656-585536	324.23	-58.927	0.148	126.52	82.49	118.71	0.88	0.68	0.71	FR II	19.95	8000047919002850	
9501	J213656-612317	324.23	-61.388	0.191	727.53	527.89	727.53	1.53	0.72	0.73	FR II	16.81		
9434	J213703-505537	324.26	-50.927	0.09	84.17	43.27	77.09	0.56	0.54	0.58	FR II	22.92		
9434	J213705-490458	324.27	-49.083	0.009	73.19	38.21	73.19	3	0.50	0.54	FR II	20.94	8000081957001270	0.46
9434	J213705-523319	324.27	-52.555	0.004	56.68	21.26	40.16	0.84	0.50	0.56	FRx	26.28		
10083	J213706-555955	324.28	-53.999	0.002	52.05		52.05	3.03			single	20.04	8000063923001740	0.44
9434	J213711-512336	324.3	-51.393	0.11	50.47	14.64	48.14	1.02	0.29	0.32	FR I	22.5	8000072696004150	1.02
9434	J213713-482257	324.31	-48.383	0.003	51.7	21.82	51.7	2.73	0.40	0.44	FR I	24.02	8000083867007150	
9442	J213714-562920	324.31	-56.489	0.016	85.93	48.04	76.94	0.05	0.60	0.65	FR II	25.5		
9434	J213718-510644	324.33	-51.112	0.002	69.03		69.03	0.33			single	19.38	8000074509000190	0.51

Continued on next page

Table 4.2 – Continued from previous page

SBID	Source Name	RA (J2000) (deg)	DEC (J2000) (deg)	Flux Density (Jy)	Size (")	a (")	b (")	PA (°)	a/b _{max}	a/b _{min}	Class	Mag (r-band)	DESI ID	Z
9442	J213718-540541	324.33	-54.095	0.007	115.66	44.36	115.66	3.03	0.38	0.39	FRI	19.2	8000063923000410	0.42
9434	J213718-513005	324.33	-51.501	0.005	54.77	54.77	54.77	3.06			single	21.06		
9442	J213719-543036	324.33	-54.51	0.008	88.87	41.23	88.87	2.79	0.45	0.48	FRI	20.4	8000062230001480	0.38
9434	J213724-490015	324.35	-49.004	0.013	108.46	71.98	108.46	1.23	0.65	0.68	FRII	23.24	8000081958003260	0.94
9442	J213726-562701	324.36	-56.45	0.009	138.62	101.99	138.62	3.12	0.72	0.75	FRII	20.09	8000055661002240	0.57
9434	J213729-493453	324.37	-49.581	0.01	66.66	46.71	66.66	2.39	0.70	0.73	single	23.19	8000080067001220	1.25
9501	J213731-615950	324.38	-61.997	0.001	129.19	92.14	129.19	0.26	0.70	0.73	FRII	19.93	8000039340003870	0.3
9434	J213732-485419	324.39	-48.905	0.002	69.18	69.18	69.18	1.32			single	18.47	8000081958005980	0.32
9434	J213734-505804	324.4	-50.968	0.027	52.63	41.86	52.63	1.34			single	22.41	8000074509003040	0.94
9501	J213736-574001	324.4	-57.667	0.002	76.06	19.14	76.06	0.24	0.24	0.26	FRI	19.04	8000051723004870	0.3
9442	J213743-572040	324.43	-57.344	0.002	55.68	19.8	55.68	2.47	0.34	0.37	FRI	19.28	8000053282000720	0.27
9410	J213745-624604	324.44	-62.768	0.004	115.98	52.6	115.98	2.35	0.44	0.46	FRI	17.68	8000037320003370	0.24
9434	J213746-481332	324.45	-48.226	0.011	91.06	40.79	91.06	0.44	0.44	0.46	FRI	17.67	8000084828004720	0.24
10083	J213748-561206	324.45	-56.202	0.025	96.47	47.07	81.54	0.2	0.56	0.60	FRII	19.61	8000056464002660	0.5
9434	J213751-512330	324.46	-51.392	0.002	55.34	18.19	55.34	0.38	0.31	0.34	FRI	22.24	8000072697003870	0.89
10083	J213752-532155	324.47	-53.366	0.006	44.93	44.93	36.2	1.3			single	15.63		
10083	J213753-580549	324.47	-58.097	0.011	54.58	46.59	46.59	1.34			single	21.9	8000050952000690	0.75
9434	J213754-501746	324.48	-50.296	0.012	43.97	36.21	36.21	0.81	0.42	0.46	single	25.25	8000077266001950	0.27
9434	J213758-505513	324.49	-50.92	0.002	54.78	23.86	54.78	0.57	0.42	0.46	FRI	19.62	8000074510003930	0.27
9501	J213803-623503	324.52	-62.584	0.039	91.5	36.02	75.46	1.61	0.46	0.49	FRI			
9434	J213804-510343	324.52	-51.062	0.003	66.3	28.8	66.3	0.17	0.42	0.45	FRI			
9501	J213809-593722	324.54	-59.623	0.027	135.31	35.55	118.68	1.27	0.29	0.31	FRI	22.58	8000074510001280	0.93
9434	J213812-512914	324.55	-51.487	0.007	38.3	32.76	32.76	1.95	0.27	0.29	single	17.6	8000046435000060	0.23
9501	J213812-595149	324.55	-59.864	0.004	92.34	25.95	92.34	0.34	0.27	0.29	FRI	26.48	8000072697002210	
9501	J213812-584544	324.55	-58.762	0.003	47.01	47.01	47.01	0.9			single	18.76		
9501	J213813-623847	324.56	-62.646	0.019	46.69	44.88	44.88	2.48			single	19.39		
9501	J213815-621231	324.57	-62.209	0.002	67.83	36.06	67.83	3.09	0.49	0.53	FRx	26.41	8000037320007150	0.24
9501	J213817-581044	324.57	-58.179	0.049	75.42	70.97	70.97	0.08	0.49	0.53	single	19.15		
9434	J213817-513505	324.57	-51.585	0.005	61.53	61.53	61.53	0.43			single	23.22	8000058905001220	0.28
10083	J213818-553345	324.58	-55.563	0.001	52.04	52.04	52.04	1.69	0.74	0.79	single	17.81		
9501	J213819-624326	324.58	-62.724	0.008	100.2	65.97	86.34	1.84	0.66	0.70	FRII	22.68		
10083	J213819-534456	324.58	-53.749	0.1	93.89	58.82	86.98	1.91	0.66	0.70	FRII	16.23		
9501	J213821-605405	324.59	-60.901	0.03	110.23	48.08	110.23	1.74	0.27	0.28	single	16.28	8000042112006160	0.12
9434	J213823-513051	324.6	-51.514	0.031	173.38	173.38	173.38	0.36	0.27	0.28	FRI	16.05	8000072697001690	0.13
10083	J213823-555716	324.6	-53.954	0.002	52.05	52.05	52.05	1.42			single	21.74	8000063924002310	0.75
10083	J213825-555423	324.61	-55.906	0.109	59.87	58.21	58.21	1.56			single	19.64	8000057272004130	
9410	J213828-602555	324.62	-60.432	0.002	56.44	56.44	56.44	1.57			single			
9434	J213830-521240	324.63	-52.211	0.052	112.31	64.05	105.37	0.04	0.59	0.62	FRII	17.16	8000070014002550	0.2
10083	J213832-531453	324.64	-53.248	0.008	50.61	18.44	42.68	0.8	0.41	0.46	FRI	20.19	8000066504002250	0.51

Continued on next page

Table 4.2 – Continued from previous page

SBID	Source Name	RA (J2000) (deg)	DEC (J2000) (deg)	Flux Density (Jy)	Size (")	a (")	b (")	PA (°)	a/b _{max}	a/b _{min}	Class	Mag (r-band)	DESI ID	Z
9410	J213833-603723	324.64	-60.623	0.007	58.21	26.08	45.87	1.58	0.54	0.60	FR II	23.9		
10083	J213834-554637	324.64	-55.777	0.001	48.9	16.57	48.9		0.32	0.36	FR I	18.99	8000058086002060	0.41
9442	J213836-563814	324.65	-56.637	0.02	100.16	54.04	87.83	0.69	0.60	0.63	FR II	19.59		
10083	J213839-574648	324.66	-57.78	0.006	66.69		52.01	2.89			single	19.27	8000051724002360	0.29
10083	J213841-533310	324.67	-53.553	0.012	42.63		39.2	2.34			single	22.77		
10083	J213841-531834	324.67	-53.309	0.014	57.69	10.98	50.33	2.92	0.21	0.23	FR I	17.53	8000066505001050	0.29
9501	J213845-574648	324.69	-57.78	0.024	103.54	69.67	97.99	0.88	0.69	0.73	FR II	20.57	8000051724002340	
9442	J213847-573224	324.7	-57.54	0.017	146.95	91.84	123.61	0.44	0.73	0.76	FR II	17.73	8000052501001830	0.26
9501	J213848-584020	324.7	-58.672	0.014	203.1	163.49	187.38	1.7	0.86	0.88	FR II	21.47	8000048670002170	0.85
9434	J213849-515010	324.71	-51.836	0.075	216.01	87.05	216.01	1.41	0.40	0.41	FR I	17.24		
9434	J213850-485711	324.71	-48.953	0.012	84.75	51.92	77.14	0.25	0.65	0.70	FR II	25.77	8000081959004490	0.29
9501	J213852-625945	324.72	-62.996	0.006	80.8	47.48	67.07	1.7	0.68	0.74	FR II	17.79	8000036657003840	0.95
9434	J213854-490553	324.73	-49.098	0.001	59.98	22.17	59.98	3.13	0.35	0.39	FR I	22.44	8000081959000670	0.95
9434	J213857-493120	324.74	-49.523	0.019	55.39		46.57	3.12			single	21.37	8000080068002400	0.85
9434	J213857-481853	324.74	-48.315	0.015	111.66	68.89	98.37	1.07	0.68	0.72	FR II	22.15	8000084829001840	0.82
9434	J213901-523846	324.76	-52.646	0.034	71.99	36.06	62	1.61	0.56	0.61	FR II	21.63	8000068250004280	0.84
9434	J213904-510456	324.77	-51.082	0.032	48.85	18.87	48.85	2.44	0.37	0.41	FR I	21.04	8000074510000900	0.58
10083	J213904-550334	324.77	-55.059	0.001	55.24	23.75	55.24	0.01	0.41	0.45	FR I	19.22	8000060558001100	0.41
9434	J213906-494007	324.78	-49.669	0.014	69.66	39.85	61.86	1.24	0.62	0.67	FR II	22.83	8000079130005150	0.9
9410	J213906-614958	324.78	-61.833	0.015	74.86	31.63	59.88	3.13	0.51	0.55	FR II	20.1	8000040026001350	0.48
9501	J213908-600201	324.79	-60.034	0.002	71.45	34.16	71.45	0.61	0.46	0.50	FR I	18.68	8000044973002080	0.34
9501	J213912-582858	324.8	-58.483	0.017	65.29	38.42	64.42	2.26	0.57	0.62	FR II	22.81	8000049426002670	1.04
9434	J213913-562127	324.81	-56.358	0.02	71.55	31.11	61.88	0.71	0.48	0.52	FRx	20.76	8000056465000280	0.65
9434	J213918-505438	324.83	-50.911	0.004	88.55	54.97	88.55	1.35	0.60	0.64	FR II	22.52	8000074511004550	0.93
9434	J213919-510950	324.83	-51.164	0.002	54.03	19.97	54.03	1.95	0.35	0.39	FR I	26.32		
9434	J213920-481753	324.83	-48.298	0.004	70.07	33.69	70.07	0.35	0.46	0.50	FR I	18.7	8000084830002010	0.31
9442	J213921-563232	324.84	-56.542	0.016	47.16		37.51	1.54			single	18.14	8000055662001180	0.3
9442	J213929-563801	324.87	-56.634	0.034	90.51	43.86	95.03	2.66	0.45	0.47	FR I	17.89	8000054864003240	0.27
9501	J213932-624809	324.88	-62.803	0.001	58.84		58.84	2.42			single	24.67		
9434	J213934-503539	324.89	-50.594	0.004	63.95		63.95	2.71			single	22.03		
9434	J213936-482247	324.9	-48.38	0.034	43.32		39.26	0.44			single	20.34	8000083868006590	0.24
9434	J213937-492337	324.9	-49.394	0.013	68.97		52.69	0.95			single	17.56	8000080068005540	0.67
10083	J213937-560843	324.91	-56.145	0.002	47.89	13.52	47.89	0.78	0.27	0.30	FR I	21.63	8000056465004110	1.1
9501	J213938-590750	324.91	-59.131	0.009	81.03		81.03	0.41			single	22.29	8000047175005240	0.72
9434	J213939-521534	324.91	-52.259	0.011	62.87	30.53	58.06	2.64	0.50	0.55	FR II	21.08	8000070015002020	0.72
9434	J213941-492201	324.92	-49.367	0.004	53.88	22.36	40.47	0.46	0.52	0.59	FR II	20.48	8000060559003800	0.61
10083	J213943-545414	324.93	-54.904	0.005	50.87		50.87	2	0.49	0.51	single	20.48		
9434	J213944-511530	324.94	-51.258	0.004	113.66	56.84	113.66	3.04	0.49	0.51	FRx	24.86	8000075425001660	0.63
9434	J213947-504709	324.95	-50.786	0.006	35.15		31.51	2.02			single	20.92		

Continued on next page

Table 4.2 – Continued from previous page

SBID	Source Name	RA (J2000) (deg)	DEC (J2000) (deg)	Flux Density (Jy)	Size (")	a (")	b (")	PA (°)	a/b_{\max}	a/b_{\min}	Class	Mag (r-band)	DESI ID	Z
10083	J213947-562135	324.95	-56.36	0.011	55.39	22.8	49.87	1.24	0.44	0.48	FRI	21.51	8000056465000260	0.7
9434	J213948-485324	324.95	-48.89	0.048	112.94	78.04	107.75	1.98	0.71	0.74	FRII	21.53	8000081959005830	0.68
9434	J213949-505413	324.96	-50.904	0.009	125.99	84.63	105.07	1.43	0.79	0.83	FRII	15.73		
10083	J213956-543526	324.98	-54.591	0.03	87.15	50.16	78.96	0.43	0.62	0.66	FRII	20.25	8000062232000560	0.48
9501	J213957-591713	324.99	-59.287	0.019	179.82	106.16	152.32	2.71	0.69	0.71	FRII	17.89	8000047176001800	0.26
9410	J213958-623715	324.99	-62.621	0.035	62.09	24.74	53.06	2.9	0.45	0.49	FRI			
9501	J213959-620340	325	-62.061	0.005	94.97	31.32	94.97	1.86	0.32	0.34	FRI	18.2	8000039341001840	0.32
10083	J213959-544944	325	-54.829	0.002	55.65	55.65	55.65	3.11			single	22.89	8000061392000560	
9434	J214001-514829	325.01	-51.808	0.015	187.1	95.12	187.1	0.4	0.50	0.52	FRII	14.6		
10083	J214002-531027	325.01	-53.174	0.004	142.69	108.28	131.15	2.33	0.81	0.84	FRII	21.7	8000066505003800	0.8
10083	J214004-572147	325.02	-57.363	0.001	46.5	20.53	46.5	0.74	0.42	0.47	FRI	20.91	8000053284000360	0.49
10083	J214004-542829	325.02	-54.475	0.052	68.29	20.4	59.56	2.94	0.33	0.36	FRI	21.97	8000062232002120	0.75
9434	J214010-514414	325.04	-51.739	0.002	75.89	47.27	75.89	0.18	0.60	0.64	FRII	22.04		
9410	J214009-601152	325.04	-60.198	0.008	64.88	33.91	33.91	0.39			single	18.92		
10083	J214017-560011	325.07	-56.003	0.002	59.87	21.34	59.87	0.79	0.34	0.37	FRI	20.54	8000057273002500	0.55
9442	J214024-533546	325.1	-53.596	0.007	130.34	85.63	130.34	0.99	0.64	0.67	FRII	17.82	8000065640000520	0.28
9434	J214025-511220	325.1	-51.206	0.002	99.04	60.81	99.04		0.60	0.63	FRII	19.9	8000073602003200	0.53
9501	J214026-604644	325.11	-60.779	0.006	181.22	75.61	181.22		0.41	0.42	FRI	20.57	8000042821002700	0.57
9434	J214030-495928	325.13	-49.991	0.001	43.55	43.55	43.55	2.87			single	21.76	8000078197003020	0.81
9434	J214031-524105	325.13	-52.685	0.032	52.09	21.63	51.5	0.62	0.40	0.44	FRI	23.23		
9434	J214032-502756	325.14	-50.466	0.007	134.17	86.24	134.17	2.8	0.63	0.65	FRII	18.67	80000763444003150	0.27
9442	J214034-563202	325.15	-56.534	0.007	87.5	53.25	75.78	0.6	0.68	0.73	FRII	21.8	8000055662001270	0.74
10083	J214038-581420	325.16	-58.239	0.008	82.9	26.08	50.68	1.1	0.49	0.54	FRx	18.31	8000050188003060	0.45
9434	J214048-511146	325.2	-51.196	0.003	51.77	26.36	51.77	1.01	0.49	0.54	FRx	23.23	8000073602003390	0.28
9434	J214050-520713	325.21	-52.12	0.006	37.38	11.66	32.95	2.41	0.33	0.38	FRI	22.13	8000070905000100	0.72
10083	J214051-543443	325.21	-54.579	0.033	136.23	102.16	136.23	1.41	0.74	0.76	FRII	24.84		
10083	J214051-544655	325.21	-54.782	0.014	56.7	44.34	44.34	2.97			single	21.06	8000061393001590	0.68
9434	J214053-513044	325.22	-51.512	0.014	196.81	122.05	159.66	2.96	0.75	0.78	FRII	18.15	8000072699001910	0.24
9501	J214053-605852	325.22	-60.981	0.161	104.92	67.23	99.38	1.13	0.66	0.69	FRII	23.45		
10083	J214058-551722	325.24	-55.289	0.216	59.15	26.91	59.77	2.27	0.43	0.47	FRI	17.9	8000059730001640	0.45
9434	J214101-512358	325.26	-51.399	0.006	73.68	34.06	57.74	3.09	0.57	0.62	FRII	18.92	8000072699003710	0.45
9434	J214105-525830	325.27	-52.975	0.01	52.09	44.2	44.2	1.94			single	19.62		
9501	J214106-581518	325.28	-58.255	0.001	57.12	21.72	57.12		0.36	0.40	FRI	20.18	8000050188002760	0.56
9501	J214110-624700	325.29	-62.783	0.01	58.33	32.25	55.47	0.94	0.56	0.61	FRII	22.46	8000037321002510	0.73
9434	J214111-491500	325.3	-49.25	0.028	42.88	16.18	44.26	2.43	0.35	0.39	FRI	22.78	8000081012003420	
10083	J214114-564546	325.31	-56.763	0.001	50.65	50.65	50.65	1.09			single	22.46		
9434	J214115-520818	325.31	-52.138	0.018	44.17	42.71	42.71	2.34			single	22.08	8000070016004410	0.71
10083	J214117-545712	325.32	-54.953	0.009	145.15	116.5	138.08	0.96	0.83	0.86	FRII	23.81		
10083	J214118-553256	325.33	-55.549	0.021	52.04	47.49	47.49	3.14			single	25.86		

Continued on next page

Table 4.2 – Continued from previous page

SBID	Source Name	RA (J2000) (deg)	DEC (J2000) (deg)	Flux Density (Jy)	Size (")	a (")	b (")	PA (°)	a/b _{max}	a/b _{min}	Class	Mag (r-band)	DESI ID	Z
9501	J214119-615819	325.33	-61.972	0.028	87.66	39.73	87.66	0.54	0.44	0.47	FRI	18.24	8000039542004720	0.31
9442	J214123-562153	325.35	-56.365	0.003	92.61	48.21	92.61	2.08	0.51	0.54	FRII	21.68	8000056466000200	0.97
10083	J214127-534537	325.36	-53.76	0.007	49.18	43.45	43.45	2.28			single	18.65	8000064781001760	0.35
10083	J214129-535213	325.37	-53.87	0.002	63.49	31.81	63.49	1.68	0.48	0.52	FRx	21.62		
10083	J214130-570533	325.38	-57.093	0.005	68.67	31.44	68.67	1.92	0.44	0.48	FRI	21.85	8000054072000570	0.82
9501	J214132-595313	325.39	-59.887	0.004	110.47	47.78	110.47	2.98	0.42	0.44	FRI	20.15	8000044974005060	0.56
9434	J214133-501308	325.39	-50.219	0	54.17		54.17				single	21.07	8000077269003490	0.55
9434	J214133-482904	325.39	-48.484	0.01	55.72	22	50.04	1.37	0.42	0.46	FRI	22.6	8000083869004000	1.07
9434	J214135-510549	325.4	-51.097	0.014	71.63	38.21	62.85	2.4	0.58	0.63	FRII	24.03		
10083	J214136-582131	325.4	-58.359	0.086	74.25	28.64	66.31	2.95	0.42	0.45	FRI	18.95	8000050188000370	0.47
9501	J214139-621725	325.41	-62.29	0.011	57.14	45.42	45.42	1.64			single	19.23	8000038663002270	0.28
10083	J214139-573435	325.41	-57.576	0.029	60.38	31.62	58.81	2.07	0.52	0.56	FRII	18.01	8000052503001130	0.56
9501	J214140-585356	325.41	-58.899	0.007	144.05	88.35	144.05	1.01	0.60	0.62	FRII	20.33	8000047922002570	0.56
9501	J214142-600946	325.43	-60.163	0.004	55.98	26.44	46.94	3.09	0.53	0.59	FRII	21.23		
9501	J214152-624106	325.47	-62.685	0.001	89.33	58.19	89.33	2.13	0.63	0.67	FRII	20.67		
9434	J214152-490521	325.47	-49.089	0.002	65.49	35.02	65.49	1.93	0.52	0.56	FRII	24.1	8000081961000920	0.93
9501	J214152-581258	325.47	-58.216	0.01	80.64	35.84	80.64	2.01	0.43	0.46	FRI	20.67	8000050188003650	0.63
9442	J214155-564507	325.48	-56.752	0.001	53.77		53.77	0.33			single			
9434	J214156-494712	325.49	-49.787	0.006	39.15		33.14	2.68			single	25.26		
9434	J214203-490206	325.51	-49.035	0.005	88.43	46.8	67.88	2.85	0.67	0.72	FRII	20.17		
10083	J214205-534155	325.52	-53.699	0.023	58.6	34.99	61.26	0.54	0.55	0.60	FRII	23.52	8000064782002560	0.64
9434	J214207-483701	325.53	-48.617	0.004	54.05	23.48	54.05	0.89	0.42	0.46	FRI	19.63	8000083870000260	0.64
9434	J214211-503407	325.55	-50.569	0.021	60.6	22.09	49.2	1.69	0.43	0.47	FRI	23.79		
9501	J214212-585437	325.55	-58.91	0.06	62.93	26	57.41	1.18	0.43	0.47	FRI	22.01	8000047922002410	0.91
10083	J214213-554836	325.56	-55.81	0.003	39.38	17.2	33.5	2.61	0.48	0.56	FRx	22.81		
9434	J214214-495911	325.56	-49.986	0.001	55.83		55.83	0.03			single			
9434	J214216-512026	325.57	-51.341	0.036	44.03	11.24	43.17	0.14	0.25	0.28	FRI	18.39	8000073603000680	0.35
9501	J214217-610215	325.57	-61.038	0.01	64.64	26.91	50.42	0.71	0.51	0.56	FRII	21.59		
10083	J214221-560709	325.59	-56.119	0.009	50.5	18.87	48.15	2.57	0.37	0.41	FRI	24.04		
9434	J214223-485430	325.6	-48.908	0.024	44.71		39.92	1.38			single	22.03	8000081961006160	0.86
9434	J214223-492631	325.6	-49.442	0.039	54.2		48.86	2.92			single	19.06		
10083	J214230-550126	325.63	-55.024	0.006	95.74	65.6	88.11	0.9	0.72	0.77	FRII	16.4		
9434	J214231-490318	325.63	-49.055	0.005	69.27		69.27	2.96			single	19.5	8000081961001910	0.49
9501	J214232-611458	325.64	-61.249	0.005	95.64	36.3	95.64	0.45	0.37	0.39	FRI	17.19	800004143002890	0.18
9501	J214233-610247	325.64	-61.046	0.008	97.57	52.24	97.57	1.24	0.52	0.55	FRII	18.06	8000042115001590	0.29
9501	J214236-580047	325.65	-58.013	0.002	55.7		55.7	2.44			single	18.41	8000050954002270	0.34
9434	J214239-482445	325.66	-48.413	0.003	104.33	62.9	103.64	0.84	0.59	0.62	FRII	20.91	8000083870005930	0.64
9434	J214239-533750	325.67	-53.631	0.006	98.17	56.6	75.46	0.56	0.73	0.78	FRII	19.76	8000064782003770	0.56
10083	J214242-531810	325.68	-53.303	0.001	63.87	37.81	63.87	1.13	0.57	0.62	FRII	21.97	8000066507001190	0.86

Continued on next page

Table 4.2 – Continued from previous page

SBID	Source Name	RA (J2000) (deg)	DEC (J2000) (deg)	Flux Density (Jy)	Size (")	a (")	b (")	PA (°)	a/b _{max}	a/b _{min}	Class	Mag (r-band)	DESI ID	Z
9501	J214249-610851	325.7	-61.148	0.007	84.01	46.65	67.47	2.12	0.67	0.72	FR II	21.4	8000041413005380	0.73
9434	J214249-512110	325.71	-51.353	0.302	82.35	32.25	71.18	2.15	0.44	0.47	FR I	19.31		
10083	J214251-553308	325.71	-55.552	0.001	69.7	39.99	69.7	0.31	0.55	0.60	FR II	15.57		
9501	J214253-600857	325.72	-60.149	0.007	55.98	25.61	47.46	2.29	0.51	0.57	FR II	25.64	8000044251005710	0.28
9501	J214303-623156	325.76	-62.532	0.1	99.69		75.8	2.08			single	18.16	8000037990002750	0.95
9434	J214304-502135	325.77	-50.36	0.001	37.63		37.63	1.2	0.44	0.49	single	22.58	8000077270000360	0.83
9434	J214306-505343	325.78	-50.895	0.018	48.33	20	43.37	1.42	0.44	0.49	FR I	22.49	8000074513004150	0.83
9501	J214312-620834	325.8	-62.143	0.015	79.23	39.29	68.96	0.55	0.55	0.59	FR II	24.11	8000038663006310	0.25
9434	J214312-501544	325.8	-50.262	0.003	65.76	44.71	65.76	1.83	0.66	0.71	FR II	17.92	8000077270002310	0.18
9501	J214312-612822	325.8	-61.473	0.046	360.28	56.14	360.28	1.47	0.15	0.16	FR I	16.66	8000040718004250	0.58
9434	J214313-512450	325.8	-51.414	0.034	73.44		62.65	0.57			single	20.18	8000072700003670	0.58
9501	J214316-624522	325.82	-62.756	0.005	84.33	48.37	68.71	3.04	0.68	0.73	FR II	20.55	8000037322003500	0.58
9434	J214317-521213	325.82	-52.204	0.067	51.6	23.41	52.77	2.31	0.42	0.47	FR I	20.79	8000070017002900	0.62
9434	J214323-483649	325.85	-48.614	0.235	65.1	27.86	60.63	1.13	0.44	0.48	FR I	22.58	8000083871000290	1.02
10083	J214325-543448	325.86	-54.58	0.002	59.85	37.57	59.85	0.16	0.60	0.66	FR II	22.15	8000062234000590	0.88
10083	J214326-554018	325.86	-55.672	0.005	161.9	98.83	161.9	0.82	0.60	0.62	FR II	18.55	8000058088003700	0.31
9410	J214331-604921	325.88	-60.823	0.017	44.57		38.55	2.99			single	18.17	8000042822001450	0.32
10083	J214332-571016	325.89	-57.171	0.002	79.17	46.99	79.17	1.09	0.58	0.61	FR II	19.74	8000053285004740	0.48
9434	J214334-491948	325.89	-49.33	0.004	85.95	47.7	85.95	0.73	0.54	0.57	FR II	20.09	8000081014001330	0.54
9434	J214338-492827	325.91	-49.474	0.002	57.11	28.55	57.11	2.38	0.48	0.52	FRx			
9434	J214338-493210	325.91	-49.536	0.04	52.5	20.88	51.5	2.85	0.39	0.43	FR I	20.84	8000080071002010	0.61
9434	J214341-523650	325.92	-52.614	0.003	63.2	23.86	63.2	0.36	0.36	0.39	FR I	19.57	8000069132000190	0.43
9434	J214343-522112	325.93	-52.353	0.039	120.7	32.56	120.7	0.8	0.26	0.28	FR I	18.58	8000070018000260	0.33
9501	J214344-611620	325.93	-61.272	0.014	101.23	26.19	101.23	1.92	0.25	0.27	FR I	21.34	8000041414003200	0.7
9434	J214347-503205	325.95	-50.535	0.007	87.66	53.3	87.66	0.65	0.59	0.63	FR II	22.01	8000076346001840	0.7
9434	J214348-513714	325.95	-51.621	0.019	88.97	56.44	88.97	1.03	0.62	0.65	FR II	24.11		
9501	J214353-593611	325.97	-59.603	0.009	76.03	34.93	60	0.36	0.56	0.61	FR II	17.89	8000046438000440	0.3
10083	J214353-551138	325.97	-55.194	0.002	54.07		54.07	0.29			single	21.04	8000059732003550	0.63
9434	J214400-482055	326	-48.349	0.172	503.19	330.95	482.06	1.68	0.68	0.69	FR II	17.17		
9501	J214404-604545	326.02	-60.763	0.025	86.23	46.65	75.3	0.57	0.60	0.64	FR II	18.83	8000042823002800	0.45
9434	J214404-522935	326.02	-52.493	0.005	88.04	52.89	88.04	0.8	0.58	0.62	FR II	20.42	8000069132002340	0.35
9501	J214405-603631	326.03	-60.609	0.002	91.16	36.82	91.16	0.31	0.39	0.42	FR I	19.52	8000043534000240	0.35
9434	J214406-494215	326.03	-49.704	0.006	81.5	46.17	67.01	1.27	0.66	0.72	FR II	23.32		
9434	J214406-483220	326.03	-48.539	0.003	89.43	58.55	89.43	1.63	0.64	0.67	FR II	20.69	8000083871002190	0.63
9501	J214409-630413	326.04	-63.07	0.008	98.95	60.83	81.39	0.75	0.73	0.77	FR II	22.28	8000036659001560	0.91
9434	J214411-521228	326.05	-52.208	0.027	104.65	35.87	102.5	0.83	0.34	0.36	FR I	20.78	8000070018003200	0.58
10083	J214411-564844	326.05	-56.812	0.001	50.65	23.9	50.65	1.6	0.45	0.50	FR I	23.1	8000054867000840	
10083	J214419-565731	326.08	-56.959	0.001	52.31	25.01	52.31	0.69	0.46	0.50	FRx	23.57		
10083	J214423-570348	326.1	-57.063	0.004	64.96	27.1	64.96	1.39	0.40	0.43	FR I	20.11	8000054073001070	0.5

Continued on next page

Table 4.2 – Continued from previous page

SBID	Source Name	RA (J2000) (deg)	DEC (J2000) (deg)	Flux Density (Jy)	Size (")	a (")	b (")	PA (°)	a/b_{\max}	a/b_{\min}	Class	Mag (r-band)	DESI ID	Z
10083	J214431-580433	326.13	-58.076	0.01	50.08	23.32	43.91	2.11	0.50	0.56	FR II	23.65		
10083	J214433-572103	326.14	-57.351	0.004	41.83	18.44	38.86	2.32	0.45	0.51	FRx	23.43		
9434	J214436-502238	326.15	-50.377	0.021	60.44	16.04	60.44	0.75	0.25	0.28	FR I	18.8	8000076347004630	0.42
10083	J214438-553208	326.16	-55.536	0.011	201.98	140.64	201.98	2.42	0.69	0.71	FR II	19.63	8000058908001980	0.42
9501	J214438-622832	326.16	-62.476	0.037	136.69	98.49	129.1	1.79	0.75	0.78	FR II	21.44	8000037991005180	0.82
9434	J214439-491112	326.16	-49.187	0.01	44.67	20	39.17	1.49	0.48	0.55	FRx	22.89		
9434	J214442-504850	326.18	-50.814	0.012	138.85	112.33	138.85	2.37	0.79	0.82	FR II	23.16		
9434	J214442-531400	326.18	-53.233	0.026	116.42	80.63	105.88	1.01	0.74	0.78	FR II	17.98		
9434	J214443-485702	326.18	-48.951	0.001	70.75		70.75				single	20.08	8000081962004520	0.49
10083	J214446-572336	326.2	-57.393	0.002	75.43	34.97	75.43	1.37	0.45	0.48	FR I	22.58	8000052504004770	0.95
9501	J214451-601709	326.21	-60.286	0.037	190.89	151.39	181.58	1.05	0.82	0.85	FR II	20.57	8000044252002110	0.56
9501	J214457-590401	326.24	-59.067	0.024	131.1	88.77	116.24	2.89	0.75	0.78	FR II	19.6	8000047924000840	0.33
10635	J214458-515009	326.24	-51.836	0.32	55.23		55.92	0.63			single	20.17		
9434	J214458-493149	326.24	-49.53	0.011	34.86		33.11	2.58			single	22.09		
10635	J214502-520929	326.26	-52.158	0.026	96.8	54.41	81.45	2.53	0.65	0.69	FR II	24.29	8000070018004030	0.48
10083	J214502-561932	326.26	-56.326	0.002	68	29.98	68	2.69	0.43	0.46	FR I	20.06	8000056468001070	0.21
10635	J214502-512521	326.26	-51.423	0.022	102.29	50.98	102.29	0.34	0.49	0.51	FRx	17.16	8000072701003090	0.16
9501	J214505-630035	326.27	-63.01	0.022	54.24		48.51	0.71			single	17.24	8000036660003130	0.16
10083	J214511-532221	326.3	-53.373	0.004	50.29		50.29	2.01			single	24.41		
9434	J214512-484254	326.3	-48.715	0.026	51.48	14.29	47.82	0.93	0.28	0.32	FR I	18.7	8000082914004180	0.27
9501	J214513-614529	326.31	-61.758	0.007	72.01	34.93	59.42	1.22	0.56	0.61	FR II	23.15		
10083	J214513-571236	326.31	-57.21	0.091	115.42	41.2	115.42	2.86	0.35	0.36	FR I	15.11	8000053286002920	0.05
9434	J214516-511612	326.32	-51.27	0.006	99.95	62.8	99.95	2.71	0.61	0.64	FR II	20.6		
10635	J214518-495446	326.33	-49.913	0.017	38.87		36.79	1.07			single	24.57		
9501	J214518-603827	326.33	-60.641	0.093	50.19	16.25	45.46	1.93	0.34	0.38	FR I	19.33		
10083	J214523-541337	326.35	-54.227	0.002	56.69	21.57	56.69	2.24	0.36	0.40	FR I	20.95	8000063079002110	0.67
9434	J214523-483003	326.35	-48.501	0.003	93.33	54.58	93.33	0.43	0.57	0.60	FR II	20.54	8000083872003440	0.33
9501	J214524-611837	326.35	-61.31	0.017	96.52	59.49	83.62	1.96	0.69	0.73	FR II	17.64	8000041414001770	0.28
9501	J214533-614424	326.39	-61.74	0.037	102.32	50.64	93.99	3.09	0.52	0.55	FR II	21.61	8000040029003270	0.85
10083	J214542-564953	326.43	-56.831	0.006	84.79	44.18	84.79	3.11	0.51	0.54	FR II	21.43	8000054867000590	0.61
10083	J214546-564142	326.45	-56.695	0.003	72.96	43.56	72.96	3.11	0.58	0.62	FR II	21.2	8000054867002600	0.56
10083	J214552-541934	326.47	-54.326	0.003	102.21	51.92	102.21	1.33	0.50	0.52	FRx	17.08	8000062235000210	0.49
9434	J214558-543603	326.49	-54.601	0.002	104.41	75.9	104.41	0.11	0.71	0.74	FR II	19.71	8000069134003550	0.21
10083	J214606-522413	326.53	-52.404	0.017	177.31	116.5	144.7	1.5	0.79	0.82	FR II	18.05	8000069134003550	0.21
10083	J214609-572841	326.54	-57.478	0.007	59.09	25.06	49.89	2.19	0.48	0.53	FRx	22.08	8000052505002890	0.84
9501	J214613-584332	326.56	-58.726	0.008	147.24	102.41	153.1	2.05	0.66	0.68	FR II	21.64	8000048674002660	0.7
9434	J214614-511001	326.56	-51.167	0.004	43.59		32.71	1.43			single	21.34	8000073606002980	0.58
9434	J214616-482532	326.57	-48.426	0.017	58.72	22	50.6	0.02	0.41	0.46	FR I	23.09	8000083873005660	1.06
10635	J214618-514753	326.57	-51.798	0.003	51.93		51.93	1.16			single	20.03		

Continued on next page

Table 4.2 – Continued from previous page

SBID	Source Name	RA (J2000) (deg)	DEC (J2000) (deg)	Flux Density (Jy)	Size (")	a (")	b (")	PA (°)	a/b _{max}	a/b _{min}	Class	Mag (r-band)	DESID	Z
9434	J214618-515802	326.58	-51.967	0.044	68.5	22.63	61.65	2.74	0.35	0.38	FRI	21.12		
10083	J214618-555212	326.58	-55.87	0.023	39.38		40.4	2.64			single	16.42		
9501	J214619-595942	326.58	-59.995	0.005	66.18	28.84	66.18	0.64	0.42	0.45	FRI	18.09	8000044976003360	0.32
10083	J214620-543632	326.59	-54.609	0.003	88.41	32.64	88.41	0.09	0.36	0.38	FRI	21.66	8000062236000220	0.72
10635	J214621-523013	326.59	-52.504	0.02	58.21	21.54	48.19	2.1	0.42	0.47	FRI	20.57	8000069134001940	0.54
10083	J214621-550919	326.59	-55.155	0.104	54.9	24.41	56.23	0.79	0.42	0.45	FRI	18.61	8000059733004370	0.23
10083	J214628-553816	326.62	-55.638	0.009	67.33	34.43	67.33	0.08	0.49	0.53	FRx	17.54	8000058090004860	0.24
9501	J214631-610942	326.63	-61.162	0.003	58.15		58.15	0.25		0.53	single	18.39	8000041415005470	0.23
9434	J214632-481118	326.64	-48.188	0.004	139	72	139				FRII	21.97	8000084834004870	0.76
10083	J214638-562706	326.66	-56.452	0.011	61.49		61.49	2.09			single	20.52	8000055666003030	0.06
10635	J214641-511839	326.67	-51.311	0.021	108.95		108.95	2.1			single	14.67	8000073606000770	
10635	J214645-512030	326.69	-51.342	0.032	61.44	28.07	56.28	0.11	0.48	0.52	FRx	19.46		
10083	J214648-561118	326.7	-56.188	0.003	72.07	41.8	72.07	1.95	0.56	0.60	FRII	17.93		
9501	J214649-574933	326.71	-57.826	0.003	67.93	34.06	56.38	0.71	0.58	0.63	FRII	22.5		
9501	J214650-591813	326.71	-59.304	0.005	69.08	36	51.94	1.57	0.66	0.73	FRII	22.56	8000051728001000	0.89
9501	J214652-614023	326.72	-61.673	0.004	123.9	75.82	95.4	0.35	0.77	0.82	FRII	17.93		
10635	J214652-510742	326.72	-51.128	0.001	57.12	21.39	57.12	1.88	0.68	0.71	FRII	23.31	8000040030004640	0.88
9434	J214654-482112	326.73	-48.353	0.003	67.63	26.07	67.63	0.1	0.37	0.39	FRI	21.32	8000084835000660	0.62
9434	J214654-505638	326.73	-50.944	0.006	43.59		37.57	1.93			single	22.64	8000074515002730	1.14
10635	J214655-513545	326.73	-51.596	0.009	55.23		48.99	2.7			single	21.06	8000072702000430	0.74
9501	J214659-621237	326.75	-62.21	0.014	167.29	59.15	167.29	2.35	0.35	0.36	FRI	15.45	8000050957000720	0.29
10083	J214703-562346	326.77	-56.396	0.006	78.36	44	78.36	0.86	0.54	0.58	FRII	18.3	8000059733003440	0.76
10083	J214705-564728	326.77	-55.207	0.003	55.29	26.08	46.44	1	0.53	0.59	FRII	19.8	8000054868001700	0.44
10083	J214715-544206	326.82	-54.702	0.002	50.96		50.96	0.81			single	21.64	8000061397001100	
10083	J214716-544747	326.82	-54.796	0.013	62.96	9.4	65.96	1.01	0.14	0.15	FRI	17.36		
10083	J214717-551312	326.82	-55.22	0.003	62.39	37.36	63.51	2.77	0.57	0.61	FRII	22.73	8000059734003220	0.09
9501	J214721-623514	326.84	-62.587	0.008	101.14	61.19	82.52	1.75	0.72	0.76	FRII	16.9	8000037992001580	0.75
9501	J214724-591309	326.85	-59.219	0.002	55.9	27.89	55.9	2.89	0.48	0.52	FRx			
9501	J214725-573202	326.86	-57.601	0.011	43.74	11.01	37.17	0.65	0.28	0.32	FRI	23.58	8000063929003260	0.21
10083	J214726-535455	326.86	-53.915	0.015	170.68		170.68	1.39	0.34	0.35	FRI	18.79	8000083873004620	0.98
9434	J214726-482743	326.86	-48.462	0.016	69.15	32.31	55.18	2	0.56	0.61	FRII	22.65	8000083873001580	0.26
9434	J214727-483402	326.86	-48.567	0.011	67.63	28.46	52.78	0.96	0.51	0.57	FRII	18.05		
10635	J214728-490350	326.87	-49.064	0.002	99.62	62.82	99.62	0.52	0.62	0.65	FRII	23.27		
10083	J214732-555422	326.88	-55.906	0.002	86.81	46.63	86.81	0.22	0.52	0.55	FRII	22.75	8000057277004590	1.08
9501	J214732-605125	326.88	-60.857	0.022	101.33	44.94	101.33	2.81	0.43	0.45	FRI	21.68		
9501	J214732-595555	326.89	-59.932	0.404	89.17	32.56	81.5	0.76	0.39	0.41	FRI	18.28	8000044977004810	0.29

Continued on next page

Table 4.2 – Continued from previous page

SBID	Source Name	RA (J2000) (deg)	DEC (J2000) (deg)	Flux Density (Jy)	Size (")	a (")	b (")	PA (°)	a/b _{max}	a/b _{min}	Class	Mag (r-band)	DESI ID	Z
10083	J214732-551325	326.89	-55.224	0.494	58.72	18.97	58.49	2.69	0.31	0.34	FRI	22.12		
10083	J214733-562537	326.89	-56.427	0.198	224.76	168.76	205.32	2.54	0.81	0.83	FRII	20.22	8000055666003840	0.56
9501	J214734-584947	326.89	-58.83	0.026	116.01	52.5	116.01	2.02	0.44	0.46	FRI	18.71	8000048675001110	0.4
10083	J214737-542501	326.91	-54.417	0.007	43.09	14.14	38.17	2.38	0.35	0.40	FRI	23.2		
9501	J214740-583900	326.92	-58.65	0.016	100.25	56.85	84.37	2.25	0.65	0.69	FRII	21.04	8000048675004960	0.77
10635	J214742-532021	326.93	-53.339	0.006	107.53	80.62	101.9	0.79	0.77	0.81	FRII	21.84		
10083	J214745-565121	326.94	-56.856	0.049	50.96		47.44	2.85			single	21.89	8000054869000260	0.79
9501	J214758-582113	326.99	-58.354	0.11	297.66	248.23	291.01	2.06	0.85	0.86	FRII	19.58	8000050192000600	0.75
10083	J214759-570336	327	-57.06	0.002	55.6		55.6	1.3			single	21.38	8000054075001030	0.71
10083	J214800-571546	327	-57.263	0.016	130.94	48.21	110.96	2.99	0.42	0.44	FRI	16.82	8000053288002330	0.13
9434	J214802-513838	327.01	-51.644	0.001	38.46	12.58	38.46		0.31	0.35	FRI	20.41	8000071804003190	0.5
10083	J214803-535957	327.01	-53.999	0.013	41.69	14.25	41.69	2.29	0.32	0.36	FRI	19.24		
10083	J214808-573841	327.04	-57.645	0.013	63.4	16.5	51.91	2.97	0.30	0.33	FRI	16.89		
9434	J214809-502436	327.04	-50.41	0.002	62.53	27.91	62.53	1.1	0.43	0.46	FRI	20.95	8000076349003440	0.75
10083	J214822-551310	327.1	-55.219	0.009	65.63	37.59	65.63	0.21	0.55	0.60	FRII	22.68	8000059734003310	1.08
10083	J214825-542627	327.11	-54.441	0.002	90.59	60.6	90.59	2.55	0.65	0.69	FRII	20.6		
10083	J214826-571411	327.11	-57.236	0.199	304.62	88.87	304.62	1.92	0.29	0.29	FRI	15.46		
10083	J214835-552514	327.15	-55.421	0.015	90.67	27.78	67.16	0.86	0.40	0.43	FRI	17.12	8000058911004080	0.19
9501	J214836-593541	327.15	-59.595	0.027	173.3	134.15	160.84	0.36	0.82	0.85	FRII	22.48	8000046440000760	0.7
9434	J214837-525159	327.16	-52.866	0.006	87.27	45.31	87.27	1.71	0.50	0.53	FRII	19.32		
10083	J214839-571958	327.16	-57.333	0.007	73.37	36.13	73.37	2.61	0.48	0.51	FRx	16.76	8000053288000880	0.15
9501	J214839-612953	327.17	-61.498	0.001	72.2	29.35	72.2	2.37	0.39	0.42	FRI	20	8000040721003260	0.54
9501	J214840-625529	327.17	-62.925	0.002	59.11	15.06	59.11	0.01	0.24	0.27	FRI	20.75	8000036661005150	0.46
9501	J214841-572800	327.17	-57.467	0.007	98.18	62.45	81.39	2.73	0.74	0.79	FRII	19.37	8000052507002840	0.53
9501	J214844-583915	327.19	-58.654	0.001	61.62	28.13	61.62	3.02	0.44	0.48	FRI	20.44	8000048675004570	0.54
10083	J214844-582436	327.19	-58.41	0.008	57.98	20.4	48.69	2.01	0.40	0.44	FRI			
9434	J214845-524027	327.19	-52.674	0.014	46.45	21.63	46.45	2.3	0.44	0.49	FRI	20.61		
10083	J214845-531524	327.19	-53.257	0.003	50.29		50.29	1.79			single	23.4		
10083	J214849-543651	327.2	-54.614	0.001	54.97	27.75	54.97		0.48	0.53	FRx	17.69		
10083	J214850-562325	327.21	-56.39	0.014	60.76	30.27	54.02	1.78	0.54	0.59	FRII	21.23	8000055667004640	0.82
10635	J214850-492458	327.21	-49.416	0.001	99.62	63.55	99.62	0.65	0.62	0.65	FRII	24.8	8000080074004730	
10083	J214859-564949	327.25	-56.83	0.13	50.96	20	48.79	3.1	0.39	0.43	FRI	22.74	8000054869000670	0.91
10083	J214903-571659	327.26	-57.283	0.002	61.84		61.84	0.61			single			
9434	J214907-481115	327.28	-48.188	0.01	113.07	63.98	113.07		0.55	0.58	FRII	16.88	8000084836004480	0.16
9501	J214907-614548	327.28	-61.763	0.021	103.39	46.78	103.39	0.16	0.44	0.46	FRI	17.49	8000040031002640	0.22
9501	J214917-610021	327.32	-61.006	0.001	52.05	22.81	52.05		0.42	0.46	FRI	19.55	8000042118002840	0.46
10083	J214920-540947	327.33	-54.163	0.017	72.71	32.28	71.23	1.63	0.44	0.47	FRI	18.18		
9501	J214921-592234	327.34	-59.376	0.003	100.07	63.42	100.07	1.2	0.62	0.65	FRII	18.53	8000046441005840	0.3
10083	J214921-550258	327.34	-55.049	0.002	51.69	23.06	51.69	0.64	0.43	0.47	FRI	99		

Continued on next page

Table 4.2 – Continued from previous page

SBID	Source Name	RA (J2000) (deg)	DEC (J2000) (deg)	Flux Density (Jy)	Size (")	a (")	b (")	PA (°)	a/b _{max}	a/b _{min}	Class	Mag (r-band)	DESI ID	Z
10635	J214923-494855	327.35	-49.815	0.01	261.37	175.07	261.37	1.92	0.66	0.68	FR II	17.59	8000079137001220	0.2
10635	J214928-491943	327.37	-49.329	0.056	50.15	17.89	47.91	2.65	0.35	0.39	FRI	20.12		
10083	J214928-565326	327.37	-56.891	0.003	50.96		50.96	2.2			single	20.29	8000054076004100	
10083	J214930-543446	327.38	-54.579	0.003	63.76	34.53	53.19	0.16	0.62	0.68	FR II	22.43		
9501	J214932-621738	327.38	-62.294	0.145	90.22	50.99	83.04	1.1	0.60	0.63	FR II	22.74	800003866002520	0.75
9501	J214935-583742	327.4	-58.628	0.003	117.2	84.95	117.2	2.88	0.71	0.74	FR II	24.43		
10083	J214939-554039	327.41	-55.678	0.005	71.41	40.69	71.41	2.19	0.55	0.59	FR II	21.37	8000058092004000	
10083	J214940-551347	327.42	-55.23	0.007	95.25	54.85	95.25	2.9	0.56	0.59	FR II	18.27	8000059735002510	0.27
10083	J214942-555352	327.43	-55.898	0.013	58.46		46.85	2.12			single	20.26	8000057278004970	0.71
10635	J214943-491337	327.43	-49.227	0.036	50.15	21.26	51.19	2.35	0.40	0.44	FRI	18.92	8000081018003590	0.34
9501	J214945-624700	327.44	-62.783	0.007	86.48	52.04	72.7	0.06	0.69	0.74	FR II	23.79		
9501	J214951-591101	327.47	-59.184	0.052	88.72	36.88	73.63	1.31	0.48	0.52	FRx	20.01	8000047181004360	0.4
9501	J214953-591917	327.47	-59.321	0.022	99.44	49.9	99.24	0.09	0.49	0.52	FRx	16.85	8000047181000900	0.28
10083	J214957-563133	327.49	-56.526	0.012	87.41	47.54	76.02	0.14	0.61	0.65	FR II	21.93	8000055667001900	0.77
9501	J214959-592326	327.5	-59.391	0.008	121.65	48.8	121.65	3.05	0.39	0.41	FRI	19.89	8000046441005420	0.37
10083	J215001-545450	327.51	-54.964	0.002	46.96		46.96	2.91			single	23.02		
10083	J215001-554141	327.51	-55.695	0.002	66.32		66.32	1.91			single	20.74	8000058092003710	0.64
10083	J215003-552918	327.51	-55.488	0.002	77.01	39.76	77.01	2.99	0.50	0.53	FR II	22.83		
9434	J215004-501256	327.52	-50.216	0.01	91.64	46.53	71.62	2.04	0.63	0.67	FR II	19.07	8000077274002490	0.45
10083	J215015-534417	327.57	-53.738	0.002	76.64		76.64	2.67			single	18.67	8000064786002260	0.32
10083	J215017-554226	327.57	-55.707	0.004	62.69		62.69	1.54			single			
9434	J215021-500557	327.59	-50.099	0.003	57.41		57.41	1.96			single	19.85	8000078204000300	0.54
10635	J215021-483600	327.59	-48.6	0.003	95.93	65.06	95.93	1.12	0.66	0.70	FR II	23.72		
9501	J215023-582248	327.6	-58.38	0.006	130.28	74.82	96.19	3.05	0.76	0.80	FR II	23.2	8000049431005680	
9501	J215023-621023	327.6	-62.173	0.174	474.74	197.95	474.74	2.66	0.41	0.42	FRI	14.71	8000038667004780	0.05
9501	J215027-621013	327.62	-62.17	0.104	140.8	42.6	140.8	2.47	0.30	0.31	FRI	14.81	8000038667005130	0.07
10635	J215028-515235	327.62	-51.876	0.001	69.8	45.51	69.8		0.63	0.68	FR II	22.78		
9434	J215028-490340	327.62	-49.061	0.043	234.94	85.44	192.18	1.93	0.44	0.45	FRI	15.59	8000081966001670	0.1
9501	J215032-625509	327.63	-62.919	0.003	117.94	77.23	117.94	2.53	0.64	0.67	FR II	22.3	8000036662004890	1.02
9501	J215032-590316	327.64	-59.054	0.012	80.98	49.63	71.83	0.74	0.67	0.72	FR II	24.48	8000047926001520	
10083	J215034-525212	327.64	-52.87	0.064	51.29		52.93	1.1			single	25.02		
10083	J215036-533004	327.65	-53.501	0.012	74.7		74.7	0.95			single	18.84	8000065646002030	
10083	J215037-570615	327.66	-57.104	0.002	80.15	41.47	80.15	2.17	0.50	0.53	FR II	24.94		
10635	J215038-490501	327.66	-49.084	0.001	51.78		51.78	0.37			FR II	19.37	8000081966001110	0.34
9501	J215039-581941	327.66	-58.328	0.01	39.44		38.26	0.93			single	20.43	8000050193001490	0.57
9434	J215041-505335	327.67	-50.893	0.002	54.56	11.71	54.56	2.95	0.21	0.23	FRI	22.25	8000074518003600	0.83
10083	J215043-534457	327.68	-53.749	0.003	74.82	39.98	74.82	0.65	0.52	0.55	FR II	19.9		
9501	J215047-614552	327.7	-61.764	0.002	64.97		64.97	0.9			single	14.47	8000040032002700	0.04
10083	J215050-544342	327.71	-54.728	0.013	78.69	42.52	68.88	0.68	0.60	0.64	FR II	23.47		

Continued on next page

Table 4.2 – Continued from previous page

SBID	Source Name	RA (J2000) (deg)	DEC (J2000) (deg)	Flux Density (Jy)	Size (")	a (")	b (")	PA (°)	a/b _{max}	a/b _{min}	Class	Mag (r-band)	DESID	Z
10083	J215051-555956	327.72	-55.999	0.006	95.87	43.86	95.87	1.18	0.45	0.47	FRI	19.31	8000057279002360	0.39
9501	J215051-580139	327.72	-58.028	0.005	240.03	202.62	240.03	1.34	0.84	0.85	FRII	20.52		
10635	J215055-531450	327.73	-53.247	0.001	59.61	59.61	59.61	3.03	0.64	0.68	single	23.15		
10635	J215056-494825	327.73	-49.807	0.004	89.07	59.03	89.07	0.65	0.64	0.63	FRII	23.23		
9434	J215100-514635	327.75	-51.776	0.007	63.94	32.56	54.5	1.73	0.57	0.63	FRII	23.44		
9501	J215106-574055	327.78	-57.682	0.417	530.85	114.9	429.38	0.46	0.27	0.27	FRI	19.06		
10635	J215107-505222	327.78	-50.873	0.002	86.82	54.01	86.82	0.85	0.60	0.64	FRII	17.62	8000075432000010	0.2
10083	J215112-533704	327.8	-53.618	0.001	67.65	67.65	67.65	0.27	0.26	0.26	single	19.39	8000065647000120	0.39
10083	J215113-551501	327.8	-55.25	0.002	41.61	10	41.61	2.28	0.23	0.26	FRI	21.21	8000059736002220	
10635	J215116-494151	327.82	-49.698	0.021	51.89	22.63	47.19	2.33	0.46	0.51	FRx	19.01		
10083	J215119-545217	327.83	-54.871	0.125	56.22	21.26	57.1	0.83	0.36	0.39	FRI	21.09		
10635	J215120-510644	327.83	-51.112	0.004	60.62	27.15	60.62	1.76	0.43	0.47	FRI	22.25		
10635	J215124-515734	327.85	-51.959	0.003	73.45	73.45	73.45	3.06	0.23	0.24	single	21.35	8000074518000180	0.86
9501	J215127-615826	327.87	-61.974	0.003	60.33	60.33	60.33	3.14	0.23	0.24	single	20.22	8000039347003940	0.57
9501	J215138-600936	327.91	-60.16	0.062	100.16	28.73	69.48	1.57	0.39	0.43	FRx	16.87	8000044255005630	0.21
9434	J215139-495104	327.92	-49.851	0.136	134.94	22.8	124.68	0	0.23	0.24	single	17.9	8000079138000460	0.22
9434	J215140-525943	327.92	-52.995	0.011	56.12	22.8	46.2	2.54	0.47	0.52	FRI	19.97		
10083	J215141-560944	327.92	-56.162	0.034	48.21	20	49.4	2.42	0.39	0.43	FRx	20.43	8000056472004570	0.58
10635	J215146-513318	327.95	-51.555	0.001	51.01	14.95	51.01	1.29	0.28	0.31	FRI	20.24	8000072705001160	
10635	J215147-483519	327.95	-48.589	0.001	60.56	31.49	60.56	0.56	0.50	0.54	FRx	24.7		
10083	J215150-562608	327.96	-56.436	0.113	159.51	109.29	153.53	0.6	0.70	0.72	FRII	21.96	8000055668003700	0.8
9501	J215150-622857	327.96	-62.483	0.009	63.93	30.53	56.32	1	0.52	0.57	FRI	23.32		
10083	J215154-545407	327.98	-54.902	0.013	84.69	56.34	75.39	1.68	0.72	0.77	FRII	19.25	8000060566003560	0.48
9501	J215154-622007	327.98	-62.335	0.024	332.96	281.6	332.96	2.95	0.84	0.85	FRII	22.7	8000038668000360	1.17
10635	J215157-523245	327.99	-52.546	0.022	74.93	28.11	62.11	0.96	0.44	0.47	FRI	22.19	8000069137001370	1.02
9501	J215157-622751	327.99	-62.464	0.007	50.45	22.09	43.18	0	0.48	0.54	FRx	22.54		
10083	J215159-525954	328	-52.998	0.05	86.19	44.72	80.66	0.24	0.54	0.57	FRII	22		
10635	J215200-522136	328	-52.36	0.002	81.21	49.16	81.21	0.89	0.59	0.62	FRII	20.28	80000700230000390	0.28
9501	J215200-612112	328	-61.353	0.005	45.63	37.32	37.32	0.86	0.64	0.66	single	21.62	8000041418000550	0.85
10635	J215201-495313	328	-49.887	0.007	161.52	105.42	161.52	1.7	0.64	0.66	FRII	17.25	8000079138000050	0.21
10635	J215201-500711	328.01	-50.12	0.004	87.23	23.83	87.23	1.63	0.27	0.28	FRI	20.17	8000078205000030	0.72
10083	J215201-555214	328.01	-55.871	0.007	145.55	78.73	145.55	2.83	0.53	0.55	FRII	20.91	8000058093000250	0.68
9501	J215203-580719	328.01	-58.122	0.004	49.23	31.87	31.87	1.56	0.50	0.54	single	20.01	8000050959000090	0.62
10083	J215208-554022	328.03	-55.673	0.083	84.82	38.21	73.32	3.13	0.50	0.54	FRII	20.57	8000058093003450	0.68
10083	J215213-554223	328.06	-55.706	0.014	54.47	43.39	43.39	0.14	0.46	0.46	single	17.48		
10635	J215213-523954	328.06	-52.665	0.002	57.29	57.29	57.29	0.49	0.42	0.46	single	23.27		
10635	J215215-520438	328.06	-52.077	0.008	57.17	21.54	48.97	0.43	0.42	0.40	FRI	23.02		
10635	J215219-490429	328.08	-49.075	0.025	50.15	18.44	48.09	3.07	0.36	0.40	FRI	23.58		
9434	J215220-492303	328.09	-49.384	0.008	57.58	21.26	46.45	0.85	0.43	0.48	FRI	25.02		

Continued on next page

Table 4.2 – Continued from previous page

SBID	Source Name	RA (J2000) (deg)	DEC (J2000) (deg)	Flux Density (Jy)	Size (")	a (")	b (")	PA (°)	a/b _{max}	a/b _{min}	Class	Mag (r-band)	DESI ID	Z
9501	J215222-602221	328.09	-60.373	0.002	110.53	70.77	110.53	0.78	0.63	0.66	FR II	20.01	8000044256000000	0.58
10635	J215222-483702	328.09	-48.617	0.005	56.2		56.2	0.5			single	20.67	8000083877000180	
10635	J215222-495426	328.09	-49.907	0.002	77.13		77.13	0.5			single	16.88	8000078205003590	0.1
10083	J215227-532736	328.11	-53.46	0.022	107.84	84.76	110.23	1.93	0.75	0.79	FR II	25.42		
9501	J215228-611108	328.12	-61.186	0.003	61.96	26.92	55.13	2.59	0.47	0.51	FRx	19.71	8000041418004660	0.47
9501	J215228-581447	328.12	-58.246	0.012	96.02	33.77	96.48	0.71	0.34	0.36	FRI	18.3	8000050194003040	0.23
9501	J215235-584407	328.15	-58.735	0.016	104.9	53.2	89.17	0.12	0.58	0.61	FR II	18.65	8000048677002870	
10083	J215237-555557	328.15	-55.933	0.001	64.97	29.21	64.97		0.43	0.47	FRI	22.84	8000057280003970	1.06
10635	J215239-482514	328.16	-48.421	0.044	109.84	30.41	109.84	1.12	0.27	0.28	FRI	17.63	8000083877004490	0.25
9501	J215240-580145	328.17	-58.029	0.006	110.25	78.8	107.22	2.26	0.72	0.75	FR II	18.72		
10083	J215245-534714	328.19	-53.787	0.003	79.05	43.61	79.05	2.72	0.53	0.57	FR II	21.72	8000064788001400	
10083	J215247-491141	328.19	-49.195	0.029	193.7	146.89	182.02	0.45	0.80	0.82	single	21.07	8000056472002580	
10083	J215249-562337	328.21	-56.394	0.002	45.83		45.83	0.56			FR II	20.32	8000081020004240	0.61
10083	J215250-543742	328.21	-54.628	0.006	84.69	52.62	74.42	2.99	0.68	0.73	single	18.31	8000055669005030	0.28
10635	J215252-483723	328.22	-48.623	0.009	69.61		69.61	0.71			FR II	20.64	8000061400003970	0.64
9501	J215254-592054	328.23	-59.348	0.111	106.77	49.03	99.51	1.7	0.48	0.51	FRx	15.27	8000047182000520	0.62
10635	J215256-515610	328.23	-51.936	0.009	124.24	75.94	124.24	0.3	0.60	0.62	FR II	21.65	8000070913003540	0.73
10083	J215258-562706	328.24	-56.452	0.002	45.83		45.83	0.49			single	24.17		
10635	J215258-511048	328.24	-51.118	0.013	57.8	14.82	51	1.41	0.28	0.31	FRI	21.77	8000073610003230	0.47
10083	J215259-555852	328.25	-55.981	0.371	51.83	16.12	51.83	2.64	0.30	0.33	FRI	22.88	8000057280002950	
9501	J215300-584216	328.25	-58.704	0.001	66.36		66.36				single	20.42	8000048677003510	0.58
10083	J215300-535614	328.25	-53.937	0.007	137.12	52.8	137.12	0.46	0.38	0.39	FRI	18.74	8000063933003270	0.32
9501	J215300-625218	328.25	-62.872	0.04	72.94	26.68	65.38	3.03	0.39	0.42	FRI	20.9	8000037327000220	0.56
10083	J215303-560807	328.27	-56.135	0.004	51.43	18.44	51.43	2.88	0.34	0.38	FRI	19.49	8000056473005120	0.47
10635	J215304-514600	328.27	-51.767	0.005	51.01	15.76	37.51	2.59	0.39	0.45	FRI	19.64	8000071807001800	0.36
10635	J215305-510445	328.27	-51.079	0.003	149.6	96.29	149.6	0.66	0.63	0.65	FR II	22.1	8000074519000780	0.94
9501	J215310-592650	328.29	-59.447	0.003	191.06	155.9	165.78	2.43	0.93	0.95	FR II	21.6	8000046443004030	0.71
10083	J215312-565242	328.3	-56.878	0.001	79.98	56.71	79.98	0.99	0.69	0.73	FR II	22.7		
10635	J215317-500419	328.32	-50.072	0.002	97.86	62.2	97.86	0.83	0.62	0.65	FR II	23.14	8000078206001030	
10635	J215317-502411	328.32	-50.403	0.007	116.99	74.24	96.19	1.64	0.75	0.79	FR II	23.32		
10083	J215319-552014	328.33	-55.337	0.003	93.77	60.43	93.77	2.57	0.63	0.66	FR II	23.59	8000059737000450	
10635	J215321-481819	328.34	-48.305	0.006	141.16	93.78	141.16	1.49	0.65	0.68	FR II	20.7	8000084839001260	0.57
9434	J215323-514826	328.35	-51.807	0.018	99.13	36.88	82.59	0.18	0.43	0.46	FRI	19.3		
9501	J215324-584037	328.35	-58.677	0.004	74.6		74.6	2.6	0.64	0.69	single	21.41	8000048678004040	0.72
10635	J215326-491633	328.36	-49.276	0.028	78.57	49.53	74.42	0.78	0.64	0.69	FR II	24.76	8000081021002070	
10635	J215327-485000	328.36	-48.833	0.018	78.57	40.79	72.22	0.23	0.55	0.59	FR II	23.38	8000082920000970	
10635	J215329-515956	328.37	-51.999	0.017	49.38		45.41	1.42			single	20.67	8000070913002270	0.67
10635	J215330-502105	328.38	-50.351	0.014	72.75		60.73	2.2			single	19.89	8000077276000340	0.37

Continued on next page

Table 4.2 – Continued from previous page

SBID	Source Name	RA (J2000) (deg)	DEC (J2000) (deg)	Flux Density (Jy)	Size (")	a (")	b (")	PA (°)	a/b _{max}	a/b _{min}	Class	Mag (r-band)	DESI ID	Z
10083	J215334-574911	328.39	-57.82	0.007	140.43	30.63	140.43		0.21	0.22	FRI	19.94		
10083	J215335-540730	328.4	-54.125	0.004	68.25	44.05	60.25	0.87	0.70	0.76	FRII	16.95		
10635	J215336-502850	328.4	-50.481	0.1	125.03	85.99	125.03	2.99	0.67	0.70	FRII	20.89	8000076353001820	0.63
10083	J215342-573700	328.43	-57.617	0.037	117.78	19.32	117.78	2.36	0.16	0.17	FRI	15.43	8000052509000300	0.07
9434	J215343-484239	328.43	-48.711	0.003	97.47		97.47	3.02			single	22.51	8000082920003240	1
10083	J215343-565255	328.43	-56.882	0.015	41.22		38.78	2.51			single	19.76	8000054078004520	0.42
9501	J215355-584830	328.48	-58.808	0.002	75.3	37.8	75.3	1.17	0.49	0.52	FRx	17.81	8000048678001280	0.27
10083	J215400-553900	328.5	-55.65	0.014	45.59	9.99	42.24	0.18	0.22	0.25	FRI	21.03	8000058094003520	0.66
10635	J215400-511320	328.5	-51.222	0.002	68.27	34.83	68.27	0.88	0.49	0.53	FRx	23.71	8000073610002550	
9501	J215403-592005	328.51	-59.335	0.001	53.02		53.02	1.27			single	17.2	8000047183000820	0.22
10635	J215406-521007	328.53	-52.169	0.176	51.01	18	51.01	0.82	0.34	0.37	FRI	23.62		
9501	J215409-602201	328.54	-60.367	0.01	54.94	22.09	44.31	1.45	0.47	0.53	FRx	22.15	8000044257000260	1.05
9501	J215410-591906	328.54	-59.318	0.002	59.62		59.62	2.53			single	26.24		
10635	J215410-522349	328.55	-52.397	0.008	66.11	31.62	56.25	0.97	0.54	0.59	FRII			
9501	J215412-610552	328.55	-61.098	0.017	125.73	35.21	125.73	0.22	0.27	0.29	FRI	17.4	8000042120000570	0.24
10083	J215417-542913	328.57	-54.487	0.004	56.27		56.27	1.22			single	21.93	8000062240002320	0.78
9501	J215423-602538	328.6	-60.427	0.022	56.53		44.82	2.48			single	20.47	8000061401000090	0.68
10083	J215424-545204	328.6	-54.868	0.002	61.18		61.18	2.4			single	20.89	8000070914001120	
10635	J215426-520437	328.61	-52.077	0.004	96.3	57	96.3	0.13	0.58	0.61	FRII	17.21		
9501	J215431-620534	328.63	-62.093	0.001	89.78	63.89	89.78		0.69	0.73	FRII	24.8		
9501	J215432-613617	328.64	-61.605	0.019	98.24	45.69	98.24	2.83	0.45	0.48	FRI	18.79	8000040723000380	0.34
10635	J215444-483422	328.68	-48.573	0.014	75.23	39.85	65.05	1.88	0.59	0.64	FRII	22.58	8000083878000990	1.05
9501	J215447-605657	328.7	-60.949	0.001	49.9		49.9	0.25			single	16.76		
10635	J215447-524605	328.7	-52.768	0.096	72.25	31.63	67.54	2	0.45	0.49	FRI	17.21	8000068259001290	0.26
10083	J215455-543845	328.73	-54.646	0.001	57.57	29.06	57.57	0.04	0.48	0.53	FRx	21.33	8000061401004080	0.78
10635	J215456-514340	328.73	-51.728	0.304	85.82	50.48	85.82	1.03	0.57	0.61	FRII	18.55	8000071808002810	0.25
10635	J215456-521827	328.73	-52.308	0.002	81.1	47.65	81.1	1.03	0.57	0.61	FRII	18.82	8000070025001250	0.23
9501	J215456-612739	328.74	-61.461	0.003	53.32		53.32	0.42			single	21.27	8000040724004060	0.64
10635	J215503-504800	328.76	-50.8	0.007	106.74	52.11	106.74	1.55	0.48	0.50	FRI	15.62		
9501	J215504-621435	328.77	-62.243	0.004	80.91	46.82	66.79	1.19	0.68	0.73	FRII	19.73	8000038669003400	0.53
10083	J215506-535340	328.78	-53.894	0.022	91.88	69.86	93.86	1.34	0.72	0.76	FRII	21.78	8000063934004290	0.86
9501	J215506-584139	328.78	-58.694	0.004	81.17		81.17	1.24			single	19.27	8000048678003690	0.45
10635	J215512-524254	328.8	-52.715	0.014	47.62		44.42	0.13			single	17.62	8000068260002520	0.24
10635	J215515-492526	328.81	-49.424	0.001	79.36		79.36				single	22.01	8000080078004480	0.77
10083	J215517-525543	328.82	-52.929	0.008	86.19	55.56	86.19	3.03	0.63	0.66	FRII	21.3	8000067384002930	0.62
10083	J215520-544026	328.83	-54.674	0.004	74.47	36.4	60.96	0.91	0.57	0.62	FRII	20.51	8000061401003610	0.48
10083	J215520-572649	328.84	-57.447	0.025	46.1		46.28	2.41			single	18.61	8000052510003610	0.28
9501	J215524-590911	328.85	-59.153	0.045	364.19	75.58	364.19	3.08	0.21	0.21	FRI	21.13		
9501	J215525-593043	328.85	-59.512	0.004	57.66	25.06	57.66	2.71	0.42	0.45	FRI	20.63	8000046444003000	0.67

Continued on next page

Table 4.2 – Continued from previous page

SBID	Source Name	RA (J2000) (deg)	DEC (J2000) (deg)	Flux Density (Jy)	Size (")	a (")	b (")	PA (°)	a/b _{max}	a/b _{min}	Class	Mag (r-band)	DESI ID	Z
10635	J215534-505400	328.89	-50.9	0.018	55.16	16.71	51.06	0.53	0.31	0.34	FRI	22.45	8000074521002590	0.58
10083	J215538-562346	328.91	-56.396	0.005	37.07	31.43	31.43	1.39			single	19.96	8000055671005130	0.46
10083	J215541-565201	328.92	-56.867	0.001	59.81		59.81	2.77			single	19.58	8000054873000200	0.46
10635	J215543-490800	328.93	-49.133	0.387	63.55	22.8	69.36	0.97	0.32	0.34	FRI	23.81		
10083	J215543-540024	328.93	-54.007	0.363	79.17	30.53	73.26	2.01	0.40	0.43	FRI	19.93	8000063934002250	0.46
10083	J215545-571556	328.94	-57.266	0.02	129.55	73.89	129.55	0.96	0.56	0.58	FRII	20.21	8000053292002170	0.58
10635	J215551-482839	328.96	-48.478	0.086	79.98	39.45	77.79	0.91	0.49	0.52	FRx	19.51		
10083	J215552-564231	328.97	-56.709	0.001	73.13	40.96	73.13	0.19	0.54	0.58	FRII	20.58	8000054873003500	0.46
10083	J215555-561228	328.98	-56.208	0.005	42.71		36.12	1.33			single	20.47	8000056474003790	0.61
9501	J215556-574229	328.99	-57.708	0.005	109.12	81.06	109.12	1.2	0.73	0.76	FRII	17.77	8000051733002490	0.29
10083	J215558-540701	328.99	-54.117	0.003	108.63	55.57	108.63	0.58	0.50	0.52	FRII	18.31	8000063934000180	0.28
10635	J215558-515836	328.99	-51.977	0.008	84.84	44.27	84.84	1.41	0.51	0.54	FRII	22.12	8000070915002830	0.82
10635	J215604-511508	329.02	-51.252	0.003	141.52	88.35	141.52	1.99	0.61	0.64	FRII	20.17	8000073612001700	0.48
10083	J215605-543152	329.02	-54.531	0.004	93.99	27.53	93.99	0.88	0.29	0.30	FRI	19.57		
10635	J215607-514347	329.03	-51.73	0.008	68.02	39.7	58.73	2.27	0.65	0.71	FRII	24.23		
10635	J215609-511956	329.04	-51.332	0.019	353.22	309.74	338.65	0.77	0.91	0.92	FRII	16.91		
9501	J215611-594930	329.05	-59.825	0.002	75.51	42.68	75.51	1.95	0.55	0.58	FRII	22.32	8000045711001200	0.8
10635	J215615-512837	329.06	-51.477	0.038	137.43	95.09	132.35	0.96	0.71	0.73	FRII	17.46	8000072708002760	0.22
10635	J215616-521215	329.07	-52.204	0.007	96.3	66.21	88.14	1.98	0.73	0.77	FRII	19.44	8000070025003470	0.5
10083	J215617-573351	329.07	-57.564	0.004	58.21	23.22	49.1	2.36	0.45	0.50	FRI	19.75	8000052511001470	0.59
9501	J215622-580044	329.09	-58.012	0.002	103.71	75.01	103.71	1.16	0.71	0.74	FRII	19.01	8000050962001330	0.34
10083	J215624-554525	329.1	-55.757	0.006	141.28	99.04	124.82	0.8	0.78	0.81	FRII	19.05	8000058096001150	0.39
10635	J215630-530743	329.13	-53.129	0.002	61.82		61.82	1.54			single	19.45	8000066515003970	0.35
10635	J215631-482722	329.13	-48.456	0.003	75.23	44.86	75.23	2.68	0.58	0.62	FRII	15.75		
10635	J215634-514242	329.15	-51.712	0.001	60.83	33.46	60.83	1.06	0.53	0.57	FRII	25.48		
10635	J215641-485457	329.17	-48.916	0.049	74.65	24.82	64.53	0.16	0.37	0.40	FRI	18.56	8000081970004500	0.24
10083	J215641-552641	329.17	-55.445	0.001	46.72	16.11	46.72		0.33	0.36	FRI	24.63		
9501	J215641-613133	329.17	-61.526	0.004	53.32		53.32	1.59			single	17.7		
10635	J215643-520008	329.18	-52.002	0.043	96.28	52.61	83.49	2.98	0.61	0.65	FRII	20.99	8000070915002370	0.59
9501	J215644-584930	329.18	-58.825	0.03	79.17	44.41	73.18	2.57	0.59	0.63	FRII	24.57		
10083	J215645-543119	329.19	-54.522	0.003	93.99	41.97	93.99	0.69	0.43	0.46	FRI	20.85		
9501	J215645-593133	329.19	-59.526	0.01	149.62	80.7	149.62	1	0.53	0.55	FRII	20.48	8000046445001190	0.55
10635	J215646-535136	329.19	-53.86	0.012	91.11	59.63	91.11	1.04	0.64	0.67	FRII	24.22		
10083	J215647-560345	329.2	-56.063	0.003	54.47	23.32	54.47	2.09	0.41	0.45	FRI	20.42	8000057282001310	0.58
9501	J215648-625157	329.2	-62.866	0.013	98.48	55.46	82.84	2.73	0.65	0.69	FRII	22.65	8000037329000170	0.94
9501	J215649-603630	329.21	-60.608	0.007	57.11	24.08	47.33	2.28	0.48	0.54	FRx	21.13	8000043541000460	0.66
9501	J215649-605034	329.21	-60.843	0.001	50.52	14.01	50.52	0.38	0.26	0.29	FRI	24.08		
10635	J215650-483332	329.21	-48.559	0.017	85.6		63.2	1.19			single	17.66	8000083880001280	0.2
9501	J215652-613848	329.22	-61.647	0.025	45.63		42.08	2.8			single	22.24	8000040035005730	0.98

Continued on next page

Table 4.2 – Continued from previous page

SBID	Source Name	RA (J2000) (deg)	DEC (J2000) (deg)	Flux Density (Jy)	Size (")	a (")	b (")	PA (°)	a/b _{max}	a/b _{min}	Class	Mag (r-band)	DESI ID	Z
10083	J215655-531417	329.23	-53.238	0.002	67.57	43.86	67.57	2.32	0.63	0.67	FR II	25.31		
9501	J215700-575704	329.25	-57.951	0.032	78.23	35.38	78.23	2.49	0.44	0.47	FR I	17.33	8000050962002040	0.21
9501	J215704-573801	329.27	-57.634	0.001	56.13	20.87	56.13		0.36	0.39	FR I	17.07		
9501	J215704-603629	329.27	-60.608	0.006	41.53	16.25	37.33	1.64	0.41	0.47	FR I	20.09	8000043541000430	0.62
10635	J215709-481937	329.29	-48.327	0.102	177.23	74.98	157.86	0.5	0.47	0.48	FR I	17.82	8000084841001000	
10083	J215712-540907	329.3	-54.152	0.008	56	28.07	50.4	1.61	0.53	0.59	FR II	19.72		
9501	J215714-613334	329.31	-61.559	0.003	70.85		70.85	2.23			single	17.51	8000040725001630	0.27
10635	J215715-483638	329.32	-48.611	0.019	146.83	104.8	132.93	1.92	0.77	0.80	FR II	16.76	8000083880000380	0.19
10635	J215716-512118	329.32	-51.355	0.008	75.63	32.06	59.34	0.1	0.52	0.56	FR II	23.23		
9501	J215716-625447	329.32	-62.913	0.006	114.06	73.09	114.06	0.63	0.63	0.66	FR II	21.18	8000036665005650	0.75
10083	J215716-541914	329.32	-54.321	0.09	48.44	16.12	46.89	2.61	0.33	0.36	FR I	24.82		
10635	J215717-490717	329.32	-49.121	0.002	63.55	18.42	63.55	0.89	0.28	0.30	FR I	20.73	8000081971000080	0.56
9501	J215721-581311	329.34	-58.22	0.004	101.04		101.04	1.81			single	14.6	8000050197002530	0.05
10083	J215722-540253	329.34	-54.048	0.004	60.32	23.09	60.32	0.79	0.37	0.40	FR I	23.12	8000063935001590	1.02
9501	J215724-574326	329.35	-57.724	0.001	63.3	35.99	63.3		0.55	0.59	FR II	19.36	8000051734002650	0.4
10083	J215726-580547	329.36	-58.096	0.006	69.77	37.78	56.4	0.85	0.64	0.70	FR II	19.15	8000050962000340	0.48
9501	J215726-611513	329.36	-61.254	0.003	69.46	34.06	53.15	0.09	0.61	0.67	FR II	23.22	8000041420003190	1.07
10635	J215728-520606	329.37	-52.102	0.021	63.24	29.12	58.2	0.33	0.48	0.52	FRx	23.31		
10083	J215738-553644	329.41	-55.612	0.001	54.6	24.44	54.6	3.01	0.43	0.47	FR I	20.27		
10083	J215738-563431	329.41	-56.575	0.001	45.35		45.35	2.37			single	21.23	8000055672001100	0.72
10635	J215739-512825	329.41	-51.474	0.016	83.52	38.21	67.96	2.3	0.54	0.58	FR II	23.31	8000072709002650	
9501	J215744-614832	329.44	-61.809	0.009	68.51		68.51	1.77			single	16.81	8000040035001790	
10083	J215748-564938	329.45	-56.827	0.001	58.28	24.33	50.13	0.14	0.46	0.51	FRx	21.95	8000054874001120	0.87
9501	J215749-582315	329.45	-58.388	0.003	87.25	49.81	67.4	1.46	0.71	0.77	FR II	22.35	8000049435004290	0.94
9501	J215751-585023	329.46	-58.84	0.013	210.7	142.05	210.7	0.09	0.67	0.68	FR II	17.33	8000048680000670	0.23
10083	J215751-544411	329.47	-54.736	0.028	74.97	40.05	63.69	0.06	0.61	0.65	FR II	19.8		
10635	J215752-485943	329.47	-48.995	0.01	52.4		44.58	0.05			single	21.66	8000081971002520	0.77
10635	J215755-514551	329.48	-51.764	0.001	59.41	23.36	59.41	1.42	0.38	0.41	FR I			
10083	J215759-534234	329.5	-53.709	0.01	45.92	16	38.73	1.62	0.39	0.44	FR I	23.06		
10635	J215759-521108	329.5	-52.186	0.013	53.37		49.51	0.7			single	20.88	8000070026003950	
10083	J215802-543411	329.51	-54.57	0.001	53.87	30.1	53.87		0.53	0.59	FR II	26.18	8000062242001070	
10083	J215806-572526	329.53	-57.424	0.032	41.7	14.56	41.6	1.09	0.33	0.37	FR I	23.92	8000052512004290	0.47
9501	J215808-595646	329.53	-59.946	0.001	45.93	17.3	45.93	2.72	0.36	0.40	FR I	19.62	800004982003860	0.7
10083	J215811-560629	329.55	-56.108	0.023	84.82	44.94	72.33	1.93	0.60	0.64	FR II	21.65	8000057283000420	0.78
10635	J215812-502241	329.55	-50.378	0.002	86.48	26.41	86.48	0.24	0.30	0.31	FR I	22.01	8000076356003620	
9501	J215815-625004	329.57	-62.834	0.006	118.32	61.74	88.41	1.94	0.68	0.72	FR II	22.06		
10635	J215816-491717	329.57	-49.288	0.014	115.1	74.58	115.1	1.74	0.63	0.66	FR II	22.55		
10083	J215816-553132	329.57	-55.526	0.016	97.04	47.61	97.04	0.41	0.48	0.50	FRx	21.24		
10635	J215817-484155	329.57	-48.699	0.001	58.51		58.51	0.71			single	23.44	8000082923003810	

Continued on next page

Table 4.2 – Continued from previous page

SBID	Source Name	RA (J2000) (deg)	DEC (J2000) (deg)	Flux Density (Jy)	Size (")	a (")	b (")	PA (°)	a/b _{max}	a/b _{min}	Class	Mag (r-band)	DESID	Z
9501	J215819-622047	329.58	-62.346	0.08	86.77	11.46	69.87	0.08	0.16	0.17	FRI	19.91	8000038671000770	0.66
10083	J215820-560918	329.58	-56.155	0.018	40.68	38.72	38.72	0.47			single	20.42	8000056476004280	0.59
9501	J215821-602400	329.59	-60.4	0.035	104.73	54.66	91.28	3.13	0.58	0.62	FRII	21.99		
10635	J215822-500133	329.59	-50.026	0.014	117.76	69.48	117.76	1.02	0.58	0.60	FRII	23.16		
9501	J215826-601817	329.61	-60.305	0.001	50.86	60.16	50.86	1.48	0.59	0.63	single	23.11	8000044259001730	
10635	J215830-484300	329.63	-48.717	0.075	99.62	246.71	98.7	3.07	0.59	0.85	FRII	23.6	8000082923003500	
10635	J215830-510029	329.63	-51.008	0.01	293.95	246.71	292.44	2.78	0.84	0.85	FRII	18.73	8000074523001620	
10083	J215831-542800	329.63	-54.467	0.02	51.57	24.8	51.57	0.19	0.46	0.51	FRx	20.32	8000062243002600	0.48
10083	J215832-555137	329.64	-55.86	0.035	62.4	16.22	53.3	0.33	0.29	0.32	FRI	15.75	8000058097000160	0.15
10083	J215835-564411	329.65	-56.736	0.024	68.99	23.32	59.31	0.58	0.38	0.41	FRI	21.83	8000054875003060	0.8
9501	J215838-603833	329.66	-60.643	0.062	205.25	34.21	210.23	2.53	0.16	0.16	FRI	14.87	8000042830005300	0.07
10083	J215845-573739	329.69	-57.628	0.02	53.75	24.08	48.68	1.5	0.47	0.52	FRx	99		
9501	J215849-581112	329.7	-58.187	0.003	54.15	70.88	54.15	3	0.56	0.58	single	18.69	8000050197003070	0.39
10635	J215851-513100	329.72	-51.517	0.081	114.3	70.88	124.66	2.77	0.56	0.56	FRII	22.66		
10635	J215852-530543	329.72	-53.095	0.001	58.29	31.46	58.29	0.54	0.52	0.56	FRII	21.76	8000067386000610	0.72
10635	J215857-513412	329.74	-51.57	0.006	68.81	30.07	51.73	1.64	0.55	0.61	FRII	22.25	8000072710000910	0.94
10635	J215857-482829	329.74	-48.475	0.002	76.8	45.4	76.8	2.8	0.57	0.61	FRII	22.92		
10083	J215902-560504	329.76	-56.084	0.004	63.96	19.38	63.96	1.68	0.29	0.32	FRI	17.98	8000057284000810	0.29
10635	J215903-531710	329.76	-53.286	0.016	167.21	116.16	149.12	3.09	0.77	0.79	FRII	22.59	8000066517001380	0.71
9501	J215906-585938	329.78	-58.994	0.042	58.31	19.8	49.77	0.74	0.38	0.42	FRI	20.96	8000047931002400	0.67
10083	J215907-560308	329.78	-56.052	0.004	47.73	33.75	47.73	0.16	0.49	0.53	single	19.25	8000057284001180	0.52
9501	J215912-582657	329.8	-58.449	0.003	65.74	33.75	65.74	1.12	0.49	0.53	FRx	22.19	8000049436002870	0.77
10635	J215912-512325	329.8	-51.39	0.002	66.94	66.94	66.94	0.12	0.44	0.46	single	20.58	8000072710004020	0.46
10635	J215913-503840	329.81	-50.644	0.013	94.74	35.18	78.24	1.22	0.44	0.46	FRI	17.38	8000075437002870	0.21
10083	J215916-532540	329.82	-53.428	0.003	53.12	16.86	36.95	1.53	0.43	0.49	FRI	18.83	8000065651002600	0.32
10083	J215921-561605	329.84	-56.268	0.086	46.6	46.49	46.49	2.23	0.64	0.67	single	20.24	8000056476002200	0.5
10635	J215926-495642	329.86	-49.945	0.001	111.6	56.27	111.6	2.3	0.49	0.52	FRx	24.04		
9501	J215927-601829	329.86	-60.308	0.005	136.64	87.52	136.64	1.2	0.63	0.65	FRII	18.99	8000044259001680	0.35
10083	J215931-572307	329.88	-57.385	0.003	80.92	26.82	80.92	0.22	0.32	0.34	FRI	19.2	8000052512004940	0.32
10083	J215933-572023	329.88	-57.34	0.103	96.32	63.56	96.74	0.5	0.64	0.67	FRII	18.3		
10635	J215933-513902	329.89	-51.651	0.01	93.11	93.11	93.11	2.3	0.49	0.52	single	17.4	8000071811003440	0.22
9501	J215938-625331	329.91	-62.892	0.002	84.81	84.81	84.81	0.44	0.44	0.44	single	17.09	8000036667005210	0.15
10635	J215938-504035	329.91	-50.676	0.001	48.57	48.57	48.57	2.83	0.37	0.40	single	22.11	8000075437002450	0.73
10083	J215940-524358	329.92	-52.733	0.12	67.23	24	62.28	0.18	0.37	0.40	FRI	18.22	8000068262002680	
9501	J215944-623136	329.94	-62.527	0.005	77.48	45.67	77.48	2.02	0.57	0.61	FRII	23.05		
10083	J215948-543915	329.95	-54.654	0.053	155.13	50.27	156.72	1.33	0.32	0.33	FRI	19.77	8000061404003310	0.45
10083	J215953-563410	329.97	-56.569	0.007	104	66.02	104	2.69	0.62	0.65	FRII	17.54	8000055673001080	0.22
10635	J215955-511539	329.98	-51.261	0.003	66.94	66.94	66.94	2.92	0.33	0.36	single	20.37	8000073614001750	0.68
9501	J215958-593923	330	-59.656	0.032	75.3	23.42	68.38	1.57	0.33	0.36	FRI	20.15	8000045713004180	0.5

Continued on next page

Table 4.2 – Continued from previous page

SBID	Source Name	RA (J2000) (deg)	DEC (J2000) (deg)	Flux Density (Jy)	Size (")	a (")	b (")	PA (°)	a/b _{max}	a/b _{min}	Class	Mag (r-band)	DESI ID	Z
10083	J215959-570924	330	-57.157	0.015	65.62	26.83	65.62	2.41	0.39	0.43	FR I	19.62		
10083	J220001-544350	330.01	-54.731	0.006	48.31	21.26	42.59	2.33	0.47	0.53	FRx	19.99	8000061404002390	0.53
10635	J220004-492925	330.02	-49.49	0.003	63.15	21.13	63.15	0.09	0.32	0.35	FR I	18.88	8000080081002610	0.28
9501	J220005-624457	330.02	-62.749	0.015	62.42		50.93	3.13			single	18.47	8000037330002990	0.4
9501	J220007-591800	330.03	-59.3	0.003	98.73	17.01	98.73	2.41	0.17	0.18	FR I	19.52	8000047186001580	0.46
9501	J220010-590811	330.04	-59.136	0.004	83.38	42.19	61.23	3.06	0.66	0.72	FR II	20.69	8000047186004440	
9501	J220011-602732	330.05	-60.459	0.103	181.05	115.6	169.47	1.05	0.67	0.69	FR II	20.11		
10083	J220011-554636	330.05	-55.777	0.003	81.19	42.06	81.19	2.74	0.50	0.53	FR II	20.72	8000043542003290	0.48
10083	J220016-554947	330.07	-55.83	0.004	62.4	36.06	55.92	1.92	0.62	0.67	FR II	19.85		
10083	J220017-561859	330.07	-56.316	0.009	46.6		36.77	2.93			single	20.47	8000056477001220	0.65
10083	J220021-572120	330.09	-57.356	0.021	73.91	26.93	59.1	0.81	0.44	0.48	FR I	22.68	8000053295000450	1.09
9501	J220028-603613	330.12	-60.604	0.013	72.75	26.72	55.57	1.62	0.46	0.50	FRx	17.96	8000043542000510	0.24
10083	J220032-571326	330.13	-57.224	0.011	162.91	134.84	154.64	0.44	0.86	0.89	FR II	21.15	8000053295003000	0.7
10635	J220032-490829	330.13	-49.141	0.007	60.86	31.26	53.42	1.57	0.56	0.61	FR II	23.7		
10083	J220032-531809	330.14	-53.303	0.001	53.12		53.12	0.86			single	19.96	8000066518001140	0.54
10635	J220033-520415	330.14	-52.071	0.021	89.9	27.17	89.9	2.7	0.29	0.31	FR I	18.88	8000070918000960	0.46
10083	J220040-541516	330.17	-54.254	0.005	60.88		60.88	1.98			single	17.91	8000063088002210	0.23
10083	J220044-545049	330.19	-54.847	0.001	74.28		74.28	2.33			single	19.61		
10635	J220045-492302	330.19	-49.384	0.27	90.91	35.44	74.37	1.84	0.46	0.49	FR I	24.06		
10083	J220048-524619	330.2	-52.772	0.005	84.96	52.35	84.96	0.86	0.60	0.63	FR II	23.48	8000068263001910	0.2
10083	J220048-533626	330.2	-53.607	0.063	98.36	58.14	90.23	3.07	0.63	0.66	FR II	17.95	8000065652000320	0.54
10083	J220054-540401	330.23	-54.067	0.024	122.72	74.19	116.14	0.67	0.63	0.65	FR II	19.75	8000063937000960	0.23
10635	J220054-522320	330.23	-52.389	0.002	106.39	61.83	106.39	0.79	0.57	0.60	FR II	17.92	8000069143004780	0.23
10083	J220055-552806	330.23	-55.468	0.008	59.56	39.29	57.67	1.86	0.65	0.71	FR II	26.18		
10083	J220057-531103	330.24	-53.184	0.037	225.82	172.29	197.03	3.01	0.86	0.89	FR II	20.7	8000066518003420	0.74
10083	J220059-532922	330.25	-53.489	0.221	158.73	120.43	160.56	0.63	0.74	0.76	FR II	23.12	8000065652001910	0.67
9501	J220109-593955	330.29	-59.665	0.296	103.91	59.46	96.82	2.33	0.60	0.63	FR II	21.41	8000045713004120	0.81
10635	J220111-521550	330.3	-52.264	0.001	57.92	28.69	57.92		0.47	0.52	FRx	22.65	8000070028002280	0.81
10635	J220114-504557	330.31	-50.766	0.047	65.44	31.11	63.29	2.44	0.47	0.51	FRx	23.81		
9501	J220115-624946	330.31	-62.829	0.009	74.46	38.47	61.7	1.71	0.60	0.65	FR II	21.73	8000037331001020	0.85
10635	J220115-531734	330.32	-53.293	0.007	47.55		36.26	1.65			single	26.16	8000066518001300	
10635	J220116-500228	330.32	-50.041	0.042	274.16	138.76	274.16	2.89	0.50	0.51	FR II	15.98	8000078211001160	0.1
9501	J220117-585735	330.32	-58.96	0.011	80.76	42.53	68.16	2.32	0.60	0.65	FR II	19.05	8000047932002700	0.44
10635	J220120-494717	330.34	-49.788	0.001	64.61	29.91	64.61	0.75	0.45	0.48	FR I	24.59		
10083	J220133-551502	330.39	-55.251	0.025	108.11	67.23	95.54	1.98	0.69	0.72	FR II	18.56		
10083	J220136-535743	330.4	-53.962	0.198	50.12	18.44	50.6	0.6	0.35	0.38	FR I	24.15		
10083	J220137-543738	330.41	-54.627	0.001	45.33		45.33	1.52	0.32	0.34	single	21.27	8000061405004290	0.55
10083	J220139-564629	330.41	-56.775	0.076	65.35	24.33	73.31	2.25	0.32	0.34	FR I	18.15		
10083	J220150-524756	330.46	-52.799	0.002	68.71		68.71	0.69			single	17.65	8000068264001180	0.22

Continued on next page

Table 4.2 – Continued from previous page

SBID	Source Name	RA (J2000) (deg)	DEC (J2000) (deg)	Flux Density (Jy)	Size (")	a (")	b (")	PA (°)	a/b _{max}	a/b _{min}	Class	Mag (r-band)	DESI ID	Z
10635	J220151-492640	330.46	-49.444	0.024	97.28	63.78	94.03	2.18	0.66	0.70	FR II	19.57	8000080083003380	0.48
10635	J220152-503611	330.47	-50.603	0.093	114.56	61.61	107.85	0.65	0.56	0.58	FR II	23.06	8000076580000350	
9501	J220156-621416	330.48	-62.238	0.004	107.12	66.2	107.12	1.11	0.60	0.63	FR II	21.4	8000038672003750	0.83
10083	J220156-562439	330.49	-56.411	0.027	61.89	51.18	51.18	2.11			single	18.44	8000055674004240	0.24
10083	J220202-574505	330.52	-57.751	0.006	38.95	30.85	33.34	2.94			single	22.61	8000051736002410	0.73
10635	J220206-485531	330.53	-48.925	0.004	60.69	60.69	60.69	2.13	0.49	0.53	FRx	20.18	8000081974003970	0.53
10635	J220212-492522	330.55	-49.423	0.083	104.02	52.04	104.02	1.67	0.49	0.51	FRx	17.79		
9501	J220212-575636	330.55	-57.943	0.003	94.46	58.72	94.46	0.45	0.61	0.64	FR II	21.12	8000050965002800	0.52
10083	J220218-532527	330.58	-53.424	0.004	93.84	45.56	93.84	0.03	0.47	0.50	FRI	18.59	8000065653003270	0.36
10635	J220218-523107	330.58	-52.519	0.002	70.62	28.49	70.62		0.39	0.42	FRI	24.47		
10635	J220220-500642	330.59	-50.112	0.033	82.42	52.5	81.54	2.28	0.62	0.66	FR II	20.75		
10083	J220220-545254	330.59	-54.882	0.058	239.79	201.04	248.27	1.4	0.80	0.82	FR II	22.03	8000060572004450	0.92
10635	J220223-520615	330.6	-52.104	0.033	114.3	64.03	111.7	0.22	0.56	0.59	FR II	18.87	8000070919000330	0.11
10635	J220224-504530	330.6	-50.758	0.007	65.44	28.28	49.26	0.6	0.55	0.60	FR II	24.47		
10635	J220224-490053	330.6	-49.015	0.04	60.86	28.43	54.81	2.49	0.50	0.54	FRx	21.75	8000081974002070	0.7
9501	J220232-591136	330.63	-59.193	0.003	56	16.22	56	1.84	0.28	0.30	FRI	21.23	8000047187003190	0.61
10083	J220232-571210	330.63	-57.203	0.018	71.36	34.18	61.63	1.77	0.53	0.58	FR II	22.02	8000053296003710	0.87
9501	J220233-591630	330.64	-59.275	0.014	188.83	134.65	188.83	2.73	0.70	0.72	FR II	17.92		
10083	J220233-560624	330.64	-56.107	0.001	85.48	60.21	85.48	1.14	0.68	0.73	FR II	27.97	8000057286000480	
10635	J220238-524149	330.66	-52.697	0.006	67.42	40.29	67.42	1.92	0.58	0.62	FR II	22.31	8000068264002980	0.82
10083	J220239-552335	330.66	-55.393	0.019	46.44		46.02	2.42			single	20.72	8000058919004080	0.62
10083	J220241-564657	330.67	-56.783	0.004	46.32	21.54	38.71	2.68	0.52	0.59	FR II	24.25		
10083	J220243-541049	330.68	-54.18	0.001	52.36	23.54	52.36	3.12	0.43	0.47	FRI	21.02	8000063089003350	0.59
9501	J220244-602900	330.69	-60.483	0.026	89.97	47.47	84	1.37	0.55	0.58	FR II	18.99	8000043544003660	0.41
10083	J220248-551907	330.7	-55.319	0.009	66.78	24.72	66.78	2.57	0.36	0.38	FRI	19.88	8000059742001050	
9501	J220248-583711	330.7	-58.62	0.002	70.54	21.94	70.54	1.58	0.30	0.32	FRI	22.64		
10083	J220249-572808	330.71	-57.469	0.108	66.37		66.72	2.93			single	15.5	8000052514002770	0.11
10083	J220252-543727	330.72	-54.624	0.018	91.12	53.81	81.29	2.28	0.64	0.68	FR II	20.53	8000062245000060	0.68
10635	J220252-522123	330.72	-52.356	0.012	140.68	93.38	124.4	0.83	0.74	0.77	FR II	20	8000070029000710	0.57
10083	J220253-561522	330.72	-56.256	0.002	43.12	10.2	43.12	0.18	0.22	0.25	FRI			
9501	J220256-601705	330.74	-60.285	0.18	46.34	16.12	46.34	0.92	0.33	0.37	FRI	22.7		
9501	J220258-585023	330.74	-58.84	0.002	65		65	0.08			single	23.66		
10635	J220259-520206	330.75	-52.035	0.012	67.42		56.08	2.69			single	22.19		
10635	J220259-493400	330.75	-49.567	0.003	54.11		54.11	1.77			single	21.28	8000080083000960	
10083	J220302-533810	330.76	-53.636	0.008	58.52	30.27	52.95	1.42	0.55	0.60	FR II	23.44		
9501	J220306-592338	330.78	-59.394	0.001	64.59		64.59	0.01			single	19.52	8000046448004470	0.48
10083	J220312-570752	330.8	-57.131	0	27.34		30.14				single	23.24	8000053296005040	1.07
10083	J220312-583418	330.8	-58.572	0.008	86.94		86.94	2.45			single	20.97	8000049438000700	0.83
10635	J220314-485751	330.81	-48.964	0.673	80.05	29.73	80.48	0.48	0.36	0.38	FRI	20.37	8000081975003340	0.42

Continued on next page

Table 4.2 – Continued from previous page

SBID	Source Name	RA (J2000) (deg)	DEC (J2000) (deg)	Flux Density (Jy)	Size (")	a (")	b (")	PA (°)	a/b _{max}	a/b _{min}	Class	Mag (r-band)	DESI ID	Z
10083	J220314-531216	330.81	-53.204	0.047	46.6	19.7	46.45	0.49	0.40	0.45	FRI	19.92	8000066519002740	0.46
9501	J220322-622736	330.84	-62.46	0.095	56.9	23.32	53.07	2.68	0.42	0.46	FRI	20.17		
10083	J220328-555219	330.87	-55.872	0.021	87.12	55.79	85.48	2.92	0.63	0.67	FRII	15.69	8000058100000040	0.1
9501	J220333-590355	330.89	-59.065	0.013	73.54	70.81	70.81	1.82			single	19.13	8000047933000970	0.41
10083	J220333-572845	330.89	-57.479	0.021	71.06	71.06	71.06	1			single	22.78	8000052515002880	0.53
10635	J220334-501422	330.89	-50.239	0.003	55.63	55.63	55.63	0.94			single	20.14	8000077283001880	
10083	J220335-565123	330.9	-56.856	0.001	45.35	45.35	45.35	0.58			single	19.79		
10083	J220335-554655	330.9	-55.782	0.013	43.65	38.52	38.52	1.7	0.65	0.69	single	21.94	8000058100001650	0.97
9501	J220336-594356	330.9	-59.732	0.011	103.91	53.67	80.02	0.43			FRII	22.39	8000045714002930	0.9
10083	J220337-540751	330.9	-54.131	0.012	41.56	38.91	38.91	2.56			single	24.03		
10635	J220340-520016	330.92	-52.004	0.002	59.29	59.29	59.29	0.7			single	21.27	8000070920002080	0.83
10083	J220342-543432	330.93	-54.576	0.005	58.68	22.23	58.68	0.79	0.36	0.40	FRI	19.18	8000062246000750	0.34
10635	J220348-500553	330.95	-50.098	0.009	66.77	46.47	46.47	0.66			single	15.9	8000078212000390	0.07
9501	J220349-615501	330.96	-61.917	0.006	48.01	34.21	34.21	0.11			single	18.14		
10083	J220353-561254	330.97	-56.215	0.029	83.35	42.05	70.46	1.45	0.58	0.62	FRII	18.52	8000056479002910	0.4
9501	J220354-624419	330.98	-62.739	0.004	69.91	15.86	69.91	0.61	0.22	0.24	FRI	20.28	8000037332003270	0.66
10635	J220354-482706	330.98	-48.452	0.003	112.31	85.17	112.31	0.79	0.74	0.78	FRII	21.6	8000083884004170	0.88
10635	J220357-513523	330.99	-51.59	0.024	127.09	86.83	110.95	3.03	0.77	0.80	FRII	19.04	8000072713000520	
9501	J220358-573630	330.99	-57.608	0.002	75.9	22.25	75.9	1.23	0.28	0.30	FRI	19.85	8000052515000400	0.53
10083	J220403-560935	331.01	-56.16	0.004	46.6	33.01	33.01	0.97			single	18.64	8000056479004030	0.39
10635	J220403-520043	331.02	-52.012	0.003	59.29	32.35	32.35	1.46			single	23.34		
9501	J220417-584434	331.07	-58.743	0.027	95.73	30.07	81.65	1.75	0.36	0.38	FRI	18.55		
10635	J220417-491622	331.07	-49.273	0.009	87.76	62.03	84.42	1.76	0.71	0.76	FRII	20.92		
9501	J220419-585045	331.08	-58.846	0.003	137.58	108.81	124.05	2.86	0.86	0.90	FRII			
9501	J220424-605907	331.1	-60.985	0.042	77.31	34	65.7	1.03	0.50	0.54	FRx	25.23	8000042125003220	
10635	J220434-495857	331.14	-49.983	0.001	51.55	22.12	51.55		0.41	0.45	FRI	15.86		
10083	J220436-543101	331.15	-54.517	0.001	51.35	51.35	51.35	2.61			single	21.36		
10635	J220441-511414	331.17	-51.237	0.003	49.18	19.45	49.18	1.84	0.38	0.42	FRI	19.72		
9501	J220441-623713	331.17	-62.62	0.042	206.19	134.12	206.19	1.15	0.64	0.66	FRII	14.87		
10635	J220445-520407	331.19	-52.069	0.007	67.42	62.45	62.45	1.18			single	15.5	8000070920000910	0.07
10083	J220447-545704	331.2	-54.951	0.001	80.98	39.77	80.98	0.11	0.48	0.51	FRx	21.53	8000060573002820	0.77
10635	J220449-510048	331.21	-51.013	0.012	85.94	38.88	85.94	2.92	0.44	0.47	FRI	22.08	8000074527001570	0.86
9501	J220450-580644	331.21	-58.112	0.043	52.8	10.83	45.93	2.74	0.22	0.25	FRI	13.88		
10083	J220455-555426	331.23	-55.907	0.082	138.03	109.39	125.98	3.12	0.85	0.89	FRII	17.16		
10635	J220457-510303	331.24	-51.051	0.004	97.58	66.77	97.58	0.45	0.67	0.70	FRII	21.58	8000074527001040	0.77
9501	J220504-595450	331.27	-59.914	0.004	109.18	66.66	109.18	0.46	0.60	0.62	FRII	25.28	8000044986003970	0.83
9501	J220505-602641	331.27	-60.445	0.001	51.64	24.34	51.64	2.22	0.45	0.50	FRI	21.78	8000043545004010	0.83
10635	J220507-523317	331.28	-52.555	0.377	114.3	71.39	116.09	0.27	0.60	0.63	FRII	23.44		
9501	J220512-590647	331.3	-59.113	0.05	54.93	21.63	49.3	2.64	0.42	0.46	FRI	22		

Continued on next page

Table 4.2 – Continued from previous page

SBID	Source Name	RA (J2000) (deg)	DEC (J2000) (deg)	Flux Density (Jy)	Size (")	a (")	b (")	PA (°)	a/b _{max}	a/b _{min}	Class	Mag (r-band)	DESI ID	Z
9501	J220517-621620	331.32	-62.272	0.01	169.43	112.64	169.43	2.73	0.66	0.67	FR II	21.14	8000038674002700	0.55
10635	J220517-510653	331.32	-51.115	0.135	79.47	22.36	70.26	1.01	0.31	0.33	FRI	21.42		
10083	J220525-554332	331.36	-55.726	0.002	49.45	49.45	49.45	1.13			single	23.76	8000058101002350	
10083	J220528-552856	331.37	-55.482	0.003	46.17	46.17	46.17	2.26			single	20.18	8000058920002240	0.7
10083	J220531-574252	331.38	-57.714	0.004	45.08	33.27	33.27	1.17			single	24.01		
10083	J220532-551456	331.39	-55.249	0.026	62.76	28.64	57.12	2.73	0.48	0.52	FRx	21.11	8000059744002280	0.67
10083	J220533-563705	331.39	-56.618	0	50.27	29.75	50.27		0.56	0.62	FR II	25.59		
10635	J220541-520322	331.42	-52.056	0.01	83.26	28.84	63.36	2.16	0.44	0.47	FRI	21.3	8000070921001350	0.79
10083	J220542-533300	331.43	-53.55	0.005	113.18	68.05	113.18	1.11	0.59	0.61	FR II	23.98		
9501	J220544-614752	331.43	-61.798	0.004	199.54	162.02	199.54	3.07	0.80	0.82	FR II	22.08	8000040039002110	0.74
10635	J220546-513238	331.44	-51.544	0.023	89.56	49.12	87.63	0.87	0.55	0.58	FR II	21.01	8000072714001250	0.41
9501	J220547-621200	331.45	-62.2	0.034	107.12	47.71	92.43	2.15	0.50	0.53	FR II	17.86	8000038674004670	
10635	J220548-491739	331.45	-49.294	0.002	76.52	42.6	76.52	1.61	0.54	0.58	FR II	20.29		
10635	J220548-522240	331.45	-52.378	0.002	71.78	34.75	71.78	1.77	0.47	0.50	FRx	19.97	8000070031000020	0.37
10635	J220549-492623	331.46	-49.44	0.003	56.26	31.96	31.96	1.31			single	24.15		
9501	J220550-600710	331.46	-60.119	0.003	98.81	52.4	98.81	1.98	0.52	0.54	FR II	21.2	8000044986000090	0.63
10083	J220555-553243	331.48	-55.545	0.031	43.8	14.64	41.5	2.37	0.33	0.38	FRI	18.7	8000058921001410	
9501	J220557-581400	331.49	-58.233	0.001	64.27	64.27	64.27	1.02			single	25.08	8000050201002560	
10635	J220600-501708	331.5	-50.286	0.004	66.3	30.36	66.3	2.85	0.44	0.48	FRI	18.18	8000077284001450	0.29
9501	J220600-622446	331.5	-62.413	0.006	56.9	42.6	42.6	1.14			single	21.55		
10635	J220602-502543	331.51	-50.429	0.003	53.53	16.83	53.53	2.91	0.30	0.33	FRI	22.15	8000076561002770	0.24
10083	J220604-562041	331.52	-56.345	0.025	127.45	99.05	118.78	3.12	0.82	0.85	FR II	20.96	8000056480000520	0.54
10083	J220607-525816	331.53	-52.971	0.007	77.47	40.57	65.9	1.18	0.59	0.64	FR II	20.65	8000067391002210	
9501	J220609-605113	331.54	-60.854	0.006	88.47	56.86	79.71	2.52	0.69	0.74	FR II	19.59	8000052516001460	0.57
9501	J220614-573238	331.56	-57.544	0.04	80.83	47.1	77.93	0.15	0.59	0.62	FR II	19.28	8000044986000040	0.45
9501	J220616-600727	331.57	-60.124	0.002	62.51	62.51	62.51	0.2			single	23.19		
10635	J220616-504010	331.57	-50.669	0.024	53.53	20.4	49.09	3.07	0.40	0.44	FRI	24.01		
9501	J220617-605415	331.57	-60.904	0.005	43.14	17.89	36.94	0.4	0.45	0.52	FRx	24.01		
9501	J220624-581721	331.6	-58.289	0.009	96.87	46.92	96.87	1.34	0.47	0.50	FRI	17.69	8000050201001330	0.23
9501	J220626-605634	331.61	-60.943	0.058	69.54	32.8	62.11	2.29	0.51	0.55	FR II	26.04		
10083	J220630-570722	331.63	-57.123	0.013	49.99	20.1	42.64	1.71	0.45	0.50	FRx	22.61		
10083	J220632-570549	331.64	-57.097	0.003	102.84	76.06	92.69	1.4	0.80	0.84	FR II	23.06		
10635	J220638-512743	331.66	-51.462	0.007	183.25	129.93	156.37	1.46	0.82	0.84	FR II	19.58	8000072715002400	0.46
10635	J220638-501450	331.66	-50.247	0.036	58.62	55.01	55.01	1.13			single	20.95	8000077285002250	
10635	J220641-523923	331.67	-52.656	0.008	59.93	44.85	44.85	0.61	0.66	0.69	single	21.6	8000068267003080	0.78
9501	J220641-604603	331.67	-60.768	0.005	106	71.53	106	0.57	0.62	0.64	FR II	23.07	8000042834002970	
10083	J220643-571949	331.68	-57.33	0.006	243.03	152.85	243.03	0.83	0.62	0.64	FR II	18.04	8000053298001280	0.27
10083	J220644-550803	331.68	-55.134	0.003	64.78	33.56	64.78	0.83	0.50	0.54	FRx	26.05		
10083	J220646-580219	331.69	-58.039	0.008	78.39	41.04	66.52	0.84	0.59	0.64	FR II	20.64	8000050967001540	0.62

Continued on next page

Table 4.2 – Continued from previous page

SBID	Source Name	RA (J2000) (deg)	DEC (J2000) (deg)	Flux Density (Jy)	Size (")	a (")	b (")	PA (°)	a/b _{max}	a/b _{min}	Class	Mag (r-band)	DESI ID	Z
10083	J220651-562135	331.71	-56.36	0.001	45.66	17.03	45.66		0.35	0.39	FRI	21.05		
10635	J220653-502638	331.72	-50.444	0.002	67.81	28.07	67.81	0.48	0.40	0.43	FRI	22.35		
10635	J220655-511818	331.73	-51.305	0.002	75.73		75.73	1.07			single	19.63	8000073619000960	0.46
10083	J220659-563443	331.75	-56.579	0.008	91.48	58.06	86.41	1.55	0.65	0.69	FRII	19.27	8000055677000650	0.48
9501	J220700-594908	331.75	-59.819	0.003	48.99	13.41	48.99	0.18	0.26	0.29	FRI	18.75	8000045716001080	0.34
10635	J220701-500715	331.76	-50.121	0.025	58.62		54.94	0.84			single	18.81	8000078215000010	0.41
10635	J220702-514643	331.76	-51.779	0.005	46.11		45.17	2.13			single	19.15	8000071815001520	0.43
10635	J220704-491341	331.77	-49.228	0.015	63.46	34.23	65.64	0.13	0.50	0.54	FRII	23.05	8000081029003310	0.9
10635	J220704-492053	331.77	-49.348	0.003	76.52	50.08	76.52	0.61	0.63	0.68	FRII	16.61		
10635	J220707-524406	331.78	-52.735	0.006	55.24	20.59	55.24	0.54	0.36	0.39	FRI	24.84		
9501	J220709-593323	331.79	-59.556	0.004	56.11	22.36	39.69	1.09	0.53	0.60	FRII	21.67		
9501	J220713-580611	331.81	-58.103	0.003	87.94		87.94	0.84			single	14.59		
10083	J220718-542116	331.83	-54.354	0.016	159.25	117.04	159.25	1.77	0.72	0.75	FRII	21.42	8000050968000410	0.66
10083	J220718-574014	331.83	-57.671	0.005	69.77	31.03	55.35	1.94	0.54	0.59	FRII	21.69	8000051739003670	0.07
10083	J220723-565805	331.85	-56.968	0.003	117.72	93.74	117.72	0.26	0.78	0.81	FRII	20.38		
9501	J220725-595618	331.86	-59.938	0.002	56.96	31.14	56.96	0.18	0.52	0.57	FRII	23.05		
10083	J220727-553334	331.86	-55.559	0.052	92.99	55.03	84.28	2.82	0.63	0.67	FRII	23.95		
9501	J220728-613115	331.87	-61.521	0.008	49.62		40.56	2.62			single	22.98		
10635	J220731-492341	331.88	-49.395	0.003	79.88		79.88	0.63			single	17.64	8000080086005080	0.21
9501	J220735-610918	331.9	-61.155	0.007	71.57	40.5	62.35	2.61	0.62	0.68	single	22.01	8000041425004780	0.57
9501	J220735-580508	331.9	-58.086	0.009	56.02		43.73	2			FRII	21.11	8000050968000650	0.66
10083	J220737-571835	331.91	-57.31	0.037	213.62	63.56	213.62	0.65	0.29	0.30	FRI	15.55	8000053298001210	0.1
9501	J220740-583148	331.92	-58.53	0.009	164.18	98.13	128.24	0.77	0.75	0.78	FRI	21.02	8000049441001520	0.64
10635	J220741-510538	331.92	-51.094	0.021	52.43	14.92	48.85	2.15	0.29	0.32	FRI	20.92		
9501	J220743-602254	331.93	-60.382	0.02	70.21		70.21	2.28			single	18.18	8000043546005390	0.26
10083	J220748-541610	331.95	-53.61	0.034	87.07	28.84	90.22	2.16	0.31	0.33	FRI	18.73	8000065656000190	0.41
10083	J220753-532637	331.97	-53.444	0.039	95.74	60.83	96.32	1.08	0.62	0.65	FRII	23.71	8000063092001550	
10083	J220804-533111	332.02	-53.52	0.002	87.07		87.07	1.74			single	19.25	8000065657001700	0.31
10083	J220805-562202	332.02	-56.367	0.001	85.57		85.57	1.07			single	16.62		
10635	J220806-521035	332.03	-52.176	0.005	57.58		57.58	2.16			single	19.24	8000070033002940	0.36
9501	J220807-600053	332.03	-60.015	0.008	106.39		93.34	0.41	0.57	0.61	single	18	8000044987002000	0.2
9501	J220809-615420	332.04	-61.906	0.003	48.01		48.01	2.05			single	23.92		
9501	J220820-623556	332.08	-62.599	0.029	85.53	30.07	65.71	1.55	0.44	0.48	FRI	19.74	8000038002000580	0.36
10083	J220820-531545	332.09	-53.263	0.004	72.86	34.35	72.86	2.94	0.46	0.49	FRI	19.76		
10083	J220825-561251	332.11	-56.214	0.003	42.78	17.2	38.7	2.52	0.42	0.48	FRI	22.03	8000056481002740	0.85
9501	J220828-591223	332.12	-59.206	0.1	64.68	32.31	62.99	1.1	0.49	0.53	FRx	20.79	8000047190002780	0.65
10635	J220833-521056	332.14	-52.182	0.005	96.21	35.79	96.21	2.11	0.36	0.38	FRI	18.43	8000070033002860	0.24
10083	J220835-562928	332.15	-56.491	0.002	111.08	81.18	111.08	0.72	0.71	0.75	FRII	23.71		

Continued on next page

Table 4.2 – Continued from previous page

SBID	Source Name	RA (J2000) (deg)	DEC (J2000) (deg)	Flux Density (Jy)	Size (")	a (")	b (")	PA (°)	a/b_{\max}	a/b_{\min}	Class	Mag (r-band)	DESID	Z
10083	J220840-525901	332.17	-52.984	0.004	50.02	22.36	38.73	3.02	0.54	0.62	FRII	24.97		
10635	J220849-522607	332.21	-52.435	0.032	138.47	50.48	102.09	2.26	0.48	0.51	FRx	15.28	8000069148002610	0.1
10635	J220852-500755	332.22	-50.132	0.015	130.74	87.32	116.48	0.33	0.73	0.77	FRII	18.08	8000077286004140	0.21
10635	J220854-500222	332.23	-50.039	0.001	39.83	14.82	39.83		0.35	0.40	FRI	18.56	8000078216001500	0.26
10083	J220854-555325	332.23	-55.89	0.002	72.29	44.27	72.29	0.09	0.59	0.63	FRII	18.91	8000057289003750	0.39
10083	J220900-553609	332.25	-55.603	0.04	55.24		55.05	1.98			single	20.94	8000058922000440	0.78
9501	J220905-623728	332.27	-62.624	0.002	124.35	96.99	124.35	0.53	0.76	0.80	FRII	19.86	8000038002000060	0.38
10635	J220905-501115	332.27	-50.188	0.074	58.62	24.08	52.61	2.3	0.44	0.48	FRI			
10083	J220910-572331	332.29	-57.392	0.001	50.12	24.6	50.12	3.12	0.47	0.52	FRx	19.86	8000052518004000	0.24
9501	J220916-601833	332.32	-60.309	0.003	56.98	27.12	56.98	0.74	0.46	0.50	FRI	24.97		
10083	J220921-570416	332.34	-57.071	0.023	96.32	59.06	85.77	0.47	0.67	0.71	FRII	20.69	8000054087000720	0.27
10635	J220923-512600	332.35	-51.433	0.011	157.05	101.36	124.3	2.28	0.80	0.83	FRII	18.58	8000072716002890	0.36
9501	J220933-583618	332.39	-58.605	0.029	76.58	34.97	76.58	2.73	0.44	0.47	FRI	20.06		
10083	J220936-525359	332.4	-52.9	0.002	65.62		65.62	0.8			single	20.3	8000067393003320	0.54
10635	J220939-510857	332.41	-51.149	0.009	52.43		42.2	0.02			single	18.73	8000073620003480	0.35
10635	J220939-484706	332.42	-48.785	0.002	66.67		66.67	1.31			single	22.39	8000082931002250	1.03
9501	J220942-601939	332.43	-60.328	0.054	137.58	100.03	128.1	1.55	0.77	0.80	FRII	23.36		
10635	J220943-525309	332.43	-52.886	0.006	57.18	24.08	47.15	0.78	0.49	0.54	FRx	99		
10083	J220945-530933	332.44	-53.159	0.006	75.68	32.64	75.68	0.77	0.42	0.45	FRI	20.07	8000066523003830	0.47
10083	J220947-553449	332.45	-55.58	0.087	85.28	11.23	81.55	0.12	0.13	0.14	FRI	15.74	8000058923000730	0.17
10083	J220958-525915	332.5	-52.988	0.038	94.45	45.4	94.45	0.68	0.47	0.49	FRI	22.96	8000067393001990	
9501	J220959-621658	332.5	-62.283	0.001	53.64	30.84	53.64		0.55	0.60	FRII	23.13		
10635	J221000-494910	332.5	-49.819	0.004	94.08	63.46	94.08	1.99	0.66	0.69	FRII	21.85	8000079150001200	0.67
10635	J221004-513958	332.52	-51.666	0.064	87.4	43.08	83.3	1.17	0.50	0.53	FRII	19.28	8000071817003690	0.42
10083	J221007-555726	332.53	-55.957	0.006	89.57	59.46	80.57	2.25	0.72	0.76	FRII	22.97		
10635	J221007-515508	332.53	-51.919	0.002	54.55		54.55	0.79			single	24.27	8000070924003580	
10635	J221010-500539	332.55	-50.094	0.021	73.75	34.41	64.12	2.54	0.52	0.56	FRII	20.95	8000078217000430	0.77
9501	J221018-601612	332.58	-60.27	0.059	89.33	44.05	79.08	2.45	0.54	0.58	FRII	22.93	8000044265002540	
9501	J221018-581139	332.58	-58.194	0.002	67.84	39.43	67.84	1.47	0.56	0.60	FRII	23.86		
9501	J221019-600635	332.58	-60.11	0.095	107.03	53.37	91.85	0.15	0.57	0.60	FRII	18.7		
10635	J221021-492937	332.59	-49.494	0.003	80.36	49.25	80.36	0.89	0.59	0.63	FRII	16.15	8000080088003010	0.13
10635	J221027-494102	332.62	-49.684	0.006	112.49	40.98	112.49	1.21	0.36	0.37	FRI	17.46	8000079150003580	0.2
10635	J221030-502715	332.63	-50.454	0.025	204.19	153.82	204.19	1.32	0.74	0.76	FRII	20.45		
10083	J221032-534845	332.64	-53.813	0.021	43.25		39.69	0.66			single	22	8000064798000870	0.86
10083	J221032-550836	332.64	-55.143	0.013	91.77	45.22	91.77	0.01	0.48	0.51	FRx	18.06		
10635	J221032-493658	332.64	-49.616	0.002	63.79		63.79	1.13			single	20.01	8000080088000200	0.51
9501	J221035-610814	332.65	-61.137	0.002	52.61		52.61	0.85			single	20.24		
10635	J221038-503352	332.66	-50.564	0.012	114.61	55.18	114.61	2.5	0.47	0.49	FRI	20.42	8000076364000620	0.49
10635	J221039-494153	332.67	-49.698	0.004	55.01		55.01	2.08			single	20.91	8000079151003760	0.57

Continued on next page

Table 4.2 – Continued from previous page

SBID	Source Name	RA (J2000) (deg)	DEC (J2000) (deg)	Flux Density (Jy)	Size (")	a (")	b (")	PA (°)	a/b _{max}	a/b _{min}	Class	Mag (r-band)	DESI ID	Z
10635	J221042-491433	332.68	-49.243	0.004	71.21	37.38	71.21	1.92	0.51	0.54	FR II	24.66	8000081032003430	
10083	J221046-553032	332.7	-55.509	0.001	48.74		48.74	0.08			single	23.73		
9501	J221050-593818	332.71	-59.638	0.044	216.03	118.73	201.56	2.62	0.58	0.60	FR II	19.32	8000045718004630	0.42
9501	J221053-582100	332.72	-58.35	0.006	56.89	19.7	38.67	1.14	0.48	0.54	FRx	23	8000050204000490	0.25
10635	J221055-520702	332.73	-52.117	0.026	59.99	25.61	60.46	0.94	0.41	0.44	FR I	19.09	8000070924000150	0.39
10083	J221056-554909	332.73	-55.819	0.013	98.92	74.41	102.49	2.49	0.71	0.74	FR II	21.79	8000058104001170	0.66
10635	J221058-501540	332.74	-50.261	0.016	105.81	49.4	98.1	2.16	0.49	0.52	FRx	17.77	8000077288001710	0.22
10635	J221103-501734	332.77	-50.293	0.104	74.32	28.64	70.72	0.26	0.39	0.42	FR I	23.45		
10083	J221106-564549	332.78	-56.764	0	46.1	20.61	46.1		0.42	0.47	FR I	22.42		
9501	J221109-623752	332.79	-62.631	0.014	159.11	48.58	159.11	2.54	0.30	0.31	FR I	18.48	800003735005580	0.37
10083	J221119-532823	332.83	-53.473	0.084	52.87	21.26	46.19	1.36	0.44	0.49	FR I	18.84		
10635	J221120-491226	332.83	-49.207	0.007	86.86	63.53	86.31	2.07	0.72	0.76	FR II	21.04		
10083	J221121-531636	332.84	-53.277	0.003	76.5	52.69	76.5	2.47	0.67	0.71	FR II	20.45	8000066524001410	0.48
10635	J221129-523056	332.87	-52.516	0.02	101.58	64	91.93	3.05	0.68	0.72	FR II	17.67	8000069149001310	0.31
10083	J221130-535256	332.88	-53.882	0.002	59.7	18.43	59.7	2.22	0.30	0.32	FR I	20.88	8000063943003410	0.63
10083	J221131-554003	332.88	-55.668	0.009	119.2	80.4	101.57	0.09	0.77	0.81	FR II	15.69		
9501	J221131-582548	332.88	-58.43	0.016	63.67	29.53	55.92	2.23	0.51	0.55	FR II	19.79	8000049443003130	0.37
9501	J221131-611439	332.88	-61.244	0.002	73.3	35.43	73.3	0.34	0.47	0.50	FRx	23.85		
10083	J221131-561857	332.88	-56.316	0.016	96.32	23.33	63.81	2.05	0.35	0.38	FR I	19.81	8000056483001180	0.5
10635	J221135-522014	332.9	-52.337	0.002	63.48	23.3	63.48	1.29	0.35	0.38	FR I	20.36	8000070035000660	0.49
10635	J221139-483023	332.91	-48.506	0.036	130.82	88.11	123.71	0.88	0.70	0.73	FR II	16.79	8000083889003240	0.2
9501	J221139-582530	332.91	-58.425	0.004	122.45	70.62	122.45	2.16	0.57	0.59	FR II	21.42	8000049443003350	0.67
10083	J221139-564516	332.92	-56.754	0.012	138.45	95.95	138.45	3.1	0.68	0.71	FR II	22.83	8000054882001700	0.99
9501	J221141-620210	332.92	-57.134	0.002	152.99	114.07	152.99	2.21	0.73	0.76	FR II	21.53	8000039556002660	0.75
10083	J221144-561949	332.94	-56.33	0.016	54.93	18.44	46.6	2.98	0.38	0.42	FR I	20.13	8000042836005480	0.55
9501	J221148-603908	332.95	-60.652	0.007	93.84	57.74	79.66	1.34	0.70	0.75	FR II	17.78	8000053301001060	0.26
10083	J221149-571920	332.96	-57.322	0.008	53.43	22.2	53.43	0.49	0.40	0.44	FR I	23.27		
10635	J221155-490016	332.98	-49.004	0.003	61.13	35.73	61.13	1.08	0.56	0.61	FR II	19.85		
10083	J221158-543012	332.99	-54.503	0.011	52.15	43.49	43.49	2.23	0.77	0.81	single	21.99	8000055680000490	0.93
10083	J221201-563554	333	-56.598	0.006	117.03	86.94	110.33	1.42	0.41	0.44	FR II	19.64	8000038003004370	0.4
9501	J221204-622650	333.02	-62.447	0.009	64.19	27.2	64.19	1.96	0.41	0.44	FR I	18.72	8000066525001230	0.39
10083	J221204-531703	333.03	-53.284	0.021	58.53	52.27	52.27	0.6			single	20.63	8000054088002110	0.65
10083	J221206-565810	333.03	-56.969	0.003	52.27		52.27	0.6			single	21.15	8000042129000590	0.53
9501	J221207-610612	333.03	-61.103	0.006	69.62	31.96	69.62	0.08	0.44	0.48	FR I	16.38		
9501	J221208-612126	333.04	-61.357	0.001	78.91	48.87	78.91		0.60	0.64	FR II	17.6	8000079152000950	0.26
10635	J221210-494955	333.05	-49.832	0.028	96.1	27.78	96.1	1.13	0.28	0.30	FRx	20.69	8000048687001170	0.64
9501	J221212-584621	333.05	-58.773	0.079	82.76	41.18	79.96	1.05	0.50	0.53	FRx	23.52		
10083	J221212-563356	333.05	-56.566	0.002	97.28	72.91	97.28	3.14	0.73	0.77	FR II			

Continued on next page

Table 4.2 – Continued from previous page

SBID	Source Name	RA (J2000) (deg)	DEC (J2000) (deg)	Flux Density (Jy)	Size (")	a (")	b (")	PA (°)	a/b _{max}	a/b _{min}	Class	Mag (r-band)	DESI ID	Z
10083	J221213-575941	333.06	-57.995	0.021	47.98	25.3	50.33	1.07	0.48	0.53	FRx	21.24	8000050970002070	0.75
10635	J221216-515928	333.07	-51.991	0.003	65.23	32.54	65.23	1.64	0.48	0.52	FRx			
9501	J221217-603702	333.07	-60.617	0.002	66.13	37.2	66.13	3.09	0.54	0.58	FRII	23.99		
9501	J221217-602943	333.07	-60.495	0.008	146.55	120.65	146.55	0.58	0.81	0.84	FRII	21		
9501	J221220-592911	333.08	-59.486	0.003	51.52	17.09	51.52	3.06	0.34	0.38	single	21.53		
10083	J221220-541653	333.09	-54.281	0.028	48.02	17.09	47.15	0.37	0.34	0.38	FR I	22.98		
10635	J221221-494051	333.09	-49.681	0.061	135.23	90.62	114.37	2	0.78	0.81	FRII	20.66	8000079152004410	0.41
9501	J221222-620059	333.09	-62.016	0.002	54.72	28.3	54.72	1.59	0.49	0.54	FRx	22.61	8000039557003030	0.79
9501	J221224-613433	333.1	-61.576	0.017	170.51	123.98	170.51	1.81	0.72	0.74	FRII	15.3	8000040732001000	0.1
10635	J221226-483941	333.11	-48.661	0.009	51.46	31.18	43.28	1.09	0.57	0.63	single	21.53	8000082932005240	0.91
10083	J221226-533207	333.11	-53.535	0.01	58.18	31.18	51.94	2.68	0.57	0.63	FRII	20.53	8000065659001470	0.62
9501	J221226-620641	333.11	-62.111	0.002	43.18	43.18	43.18	1.08	0.49	0.53	single	23.66		
9501	J221228-611127	333.12	-61.191	0.002	62.17	31.42	62.17	0.8	0.49	0.53	FRx	17.88	8000041428004100	0.24
10083	J221234-544004	333.14	-54.668	0.003	119.49	84.74	119.49	2.88	0.69	0.72	FRII	19.37		
10083	J221235-570616	333.15	-57.104	0.085	96.32	56.32	87.05	1.88	0.63	0.67	FRII	23.48		
10083	J221237-533554	333.16	-53.598	0.003	91.54	61.83	91.54	2.04	0.66	0.69	FRII	19.33		0.4
10083	J221240-565801	333.17	-56.967	0.002	120.59	99.39	120.59	2.5	0.81	0.84	FRII	24.16		
10083	J221246-530700	333.19	-53.117	0.011	50.56	44.99	44.99	1.05	0.56	0.56	single	21.91	8000067395000150	0.72
10083	J221247-565432	333.2	-56.909	0.004	74.68	40.7	74.68	1.73	0.53	0.53	FRII	18.28	8000054089003800	0.25
9501	J221253-603327	333.22	-60.558	0.002	54.02	54.02	54.02	0.25	0.25	0.25	single	21.95	8000043549001700	0.65
9501	J221254-603657	333.23	-60.616	0.003	66.18	66.18	66.18	2.34	0.38	0.43	single	21.99		
10083	J221257-543445	333.24	-54.579	0.01	44.62	18.44	45.47	2.02	0.38	0.43	single	20.85	8000062251000810	0.69
10083	J221257-562630	333.24	-56.442	0.053	46.74	18.44	45.47	2.02	0.38	0.43	FR I	19.93		
10083	J221300-535320	333.25	-53.889	0.082	95.74	54.59	91.68	0.49	0.58	0.61	FRII	21.05	8000063944003260	0.5
10083	J221301-563103	333.25	-56.518	0.015	41.84	20.09	77.29	0.15	0.25	0.27	single	21.48	8000055680001730	0.58
9501	J221303-625743	333.27	-62.962	0.004	77.29	20.09	77.29	0.15	0.25	0.27	FR I	21.17	8000036673004110	0.78
9501	J221304-602249	333.27	-60.38	0.002	89.84	56.41	89.84	0.75	0.61	0.65	FRII	22.57	8000043549006360	0.82
10635	J221305-514240	333.27	-51.711	0.136	72.49	29.73	65.95	1.94	0.43	0.47	FR I	22.5	8000071819002330	0.8
9501	J221306-582119	333.28	-58.355	0.005	112.16	82.4	112.16	2.69	0.72	0.75	FRII	20.34	8000050205000400	0.67
10635	J221307-500521	333.28	-50.089	0.004	56.15	56.15	56.15	2.74	0.42	0.45	single	20.71	8000078218000570	0.85
10083	J221308-534633	333.29	-53.776	0.006	60.04	26	60.04	0.26	0.42	0.45	FR I	21.89	8000064800001490	0.85
10083	J221308-541637	333.29	-54.277	0.063	77.59	26.68	64.84	0.75	0.40	0.43	FR I	17.8		
9501	J221315-611008	333.32	-61.169	0.082	61.76	31.62	61.76	2.49	0.49	0.53	FRx	22.18	8000041428004750	0.7
10635	J221319-493257	333.33	-49.549	0.01	70.92	29.13	70.92	0.72	0.40	0.43	FR I	20.83	8000080090001440	0.58
9501	J221324-574957	333.35	-57.833	0.012	65.46	32.98	65.46	0.39	0.49	0.52	FRx	23.89	8000051742000790	
10083	J221325-562240	333.35	-56.378	0.013	96.32	57.28	82.17	1.34	0.68	0.72	FRII	23.19		
9501	J221326-582431	333.36	-58.409	0.009	70.3	49.06	70.3	2.21	0.67	0.72	FRII			
10083	J221329-530338	333.37	-53.061	0.019	76.92	76.92	76.92	0.79	0.78	0.82	single	23.95		
9501	J221330-594128	333.38	-59.691	0.006	131.35	80.33	100.33	0.73	0.78	0.82	FRII	22.86	8000045719003330	

Continued on next page

Table 4.2 – Continued from previous page

SBID	Source Name	RA (J2000) (deg)	DEC (J2000) (deg)	Flux Density (Jy)	Size (")	a (")	b (")	PA (°)	a/b _{max}	a/b _{min}	Class	Mag (r-band)	DESI ID	Z
10635	J221331-501738	333.38	-50.294	0.006	114.59	75.27	114.59	1.96	0.64	0.67	FR II	19.47	8000077289001200	0.44
10083	J221334-533505	333.39	-53.585	0.005	51.63	21.89	51.63	2.82	0.40	0.45	FRI	19.74	8000065660000730	0.43
10635	J221336-502633	333.4	-50.443	0.054	73.75	36.15	64.87	3.08	0.54	0.58	FR II	24.48		
10083	J221337-560819	333.41	-56.139	0.005	40.21		33.58	0.41			single	18.25	8000056484004150	0.32
10635	J221338-505704	333.41	-50.951	0.017	52.43	21.54	46.3	2.76	0.44	0.49	FRI	20.22	8000074532002910	
10083	J221340-562827	333.42	-56.474	0.025	96.32	58.31	87.24	1.04	0.65	0.69	FR II	19.57	8000055681002580	0.3
10635	J221340-504900	333.42	-50.817	0.009	84.19	56.04	81.12	1.6	0.67	0.71	FR II	23.53	8000075446000630	
9501	J221340-593016	333.42	-59.504	0.013	52.82	19.78	47.91	1.79	0.39	0.44	FRI	22.64	8000046453002240	0.94
9501	J221343-594230	333.43	-59.708	0.003	61.54	22.51	61.54	3.03	0.35	0.38	FRI	19.78	8000045720003310	0.37
9501	J221343-585917	333.43	-58.988	0.001	69.13	42.18	69.13	0.08	0.59	0.63	FR II	19.63	8000047938001450	0.48
10635	J221347-511528	333.45	-51.258	0.05	72.49	36.88	67.8	2.25	0.52	0.56	FR II	16.56	8000073623001650	0.19
10083	J221348-561257	333.45	-56.216	0.022	101.42	52.7	86.06	2.25	0.60	0.63	FR II	18.59	8000056484002660	0.32
10635	J221349-520933	333.46	-52.159	0.006	98.87	58.29	82.68	0.35	0.68	0.73	FR II	19.19	8000070036003520	0.36
10083	J221353-535009	333.47	-53.836	0.012	56.9	22.51	51.77	2.79	0.41	0.46	FRI	21.17	8000064800000620	0.73
10635	J221354-501318	333.48	-50.222	0.004	77.9		77.9	0.55			single	24.7		
10083	J221358-570538	333.49	-57.093	0.001	47.25		47.25				single	21.33	8000054089000480	0.64
10083	J221401-561924	333.51	-56.323	0.006	168.45	108.63	168.45	2.09	0.64	0.65	FR II	18.05	8000056484001070	0.29
9501	J221404-573917	333.52	-57.655	0.004	62.1	32	50.05	1.57	0.61	0.67	FR II	22.91	8000051743003600	0.83
10635	J221406-510835	333.53	-51.143	0.004	52.43		52.43	0.22			single	20.76	8000073623003740	0.7
10083	J221408-561249	333.53	-56.214	0.021	115.62	73.86	99.93	0.62	0.72	0.76	FR II	15.93		
9501	J221409-573516	333.54	-57.588	0.014	99.27	36.96	85.38	0.61	0.42	0.45	FRI	17.86	8000052520000540	0.26
10635	J221409-494518	333.54	-49.755	0.001	61.21	27.35	61.21	1.99	0.43	0.47	FRI	21.26	8000079153002070	0.71
10083	J221409-563320	333.54	-56.556	0.002	80.87	48.42	80.87	2.65	0.58	0.62	FR II	23.83		
10635	J221410-523743	333.54	-52.629	0.005	77.46	30.86	77.46	0.73	0.39	0.41	FRI	16.13	8000068271002450	0.1
9501	J221416-612138	333.57	-61.361	0.003	85.76	44.58	85.76	0.29	0.51	0.54	FR II	18.74	8000041428000190	0.26
10635	J221419-493215	333.58	-49.538	0.008	89.23		89.23	0.24			single	21.55		
10083	J221420-561231	333.59	-56.209	0.012	62.71	27.2	55.05	1.3	0.47	0.52	FRx	20.61	8000056485003050	0.57
10635	J221422-510157	333.59	-51.033	0.024	57.68	24.74	51.99	1.77	0.45	0.50	FRI			
10635	J221422-524541	333.6	-52.761	0.001	66.18	28.6	66.18	3.14	0.42	0.45	FRI	21.33		
10635	J221423-483425	333.6	-48.574	0.033	48.2	21.54	46.92	2.4	0.44	0.48	FRI	18.87	8000083891001140	0.29
9501	J221432-620644	333.63	-62.112	0.023	82.55	30	64.66	2.17	0.45	0.48	FRI	19.21	8000039358000420	0.25
9501	J221432-614616	333.64	-61.771	0.078	53.82		51.63	1.69			single	21.38	8000040043002480	0.64
10083	J221435-555834	333.65	-55.976	0.006	100.63	76.84	95.6	0.73	0.78	0.83	FR II	23.84		
10083	J221436-551322	333.65	-55.223	0.06	48.02	15.62	50.03	2.74	0.30	0.33	FRI	19.24		
9501	J221436-610913	333.65	-61.154	0.004	104.48	60.62	104.48	1.27	0.57	0.59	FR II	18.35	80000414290005140	0.22
9501	J221437-611714	333.66	-61.287	0.002	89.28	46.73	89.28	2.07	0.51	0.54	FR II	23.78		
9501	J221439-572506	333.66	-57.385	0.002	88.92	51.69	88.92	0.71	0.57	0.60	FR II	20.87		
10635	J221441-531410	333.67	-53.236	0.008	46.32		39.85	0.97			single	23.35		
10083	J221445-561236	333.69	-56.21	0.011	113.52	77.25	100.76	2.76	0.75	0.79	FR II	22.8	8000056485003130	1.03

Continued on next page

Table 4.2 – Continued from previous page

SBID	Source Name	RA (J2000) (deg)	DEC (J2000) (deg)	Flux Density (Jy)	Size (")	a (")	b (")	PA (°)	a/b _{max}	a/b _{min}	Class	Mag (r-band)	DESI ID	Z
10635	J221446-512455	333.7	-51.415	0.01	70	21.76	51.05	1.21	0.41	0.45	FRI	17.72		
9501	J221450-612014	333.71	-61.337	0.097	77.2	27.86	67.79	2.92	0.40	0.43	FRI	19.39	8000041429001030	0.36
10083	J221452-535224	333.72	-53.873	0.09	177.81	117.07	155.44	3.01	0.74	0.77	FRII	15.56	8000063945004070	0.11
10635	J221453-481443	333.72	-48.245	0.146	71.66	31.35	68.27	0.07	0.44	0.48	FRI	16.65		
10083	J221455-532102	333.73	-53.351	0.122	82.47	27.04	76.71	2.67	0.34	0.36	FRI	17.58		
10635	J221455-524213	333.73	-52.704	0.009	71.43	57.24	1.8				single	20.89	8000068272001650	0.68
9501	J221503-573224	333.77	-57.54	0.001	72.15	42.37	72.15	0.5	0.57	0.61	FRII	21.55	8000052521001540	0.79
10635	J221507-531823	333.78	-53.306	0.003	54.41	20.31	54.41	1.48	0.36	0.39	FRI	18.5	8000066526001180	0.36
10083	J221508-564119	333.79	-56.689	0.003	76.97	40.57	76.97	2.97	0.51	0.54	FRII	20.67	8000054884002910	0.6
10635	J221510-522629	333.8	-52.441	0.16	78.19	34.06	72.31	1.44	0.46	0.49	FRI	22.29	8000069151002880	1.02
10635	J221511-484527	333.8	-48.758	0.054	86.34	57.72	85.3	1.81	0.66	0.70	FRII	20.69		
10635	J221516-520253	333.82	-52.048	0.007	67.55	32.43	67.55	2.51	0.46	0.50	FRI	17.99	8000070927001670	0.28
10083	J221518-531540	333.83	-53.261	0.005	51.3	40.25	40.25	0.74			single	17.86	8000066527001530	0.24
10635	J221520-482338	333.84	-48.394	0.005	59.53	43.2	43.2	0.96			single	20.67		
10635	J221528-514023	333.87	-51.673	0.003	62.45	20.35	62.45	2.62	0.31	0.34	FRI	23.34		
10635	J221528-511234	333.87	-51.21	0.001	52.43	52.43	1.62				single	20.05	8000073624003100	0.52
9501	J221533-585527	333.88	-59.318	0.098	114.47	65.42	101.45	1.15	0.63	0.66	FRII	19.23	8000047194000990	0.45
10635	J221534-512539	333.89	-58.924	0.039	271.78	222.37	296.33	1.07	0.74	0.76	FRII	20.82	8000047939002730	0.82
10083	J221535-551917	333.9	-55.321	0.002	88.55	41.81	88.55	2.25	0.46	0.49	FRI	18.06	8000072720003420	0.27
10083	J221538-562526	333.91	-56.474	0.003	51.38	16.69	51.38	2.56	0.31	0.34	FRI	22.28	8000059750000940	0.69
10083	J221539-563137	333.92	-56.527	0.002	42.18	41.04	41.04	0.23			single	22.34	8000055682002760	0.98
10635	J221541-521756	333.93	-52.299	0.003	64.44	36.44	64.44	1.45	0.54	0.59	FRII	20.93	8000055682001710	0.63
10083	J221553-570721	333.97	-57.123	0.006	77.81	77.81	0.89				single	20		
9501	J221554-590236	333.98	-59.043	0.003	63.77	26.14	54.19	1.67	0.46	0.51	FRx	20.02	8000054091000030	0.57
9501	J221601-580856	334	-58.149	0.034	55.21	20.4	55.21	1.36	0.35	0.39	FRI	22.04	8000047940001280	0.82
10635	J221605-511532	334.02	-51.259	0.006	72.08	36.01	64.37	2.49	0.54	0.58	FRII	13.99	8000050206003590	0.04
10083	J221609-551839	334.04	-55.311	0.012	99.57	60.48	81.66	0.24	0.72	0.76	FRII	19.58		
10083	J221613-562019	334.05	-56.339	0.016	69.29	27.86	58.94	0.34	0.45	0.49	FRI	24.79		
10635	J221613-500341	334.06	-50.061	0.068	64.44	41.23	64.35	2.02	0.62	0.67	FRII	18.37	8000056486000790	
10635	J221614-532702	334.06	-53.451	0.019	83.56	37.74	73.9	0.59	0.49	0.53	FRx	24.41		
10635	J221618-522635	334.08	-52.443	0.015	107.01	33.41	107.01	0.43	0.31	0.32	FRI	15.32	8000065662002350	0.08
10635	J221623-505053	334.1	-50.848	0.078	76.68	38.21	76.68	0.98	0.48	0.52	FRx	19.81	8000069152003150	0.6
10635	J221624-523751	334.1	-52.631	0.227	84.19	40.2	77.81	0.12	0.50	0.53	FRII	23.36		
10635	J221625-483656	334.1	-48.616	0.004	78.08	23.78	78.08	2.24	0.30	0.31	FRI	17.65	8000068272002530	0.37
10083	J221629-574129	334.12	-57.691	0.009	84.55	33.73	54.7	1.58	0.59	0.65	FRII	18.6	8000083893000520	0.37
10635	J221630-513702	334.13	-51.617	0.021	67.26	20.59	41.65	2.08	0.47	0.53	FRx	23.41	8000051744002710	0.66
9501	J221639-600853	334.17	-60.148	0.007	49.83	13.09	48.6	2.91	0.26	0.28	FRI	21.47	8000072721000130	0.66
10083	J221646-544420	334.19	-54.739	0.005	93.77	52.95	76.55	0.22	0.67	0.72	FRII	20.42	8000044268004530	1.17
					74.97		74.97				single	22.32	8000061414002750	1.17

Continued on next page

Table 4.2 – Continued from previous page

SBID	Source Name	RA (J2000) (deg)	DEC (J2000) (deg)	Flux Density (Jy)	Size (")	a (")	b (")	PA (°)	a/b _{max}	a/b _{min}	Class	Mag (r-band)	DESI ID	Z
10635	J221648-532419	334.2	-53.405	0.013	107.31	33.42	92.76	2.54	0.35	0.37	FRI	16.23		
10635	J221649-514419	334.21	-51.739	0.008	46.05	40.23	68.78	1.69	0.47	0.51	single	20.62	8000071821002430	0.64
10635	J221651-524013	334.21	-52.67	0.007	68.78	33.83	68.78	0.16	0.47	0.51	FRx	23.63		
9501	J221655-581442	334.23	-58.245	0.061	43.43	40.72	40.72	2.76	0.67	0.70	single	18.13	8000050207002360	0.86
10635	J221705-495211	334.27	-49.87	0.004	125.09	85.29	125.09	0.73	0.67	0.70	FRII	21.94	8000079155000170	0.45
9501	J221710-604430	334.3	-60.742	0.002	53.08	53.08	53.08	3.12	0.28	0.29	single	20.03	8000042839002560	0.09
9501	J221711-621426	334.3	-62.241	0.009	158.46	45.77	158.46	1.24	0.28	0.29	FRx	15.91	8000038679003020	0.3
10635	J221711-491710	334.3	-49.286	0.001	57.98	57.98	57.98				single	19.57	8000081036001650	
9501	J221714-582144	334.31	-58.362	0.001	61.92	61.92	61.92	1.61	0.25	0.27	single	23.24	8000050207000310	
10635	J221717-490746	334.32	-49.129	0.002	90.33	90.33	90.33	0.71	0.25	0.27	single	23.26	8000043551001860	0.41
9501	J221718-603208	334.33	-60.536	0.001	45.41	11.77	45.41	1.12	0.52	0.55	FRx	19.81		
10635	J221721-502926	334.34	-50.491	0.004	87.75	46.67	87.75	2.01	0.52	0.55	FRx	24.41		
10083	J221725-551852	334.36	-55.314	0.01	63.15	31.62	56.9	1.23	0.53	0.58	FRx	19.81	8000059751001130	0.5
10635	J221725-512438	334.36	-51.411	0.007	72.12	29.95	72.12	1.49	0.40	0.43	FRx	20.67	8000072721003850	0.67
10635	J221728-532427	334.37	-53.408	0.005	64.44	64.44	64.44	1.74	0.52	0.56	single	18.1	8000065662003110	0.28
9501	J221729-630206	334.37	-63.035	0.011	72.09	39.11	72.09		0.52	0.56	FRx	22.8	8000036675002960	1.03
9501	J221731-605653	334.38	-60.948	0.01	75.18	38	61.82	3.09	0.59	0.64	FRx	19.07	8000042132003780	0.44
9501	J221732-593141	334.39	-59.528	0.091	61.1	23.41	57.56	2.22	0.39	0.43	FRx	18.43	8000046455001800	0.28
10635	J221734-511845	334.39	-51.313	0.016	63.34	34.53	60.17	1.72	0.55	0.60	FRx	17.39		
10635	J221737-484713	334.41	-48.787	0.019	86.34	47.07	78.98	0.22	0.58	0.62	FRx	25.03		
9501	J221738-623055	334.41	-62.515	0.009	41.06	36.9	36.9	3.13	0.80	0.83	single	18.3	8000038006002730	0.32
9501	J221738-611828	334.41	-61.308	0.004	197.47	160.9	197.47	2.6	0.80	0.83	FRx	21.88	8000041430001660	0.71
10083	J221739-564331	334.41	-56.725	0.001	64.56	37.26	64.56	0.57	0.56	0.60	FRx	19.85	8000054885002270	0.35
10083	J221740-544936	334.42	-54.827	0.028	82.72	49.06	82.72		0.58	0.61	FRx	21.31	8000061414000900	0.61
10635	J221747-500844	334.45	-50.146	0.031	48.92	16	46.3	1.34	0.33	0.37	FRx	23.88		
10635	J221750-494552	334.46	-49.764	0.02	64.59	30.46	62.54	1.11	0.47	0.51	FRx	24.25		
9501	J221757-603713	334.49	-60.62	0.005	59.68	32.44	49.35	2.51	0.63	0.69	FRx	20.78	8000043551000170	0.53
10635	J221803-504326	334.51	-50.724	0.011	61.78	16.48	53.45	0.97	0.29	0.32	FRx	19.5	8000075449002130	0.29
10635	J221817-495936	334.57	-49.993	0.011	164.19	130.23	158.3	0.2	0.81	0.84	FRx	21.02		
9501	J221823-594521	334.6	-59.756	0.001	54.76	26.67	54.76	1.46	0.47	0.51	FRx	18.47	8000045722002280	0.29
10083	J221824-564829	334.6	-56.808	0.006	51.51	24.08	51.51	0.89	0.45	0.49	FRx	16.18		
9501	J221828-600034	334.62	-60.009	0.024	54.41	22.63	43.3	0.01	0.49	0.55	FRx	99	8000044992001990	0.55
10635	J221830-503721	334.63	-50.623	0.049	61.78	55.86	55.86	1.66	0.63	0.66	single	23.55		
10635	J221841-492810	334.67	-49.469	0.004	133.93	86.14	133.93	1.6	0.63	0.66	FRx	20.58	8000080094003790	0.54
10635	J221849-491335	334.7	-49.226	0.016	138.33	47	138.33	1.76	0.33	0.35	FRx	14.73	8000081037003120	0.05
10083	J221849-550756	334.71	-55.132	0.003	65.58	28.77	65.58		0.42	0.46	FRx	20.78	8000059752004890	0.68
10635	J221850-492229	334.71	-49.375	0.002	75.85	35.35	75.85	1.34	0.45	0.48	FRx	18.17	8000081037000040	0.29
10635	J221852-513654	334.72	-51.615	0.013	81.15	37.36	69.67	0.28	0.52	0.56	FRx	22.49	8000072722000020	0.86
10635	J221853-491036	334.72	-49.177	0.21	64.05	26.83	70.85	0.88	0.37	0.39	FRx	21.19	8000081037004420	

Continued on next page

Table 4.2 – Continued from previous page

SBID	Source Name	RA (J2000) (deg)	DEC (J2000) (deg)	Flux Density (Jy)	Size (")	a (")	b (")	PA (°)	a/b_{\max}	a/b_{\min}	Class	Mag (r-band)	DESI ID	Z
10635	J221901-512022	334.76	-51.339	0.03	69.6	27.78	65.49	1.09	0.41	0.44	FRI	17.99	8000073626000630	0.27
10635	J221901-525853	334.76	-52.981	0.03	240.42	77.81	240.42	2.35	0.32	0.33	FRI	16.51	8000067398001430	0.09
9501	J221909-573247	334.79	-57.546	0.003	48.89	48.89	48.89	1.63	0.72	0.75	single	21.65	8000052523001240	0.79
10635	J221911-481519	334.8	-48.255	0.02	111.67	80.53	109.45	1.33	0.72	0.75	FRII	20.48	8000084856003630	
9501	J221912-621330	334.8	-62.225	0.001	55.6	28.93	55.6	0.18	0.50	0.54	FRx	21.72	8000038680003700	0.81
10635	J221912-513007	334.8	-51.502	0.001	79.72	79.72	79.72	0.93	0.93	0.93	single	22.29		
10635	J221912-513305	334.8	-51.551	0.002	86.88	36.49	86.88	1.28	0.41	0.43	FRI	23.65		
9501	J221913-583726	334.81	-58.624	0.005	116.02	71	90.19	1.25	0.77	0.81	FRII	22.54	8000048691003230	
9501	J221915-580213	334.81	-58.037	0.021	72.69	36.06	64.63	0.06	0.54	0.58	FRII	22.56	8000050974001210	1.13
10635	J221918-534151	334.83	-53.698	0.004	143.33	85.56	143.33	1.45	0.59	0.61	FRII	17.63	8000064804002390	0.23
10635	J221920-512801	334.84	-51.467	0.045	81.15	49.03	78.77	2.86	0.60	0.64	FRII	15.74		
9501	J221928-601021	334.87	-60.173	0.008	85.68	32.13	85.68	2.7	0.36	0.39	FRI	99	8000044269004000	0.77
9501	J221934-600145	334.9	-60.029	0.075	239.88	123.85	204.62	0.53	0.60	0.61	FRII	17.44	8000044993001450	0.2
9501	J221941-612602	334.92	-61.434	0.055	65.26	28.43	60.58	0.77	0.45	0.49	FRI	20.01	8000040735004200	0.46
10635	J221948-513551	334.95	-51.598	0.001	61.45	23.18	61.45	1.44	0.33	0.36	single	17.31	8000072723000390	0.19
10635	J221959-504834	335	-50.809	0.017	87.75	67.08	67.08	0.57	0.33	0.36	FRI	19.78	8000075450001140	0.48
9501	J222001-580817	335.01	-58.138	0.072	60.99	52.11	52.11	0.07	0.58	0.61	single	18.88	8000050209003660	0.26
10635	J222007-490135	335.03	-49.026	0.028	102.02	54.97	93.08	0.71	0.58	0.61	FRII	17.58	8000081986002710	0.99
10635	J222009-524932	335.04	-52.826	0.016	79.82	48.7	72.34	2.77	0.65	0.70	FRII	23.12	8000044993000810	0.99
9501	J222021-600427	335.09	-60.074	0.004	124.25	46.84	124.25	2.04	0.37	0.38	FRI	20.68	8000074537000690	0.79
9501	J222022-620159	335.1	-62.033	0.003	57.93	23.24	57.93	0.62	0.38	0.42	FRI	23.67	8000070040003890	1.14
10635	J222027-510525	335.12	-51.09	0.008	58.53	46.32	46.32	1.21	0.32	0.35	single	18.64	8000069155000710	0.48
10635	J222034-520845	335.14	-52.146	0.347	51.86	18.11	53.98	0.13	0.32	0.35	FRI	20.37		
10635	J222040-523444	335.17	-52.579	0.003	56.74	18.44	56.74	0.9	0.31	0.34	FRI	22.36		
9501	J222041-611947	335.17	-61.33	0.008	80.82	19.71	80.82	0.27	0.24	0.25	FRI	19.95		
10635	J222046-521535	335.19	-52.26	0.009	103.65	23.24	103.65	1.13	0.38	0.42	single	17.74		
10635	J222046-485438	335.19	-48.911	0.016	174.41	120.88	162.9	0.89	0.73	0.75	FRII	20.37		
10635	J222048-534553	335.2	-53.765	0.055	93.03	42.94	79.67	2.05	0.52	0.56	FRII	23.66		
10635	J222050-513615	335.21	-51.604	0.005	53.15	18.09	53.15	2.71	0.33	0.36	FRI	20.7	8000072724000300	0.58
10635	J222055-532314	335.23	-53.387	0.003	111.5	69.12	111.5	0.75	0.61	0.63	FRII	17.52		
10635	J222057-522525	335.24	-52.424	0.01	52.61	45.46	45.46	1.46	0.61	0.63	single	17.42	8000069155003520	0.19
10635	J222058-515011	335.25	-51.836	0.015	60.76	50.48	50.48	0.31	0.67	0.69	single	23.21		
10635	J222106-501823	335.28	-50.306	1.566	154.2	102.43	151.36	0.04	0.67	0.69	FRII	18.04	8000077294001400	0.31
10635	J222106-484037	335.28	-48.677	0.008	65.99	33.11	57.05	0.41	0.56	0.61	FRII	20.41	8000082938005040	0.6
9501	J222106-613331	335.28	-61.559	0.002	53.49	53.49	53.49	2.28	0.61	0.61	single	21.33	8000040736001510	0.88
10635	J222107-502016	335.28	-50.338	0.004	61.4	61.4	61.4	1.99	0.53	0.53	single	18.4	8000077294000790	0.37
10635	J222116-495111	335.32	-49.853	0.003	73.15	73.15	73.15	1.53	0.53	0.53	single	22.1	8000079157000540	0.91
10635	J222122-532017	335.34	-53.338	0.002	64.44	64.44	64.44	1.67	0.49	0.52	single	18.69	8000084858001390	
10635	J222125-481922	335.36	-48.323	0.003	65.94	33.27	65.94	1.41	0.49	0.52	FRx	18.69		

Continued on next page

Table 4.2 – Continued from previous page

SBID	Source Name	RA (J2000) (deg)	DEC (J2000) (deg)	Flux Density (Jy)	Size (")	a (")	b (")	PA (°)	a/b_{\max}	a/b_{\min}	Class	Mag (r-band)	DESI ID	Z
10635	J222125-493532	335.36	-49.592	0.003	48.99	19.64	48.99	1.12	0.26	0.28	single	16.99	8000080095000640	0.26
9501	J222136-621239	335.4	-62.211	0.002	73.59	122.37	73.59	1.95	0.76	0.79	FRI	22.29	8000038681004060	0.92
10635	J222144-505001	335.43	-50.834	0.025	158.09	122.37	158.09	2.96	0.76	0.79	FRII	20.61	8000075451000960	0.43
10635	J222145-503732	335.44	-50.626	0.006	158.09	110.16	136.5	1.8	0.79	0.82	FRII	23.12		
10635	J222148-493210	335.45	-49.536	0.017	112.22	68.12	98.52	1.61	0.67	0.71	FRII	20.74	8000080096001850	0.65
10635	J222203-534107	335.52	-53.685	0.021	45.12		46	2.31			single	19.23	8000064805002410	0.48
9501	J222231-593415	335.63	-59.571	0.054	44.63	10.3	44.92	2.49	0.22	0.24	FRI	17.24	8000046458001020	0.25
10635	J222237-481922	335.66	-48.323	0.018	94.5	64.5	90.69	1.68	0.69	0.73	FRII	20.51	8000084858001420	
9501	J222239-595832	335.66	-59.976	0.031	53.74	24.33	49.85	1.71	0.46	0.51	FRx	23.84		
10635	J222241-530314	335.67	-53.054	0.005	61.39	32.61	61.39	1.49	0.51	0.55	FRII	23.97		
10635	J222243-492636	335.68	-49.443	0.073	64.05	25.06	67.52	0.99	0.36	0.39	FRI	16	8000080096003890	0.06
10635	J222252-513802	335.72	-51.634	0.061	79.78	25.61	73.94	0.9	0.34	0.36	FRI	23.87		
10635	J222252-485229	335.72	-48.875	0.003	63.96	25.38	63.96	0.11	0.38	0.41	FRI	22.38		
9501	J222258-593706	335.74	-59.618	0.005	137.79	92.1	137.79	0.48	0.66	0.68	FRII	23.3	8000082939000080	0.96
10635	J222301-523035	335.75	-52.51	0.005	96.51	62.1	81.97	1.3	0.74	0.78	FRII	22.43	8000069156002210	0.71
10635	J222311-525317	335.8	-52.888	0.006	96.14	29.95	68.48	1.85	0.42	0.45	FRI	18.91	8000067401003860	0.37
10635	J222314-530447	335.81	-53.08	0.005	78.71	29.21	78.71	0.54	0.36	0.38	FRI	19.23	8000067401000710	0.3
10635	J222317-501509	335.82	-50.253	0.032	79.19	50.17	75.63	0.4	0.64	0.69	FRII	23.82	8000077295002880	
10635	J222319-502951	335.83	-50.498	0.012	87.03	42.74	87.03	0.83	0.48	0.51	FRx	22.31	8000076372002490	1.12
10635	J222325-524757	335.86	-52.799	0.011	59.57	27.2	50.81	2.54	0.51	0.56	FRII	22.11	8000068277001380	0.76
10635	J222338-513555	335.91	-51.599	0.002	65.01	21.34	65.01	1.08	0.32	0.34	FRI	21.01	8000072725000410	0.7
10635	J222338-515628	335.91	-51.941	0.017	64.3	28.64	55.06	0.5	0.50	0.54	FRx	24.56		
10635	J222354-504945	335.98	-50.829	0.035	132.38	70.57	110.07	1.69	0.63	0.66	FRII	22.2	8000075452000770	0.95
10635	J222402-490236	336.01	-49.043	0.003	51.95		51.95	0.98			single	21.87	8000081988001920	0.84
10635	J222421-490321	336.09	-49.056	0.016	55.06	24.74	50.58	2.97	0.47	0.51	FRx	24.53		
10635	J222438-530110	336.16	-53.019	0.022	61.4	25.61	57.99	0.66	0.42	0.46	FRI	21.21	8000067402001830	0.63
10635	J222439-525721	336.17	-52.956	0.048	96.51	55.17	93.89	0.78	0.57	0.60	FRII	17.54		
10635	J222441-491905	336.17	-49.318	0.056	116.45	67.47	102.7	0.25	0.64	0.67	FRII	20.84	8000081041001530	0.44
10635	J222443-510640	336.18	-51.111	0.049	47.23	10.17	51.36	0.75	0.19	0.21	FRI	23.26		
10635	J222451-483943	336.21	-48.662	0.013	103.78	69.97	91.46	2.09	0.74	0.79	FRII	18.87	8000082941005630	0.37
10635	J222452-522402	336.22	-52.401	0.004	72.09	30	72.09	2.15	0.40	0.43	FRI	22.27	8000069157003990	0.52
10635	J222502-525235	336.26	-52.876	0.011	61.4	18.44	44.13	2.29	0.40	0.44	FRI	19.15	8000067402004290	0.47
10635	J222503-530139	336.27	-53.028	0.031	111.5	71.02	107.57	0.52	0.65	0.68	FRII	18.83	8000067402001760	0.47
10635	J222506-515033	336.28	-51.843	0.002	54.13		54.13	1.81			single	23.13		
10635	J222513-501609	336.31	-50.269	0.108	64.05	27.78	66.23	2.15	0.40	0.44	FRI	22.52	8000077297002310	0.87
10635	J222540-515638	336.42	-51.944	0.002	114.11	78.02	114.11	1.82	0.67	0.70	FRII	20.83	8000070933002650	0.58
10635	J222548-513944	336.45	-51.662	0.026	133.42	84.24	124.46	1.58	0.66	0.69	FRII	16.3	8000071827003320	0.14
10635	J222604-514936	336.52	-51.827	0.003	46.49	18.97	46.49	2.85	0.39	0.43	FRI	25.07	8000071827000780	0.73
10635	J222615-515458	336.56	-51.916	0.011	51.15		47.06	0.32			single	21.27	8000070934004110	0.73

Continued on next page

Table 4.2 – Continued from previous page

SBID	Source Name	RA (J2000) (deg)	DEC (J2000) (deg)	Flux Density (Jy)	Size (")	a (")	b (")	PA (°)	a/b_{\max}	a/b_{\min}	Class	Mag (r-band)	DESI ID	Z
10635	J222623-523036	336.6	-52.51	0.026	96.51	63.08	87.91	1.45	0.70	0.74	FRII	19.62	8000069158001970	0.49
10635	J222636-515254	336.65	-51.882	0.018	114.11	78.41	103.45	1.45	0.74	0.78	FRII	23.33		

Chapter 5

Alignment of DRAGNs

Context

In this chapter, I investigate the claim that the major axis of nearby (within a few degrees separation) radio sources tend to be aligned, using the G23 and EMU-PS data sets. If this is true, then the difference in Position Angles (PAs) of nearby sources should be close to zero. Alternatively, a null result would be that the radio sources are randomly aligned in which case the distribution of the difference in position angles should be uniform between -90 and $+90$ degrees. Since the direction of radio galaxy jets is determined by the angular momentum axis of the Supermassive Black Hole (SMBH) that drives the Active Galactic Nuclei (AGN) activity in the host galaxy, any observed jet alignment would therefore imply an alignment of the angular momentum axes of central black holes on scales of several tens of megaparsecs or greater. An alignment such as this could only have arisen during the time of formation and would suggest that angular momentum features of similar scale were embedded in the local large-scale cosmic structure in the early Universe.

In Chapter 5.2, I describe how the major axis of the sample is determined, followed by the statistical methods undertaken in Chapter 5.3. My results and analysis are presented in Chapter 5.4. I end with a comparison with previous studies in Chapter 5.3.

5.1 Introduction

There has been some compelling evidence (see Chapter 1) for a preferential direction in the orientation of quasar optical polarizations on gigaparsec scales. Early attempts to explain the preferential orientation involved systematic effects introduced by a global rotation of the Universe (Birch, 1982), but the evidence for this global rotation has been heavily disputed (e.g. Phinney and Webster, 1983; Bietenholz and Kronberg, 1984; Kendall and Young, 1984). The link between quasar optical polarization and host galaxy

PA (Joshi *et al.*, 2007; Borguet *et al.*, 2008, 2011) prompts the thought that the objects themselves are aligned, perhaps along the large scale structure the quasars reside in. As such, various radio polarization studies and radio structure position angle studies have found preferential orientation of quasar axes with respect to each other or to major axes of hosting large quasar groups (Pelgrims and Hutsemékers, 2015; Taylor and Jagannathan, 2016; Contigiani *et al.*, 2017; Osinga *et al.*, 2020). The field at present seems to have converged to the conclusion that the orientation of AGNs seems to be influenced by the large scale structure they inhabit. In this project, I will attempt to explore this hypothesis using the PA of Double Radio sources Associated with Galactic Nuclei (DRAGNs), primarily using data from the Evolutionary Map of the Universe (EMU) Pilot Survey 1 and the Galaxy And Mass Assembly (GAMA)-23 field.

5.2 Determining Major Axis

I measure orientations of radio sources by using the PA of the long axis of the enclosing box determined from the Fanaroff-Riley (FR) ratio algorithm (more details in Chapter 2). I then measure the difference $dPA_{ij} = PA_i - PA_j$ of pairs of galaxies i and j and see if that tends to be close to zero in various circumstances. However, it must be noted that this might be a subtle effect, so instead, I'm looking for a slight overdensity of points with $dPA \sim 0$ compared to other angles. So for each field containing n galaxies, I will have a table of the $n(n-1)/2$ values of dPA_{ij} .

Due to the rotational symmetry of this data, the period is π radians. As circular statistical tests expect the data to have a period of 2π radians, I have doubled each source angle to match this assumption for the tests.

The orientation of the major axis of each source was measured by using weighted Principal Component Analysis (PCA) where each non-background pixel has a position and a weight (intensity). To perform weighted PCA, I am required to convert the set of pixels into vectors. The vectors associated to each pixel begin at the origin (the centre of the source taken from the catalogue), and finish at the pixel centre. To ensure that the pixel intensity is taken into account, it is used as the weight for each vector in weighted PCA. The major axis of each source is taken as the first principal component. The background was separated from the source using standard deviation. All this is done with the ratio algorithm which I describe in Chapter 2. I give an example of a well-measured source's PA in Figure 5.1.

5.3 Statistical methods

The third part of my project is to find whether the selected sources have a preferential PA, either globally or locally. To determine the alignment on the sky (i.e., the celestial sphere), an appropriate statistical method must be used. In particular, it must account for the circular nature of PAs. Since a PA of 89 degrees is very close to a PA of -89 degrees, standard statistical definitions such as the mean do not

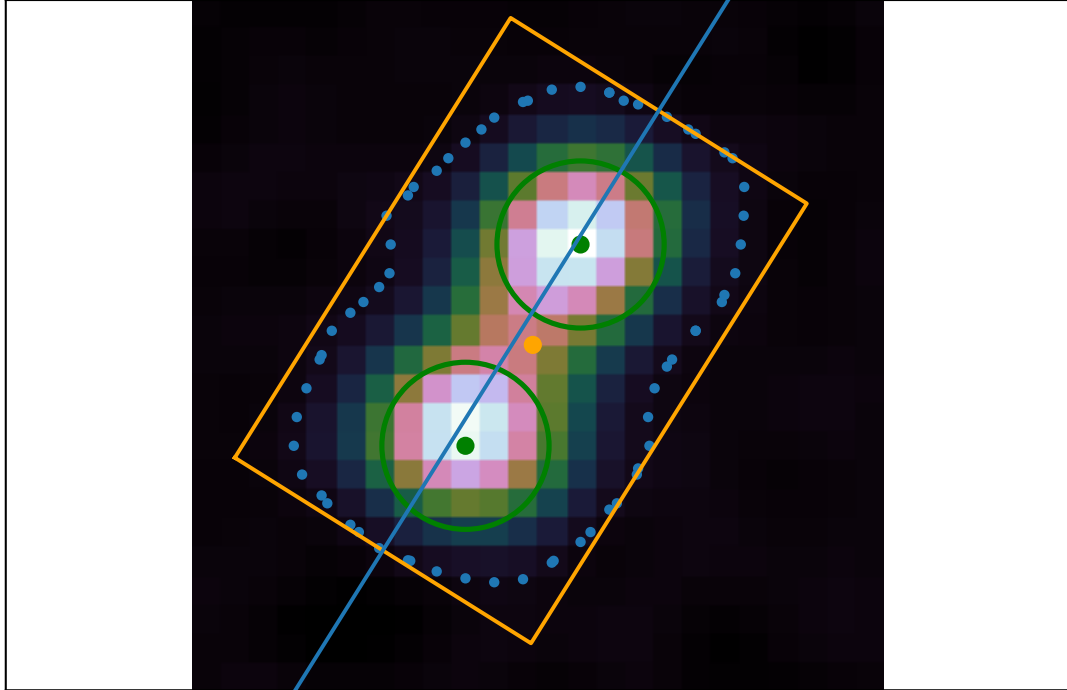


Figure 5.1: An example radio image of a DRAGN showing the morphological features extracted and position angle shown in the blue line. The orange dot is the IR host coordinates, the green dots are the centroids of the detected blobs (green circles), the blue dots represent the contour and the orange box represents the fitting bounding box of that contour.

apply. When considering the alignment of PAs on a sphere, I cannot simply compare angles that are defined on different parts of the sphere. To tackle these problems, the notion of parallel transport and the dispersion measure are introduced in Chapter 2.

5.4 Results and Analysis

I first examine the uniformity of the PAs of the sources across both the G23 and EMU-PS images to detect any systematic effects. The distribution of PAs is given in Figure 5.2. If there are no systematic effects, I will expect the PAs to be uniformly distributed across this large area of the sky. From Figure 5.2, it can be seen that although the distribution is not quite uniform, there are no major systematic effects present. I then applied the Kolmogorov-Smirnov (K-S) test to see if the distribution is consistent with a uniform distribution of sources (e.g. Frommert *et al.*, 2012). The K-S test yielded a p-value of 0.017, which is strong indication for rejecting the null hypothesis. The null hypothesis in this case is that the distribution of PAs is uniform over the full sample. This points to a possible systematic (survey-wide) bias in my sample. Depending on the nature of the effect causing the alignment, the local alignment signal may vary, either becoming stronger or weaker.

It is unclear what is causing this bias. For example, my measured PAs refer to the PA of DRAGNs

Table 5.1: The parameters used to divide the initial source sample into three equal flux density f bins. Units are in Jansky.

Bin No.	Flux Range
1	$f \leq 0.0046$
2	$0.0046 < f < 0.01495$
3	$0.01495 < f$

which are typically many synthesised beam-widths wide (i.e. the source examined is the aggregation of many beams), and so the PA of an elliptical synthesised beam will not significantly affect the PAs. Future work will explore what is causing this bias, and whether it might affect the tests in this chapter. However, any such effect will be minimised by comparing the sample with a randomized control sample, as described in the next section.

5.4.1 Two-dimensional analysis

I compare the results for the observed samples with those for control samples of 1000 simulated randomly distributed PAs to see if the hypothesis of uniformity in PAs holds up across different angular scales, and if so, at what Significance level (SL). In order to maintain a consistent global PA distribution and source positions, I generated these control samples by randomly shuffling the PAs among the sources. This process should remove any instrumental bias that is common to all the observations.

By probing the statistic, S_n , for varying numbers of nearest neighbours, each sample was checked for local alignment. A circular aperture with a radius extending to the n -th neighbour of each source is drawn to express the statistic in terms of angular scale. In taking the median angular radius of all these apertures, I converted the number of nearest neighbours to an approximate corresponding angular scale. This dependency is shown in Figure 5.3 for both the G23 and EMU-PS.

The SL at which the null hypothesis of the PAs being uniformly distributed should be rejected as a function of the number of nearest neighbors n (or corresponding angular scale) is shown in Figure 5.4. With a SL of $< 10^{-5}$, this plot shows that there is strong evidence to reject the hypothesis of uniformity in radio source PAs on angular scales of ~ 4 degrees.

To further investigate the effect, I divide the sample into three equal flux density bins, each with the maximum number of sources, as given in Table 5.1.

Figure 5.5 depicts the SL of PA alignment as a function of angular distance for the three flux density bins. The highest flux density bin exhibits evidence of alignment up to scales of approximately 4 degrees, whereas all other bins are consistent with uniform distributions. Unfortunately, the lowest flux bin gave me a null result due to the S_L being 0, so I don't show it here. Thus the observed effect in the overall sample is most likely caused only by the sources with the highest flux density.

As the EMU-PS is spread over ten tiles (pointings), I decided to also run an analysis on the tiles

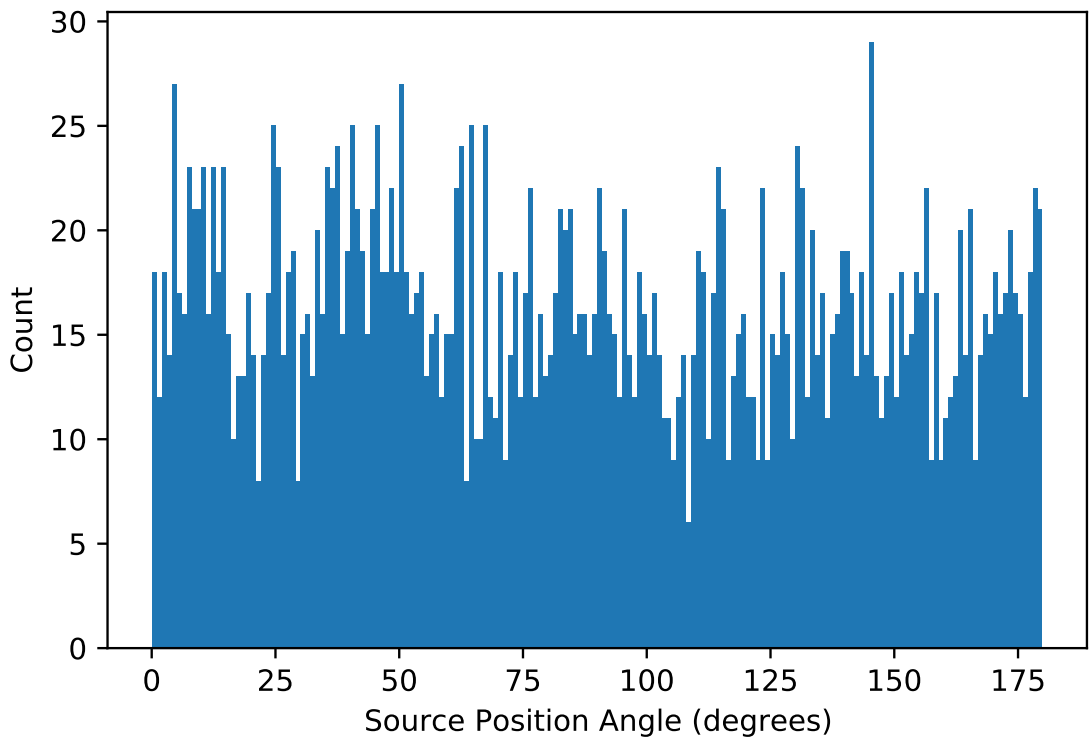
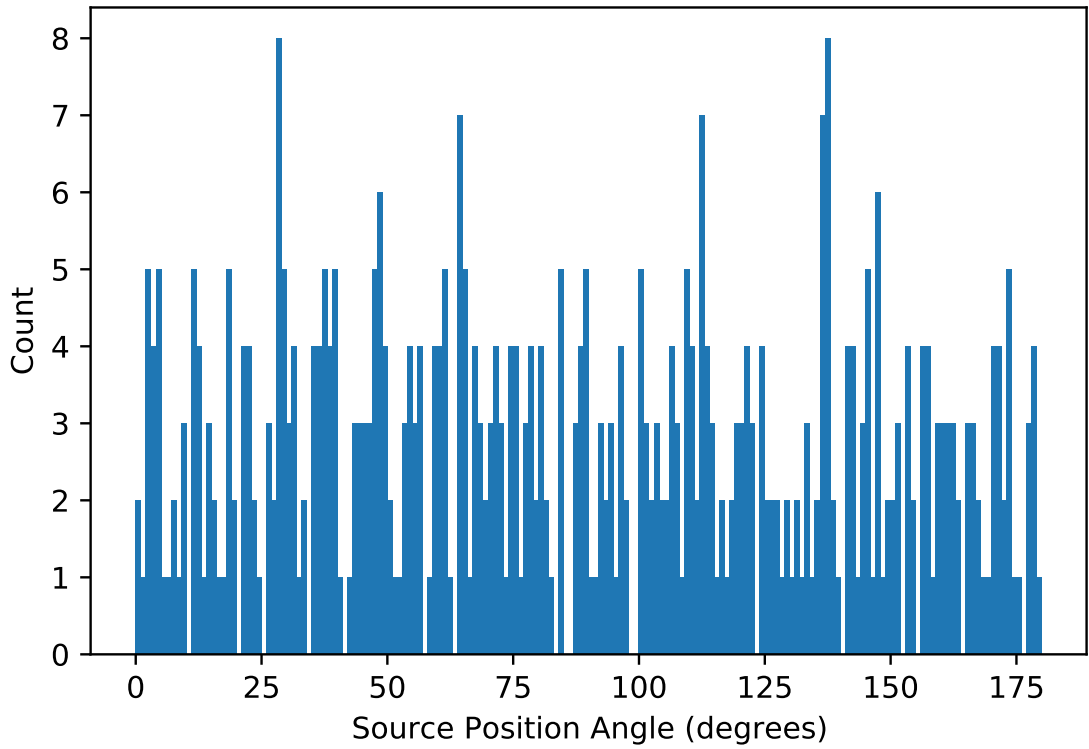


Figure 5.2: The distribution of PAs of the selected sources in the EMU-PS. Obvious systematic effects do not seem to be present.

individually to see if one tile was contributing solely to the observed effect, or if it was spread evenly overall. It must be noted that this results in smaller sample sizes per tile, resulting in a lower statistical

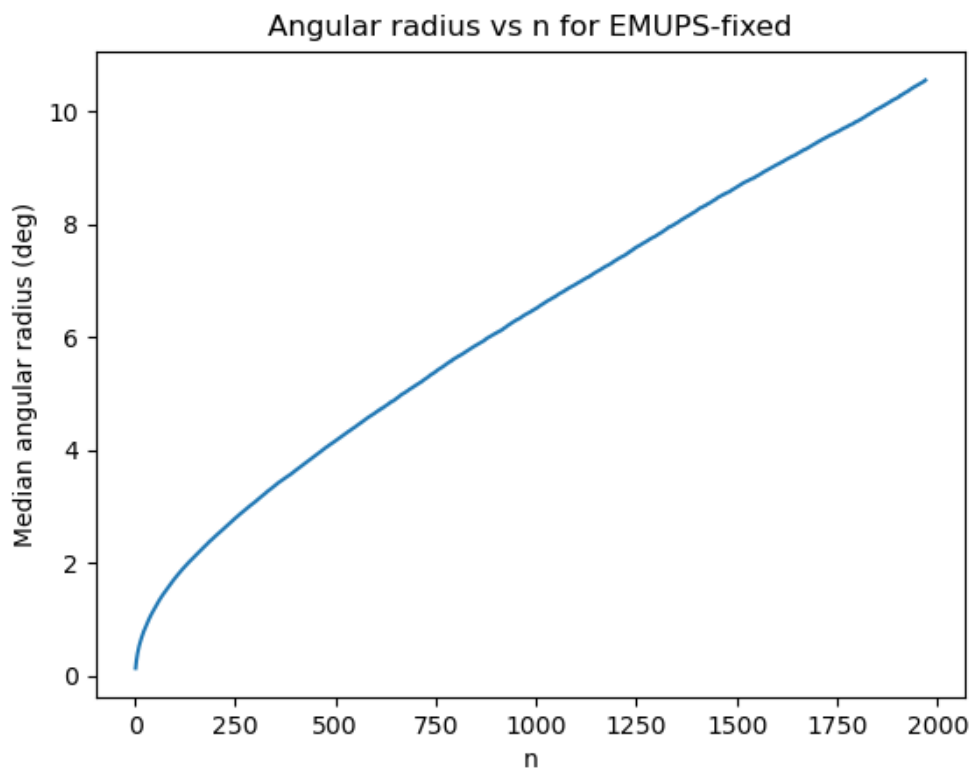
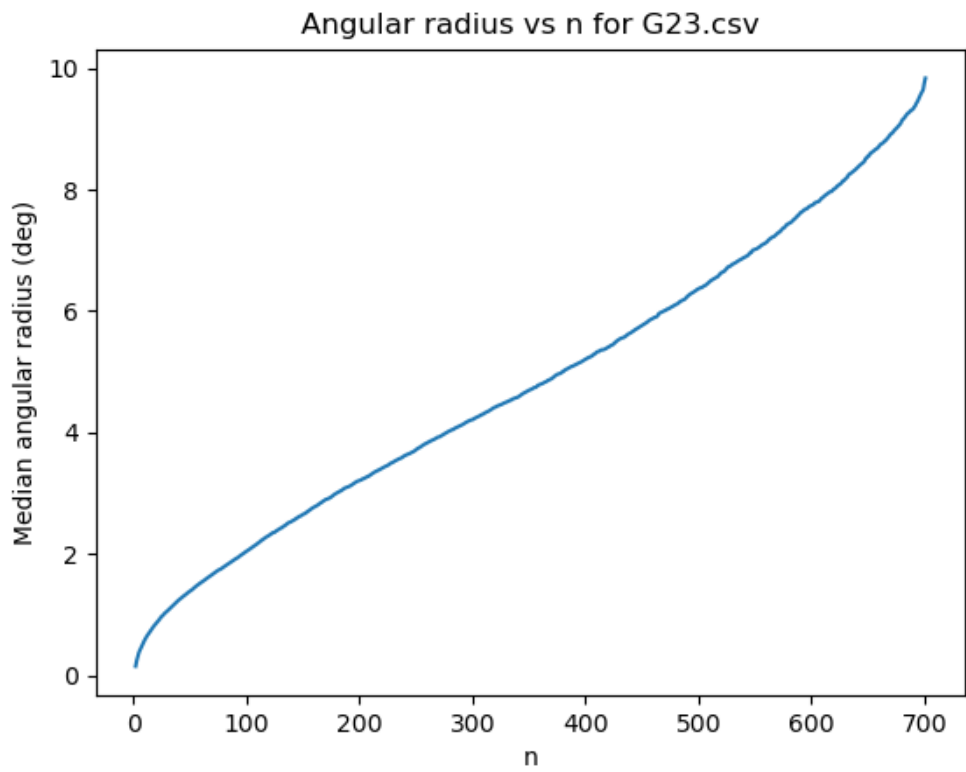


Figure 5.3: The median angular radius pertaining to a circular aperture drawn around every source with an angular radius bound by each source's n -th neighbor: G23 (top) and EMU-PS (bottom).

significance.

Again, I plot the distribution of PAs (Figure 5.6), median angular radius (Figure 5.7) and the logarithm of the SL (Figure 5.8) for the sources in each tile.

For a majority of the tiles, there is no obvious significance. However, tile 9442 (coincidentally the center tile of the EMU-PS survey, see Figure 2.5 in Chapter 4) with 287 sources, shows strong evidence for alignment up to scales of 1.25 degrees.

I plot the PAs of the sources in this tile specially to see if any obvious effect can be seen (Figure 5.9).

At a glance, they seem rather scattered. However, there are a few groups of PAs where potential alignment might exist.

To determine which specific sources are responsible for the observed signal, I examine which sources have the strongest alignment effect in 2D space. I thus make use of $d_{i,n}|_{\max}$, the calculated maximum dispersion measure (Equation 2.12), which measures the alignment significance of a source, i , and its nearest neighbors, n . I plot in Figure 5.10 the maximum dispersion as a function of right ascension and declination for every source in the initial sample of 2945 sources.

This figure shows that there is no single region with the most pronounced alignment, but instead, there is an alternation between regions of strong and weak alignment. This contradicts the observed effect being the result of a survey-wide systematic effect, as all sources would then have similar maximum dispersion regardless of position. However, it is also clear that there are regions of high dispersion (i.e. stronger alignment), indicated by lighter colours in Figure 5.10. In future work, I plan to explore whether this corresponds to astrophysical phenomena such as clusters of galaxies.

5.4.2 Three-dimensional analysis

After removing from the sample all sources without a photometric redshift from Dark Energy Spectroscopic Instrument (DESI), I performed an analysis of alignment uniformity using 3D source positions similar to (Osinga *et al.*, 2020). For this analysis, I only considered the EMU-PS sample, as the G23 sample had too small a sample to work with. This reduced the size of the EMU-PS sample to 1779 sources. The analysis uses the same statistical method as the two-dimensional analysis. The only distinction between the 2D and 3D analysis is that 3D source positions are now used to determine the n nearest neighbours for each source. The distribution of angular radius of these sources is shown in Figure 5.11.

To repeat the analysis in three dimensional space, I assign each source a position according to their right ascension, α , declination, δ , and comoving distance, r , in 3D space as follows:

Table 5.2: The parameters used to divide the selected sample of 1779 sources into three equal redshift z bins.

Bin No.	Redshift
1	$z \leq 0.0384$
2	$0.384 < z < 0.663$
3	$0.663 < z$

$$\begin{aligned}
 x &= r \cos \alpha \cos \delta \\
 y &= r \sin \alpha \cos \delta \\
 z &= r \sin \delta
 \end{aligned}
 \tag{5.1}$$

The comoving distance, r , is calculated using the Ned Wright cosmology calculator (Wright, 2006). The nearest neighbours were then computed using these 3D positions to probe for alignment on local scales. Running the K-S test yields a p-value of 1.0 per cent, indicating that there is insufficient evidence to reject the null hypothesis for PA uniformity in this sample.

Figure 5.12 depicts the SL at which the hypothesis of uniformity in PAs can be rejected for the 1779 sources that have a redshift. The 3D analysis shows evidence for an alignment effect up to scales of around 1 degree.

Similar to what I did in the 2D analysis, I divide the sample into three equal bins and have the maximum number of sources in every bin, as given in Table 5.2. However, this time they are in terms of redshift bins in order to further investigate the effect in 3D space.

Figure 5.13 shows the SL of PA alignment for the three redshift bins as a function of angular distance. The highest and lowest redshift bins show evidence up to scales of roughly 1.7 degrees for alignment, while the middle bin result is consistent with a uniform distribution. This shows that the effect observed in the total sample is dominated by the highest and lowest redshift sources, or by sources without a measured redshift.

5.5 Comparison with previous studies

I cannot be certain whether the observed effect is real or a result of particular biases. To gain more insight into this, I will compare the results of this study to what previous studies of AGN alignments have found.

Table 5.3 shows the parameters and results of this study and three previous studies of radio structure alignment (see Table for references). Taylor and Jagannathan (2016) studied an area of 1.2 square degrees, which limited their study of finding alignment to just this area. As a result, their angular scale of 1

Table 5.3: Comparison of this work with previous studies. The table shows the parameters of the previous studies that have found alignment effects, their significance level and the angular scale of the effect found.

Study	Frequency	RMS (mJy/beam)	Resolution (arcsec)	Study area (deg ²)	Significance (per cent)	Scale (deg)	No. of sources
This study	888 MHz	0.025	12x10	270	<0.1	4	2945
Osinga ¹	150 MHz	0.071	6x6	424	<0.1	5	7555
Contigiani ²	1.4 GHz	0.015	5x5	7000	<2	1.5	30059+11674
Taylor ³	612 MHz	0.01	6.1x5.1	1.2	<0.1	1	65

¹ Osinga *et al.* 2020

² Contigiani *et al.* 2017

³ Taylor and Jagannathan 2016

degree for an alignment effect could be underestimated while still agreeing with my findings. However, Contigiani *et al.* (2017) having probed an area of 7000 square degrees had no such limitation. A resulting effect was found by the team on scales smaller than 2.5 degrees, with the strongest alignment signal at 1.5 degrees. Contigiani *et al.* (2017) also limited their search to angular scales < 2.5 degrees, and while the scale of the maximum effect differs between our studies, this suggests that the signal may be present on larger scales in the Faint Images of the Radio Sky at Twenty-centimeters (FIRST) survey as well. With LOFAR Two-Metre Sky Survey (LoTSS), Osinga *et al.* (2020) studied an area comparable with the EMU-PS, and the results of my study seem to agree considerably with theirs.

If the radio structures are indeed aligned over the scales found in this study, this might come from an alignment of the AGNs that power these radio structures, with the large scale structure. There has been evidence for the preferential orientation of AGN to their hosting structures, which was found in the alignment of optical polarization of quasars and the surrounding large quasar groups (Hutsemékers *et al.*, 2014). Since the radio structures of AGN are found to be correlated to the optical polarization (Antonucci, 1983; Lister, 2001; Joshi *et al.*, 2007), the results of this study might corroborate this finding, if the alignment effect is found to follow the orientation of large scale structures in the observed area of the sky. If the AGNs are indeed aligned with respect to the large scale structure in which they reside in, angular momentum transfer from matter as it gravitationally collapses during the early stages of galaxy formation could be a possible cause. It has been found that in N-body simulations, the tidal forces imparted on collapsing halos influence the spin and shape of galaxies (e.g. White, 1984; Codis *et al.*, 2012; Laigle *et al.*, 2015). This supercluster scale mechanism may perhaps also impact the spin of the central SMBHs of these galaxies, resulting in AGNs alignment.

Another explanation might lie in a different effect of large scale structures on AGNs. Radio-loud AGNs are believed to be the result of the accretion of cold matter on the SMBH, and a way to accomplish this is by merging with gas-rich systems (Hardcastle *et al.*, 2007b). As a result, radio-loud AGNs are thought to be associated with mergers, which is supported by both observations and simulations (e.g. Chiaberge *et al.*, 2015; Croton *et al.*, 2006). If these mergers happen along the filaments of large

scale cosmic structure preferentially, they may cause the central SMBHs to orient in a specific direction, resulting in radio jet alignment.

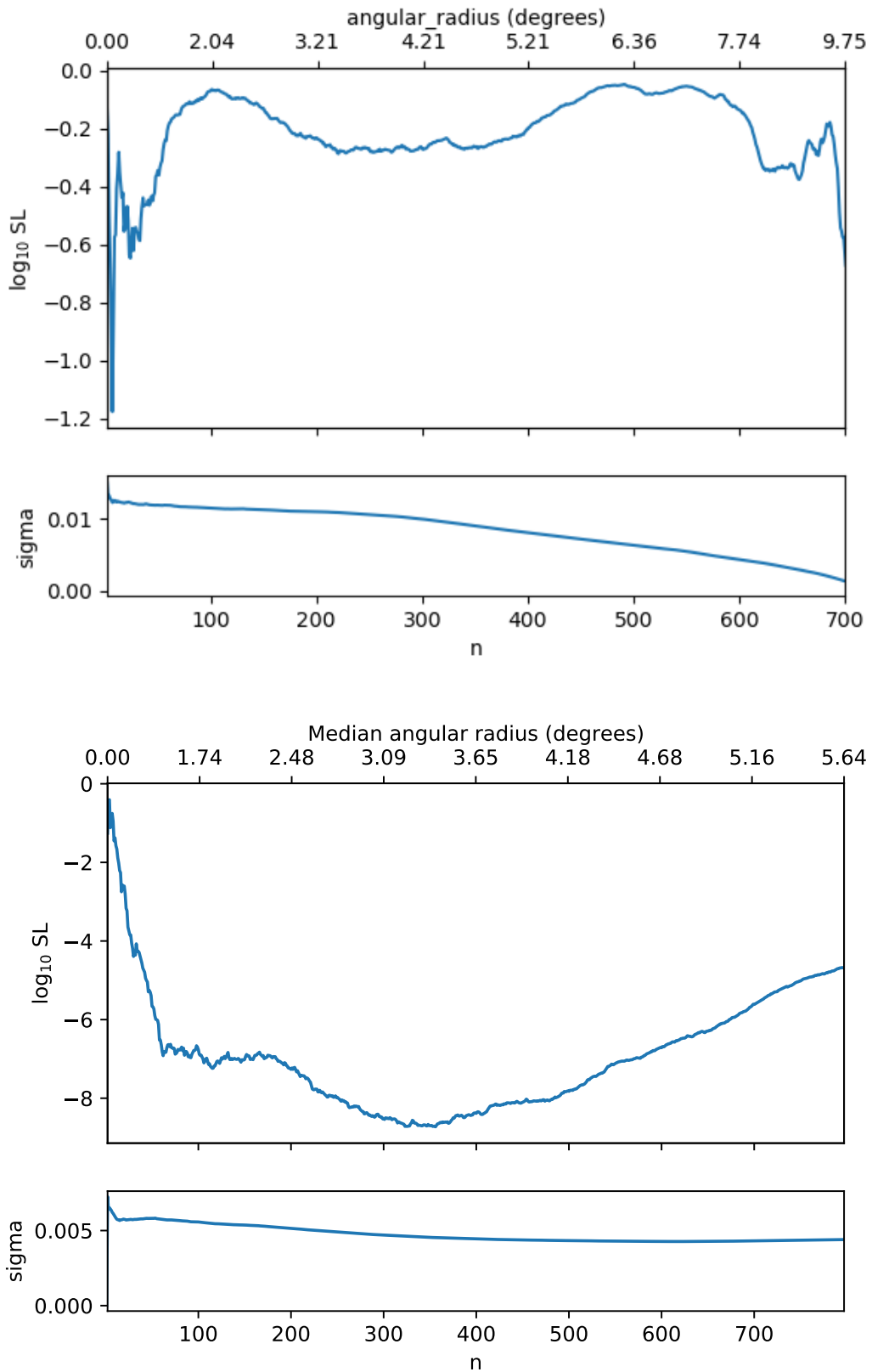


Figure 5.4: The logarithm of the significance level at which uniformity in PAs should be rejected as a function of n , the number of nearest neighbours for the G23 (top) and EMU-PS (bottom) samples, after comparison with a control sample, as described by Equation 2.15. The angular scale conversion is shown in Figure 5.3. The sample standard deviation of the simulated datasets is also plotted. This result shows that neighbouring sources in EMU-PS are probably not randomly oriented with respect to each other.

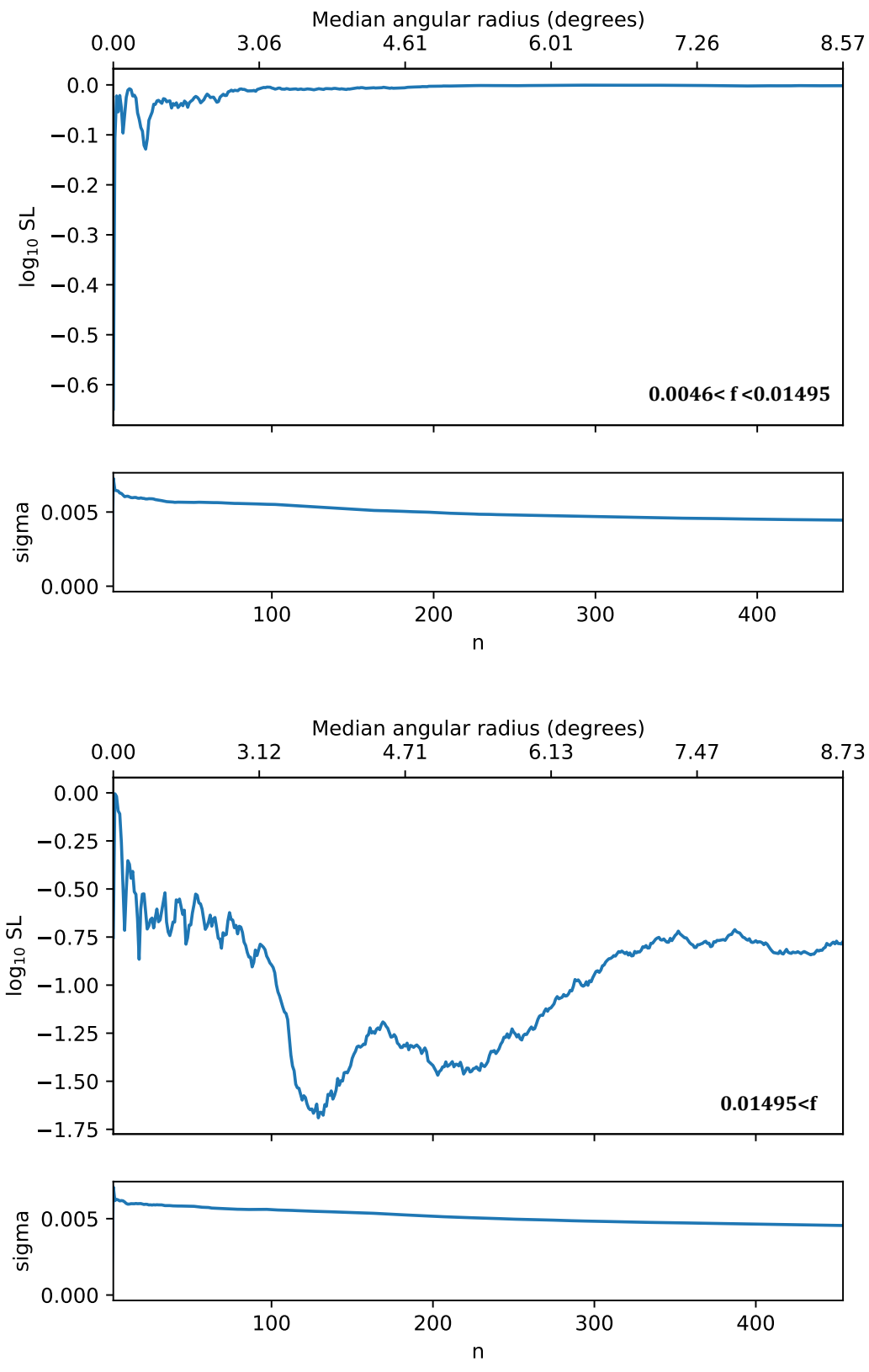


Figure 5.5: The logarithm of the significance level with the sample divided into three equal flux density bins, as defined in Table 5.1. Only two of the bins are shown, as described in the text.

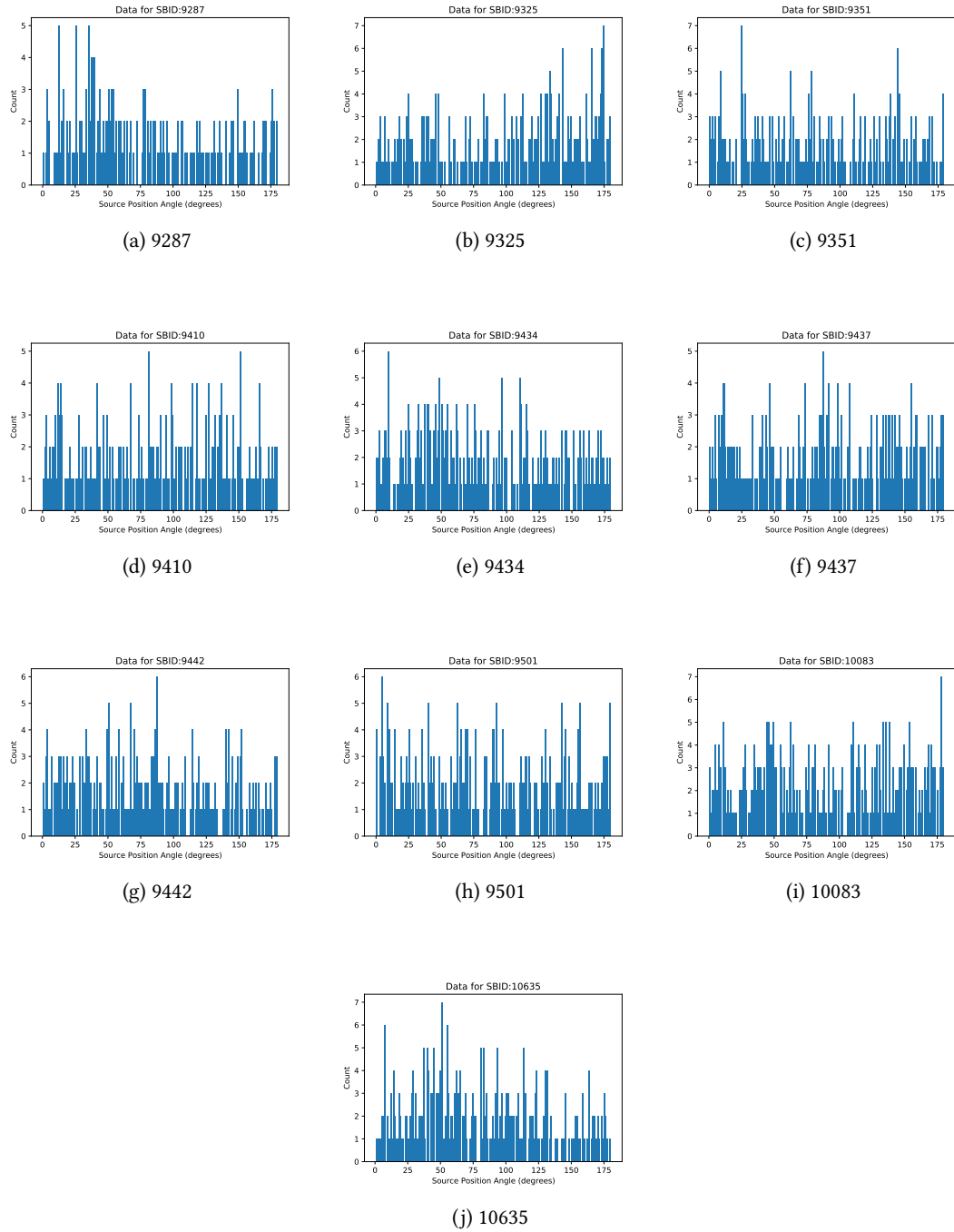
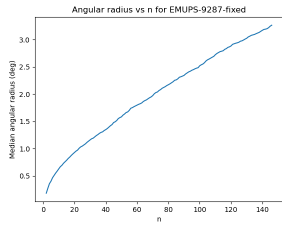
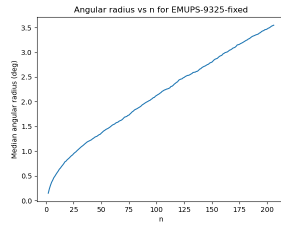


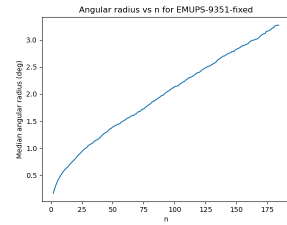
Figure 5.6: The distribution of position angles of the individual ten tiles of the EMU-PS. The SBID of each tile is given below the plot.



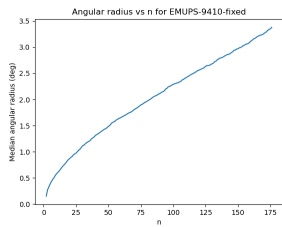
(a) 9287



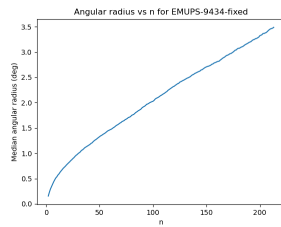
(b) 9325



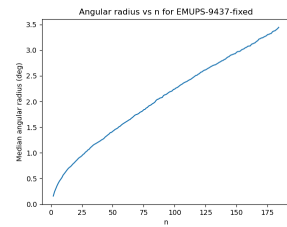
(c) 9351



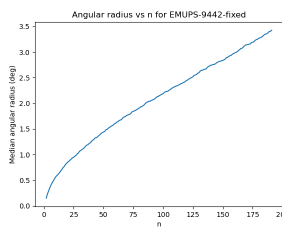
(d) 9410



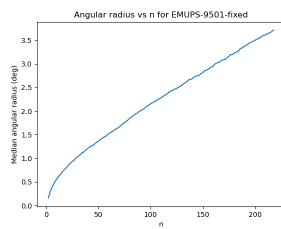
(e) 9434



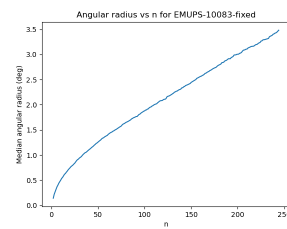
(f) 9437



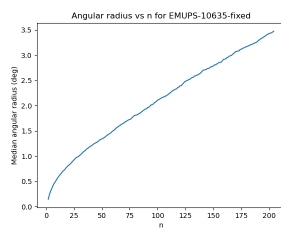
(g) 9442



(h) 9501



(i) 10083



(j) 10635

Figure 5.7: The median angular radius as a function of the number of neighbours across the individual ten tiles of the EMU-PS. The SBID of each tile is given below the plot.

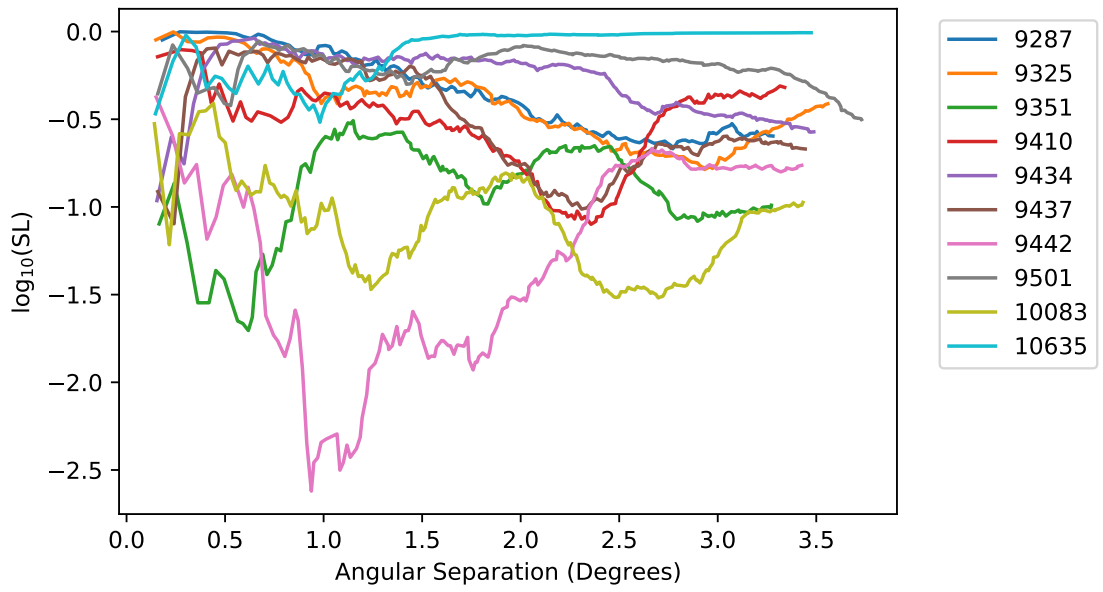


Figure 5.8: The logarithm of the significance level at which the hypothesis of PA uniformity should be rejected as a function of n , the number of nearest neighbors for each EMU-PS tile. The conversion to angular scale is shown in Figure 5.7.

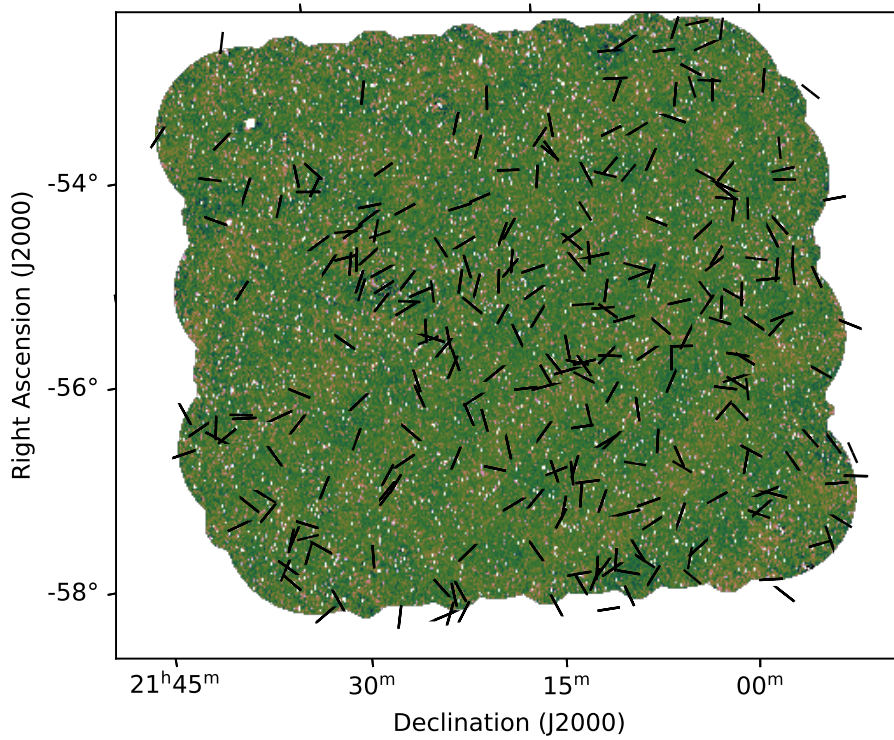


Figure 5.9: A plot showing the PAs of all sources (287) in tile SBID 9442, which is shown to have the most significance as per Figure 5.8.

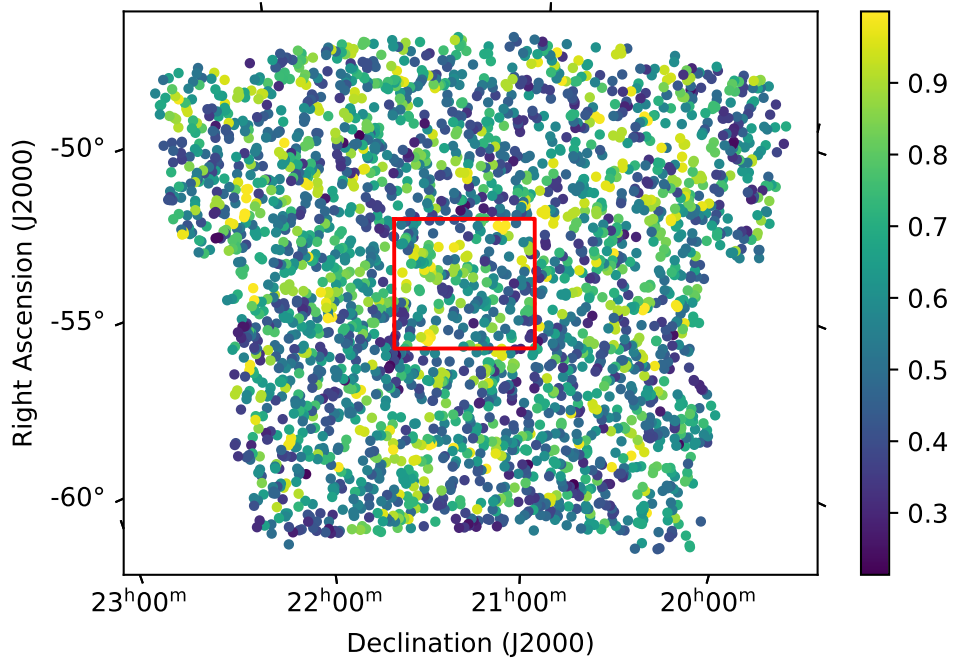


Figure 5.10: A scatter plot displaying the strength of alignment signal or the maximum dispersion measure (see Equation 2.12) for every source in the selected EMU-PS sample of 2945 radio sources, plotted as a function of right ascension and declination. Lighter colours show a greater dispersion, indicating a greater degree of alignment. The red box indicates tile SBID 9442 which showed the most prominent alignment.

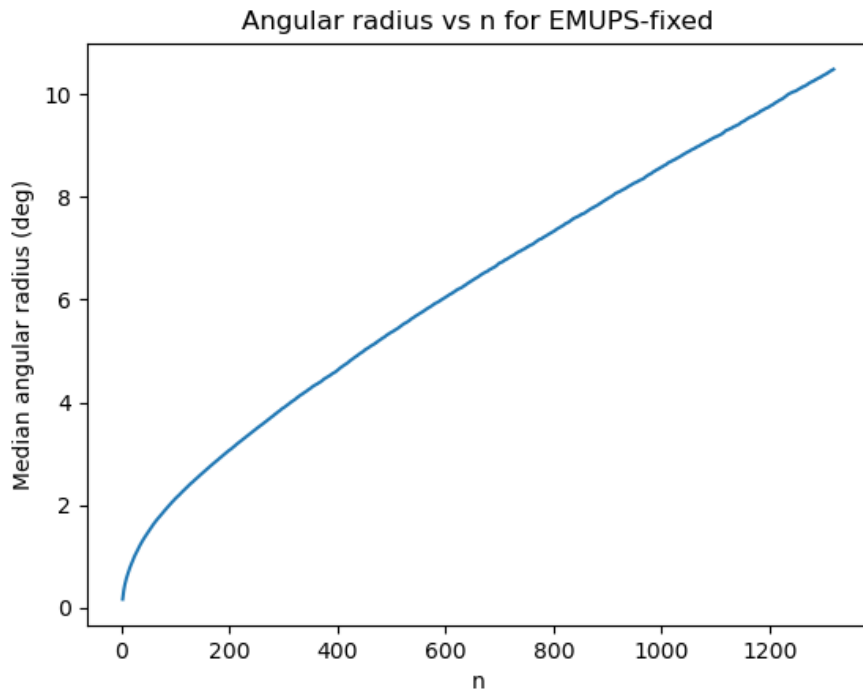


Figure 5.11: The median angular radius as a function of the number of neighbours of the complete sample of the EMU-PS, including only sources with a photometric DESI redshift.

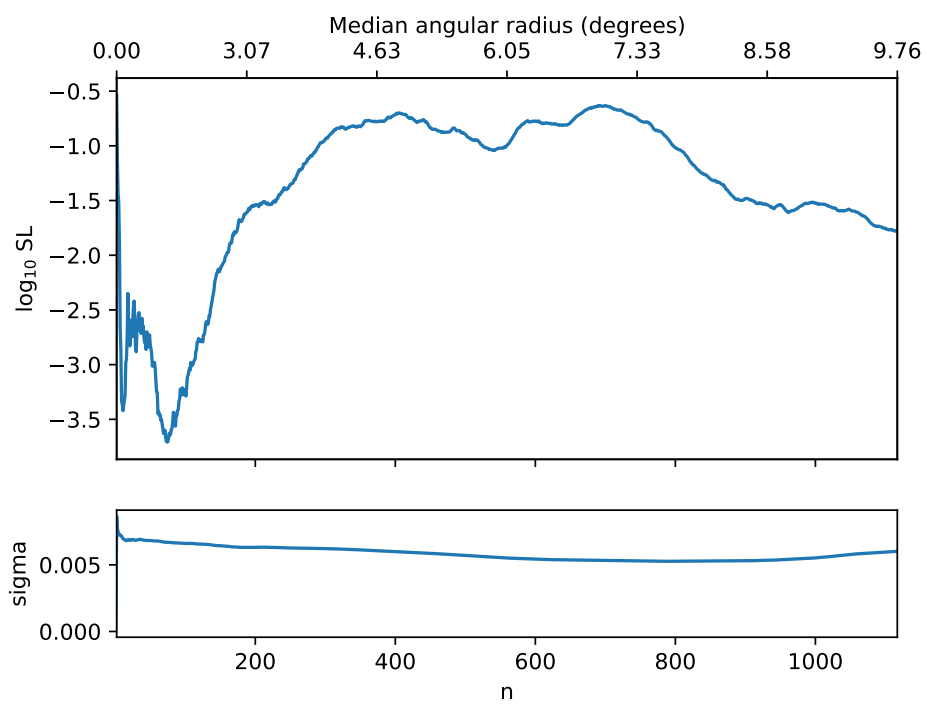


Figure 5.12: Logarithm of the significance level for which uniformity in position angles as a function of the number of nearest neighbors n should be rejected for the EMU-PS sample. This includes only sources with a photometric redshift available.

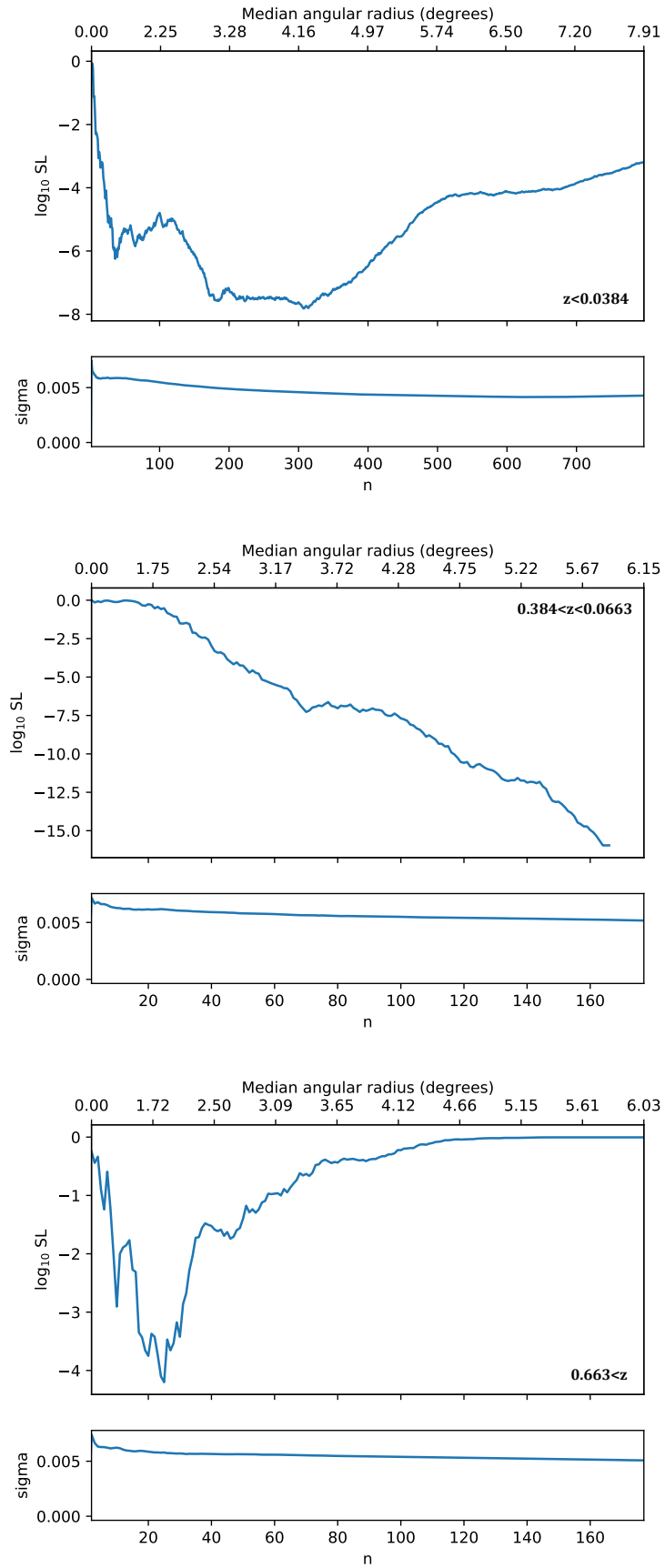


Figure 5.13: Logarithm of the significance level with the sample divided into three equal redshift bins, as defined in Table 5.2. The highest and lowest bins show significance for alignment.

Chapter 6

Summary and Future Work

6.1 Summary

Throughout this thesis, I have studied the radio-loud Active Galactic Nuclei (AGN) population in the nearby Universe using interferometric arrays of radio telescopes equipped with phased array feeds.

Future radio surveys will undoubtedly produce sensitive maps of the entire sky. Several of the latest and upcoming instruments have been (or are being) specifically designed to do so.

6.1.1 A catalogue of DRAGNs

In Chapter 3 and Chapter 4, I have manually put together a large catalogue of Double Radio sources Associated with Galactic Nuclei (DRAGNs) in the Galaxy And Mass Assembly (GAMA)-23 and Evolutionary Map of the Universe (EMU) Pilot Survey respectively using Australian Square Kilometre Array Pathfinder (ASKAP) data. This is the largest catalogue of its kind. It is not only used in the studies outlined in this thesis but will also be used as a training set for Machine Learning (ML) algorithms to classify the rest of the EMU survey, and possible other surveys as well. I also find populations that do not fit in the original Fanaroff-Riley Class I (FRI) and Fanaroff-Riley Class II (FR II) definition, including HYbrid MORphology Radio Sources (HyMoRS), and a new class of sources I term FRx whose classification is ambiguous because of resolution effects.

My results agree with the study done by Mingo *et al.* (2019), and show that whether a source is FRI and FR II morphology does not depend on radio luminosity. DRAGNs can also be found over a wide range of radio luminosity with a significant luminosity overlap in between the two classes.

6.1.2 Fanaroff-Riley classification with ASKAP/EMU

I have conducted a morphological investigation of DRAGNs in the GAMA-23 and EMU Pilot Survey using ASKAP data. In particular, I explore the correlation between peak radio luminosity and Fanaroff/Riley

(1974) classifications. My analysis confirms previous findings that radio luminosity does not unambiguously define whether a source is [FRI](#) or [FR II](#). The ‘break’ that has been seen to exist between [FRI](#) and [FR II](#) populations is not obvious in my sample. The cause for this remains unknown and I intend to explore this further. I find no significant evidence for the redshift distributions of the two classes to differ, except for sensitivity effects.

6.1.3 Alignment of Radio Sources

I have studied the mutual alignment of radio sources within the G23 and [EMU](#) Pilot survey (primarily the latter). This is done by determining the Position Angles ([PAs](#)) of both catalogues. I find evidence of a local alignment with the EMU-PS on scales smaller than 5 degrees. The statistical probability of this happening by chance is less than 0.1 per cent. My result supports evidence reported by 3 studies of radio jet alignment. A possible explanation for the alignment could lie in the origin of radio-loud [AGNs](#), and the cosmic web. The new generation of high resolution radio interferometers, such as the Square Kilometre Array ([SKA](#)) and the Low-Frequency Array ([LOFAR](#)), will undoubtedly expand the cosmological prospects of alignment and radio astronomy in general.

6.2 Future Work

6.2.1 Radio

The future of radio astronomy studies is looking bright, with funding secured for a cryogenically cooled Phased Array Feed ([PAF](#)) on the Parkes telescope, and the Square Kilometre Array ([SKA](#)) precursors [ASKAP](#) and MeerKAT (the Karoo Array Telescope, [Jonas and MeerKAT Team, 2016](#)) becoming fully operational. These instruments are all leading to the construction and operation of the [SKA](#) mid-frequency array (SKA1-MID, covering 350 megahertz to at least 15 gigahertz), as well as the low-frequency array (SKA-LOW, covering 50 to 350 megahertz). The former will be an array of ~ 200 MeerKAT dish antennas, including the current 64 that make up MeerKAT, while the latter will have 512 array stations, each with 256 antennas. The large number of antennas of SKA1-MID and SKA-LOW will result in having higher angular resolution and sensitivity and require less time for observing, compared with [SKA](#) precursors. However, SKA1-MID will not have the wide Field of View ([FoV](#)) of [ASKAP](#) as it will use feed horn receivers rather than [PAFs](#). With SKA1-MID a number of years away from completion and my work specifically depending on [ASKAP](#), I focus in the rest of this section on the future with respect to [ASKAP](#), and the [EMU](#) survey in particular.

Pilot survey observations for the [ASKAP](#) survey science projects (e.g. [EMU](#), [DINGO](#), [WALLABY](#), [FLASH](#), [GASKAP](#)) are currently underway using the full 36 antenna array (ASKAP-36) with successful processing of the full observations taking place at the Pawsey Supercomputing Centre. The [EMU](#) Pilot

Survey phase 2 completed recently, and the full survey is expected to start within the next year after the pilot observations are finished and the observing and data processing strategies have been validated and finalised.

6.2.2 Multi-wavelength

A complete picture of galaxy evolution requires multi-wavelength observations to provide information not available at radio wavelengths. Just as there are new radio facilities under construction and beginning operation, there are numerous optical and Infrared (IR) instruments and telescopes that will be coming online in the next decade. These will include photometric: the Legacy Survey of Space and Time (LSST, Ivezic *et al.*, 2019) on the recently renamed Vera C. Rubin Observatory (VRO, formerly the Large Synoptic Survey Telescope), spectroscopic: the 4-metre Multi-Object Spectrograph Telescope (4MOST, de Jong *et al.*, 2019) on the Visible and Infrared Survey Telescope for Astronomy (VISTA, Sutherland *et al.*, 2015) and integral field spectroscopy: the Multi Unit Spectroscopic Explorer (MUSE, Bacon *et al.*, 2010) on the European Southern Observatory (ESO) Very Large Telescope (VLT), the WHT Enhanced Area Velocity Explorer (WEAVE, Dalton *et al.*, 2016) multi-object survey spectrograph on the William Herschel Telescope (WHT) and the Hector (Bland-Hawthorn, 2015) multi-integral field unit spectrograph on the Anglo-Australian Telescope (AAT), the successor to the Sydney-AAO Multi-object Integral field spectrograph (SAMI, Croom *et al.*, 2012). In addition to galaxy properties derived from optical and IR measurements (e.g. star formation rate and stellar mass), spectroscopic instruments will provide spectroscopic redshifts for all observed galaxies. Spectroscopic redshifts will be more accurate than photometric redshifts provided by surveys and will be vital for future studies. However, even with these new instruments, spectroscopic redshifts will be available for only a tiny fraction of radio sources.

6.2.3 Classification

The classifications done in this work have been purely manual. One of the things that I plan to do is to compare my classifications with those based on catalogues from automated source finders, such as the recent study by Gürkan *et al.* (2022b) on the G23 field. The aim is to see how manual and automated classification differs results-wise.

A new Citizen Science project (RGZ2-EMU) for EMU is being developed by Eleni Vardoulaki, Hongming Tang and their team. It's aiming to identify sources in the full EMU survey, building upon the success of Radio Galaxy Zoo (RGZ; Banfield *et al.*, 2015). The first initial test-run will be on the EMU Pilot Survey, and a key test will be to compare the results of RGZ2-EMU with my catalogue.

A key aspect of my classification system is based on the Fanaroff-Riley (FR) ratio, and I aim to explore the boundaries further. Based on the conditions I gave in Chapter 2 to determine what makes a source FRI or FR II, if the value of c was changed, the resulting a/b ratio and thus the classification would also

change. This would naturally change the luminosity divide between the two populations.

6.2.4 Machine-Learning

The new and upcoming next generation of radio observatories such as the Australian Square Kilometre Array Pathfinder (*ASKAP*), the Expanded Karl G. Jansky Very Large Array (EVLA; Perley *et al.*, 2011), and the Square Kilometre Array (*SKA*; Braun *et al.*, 2015; Quinn *et al.*, 2015; Dewdney *et al.*, 2009) will yield massive volumes of radio imaging data.

For example, the *EMU* survey conducted by *ASKAP* is expected to discover 40 million radio sources, and *SKA* is expected to generate about 3 zetabytes of raw data (150 terabytes per day; Garofalo *et al.*, 2017) including images, catalogues and redshifts. It is not possible to process and analyse this massive amount of data using the traditional method of visual examination. The only real possibility for automatically and quickly processing and analysing large amounts of imaging data (including morphological classification) is in the development of new automatic algorithms. Another aspect to consider when dealing with such streams of data is the computational complexity, which will also contribute to the costs of data processing.

ML algorithms have successfully provided new tools and opportunities for processing astronomical data from surveys in recent years (e.g. Alger *et al.*, 2018; Alhassan *et al.*, 2018; Aniyan and Thorat, 2017; Lukic *et al.*, 2018; Wu *et al.*, 2019; Galvin *et al.*, 2020; Ralph *et al.*, 2019). Deep learning methods, specifically Convolutional Neural Network (CNN; LeCun, 1989) have become widely used in the field of astronomy and astrophysics for detecting and classifying celestial objects. However, Aniyan and Thorat (2017) was the first to present deep learning classification of radio images, demonstrating that neural networks can accurately identify different classes of Radio Galaxies (RGs).

The ultimate goal is to automate the morphological classification process of radio sources by developing a ML classifier capable of accurately classifying large numbers of RGs. As this work has produced FR catalogs with the G23 and EMU-PS data sets, they would provide a good training set for use with e.g. Parallelized rotation and flipping Invariant Kohonen (PINK; Polsterer *et al.*, 2015; Galvin *et al.*, 2019). PINK is a self-organised map method of reducing the dimensionality of the data and reduce the number of images which will need to be classified by the human eye.

For all these automated techniques, training and testing with supervised algorithms require large sets of ‘ground-truth’ sources that have been selected by eye. My manually-selected catalogue of labelled FRI and FRII sources is the largest yet produced, and is already in high demand by groups developing these algorithms for *EMU*. The work will build on the results in this thesis, and I will help develop these tools to classify sources from the *EMU* survey.

6.2.5 Simulations

Full interpretation of observational results will also require comparison with theoretical models and predictions. Current and future large scale cosmological N-body/hydrodynamical simulations that have synergies with radio and multi-wavelength observations include IllustrisTNG (Weinberger *et al.*, 2017; Pillepich *et al.*, 2018), Synthetic Universe For Surveys (SURFS, Elahi *et al.*, 2018), Evolution and Assembly of Galaxies and their Environments (EAGLE, Schaye *et al.*, 2015), and the Genesis theoretical simulations (Poulton *et al.*, 2020). These simulations model the physical processes acting in and around galaxies from their formation in the simulations at high redshift, down to more recent times to provide predictions and aid in interpreting the observational data. Observations from current and future surveys will also inform the simulations through the testing of simulation parameters, and will be used to constrain the simulation models and enable the incorporation of updated model parameters and physical models into simulations. The knowledge gained by combining radio and multi-wavelength surveys with simulations will provide a more accurate picture of galaxy evolution, and in particular those with double structure.

Specifically, I plan to compare the properties (such as the redshift and luminosity distribution) of my catalogue with widely-used simulations such as SKA Design Study (SKADS, Wilman *et al.*, 2008) and Tiered Radio Extragalactic Continuum Simulation (T-RECS, Bonaldi *et al.*, 2019) to test how closely these simulations match the real radio sky.

6.2.6 Alignment of DRAGNs

In this project, I have shown that nearby DRAGNs seem to be mutually aligned with each other, even clustering in some areas. I plan to extend this work by subdividing my samples by properties of the sources such as their redshift, flux density, the type of galaxy, luminosity, etc.

A key question from this work is to find what the astrophysical mechanism that is giving cause to this alignment is. Presumably, from similar studies, it is in some way related to the structure of the cosmic web, which influences the shape and spin of galaxies. In further work, I will explore the clustering properties of this alignment, and compare it to known galaxy clusters and the density distribution on the sky of galaxies. One particularly critical test will be to limit this comparison to galaxies with known redshifts.

I also plan to extend this analysis to other survey fields now becoming available with ASKAP, assuming that the classifications in these fields will be performed using ML tools trained on my catalogues.

6.3 Epilogue

I hope that by training ML methods on samples like my catalogue, and using Citizen Science Techniques, nobody ever again has to identify 3000 or so radio sources by eye!

References

- Abbott, T. M. C., Abdalla, F. B., Allam, S., Amara, A., *et al.* (2018). The Dark Energy Survey: Data Release 1. *ApJS*, 239(2):18.
- Abbott, T. M. C., Abdalla, F. B., Avila, S., Banerji, M., *et al.* (2019). Dark Energy Survey year 1 results: Constraints on extended cosmological models from galaxy clustering and weak lensing. *Phys. Rev. D*, 99(12):123505.
- Alexander, P. (2000). Evolutionary models for radio sources from compact sources to classical doubles. *MNRAS*, 319(1):8.
- Alexander, P. (2006). Models of young powerful radio sources. *MNRAS*, 368(3):1404.
- Alger, M. J., Banfield, J. K., Ong, C. S., Rudnick, L., *et al.* (2018). Radio Galaxy Zoo: machine learning for radio source host galaxy cross-identification. *MNRAS*, 478(4):5547.
- Alhassan, W., Taylor, A. R., and Vaccari, M. (2018). The FIRST Classifier: compact and extended radio galaxy classification using deep Convolutional Neural Networks. *MNRAS*, 480(2):2085.
- Alsaberi, R. Z. E., Maitra, C., Filipović, M. D., Bozzetto, L. M., *et al.* (2019). Discovery of a pulsar-powered bow shock nebula in the Small Magellanic Cloud supernova remnant DEM S5. *MNRAS*, 486(2):2507.
- An, T., and Baan, W. A. (2012). The Dynamic Evolution of Young Extragalactic Radio Sources. *ApJ*, 760(1):77.
- Andernach, H. J. (1995). Radio-Optical Orientation of Elliptical Galaxies, *Astronomical Society of the Pacific Conference Series*, vol. 86, page 69. Astronomical Society of the Pacific.
- Angel, J. R. P., and Stockman, H. S. (1980). Optical and infrared polarization of active extragalactic objects. *ARA&A*, 18:321.
- Aniyan, A. K., and Thorat, K. (2017). Classifying Radio Galaxies with the Convolutional Neural Network. *ApJS*, 230(2):20.
- Antonucci, R. (1993). Unified models for active galactic nuclei and quasars. *ARA&A*, 31:473.

- Antonucci, R. R. J. (1983). Optical polarization position angle versus radio structure axis in Seyfert galaxies. *Nature*, 303(5913):158.
- Antonucci, R. R. J., and Miller, J. S. (1985). Spectropolarimetry and the nature of NGC 1068. *ApJ*, 297:621.
- Avila-Reese, V. (2007). Understanding Galaxy Formation and Evolution. In Solar, Stellar and Galactic Connections Between Particle Physics and Astrophysics, *Astrophysics and Space Science Proceedings*, vol. 2, page 115.
- Baade, W., and Minkowski, R. (1954). Identification of the Radio Sources in Cassiopeia, Cygnus A, and Puppis A. *ApJ*, 119:206.
- Bacon, R., Accardo, M., Adjali, L., Anwand, H., *et al.* (2010). The MUSE second-generation VLT instrument. In McLean, I. S., Ramsay, S. K., and Takami, H. (Eds.), Ground-based and Airborne Instrumentation for Astronomy III, *Society of Photo-Optical Instrumentation Engineers (SPIE) Conference Series*, vol. 7735, page 773508.
- Bagchi, J., Durret, F., Neto, G. B. L., and Paul, S. (2006). Giant Ringlike Radio Structures Around Galaxy Cluster Abell 3376. *Science*, 314(5800):791.
- Bagchi, J., Vivek, M., Vikram, V., Hota, A., *et al.* (2014). Megaparsec Relativistic Jets Launched from an Accreting Supermassive Black Hole in an Extreme Spiral Galaxy. *ApJ*, 788(2):174.
- Baldi, R. D., and Capetti, A. (2008). Recent star formation in nearby 3CR radio-galaxies from UV HST observations. *A&A*, 489(3):989.
- Baldi, R. D., Capetti, A., and Giovannini, G. (2015). Pilot study of the radio-emitting AGN population: the emerging new class of FR 0 radio-galaxies. *A&A*, 576:A38.
- Baldi, R. D., Torresi, E., Migliori, G., and Balmaverde, B. (2019). The High Energy View of FR0 Radio Galaxies. *Galaxies*, 7(3):76.
- Baldry, I. K., Liske, J., Brown, M. J. I., Robotham, A. S. G., *et al.* (2018). Galaxy And Mass Assembly: the G02 field, Herschel-ATLAS target selection and data release 3. *MNRAS*, 474(3):3875.
- Baldry, I. K., Robotham, A. S. G., Hill, D. T., Driver, S. P., *et al.* (2010). Galaxy And Mass Assembly (GAMA): the input catalogue and star-galaxy separation. *MNRAS*, 404(1):86.
- Baldwin, J. E., Boysen, R. C., Hales, S. E. G., Jennings, J. E., *et al.* (1985). The 6C survey of radio sources - I. Declination zone delta > +80. *MNRAS*, 217:717.
- Banfield, J. K., Wong, O. I., Willett, K. W., Norris, R. P., *et al.* (2015). Radio Galaxy Zoo: host galaxies and radio morphologies derived from visual inspection. *MNRAS*, 453(3):2326.

- Barthel, P. D., and Arnaud, K. A. (1996). Anomalous radio-loudness of Cygnus A and other powerful radio galaxies. *MNRAS*, 283(2):L45.
- Batschelet, E. (1981). Circular statistics in biology / Edward Batschelet. Academic Press London.
- Battye, R. A., and Browne, I. W. A. (2009). Radio and optical orientations of galaxies. *MNRAS*, 399(4):1888.
- Baum, S. A., Heckman, T. M., and van Breugel, W. (1992). Spectroscopy of Emission-Line Nebulae in Powerful Radio Galaxies: Interpretation. *ApJ*, 389:208.
- Baum, S. A., Zirbel, E. L., and O'Dea, C. P. (1995). Toward Understanding the Fanaroff-Riley Dichotomy in Radio Source Morphology and Power. *ApJ*, 451:88.
- Begelman, M. C., Blandford, R. D., and Rees, M. J. (1984). Theory of extragalactic radio sources. *Reviews of Modern Physics*, 56(2):255.
- Bertin, E., Mellier, Y., Radovich, M., Missonnier, G., *et al.* (2002). The TERAPIX Pipeline. In Bohlender, D. A., Durand, D., and Handley, T. H. (Eds.), *Astronomical Data Analysis Software and Systems XI, Astronomical Society of the Pacific Conference Series*, vol. 281, page 228.
- Best, P. N. (2009). Radio source populations: Results from SDSS. *Astronomische Nachrichten*, 330(2):184.
- Best, P. N., and Heckman, T. M. (2012). On the fundamental dichotomy in the local radio-AGN population: accretion, evolution and host galaxy properties. *MNRAS*, 421(2):1569.
- Bicknell, G. V. (1986). A Model for the Surface Brightness of a Turbulent Low Mach Number Jet. III. Adiabatic Jets of Arbitrary Density Ratio: Application to NGC 315. *ApJ*, 305:109.
- Bicknell, G. V. (1994). Extragalactic radio sources and the role of relativistic jets. *Australian Journal of Physics*, 47:669.
- Bicknell, G. V. (1995). Relativistic Jets and the Fanaroff-Riley Classification of Radio Galaxies. *ApJS*, 101:29.
- Bietenholz, M. F. (1986). Determining dependences between directional quantities and position on a sphere. *AJ*, 91:1249.
- Bietenholz, M. F., and Kronberg, P. P. (1984). Is there really evidence for universal rotation? *ApJ*, 287:L1.
- Bilicki, M., Hoekstra, H., Brown, M. J. I., Amaro, V., *et al.* (2018). Photometric redshifts for the Kilo-Degree Survey. Machine-learning analysis with artificial neural networks. *A&A*, 616:A69.
- Birch, P. (1982). Is the Universe rotating? *Nature*, 298(5873):451.

- Bland-Hawthorn, J. (2015). The Hector Survey: integral field spectroscopy of 100,000 galaxies. In Ziegler, B. L., Combes, F., Dannerbauer, H., and Verdugo, M. (Eds.), *Galaxies in 3D across the Universe*, vol. 309, pages 21–28.
- Blandford, R. D., and Rees, M. J. (1974). A “twin-exhaust” model for double radio sources. *MNRAS*, 169:395.
- Blandford, R. D., and Rees, M. J. (1974). A ‘Twin-Exhaust’ Model for Double Radio Sources. *Monthly Notices of the Royal Astronomical Society*, 169(3):395.
- Blundell, K. M., Rawlings, S., and Willott, C. J. (1999). The Nature and Evolution of Classical Double Radio Sources from Complete Samples. *AJ*, 117(2):677.
- Bolton, J. G., Stanley, G. J., and Slee, O. B. (1949). Positions of Three Discrete Sources of Galactic Radio-Frequency Radiation. *Nature*, 164(4159):101.
- Bonaldi, A., Bonato, M., Galluzzi, V., Harrison, I., *et al.* (2019). The Tiered Radio Extragalactic Continuum Simulation (T-RECS). *MNRAS*, 482(1):2.
- Borguet, B., Hutsemékers, D., Letawe, G., Letawe, Y., *et al.* (2008). Evidence of a type 1/type 2 dichotomy in the correlation between quasar optical polarization and host-galaxy/extended emission position angles. *A&A*, 478(2):321.
- Borguet, B., Hutsemékers, D., Letawe, G., Letawe, Y., *et al.* (2011). New Insights into the Quasar Type 1/Type 2 Dichotomy from Correlations between Quasar Host Orientation and Polarization. In Bastien, P., Manset, N., Clemens, D. P., and St-Louis, N. (Eds.), *Astronomical Polarimetry 2008: Science from Small to Large Telescopes*, *Astronomical Society of the Pacific Conference Series*, vol. 449, page 459.
- Braun, R., Bourke, T., Green, J. A., Keane, E., *et al.* (2015). Advancing Astrophysics with the Square Kilometre Array. In *Advancing Astrophysics with the Square Kilometre Array (AASKA14)*, page 174.
- Briggs, D. S. (1995). High Fidelity Deconvolution of Moderately Resolved Sources. Ph.D. thesis, New Mexico Institute of Mining and Technology.
- Buttiglione, S., Capetti, A., Celotti, A., Axon, D. J., *et al.* (2010). An optical spectroscopic survey of the 3CR sample of radio galaxies with $z < 0.3$. II. Spectroscopic classes and accretion modes in radio-loud AGN. *A&A*, 509:A6.
- Capaccioli, M., and Schipani, P. (2011). The VLT Survey Telescope Opens to the Sky: History of a Commissioning. *The Messenger*, 146:2.
- Capetti, A., Massaro, F., and Baldi, R. D. (2017a). FRICAT: A FIRST catalog of FR I radio galaxies. *A&A*, 598:A49.

- Capetti, A., Massaro, F., and Baldi, R. D. (2017b). FRICAT: A FIRST catalog of FR II radio galaxies. *A&A*, 601:A81.
- Cavagnolo, K. W., McNamara, B. R., Nulsen, P. E. J., Carilli, C. L., *et al.* (2010). A Relationship Between AGN Jet Power and Radio Power. *ApJ*, 720(2):1066.
- Cegłowski, M., Gawroński, M. P., and Kunert-Bajraszewska, M. (2013). Orientation of the cores of hybrid morphology radio sources. *A&A*, 557:A75.
- Celotti, A., and Fabian, A. C. (1993). The kinetic power and luminosity of parsec-scale radio jets - an argument for heavy jets. *MNRAS*, 264:228.
- Chiaberge, M., Gilli, R., Lotz, J. M., and Norman, C. (2015). Radio Loud AGNs are Mergers. *ApJ*, 806(2):147.
- Coble, K., Bonamente, M., Carlstrom, J. E., Dawson, K., *et al.* (2007). Radio Sources toward Galaxy Clusters at 30 GHz. *AJ*, 134(3):897.
- Codis, S., Pichon, C., Devriendt, J., Slyz, A., *et al.* (2012). Connecting the cosmic web to the spin of dark haloes: implications for galaxy formation. *MNRAS*, 427(4):3320.
- Condon, J. J. (1992a). Radio emission from normal galaxies. *ARA&A*, 30:575.
- Condon, J. J. (1992b). Radio emission from normal galaxies. *ARA&A*, 30:575.
- Contigiani, O., de Gasperin, F., Miley, G. K., Rudnick, L., *et al.* (2017). Radio Galaxy Zoo: cosmological alignment of radio sources. *MNRAS*, 472(1):636.
- Crawford, E., Norris, R. P., and Polsterer, K. (2017). WTF? Discovering the Unexpected in Next-Generation Radio Continuum Surveys, *Astronomical Society of the Pacific Conference Series*, vol. 512, page 109. Astronomical Society of the Pacific.
- Croom, S. M., Lawrence, J. S., Bland-Hawthorn, J., Bryant, J. J., *et al.* (2012). The Sydney-AAO Multi-object Integral field spectrograph. *MNRAS*, 421(1):872.
- Croston, J. H., Ineson, J., and Hardcastle, M. J. (2018). Particle content, radio-galaxy morphology, and jet power: all radio-loud AGN are not equal. *MNRAS*, 476(2):1614.
- Croton, D. J., Springel, V., White, S. D. M., De Lucia, G., *et al.* (2006). The many lives of active galactic nuclei: cooling flows, black holes and the luminosities and colours of galaxies. *MNRAS*, 365(1):11.
- Cutri, R. M., Wright, E. L., Conrow, T., Fowler, J. W., *et al.* (2013). Explanatory Supplement to the AllWISE Data Release Products. Explanatory Supplement to the AllWISE Data Release Products, by R. M. Cutri *et al.*

- Cutri, R. M., Wright, E. L., Conrow, T., Fowler, J. W., *et al.* (2021). VizieR Online Data Catalog: AllWISE Data Release (Cutri+ 2013). *VizieR Online Data Catalog*, II/328.
- Dalton, G., Trager, S., Abrams, D. C., Bonifacio, P., *et al.* (2016). Final design and progress of WEAVE: the next generation wide-field spectroscopy facility for the William Herschel Telescope. In Evans, C. J., Simard, L., and Takami, H. (Eds.), *Ground-based and Airborne Instrumentation for Astronomy VI, Society of Photo-Optical Instrumentation Engineers (SPIE) Conference Series*, vol. 9908, page 99081G.
- de Jong, J. T. A., Kuijken, K., Applegate, D., Begeman, K., *et al.* (2013). The Kilo-Degree Survey. *The Messenger*, 154:44.
- de Jong, R. S., Agertz, O., Berbel, A. A., Aird, J., *et al.* (2019). 4MOST: Project overview and information for the First Call for Proposals. *The Messenger*, 175:3.
- De Young, D. S. (1993). On the Relation between Fanaroff-Riley Types I and II Radio Galaxies. *ApJ*, 405:L13.
- DeBoer, D. R., Gough, R. G., Bunton, J. D., Cornwell, T. J., *et al.* (2009). Australian SKA Pathfinder: A High-Dynamic Range Wide-Field of View Survey Telescope. *IEEE Proceedings*, 97(8):1507.
- Dermer, C. D., and Giebels, B. (2016). Active galactic nuclei at gamma-ray energies. *Comptes Rendus Physique*, 17(6):594.
- Dewdney, P. E., Hall, P. J., Schilizzi, R. T., and Lazio, T. J. L. W. (2009). The Square Kilometre Array. *IEEE Proceedings*, 97(8):1482.
- Driver, S. P., Hill, D. T., Kelvin, L. S., Robotham, A. S. G., *et al.* (2011). Galaxy and Mass Assembly (GAMA): survey diagnostics and core data release. *MNRAS*, 413(2):971.
- Einasto, M., Saar, E., Martínez, V. J., Einasto, J., *et al.* (2008). Toward Understanding Rich Superclusters. *The Astrophysical Journal*, 685(1):83.
- Elahi, P. J., Welker, C., Power, C., Lagos, C. d. P., *et al.* (2018). SURFS: Riding the waves with Synthetic Universe For Surveys. *MNRAS*, 475(4):5338.
- Falle, S. A. E. G. (1991). Self-similar jets. *MNRAS*, 250:581.
- Fanaroff, B. L., and Riley, J. M. (1974). The morphology of extragalactic radio sources of high and low luminosity. *MNRAS*, 167:31.
- Feain, I. J., Cornwell, T. J., Ekers, R. D., Calabretta, M. R., *et al.* (2011). The Radio Continuum Structure of Centaurus A at 1.4 GHz. *ApJ*, 740(1):17.
- Fisher, N. I. (1995). *Statistical Analysis of Circular Data*. Cambridge University Press.

- Flaugher, B., Diehl, H. T., Honscheid, K., Abbott, T. M. C., *et al.* (2015). The Dark Energy Camera. *AJ*, 150(5):150.
- Frommert, M., Durrer, R., and Michaud, J. (2012). The Kolmogorov-Smirnov test for the CMB. *JCAP*, 2012(1):009.
- Galvin, T. J., Huynh, M., Norris, R. P., Wang, X. R., *et al.* (2019). Radio Galaxy Zoo: Knowledge Transfer Using Rotationally Invariant Self-organizing Maps. *PASP*, 131(1004):108009.
- Galvin, T. J., Huynh, M. T., Norris, R. P., Wang, X. R., *et al.* (2020). Cataloguing the radio-sky with unsupervised machine learning: a new approach for the SKA era. *MNRAS*, 497(3):2730.
- Garofalo, M., Botta, A., and Ventre, G. (2017). Astrophysics and Big Data: Challenges, Methods, and Tools. In Brescia, M., Djorgovski, S. G., Feigelson, E. D., Longo, G., *et al.* (Eds.), *Astroinformatics*, vol. 325, pages 345–348.
- Gawroński, M. P., Marecki, A., Kunert-Bajraszewska, M., and Kus, A. J. (2006). Hybrid morphology radio sources from the FIRST survey. *A&A*, 447(1):63.
- Gendre, M. A., Best, P. N., Wall, J. V., and Ker, L. M. (2013). The relation between morphology, accretion modes and environmental factors in local radio AGN. *MNRAS*, 430(4):3086.
- Ghez, A. M., Salim, S., Hornstein, S. D., Tanner, A., *et al.* (2005). Stellar Orbits around the Galactic Center Black Hole. *ApJ*, 620(2):744.
- Ghisellini, G., and Celotti, A. (2001). Relativistic large-scale jets and minimum power requirements. *MNRAS*, 327(3):739.
- Gopal-Krishna, and Wiita, P. J. (1988). Hot gaseous coronae of early-type galaxies and their radio luminosity function. *Nature*, 333(6168):49.
- Gopal-Krishna, and Wiita, P. J. (2000). Extragalactic radio sources with hybrid morphology: implications for the Fanaroff-Riley dichotomy. *A&A*, 363:507.
- Gopal-Krishna, and Wiita, P. J. (2001). The Fanaroff-Riley transition and the optical luminosity of the host elliptical galaxy. *A&A*, 373:100.
- Govoni, F., Falomo, R., Fasano, G., and Scarpa, R. (2000). The optical properties of low redshift radio galaxies. *A&A*, 353:507.
- Grandi, P., Torresi, E., Macconi, D., Boccardi, B., *et al.* (2021). Jet-Accretion System in the Nearby mJy Radio Galaxies. *ApJ*, 911(1):17.

- Gunawardhana, M. L. P., Hopkins, A. M., Bland-Hawthorn, J., Brough, S., *et al.* (2013). Galaxy And Mass Assembly: evolution of the H α luminosity function and star formation rate density up to $z < 0.35$. *MNRAS*, 433(4):2764.
- Gürkan, G., Prandoni, I., O'Brien, A., Raja, W., *et al.* (2022a). Deep ASKAP EMU Survey of the GAMA23 field: properties of radio sources. *MNRAS*, 512(4):6104.
- Gürkan, G., Prandoni, I., O'Brien, A., Raja, W., *et al.* (2022b). Deep ASKAP EMU Survey of the GAMA23 field: Properties of radio sources. *arXiv e-prints*, arXiv:2203.14727.
- Guzman, J., Whiting, M., Voronkov, M., Mitchell, D., *et al.* (2019). ASKAPsoft: ASKAP science data processor software. Astrophysics Source Code Library, record ascl:1912.003.
- Hardcastle, M. (2018a). Interpreting radiative efficiency in radio-loud AGNs. *Nature Astronomy*, 2:273.
- Hardcastle, M. J. (2018b). A simulation-based analytic model of radio galaxies. *MNRAS*, 475(2):2768.
- Hardcastle, M. J., Croston, J. H., and Kraft, R. P. (2007a). A Chandra Study of Particle Acceleration in the Multiple Hot Spots of Nearby Radio Galaxies. *ApJ*, 669(2):893.
- Hardcastle, M. J., Evans, D. A., and Croston, J. H. (2007b). Hot and cold gas accretion and feedback in radio-loud active galaxies. *MNRAS*, 376(4):1849.
- Hardcastle, M. J., Evans, D. A., and Croston, J. H. (2009). The active nuclei of $z \lesssim 1.0$ 3CRR radio sources. *MNRAS*, 396(4):1929.
- Hardcastle, M. J., and Krause, M. G. H. (2013). Numerical modelling of the lobes of radio galaxies in cluster environments. *MNRAS*, 430(1):174.
- Hardcastle, M. J., Williams, W. L., Best, P. N., Croston, J. H., *et al.* (2019). Radio-loud AGN in the first LoTSS data release. The lifetimes and environmental impact of jet-driven sources. *A&A*, 622:A12.
- Harwood, J. J., Vernstrom, T., and Stroe, A. (2020). Unveiling the cause of hybrid morphology radio sources (HyMoRS). *MNRAS*, 491(1):803.
- Hawley, D. L., and Peebles, P. J. E. (1975). Distribution of observed orientations of galaxies. *AJ*, 80:477.
- Hay, S. G., and O'Sullivan, J. D. (2008). Analysis of common-mode effects in a dual-polarized planar connected-array antenna. *Radio Science*, 43(6):23.
- Heckman, T. M. (1980). An optical and radio survey of the nuclei of bright galaxies. Activity in normal galactic nuclei. *A&A*, 500:187.
- Heckman, T. M., Smith, E. P., Baum, S. A., van Breugel, W. J. M., *et al.* (1986). Galaxy Collisions and Mergers: The Genesis of Very Powerful Radio Sources? *ApJ*, 311:526.

- Helou, G., Soifer, B. T., and Rowan-Robinson, M. (1985). Thermal infrared and nonthermal radio : remarkable correlation in disks of galaxies. *ApJ*, 298:L7.
- Hill, G. J., and Lilly, S. J. (1991). A Change in the Cluster Environments of Radio Galaxies with Cosmic Epoch. *ApJ*, 367:1.
- Hill, G. J., and Rawlings, S. (2003). The TOOT survey: status and early results. *New A Rev.*, 47(4-5):373.
- Hoffmeister, C. (1929). 354 neue Veränderliche. *Astronomische Nachrichten*, 236:233.
- Hogg, D. W. (1999). Distance measures in cosmology. *arXiv e-prints*, astro-ph/9905116.
- Honscheid, K., and DePoy, D. L. (2008). The Dark Energy Camera (DECam). *arXiv e-prints*, arXiv:0810.3600.
- Hopkins, A. M., Driver, S. P., Brough, S., Owers, M. S., *et al.* (2013). Galaxy And Mass Assembly (GAMA): spectroscopic analysis. *MNRAS*, 430(3):2047.
- Hota, A., Sirothia, S. K., Ohyama, Y., Konar, C., *et al.* (2011). Discovery of a spiral-host episodic radio galaxy. *MNRAS*, 417(1):36.
- Hotan, A. W., Bunton, J. D., Chippendale, A. P., Whiting, M., *et al.* (2021). Australian square kilometre array pathfinder: I. system description. *PASA*, 38:e009.
- Hubble, E. P. (1922). A general study of diffuse galactic nebulae. *ApJ*, 56.
- Hubble, E. P. (1926). Extragalactic nebulae. *ApJ*, 64.
- Hurley-Walker, N., Callingham, J. R., Hancock, P. J., Franzen, T. M. O., *et al.* (2017). GaLactic and Extragalactic All-sky Murchison Widefield Array (GLEAM) survey - I. A low-frequency extragalactic catalogue. *MNRAS*, 464(1):1146.
- Hutsemekers, D. (1998). Evidence for very large-scale coherent orientations of quasar polarization vectors. *A&A*, 332:410.
- Hutsemékers, D., Braibant, L., Pelgrims, V., and Sluse, D. (2014). Alignment of quasar polarizations with large-scale structures. *A&A*, 572:A18.
- Hutsemékers, D., Cabanac, R., Lamy, H., and Sluse, D. (2005). Mapping extreme-scale alignments of quasar polarization vectors. *A&A*, 441(3):915.
- Hutsemékers, D., and Lamy, H. (2001). Confirmation of the existence of coherent orientations of quasar polarization vectors on cosmological scales. *A&A*, 367:381.

- Hutsemékers, D., Payez, A., Cabanac, R., Lamy, H., *et al.* (2011). Large-Scale Alignments of Quasar Polarization Vectors: Evidence at Cosmological Scales for Very Light Pseudoscalar Particles Mixing with Photons ? In Bastien, P., Manset, N., Clemens, D. P., and St-Louis, N. (Eds.), *Astronomical Polarimetry 2008: Science from Small to Large Telescopes, Astronomical Society of the Pacific Conference Series*, vol. 449, page 441.
- Ineson, J., Croston, J. H., Hardcastle, M. J., Kraft, R. P., *et al.* (2015). The link between accretion mode and environment in radio-loud active galaxies. *MNRAS*, 453(3):2682.
- Ishwara-Chandra, C. H., and Saikia, D. J. (1999). Giant radio sources. *Monthly Notices of the Royal Astronomical Society*, 309(1):100.
- Ivezić, Ž., Kahn, S. M., Tyson, J. A., Abel, B., *et al.* (2019). LSST: From Science Drivers to Reference Design and Anticipated Data Products. *ApJ*, 873(2):111.
- Jain, P., Narain, G., and Sarala, S. (2004). Large-scale alignment of optical polarizations from distant QSOs using coordinate-invariant statistics. *MNRAS*, 347(2):394.
- Jennison, R. C., and Das Gupta, M. K. (1953). Fine Structure of the Extra-terrestrial Radio Source Cygnus I. *Nature*, 172(4387):996.
- Johnston, S., Bailes, M., Bartel, N., Baugh, C., *et al.* (2007). Science with the Australian Square Kilometre Array Pathfinder. *PASA*, 24(4):174.
- Johnston, S., Taylor, R., Bailes, M., Bartel, N., *et al.* (2008). Science with ASKAP. The Australian square-kilometre-array pathfinder. *Experimental Astronomy*, 22(3):151.
- Jonas, J., and MeerKAT Team (2016). The MeerKAT Radio Telescope. In *MeerKAT Science: On the Pathway to the SKA*, page 1.
- Jones, T. W., O'Dell, S. L., and Stein, W. A. (1974). Physics of Compact Nonthermal Sources. I. Theory of Radiation Processes. *ApJ*, 188:353.
- Joseph, T. D., Filipović, M. D., Crawford, E. J., Bojčić, I., *et al.* (2019). The ASKAP EMU Early Science Project: radio continuum survey of the Small Magellanic Cloud. *MNRAS*, 490(1):1202.
- Joshi, S. A., Battye, R. A., Browne, I. W. A., Jackson, N., *et al.* (2007). A survey of polarization in the JVAS/CLASS flat-spectrum radio source surveys - II. A search for aligned radio polarizations. *MNRAS*, 380(1):162.
- Joye, W. A., and Mandel, E. (2003). New Features of SAOImage DS9. In Payne, H. E., Jedrzejewski, R. I., and Hook, R. N. (Eds.), *Astronomical Data Analysis Software and Systems XII, Astronomical Society of the Pacific Conference Series*, vol. 295, page 489.

- Kaiser, C. R., and Alexander, P. (1997). A self-similar model for extragalactic radio sources. *MNRAS*, 286(1):215.
- Kaiser, C. R., and Best, P. N. (2007). Luminosity function, sizes and FR dichotomy of radio-loud AGN. *MNRAS*, 381(4):1548.
- Kaiser, C. R., and Cotter, G. (2002). The death of FR II radio sources and their connection with radio relics. *MNRAS*, 336(2):649.
- Kaiser, C. R., Dennett-Thorpe, J., and Alexander, P. (1997). Evolutionary tracks of FR II sources through the P-D diagram. *MNRAS*, 292(3):723.
- Kapińska, A. D., Terentev, I., Wong, O. I., Shabala, S. S., *et al.* (2017). Radio Galaxy Zoo: A Search for Hybrid Morphology Radio Galaxies. *AJ*, 154(6):253.
- Karson, M. J. (1968). Handbook of Methods of Applied Statistics. Volume I: Techniques of Computation Descriptive Methods, and Statistical Inference. Volume II: Planning of Surveys and Experiments. I. M. Chakravarti, R. G. Laha, and J. Roy, New York, John Wiley; 1967, \$9.00. *Journal of the American Statistical Association*, 63:1047.
- Kauffmann, G., and Haehnelt, M. (2000). A unified model for the evolution of galaxies and quasars. *MNRAS*, 311(3):576.
- Kaviraj, S., Shabala, S. S., Deller, A. T., and Middelberg, E. (2015). Radio AGN in spiral galaxies. *MNRAS*, 454(2):1595.
- Kawakatu, N., Kino, M., and Nagai, H. (2009). On the Origin of Fanaroff-Riley Classification of Radio Galaxies: Deceleration of Supersonic Radio Lobes. *ApJ*, 697(2):L173.
- Kellermann, K. I., Sramek, R., Schmidt, M., Shaffer, D. B., *et al.* (1989). VLA Observations of Objects in the Palomar Bright Quasar Survey. *AJ*, 98:1195.
- Kendall, D. G., and Young, G. A. (1984). Indirectional statistics and the significance of an asymmetry discovered by Birch. *MNRAS*, 207:637.
- Kewley, L. J., Groves, B., Kauffmann, G., and Heckman, T. (2006). The host galaxies and classification of active galactic nuclei. *MNRAS*, 372(3):961.
- Khachikian, E. Y., and Weedman, D. W. (1974). An atlas of Seyfert galaxies. *ApJ*, 192:581.
- Komissarov, S. S. (1988). Relativistic Jet Deceleration in Weak Extragalactic Radio Sources. *Ap&SS*, 150(1):59.

- Kormendy, J., and Richstone, D. (1995). Inward Bound—The Search For Supermassive Black Holes In Galactic Nuclei. *ARA&A*, 33:581.
- Koski, A. T. (1978). Spectrophotometry of Seyfert 2 galaxies and narrow-line radio galaxies. *ApJ*, 223:56.
- Krause, M., Alexander, P., Riley, J., and Hopton, D. (2012). A new connection between the jet opening angle and the large-scale morphology of extragalactic radio sources. *MNRAS*, 427(4):3196.
- Kuijken, K. (2011). OmegaCAM: ESO’s Newest Imager. *The Messenger*, 146:8.
- Kuijken, K., Heymans, C., Dvornik, A., Hildebrandt, H., *et al.* (2019). The fourth data release of the Kilo-Degree Survey: ugri imaging and nine-band optical-IR photometry over 1000 square degrees. *A&A*, 625:A2.
- Kumari, S., and Pal, S. (2021). Search for hybrid morphology radio galaxies from FIRST survey at 1400 MHz. *arXiv e-prints*, arXiv:2104.14469.
- Laigle, C., Pichon, C., Codis, S., Dubois, Y., *et al.* (2015). Swirling around filaments: are large-scale structure vortices spinning up dark haloes? *MNRAS*, 446(3):2744.
- Laing, R. A., and Bridle, A. H. (2002). Dynamical models for jet deceleration in the radio galaxy 3C 31. *MNRAS*, 336(4):1161.
- Laing, R. A., and Bridle, A. H. (2014). Systematic properties of decelerating relativistic jets in low-luminosity radio galaxies. *MNRAS*, 437(4):3405.
- Laing, R. A., Guidetti, D., Bridle, A. H., Parma, P., *et al.* (2011). Deep imaging of Fanaroff-Riley Class I radio galaxies with lobes. *MNRAS*, 417(4):2789.
- Laing, R. A., Jenkins, C. R., Wall, J. V., and Unger, S. W. (1994). Spectrophotometry of a Complete Sample of 3CR Radio Sources: Implications for Unified Models, *Astronomical Society of the Pacific Conference Series*, vol. 54, page 201. Astronomical Society of the Pacific.
- Laing, R. A., Riley, J. M., and Longair, M. S. (1983). Bright radio sources at 178 MHz : flux densities, optical identifications and the cosmological evolution of powerful radio galaxies. *MNRAS*, 204:151.
- Landler, L., Ruxton, G., and Malkemper, P. (2019). The Hermans–Rasson test as a powerful alternative to the Rayleigh test for circular statistics in biology. *BMC Ecology*, 19.
- Lang, D. (2014). unWISE: Unblurred Coadds of the WISE Imaging. *AJ*, 147(5):108.
- Leahy, D. A., Hopkins, A. M., Norris, R. P., Marvil, J., *et al.* (2019). ASKAP commissioning observations of the GAMA 23 field. *PASA*, 36:e024.

- Leahy, J. P. (1993). DRAGNs. In Röser, H.-J., and Meisenheimer, K. (Eds.), *Jets in Extragalactic Radio Sources*, vol. 421, page 1. Springer.
- LeCun, Y. (1989). Generalization and Network Design Strategies. In Pfeifer, R., Schreter, Z., Fogelman, F., and Steels, L. (Eds.), *Connectionism in Perspective*. Elsevier, Zurich, Switzerland. An extended version was published as a technical report of the University of Toronto.
- Ledlow, M. J., and Owen, F. N. (1996). 20 CM VLA Survey of Abell Clusters of Galaxies. VI. Radio/Optical Luminosity Functions. *AJ*, 112:9.
- Lin, Y.-T., Shen, Y., Strauss, M. A., Richards, G. T., *et al.* (2010). On the Populations of Radio Galaxies with Extended Morphology at $z < 0.3$. *ApJ*, 723(2):1119.
- Liske, J., Baldry, I. K., Driver, S. P., Tuffs, R. J., *et al.* (2015). Galaxy And Mass Assembly (GAMA): end of survey report and data release 2. *MNRAS*, 452(2):2087.
- Lister, M. L. (2001). Parsec-Scale Jet Polarization Properties of a Complete Sample of Active Galactic Nuclei at 43 GHz. *ApJ*, 562(1):208.
- Lorensen, W. E., and Cline, H. E. (1987). Marching Cubes: A High Resolution 3D Surface Construction Algorithm. *SIGGRAPH Comput. Graph.*, 21(4):163.
- Lukic, V., Brüggem, M., Banfield, J. K., Wong, O. I., *et al.* (2018). Radio Galaxy Zoo: compact and extended radio source classification with deep learning. *MNRAS*, 476(1):246.
- Ma, Z., Xu, H., Zhu, J., Hu, D., *et al.* (2019). A Machine Learning Based Morphological Classification of 14,245 Radio AGNs Selected from the Best-Heckman Sample. *ApJS*, 240(2):34.
- Mackay, C. D. (1971). Observations of the structure of radio sources in the 3C catalogue V. The properties of sources in a complete sample. *MNRAS*, 154:209.
- Magorrian, J., Tremaine, S., Richstone, D., Bender, R., *et al.* (1998). The Demography of Massive Dark Objects in Galaxy Centers. *AJ*, 115(6):2285.
- Mahatma, V. H., Hardcastle, M. J., Williams, W. L., Best, P. N., *et al.* (2019). LoTSS DR1: Double-double radio galaxies in the HETDEX field. *A&A*, 622:A13.
- Mahatma, V. H., Hardcastle, M. J., Williams, W. L., Brienza, M., *et al.* (2018). Remnant radio-loud AGN in the Herschel-ATLAS field. *MNRAS*, 475(4):4557.
- Mainzer, A., Bauer, J., Cutri, R. M., Grav, T., *et al.* (2014). Initial Performance of the NEOWISE Reactivation Mission. *ApJ*, 792(1):30.

- Mardia, K. V. (1975). Statistics of Directional Data. *Journal of the Royal Statistical Society. Series B (Methodological)*, 37(3):349.
- Marocco, F., Eisenhardt, P. R. M., Fowler, J. W., Kirkpatrick, J. D., *et al.* (2020). The CatWISE2020 Catalog. *arXiv e-prints*, arXiv:2012.13084.
- Marocco, F., Eisenhardt, P. R. M., Fowler, J. W., Kirkpatrick, J. D., *et al.* (2021). The CatWISE2020 Catalog. *ApJS*, 253(1):8.
- Matthews, T. A., Morgan, W. W., and Schmidt, M. (1964). A Discussion of Galaxies Identified with Radio Sources. *ApJ*, 140:35.
- McCarthy, P. J. (1993). High redshift radio galaxies. *ARA&A*, 31:639.
- McGilchrist, M. M., Baldwin, J. E., Riley, J. M., Titterton, D. J., *et al.* (1990). The 7C survey of radio sources at 151 MHz - two regions centered at RA 10h 28m, dec. 41 and RA 06h 28m, DEC 45. *MNRAS*, 246:110.
- Meier, D. L. (1999). A Magnetically Switched, Rotating Black Hole Model for the Production of Extragalactic Radio Jets and the Fanaroff and Riley Class Division. *ApJ*, 522(2):753.
- Meier, D. L., Edgington, S., Godon, P., Payne, D. G., *et al.* (1997). A magnetic switch that determines the speed of astrophysical jets. *Nature*, 388(6640):350.
- Meisner, A. M., Lang, D., Schlafly, E. F., and Schlegel, D. J. (2019). unWISE Coadds: The Five-year Data Set. *PASP*, 131(1006):124504.
- Meisner, A. M., Lang, D., and Schlegel, D. J. (2017a). Deep Full-sky Coadds from Three Years of WISE and NEOWISE Observations. *AJ*, 154(4):161.
- Meisner, A. M., Lang, D., and Schlegel, D. J. (2017b). Full-depth Coadds of the WISE and First-year NEOWISE-reactivation Images. *AJ*, 153(1):38.
- Miley, G. (1980). The structure of extended extragalactic radio sources. *ARA&A*, 18:165.
- Miley, G., and De Breuck, C. (2008). Distant radio galaxies and their environments. *A&A Rev*, 15(2):67.
- Mingo, B., Croston, J. H., Hardcastle, M. J., Best, P. N., *et al.* (2019). Revisiting the Fanaroff-Riley dichotomy and radio-galaxy morphology with the LOFAR Two-Metre Sky Survey (LoTSS). *MNRAS*, 488(2):2701.
- Mingo, B., Hardcastle, M. J., Croston, J. H., Dicken, D., *et al.* (2014). An X-ray survey of the 2 Jy sample - I. Is there an accretion mode dichotomy in radio-loud AGN? *MNRAS*, 440(1):269.
- Minkowski, R. (1960). A New Distant Cluster of Galaxies. *ApJ*, 132:908.

- Miraghaei, H., and Best, P. N. (2017). The nuclear properties and extended morphologies of powerful radio galaxies: the roles of host galaxy and environment. *MNRAS*, 466(4):4346.
- Mulder, K., and Klugkist, I. (2020). Bayesian tests for circular uniformity. *Journal of Statistical Planning and Inference*, 211.
- Norris, R. P., Afonso, J., Appleton, P. N., Boyle, B. J., *et al.* (2006). Deep ATLAS Radio Observations of the Chandra Deep Field-South/Spitzer Wide-Area Infrared Extragalactic Field. *AJ*, 132(6):2409.
- Norris, R. P., Hopkins, A. M., Afonso, J., Brown, S., *et al.* (2011). EMU: Evolutionary Map of the Universe. *PASA*, 28(3):215.
- Norris, R. P., Marvil, J., Collier, J. D., Kapińska, A. D., *et al.* (2021). The Evolutionary Map of the Universe pilot survey. *PASA*, 38:e046.
- Osinga, E., Miley, G. K., van Weeren, R. J., Shimwell, T. W., *et al.* (2020). Alignment in the orientation of LOFAR radio sources. *A&A*, 642:A70.
- Osterbrock, D. E. (1977). Spectrophotometry of Seyfert 1 galaxies. *ApJ*, 215:733.
- Owen, F. N. (1993). Steps Toward a Radio H-R Diagram, vol. 421, page 273. Springer.
- Owen, F. N., and Laing, R. A. (1989). CCD surface photometry of radio galaxies -I. FR class I and II sources. *MNRAS*, 238:357.
- Owen, F. N., and Ledlow, M. J. (1994). The FRI/II Break and the Bivariate Luminosity Function in Abell Clusters of Galaxies, *Astronomical Society of the Pacific Conference Series*, vol. 54, page 319. Astronomical Society of the Pacific.
- Panwar, M., Prabhakar, Sandhu, P. K., Wadadekar, Y., *et al.* (2020). Alignment of radio galaxy axes using FIRST catalogue. *MNRAS*, 499(1):1226.
- Parzen, E. (1962). On Estimation of a Probability Density Function and Mode. *The Annals of Mathematical Statistics*, 33(3):1065 .
- Pelgrims, V., and Hutsemékers, D. (2015). Polarization alignments of quasars from the JVAS/CLASS 8.4-GHz surveys. *MNRAS*, 450(4):4161.
- Perley, R. A., Chandler, C. J., Butler, B. J., and Wrobel, J. M. (2011). The Expanded Very Large Array: A New Telescope for New Science. *ApJ*, 739(1):L1.
- Perucho, M., and Martí, J. M. (2007). A numerical simulation of the evolution and fate of a Fanaroff-Riley type I jet. The case of 3C 31. *MNRAS*, 382(2):526.
- Phinney, E. S., and Webster, R. L. (1983). Is there evidence for universal rotation? *Nature*, 301(5902):735.

- Pillepich, A., Nelson, D., Hernquist, L., Springel, V., *et al.* (2018). First results from the IllustrisTNG simulations: the stellar mass content of groups and clusters of galaxies. *MNRAS*, 475(1):648.
- Planck Collaboration IV (2020). Planck 2018 results. VI. Cosmological parameters. *A&A*, 641:A6.
- Polsterer, K. L., Gieseke, F., and Igel, C. (2015). Automatic Galaxy Classification via Machine Learning Techniques: Parallelized Rotation/Flipping INvariant Kohonen Maps (PINK). In Taylor, A. R., and Rosolowsky, E. (Eds.), *Astronomical Data Analysis Software and Systems XXIV (ADASS XXIV)*, *Astronomical Society of the Pacific Conference Series*, vol. 495, page 81.
- Poulton, R. J. J., Power, C., Robotham, A. S. G., and Elahi, P. J. (2020). Extracting galaxy merger time-scales - I. Tracking haloes with WHEREWOLF and spinning orbits with ORBWEAVER. *MNRAS*, 491(3):3820.
- Prestage, R. M., and Peacock, J. A. (1988). The cluster environments of powerful radio galaxies. *MNRAS*, 230:131.
- Quinn, P., Axelrod, T., Bird, I., Dodson, R., *et al.* (2015). Delivering SKA Science. In *Advancing Astrophysics with the Square Kilometre Array (AASKA14)*, page 147.
- Ralph, N. O., Norris, R. P., Fang, G., Park, L. A. F., *et al.* (2019). Radio Galaxy Zoo: Unsupervised Clustering of Convolutionally Auto-encoded Radio-astronomical Images. *PASP*, 131(1004):108011.
- Ramos Almeida, C., Bessiere, P. S., Tadhunter, C. N., Pérez-González, P. G., *et al.* (2012). Are luminous radio-loud active galactic nuclei triggered by galaxy interactions? *MNRAS*, 419(1):687.
- Rawlings, S. (2002). Cosmological Studies from Radio Source Samples. In Pramesh Rao, A., Swarup, G., and Gopal-Krishna (Eds.), *The Universe at Low Radio Frequencies*, vol. 199, page 34.
- Rayleigh, J. W. S. (1880). XII. On the resultant of a large number of vibrations of the same pitch and of arbitrary phase. *The London, Edinburgh, and Dublin Philosophical Magazine and Journal of Science*, 10(60):73.
- Rees, G. A., Spitler, L. R., Norris, R. P., Cowley, M. J., *et al.* (2016). Radio galaxies in ZFOURGE/NMBS: no difference in the properties of massive galaxies with and without radio-AGN out to $z = 2.25$. *MNRAS*, 455(3):2731.
- Renzini, A., and Daddi, E. (2009). Journeying the Redshift Desert. *arXiv e-prints*, arXiv:0906.4662.
- Reynolds, C. S., Di Matteo, T., Fabian, A. C., Hwang, U., *et al.* (1996a). The ‘quiescent’ black hole in M87. *MNRAS*, 283(4):L111.
- Reynolds, C. S., Fabian, A. C., Celotti, A., and Rees, M. J. (1996b). The matter content of the jet in M87: evidence for an electron-positron jet. *MNRAS*, 283(3):873.

- Reynolds, J. (1994). A revised flux scale for the AT Compact Array. Tech. Rep. AT/39.3/040, Australia Telescope National Facility.
- Richstone, D., Ajhar, E. A., Bender, R., Bower, G., *et al.* (1998). Supermassive black holes and the evolution of galaxies. *Nature*, 385(6701):20.
- Robotham, A., Driver, S. P., Norberg, P., Baldry, I. K., *et al.* (2010). Galaxy and Mass Assembly (GAMA): Optimal Tiling of Dense Surveys with a Multi-Object Spectrograph. *PASA*, 27(1):76.
- Rottgering, H. J. A., Wieringa, M. H., Hunstead, R. W., and Ekers, R. D. (1997). The extended radio emission in the luminous X-ray cluster A3667. *MNRAS*, 290(4):577.
- Rusk, R. (1990). Optical Polarization Properties of Compact Radio Sources. *JRASC*, 84:199.
- Sabater, J., Best, P. N., Hardcastle, M. J., Shimwell, T. W., *et al.* (2019). The LoTSS view of radio AGN in the local Universe. The most massive galaxies are always switched on. *A&A*, 622:A17.
- Sadler, E. M., Ekers, R. D., Mahony, E. K., Mauch, T., *et al.* (2014). The local radio-galaxy population at 20 GHz. *MNRAS*, 438(1):796.
- Saripalli, L. (2012). Understanding the Fanaroff-Riley Radio Galaxy Classification. *AJ*, 144(3):85.
- Schaye, J., Crain, R. A., Bower, R. G., Furlong, M., *et al.* (2015). The EAGLE project: simulating the evolution and assembly of galaxies and their environments. *MNRAS*, 446(1):521.
- Scheuer, P. A. G. (1974). Models of extragalactic radio sources with a continuous energy supply from a central object. *MNRAS*, 166:513.
- Schlafly, E. F., Green, G. M., Lang, D., Daylan, T., *et al.* (2018). The DECam Plane Survey: Optical Photometry of Two Billion Objects in the Southern Galactic Plane. *ApJS*, 234(2):39.
- Schlafly, E. F., Meisner, A. M., and Green, G. M. (2019). The unWISE Catalog: Two Billion Infrared Sources from Five Years of WISE Imaging. *ApJS*, 240(2):30.
- Schmidt, M. (1963). 3C 273 : A Star-Like Object with Large Red-Shift. *Nature*, 197(4872):1040.
- Seyfert, C. K. (1943). Nuclear Emission in Spiral Nebulae. *ApJ*, 97:28.
- Seymour, N., Dwelly, T., Moss, D., McHardy, I., *et al.* (2008). The star formation history of the Universe as revealed by deep radio observations. *MNRAS*, 386(3):1695.
- Seymour, N., Huynh, M., Dwelly, T., Symeonidis, M., *et al.* (2009). Investigating the far-IR/radio correlation of star-forming Galaxies to $z = 3$. *MNRAS*, 398(3):1573.
- Shabala, S. S. (2018). The role of environment in the observed Fundamental Plane of radio active galactic nuclei. *MNRAS*, 478(4):5074.

- Shabala, S. S., Ash, S., Alexander, P., and Riley, J. M. (2008). The duty cycle of local radio galaxies. *MNRAS*, 388(2):625.
- Shimwell, T. W., Röttgering, H. J. A., Best, P. N., Williams, W. L., *et al.* (2017). The LOFAR Two-metre Sky Survey. I. Survey description and preliminary data release. *A&A*, 598:A104.
- Shimwell, T. W., Tasse, C., Hardcastle, M. J., Mechev, A. P., *et al.* (2019). The LOFAR Two-metre Sky Survey. II. First data release. *A&A*, 622:A1.
- Singal, A. K., and Rajpurohit, K. (2014). Fanaroff-Riley dichotomy of radio galaxies and the Malmquist bias. *MNRAS*, 442(2):1656.
- Smith, E. P., and Heckman, T. M. (1989). Multicolor Surface Photometry of Powerful Radio Galaxies. II. Morphology and Stellar Content. *ApJ*, 341:658.
- Smith, M. D., and Donohoe, J. (2019). The morphological classification of distant radio galaxies explored with three-dimensional simulations. *MNRAS*, 490(1):1363.
- Stockman, H. S., Angel, J. R. P., and Miley, G. K. (1979). Alignment of the optical polarization with the radio structure of QSOs. *ApJ*, 227:4.
- Sutherland, W., Emerson, J., Dalton, G., Atad-Ettdgui, E., *et al.* (2015). The Visible and Infrared Survey Telescope for Astronomy (VISTA): Design, technical overview, and performance. *A&A*, 575:A25.
- Tadhunter, C. (2016). Radio AGN in the local universe: unification, triggering and evolution. *A&A Rev.*, 24(1):10.
- Tang, H., Scaife, A. M. M., Wong, O. I., Kapińska, A. D., *et al.* (2020). Radio Galaxy Zoo: new giant radio galaxies in the RGZ DR1 catalogue. *MNRAS*, 499(1):68.
- Taylor, A. R., and Jagannathan, P. (2016). Alignments of radio galaxies in deep radio imaging of ELAIS N1. *MNRAS*, 459(1):5.
- Tchekhovskoy, A., and Bromberg, O. (2016). Three-dimensional relativistic MHD simulations of active galactic nuclei jets: magnetic kink instability and Fanaroff-Riley dichotomy. *MNRAS*, 461(1):5.
- Thorat, K., Saripalli, L., and Subrahmanyan, R. (2013). Environments of extended radio sources in the Australia Telescope Low-Brightness Survey. *MNRAS*, 434(4):2877.
- Turner, R. J., and Shabala, S. S. (2015). Energetics and Lifetimes of Local Radio Active Galactic Nuclei. *ApJ*, 806(1):59.
- Ulrich, M.-H., Maraschi, L., and Urry, C. M. (1997). Variability of Active Galactic Nuclei. *ARA&A*, 35:445.

- Urry, C. M., and Padovani, P. (1995). Unified Schemes for Radio-Loud Active Galactic Nuclei. *PASP*, 107:803.
- Urry, M. (2003). The AGN Paradigm for Radio-Loud Objects, *Astronomical Society of the Pacific Conference Series*, vol. 290, page 3. Astronomical Society of the Pacific.
- van der Walt, S., Schönberger, J. L., Nunez-Iglesias, J., Boulogne, F., *et al.* (2014). scikit-image: image processing in Python. *PeerJ*, 2:e453.
- van Haarlem, M. P., Wise, M. W., Gunst, A. W., Heald, G., *et al.* (2013). LOFAR: The LOw-Frequency ARray. *A&A*, 556:A2.
- van Weeren, R. J., Brügger, M., Röttgering, H. J. A., Hoeft, M., *et al.* (2011). Radio continuum observations of new radio halos and relics from the NVSS and WENSS surveys. Relic orientations, cluster X-ray luminosity, and redshift distributions. *A&A*, 533:A35.
- Vardoulaki, E., Gozaliasl, G., Finoguenov, A., Jiménez-Andrade, E. F., *et al.* (2021). The M^* -Mhalo relation at $0.08 < z < 1.53$ in COSMOS: the role of AGN radio-mode feedback. *arXiv e-prints*, arXiv:2104.04288.
- Verschuur, G., Kellermann, K., and Bouton, E. (1988). Galactic and Extragalactic Radio Astronomy. Astronomy and astrophysics library. Springer.
- Villarreal Hernández, A. C., and Andernach, H. (2018). A Search for Extended Radio Sources in 1.3 sr of the VLA Sky Survey (VLASS). *arXiv e-prints*, arXiv:1808.07178.
- Volonteri, M., Haardt, F., and Madau, P. (2003). The Assembly and Merging History of Supermassive Black Holes in Hierarchical Models of Galaxy Formation. *ApJ*, 582(2):559.
- Wang, Y., Knigge, C., Croston, J. H., and Pavlovski, G. (2011). The entrainment-limited evolution of FR II sources: maximum sizes and a possible connection to FR Is. *MNRAS*, 418(2):1138.
- Weinberger, R., Springel, V., Hernquist, L., Pillepich, A., *et al.* (2017). Simulating galaxy formation with black hole driven thermal and kinetic feedback. *MNRAS*, 465(3):3291.
- White, S. D. M. (1984). Angular momentum growth in protogalaxies. *ApJ*, 286:38.
- Whiting, M., Voronkov, M., Mitchell, D., and Askap Team (2017). Early Science Pipelines for ASKAP. In Lorente, N. P. F., Shortridge, K., and Wayth, R. (Eds.), *Astronomical Data Analysis Software and Systems XXV, Astronomical Society of the Pacific Conference Series*, vol. 512, page 431.
- Whiting, M. T. (2020). High-performance Pipeline Processing for ASKAP. In Ballester, P., Ibsen, J., Solar, M., and Shortridge, K. (Eds.), *Astronomical Data Analysis Software and Systems XXVII, Astronomical Society of the Pacific Conference Series*, vol. 522, page 469.

- Williams, W. L., Hardcastle, M. J., Best, P. N., Sabater, J., *et al.* (2019). The LOFAR Two-metre Sky Survey. III. First data release: Optical/infrared identifications and value-added catalogue. *A&A*, 622:A2.
- Willis, A. G., Strom, R. G., and Wilson, A. S. (1974). 3C236, DA240; the largest radio sources known. *Nature*, 250(5468):625.
- Wilman, R. J., Miller, L., Jarvis, M. J., Mauch, T., *et al.* (2008). A semi-empirical simulation of the extragalactic radio continuum sky for next generation radio telescopes. *MNRAS*, 388(3):1335.
- Wilson, A. S., and Colbert, E. J. M. (1995). The Difference between Radio-loud and Radio-quiet Active Galaxies. *ApJ*, 438:62.
- Wing, J. D., and Blanton, E. L. (2011). Galaxy Cluster Environments of Radio Sources. *AJ*, 141(3):88.
- Wright, E. L. (2006). A Cosmology Calculator for the World Wide Web. *PASP*, 118(850):1711.
- Wright, E. L., Eisenhardt, P. R. M., Mainzer, A. K., Ressler, M. E., *et al.* (2010). The Wide-field Infrared Survey Explorer (WISE): Mission Description and Initial On-orbit Performance. *AJ*, 140:1868-1881.
- Wu, C., Wong, O. I., Rudnick, L., Shabala, S. S., *et al.* (2019). Radio Galaxy Zoo: CLARAN - a deep learning classifier for radio morphologies. *MNRAS*, 482(1):1211.
- Wyithe, J. S. B., and Loeb, A. (2003). Self-regulated Growth of Supermassive Black Holes in Galaxies as the Origin of the Optical and X-Ray Luminosity Functions of Quasars. *ApJ*, 595(2):614.
- Yates, P. M., Shabala, S. S., and Krause, M. G. H. (2018). Observability of intermittent radio sources in galaxy groups and clusters. *MNRAS*, 480(4):5286.
- Yew, M., Filipović, M. D., Roper, Q., Collier, J. D., *et al.* (2018). A Multi-Frequency Study of the Milky Way-Like Spiral Galaxy NGC 6744. *PASA*, 35:e015.
- Yew, M., Filipović, M. D., Stupar, M., Points, S. D., *et al.* (2021). New optically identified supernova remnants in the Large Magellanic Cloud. *MNRAS*, 500(2):2336.
- Yun, M. S., Reddy, N. A., and Condon, J. J. (2001). Radio Properties of Infrared-selected Galaxies in the IRAS 2 Jy Sample. *ApJ*, 554(2):803.
- Zirbel, E. L. (1997). The Megaparsec Environments of Radio Galaxies. *ApJ*, 476(2):489.
- Zirbel, E. L., and Baum, S. A. (1995). On the FR I/FR II Dichotomy in Powerful Radio Sources: Analysis of Their Emission-Line and Radio Luminosities. *ApJ*, 448:521.
- Zou, H., Gao, J., Zhou, X., and Kong, X. (2019). Photometric Redshifts and Stellar Masses for Galaxies from the DESI Legacy Imaging Surveys. *ApJS*, 242(1):8.

Zou, H., Gao, J., Zhou, X., and Kong, X. (2020). *VizieR Online Data Catalog: DESI photz and stellar masses galaxies* (Zou+, 2019). *VizieR Online Data Catalog*, J/ApJS/242/8.

Appendix A

**A Second Epoch Chandra
Observation of the Spiral Galaxy
NGC 6744**

This chapter is a reproduction of: Yew, M., Filipović, M. D., Roper, Q., Collier, J. D., *et al.* (2018). A Multi-Frequency Study of the Milky Way-Like Spiral Galaxy NGC 6744. *PASA*, 35:e015

A SECOND EPOCH CHANDRA OBSERVATION OF THE SPIRAL GALAXY NGC 6744

Miranda Yew¹, Evan J. Crawford¹, Miroslav D. Filipović¹, Eric M. Schlegel²
and Thomas G. Pannuti³

¹*Western Sydney University, Locked Bag 1797, Penrith, NSW 2751, Australia*
E-mail: *e.crawford@westernsydney.edu.au*

²*The University of Texas, One UTSA Circle, San Antonio, 78249, Texas*

³*Space Science Center, Department of Physics, Earth Science and Space Systems
Engineering, Morehead State University, Morehead, KY 40351, USA*

SUMMARY: We present a follow-up X-ray study of the intermediate spiral SAB(r)bc type galaxy NGC 6744, using newly available data from the *Chandra* X-ray telescope. In this study we found a total of 134 X-ray sources; of which 7 had no broad-band flux; 62 sources were in common between the two datasets; 25 sources of the old data that are in the new with no counterparts in overlapping region; 20 sources in the new data that have no counterpart in the old overlapping region; and 5 sources that are in the new with no overlapping region. We also find 15 sources in the old dataset with no overlapping region in the new.

Key words. spiral galaxies: active ISM: supernova remnants (ISM:) H II regions
techniques: image processing infrared: galaxies X-rays: general radio continuum:
galaxies

1. INTRODUCTION

The galaxy NGC 6744, an intermediate spiral SAB(r)bc type galaxy is one of the most prominent spiral galaxies near to our local volume of the Universe. At a distance of 9.2 ± 0.4 Mpc (Tully et al. 2013), NGC 6744 is inclined at $50^\circ \pm 4^\circ$ to our line of sight (Ryder et al. 1999). Its morphology was studied by de Vaucouleurs (1963) and was suggested to be similar to our Galaxy; the Milky Way, additionally hosting a central ring structure. Evidence of the galaxy still actively forming stars is in the star-formation rate (SFR) which Yew et al. (2018) reported to be in the range $2.8 - 4.7 M_\odot \text{ yr}^{-1}$.

NGC 6744 has been studied previously in the radio and X-ray wavebands but it was not until Yew et. al (2018) that infrared observations of this galaxy

were also examined in detail. The previously published studies of this galaxy include an investigation of its H I disk (Ryder 1995; Ryder et al. 1999), and an X-ray study by Fabbiano et al. (1992) analysing an *Einstein* Imaging Proportional Counter image of NGC 6744. The work of Yew et al. (2018) contained a comprehensive examination of the properties of this intriguing galaxy using a combination of X-ray, infrared and radio observations.

In this paper, we consider a new pointed observation made of NGC 6744 with the *Chandra* X-ray Observatory (Weisskopf et al. 2000) in combination an archival pointed observation made of the galaxy that was the subject of analysis by Yew et al. (2018). The present paper may be considered to be a continuation of a group of studies on nearby galaxies including the Large Magellanic Cloud (Hughes et al. 2007), the Small Magellanic Cloud (Filipović et al. 2005;

Wong et al. 2011a,b; Crawford et al. 2011; Haberl et al. 2012; Wong et al. 2012; Sturm et al. 2013), NGC 300 (Payne et al. 2004; Millar et al. 2011; Galvin et al. 2012b; Millar et al. 2012), NGC 55 (O'Brien et al. 2013), M 31 (Galvin et al. 2012a; Galvin & Filipović 2014), NGC 7793 (Pannuti et al. 2011; Dopita et al. 2012; Galvin et al. 2014), and NGC 45 (Pannuti et al. 2015). The aim of the present paper study is to compare the two *Chandra* observations of this galaxy and to analyze any changes in the properties of the detected discrete X-ray sources. The layout of this paper may be described as follows: in Section 2 we describe the observations and data reduction techniques and in Section 3 we present our results and discussion. Finally, in Section 4 we summarise our findings.

2. *Chandra* X-ray OBSERVATIONS

The new X-ray data were obtained by the *Chandra* X-ray Observatory Advanced CCD Imaging Spectrometer (ACIS; PI: Garmire; observation ID 18484) on 2016 June 30 with an effective exposure time of 49.46 ks. The *Chandra* data cover most of NGC 6744's optical extent (see Figure 1); the 20' major axis of NGC 6744 exceeds the 17'×17' ACIS-I field of view on the sky (which corresponds to 11.3×11.3 kpc at the assumed distance to NGC 6744). The nominal FWHM of the point spread function of the X-ray telescope is 0.5'' on-axis, but this value increases towards the edge of the detector. We compare this new observation to the observation analyzed by Yew et al. (2018) – that is, ObsID 15384, which was conducted on 2014 May 5 with an effective exposure time 52.79 ks. More details about this observation are presented in Table 1.

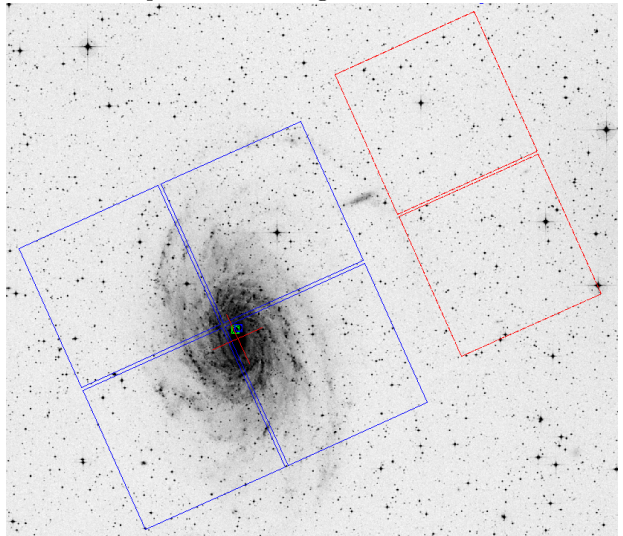
The X-ray data reduction techniques used standard tools within the *Chandra* Interactive Analysis of Observations (CIAO; Fruscione et al. 2006) version 4.8 package with CALDB version 4.7.2 and followed the standard *Chandra* ACIS data analysis thread¹.

Table 1. Details of the two *Chandra* X-ray datasets (15383 and 18484) used in this study.

Observation ID	Date	Exp. Time (ksec)	Nominal Roll (deg)
15384	2014-05-19	52.79	67.214
18454	2016-06-29	49.46	18.048

Exposure-corrected images and exposure maps were created from events files using the reprocessing script `chandra_repro`. Images in five energy bands were created using the `fluximage` task. The five bands considered in this paper are the following: (1) broad band with energies 0.5–7.0 keV and effective energy 2.3 keV; (2) ultra-

soft band with energies 0.2–0.5 keV and effective energy 0.4 keV; (3) soft band with energies 0.5–1.2 keV and effective energy 0.92 keV; (4) medium band with energies 1.2–2.0 keV and effective energy 1.56 keV; and (5) the hard band with energies 2.0–7.0 keV and effective energy 3.8 keV. As the characterization of the ACIS response is not well defined below ~ 0.5 keV (Prigozhin et al. 1998), we have excluded the ultrasoft band from our analysis (Yew et al. (2018) excluded this band from analysis for the same reason). Using the task `mkpsfmap`, the exposure-corrected images were utilized to produce a point spread function (PSF) map which provides information on the PSF at each pixel in the image.



¹<http://cxc.harvard.edu/ciao/threads/>

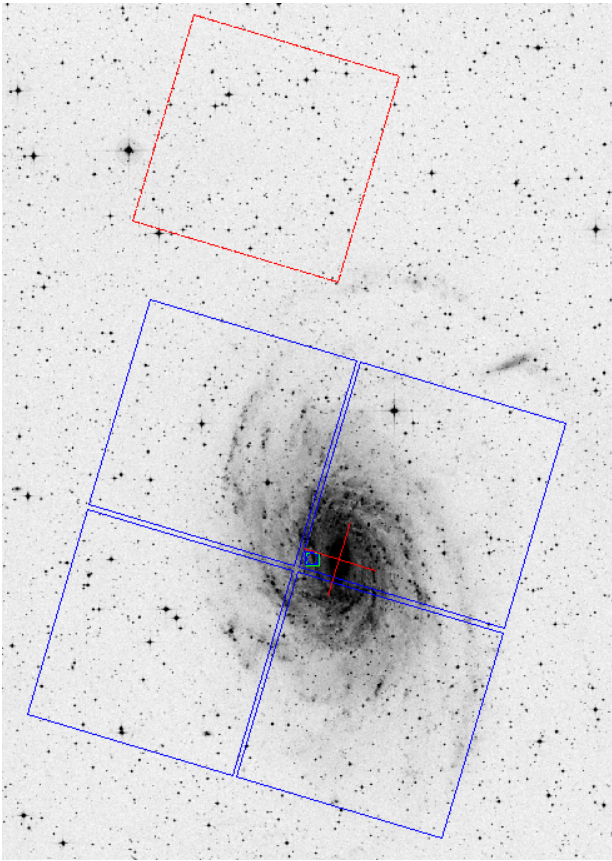


Figure 1. ACIS-I CCD chip footprints overlaid on the optical DSS2 image of NGC 6744 from both observations 15384 (top) from Yew et. al (2018) and 18484 (bottom). The optional CCD chips have also been included for comparison. The red cross represents the centre of NGC 6744, the aimpoint is the green square and the nominal aimpoint is the blue square in the centre of the image. North is up and east is to the left.

The PSF map along with the exposure-corrected images were then fed through the wavelet detection algorithm `wavdetect` in CIAO with scales of 1,2,4 and 8. Once the images were obtained, a catalogue was compiled and hardness ratios (HR) were calculated for each point source. This ratio is calculated as a normalised difference of the exposure-corrected integrated flux between two energy bands where E is the X-ray intensity:

$$HR = \frac{E_{\text{Upper}} - E_{\text{Lower}}}{E_{\text{Upper}} + E_{\text{Lower}}}. \quad (1)$$

We calculated two hardness ratios, HR_1 and HR_2 , between medium and soft bands and between hard and medium bands, respectively. Broad-band fluxes were estimated assuming a power-law spectrum of $\Gamma = 1.7$ and a Galactic foreground column density N_H of 0.061×10^{22} atoms cm^{-2} (Fabbiano et al. 1992) to convert count rates to fluxes using *Sherpa* (Freeman et al. 2001).

3. RESULTS AND DISCUSSION

3.1. X-ray Sources in NGC 6744

The 18454 (2016) dataset has a different nominal roll, giving a different FOV compared to the 15384 (2014) dataset as seen in Figure 1. We detect a total of 134 sources in the new 2016 *Chandra* observations of NGC 6744. Of these 134 sources, we find 62 sources in common between 15384 (2014) data (where we detected 117 X-ray sources) and new 18454 (2016) (see Table 2).

After stacking the images from the 15384 (2014) data and the 18454 (2016) data, we found 25 sources from the 15384 (2014) data that had no 18454 (2016) counterpart and 20 sources from the 18454 (2016) data that had no 15384 (2014) counterpart. Additionally, outside of the region where the images overlapped, we found 5 sources in the 18454 (2016) data. We also find 15 sources in the 15384 (2014) data that were outside of the region where the images overlapped.

Comparing with Yew et. al (2018), out of the 62 X-ray sources found in common between the datasets 15384 and 18454, we find 5 sources that had a classification. J190908–634638, J190919–635330 are classified as strong SNR candidates; J191042–634553 and J191107–634823 are classified as less robust SNR candidates; source J190946–635129 is the central AGN.

We also calculate the separation between sources in common (Δ) as well as their corresponding fluxes.

We found the average change of flux to be -7.89×10^{15} ergs $\text{s}^{-1} \text{cm}^{-2}$ and the change of position to be $1.750''$ (excluding sources which had a change of position value > 4 ; see Table 3). There are a few sources which have a change of flux > 10 e.g. source J190936–634840 with a change of flux of 70.40×10^{-15} and source J190845–634817 with a change of flux of -385.0×10^{-15} .

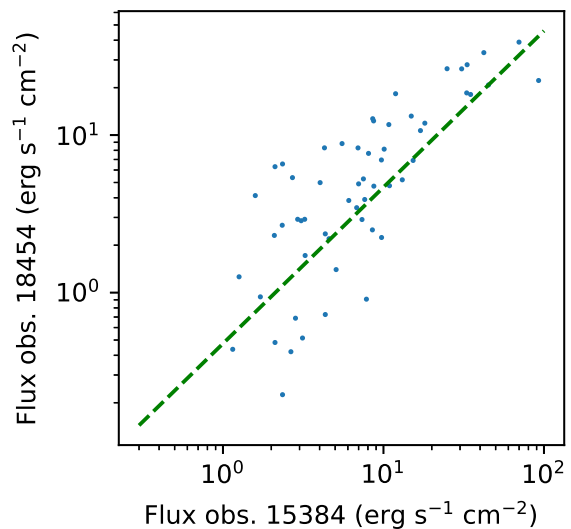


Figure 2. A plot of the flux of 18484 (vertical axis and 15384 (horizontal axis) from Yew et. al (2018) show on a logarithmic scale. The dashed green line is a line of best fit and has a slope of 0.430.

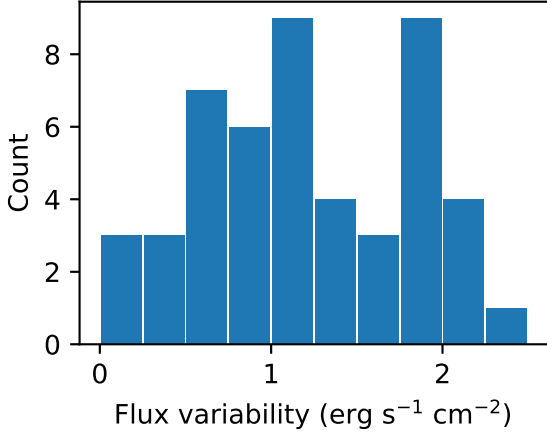


Figure 3. A histogram plot showing the flux variability of the 15384 against the 18484 dataset.

For further comparison, we plotted the flux of the old data-set 15384 against the new 18484 (see Figure 2) Additionally, we also plotted the difference in position as a histogram plot (RA and DEC) of the new 18484 data set in Figure 3 as well as the hardness ratios in Figure 4

Lastly, we also compared with radio data which was used in Yew et. al (2018). Out of the 20 new source found in 18484, after comparison with radio and optical, we found 4 sources with either a radio and/or optical counterpart (see Table 4).

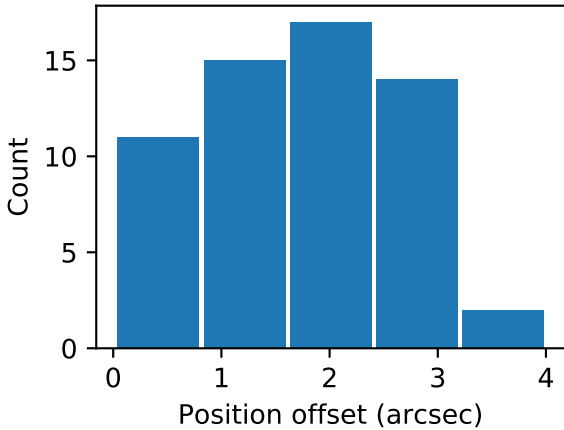


Figure 4. A histogram plot of the difference in position of the 18484 dataset. Comparing this to Figure 10 in Kim et al. 2007, we find the data agrees with the trend.

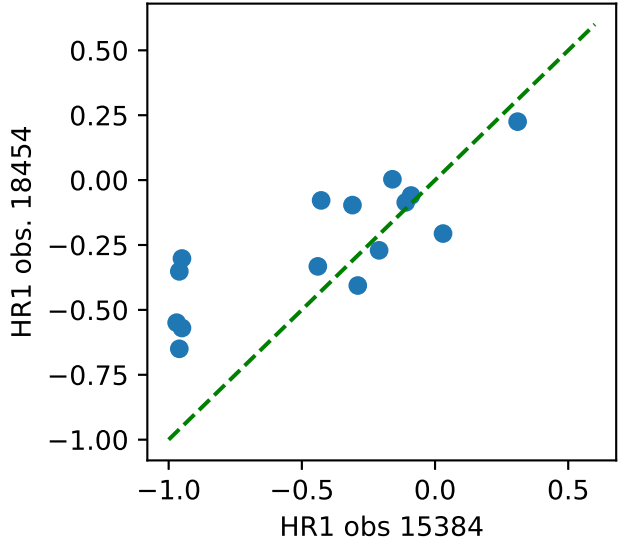


Figure 5. A comparison plot of HR1 between obs. 15384 and 18484. The green dashed line is a linear line from -1 to 1.

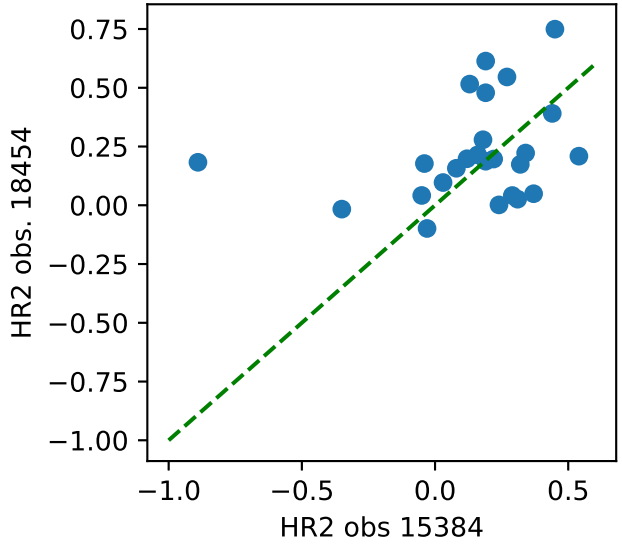


Figure 6. A comparison plot of HR2 between obs. 15384 and 18484. The green dashed line is a linear line from -1 to 1.

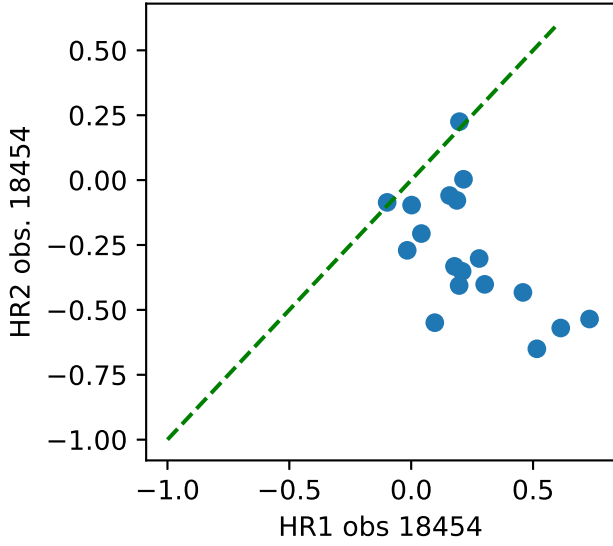


Figure 7. A comparison of the hardness ratios HR1 and HR2 of 18484.

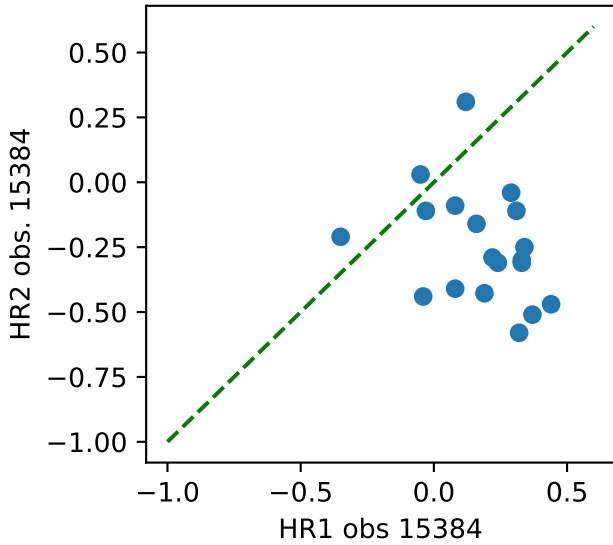


Figure 7. A comparison of the hardness ratios HR1 and HR2 of 15384.

4. CONCLUSION

We present a catalogue of the discrete X-ray in NGC 6744 from recent *Chandra* data. Our multi-frequency analysis of the available observations have led to the following results:

- We find a total of 134 X-ray sources; 62 sources in common between the two datasets, 32 new sources in 18454 of which 7 do not have a broad flux value and 5 do not overlap with 15384 dataset FOV, 40 sources from 15384 without 18454 counterpart; of which 25 were in overlapped FOV and remaining 15 were outside of overlapping FOV area.
- We find a somewhat consistent trend after plotting the flux with only a few sources going off to the far extreme. A majority of our sources lie close to the line of best fit.
- The type Ic supernova SN2005at was not detected in the X-ray data in Yew et. al (2018) with observation ID 15384. Likewise, in the new data presented in this paper with observation ID 18454, SN2005at could not be detected either.

Table 4. Listing the new sources discovered in 18484 that had a radio and/or optical counterpart. Names are taken from radio table in Yew et. al (2018) with exception of source 3 which only had an optical counterpart.

Source Name	Radio	Optical
J190945-635314	Y	Y
J190953-635059	Y	N
J190956-635500	N	Y
J190958-635739	Y	Y

Acknowledgements – This research has made use of data obtained from the *Chandra* Data Archive and the *Chandra* Source Catalog and software provided by the *Chandra* X-ray Center (CXC) in the application packages CIAO, ChIPS, and Sherpa. The authors would also like to thank Quentin Parker for his contributions.

REFERENCES

- Crawford E. J., Filipović M. D., de Horta A. Y., Wong G. F., Tothill N. F. H., Drašković D., Collier J. D., Galvin T. J., 2011, *Serb. Astron. J.*, **183**, 95
- de Vaucouleurs G., 1963, *Astrophys. J.*, **138**, 934
- Dopita M. A., Payne J. L., Filipović M. D., Pannuti T. G., 2012, *Mon. Not. R. Astron. Soc.*, **427**, 956
- Fabbiano G., Kim D.-W., Trinchieri G., 1992, *Astrophys. J. Suppl. Ser.*, **80**, 531
- Filipović M. D., Payne J. L., Reid W., Danforth C. W., Staveley-Smith L., Jones P. A., White G. L., 2005, *Mon. Not. R. Astron. Soc.*, **364**, 217
- Freeman P., Doe S., Siemiginowska A., 2001, in Starck J.-L., Murtagh F. D., eds, Proc. SPIE Vol. 4477, Astronomical Data Analysis. pp 7687, Bellingham WA 982270010 USA (arXiv:astro-ph/0108426), doi:10.1117/12.447161
- Fruscione A., et al., 2006, in Society of Photo-Optical Instrumentation Engineers (SPIE) Conference Series. pp 62701V, Bellingham WA 982270010 USA, doi:10.1117/12.671760
- Galvin T. J., Filipović M. D., 2014, *Serb. Astron. J.*, **189**, 15
- Galvin T. J., Filipović M. D., Crawford E. J., Tothill N. F. H., Wong G. F., De Horta A. Y., 2012a, *Serb. Astron. J.*, **184**, 41
- Galvin T. J., et al., 2012b, *Astrophys. Space Sci.*, **340**, 133
- Galvin T. J., et al., 2014, *Astrophys. Space Sci.*, **353**, 603
- Haberl F., et al., 2012, *Astron. Astrophys.*, **545**, A128
- Hughes A., Staveley-Smith L., Kim S., Wolleben M., Filipović M., 2007, *Mon. Not. R. Astron. Soc.*, **382**, 543
- Kim, Minsun, Wilkes, Belinda J., Kim, Dong-Woo, Green, Paul J., Barkhouse, Wayne A., Lee, Myung Gyoon, Silverman, John D., Tananbaum, Harvey D., 2007, *Astrophys. Space Sci.*, **169**, 401
- Millar W. C., White G. L., Filipović M. D., Payne J. L., Crawford E. J., Pannuti T. G., Staggs W. D., 2011, *Astrophys. Space Sci.*, **332**, 221
- Millar W. C., White G. L., Filipović M. D., 2012, *Serb. Astron. J.*, **184**, 19
- O'Brien A. N., et al., 2013, *Astrophys. Space Sci.*, **347**, 159
- Pannuti T. G., Schlegel E. M., Filipović M. D., Payne J. L., Petre R., Harrus I. M., Staggs W. D., Lacey C. K., 2011, *Astron. J.*, **142**, 20
- Pannuti T. G., et al., 2015, *Astron. J.*, **150**, 91
- Payne J. L., Filipović M. D., Pannuti T. G., Jones P. A., Duric N., White G. L., Carpano S., 2004, *Astron. Astrophys.*, **425**, 443
- Prigozhin G. Y., Rasmussen A., Bautz M. W., Ricker G. R., 1998, in Hoover R. B., Walker A. B., eds, Proc. SPIE Vol. 3444, X-ray Optics, Instruments, and Missions. pp 267275, Bellingham WA 982270010 USA, doi:10.1117/12.331291
- Ryder S. D., 1995, *ApJ*, **444**, 610
- Ryder S. D., Walsh W., Malin D., 1999, *Publ. Astron. Soc. Aust.*, **16**, 84
- Sturm R., et al., 2013, *Astron. Astrophys.*, **558**, A3
- Tully, R. B., Courtois, H. M., Dolphin, A. E., Fisher, J. R., Héraudeau, P., Jacobs, B. A., Karachentsev, I. D., et al. 2013, *Astron. J.*, **146**, 86
- Weisskopf M. C., Tananbaum H. D., Van Speybroeck L. P., O'Dell S. L., 2000, in Truemper J. E., Aschenbach B., eds, Proc. SPIE Vol. 4012, X-ray Optics, Instruments, and Missions III. pp 216, Munich, Germany (arXiv:astro-ph/0004127), doi:10.1117/12.391545
- Wong G. F., Filipović M. D., Crawford E. J., de Horta A. Y., Galvin T., Drašković D., Payne J. L., 2011a, *Serb. Astron. J.*, **182**, 43
- Wong G. F., et al., 2011b, *Serb. Astron. J.*, **183**, 103
- Wong G. F., Filipović M. D., Crawford E. J., Tothill N. F. H., De Horta A. Y., Galvin T. J., 2012, *Serb. Astron. J.*, **185**, 53
- Yew, M., Filipović, M. D., Roper, Q., Collier, J. D., Crawford, E. J., Jarrett, T. H., Tothill, N. F. H., O'Brien, A. N., et al. 2018, *Publ. Astron. Soc. Aust.*, **35**, e015

Table 2. X-ray source catalogue showing 62 sources in common between datasets 15384 and 18454. The changes in flux and Hardness Ratios were calculated between values of the dataset 15384 presented in Yew et. al (2018) with that of the dataset 18454 presented in this work. Source J190946-635129 is the central black hole.

X-ray Source Name	RA (J2000) (h m s)	DEC (J2000) ($^{\circ}$ ' ")	Δ Separation (")	E_{Broad} (ergs s $^{-1}$ cm $^{-2}$) ($\times 10^{-15}$)	Δ Flux (ergs s $^{-1}$ cm $^{-2}$) ($\times 10^{-15}$)	HR_1	HR_2	ΔHR_1	ΔHR_2
J190845-634817	19:08:44.9	-63:48:17.34	0.867	438.00	-385.0	-0.078	0.187	-0.349	0.003
J190848-635240	19:08:49.1	-63:52:34.09	6.830	4.99	-0.960	1	0.183	-0.07	-1.070
J190859-635735	19:08:58.8	-63:57:35.39	3.970	2.68	-0.337				
J190908-635719	19:09:08.6	-63:57:21.53	2.110	4.74	3.970	-0.65	0.516	-0.31	-0.386
J190908-634638	19:09:08.4	-63:46:38.46	0.774	18.10	16.80	1	0.042	-1.04	0.249
J190909-635651	19:09:09.3	-63:56:51.25	1.690	5.27	2.230	1	-1	-1.98	1.28
J190911-634529	19:09:12.1	-63:45:28.78	1.480	2.35	2.130				
J190916-635615	19:09:16.0	-63:56:12.33	3.150	2.86	0.210				
J190919-635330	19:09:19.9	-63:53:30.53	0.020	0.69	2.142	1	0.375	-1	-0.375
J190921-635252	19:09:21.2	-63:52:44.79	7.510	4.13	-2.540	-0.044	-1	0.044	1
J190924-635355	19:09:24.8	-63:53:55.24	0.090	2.91	4.440		1	-0.3	-0.67
J190926-635742	19:09:26.7	-63:57:41.01	1.340	1.72	1.530				
J190929-635458	19:09:29.7	-63:54:58.19	2.280	3.84	2.240		1	-0.98	-0.45
J190930-635240	19:09:30.8	-63:52:43.28	2.530	1.26	4.190				
J190931-635638	19:09:31.1	-63:56:39.86	1.790	0.42	2.230				
J190934-635657	19:09:34.1	-63:56:57.98	2.080	0.43	0.713				
J190934-635534	19:09:34.7	-63:55:34.84	0.776	11.70	-0.857	-0.271	-0.016	0.061	-0.334
J190935-635745	19:09:35.7	-63:57:45.16	0.820	5.37	-2.660				
J190936-634840	19:09:36.0	-63:48:40.97	1.930	22.20	70.40	-0.206	0.042	0.236	-0.092
J190937-634948	19:09:37.1	-63:49:48.32	1.040	0.52	2.620				
J190939-635027	19:09:39.1	-63:50:28.12	1.350	3.90	3.740				
J190939-634956	19:09:40.2	-63:49:49.22	2.640	4.77	6.130				
J190941-635359	19:09:41.0	-63:53:59.29	2.090	33.40	8.840	0.003	0.215	-0.163	-0.055
J190944-634916	19:09:43.9	-63:49:17.38	2.830	12.30	-3.620				
J190945-635214	19:09:45.6	-63:52:16.24	3.250	2.92	0				
J190945-635250	19:09:45.6	-63:52:16.24	6.250	2.92	0.310				
J190946-635325	19:09:46.2	-63:53:24.85	0.180	10.70	6.320	-0.352	0.209	-0.421	-0.331
J190946-635129	19:09:46.3	-63:51:28.25	1.600	12.70	-4.130	-0.549	0.097	-0.421	-0.067
J190946-634902	19:09:46.8	-63:49:01.09	1.320	8.29	-1.350	-0.301	0.279	-0.648	-0.099
J190947-635547	19:09:47.3	-63:55:47.00	1.319	2.31	0.217				
J190948-634940	19:09:48.0	-63:49:40.33	1.380	18.30	-6.400	-1	1	1.040	-0.070
J190948-635023	19:09:48.2	-63:50:22.62	2.810	0.94	0.770				
J190950-635032	19:09:49.7	-63:50:32.36	2.000	2.36	1.980				
J190951-634953	19:09:51.8	-63:49:51.37	2.790	20.80	24.30				
J190952-635749	19:09:52.3	-63:57:48.28	2.460	8.30	-4.010	1	0.479	-1.980	-0.289
J190953-635014	19:09:52.3	-63:50:16.00	2.000	3.46	3.350				
J190953-635636	19:09:53.4	-63:56:34.11	2.000	6.56	-4.210	-0.402	0.301	0.402	-0.301
J190955-635208	19:09:55.7	-63:52:10.23	1.430	8.14	1.960	1	0.026	-0.110	12.00
J191002-635336	19:10:02.0	-63:53:33.89	2.540	6.95	2.760	1	-1	-0.310	-0.330
J191002-635004	19:10:02.5	-63:50:04.22	1.990	775.00	-349.0	-0.060	0.158	1.520	0.508
J191008-635645	19:10:08.7	-63:56:45.36	1.440	0.48	1.630				
J191009-635431	19:10:09.7	-63:54:31.48	0.788	2.50	3.410	-0.535	0.732	0.535	-0.732
J191013-634723	19:10:13.6	-63:47:23.44	2.040	11.90	6.200	-0.570	0.614	-0.380	-0.424
J191018-635514	19:10:18.0	-63:55:13.76	1.460	26.30	4.380	0.225	0.198	0.085	-0.078
J191020-634916	19:10:20.1	-63:49:16.84	0.090	28.00	5.240	-0.090	-0.100	-0.024	0.069
J191024-635039	19:10:24.2	-63:50:39.09	1.350	0.73	3.610				
J191025-635150	19:10:25.8	-63:51:50.87	2.730	4.90	2.100				
J191025-635150	19:10:25.8	-63:51:50.87	1.340	26.40	-1.470	-0.096	0.002	-0.214	0.238
J191026-635300	19:10:26.7	-63:53:00.28	0.110	2.24	7.490	1	0.449	-1	-0.449
J191035-635008	19:10:35.0	-63:50:08.55	2.870	8.83	-3.310	-0.433	0.458	0.433	-0.458
J191036-635926	19:10:36.8	-63:59:26.29	2.270	13.20	1.700	1	0.174	-1.950	0.146
J191042-634553	19:10:42.9	-63:45:53.08	2.680	5.20	7.900	1	0.546	-1.950	-0.276
J191045-635240	19:10:45.1	-63:52:40.64	0.070	2.20	2.380	1	0.470	-1	-0.471
J191045-634830	19:10:45.3	-63:48:30.80	2.750	1.40	3.670	1	0.749	-1.99	-0.299
J191046-635023	19:10:46.3	-63:50:23.24	2.320	6.90	8.400	1	0.222	-1.25	0.118
J191055-634718	19:10:55.1	-63:47:18.31	2.030	7.65	0.420	1	0.050	-1.51	0.321
J191056-634548	19:10:56.8	-63:45:48.98	0.270	38.90	31.00	-0.410	0.197	0.116	0.023
J191106-635044	19:11:06.5	-63:50:44.21	2.730	0.91	6.920				
J191107-634823	19:11:07.3	-63:48:23.50	4.790	6.30	-4.190	1	0.391	-1.470	0.049
J191109-635258	19:11:09.5	-63:52:58.05	0.703	18.50	14.50	-0.332	0.178	-0.108	-0.278

Table 3. X-ray source catalogue showing 25 sources new in dataset 18454. The first 20 sources are in regions overlapping with dataset 15384 while the last 5 sources are in regions not overlapping.

X-ray Source Name	RA (J2000) (h m s)	DEC (J2000) ($^{\circ}$ $'$ $''$)	E_{Broad} ($\text{ergs s}^{-1} \text{cm}^{-2}$) ($\times 10^{-15}$)	HR_1	HR_2
J190900-634717	19:09:00.3	-63:47:17.65	0.196		
J190903-634935	19:09:03.6	-63:49:35.16	5.100	0.843	0.332
J190905-635700	19:09:05.7	-63:57:00.69	5.680	0.510	-0.085
J190927-634534	19:09:27.1	-63:45:34.34	1.250	-0.486	-0.805
J190930-635001	19:09:30.7	-63:50:01.07	6.220	0.322	-0.253
J190936-635536	19:09:36.6	-63:55:36.46	3.780	0.005	-0.494
J190941-635341	19:09:41.7	-63:53:41.05	1.920	0.389	-0.196
J190942-635436	19:09:42.2	-63:54:36.35	1.710	0.559	-0.036
J190945-635311	19:09:45.1	-63:53:11.91	2.870	0.106	-0.421
J190952-635057	19:09:52.7	-63:50:57.11	2.520	0.515	-0.079
J190956-635500	19:09:56.4	-63:55:00.78	6.210	0.793	0.250
J190956-635024	19:09:56.9	-63:50:24.43	2.090	0.591	-0.002
J190958-635740	19:09:58.7	-63:57:40.56	1.930	0.565	-0.029
J191004-635341	19:10:04.7	-63:53:41.02	3.190	0.121	-0.410
J191013-635403	19:10:13.5	-63:54:03.56	3.030	0.806	0.270
J191017-635027	19:10:17.2	-63:50:27.89	10.45	0.503	-0.091
J191022-635455	19:10:22.3	-63:54:55.12	2.430	0.443	-0.147
J191025-635026	19:10:25.5	-63:50:26.42	2.930	-0.210	-0.638
J191029-634759	19:10:29.8	-63:47:59.85	0.692	0.807	0.271
J191048-635308	19:10:48.6	-63:53:08.25	0.370	0.922	0.500
J190925-640015	19:09:25.2	-64:00:15.98	3.050	0.593	-0.001
J190954-633538	19:09:54.7	-63:35:38.81	48.90	0.717	0.144
J190955-640038	19:09:55.9	-64:00:38.35	90.70	0.694	0.103
J191005-633824	19:10:05.8	-63:38:24.48	62.50	0.246	-0.314
J191127-635614	19:11:27.9	-63:56:14.96	4.050	0.639	0.050

Appendix B

New Optically Identified Supernova Remnants in the Large Magellanic Cloud

This chapter is a reproduction of: Yew, M., Filipović, M. D., Stupar, M., Points, S. D., *et al.* (2021). New optically identified supernova remnants in the Large Magellanic Cloud. *MNRAS*, 500(2):2336

New Optically Identified Supernova Remnants in the Large Magellanic Cloud

Miranda Yew¹, Miroslav D. Filipović¹, [★] Milorad Stupar¹, Sean D. Points², Manami Sasaki³, Pierre Maggi⁴, Frank Haberl⁵, Patrick J. Kavanagh⁶, Quentin A. Parker^{7,8}, Evan J. Crawford¹, Branislav Vukotić⁹, Dejan Urošević^{10,11}, Hidetoshi Sano^{12,13}, Ivo R. Seitenzahl¹⁴, Gavin Rowell¹⁵, Denis Leahy¹⁶, Luke M. Bozzetto¹, Chandreyee Maitra⁵, Howard Leverenz¹, Jeffrey L. Payne¹, Laurence A. F. Park¹, Rami Z. E. Alsaberi¹ and Thomas G. Pannuti¹⁷

¹Western Sydney University, Locked Bag 1797, Penrith South DC, NSW 2751, Australia

²Cerro Tololo Inter-American Observatory/NSF's NOIRLab, Casilla 603, La Serena, Chile

³Remeis Observatory and ECAP, Universität Erlangen-Nürnberg, Sternwartstraße 7, D-96049 Bamberg, Germany

⁴Observatoire Astronomique de Strasbourg, Université de Strasbourg, CNRS, 11 rue de l'Université, F-67000 Strasbourg, France

⁵Max-Planck-Institut für extraterrestrische Physik, Gießenbachstraße 1, D-85748 Garching, Germany

⁶School of Cosmic Physics, Dublin Institute for Advanced Studies, 31 Fitzwilliam Place, Dublin 2, Ireland

⁷Department of Physics, University of Hong Kong, Hong Kong

⁸Laboratory for Space Research, The University of Hong Kong, Hong Kong

⁹Astronomical Observatory, Volgina 7, PO Box 74 11060 Belgrade, Serbia

¹⁰Department of Astronomy, Faculty of Mathematics, University of Belgrade, Studentski trg 16, 11000 Belgrade, Serbia

¹¹Isaac Newton Institute of Chile, Yugoslavia Branch

¹²Institute for Advanced Research, Nagoya University, Chikusa-ku, Nagoya 464-8601, Japan

¹³National Astronomical Observatory of Japan, Mitaka, Tokyo 181-8588, Japan

¹⁴School of Science, University of New South Wales, Australian Defence Force Academy, Canberra, ACT 2600, Australia

¹⁵School of Physical Sciences, University of Adelaide, North Terrace, Adelaide, SA 5005, Australia

¹⁶Department of Physics and Astronomy, University of Calgary, University of Calgary, Calgary, Alberta, T2N 1N4, Canada

¹⁷Space Science Center, Department of Physics, Earth Science and Space Systems Engineering, Morehead State University, Morehead, KY 40351, USA

Accepted XXX. Received YYY; in original form ZZZ

ABSTRACT

We present a new optical sample of three Supernova Remnants (SNRs) and 16 Supernova Remnant (SNR) candidates in the Large Magellanic Cloud (LMC). These objects were originally selected using deep H α , [S II] and [O III] narrow-band imaging. Most of the newly found objects are located in less dense regions, near or around the edges of the LMC's main body. Together with previously suggested MCSNR J0541–6659, we confirm the SNR nature for two additional new objects: MCSNR J0522–6740 and MCSNR J0542–7104. Spectroscopic follow-up observations for 12 of the LMC objects confirm high [S II]/H α emission-line ratios ranging from 0.5 to 1.1. We consider the candidate J0509–6402 to be a special example of the remnant of a possible type Ia Supernova (SN) which is situated some 2° (~1.75 kpc) north from the main body of the LMC. We also find that the SNR candidates in our sample are significantly larger in size than the currently known LMC SNRs by a factor of ~2. This could potentially imply that we are discovering a previously unknown but predicted, older class of large LMC SNRs that are only visible optically. Finally, we suggest that most of these LMC SNRs are residing in a very rarefied environment towards the end of their evolutionary span where they become less visible to radio and X-ray telescopes.

Key words: ISM: supernova remnants – techniques: spectroscopic – (galaxies:) Magellanic Clouds

1 INTRODUCTION

SNRs play a major role in our understanding of Supernovae (SNe), the interstellar medium (ISM), and the evolution of galaxies as a whole. They are generally divided into two categories according to their progenitors: core-collapse and thermonuclear (type Ia) SNRs. Core-collapse SNRs, as their name suggests, result from massive stars undergoing core collapse. Thermonuclear SNRs are remnants of type Ia SNe occurring when a massive white dwarf in a binary system experiences a runaway thermonuclear fusion reaction resulting in the explosive release of nuclear energy (for a review see e.g. Hillebrandt et al. 2013). These two types of SNe eject heavy elements into the ISM and heat it. SNe create shock waves that compress magnetic fields and efficiently accelerate particles such as energetic cosmic rays observed throughout the Galaxy. Therefore, a complete study of the properties of these two types of SNRs in galaxies can provide an opportunity to understand the origin of cosmic rays, the star formation history and chemical evolution of galaxies.

In general, SNRs are characterised by their simultaneous exhibition of diffuse X-ray emission, their non-thermal radio spectral index, and their high $[S\ II]/H\alpha$ ratios as these signatures are produced by high-velocity shocks. We utilise the criteria given in Filipovic et al. (1998b, Sect. 4.1) to establish bona-fide SNRs from SNR candidates. In the simplest form, source X-ray and/or radio confirmation in addition to the high optical $[S\ II]/H\alpha$ ratio is necessary for an object to be established as a bona-fide SNR. Otherwise, if a source satisfies only one of these three multi-frequency criteria, we consider it to be an SNR candidate.

Various surveys of SNRs in our Galaxy and nearby galaxies have been carried out at radio, X-ray, Infrared (IR) and optical wavelengths. The first extragalactic SNR candidates were identified in the LMC by Mathewson & Healey (1964) and later confirmed with a combination of radio and optical techniques by Westerlund & Mathewson (1966). To date, a total of 60 SNRs have been confirmed in the LMC with an additional 14 suggested candidates (Maggi et al. 2016; Bozzetto et al. 2017; Maitra et al. 2019). However, sensitivity and resolution limitations severely reduce the effectiveness of the past & present generations of radio and X-ray searches for SNRs in galaxies beyond the Small & Large Magellanic Clouds (MCs) (Goss et al. 1980; Long et al. 1981; Cowan & Branch 1985; Matonick & Fesen 1997; Matonick et al. 1997; Millar et al. 2012; Galvin & Filipovic 2014; Sasaki et al. 2018; Lin et al. 2020; Sasaki 2020). As a result, optical studies have produced the largest number (~1200) of new extra-Magellanic SNR candidates. Optical extragalactic searches for SNRs are mainly done by using an emission line ratio criterion of the form $[S\ II]/H\alpha > 0.4\text{--}0.5$ (Mathewson & Clarke 1973; Dodorico et al. 1980; Fesen 1984; Matonick & Fesen 1997; Blair & Long 1997; Dopita et al. 2010b; Lee & Lee 2014; Vučićić et al. 2019b,a, 2018; Lin et al. 2020). This criterion separates shock-ionisation from photoionisation in SNRs from H II regions and Planetary Nebulae (PNe) (Frew & Parker 2010). SNR radiative shocks collisionally excite sulphur ions in the extended recombination region resulting in S^+ , hence the larger contribution of $[S\ II]$ accounting for an increase of the $[S\ II]$ to $H\alpha$ ratio. In typical H II regions, sulphur exists predominantly in the form of S^{++} , yielding low $[S\ II]$ to $H\alpha$ emission ratios. Ratios from narrow-band imaging are usually verified spectroscopically, since $[N\ II]$ lines at 6548 and 6584Å can contaminate the $H\alpha$ images at an unknown and variable level. Spectroscopic observations of such emission nebulae also can provide other evidence of shock heating, such as strong $[O\ I]\ \lambda 6300$ emission, elevated $[N\ II]$ to $H\alpha$ with respect to H II re-

gions, or high $[O\ III]$ electron temperatures, verifying the candidate as being a SNR (Blair et al. 1981, 1982; Long et al. 1990; Smith et al. 1993; Blair & Long 1997). Although somewhat biased as an isolated criterion, this method is proven and a good way of identifying ordinary radiatively cooling SNRs in nearby galaxies. We note that young, Balmer-dominated SNRs (Chevalier et al. 1980) would be missed by this criterion.

The LMC galaxy, the target of this study, lies towards the south ecliptic pole and is in one of the coldest parts of the radio sky, uncontaminated by Galactic foreground emission (Haynes et al. 1991; Reid & Parker 2010). The LMC's position and its known distance of 50 kpc (di Benedetto 2008) makes the LMC arguably an ideal galaxy in which to study SNRs in our Local Group of galaxies. LMC objects can also be assumed to be located at approximately the same distance even with the tilt (inclination) of the LMC at 23° toward the line of sight (Subramanian & Subramaniam 2010). This tilt introduces <10 per cent of additional uncertainty in diameter estimates.

Apart from the above mentioned LMC SNR survey papers, there are a number of studies focusing on particular LMC SNRs, such as N 103B and N 132D. Some recent studies include: Bojičić et al. (2007); Cajko et al. (2009); Crawford et al. (2008, 2010); Crawford et al. (2014a); Bozzetto et al. (2010); Grondin et al. (2012); Bozzetto et al. (2017); de Horta et al. (2012); De Horta et al. (2014); Kavanagh et al. (2013); Brantseg et al. (2014); Kavanagh et al. (2016, 2015c,b,a); Reid et al. (2015); Maggi et al. (2014); Warth et al. (2014); Bozzetto & Filipović (2014); Bozzetto et al. (2015, 2013, 2014a); Bozzetto & Filipović (2014); Bozzetto et al. (2014b, 2012a,b,d,c); Leahy (2017); Ghavamian et al. (2017); Dopita et al. (2018); Maitra et al. (2019); Alsaberi et al. (2019a); Seitzzahl et al. (2019); Leahy et al. (2019); Pennock et al. (2020).

In this paper, we present new optical narrow band imaging data for 19 LMC objects. For 12 of these 19 objects we also have spectroscopic follow-up observations. The nebular lines detected include $[O\ III]\ 4959/5007\text{Å}$, $[O\ I]\ 6300/6364\text{Å}$, $[S\ II]\ 6716/6731\text{Å}$, and hydrogen Balmer lines, $H\alpha$, $H\beta$, $H\gamma$ and $H\delta$. Further, $[N\ II]\ 6548/6583\text{Å}$ ratio (and line detection) are generally common in SNR spectra, but in the MCs, due to a low abundance of nitrogen (see Dopita 1979; Russell & Dopita 1990; Dopita et al. 2019) these lines are not necessarily detected, or if they are seen they are usually not as intense compared with the same lines of SNRs in the Milky Way (MW) or in other galaxies. These optical lines are common for evolved SNRs, i.e., for remnants whose interiors are in the cooling phase while their shells are merging with the ISM. Compared with old SNRs, younger ones show many more lines in their optical spectra, although they do not share the same spectral classification such as the type of SN explosion and the surrounding ISM. Likewise, in the LMC we notice the existence of non-radiative Balmer dominated and oxygen rich SNRs (see Smith et al. 1991; Vogt & Dopita 2011; Seitzzahl et al. 2018; Vogt et al. 2018) like others discovered in the Galaxy or other galaxies but, somewhat surprisingly, not in M 33 (Long et al. 2010; Lin et al. 2020).

The layout of this paper is as follows: In Section 2 we describe the observations and imaging techniques. In Section 3 we present our results on the 19 LMC objects studied and in Section 4 we investigate the true nature of these objects. Finally, in Section 5 we summarise our findings.

2 OPTICAL AND X-RAY OBSERVATIONS

2.1 Magellanic Cloud Emission Line Survey (MCELS) Observations

We used images from the Magellanic Cloud Emission Line Survey (MCELS; Smith & MCELS Team 1999). These images were taken at the UM/CTIO (University of Michigan) Curtis Schmidt telescope at Cerro Tololo Inter-American Observatory (CTIO). The detector, a Tek 2048 × 2048 CCD with 24 μm pixels, had a scale of 2.3'' per pixel and a resulting angular resolution of approximately 4.6''. The narrowband images were taken with filters centered on the [O III] (λ_c 5008Å, FWHM=50Å), H α + [N II] (λ_c 6563Å, FWHM=30Å), and [S II] (λ_c 6724Å, FWHM=50Å) emission-lines along with green (λ_c 5130Å, FWHM=155Å) and red (λ_c 6850Å, FWHM=95Å) continuum filters. The optical data were reduced using the IRAF¹ software package for bias subtraction and flat-field correction. The astrometry was derived from stars in the Two Micron All Sky Survey (2MASS) J-band catalog (Skrutskie et al. 2006). The data were flux-calibrated using observations of spectro-photometric standard stars (Hamuy et al. 1994, 1992) and then continuum subtracted. More details about MCELS observations can be found in Points et al. (2019)².

In Table 1 we list all 19 objects studied in this paper. In Col. 2 we list the date of the spectroscopic observations for objects listed in Table 2; source name and its central position (RA and DEC) are listed in Cols. 3, 4 and 5; source extent as major and minor axis/diameter are listed in Col. 6 (in arcsec) while in Col. 7 we show the average of major and minor axes converted to parsecs for a distance of 50 kpc; the position angle (PA; Col. 8) is measured from north to east. [S II]/H α from MCELS in Col. 9 represent the average measured value within the SNR candidate extent after subtracting local noise. Only values > 5 σ of the local noise were used and [S II] value provided in Col. 9 is the sum of the 6716Å and 6731Å lines. In Col. 10 we show the number of massive OB stars found within ~100 pc radius as well as within the object's extent as measured in (Col. 6).

2.2 WiFeS

The Wide-Field Spectrograph (WiFeS; Dopita et al. 2007; Dopita et al. 2010a) was used to obtain the integral field spectra of 12 MCELS selected objects (see Section 3.1 for more details). This integral field unit (IFU) is mounted on the Australia National University (ANU) 2.3-m telescope at the Siding Spring Observatory (SSO). The spectrograph is an image slicer, consisting of a combination of 25 × 1'' wide adjacent slits each 38'' in length to yield an effective 25'' × 38'' field of view on the sky.

We performed our WiFeS spectral observation between October 21 and 23, 2017 as well as on September 7, 2019 using the RT560 dichroic as a beam splitter to send light to both the blue and red arms of the spectrograph. However, only the September 7, 2019 observation was done under excellent atmospheric (photometric) conditions. Each observation was 20–50 minutes in length and we used Nod-and-Shuffle techniques as per Dopita et al. (2007). In the blue arm, the medium resolution grating with 708 lines mm⁻¹ (B3000;

~51.7 Å mm⁻¹) was used and for the red arm we used the higher resolution grating of 1200 lines mm⁻¹ (R7000; ~29.0 Å mm⁻¹). According to Dopita et al. (2010a, Table 2), the R7000 grating actually achieves R~6800 (~45 km s⁻¹) and the B3000 grating is actually R ~2900 (~105 km s⁻¹). At H α , this means that R7000 grating has a resolution of just under 1 Å (0.965) (Figure A5) and at H β B3000 has a resolution of about 1.67 Å.

Our choice of gratings provided overlapping blue and red spectra with a coverage from ~3400 to 7000 Å. Dopita et al. (2007) and Dopita et al. (2010a) presented the on-telescope end-to-end transmission of the WiFeS spectrograph, including the telescope, atmosphere and detectors. According to this work, the transmission of the R7000 grating (which we used for the red arm observations) at the wavelength of the [S II] sulphur lines is 12.5 per cent lower compared to the transmission at the wavelength of H α . This transmission correction was applied to all of our relative flux observations of the [S II] lines to H α .

After the data reduction of the WiFeS observations, which was performed with the PyWiFeS pipeline (Version 0.7.0 e.g. Childress et al. 2014), the final product is a 3D spectral data cube with R.A., Dec and λ as the third dimension. Using a circular or square aperture, summed 1D spectra were extracted from the cube (see example in Stupar et al. 2018). For our sample of obtained cubes, we used circular apertures between 5'' and 10'' positioned at the brightest parts of the SNR filaments to extract 1D spectra (see example in Figure A6 (bottom right)). We used the IRAF splot routine to subtract the sky. The same results were achieved using Starlink Splat routine. [O I] spectral lines at 6300/6363 Å are frequently present in the spectrum of SNRs and are good SNR indicators especially in their young phase. However, they are also present in the spectrum of the night sky. Therefore, distinguishing whether such lines belong to the object or they are from the night sky is of essential importance. To resolve this problem, spectra with the presence of these lines were first checked on 2D data and then their wavelengths were measured. If the wavelengths were exactly 6300/6360 Å, then the lines definitely belong to the night sky and are deleted from the 1D spectra. If the lines were shifted for some 5–6 Å (our usual shift for the LMC) its assumed they originate from the given object, and therefore, the lines are kept in the 1D spectrum. We present details in Section A for all 12 spectroscopically observed objects. Also, Tables 1 and 2 provide aperture positions, relative intensities, and ratios of observed lines.

We note that the intrinsically fainter blue flux of three sources produced very weak blue spectra, so that these three candidates only have data for the red part of spectrum (see Table 2). The blue spectra of other candidates should be taken with the understanding that we have not applied individual reddening corrections. For one object, J0548–6941, we have determined physical fluxes of the observed lines (see Table 2). The fluxes were determined by calibration against the spectrophotometric standard star LTT1020.

Some line ratios are set by atomic physics. Specifically, the ¹D₂ → ³P doublet ratios [O III] 5007/4959Å and [N II] 6583/6548Å must both be ~2.9 (Acker et al. 1989), which makes measuring the flux of the fainter blue lines ([O III]4959Å and [N II]6548Å) difficult in several cases (e.g. source J0542–7104 (Figure A18) where [O III]4959Å is hardly above the background fluctuations). To avoid adding noise, we measure only the brighter red component of the doublets, and multiply by (1+1/3) to calculate [N II]/H α and [O III]/H α ratios.

¹ Image Reduction and Analysis Facility (IRAF) is distributed by the National Optical Astronomy Observatory (NOAO), which is operated by the Association of Universities for Research in Astronomy (AURA) under a cooperative agreement with the National Science Foundation (NSF).

² Data can be found in: <ftp://ftp.ctio.noao.edu/pub/points/MCELS/LMC/>

2.3 XMM-Newton data

To search for X-ray emission from our candidate SNRs we created an up-to-date mosaic of all *XMM-Newton* (Jansen et al. 2001) observations available in the LMC area. This included all archival observations that were public up to July 2020, as well as recent observations from projects with author involvement centred within 4° around R.A.(J2000)= $05^h 22^m 00^s$ and Dec(J2000)= $-68^\circ 30' 00''$ (for more detailed descriptions see Maggi et al. 2016; Sturm et al. 2013; Haberl et al. 2012). Observations were processed with *XMM-Newton* science analysis software SAS version 17.0.0. We combined the data from the European Photon Imaging Camera, EPIC-pn and EPIC-MOS (Strüder et al. 2001; Turner et al. 2001) and created images in the 0.3–0.7 keV, 0.7–1.1 keV and 1.1–4.2 keV energy bands which were combined with an RGB image. From EPIC-pn we used only single- and double-pixel events ($\text{PATTERN} \leq 4$), and from EPIC-MOS all single- to quadruple-pixel events ($\text{PATTERN} \leq 12$). The X-ray properties of the detected SNRs as revealed by our *XMM-Newton* mosaic will be discussed in future papers including (Kavanagh et al. 2020).

2.4 Magellanic Clouds Photometric Survey

It is very important to understand the type of stellar environment the progenitor of these objects came from. Because of that, we make use of data from the Magellanic Clouds Photometric Survey (MCPS; Zaritsky et al. 2004) in order to construct colour-magnitude diagrams. This way we identify blue stars more massive than $\sim 8 M_\odot$ within a 100 pc ($6.9'$) radius of objects selected in this study. This allows us to see the prevalence of early-type stars close to the remnant candidates.

3 RESULTS

From careful examination of the MCELS images, we select 19 LMC objects and classify them as potential new SNR candidates. We base this classification on their morphological characteristics as well as their $[\text{S II}]/\text{H}\alpha$ ratios (see Table 1 and Figure 1 for their positions across the LMC field). We include in our sample MCSNR J0541–6659, which was previously classified as an SNR by Grondin et al. (2012) using X-ray observations (Figure A17) but never confirmed spectroscopically.

Figures A1, A3, A4, A5, A6, A8, A9, A11, A16, A18, A19 and A21 show the 12 spectroscopically studied LMC objects with their associated WiFeS spectra and the MCELS images (namely: $\text{H}\alpha$, $[\text{S II}]$, $[\text{O III}]$ and the ratio $[\text{S II}]/\text{H}\alpha$).

In Figures A2, A7, A12, A13, A14, A15 and A20 we show seven additional MCELS objects, which we propose as new LMC SNRs or SNR candidates. However, we have not yet obtained any spectroscopic follow-up observations of these objects. Three of these seven objects are detected in X-rays which additionally support their classification as SNRs. Because of the lack of spectroscopic confirmation as well as the lack of confirmed detections at other frequencies, we assign a lower confidence classification (as SNR candidates) for the four remaining sources in this sample of seven objects.

3.1 Optical Identification of Newly Selected LMC objects

It is well established that the most reliable SNR diagnostic of optical spectral observations is the ratio of the $[\text{S II}]/\text{H}\alpha$ lines. This

confirms the presence of radiative shock(s) and a ratio of >0.4 suggests an SNR origin. However, we note that $[\text{S II}]/\text{H}\alpha$ can also reach 0.4 (and higher) in ionisation fronts as well as in diffuse gas ionised by a diluted UV flux. A good example is NGC 7793 where the optical search for SNRs was severely complicated by extensive diffuse $[\text{S II}]/\text{H}\alpha$ photoionised gas throughout the galaxy and rises well above the value of 0.4 (Blair & Long 1997). The $[\text{S II}]/\text{H}\alpha$ ratio alone is thus not sufficient to robustly confirm an SNR classification as X-ray and/or radio confirmation is also needed. All discrete objects in Table 2 satisfy these optical criteria indicating their possible SNR nature. The shell structure of the observed sample, clearly seen on MCELS images in $\text{H}\alpha$, $[\text{S II}]$ and $[\text{O III}]$ light, also supports the fact that these objects are excellent SNR candidates.

Additionally, the existence of $[\text{O III}]$ emission that is localised to a thin shell is another indicator that the source is indeed of SNR origin as it traces out the radiative cooling zone. But if it is extended, especially in the inner part of the nebula, it is more typical of a high (photo-)ionisation nebula, and argues against an SNR interpretation.

In Figure 2 we show the ratio of the $[\text{S II}]\lambda 6716$ and $[\text{S II}]\lambda 6731$ lines versus $\log(\text{H}\alpha/([\text{S II}]\lambda 6716 + [\text{S II}]\lambda 6731))$ for the sample of our 12 spectroscopically studied LMC objects (following Sabbadin et al. (1977)). This diagram maps the locations in this graph that would be occupied by H II regions, SNRs and PNe. This diagram is based on Galactic SNRs, H II regions and PNe and is representative of nearby galaxies such as the LMC.

Using our high resolution spectroscopic observations, we find one of the initially selected SNR candidates having an elevated $[\text{S II}]/\text{H}\alpha$ ratio which is just out of the range expected for SNRs (J0549–6633; marked in red in Figure 2). We still classify this object, though, as a somewhat more likely SNR candidate than a (super)bubble (see Appendix A19). The rest of our sample nicely fits in the group of older SNRs because of the higher ratio of sulphur lines – just as it is predicted by Sabbadin et al. (1977). This is in agreement with the findings of Long et al. (2018) for M33 SNRs where some very large shells with elevated $[\text{S II}]$ emission were seen. Recently, Fesen et al. (2020) also found a new large optically visible but radio and X-ray faint Galactic SNR.

Sabbadin et al. (1977) also use a diagram of $\text{H}\alpha/[\text{N II}]$ vs. $\text{H}\alpha/[\text{S II}]$ (in log scale, their Fig. 2). H II regions have smaller $[\text{N II}]/\text{H}\alpha$ ratios than SNR which adds another tool to separate these two group of sources. A very low value for our candidates J0502–6739 (looks more like H II region) and J0542–7104 casts some doubts on their classification as SNR candidates from the spectroscopic point of view. Certainly, Sabbadin et al. (1977) estimates were for MW objects, and as we mentioned earlier (see Section 1) the LMC has nitrogen deficiency.

In Table 2 we also show the ratio of $[\text{N II}]/\text{H}\alpha$ lines with a median (for this sample) of ~ 0.27 ($\text{SD}=0.10$). This is a somewhat lower than expected ratio compared to Galactic SNRs, but it is acceptable because of the overall lower nitrogen abundance of the LMC compared to the MW (see also Reid et al. 2015). Depending on the local abundance in the Galaxy (see example in Stupar et al. 2018), this ratio for SNRs could vary by as much as a factor of ~ 2 (or even more). In the blue part of the spectrum, we detected the oxygen line $[\text{O III}]\lambda 5007$ in six SNR candidates (MCSNR J0541–6659, J0444–6758, J0455–6830, J0517–6757, MCSNR J0542–7104 and J0548–6941). The presence of this line suggests that the shock velocity is between 80 km s^{-1} and 140 km s^{-1} because a speed of over 140 km s^{-1} would produce more $\text{H}\beta$ emission than the oxygen line which becomes relatively weak. However, spectra of these six putative remnants (and their relative intensities as listed in Table 2) show a rather strong $[\text{O III}]\lambda 5007$ line. The exception is again

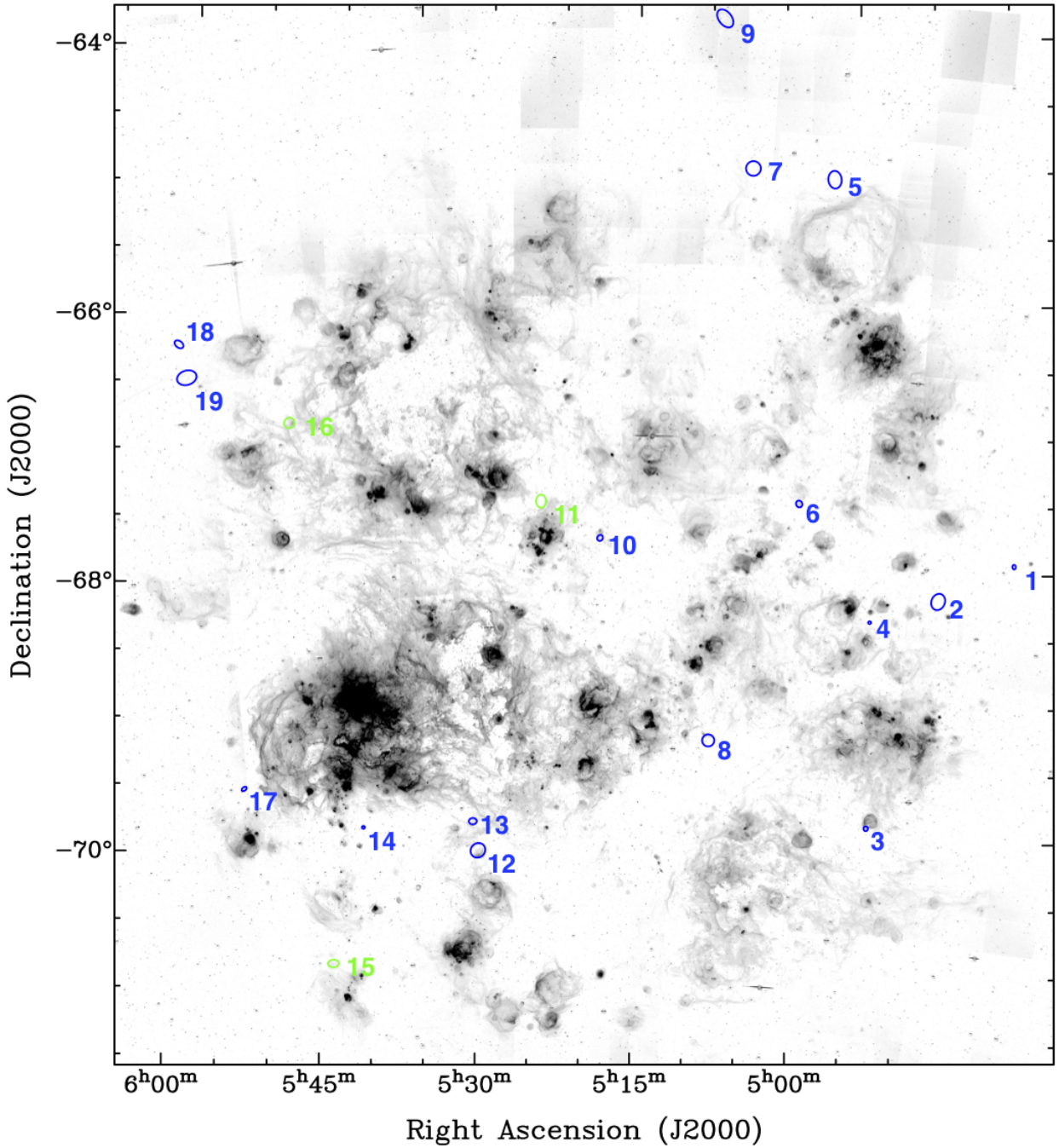


Figure 1. The positions of 16 new SNR candidates in the LMC are marked in blue. Previously classified X-ray SNR — MCSNR J0541–6659 and here classified MCSNR 0522–6740 and MCSNR J0542–7104 are marked in green colour with corresponding numbers as in Table 1 (Col. 1). Background (grey scale) image is MCELS $H\alpha$.

MCSNR J0541–6659 where $H\beta$ is much stronger than the usually strong $[O\text{ III}]\lambda 5007$ line. The last column in Table 2 presents electron densities for the given sample calculated on the basis of the $[S\text{ II}]\lambda 6716/[S\text{ II}]\lambda 6731$ line ratios with an assumed electron temperature of 10 000 K. Assessment of values in this column suggests an overall older SNR population including five objects that are at a low electron density (e.g. out of the electron density function; marked with LDL (low density limit) in the last column of Table 2).

While these spectroscopic results suggest that our newly se-

lected objects are SNRs, we cannot take that as the final classification. Apart from a confirmation at other frequencies (Filipovic et al. 1998b; Bozzetto et al. 2017), a question arises from the fact that the shell structure and the ratio of sulphur lines with $H\alpha$ (e.g. the shock) are not seen only in SNRs. For example, a Wolf Rayet (WR) star nebula is also a source of nebulousity where shocks are observed as they are released from a WR star. However, the sizes of WR shells are certainly smaller compared to SNRs. For our sample of sources studied here, the indication of a possible WR star nebula can be

Table 1. The main characteristics of the 19 LMC objects in this study.

No.	Obs. Date	Name	RA (J2000) (h m s)	DEC (J2000) (° ' ")	$D_{maj} \times D_{min}$ (")	D_{av} (pc)	PA (°)	MCELS [S II]/H α	OB stars No.	Figure No.
(1)	(2)	(3)	(4)	(5)	(6)	(7)	(8)	(9)	(10)	(11)
1	22/10/2017	0444–6758	04 44 27.8	–67 58 13.1	124 × 92	25.9	80	0.7	1/0	A1
2	23/10/2017	0450–6818	04 50 12.4	–68 18 04.8	454 × 366	98.8	105	0.8	1/1	A2
3	not obs.	0454–7003	04 54 19.1	–70 03 30.5	129 × 121	30.3	80	0.8	18/0	A3
4	21/10/2017	0455–6830	04 55 36.8	–68 30 34.6	80 × 78	19.1	170	0.9	18/0	A4
5	22/10/2017	0500–6512	05 00 58.5	–65 12 15.3	480 × 360	100.8	80	0.8	0/0	A5
6	22/10/2017	0502–6739	05 02 02.5	–67 39 31.3	190 × 168	43.3	60	0.6	18/2	A6
7	not obs.	0506–6509	05 06 51.7	–65 09 16.6	402 × 398	97.0	170	0.6	—	A7
8	22/10/2017	0508–6928	05 08 31.8	–69 28 29.8	330 × 330	80.0	0	0.7	7/2	A8
9	22/10/2017	0509–6402	05 09 16.1	–64 02 11.3	556 × 350	106.9	50	0.7	—	A9
10	23/10/2017	0517–6757	05 17 51.1	–67 57 46.0	170 × 150	38.7	130	0.7	17/0	A11
11	not obs.	0522–6740	05 22 32.4	–67 40 56.0	360 × 270	75.6	90	1.0	7/1	A12
12	not obs.	0528–7017	05 28 46.0	–70 17 56.8	416 × 380	96.4	140	0.9	13/4	A13
13	not obs.	0529–7004	05 29 05.9	–70 04 40.6	216 × 174	47.0	0	1.0	12/0	A14
14	not obs.	0538–7004	05 38 47.2	–70 04 15.8	80 × 80	19.4	0	0.8	2/0	A15
15	23/10/2017	0541–6659	05 41 51.5	–66 59 02.8	300 × 272	69.2	0	0.5	18/2	A16
16	23/10/2017	0542–7104	05 42 37.9	–71 04 13.6	300 × 210	60.8	0	0.7	1/0	A18
17	07/09/2019	0548–6941	05 48 49.1	–69 41 18.3	156 × 95	29.5	150	0.6	4/0	A19
18	not obs.	0549–6618	05 49 30.1	–66 18 15.9	270 × 180	53.4	45	1.0	0/0	A20
19	23/10/2017	0549–6633	05 49 14.5	–66 33 43.1	540 × 390	111.2	170	1.4	0/0	A21

Table 2. The relative fluxes and most important line ratios (in the red arm) of observed emission lines for 12 LMC objects. To extract spectra from WiFeS cube we used apertures between 5 and 10 arcsec. LDL (Column 15) stands for “low density limit”. Also, J0548–6941 is the only source with physical (calibrated) flux values for which the spectroscopic standard star LTT1020 was used. All other objects are with relative flux (counts). All fluxes for J0548–6941 in units of erg cm^{−2} s^{−1} Å^{−1}. Errors in flux estimates for blue end of the spectra are in order of 17–19 per cent, and for red arm observations 23–25 per cent what can be expected for lower signal-to-noise for the higher resolution spectra, while dispersion errors are as in [Dopita et al. \(2007\)](#); [Dopita et al. \(2010a\)](#); [Childress et al. \(2014\)](#). [N II] and [S II] used in Columns 13 and 14 for the ratios relative to H α are the sum of the doublet lines. The [S II]_{6548Å} line flux is derived from that of the 6563Å line (see Sect. 2.2).

Object Name	H δ 4101Å	H γ 4342Å	H β 4861Å	[Fe II] 4890Å	[O III] 5007Å	[O I] 6300Å	H α 6563Å	[N II] 6583Å	[S II] 6716Å	[S II] 6731Å	[S II]/[S II] 6716Å/6731Å	[N II]/H α	[S II]/H α	Elect. den. (cm ^{−3})
(1)	(2)	(3)	(4)	(5)	(6)	(7)	(8)	(9)	(10)	(11)	(12)	(13)	(14)	(15)
J0444–6758			83		1085		1103	277	446	286	1.5	0.33	0.67	LDL
J0450–6818						302	1101	212	523	364	1.4	0.26	0.80	26.5
J0455–6830			100		580		1824	624	1192	838	1.4	0.46	1.10	26.5
J0500–6512							1111	152	540	359	1.5	0.18	0.81	LDL
J0502–6739		588	1563			180	5196	536	1692	1180	1.4	0.14	0.55	26.5
J0508–6928	631	1270	4260			533	22952	5073	9906	6628	1.5	0.29	0.72	LDL
J0509–6402						280	1107	224	461	373	1.2	0.27	0.75	29.8
J0517–6757		82	1420		2078	488	6284	1531	2447	1871	1.3	0.32	0.69	26.5
J0541–6659	1281	3805	12957		5944		19692	3045	5672	4120	1.4	0.21	0.50	26.5
J0542–7104			30		101	331	3688	113	1835	1198	1.5	0.04	0.82	LDL
J0548–6941	2.5×10 ^{−16}		1.1×10 ^{−15}	3.1×10 ^{−16}	1.5×10 ^{−15}		1.3×10 ^{−15}	2.5×10 ^{−16}	3.7×10 ^{−16}	2.4×10 ^{−16}	1.5	0.26	0.47	LDL
J0549–6633						731	1989	400	1618	1129	1.4	0.27	1.38	26.5

also rejected as none of our sources can be found in the recent comprehensive survey of WR stars in LMC ([Neugent et al. 2018](#)).

[Lasker \(1977\)](#) demonstrated that some LMC shell nebulae would have [S II] (6716, 6731Å) strengths of the same order as H α as well as expansion velocities of ~ 30 km s^{−1}. He argued that the ionisation is radiative and that the additional heating required to explain the strong [S II] is furnished by shocks. In summary, it is challenging to determine whether these shocks are driven by SN blasts or by stellar winds. A number of examples can be seen across the LMC in objects such as N 185, N 186 and N 70 ([Oey et al. 2002](#); [De Horta et al. 2014](#)). However, some of the objects (for example N 9; [Bozzetto et al. 2017](#)) from the [Lasker \(1977\)](#) sample were later

confirmed as a true SNRs. Essentially, if any of these large shells are driven by stellar winds, one would expect to find some massive (OB) stars in the vicinity of these objects to create those stellar winds. This would be a most straightforward way to distinguish one from the other.

Similar to SNRs and WR star nebula, (super)bubbles also show shell structure as well as shocked radiative spectra. But in most cases, inside the shell, the material is far less dense (particularly seen in H α light) and propelled by the fast stellar winds because of the loss of energy from a massive star (see [Chu 2008](#)). (Super)bubbles are also usually associated with a massive stellar population. MCELS images of the whole sample (except MCSNR J0542–7104; see later

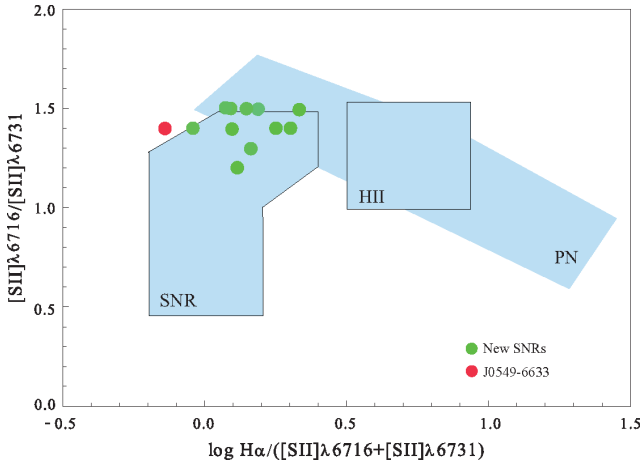


Figure 2. Ratio of $[S\text{ II}]\lambda 6716$ and $[S\text{ II}]\lambda 6731$ lines versus $\log H\alpha/([S\text{ II}]\lambda 6716+[S\text{ II}]\lambda 6731)$ for the sample of our 12 spectroscopically observed LMC objects presented in this paper. 11 objects from Table 2 fit in the designated area of SNRs while the object marked as a red dot (J0549–6633; Section A19) is slightly out. Noticeably, all these objects occupy the area suggested for older remnants as predicted by Sabbadin et al. (1977).

discussion) do not show any obvious dense material inside the shells. Thus, for our sample of objects, a classification as a (super)bubble is somewhat unlikely. One, though, should always consider a possible confusion with other nearby objects such as H II regions (Bojčić et al. 2007).

As radio-continuum objects, SNRs are well known by their non thermal emission seen at different radio frequencies. Our search for radio emission from the new optically selected sample of SNR candidates failed to detect any such emission. We searched all present-day radio surveys including the latest and most sensitive Australian Square Kilometre Array Pathfinder (ASKAP) survey of the LMC at 888 MHz (Filipović et al., in prep). Existing X-ray surveys of the LMC such as from the *Röntgen SATellite (ROSAT)* (Filipović et al. 1998a) and *XMM-Newton* (Maggi et al. 2016), with their noticeably limited area coverage compared to radio and optical data, likewise did not show any signs of SNR-like emission except for MCSNR J0542–7104 ([HP99] 1235; Section A16) as reported in Kavanagh et al. (2020; in prep.), J0454–7003 (Section A3), J0529–7004 ([HP] 1077; Section A13) and MCSR J0522–6740 (Section A11).

We did not find any infrared emission from any object in our sample (Lakićević et al. 2015, also see;). SNRs are often connected with infrared emission from the time of a SN explosion where it is suggested that the dust grains are formed within the expanding and cooling ejecta (see more details in Williams & Temim 2017; Lakićević et al. 2015). During the later SNR phase, the source of infrared emission is shock-heated dust. Usually younger SNRs emit in mid-infrared wavelengths even though some recent observations of the Small Magellanic Cloud (SMC) remnant and Pulsar Wind Nebulae (PWN) DEMSS suggest otherwise (Alsaberi et al. 2019b). In older SNRs, which is the most likely case for our sample studied here, the dominant radiation is optical (see our spectra) and UV radiation where cooled gas in a post-shock environment with low radiative shock speed (about 100 km s^{-1}) is observed. This cooler emission is in the far infrared and could explain why we saw no infrared emission in our sample of evolved remnants.

From these 19 SNR candidates, MCSNR J0522–6740, MCSNR J0541–6659 and MCSNR J0542–7104 are confirmed SNRs

(Appendix A11, A15 and A16). The remaining 16 objects studied here are all excellent new SNR candidates.

4 DISCUSSION

We found that our new LMC SNRs and SNR candidates are larger in comparison to other confirmed LMC SNRs (see Table 1) but only after excluding three smaller size objects: J0444–6758, J0455–6830 and J0538–7004. Those three were most likely previously undetected SNRs due to the confusion with larger H II regions.

To calculate the physical diameter distribution for these 16 SNRs and SNR candidates the kernel smoothing procedure described in Maggi et al. (2019) is applied (Figure 3). For comparison, the same procedure is also applied to the sample of 59 SNRs from Bozzetto et al. (2017, Fig. 8). It is evident that the sample diameters from this work have values almost two times larger (with correspondingly higher uncertainties) for the stated distribution parameters, while the smoothing bandwidth differs by about 15 per cent. We find that the average size of the 16 SNRs and SNR candidates to be 71 ± 14 pc ($SD=27$). Bozzetto et al. (2017) found that the LMC SNR population exhibits a mean diameter of 39 ± 4 pc for the earlier confirmed 59 LMC SNR. Our discovery of these 16 large LMC SNR candidates nicely agree with the Bozzetto et al. (2017) prediction that the present sample with sizes $D>40$ pc is incomplete, leaving room for a future detection of mainly large (and older) LMC SNRs (such as these 16). We also note that our new SNR size distribution is much closer to the SMC sample (Maggi et al. 2019) which is smaller in number but noticeably more complete. The sample from this work shows indications of the secondary distribution peak at ≈ 45 pc, which corresponds to the peak of the distribution for the sample from Bozzetto et al. (2017).

As mentioned earlier, Fesen et al. (2020) found a large, new optically visible but radio and X-ray faint Galactic SNR – G107.0+9.0 with an estimated size of $\sim 75 - 100$ pc, an advanced age of $\sim 100\,000$ yrs and well above the Galactic plane (250–300 pc). However, most of its large shell is not as high in $[S\text{ II}]/H\alpha$ ratio as the objects studied here. Still, one selected location where Fesen et al. (2020) obtained a spectrum does contain an elevated ratio, apparently from a relatively slow but radiative shock in an isolated emission knot. This provokes an interesting question: what would G107.0+9.0 look like if it were at the distance of the LMC? To start with, if it is anywhere close to the 30 Doradus region it would most likely be indistinguishable from the local environment which is crowded with bright H II region filaments. Or at best, we would see something similar to J0528–7017 which we study here. But, if G107.0+9.0 is positioned well outside the LMC we would most likely see it to be similar to our J0450–6818, J0500–6512, J0506–6509, J0508–6928, J0522–6740, MCSNR J0542–7104 or J0549–6618.

As in Bozzetto et al. (2017), we investigate the spatial distribution and local environment of these 19 new LMC SNRs and SNR candidates in relation to the H I peak temperature map from Kim et al. (1998). Most of these new SNR candidates (15 out of 19) are positioned near or around the edges of the LMC’s main body, in obviously less dense regions.

As argued by Long et al. (2018), the majority of the objects with high $[S\text{ II}]/H\alpha$ line ratios (>0.4) are indeed SNRs, but the distinction between H II regions and SNRs becomes far less obvious at low surface brightness, and additional criteria, such as X-ray or radio continuum detection, are needed. We also note that these outer regions of the LMC lack good X-ray coverage, and there-

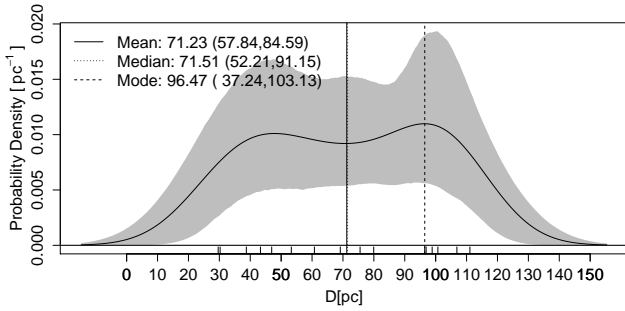


Figure 3. Smoothed diameter distribution for the samples of 16 selected and here studied LMC SNRs. The smoothing procedure and 95 per cent bootstrap confidence intervals are calculated as described in Maggi et al. (2019). The grey lines present a 95 per cent confidence interval around the smoothed distribution. The obtained value for the

smoothing bandwidth h is also designated on the plot.

fore confirmation of the true nature of these objects cannot yet be made. The recent *XMM-Newton* detection of MCSNR J0542–7104 (Kavanagh et al. 2020; in prep) and MCSNR J0522–6740 which is classified here, show that the SNR candidacy of our selected object sample is solid. Further, we report here the detection of diffuse soft X-ray emission from three of our objects with *XMM-Newton* (J0454–7003, MCSNR J0522–6740 and J0529–7004). We note that in all three cases the X-ray emission is more centrally peaked. However, the short exposures and large off-axis angles of the observations do not allow a more detailed analysis of their faint X-ray emission. Despite the lack of deeper coverage we manage to classify one of these three sources (MCSNR J0522–6740; see Appendix A11) as a new bona-fide SNR.

As discussed by Lopez & Fesen (2018), the environment and the surrounding medium influences SNR morphology. More specifically, the progenitors of Core Collapse (CC) SNe have short main-sequence lives (3 – 50 Myr) and their explosions are expected to occur within or near the dense media from which the massive stars formed. The mean H I column density in the direction of the 59 confirmed and 15 candidate remnants, from Bozzetto et al. (2017), was estimated to be $\sim 2 \times 10^{21}$ atoms cm^{-2} (with a $\text{SD}=1 \times 10^{21}$ atoms cm^{-2}). Our sub-sample of 15 new SNR objects (excluding three smaller SNR candidates and bona-fide SNR MCSNR J0541–6659 as they are possibly embedded in H II regions) show a marginally lower environmental density of $\sim 1.8 \times 10^{21}$ atoms cm^{-2} ($\text{SD}=1.3 \times 10^{21}$ atoms cm^{-2}). Therefore, we find no significant difference in the H I environment in which our new sub-sample of the LMC SNR candidates resides and evolves.

Maggi et al. (2016) argue that the relatively large population of the LMC SNRs could be a product of type Ia SNe, as we also argued for the distant candidate J0509–6402 studied here and new bona-fide SNR MCSNR J0542–7104, although it should be considered with caution. We emphasise that the H I environment around SNR candidates studied here is not vastly different from the previously established LMC SNRs sample as shown above. But the low number of massive (OB) stars within the boundaries of the SNR candidates may favour an SN type Ia origin. However, this should be taken only as indirect evidence.

The larger physical size of our SNR candidates sample could indicate their possibly older age and more evolved phase as also observed for a number of Galactic SNRs by Stupar et al. (2008),

Fesen et al. (2019) and recently Fesen et al. (2020). However, one should be very careful comparing our results from the MCs sample with MW SNRs because close to the Galactic plane the absorption is sufficient to absorb most X-ray emission for any but the young SNRs (emitting above 1 or 2 keV). When comparing with other waveband surveys such as X-ray *Chandra* or *XMM-Newton* and ASKAP/Australia Telescope Compact Array (ATCA) radio images, we find that these new LMC SNR candidates are seen almost exclusively in the optical wavelengths. However, the exception are three confirmed SNRs (MCSNR J0522–6740, MCSNR J0541–6659 and MCSNR J0542–7104) as well as two candidates (J0454–7003 and J0529–7004) which can be detected in the X-ray surveys. This could potentially imply that we are discovering a previously unknown class of large and predominantly optically visible LMC SNRs. We suggest that these SNRs are mainly residing in a very rarefied environment and are likely relatively old (>20 kyr). This would make them less visible to the present generation of radio and X-ray telescopes.

Evidently, larger (and older) remnants seen mostly in optical wavebands are radio and X-ray quiet since they are in the last dissipation phase and they almost blend with the ISM. Their emission in those domains are likely to cease because of radiative cooling and the decrease of their strong magnetic fields to the level of the galactic background. SNR non-thermal emission ends because of this dissipation and therefore is not detectable (Stupar et al. 2008).

SNRs in free expansion and Sedov phases of evolution (defined by the non-radiative shocks) can not be easily detected by the $[\text{S II}]/\text{H}\alpha$ method. In these phases, $[\text{S II}]$ emission of SNR is at best small because they are usually mixed within the local ISM (or H II regions). Even for the nearby galaxies such as the LMC, this causes a selection effect that adversely affects the detection of objects such as SNRs. In the early phases of their evolution, SNRs are mainly detected by radio and X-ray observations and (for SN type Ia) in optical bands only by Balmer lines (Lin et al. 2020). H II regions are also detected by Balmer lines and therefore to rely only on optical detection will not be sufficient especially for SNRs in the free expansion and Sedov phases. In the radiative phases of evolution, SNRs are usually not easily detected in radio and X-rays if they are distant and evolve in a low density environment. In general, this is one of the major detection challenges for distant extragalactic SNR samples where the instrumental sensitivity selection effects dominates the construction of a complete SNR sample.

We follow (and update) the Bozzetto et al. (2017) comparison of multi-frequency emission from known SNRs (60; including one from Maitra et al. (2019)) and SNR candidates (32 including 18 from this work and 14 from Bozzetto et al. (2017) as Maitra et al. (2019) confirmed MCSNR J0513–6731) in the LMC. Also, we plot a Venn diagram (Figure 4) that summarises the number of SNRs (and candidates) exhibiting emission in different electromagnetic domains. We emphasise that the lack of detected emission does not always mean that the remnant does not emit such radiation. Alternatively, it may indicate that the emission is below the sensitivity level of current surveys. Importantly, there are examples of SNRs such as the SMC SNR HFPK 334 (Crawford et al. 2014b; Joseph et al. 2019; Maggi et al. 2019), SMC IKT 23, MCSNR J0528–6713 (Crawford et al. 2010) or the Galactic Vela Jr SNR (Filipović et al. 2001; Stupar et al. 2005; Fukui et al. 2017; Maxted et al. 2018) that could not be identified in optical frequencies despite extensive searches.

Various optical, radio and X-ray SNR detection methodologies have biases as can be seen in our Venn diagrams (Figure 4 and (Bozzetto et al. 2017)). If there are no biases one would expect that all SNRs from one sample would converge to common intersection

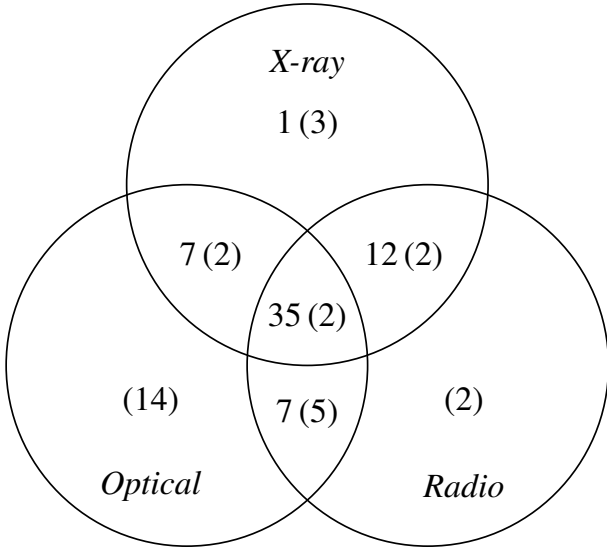


Figure 4. A Venn diagram showing 62 confirmed LMC SNRs (including three from this work). We also show (in brackets) the previously known 14 SNR candidates from [Bozzetto et al. \(2017\)](#) and the here proposed 16 new SNR candidates in different electromagnetic domains.

of all three circles of the Venn diagrams, with zero SNRs in different observational wavebands.

5 CONCLUSIONS

We study previously selected MCSNR J0541–6659 and confirm its optical SNR signature. We also classify previously unknown MCSNR J0522–6740 and MCSNR J0542–7104 as new LMC SNRs. Finally, 16 other objects studied here for the first time are good SNR candidates that require further studies to confirm their real nature.

In total, this work adds two new bona-fide SNRs to the list of 60 previously confirmed SNRs and 16 new SNR candidates to the list of 14 previously known in the LMC as per [Bozzetto et al. \(2017\)](#) and [Maggi et al. \(2019\)](#), respectively. We believe the reason as to why these SNR candidates were not detected previously is due to the fact they are mainly positioned in the outer field of the LMC where they can only be detected because of the high sensitivity of MCELS. This could mean we are looking at an unknown (but predicted) class of large and only (at this stage) optically visible SNRs. The 16 new SNRs and SNR candidates studied here have an average size of 71 pc which is almost a factor of 2 larger (71 pc vs. 39 pc) than those in [Bozzetto et al. \(2017\)](#). We suggest that this sample is older and perhaps in the last evolutionary phase of their lives.

J0509–6402 is a prime candidate of type Ia SNR situated 2° north of the LMC, in a field where low surface brightness stellar population from the LMC extend much further than the main (gaseous) body ([Mackey et al. 2018](#)). Two other candidates (J0454–7003 and J0529–7004) were found that exhibit X-ray emission but only further studies can confirm their real nature.

ACKNOWLEDGEMENTS

The MCELS was funded through the support of the Dean B. McLaughlin fund at the University of Michigan and through NSF grant 9540747. M.S. acknowledges support by the Deutsche

Forschungsgemeinschaft through the Heisenberg professor grants SA 2131/5-1 and 12-1. We thank You-Hua Chu for her comments and suggestions. B.V. was funded by the Ministry of Education, Science and Technological Development of the Republic of Serbia through the contract number 451-03-68/2020-14/200002. Lastly, we thank the referee for their very constructive and insightful comments and suggestions.

DATA AVAILABILITY

The data underlying this article will be shared on reasonable request to the corresponding author.

REFERENCES

- Acker A., Köppen J., Samland M., Stenholm B., 1989, *The Messenger*, **58**, 44
- Alsaberi R. Z. E., et al., 2019a, *Ap&SS*, **364**, 204
- Alsaberi R. Z. E., et al., 2019b, *MNRAS*, **486**, 2507
- Blair W. P., Long K. S., 1997, *ApJS*, **108**, 261
- Blair W. P., Kirshner R. P., Chevalier R. A., 1981, *ApJ*, **247**, 879
- Blair W. P., Kirshner R. P., Chevalier R. A., 1982, *ApJ*, **254**, 50
- Bojičić I. S., Filipović M. D., Parker Q. A., Payne J. L., Jones P. A., Reid W., Kawamura A., Fukui Y., 2007, *MNRAS*, **378**, 1237
- Borkowski K. J., Hendrick S. P., Reynolds S. P., 2006, *ApJ*, **652**, 1259
- Bozzetto L. M., Filipović M. D., 2014, *Ap&SS*, **351**, 207
- Bozzetto L., Filipović M., Crawford E., Bojičić I., Payne J., Mendik A., Wardlaw B., De Horta A., 2010, *Serbian Astronomical Journal*, pp 43–49
- Bozzetto L. M., Filipović M. D., Crawford E. J., Payne J. L., de Horta A. Y., Stupar M., 2012a, *Rev. Mex. Astron. Astrofis.*, **48**, 41
- Bozzetto L. M., Filipović M. D., Crawford E. J., De Horta A. Y., Stupar M., 2012b, *Serbian Astronomical Journal*, **184**, 69
- Bozzetto L. M., Filipović M. D., Urošević D., Crawford E. J., 2012c, *Serbian Astronomical Journal*, **185**, 25
- Bozzetto L. M., et al., 2012d, *MNRAS*, **420**, 2588
- Bozzetto L. M., et al., 2013, *MNRAS*, **432**, 2177
- Bozzetto L. M., et al., 2014a, *MNRAS*, **439**, 1110
- Bozzetto L. M., Filipović M. D., Urošević D., Kothes R., Crawford E. J., 2014b, *MNRAS*, **440**, 3220
- Bozzetto L. M., Filipović M. D., Haberl F., Sasaki M., Kavanagh P., Maggi P., Urošević D., Sturm R., 2015, *Publication of Korean Astronomical Society*, **30**, 149
- Bozzetto L. M., et al., 2017, *The Astrophysical Journal Supplement Series*, **230**, 2
- Brantseg T., McEntaffer R. L., Bozzetto L. M., Filipović M., Grieves N., 2014, *ApJ*, **780**, 50
- Cajko K. O., Crawford E. J., Filipović M. D., 2009, *Serbian Astronomical Journal*, **179**, 55
- Chevalier R. A., Kirshner R. P., Raymond J. C., 1980, *ApJ*, **235**, 186
- Childress M. J., Vogt P. A., Nielsen J., Sharp R. G., 2014, *Ap&SS*, **349**, 617
- Chu Y. H., 2008, *IAU Symposium*, **250**, 341
- Cowan J. J., Branch D., 1985, *ApJ*, **293**, 400
- Crawford E. J., Filipović M. D., de Horta A. Y., Stootman F. H., Payne J. L., 2008, *Serbian Astronomical Journal*, **177**, 61
- Crawford E. J., Filipović M. D., Haberl F., Pietsch W., Payne J. L., de Horta A. Y., 2010, *A&A*, **518**, A35
- Crawford E. J., Filipović M. D., McEntaffer R. L., Brantseg T., Heitritter K., Roper Q., Haberl F., Urošević D., 2014a, *The Astronomical Journal*, **148**, 99
- Crawford E. J., Filipović M. D., McEntaffer R. L., Brantseg T., Heitritter K., Roper Q., Haberl F., Urošević D., 2014b, *AJ*, **148**, 99
- De Horta A. Y., et al., 2014, *AJ*, **147**, 162
- Dodorico S., Dopita M. A., Benvenuti P., 1980, *Astronomy and Astrophysics Supplement Series*, **40**, 67

- Dopita M. A., 1979, *Australian Journal of Physics*, **32**, 123
- Dopita M., Hart J., McGregor P., Oates P., Bloxham G., Jones D., 2007, *Astrophysics and Space Science*, **310**, 255
- Dopita M., et al., 2010a, *Ap&SS*, **327**, 245
- Dopita M. A., et al., 2010b, *ApJ*, **710**, 964
- Dopita M. A., Vogt F. P. A., Sutherland R. S., Seitzzahl I. R., Ruiter A. J., Ghavamian P., 2018, *ApJS*, **237**, 10
- Dopita M. A., Seitzzahl I. R., Sutherland R. S., Nicholls D. C., Vogt F. P. A., Ghavamian P., Ruiter A. J., 2019, *AJ*, **157**, 50
- Fesen R. A., 1984, *ApJ*, **281**, 658
- Fesen R. A., Neustadt J. M. M., How T. G., Black C. S., 2019, *MNRAS*, **486**, 4701
- Fesen R. A., et al., 2020, *MNRAS*,
- Filipovic M. D., et al., 1998a, *A&AS*, **127**, 119
- Filipovic M. D., Haynes R. F., White G. L., Jones P. A., 1998b, *A&AS*, **130**, 421
- Filipović M. D., Jones P. A., Aschenbach B., 2001, in Holt S. S., Hwang U., eds, *American Institute of Physics Conference Series Vol. 565, Young Supernova Remnants*. pp 267–270, doi:10.1063/1.1377103
- Frew D. J., Parker Q. A., 2010, *Publ. Astron. Soc. Australia*, **27**, 129
- Fukui Y., et al., 2017, *The Astrophysical Journal*, **850**, 71
- Galvin T. J., Filipovic M. D., 2014, *Serbian Astronomical Journal*, **189**, 15
- Ghavamian P., Seitzzahl I. R., Vogt F. P. A., Dopita M. A., Terry J. P., Williams B. J., Winkler P. F., 2017, *ApJ*, **847**, 122
- Goss W. M., Ekers R. D., Danziger I. J., Israel F. P., 1980, *MNRAS*, **193**, 901
- Grondin M.-H., et al., 2012, *A&A*, **539**, A15
- Haberl F., Pietsch W., 1999, *A&AS*, **139**, 277
- Haberl F., et al., 2012, *A&A*, **545**, A128
- Hamuy M., Walker A. R., Suntzeff N. B., Gigoux P., Heathcote S. R., Phillips M. M., 1992, *PASP*, **104**, 533
- Hamuy M., Suntzeff N. B., Heathcote S. R., Walker A. R., Gigoux P., Phillips M. M., 1994, *PASP*, **106**, 566
- Haynes P. H., McIntyre M. E., Shepherd T. G., Marks C. J., Shine K. P., 1991, *Journal of the Atmospheric Sciences*, **48**, 651
- Henize K. G., 1956, *ApJS*, **2**, 315
- Hillebrandt W., Kromer M., Röpke F. K., Ruiter A. J., 2013, *Frontiers of Physics*, **8**, 116
- Jansen F., et al., 2001, *A&A*, **365**, L1
- Joseph T. D., et al., 2019, *MNRAS*, **490**, 1202
- Kavanagh P. J., et al., 2013, *A&A*, **549**, A99
- Kavanagh P. J., Sasaki M., Bozzetto L. M., Filipović M. D., Points S. D., Maggi P., Haberl F., 2015a, *A&A*, **573**, A73
- Kavanagh P. J., Sasaki M., Whelan E. T., Maggi P., Haberl F., Bozzetto L. M., Filipović M. D., Crawford E. J., 2015b, *A&A*, **579**, A63
- Kavanagh P. J., Sasaki M., Bozzetto L. M., Points S. D., Filipović M. D., Maggi P., Haberl F., Crawford E. J., 2015c, *A&A*, **583**, A121
- Kavanagh P. J., et al., 2016, *A&A*, **586**, A4
- Kim S., Staveley-Smith L., Dopita M. A., Freeman K. C., Sault R. J., Kesteven M. J., McConnell D., 1998, *ApJ*, **503**, 674
- Kim S., Staveley-Smith L., Dopita M. A., Sault R. J., Freeman K. C., Lee Y., Chu Y.-H., 2003, *ApJS*, **148**, 473
- Lakićević M., et al., 2015, *ApJ*, **799**, 50
- Lasker B. M., 1977, *ApJ*, **212**, 390
- Leahy D. A., 2017, *ApJ*, **837**, 36
- Leahy D., Wang Y., Lawton B., Ranasinghe S., Filipović M., 2019, *AJ*, **158**, 149
- Lee J. H., Lee M. G., 2014, *The Astrophysical Journal*, **793**, 134
- Lin C. D.-J., Chu Y.-H., Ou P.-S., Li C.-J., 2020, *The Astrophysical Journal*, **900**, 149
- Long K. S., Dodorico S., Charles P. A., Dopita M. A., 1981, *ApJ*, **246**, L61
- Long K. S., Blair W. P., Kirshner R. P., Winkler P. F., 1990, *ApJS*, **72**, 61
- Long K. S., et al., 2010, *ApJS*, **187**, 495
- Long K. S., Blair W. P., Milisavljevic D., Raymond J. C., Winkler P. F., 2018, *ApJ*, **855**, 140
- Lopez L. A., Fesen R. A., 2018, *Space Sci. Rev.*, **214**, 44
- Lopez L. A., Ramirez-Ruiz E., Huppenkothen D., Badenes C., Pooley D. A., 2011, *ApJ*, **732**, 114
- Mackey D., Koposov S., Da Costa G., Belokurov V., Erkal D., Kuzma P., 2018, *ApJ*, **858**, L21
- Maggi P., et al., 2014, *A&A*, **561**, A76
- Maggi P., et al., 2016, *A&A*, **585**, A162
- Maggi P., et al., 2019, *A&A*, **631**, A127
- Maitra C., et al., 2019, *MNRAS*, **490**, 5494
- Mathewson D. S., Clarke J. N., 1973, *ApJ*, **180**, 725
- Mathewson D. S., Healey J. R., 1964, *Symposium - International Astronomical Union*, **20**, 245
- Matonick D. M., Fesen R. A., 1997, *The Astrophysical Journal Supplement Series*, **112**, 49
- Matonick D. M., Fesen R. A., Blair W. P., Long K. S., 1997, *ApJS*, **113**, 333
- Maxted N. I., et al., 2018, *ApJ*, **866**, 76
- Millar W. C., White G. L., Filipovic M. D., 2012, *Serbian Astronomical Journal*, **184**, 19
- Neugent K. F., Massey P., Morrell N., 2018, *ApJ*, **863**, 181
- Oey M. S., 1996, *ApJ*, **465**, 231
- Oey M. S., Groves B., Staveley-Smith L., Smith R. C., 2002, *AJ*, **123**, 255
- Pennock C. M., van Loon J. T., Bell C., Filipović M., Joseph T., Vardoulaki E., 2020, arXiv e-prints, p. arXiv:2004.04531
- Points S. D., Long K. S., Winkler P. F., Blair W. P., 2019, *ApJ*, **887**, 66
- Reid W. A., Parker Q. A., 2010, *MNRAS*, **405**, 1349
- Reid W. A., Stupar M., Bozzetto L. M., Parker Q. A., Filipović M. D., 2015, *MNRAS*, **454**, 991
- Russell S. C., Dopita M. A., 1990, *ApJS*, **74**, 93
- Sabbadin F., Minello S., Bianchini A., 1977, *A&A*, **60**, 147
- Sano H., et al., 2018, *ApJ*, **867**, 7
- Sano H., et al., 2019a, *ApJ*, **873**, 40
- Sano H., et al., 2019b, *ApJ*, **881**, 85
- Sano H., et al., 2020, arXiv e-prints, p. arXiv:2007.07900
- Sasaki M., 2020, *Astronomische Nachrichten*, **341**, 156
- Sasaki M., et al., 2018, *A&A*, **620**, A28
- Schaerer D., Meynet G., Maeder A., Schaller G., 1993, *A&AS*, **98**, 523
- Seitzzahl I. R., Vogt F. P. A., Terry J. P., Ghavamian P., Dopita M. A., Ruiter A. J., Sukhbold T., 2018, *ApJ*, **853**, L32
- Seitzzahl I. R., Ghavamian P., Laming J. M., Vogt F. P. A., 2019, *Phys. Rev. Lett.*, **123**, 041101
- Skrutskie M. F., et al., 2006, *AJ*, **131**, 1163
- Smith R. C., MCELS Team 1999, in Chu Y. H., Suntzeff N., Hesser J., Bohlender D., eds, *IAU Symposium Vol. 190, New Views of the Magellanic Clouds*. p. 28
- Smith R. C., Kirshner R. P., Blair W. P., Winkler P. F., 1991, *ApJ*, **375**, 652
- Smith R. C., Kirshner R. P., Blair W. P., Long K. S., Winkler P. F., 1993, *ApJ*, **407**, 564
- Strüder L., et al., 2001, *A&A*, **365**, L18
- Stupar M., Filipović M. D., Jones P. A., Parker Q. A., 2005, *Advances in Space Research*, **35**, 1047
- Stupar M., Parker Q. A., Filipović M. D., 2008, *MNRAS*, **390**, 1037
- Stupar M., Parker Q. A., Frew D. J., 2018, *MNRAS*, **479**, 4432
- Sturm R., et al., 2013, *A&A*, **558**, A3
- Subramanian S., Subramaniam A., 2010, *A&A*, **520**, A24
- Turner M. J. L., et al., 2001, *A&A*, **365**, L27
- Vogt F., Dopita M. A., 2011, *Ap&SS*, **331**, 521
- Vogt F. P. A., Bartlett E. S., Seitzzahl I. R., Dopita M. A., Ghavamian P., Ruiter A. J., Terry J. P., 2018, *Nature Astronomy*, **2**, 465
- Vučetić M. M., Trčka A., Arbutina B., Čiprijanović A., Pavlović M. Z., Urošević D., Petrov N., 2018, *Astronomical and Astrophysical Transactions*, **30**, 379
- Vučetić M. M., Onić D., Petrov N., Čiprijanović A., Pavlović M. Z., 2019a, *Serbian Astronomical Journal*, **198**, 13
- Vučetić M. M., et al., 2019b, *A&A*, **628**, A87
- Warth G., Sasaki M., Kavanagh P. J., Filipović M. D., Points S. D., Bozzetto L. M., 2014, *A&A*, **567**, A136
- Westerlund B. E., Mathewson D. S., 1966, *MNRAS*, **131**, 371
- Williams B. J., Temim T., 2017, in *Handbook of Supernovae*, Alsabti A., Murdin P. (eds), Springer, Cham. pp 2105–2124, doi:10.1007/978-3-319-21846-5_94
- Zaritsky D., Harris J., Thompson I. B., Grebel E. K., 2004, *AJ*, **128**, 1606

de Horta A. Y., et al., 2012, *A&A*, 540, A25
 di Benedetto G. P., 2008, *MNRAS*, 390, 1762

APPENDIX A: NOTES ON INDIVIDUAL OBJECTS

Below, we present notes on each individual source from this sample. These notes also include the number of OB stars found in the vicinity of each. As explained in Section 2.4, the significance of the number of OB stars is related to the possible classification of a SNR as a likely CC or a type Ia origin. This, together with the global (galactic) and local morphological properties, can indicate the potential of each of these individual objects to have a SN origin (Lopez et al. 2011).

A1 J0444–6758 (Figure A1)

This object’s $H\alpha$ image shows patchy semi-circular diffuse emission with $D=23.6$ pc assuming the distance to the LMC of 50 kpc. This remnant candidate, as can be seen in Figure A1, is faint and it has a $[S\ II]/H\alpha$ ratio of ~ 0.67 indicating it to be likely an SNR candidate. We searched the MCPS for the massive (OB) stars in and around this object’s 100 pc boundaries and found that only one such star can be found at the far North position from the SNR candidate.

A bit of a caution for the classification of this object as an SNR candidate since $[O\ III]$ lines are quite prominent while at the same time we note an absence of the $[O\ I]$ line. The MCELS $[O\ III]$ image also shows emission concentrated in the centre rather than in a shell. Unfortunately, this area is presently poorly covered in X-ray surveys and further study is needed.

A2 J0450–6818 (Figure A2)

The $H\alpha$ image for this object shows two distinctly disjointed filaments, giving a bilateral and elliptical shell morphology. The emission lines are strongest in these areas. The $[S\ II]/H\alpha$ ratio is ~ 0.8 and has an elliptical diameter of about 116×87 pc which satisfies one of the selection criteria for the larger diameter class of SNRs known as “evolved” (Mathewson & Clarke 1973). This remnant, as seen in Figure A2, was also detected in $[O\ I]$ which boosts the SNR confirmation as it gives evidence of shock heating. As for the J0444–6758 SNR candidate, the stellar content of this object’s area shows the presence of only one nearby massive OB star.

A3 J0454–7003 (Figure A3)

This circular object is positioned at the outer south-east boundary of the large superbubble DEML25 (Oey et al. 2002). With a diameter of 30 pc (Figure A3) and no optical spectra available for this object, we use MCELS images and estimate that the overall $[S\ II]/H\alpha$ ratio of >0.8 which warrants further investigation of this object as an SNR candidate. For the larger DEML25 shell, the $[O\ III]/H\alpha$ ratio is also higher in the interaction zone (ranging around 0.8), which together with the high $[S\ II]/H\alpha$ ratio suggest a ram pressure-induced shock. We note that there is also a possible filamentary shell (“blow-out”) from the much larger and brighter DEML25 shell. There are a number of nearby OB stars in projection to J0454–7003, and their stellar content was classified by Oey (1996).

Very weak and soft (<0.7 keV) X-ray emission is seen around the centre of the ellipse marking the optical emission (Figure A3 (right)). Clearly extended soft X-ray emission is detected from

the nearby DEML25 shell. Unfortunately, the exposure of ~ 3.8 ks (EPIC-pn) is too short for a more quantitative analysis of the X-ray emission from J0454–7003.

A4 J0455–6830 (Figure A4)

The MCELS $H\alpha$ image of this SNR candidate does not show an obvious shell morphology with diffuse and scattered emission across the suggested boundaries (Figure A4). This SNR candidate has the smallest diameter ($D_{av}=17$ pc) of our sample and the $[S\ II]/H\alpha$ ratio of ~ 1.1 is one of the sample’s highest.

As in J0450–6818, this SNR candidate also exhibits prominent (bright) $[O\ III]$ lines while at the same time we did not detect an $[O\ I]$ line. The MCELS $[O\ III]$ image also shows distinctive emission that, in this case, follows the $H\alpha$ and $[S\ II]$ emission. Finally, one would expect that such a small sized SNR would be bright in X-ray emission. Unfortunately, this area is presently poorly covered in all X-ray surveys.

We also searched MCPS for massive (OB) stars near this object (100 pc radius) and found 18 very distant OB stars – none within the boundaries of this proposed SNR candidate.

A5 J0500–6512 (Figure A5)

The $H\alpha$ image shows a looped filamentary structure (Figure A5). This SNR candidate has a complex (double-shell) morphology, with the shells overlapping in the South. We estimate that this is similar in size to the J0450–6818 candidate. The $[S\ II]/H\alpha$ ratio is ~ 0.81 , typical of SNRs. The limited variety of line intensities are not surprising as the weaker lines are lost in the noise.

A6 J0502–6739 (Figure A6)

This SNR candidate structure has an average diameter of 43 pc and shows diffuse structureless emission which is slightly elongated (Figure A6). Although the $[S\ II]/H\alpha$ ratio is relatively low at ~ 0.55 , we still take this as an SNR candidate but we note possible contamination from the nearby $H\ II$ region.

As for other objects in this sample, we searched for massive stars and found the richest population of OB stars (18 with 2 inside the object boundaries) among the sample studied here.

A7 J0506–6509 (Figure A7)

The candidacy for the SNR nature of this object is prompted by its spherical (circular) shell morphology with a diameter of 90 pc (Figure A7). While there are no spectra available for this candidate, we use MCELS images and estimate that the overall $[S\ II]/H\alpha$ ratio is ~ 0.6 , which warrants further investigation of this object as an SNR candidate. We note that no nearby massive stars could be found.

A8 J0508–6928 (Figure A8)

This SNR candidate has an obvious half-shell (horse-shoe) morphology in the top-half, expanding a little past half-way (Figure A8). The $[S\ II]/H\alpha$ ratio is ~ 0.72 . This remnant also has the highest peak in $H\alpha$ in our sample but given the strength of $H\beta$ in this object, we note the stunning lack of any $[O\ III]$ emission. We find 2 massive OB stars inside the object bounds, 3 just north and 2 relatively close on the Eastern side of this SNR candidate.

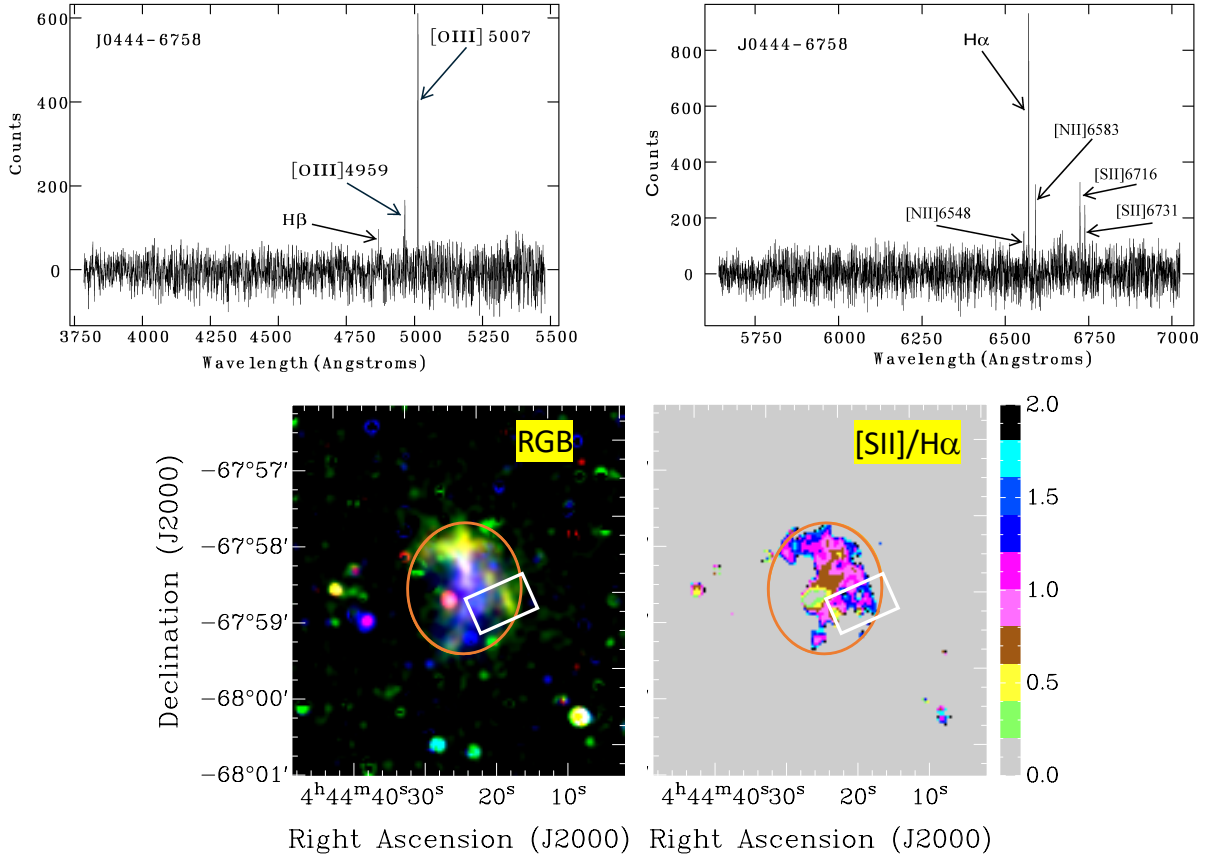


Figure A1. J0444–6758: (Top) showing the spectra from both arms (left; blue, right; red) of the spectrograph; (Bottom) colour images produced from MCELS data, where RGB corresponds to $H\alpha$, $[S\ II]$ and $[O\ III]$ while the ratio map is between $[S\ II]$ and $H\alpha$. The rectangular box (white) represents an approximate position of the WiFeS slicer. The orange ellipse indicates the extent of the optical emission seen from the object.

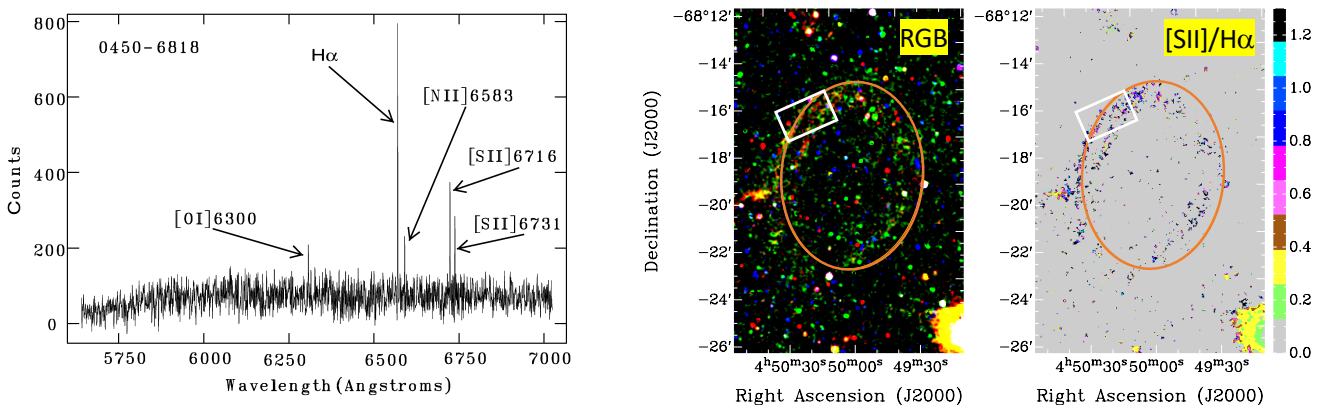


Figure A2. J0450–6818: (Left) showing the spectra from one arm (red) of the spectrograph; (Middle and right) colour images produced from MCELS data, where RGB corresponds to $H\alpha$, $[S\ II]$ and $[O\ III]$ while the ratio map is between $[S\ II]$ and $H\alpha$. The rectangular box (white) represents an approximate position of the WiFeS slicer. The orange ellipse indicates the extent of the optical emission seen from the object.

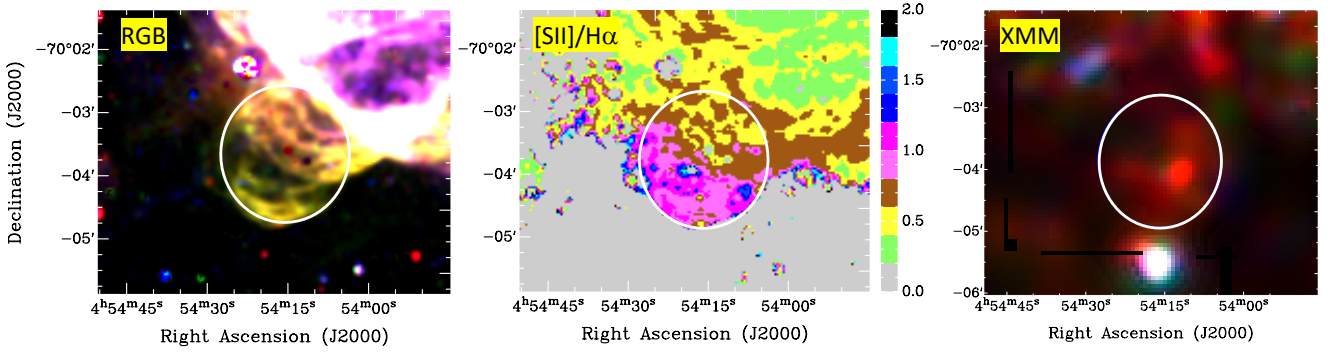


Figure A3. J0454–7003: colour images produced from MCELS data, where RGB corresponds to $H\alpha$, $[S\ II]$ and $[O\ III]$ (left) while the ratio map is between $[S\ II]$ and $H\alpha$ (middle). *XMM-Newton* EPIC RGB (R=0.3–0.7 keV band, G=0.7–1.1 keV band and B=1.1–4.2 keV band) image from the area of J0454–7003 is shown in the right panel. The white circle indicates the extent of the optical emission seen from the object. The line-shaped features in the left and bottom hand side of the image are smoothing artefacts, caused by borders of adjacent observations, which introduce steps in exposure.

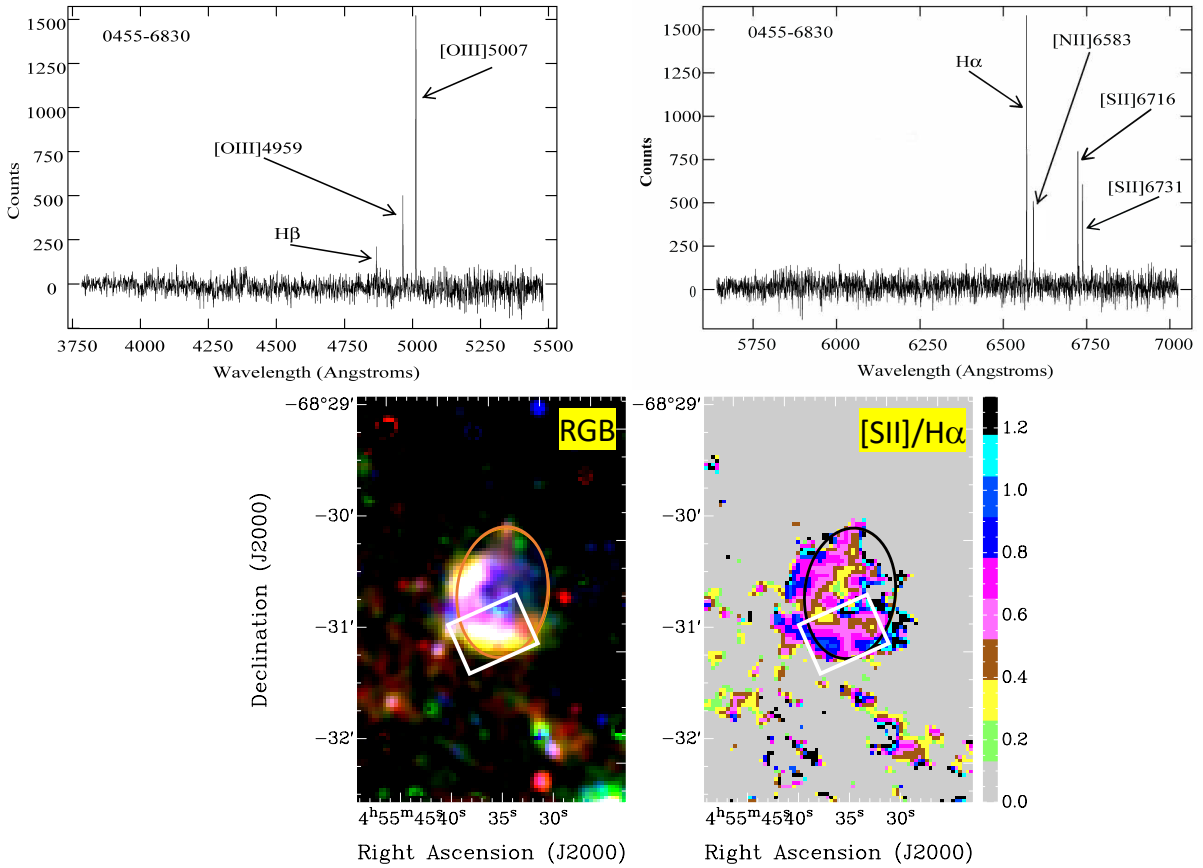


Figure A4. J0455–6830: (Top) showing the spectra from both arms (left; blue, right; red) of the spectrograph; (Bottom) colour images produced from MCELS data, where RGB corresponds to $H\alpha$, $[S\ II]$ and $[O\ III]$ while the ratio map is between $[S\ II]$ and $H\alpha$. The rectangular box (white) represents an approximate position of the WiFeS slicer. The orange/black ellipse indicates the extent of the optical emission seen from the object.

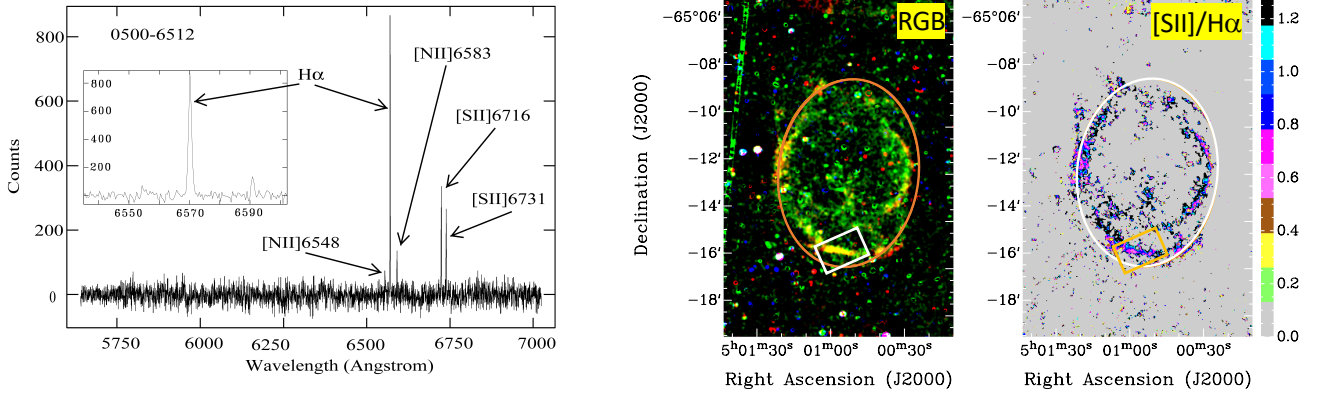


Figure A5. J0500–6512: (Left) showing the spectra from one arm (red) of the spectrograph where the inset figure represents the “zoomed-in” $H\alpha$ line. This $H\alpha$ line is detected with the broadening of 1.20 \AA while the instrument width is $\sim 1 \text{ \AA}$ ($\sim 45 \text{ km s}^{-1}$); (Middle and right) colour images produced from MCELS data, where RGB corresponds to $H\alpha$, $[S \text{ II}]$ and $[O \text{ III}]$ while the ratio map is between $[S \text{ II}]$ and $H\alpha$. The rectangular box (white/orange) represents an approximate position of the WiFeS slicer. The orange/white ellipse indicates the extent of the optical emission seen from the object.

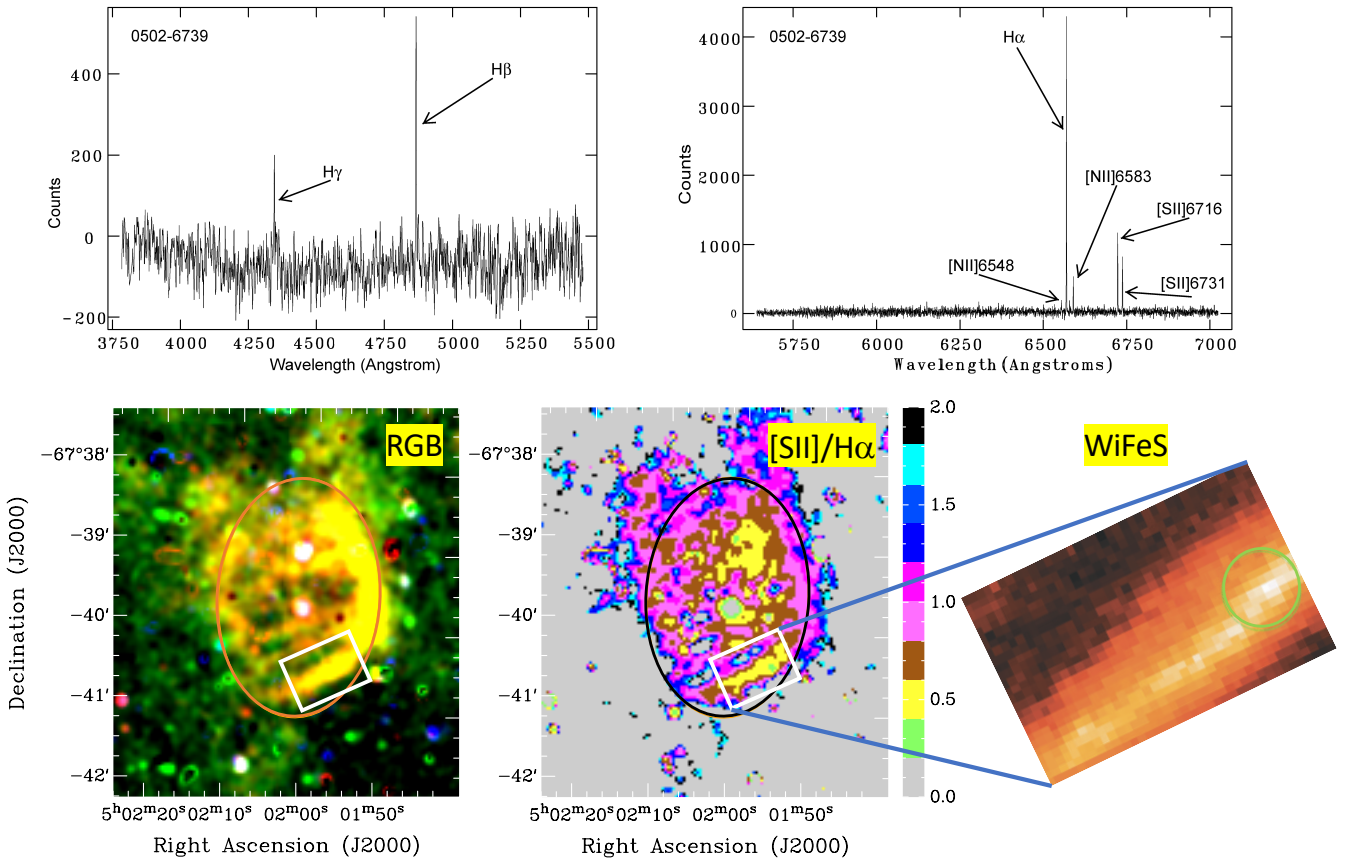


Figure A6. J0502–6739: (Top) showing the spectra from both arms (left; blue, right; red) of the spectrograph; (Bottom left and right) colour images produced from MCELS data, where RGB corresponds to $H\alpha$, $[S \text{ II}]$ and $[O \text{ III}]$ while the ratio map is between $[S \text{ II}]$ and $H\alpha$. The orange/black ellipse indicates the extent of the optical emission seen from the object. (bottom right) image of $25 \times 38 \text{ arcsec}$ (as in the white rectangular box) field of view of WiFeS spectrograph slicer which consists of 3152 slices (see Sect. 2.2). The strongest part of $H\alpha$ emission of J0502–6739 is detected on slice number 2116. The green circle represents the position of the highest flux within a 10 arcsec aperture where the 1D spectrum of all spectral lines is extracted from the cube.

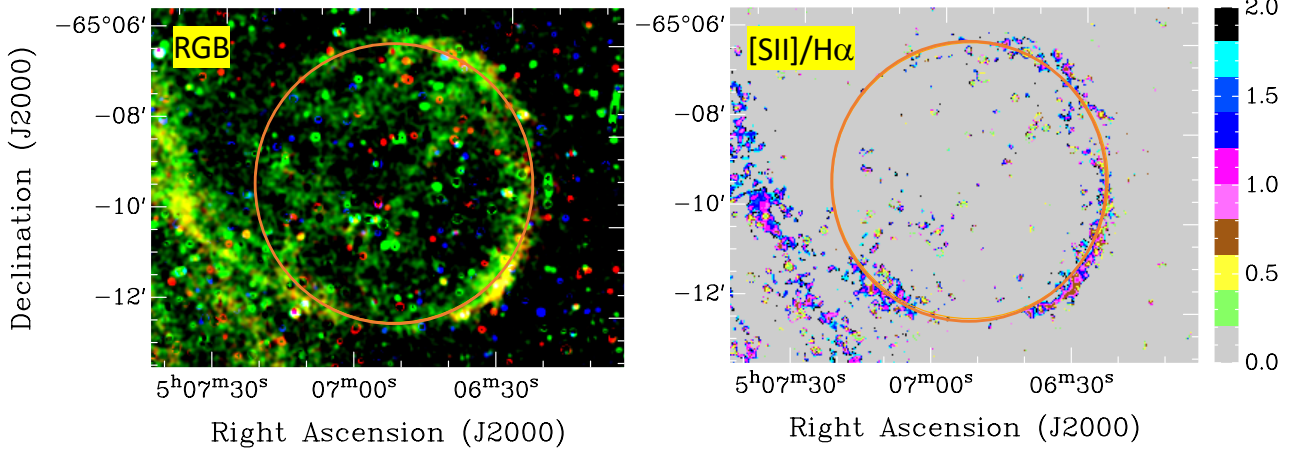


Figure A7. J0506–6509: colour images produced from MCELS data, where RGB corresponds to $H\alpha$, $[S\ II]$ and $[O\ III]$ while the ratio map is between $[S\ II]$ and $H\alpha$. The orange circle indicates the extent of the optical emission seen from the object.

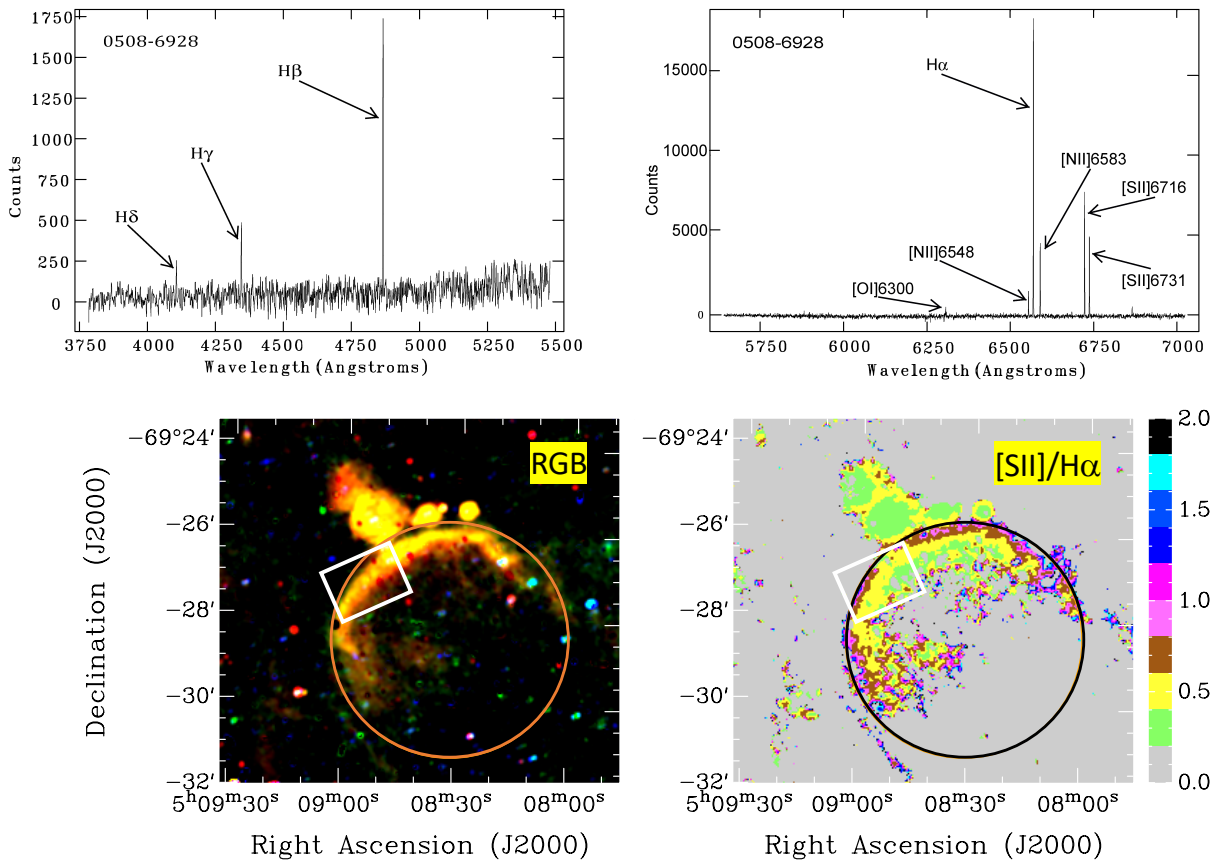


Figure A8. J0508–6928: (Top) showing the spectra from both arms (left; blue, right; red) of the spectrograph; (Bottom) colour images produced from MCELS data, where RGB corresponds to $H\alpha$, $[S\ II]$ and $[O\ III]$ while the ratio map is between $[S\ II]$ and $H\alpha$. The rectangular box (white) represents an approximate position of the WiFeS slicer. The orange/black circle indicates the extent of the optical emission seen from the object.

A9 J0509–6402 (Figures A9 and A10)

This SNR candidate lies 2° north of the LMC main body, in a field where we did not expect detection of any LMC SNRs. The MCELS $H\alpha$ and $[S\text{ II}]$ images shows a typical (shell-like) SNR morphology but somewhat elongated (Figure A9). At the same time, we report no $[O\text{ III}]$ emission in the MCELS image. Due to the size of the J0509–6402 shell $\sim 8' \times 5'$ ($\sim 116 \times 83$ pc), the SNR candidate cannot be morphologically classified as a young SNR. If confirmed as an SNR, this object would be certainly evolving in a much more rarefied environment than the rest of the known LMC SNRs. However, as can be seen in Figure A10, the eastern side of J0509–6402 might be interacting with one the northernmost $H\text{ I}$ spurs and perhaps create so called cloud-cloud interaction as seen in a number of other MCs SNRs and shells (Sano et al. 2018, 2019a,b, 2020). Sensitive X-ray and molecular gas observations are needed to confirm this possibility.

The optical spectra confirms shocks typical of SNRs which can be further confirmed using the ratio of shock sensitive $[S\text{ II}]$ lines with $H\alpha$ e.g. $[S\text{ II}]/H\alpha$ ratio of 0.75 (see Table 2) which differentiates SNRs from $H\text{ II}$ regions and planetary nebulae. The most prominent line in its spectrum is $H\alpha$, with the presence of $[O\text{ I}]$ at 6300\AA , $[N\text{ II}]$ at 6548\AA and 6583\AA as well as $[S\text{ II}]$ lines at 6717\AA and 6731\AA . All these lines are always associated with spectra of SNRs except the $[O\text{ I}]$ line which is rarely seen. We estimate that this SNR has an electron density of $\sim 30\text{ cm}^{-3}$ (for a temperature of 10 000 K) as a result of the ratio of $[S\text{ II}]$ lines. This indicates that SNR candidate J0509–6402 is most likely of a mature age. We also suggest that it might be more likely a result of a type Ia SN event because of its large distance from the main body of the LMC where massive stars are rarely found. However, one cannot completely disregard a possible core-collapse SN event as a very massive star could be ejected from the LMC main body and survive “traveling” some ~ 2 kpc (assuming a distance to the LMC of 50 kpc). While no such SN explosion is directly confirmed (so far) we suggest that only a small fraction of such SNRs would exist in any galaxy. In principle, this scenario could be applied to any CC type of SN explosion unless a given SNR doesn’t currently sit near a known OB star.

As this object is so far north of the main body of the LMC we could not search for massive stars since the area is not covered in Zaritsky et al. (2004).

A10 J0517–6757 (Figure A11)

The MCELS $H\alpha$ image (Figure A11) of this SNR candidate shows a faint, thin half-shell of emission towards the south of the object. It also shows line intensities for $H\gamma$ and $H\beta$ in its spectrum. J0517–6757 is surrounded with a number of $H\text{ II}$ regions, the most prominent of which is located just north of its suggested boundaries. Although unconfirmed, given that its $[S\text{ II}]/H\alpha$ ratio is ~ 0.69 and a somewhat typical LMC SNR size of $D=39$ pc, we nominate this object to be an SNR candidate. While we find some 17 OB stars in a 100 pc radius, none of these lie within the object’s defined shell.

We also note an adjacent semi-loop somewhat north of our SNR candidate J0517–6757 (see dashed ellipse in Figure A11). With an elevated $[S\text{ II}]/H\alpha$ ratio of 0.6 and diameter of ~ 150 arcsec (~ 36 pc), it will be further studied in our future follow up studies.

A11 MCSNR J0522–6740 (Figure A12)

This source shows a diffuse elliptical shell morphology ($D=87 \times 65$ pc) which is indicative of an evolved SNR (Figure A12

(left and middle)). It is found just outside the northern boundary of the giant $H\text{ II}$ complex LHA 120-N 44 (Henize 1956). While there are no optical spectra available for this object, the source is most prominent in the light of $[S\text{ II}]$, and we estimate from the MCELS images a very high $[S\text{ II}]/H\alpha$ ratio of ~ 1.0 . There are several isolated filaments where the $[S\text{ II}]/H\alpha$ ratio is elevated (>0.4). But, we couldn’t connect any of these with possible new SNR candidates. Seven massive OB stars are found in the vicinity, but only one within the bounds of this SNR candidate.

Although the contour plot is located in a region with low X-ray exposure (~ 10 ks EPIC-pn combining two observations), soft extended X-ray emission is significantly detected at the centre of the optical shell (Figure A12, right), most prominently in the 0.7–1.1 keV band. We analysed the X-ray spectrum of MCSNR J0522–6740 accumulated over the whole optical shell. The spectrum is thermal and reproduced by the emission of an optically-thin collisional-ionisation equilibrium plasma at LMC abundance (about half-solar). The best-fit electronic temperature is $kT_e = 0.3 \pm 0.02$ keV. This is typical for evolved SNRs, lending strong support to its confirmation as a bona-fide SNR. The amount of LMC neutral gas in front of the source is low (best-fit $N_H = 0$, and less than 10^{21} cm^{-2} at the 90% confidence level), but the total LMC line-of-sight integrated $H\text{ I}$ column at this position is only $1.6 \times 10^{21}\text{ cm}^{-2}$ (Kim et al. 2003). The 0.3–8 keV luminosity of MCSNR J0522–6740 is $L_X = 1.7 \times 10^{34}\text{ erg s}^{-1}$, potentially ranking this source among the 10 per cent faintest (so far) LMC SNRs in X-rays.

We investigate whether the prominence of the medium 0.7–1.1 keV X-ray band could be due to the presence of elevated iron abundance of SN ejecta origin, as was seen previously in several LMC and SMC SNRs (e.g. Borkowski et al. 2006; Maggi et al. 2014; Kavanagh et al. 2016; Maggi et al. 2019). When letting the oxygen and iron abundance free, fits with elevated Fe abundance are favoured despite large uncertainties (the upper value of Fe abundance is unconstrained), but the statistical improvement is moderate ($\Delta\chi^2 = 4.95$ for 2 degrees of freedom, i.e. less than 2σ). Exploring the parameter space of oxygen vs. iron abundance, the Fe/O ratio (by number) is > 3 at the 90% confidence level. This is more than twice the average LMC value of 1.4. We consider this enhancement to be indicative of a possible detection of iron ejecta. However, this evidence remains marginal given the limited exposure time and spectral resolution, and the intrinsic faintness of MCSNR J0522–6740.

Based on above findings, we suggest that MCSNR J0522–6740 is a new LMC SNR.

A12 J0528–7017 (Figure A13)

The SNR nature of J0528–7017 is drawn from its spherical (circular) shell morphology with a diameter ($D=81$ pc; Figure A13) while MCELS images indicates an overall $[S\text{ II}]/H\alpha$ ratio of ~ 0.9 . We searched MCPS images for massive (OB) stars near this object within a 100 pc radius and found 13 very distant OB stars from which 4 are within the boundaries of this proposed SNR candidate.

A13 J0529–7004 (Figure A14)

The candidacy for the SNR nature of J0529–7004 is also suggested by its spherical (circular) shell morphology with a diameter of 47 pc (Figure A14). While there are no spectra available for this candidate, we use MCELS images and found that the overall $[S\text{ II}]/H\alpha$ ratio of ~ 1.0 warrants further investigation of this object as an SNR candidate. We note that no massive stars could be found within the

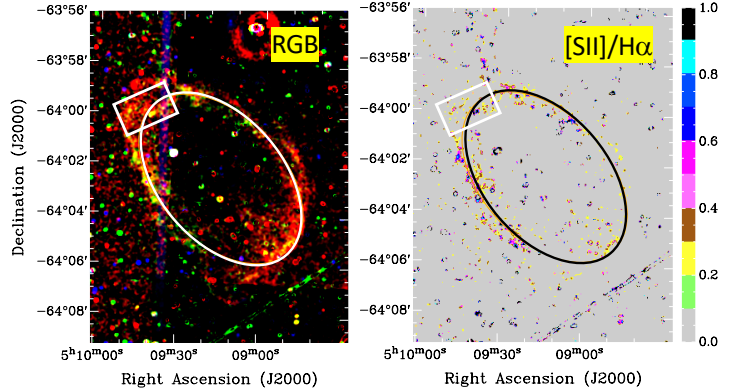
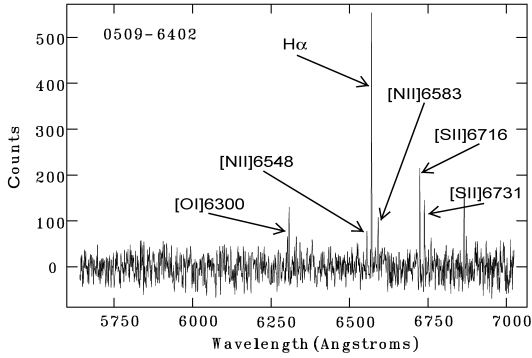


Figure A9. J0509–6402: (Left) showing the spectra from one arm (red) of the spectrograph; (Middle and right) colour images produced from MCELS data, where RGB corresponds to $H\alpha$, $[S\ II]$ and $[O\ III]$ while the ratio map is between $[S\ II]$ and $H\alpha$. The rectangular box (white) represents an approximate position of the WiFeS slicer. The white/orange ellipse indicates the extent of the optical emission seen from the object.

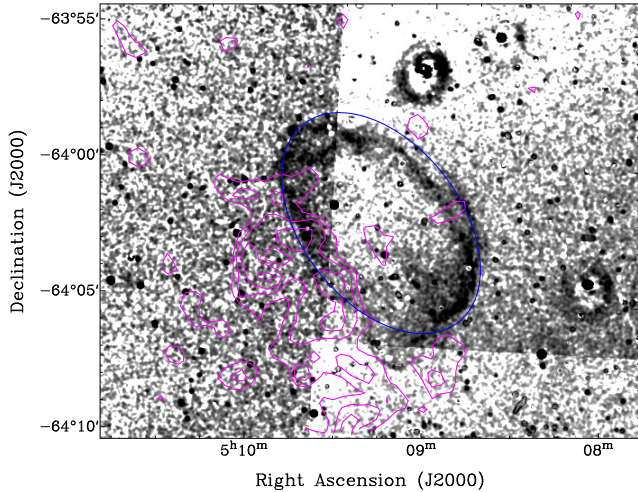


Figure A10. $H\alpha$ image of J0509–6402 overplotted with $H\ I$ contours (6, 7, 8 and 9×10^{20} atoms cm^{-2}). The blue ellipse indicates the extent of the optical emission seen from the object.

shell of this object but in a near vicinity (100 pc radius) we found 12 OB stars in the MCPs.

J0529–7004 is covered by two XMM-Newton observations, but both are at the very edge of the EPIC field of view. This results in an uneven exposure with 7.5 ks in the eastern and 25 ks in the western half of the region with optical emission. This candidate is located in an area of strong diffuse emission, but peaked soft X-ray emission is detected from J0529–7004 right at the centre of the optical emission. The position of the *ROSAT* source [HP99] 1077 is consistent with the bright spot seen in the EPIC image. The position of the *ROSAT* X-ray source source [HP99] 1077, which is about $18.5''$ away from the centre of J0529–7004, is consistent with the bright spot seen in the EPIC image.

A14 J0538–7004 (Figure A15)

This SNR candidate shows a partial filled-in shell, concentrating to the North-West (Figure A15). There are no spectra available for this candidate but the $[S\ II]/H\alpha$ ratio of ~ 0.8 that we estimate from the MCELS images is indicative of an SNR nature. However, this is the

second smallest SNR candidate in our 19 object strong sample with $D_{av} = 19.4$ pc. This would strongly argue for the presence of radio and X-ray emission which we don't see in any of our surveys despite the good coverage. Only two distant OB stars are found within the 100 pc from the object centre. As for the J0444–6758 (Section A1), we see a bright central $[O\ III]$ emission which is indicative of an $H\ II$ region. Therefore, this object is in a group of low confidence SNR candidates in this sample.

A15 MCSNR J0541–6659 (Figures A16 and A17)

This source was previously suggested as an SNR in the LMC based on its initial X-ray detection (Grondin et al. 2012). It was named [HP99] 456 in the *ROSAT* PSPC survey of the LMC (Haberl & Pietsch 1999, hereafter HP99). West of the X-ray source, there is an extended source in the optical bands. Here, for the first time, we present optical spectra of this object (see Figure A16). It has some diffuse emission towards the top left and relatively low $[S\ II]/H\alpha$ ratio of ~ 0.4 . We note a large peak in $H\alpha$ and $H\beta$ which coupled with its $[O\ III]$ value, gives a low $[O\ III]/H\beta$ ratio. Therefore, this SNR is possibly located next to an $H\ II$ region.

We obtained data from a 50 ks observation with the *Chandra* X-ray Observatory, using the ACIS-S array in VFaint mode. The SNR was observed at the aimpoint and was fully covered by the S3 chip. The observation was split into two parts with the same configuration: one observation performed on June 18, 2015 (ObsID 17675) with a net exposure time of 22 ks and another one performed 9 days later on June 27, 2015 (ObsID 16754) with a net exposure time of 29 ks. We reprocessed the data using CIAO Version 4.7 and CALDB Version 4.6.7. Using the reprocessed files, we created images in two bands: soft band (0.3–1.0 keV) and hard band (1.0–8.0 keV). We then smoothed the images adaptively using the tool *dmimgadapt* with a Gaussian kernel. We also merged the event files of the two observations and created images.

The *Chandra* images show shell-like soft X-ray emission and confirm the SNR identified with *XMM-Newton* data (Figure A17). There is some additional faint soft diffuse emission extending to the northeast, which might be caused by acceleration of gas along a negative density gradient (possible “blow out”). One should also consider that the SNR has blown out as we can see open optical filaments in that direction in the MCELS images.

Above 1 keV, extended emission is only visible in the western

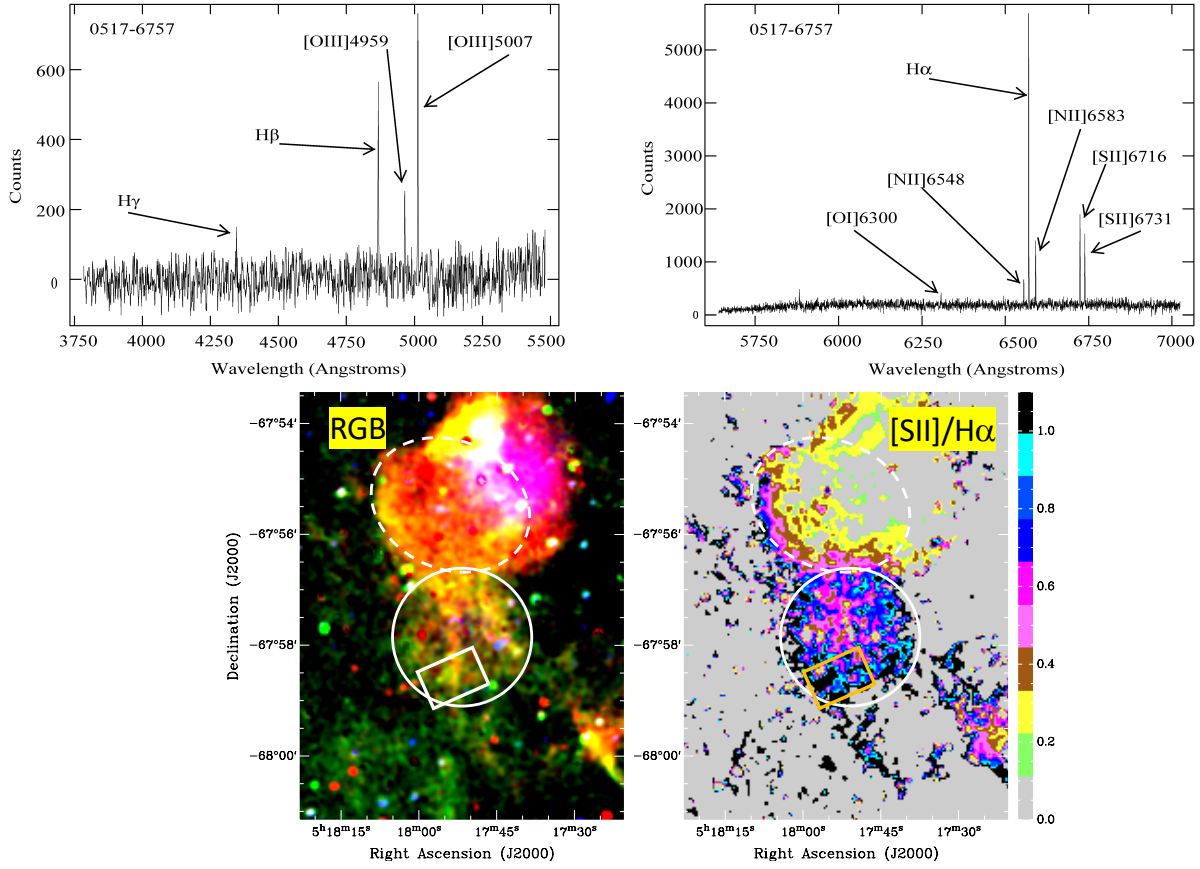


Figure A11. J0517–6757: (Top) showing the spectra from both arms (left: blue, right: red) of the spectrograph; (Bottom) colour images produced from MCELS data, where RGB corresponds to $H\alpha$, [S II] and [O III] while the ratio map is between [S II] and $H\alpha$. The rectangular box (white/orange) represents an approximate position of the WiFeS slicer. The solid white circle indicates the extent of the optical emission seen from the object while the dashed ellipse indicates possible adjacent SNR candidate that we will investigate in our future studies.

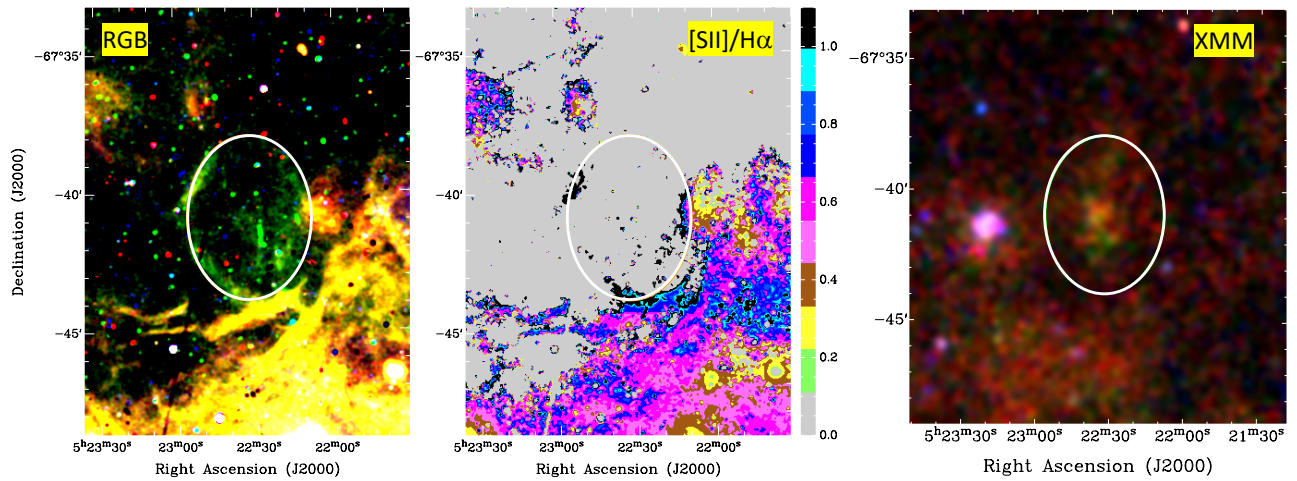


Figure A12. MCSR J0522–6740: colour images produced from MCELS data, where RGB corresponds to $H\alpha$, [S II] and [O III] (left) while the ratio map is between [S II] and $H\alpha$ (middle). *XMM-Newton* EPIC RGB (R=0.3–0.7 keV band, G=0.7–1.1 keV band and B=1.1–4.2 keV band) image from the area of MCSR J0522–6740 is shown in the right panel. The white ellipse indicates the location of the optical shell.

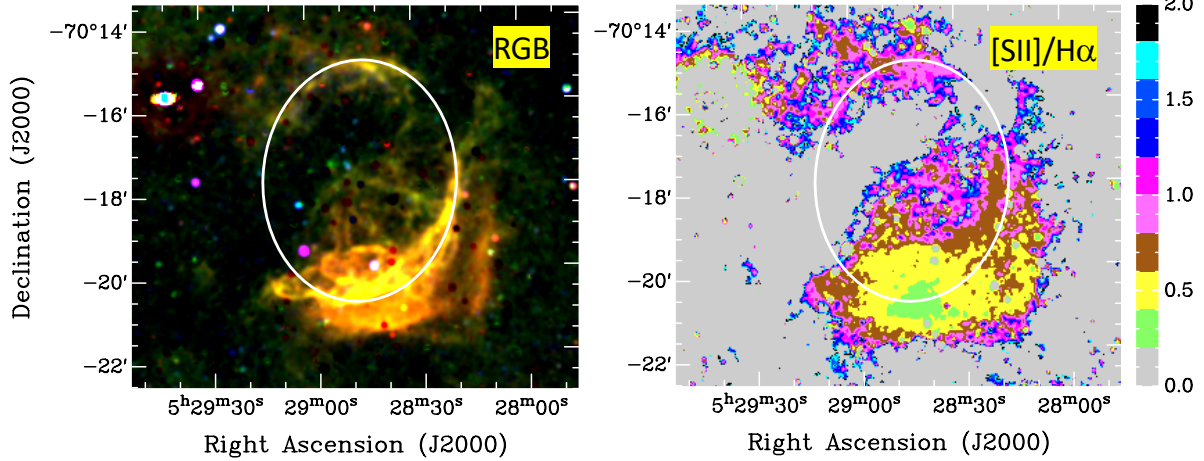


Figure A13. J0528–7017: Colour images produced from MCELS data, where RGB corresponds to $H\alpha$, $[S\text{II}]$ and $[O\text{III}]$ while the ratio map is between $[S\text{II}]$ and $H\alpha$. The white ellipse indicates the location of the optical shell.

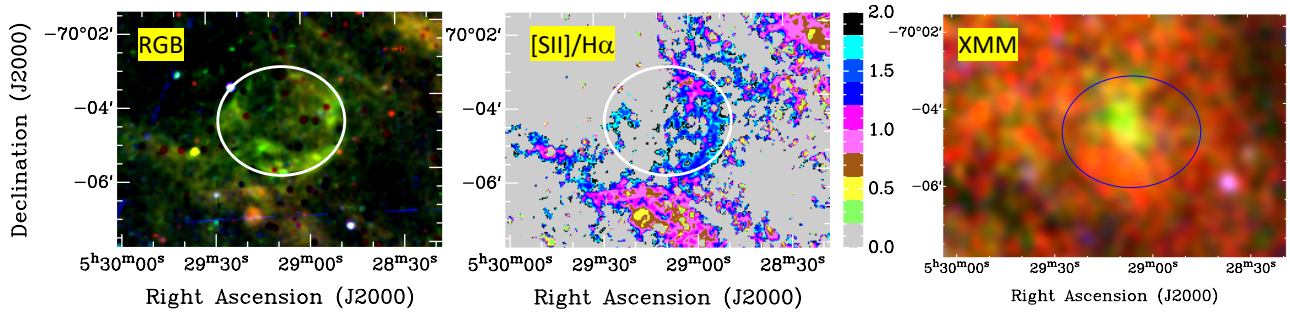


Figure A14. J0529–7004: colour images produced from MCELS data, where RGB corresponds to $H\alpha$, $[S\text{II}]$ and $[O\text{III}]$ (left) while the ratio map is between $[S\text{II}]$ and $H\alpha$ (middle). *XMM-Newton* EPIC RGB (R=0.3–0.7 keV band, G=0.7–1.1 keV band and B=1.1–4.2 keV band) image from the area of J0529–7004 (right). The white/blue ellipse indicates the location of the optical shell.

part, as had been already discovered with *XMM-Newton*. Inside the hard extended emission, which has an extent of $\sim 80'' \times 100''$, the superb spatial resolution of *Chandra* allowed us to detect two point sources: CXOU J054138.2–665817 (PSN) and CXOU J054140.4–665912 (PSS). These sources were detected by applying the source detection procedure `wavdetect` on the images of the different bands for both observations. For PSN, we only obtained ~ 20 net counts. The source is hard and only detected in the hard-band image. Source PSS has ~ 60 net counts and is detected both in the soft and the hard-band images. However, there is no indication that one of these sources might be a pulsar. In fact, according to Maggi et al. (2016), the stellar population in the region around the SNR is rather old with an age of $> 5 \times 10^7$ years for the majority of the stars (based on the Magellanic Clouds Photometric Survey, MCPS, Zaritsky et al. 2004), which indicates that most of massive stars have ended their lives (Schaerer et al. 1993). In fact, a number of OB stars can be

found within the 100 pc of the SNR centre from which only two are within its boundaries.

A16 MCSNR J0542–7104 (Figure A18)

This is a large, elliptical SNR candidate with a filled-in centre shell morphology (Figure A18) that extends to 73×51 pc. The $[S\text{II}]/H\alpha$ ratio estimated from our spectroscopic observation is ~ 0.82 which is typical of SNRs. As for a number of other objects from our sample, this SNR candidate does not show any detectable radio-continuum emission in our surveys. However, we note the detection of a source at this position in the *ROSAT* survey as HP[99] 1235. Further *XMM-Newton* follow up observations of this source will be presented in Kavanagh et al. (2020; in prep.) and we can consider this object as a bona-fide SNR. We also note that only one but very distant OB star is found at some 90 pc distance from the centre of this object.

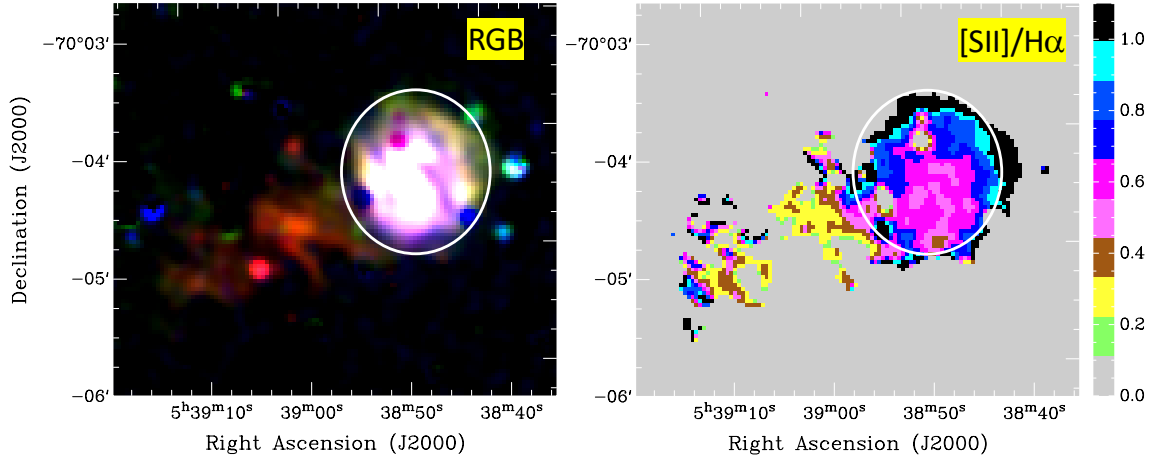


Figure A15. J0538–7004: colour images produced from MCELS data, where RGB corresponds to $H\alpha$, $[S\ II]$ and $[O\ III]$ while the ratio map is between $[S\ II]$ and $H\alpha$. The white circle indicates the location of the optical shell.

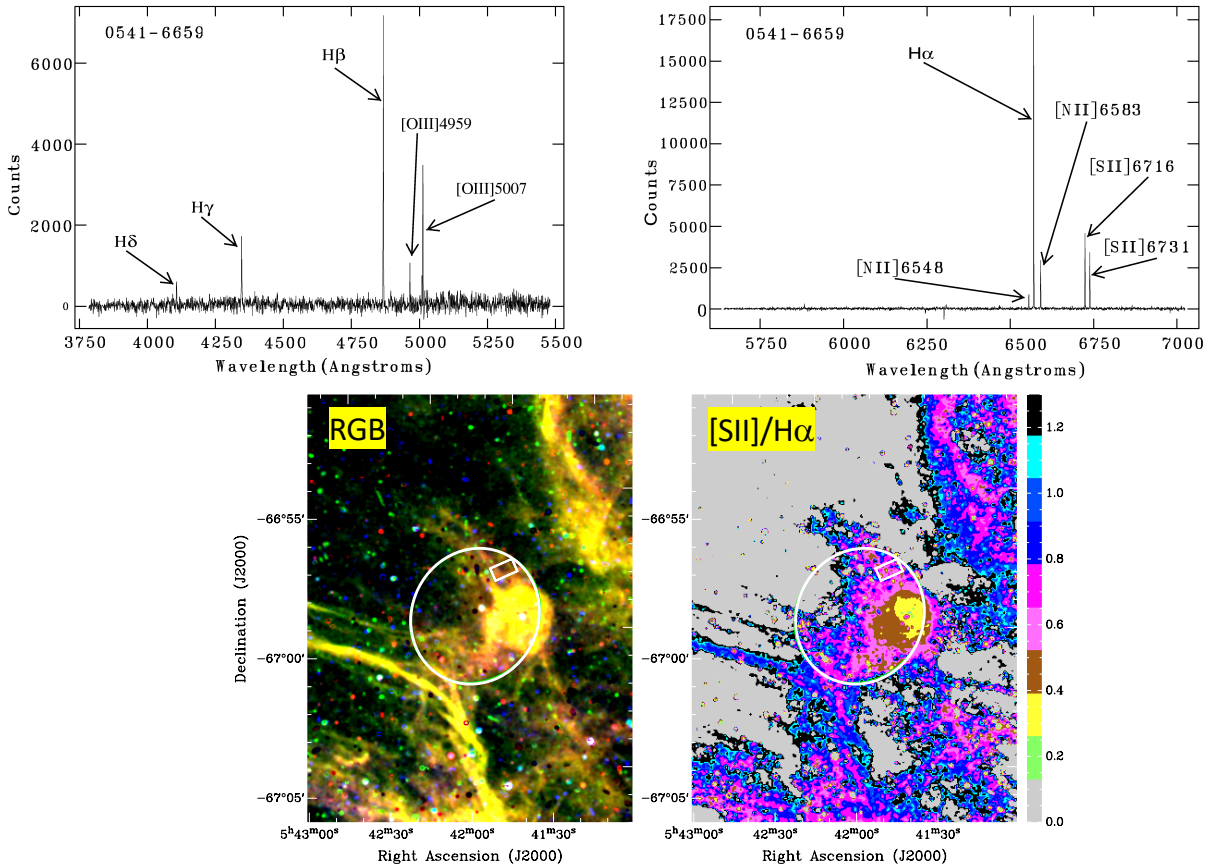


Figure A16. M3SNR J0541–6659: (Top) showing the spectra from both arms (left; blue, right; red) of the spectrograph; (Bottom) colour images produced from MCELS data, where RGB corresponds to $H\alpha$, $[S\ II]$ and $[O\ III]$ while the ratio map is between $[S\ II]$ and $H\alpha$. The rectangular box (white) represents an approximate position of the WiFeS slicer. The white circle indicates the location of the optical shell.

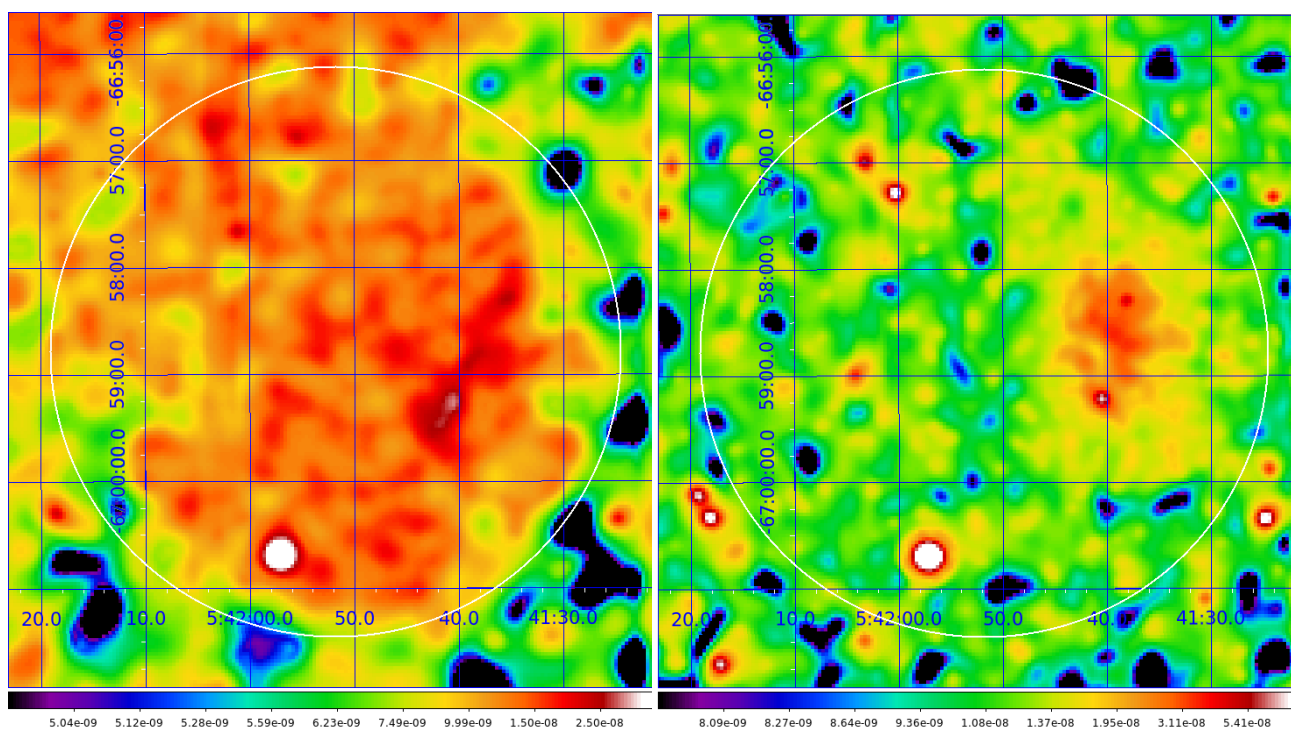


Figure A17. *Chandra* ACIS images of MGSNR J0541–6659 created from merged data of observations 16754 and 17675 (left: soft-band image, 0.3–1.0 keV; right: hard-band image, 1.0–8.0 keV). The images have been binned with a bin size of 4 pixels, smoothed adaptively, and exposure-corrected. The shell of the SNR is indicated with a white circle.

A17 J0548–6941 (Figure A19)

This candidate has an obvious half shell elongated morphology to its south-west (Figure A19) and a somewhat smaller size of 38×23 pc. It has a $[\text{S II}]/\text{H}\alpha$ ratio of ~ 0.6 (from our WiFeS spectroscopic observations) and is the only SNR candidate in the sample with a $[\text{Fe II}]$ line. We find 4 distant OB stars in the area of SNR candidate J0548–6941. This region is covered by *XMM-Newton* and reveals no X-ray emission.

A18 J0549–6618 (Figure A20)

J0549–6618 has no obvious shell morphology like many other objects in our sample but has a filled-in centre (Figure A20). There are no spectra available for this candidate but our $[\text{S II}]/\text{H}\alpha$ ratio estimates based on the MCELS images is ~ 1.0 . The stellar environment is such that we can't see any nearby massive star.

A19 J0549–6633 (Figure A21)

This SNR candidate is chosen based on its very high MCELS $[\text{S II}]/\text{H}\alpha$ ratio of 1.4 (Figure A21; Table 2). While elongated ($D=131 \times 95$ pc), it also has a centre-filled-in shell morphology but without a distinctive peak at the centre. It is the largest among all of the objects studied here and it has the highest spectroscopic $[\text{S II}]/\text{H}\alpha$ ratio at ~ 1.38 . The remnant is not only strong in $[\text{S II}]$ but is also detected in $[\text{O I}]$. As shown in Figure 2, this source is just outside of the established spectroscopic boundaries for being a SNR and as such would qualify for a (super)bubble. However, as for J0549–6618, the stellar environment shows no nearby massive stars which is a strong argument against a (super)bubble classification.

This paper has been typeset from a $\text{\TeX}/\text{\LaTeX}$ file prepared by the author.

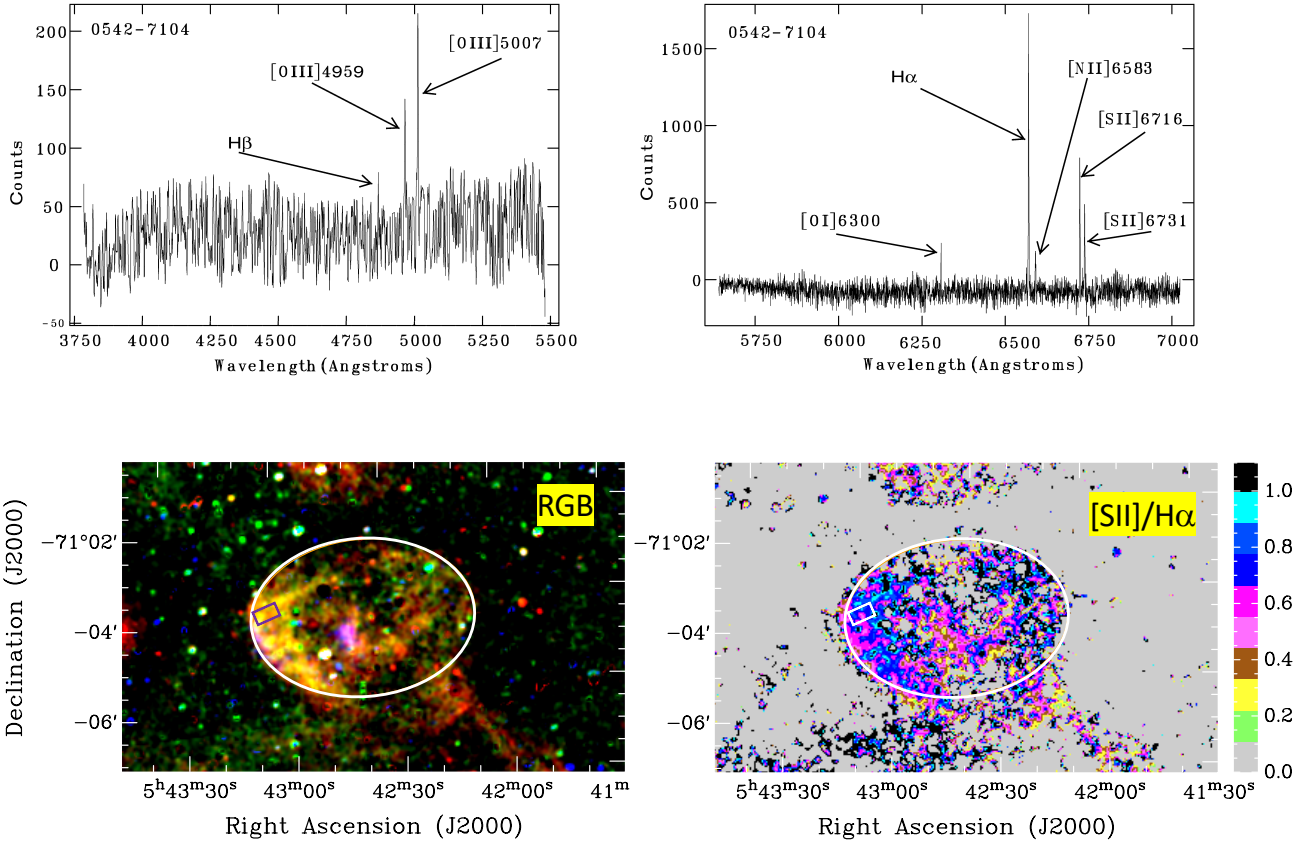


Figure A18. MGSNR J0542–7104: (Top) showing the spectra from both arms (left; blue, right; red) of the spectrograph; (Bottom) colour images produced from MCELS data, where RGB corresponds to $H\alpha$, $[S\text{II}]$ and $[O\text{III}]$ while the ratio map is between $[S\text{II}]$ and $H\alpha$. The rectangular box (magenta/white) represents an approximate position of the WiFeS slicer. The white ellipse indicates the location of the optical shell.

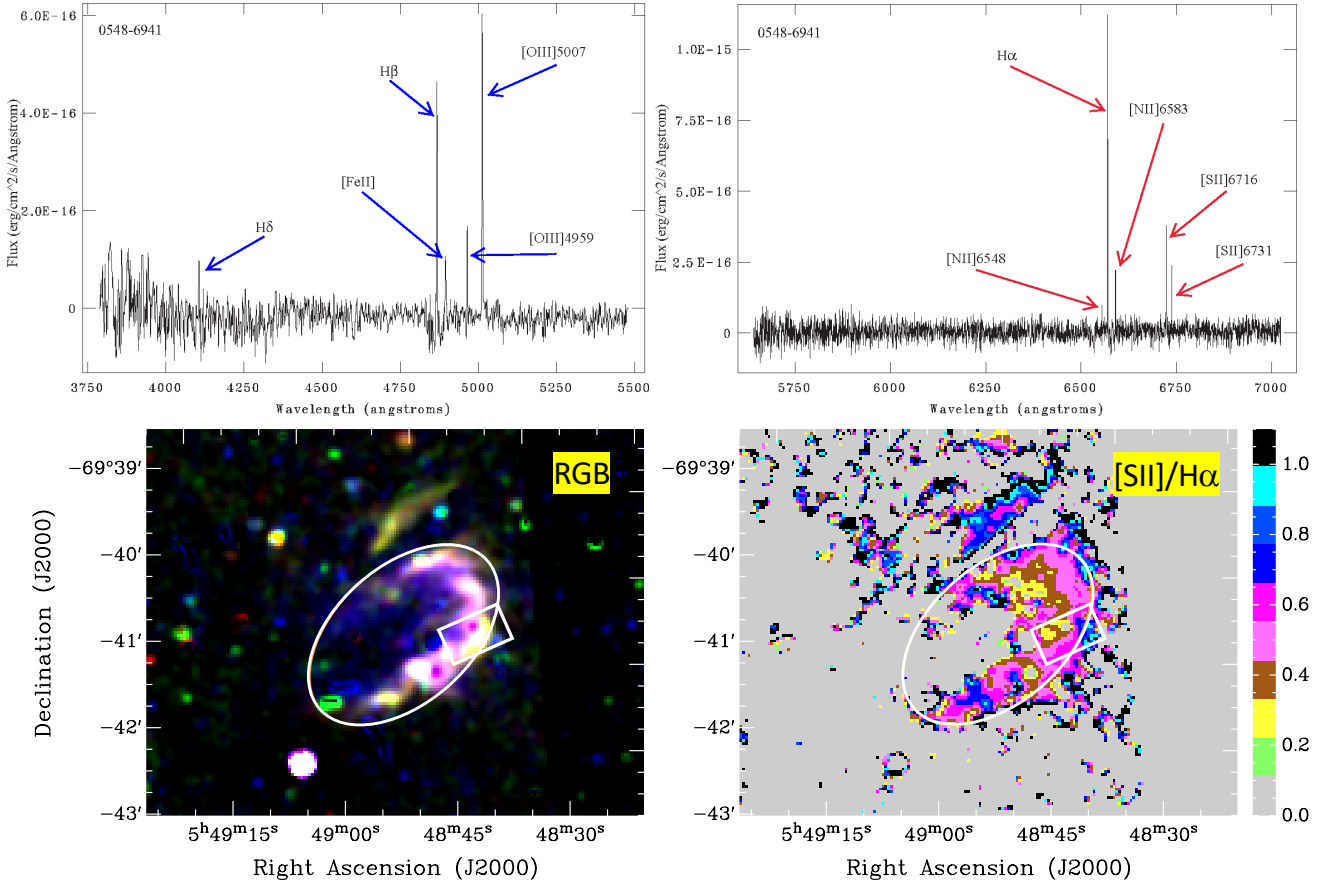


Figure A19. J0548–6941: (Top) showing the spectra from both arms (left; blue, right; red) of the spectrograph; (Bottom) colour images produced from MCELS data, where RGB corresponds to $H\alpha$, [S II] and [O III] while the ratio map is between [S II] and $H\alpha$. The rectangular box (white) represents an approximate position of the WiFeS slicer. The white ellipse indicates the location of the optical shell.

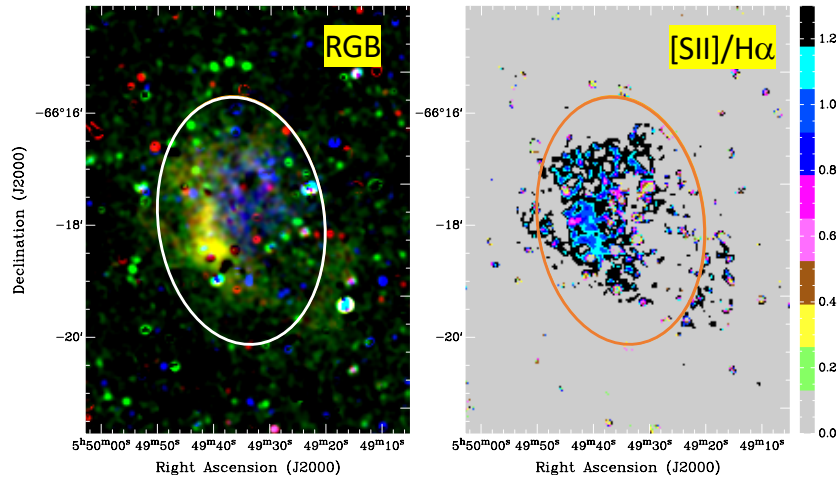


Figure A20. J0549–6618: colour images produced from MCELS data, where RGB corresponds to $H\alpha$, [S II] and [O III] while the ratio map is between [S II] and $H\alpha$. The white/orange ellipse indicates the location of the optical shell.

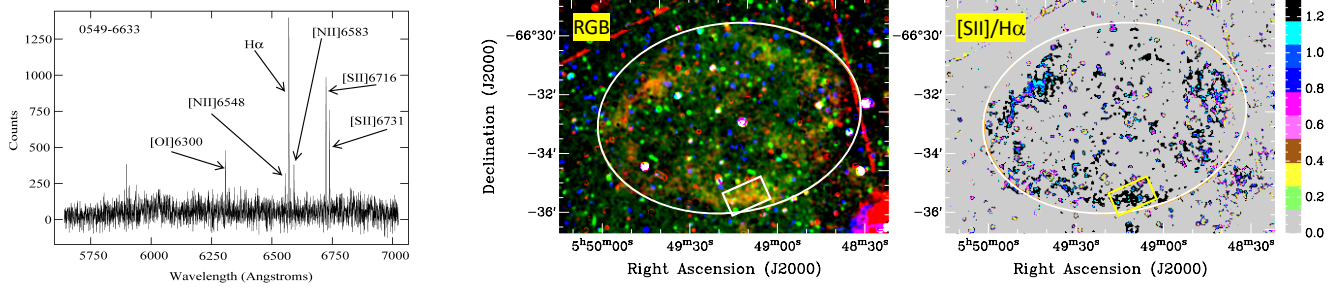


Figure A21. 0549–6633: (Left) showing the spectra from one arm (red) of the spectrograph; (Middle and right) colour images produced from MCELS data, where RGB corresponds to $H\alpha$, $[S\ II]$ and $[O\ III]$ while the ratio map is between $[S\ II]$ and $H\alpha$. The rectangular box (white/yellow) represents an approximate position of the WiFeS slicer. The white ellipse indicates the location of the optical shell.

Appendix C

Discovery of a Pulsar-powered Bow Shock Nebula in the Small Magellanic Cloud Supernova Remnant DEM S5

This chapter is a reproduction of: Alsaberi, R. Z. E., Maitra, C., Filipović, M. D., Bozzetto, L. M., *et al.* (2019). Discovery of a pulsar-powered bow shock nebula in the Small Magellanic Cloud supernova remnant DEM S5. *MNRAS*, 486(2):2507

Discovery of a Pulsar-powered Bow Shock Nebula in the Small Magellanic Cloud Supernova Remnant DEM S5

Rami Z. E. Alsaberi,^{1*} C. Maitra,² M. D. Filipović,¹ L. M. Bozzetto,¹ F. Haberl,² P. Maggi,³ M. Sasaki,⁴ P. Manjlović,^{1,5} V. Velović,⁶ P. Kavanagh,⁷ N. I. Maxted,^{1,8} D. Urošević,^{6,9} G. P. Rowell,¹⁰ G. F. Wong,^{1,8} B.-Q. For,^{11,12} A. N. O’Brien,^{1,5} T. J. Galvin,^{1,5,13} L. Staveley-Smith,^{11,12} R. P. Norris,^{1,5} T. Jarrett,¹⁴ R. Kothes,¹⁵ K. J. Luken,^{1,5} N. Hurley-Walker,¹³ H. Sano,¹⁶ D. Onić,⁶ S. Dai,⁵ T. G. Pannuti,¹⁷ N. F. H. Tothill,¹ E. J. Crawford,¹ M. Yew,¹ I. Bojčić,¹ H. Dénes,¹⁸ N. McClure-Griffiths,¹ S. Gurovich,²⁰ and Y. Fukui¹⁶

¹Western Sydney University, Locked Bag 1797, Penrith South DC, NSW 1797, Australia

²Max-Planck-Institut für extraterrestrische Physik, Giessenbachstraße, 85748 Garching, Germany

³Observatoire Astronomique de Strasbourg, Université de Strasbourg, CNRS, 11 rue de l’Université, F-67000 Strasbourg, France

⁴Remeis Observatory and ECAP, Universität Erlangen-Nürnberg, Sternwartstr. 7, 96049 Bamberg, Germany

⁵CSIRO Astronomy and Space Sciences, Australia Telescope National Facility, PO Box 76, Epping, NSW 1710, Australia

⁶Department of Astronomy, Faculty of Mathematics, University of Belgrade, Studentski trg 16, 11000 Belgrade, Serbia

⁷School of Cosmic Physics, Dublin Institute for Advanced Studies, 31 Fitzwilliam Place, Dublin 2, Ireland

⁸School of Science, University of New South Wales, Australian Defence Force Academy, Canberra, ACT 2600, Australia

⁹Isaac Newton Institute of Chile, Yugoslavia Branch

¹⁰School of Physical Sciences, The University of Adelaide, Adelaide 5005, Australia

¹¹International Centre for Radio Astronomy Research, University of Western Australia, 35 Stirling Hwy, Crawley, WA 6009, Australia

¹²ARC Centre of Excellence for All Sky Astrophysics in 3 Dimensions (ASTRO 3D)

¹³International Centre for Radio Astronomy Research, Curtin University, Bentley, WA 6102, Australia

¹⁴Astrophysics, Cosmology and Gravity Centre (ACGC), Astronomy Department, University of Cape Town, Private Bag X3, Rondebosch 7701, South Africa

¹⁵Dominion Radio Astrophysical Observatory, Herzberg Programs in Astronomy and Astrophysics, National Research Council Canada, PO Box 248, Penticton, BC V2A 6J9, Canada

¹⁶Institute for Advanced Research, Nagoya University, Chikusa-ku, Nagoya 464-8601, Japan

¹⁷Space Science Center, Department of Earth and Space Sciences, Morehead State University, Morehead, KY 40351, USA

¹⁸ASTRON - Netherlands Institute for Radio Astronomy, 7991 PD, Dwingeloo, The Netherlands

¹⁹Research School of Astronomy & Astrophysics, Australian National University, Canberra ACT 2610, Australia

²⁰Instituto de Astronomía Teórica y Experimental - Observatorio Astronómico Córdoba (IATE-OAC-UNC-CONICET), Laprida 854, X5000BGR, Córdoba, Argentina

Accepted XXX. Received YYY; in original form ZZZ

ABSTRACT

We report the discovery of a new Small Magellanic Cloud Pulsar Wind Nebula (PWN) at the edge of the Supernova Remnant (SNR) DEM S5. The pulsar powered object has a cometary morphology similar to the Galactic PWN analogs PSR B1951+32 and ‘the mouse’. It is travelling supersonically through the interstellar medium. We estimate the Pulsar kick velocity to be in the range of 700–2000 km s^{−1} for an age between 28–10 kyr. The radio spectral index for this SNR-PWN-pulsar system is flat (−0.29 ± 0.01) consistent with other similar objects. We infer that the putative pulsar has a radio spectral index of −1.8, which is typical for Galactic pulsars. We searched for dispersion measures (DMs) up to 1000 cm^{−3} pc but found no convincing candidates with a S/N greater than 8. We produce a polarisation map for this PWN at 5500 MHz and find a mean fractional polarisation of P ∼ 23 percent. The X-ray power-law spectrum (Γ ∼ 2) is indicative of non-thermal synchrotron emission as is expected from PWN-pulsar system. Finally, we detect DEM S5 in Infrared (IR) bands. Our IR photometric measurements strongly indicate the presence of shocked gas which is expected for SNRs. However, it is unusual to detect such IR emission in a SNR with a supersonic bow-shock PWN. We also find a low-velocity H I cloud of ∼ 107 km s^{−1} which is possibly interacting with DEM S5. SNR DEM S5 is the first confirmed detection of a pulsar-powered bow shock nebula found outside the Galaxy.

Key words: ISM: individual objects: DEM S5 – ISM: supernova remnants – Radio continuum: ISM – Radiation mechanisms: general – Magellanic Clouds

arXiv:1903.03226v2 [astro-ph.HE] 11 Apr 2019

1 INTRODUCTION

The Small Magellanic Cloud (SMC) is a gas-rich irregular dwarf galaxy orbiting the Milky Way (MW). However, the proper motion of both the SMC and the Large Magellanic Cloud (LMC) is high, with Besla et al. (2007, and references therein) arguing that it could be on its first passage about the MW. With a current star formation rate (SFR) of $0.021\text{--}0.05 M_{\odot} \text{ yr}^{-1}$ (For et al. 2018), it is ranked as the second nearest star forming galaxy after the LMC to the MW. The relatively nearby distance of ~ 60 kpc (Macri et al. 2006) and the low Galactic foreground absorption ($N_{\text{HI}} \sim 6 \times 10^{20} \text{ cm}^{-2}$) enables the entire source population in the SMC to be studied in X-rays down to a luminosity of $\sim 10^{33} \text{ erg s}^{-1}$ (Haberl et al. 2012c). The recent star formation activity over the last ~ 50 Myr has created an environment where supernova remnants (SNRs) and X-ray pulsars are expected to be plentiful. In line with this, a large population of high-mass X-ray binaries (HMXBs) have been discovered and extensively studied by Haberl & Sturm (2016). These objects are typically tens of millions of years old and have spin periods ranging from 1 to 1000 s. However, the younger population of neutron stars (NSs) is still largely missing.

There are only two known young SMC pulsars: an 8.02 s anomalous X-ray pulsar, CXOU J010043.1–721134, with a characteristic age of ~ 6700 yr (Tiengo et al. 2008); The second one powers the only confirmed pulsar wind nebula (PWN) in the SMC, inside the large (74.5 pc diameter) SNR IKT 16. IKT 16 hosts a suspected pulsar with a spin-down luminosity (\dot{E}) $\sim 10^{37} \text{ erg s}^{-1}$ and an age of ~ 14.7 kyr (Owen et al. 2011; Maitra et al. 2015). The PWN within IKT 16 was discovered with a dedicated *Chandra* observation, which resolved the hard (2–4.5 keV) X-ray point source seen with *XMM-Newton* into a faint and soft symmetric nebula surrounding a bright and hard point source. The symmetric morphology suggested that the PWN has not yet interacted with the reverse shock of the SNR. IKT 16 was also detected at radio continuum frequencies with a typical flat spectral energy distribution (SED)¹ but without any indication of a point source coinciding with the X-ray point source at the centre of the nebula.

Other well studied SNRs in the SMC include SXP 1062 (Haberl et al. 2012a) which hosts a young Be X-ray binary pulsar with a long spin period in the centre of the remnant. Crawford et al. (2014) investigated the SNR HFPK 334 which has a prominent X-ray point source close to the centre of the SNR. This X-ray source was considered to be a background object and not associated with the SNR. At the same time Roper et al. (2015) noted a lack of confirmed and prominent type Ia SNRs, indicating that the sample of ~ 25 SNRs in the SMC may not be representative for any normal galaxy. However and recently, Maggi et al. (in prep) list three likely type Ia SNRs in the SMC.

Bozzetto et al. (2017) showed that only five PWNe (out of some 60 confirmed SNRs) are detected so far in the LMC. A further instance was investigated for a relationship between the LMC SNR J0529–6653 and the pulsar B0529–66 (Bozzetto et al. 2012, 2017) where the displacement between the midpoint (geometric centre) of the SNR to a pulsar candidate would be consistent with typical kick velocities. How-

ever, there was no radio frequency trail of the kind seen in other SNR/PWN systems.

Pulsars and their PWNe, moving supersonically through the ambient medium, are characterised by bow shaped shocks around the pulsar and/or cometary tails (Reynolds et al. 2017). This population is characterised by Rotation-Powered Pulsars (RPPs) with ages between 10 kyr–3 Myr, with a spin-down power (\dot{E}) ranging from $10^{33}\text{--}10^{37} \text{ erg s}^{-1}$ (Kargaltsev et al. 2017). Currently, there are ~ 28 known pulsars which show indications of supersonic motion (most with measured velocities). All of them reside in our Galaxy and exhibit a wide range of morphology (c.f.: Pavan et al. 2014a,b; Kargaltsev et al. 2017; Barkov et al. 2019). Although the LMC pulsar J0537–6910 (a.k.a SNR N157 B or 30 Dor B) shows indications of some supersonic motion, its nature is yet to be firmly established. Similarly, LMC SNR N 206 (Klinger et al. 2002) shows an interesting linear tail-like feature but without an identifiable point source (pulsar) association. The other well established PWNe in the LMC do not exhibit a bow shock morphology, but a typically flat radio SED is evident and located more or less centrally within the remnant (Haberl et al. 2012b).

DEM S5 (MCSNR J0041–7336; HFPK530) is among the largest SNRs in the SMC with a size of 245.5×219.7 arcsec (71.4×63.9 pc at the distance of 60 kpc to the SMC; see Fig. 1), is X-ray faint, and has a complex shell like structure. The size of DEM S5 is measured from optical (MCELS; see section 2.3) images while both X-ray and radio images show a smaller extent. With the present sensitivity (and resolution) of our X-ray and radio observations we cannot see the complete shell of SNR DEM S5, specifically, we are unable to measure any emission in the north and north-west region of the SNR. Therefore the size of the complete shell can only be reliably measured from the optical MCELS images. While lack of sensitivity may play an important role, this could also indicate that the outer regions seen in [O III] as radiative shocks contains gas too cool to emit X-rays or radio continuum. A previous *XMM-Newton* study of DEM S5 based on observations in which the source was substantially off-axis (~ 8 arcmin) yielded poor constraints on the properties of the SNR due to statistical limitations (Filipović et al. 2008). However, an interesting outcome of the study was the detection of a soft X-ray source ~ 67.5 arcsec from the centre at RA(J2000) = $00^{\text{h}}40^{\text{m}}47.7^{\text{s}}$, and DEC(J2000) = $-73^{\circ}37'03''$. Filipović et al. (2008) noted then that the hard X-ray emission also coincided with the peak of the radio continuum image obtained with Australia Telescope Compact Array (ATCA).

Confirmation of the nature of this source is essential to refine our knowledge of pulsars in the SMC and more generally for stellar population studies of dwarf irregular galaxies. In particular, the detection of a new bow shock PWN would be of critical importance to study this small subsample of PWN systems. Furthermore, since the star formation history and metallicity of the SMC is different from that of our Galaxy, it is an interesting system for studying the pulsar population, and comparing the younger population with the plentiful older ones (HMXBs).

In this paper we present an analysis of radio and X-ray observational data of DEM S5 as follows: Section 2 details the radio X-ray and supplementary optical & Infrared (IR) data; Sections 3 and 4 respectively contain our results and

¹ Defined as $S_{\nu} \propto \nu^{\alpha}$

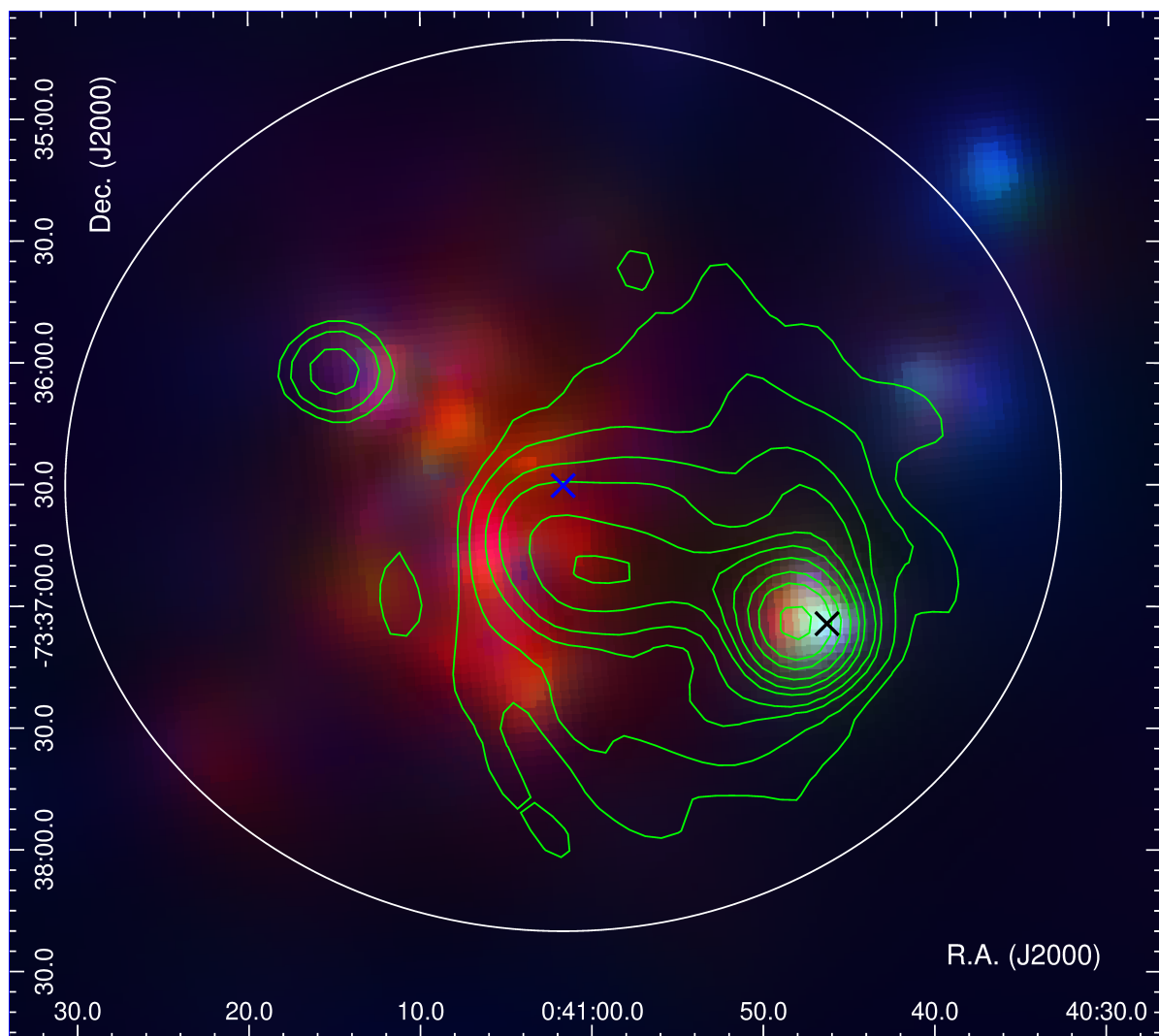


Figure 1. *XMM-Newton* EPIC RGB (R= 0.2–1 keV, G= 1–2 keV, B= 2–4.5 keV) image of DEM S5. The optical size of the SNR and the centre are marked with a white ellipse (245.5×219.7 arcsec extent) and blue cross respectively (Filipović et al. 2008). The green contours denote the 1320 MHz radio image. The contours are: 0.5, 1, 2, 3, 5, 7, 10, 15, 20, and 30 mJy beam^{-1} where we measure the local RMS (or 1σ) to be $\sim 0.1 \text{ mJy beam}^{-1}$. The beam size of the radio image is 16.3×15.1 arcsec. The position of the hard X-ray point source (2–4.5 keV) is marked with a black cross.

a discussion. Finally, concluding remarks are given in Section 5.

2 OBSERVATIONS AND DATA

2.1 Radio continuum observations

We used ATCA observational data from projects CX310 and CX403 that were taken on the 2014 December 30th and 31st; 2015 January 4th and 2017 December 22nd. These observations used the Compact Array Broadband Backend (CABB) (with 2048 MHz bandwidth) in the 6A and 6C array configuration, centred at wavelengths of 3/6 cm ($\nu = 4500\text{--}6500$ and 8000–10000 MHz; centred at 5500 and 9000 MHz), and 13 cm ($\nu = 2100$ MHz). The observations were carried out in a frequency switching mode, totaling ~ 444 minutes of integration at 4500–6500 and 8000–10000 MHz bands and 153 minutes of integration at 2100 MHz frequency. Source

PKS B1934–638 was used as the primary (flux density) calibrator for the 2014 December 30th, 2014 December 31st, and 2015 January 4th data; and source PKS B0252–712 for the 2017 December 22nd data. Source PKS B0230–790 was used as the secondary (phase) calibrator for all four observations (Table 1). The MIRIAD² (Sault et al. 1995) and KARMA³ (Gooch 1995) software packages were used to reduce and analyze the data. Images were formed using MIRIAD and the multi-frequency synthesis tasks (Sault & Wieringa 1994) therein with a Briggs weighting robust = -1 parameter for the 5500 MHz image and 0 for the 2100 MHz image. Both images were deconvolved by applying a primary beam correction. The same procedure was used for both the Q and U Stokes parameter maps (see Fig. 2).

The 2100 MHz image has a resolution of 3.7×2.9 arcsec

² <http://www.atnf.csiro.au/computing/software/miriad/>

³ <http://www.atnf.csiro.au/computing/software/karma/>

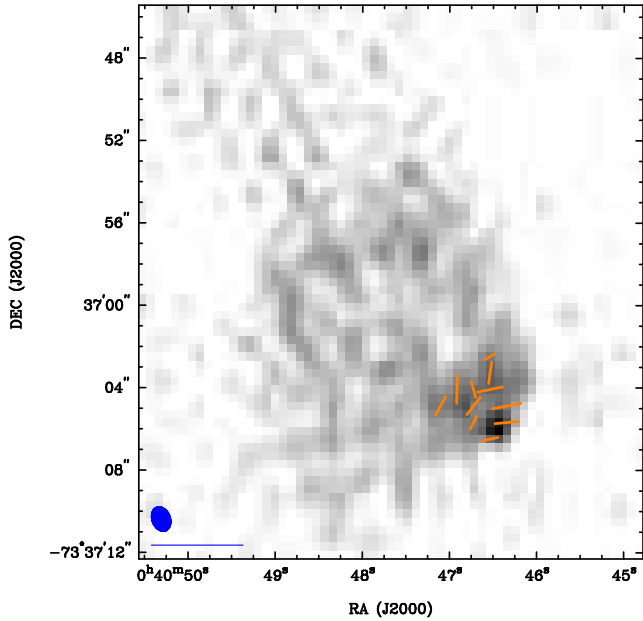


Figure 2. Fractional polarisation vectors overlaid on the 5500 MHz ATCA image of DEM S5 PWN. The blue ellipse in the lower left corner represents the synthesised beamwidth of 1.2×0.89 arcsec and the blue line below the ellipse represents a polarisation vector of 100 percent. We used `robust=-1` weighting scheme to make this image. The peak fractional polarisation value is $P = 32 \pm 7$ percent while the average polarisation is measured to be ~ 23 percent.

with position angle (PA) = 58.1 deg, while the 5500 MHz image had a resolution of 1.2×0.89 arcsec and PA = 21.3 deg. Because of the low surface brightness and lack of short spacings, we were unable to create a reliable image at 9000 MHz to sample the entire DEM S5 extended emission. However, we use the 9000 MHz image for studying point sources within the field as they are largely not affected by the above shortcomings. Our new images at 2100, 5500, and 9000 MHz have an RMS noise of 0.1, 0.013, and 0.012 mJy beam $^{-1}$ respectively.

We measured the integrated flux density of DEM S5 PWN from 11 separate images spanning a frequency range of 88 to 8640 MHz, which are summarised in Table 2. At the same time, we were able to measure the flux density from our two new CABB observations (5500 and 9000 MHz) of the two point-like sources in the field of DEM S5 which we associate with the putative pulsar and an unrelated background source (RA(J2000) = $00^{\text{h}}41^{\text{m}}14.82^{\text{s}}$, and DEC(J2000) = $-73^{\circ}35'59.9''$).

Similar to the studies of the radio continuum from the LMC by [Bozzetto et al. \(2017\)](#) and [Maggi et al. \(2018; in prep\)](#), we have used all available radio continuum data described in previous SMC surveys ([Filipovic et al. 1997, 1998; Turtle et al. 1998; Filipović et al. 2002; Payne et al. 2004; Filipović et al. 2005b; Reid et al. 2006; Payne et al. 2007; Wong et al. 2011a,b; Crawford et al. 2011; Wong et al. 2012a,b](#)). These data have been taken with the ATCA, Parkes and the Molonglo Synthesis Telescope (MOST). Additionally, we make use of Murchison Widefield Array (MWA) data from [For et al. \(2018\)](#) and [Joseph et al. \(2019, in prep.\)](#) obtained from the Australia Square Kilometre Ar-

ray Pathfinder (ASKAP) Early Science Project observations of the SMC.

In Fig. 3 we show the new ATCA radio continuum images at 5500 and 2100 MHz with the X-ray soft (0.2–1.0 keV) and hard (2–4.5 keV) band contours overlaid, obtained from *XMM-Newton*. For all radio surveys (except the MWA), we used the MIRIAD task `imfit` in order to extract source integrated flux density, extensions (diameter/axes (D) and PA). Errors in flux density measurements predominately arose from uncertainties in defining the ‘edge’ of the remnant. However, we estimate these errors to be < 10 percent.

To estimate the flux density from the MWA surveys, we cut out $\approx 3 \times 3$ deg areas around the source from the GLEAM wide-band extragalactic catalogue images ([Hurley-Walker et al. 2017; For et al. 2018](#))⁴. Using the Aegean Tools package ([Hancock et al. 2012, 2018](#))⁵, we ran the Background And Noise Estimator and the Aegean source-finder on the 170–231 MHz image to detect the SNR/PWNe. We then used the measured position as a prior and allowed the flux to vary when finding it in the 72–103, 103–134, and 139–170 MHz images (‘priorized fitting’). The errors on the integrated flux densities take into account the local RMS, the fitting errors, and the overall flux scale calibration ([Hurley-Walker et al. 2017](#), 13 percent at this low Declination). The source DEM S5 was unresolved at all MWA frequencies (as expected) so the integrated flux density is identical to the (background-subtracted) peak flux density.

2.2 X-ray observations and analysis

DEM S5 was observed serendipitously with *XMM-Newton* twice between 2006 and 2015 albeit at substantial off-axis angles. The observation details are given in Table 3. Fig. 1 displays the *XMM-Newton* EPIC RGB image of DEM S5, showing the supernova remnant in X-rays and a hard point-like X-ray source shown with a black cross in the south-west direction at a distance of 21.2 pc from the geometrical centre of the remnant. During both observations the point-like X-ray source was located on a malfunctioning CCD of MOS1 and in the case of ObsID 0764780201, the source was also outside the readout area of the PN operated in small window mode. *XMM-Newton*/EPIC ([Strüder et al. 2001; Turner et al. 2001](#)) observations were processed with the *XMM-Newton*, data analysis software SAS version 16.1.0⁶.

We searched for periods of high background flaring activity by extracting light curves in the energy range of 7.0–15.0 keV and removed the time intervals with background rates ≥ 8 and 2.5 cts ks $^{-1}$ arcmin $^{-2}$ for EPIC-PN and EPIC-MOS respectively ([Sturm et al. 2013](#)). Events were extracted using the SAS task `evselect` by applying the standard filtering criteria (`#XMMEA_EP && PATTERN<=4` for EPIC-PN and `#XMMEA_EM && PATTERN<=12` for EPIC-MOS).

In order to investigate whether the hard X-ray point-like source is extended, we extracted a radial profile centered on the source in the energy range of 1–2 keV from the EPIC-PN image (ObsID 0301170301) as the signal to noise ratio peaks in this energy range. This was fitted with a Gaussian

⁴ <http://gleam-vo.icrar.org>

⁵ <https://github.com/PaulHancock/Aegean>

⁶ Science Analysis Software (SAS): <http://xmm.esac.esa.int/sas/>

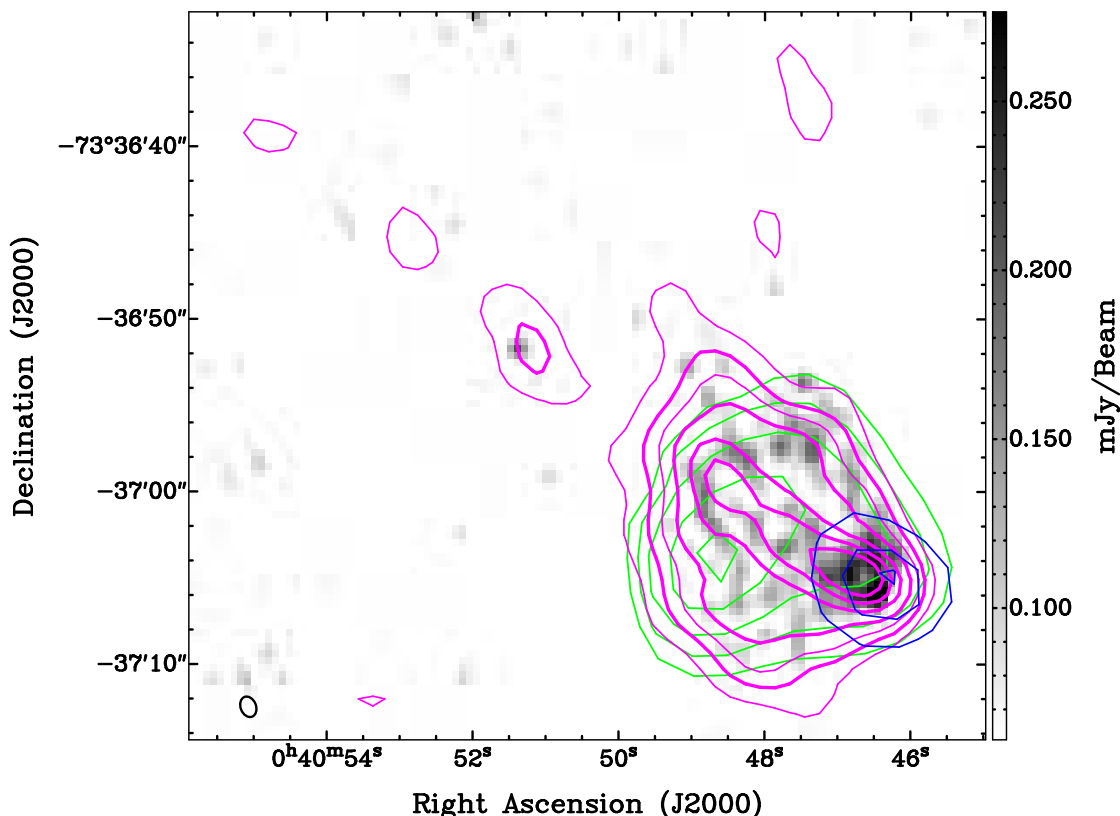


Figure 3. A zoomed in image of the point-like source (pulsar) and PWN within DEM S5 showing a comparison between the radio and X-ray wavelengths. The gray-scale image is from the ATCA observation at 5500 MHz, magenta contours are from the 2100 MHz image (0.3, 0.5, 0.7, 1, 1.5, 2, and 2.5 mJy beam⁻¹); green contours are from *XMM-Newton* (0.2–1 keV; 1.7, 1.9, 2.1, 2.3, and 2.5 × 10⁻⁵ cts s⁻¹ pixel⁻¹); and blue contours are the *XMM-Newton* (2–4.5 keV; levels are 1.1, 1.3, and 1.4 × 10⁻⁵ cts s⁻¹ pixel⁻¹). The black ellipse in the lower left corner represents the synthesised beam width of 1.2 × 0.89 arcsec. An RMS noise at 5500 MHz image is 0.013 mJy beam⁻¹ and 0.1 mJy beam⁻¹ at 2100 MHz image.

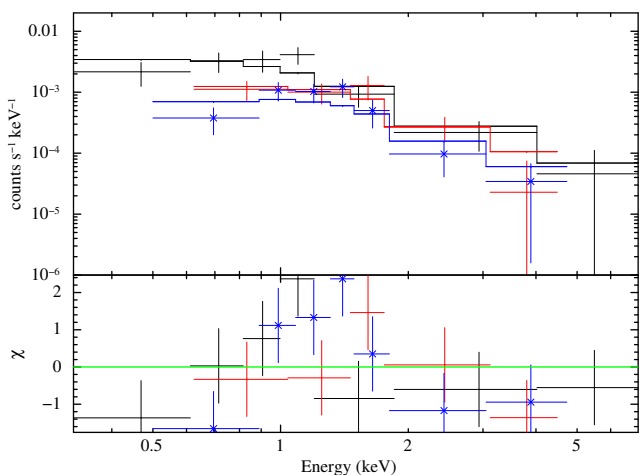


Figure 4. The upper panel shows the simultaneous spectral fit using spectra from all the available *XMM-Newton*/EPIC cameras (PN: ObsID 0301170301 in black, MOS2: ObsID 0301170301 in red and MOS2: ObsID 0764780201 in blue double crosses) along with the best-fit model. The lower panel displays the residuals after the fit. The plots have been rebinned for visual clarity.

profile and the derived width was compared to that of the *XMM-Newton* Point Spread Function (PSF) at the source position. The radial profile of the hard X-ray source is consistent with the PSF and we derived a 3σ upper limit of 14 arcsec for the X-ray extent of the PWN. To further investigate the presence of a diffuse soft X-ray emission that may be associated with the source (and as may be indicated from Fig. 3, green contours), we performed the same exercise of comparison with the PSF in the energy range of 0.5–1 keV. An additional soft X-ray emission is detected peaking at ~ 78 arcsec, which originates from the X-ray SNR with its peak in emission at this distance (see X-ray image in Fig. 1).

We extracted the spectrum of the hard X-ray point source using a circular region of radius 20 arcsec centered around the source position obtained by Filipović et al. (2008). The background was chosen from two circular regions of radius 20 arcsec north and south of the source extraction region at a similar distance to the centre of the SNR. This should remove the contribution of soft X-ray emission from the SNR DEM S5, but given the irregular morphology of the SNR some uncertainty remains.

The SAS tasks `rmfgen` and `arfgen` were used to create the redistribution matrices and ancillary files for the spectral analysis. The spectrum was binned to achieve a minimum of one count per spectral bin. The spectral analysis was per-

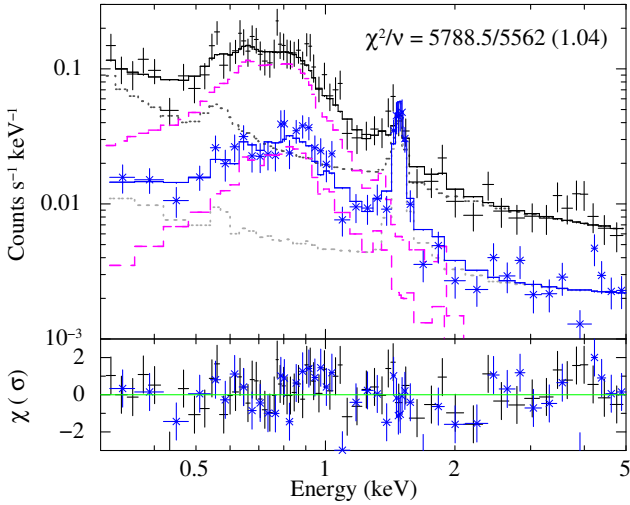


Figure 5. X-ray spectra of the diffuse emission of SNR DEM S5. Colours for data are the same as in Fig. 4, but MOS data for ObsID 0301170301 have been omitted for the sake of clarity. The total background models for PN and MOS are shown by the dotted gray lines. The SNR emission models are shown by the dashed magenta lines, as convolved with the PN and MOS spectral responses (top and bottom curves, respectively). The lower panel displays the residuals.

formed using the XSPEC fitting package, version 12.9 (Arnaud 1996) using the C-statistic. Errors were estimated at 90 percent confidence intervals. The spectra from both observations were fitted simultaneously with absorbed single-component emission models. Given the low statistics of the spectra power-law (photon index $\Gamma \sim 2$), Bremsstrahlung (temperature $kT \sim 1.7$ keV) and APEC plasma emission ($kT \sim 2.1$ keV) yield formally indistinguishable fit quality (χ^2 values of 121.2, 121.1 and 119.9, respectively, for 185 deg of freedom). The spectra with best-fit absorbed power-law model is shown in Fig. 4. The index of the emitting particles (p) has been calculated by using the equation $p = \Gamma \times 2 - 1$, where Γ is the index of the (synchrotron) energy spectrum. The p value is consistent with the expected range of $1 \leq p \leq 3$ for non-thermal emission. The spectral parameters are tabulated in Table 4. No excess absorption was required apart from the Galactic value along the line of sight to the SMC. This is in further support of the source being located at the near side of the SMC and argues against the source being a background object, as the absorption at the source position through the depth of the SMC is $N_{HI} \sim 4 \times 10^{21} \text{ cm}^{-2}$ (Stanimirovic et al. 1999). The value of Γ is consistent with typical X-ray spectral slopes observed in (Kargaltsev & Pavlov 2008) as is expected from non-thermal synchrotron emission originating from a PWN/pulsar. We further verified that the X-ray spectral shape and the flux were stable between the two *XMM-Newton* observations separated by 8-years by setting the Γ and normalizations free between the observations. A non-varying spectrum is in further support of a PWN (containing a putative pulsar unresolved in the current observations) origin of the source. The detection of a hard X-ray point source with *XMM-Newton* ascertains the fact that we are unable to further resolve the PWN/pulsar

composite, and require a higher spatial resolution on-axis *Chandra* observation for the purpose.

In parallel, we extracted spectra for the diffuse X-ray emission in the east part of the SNR. For such faint *extended* emission we did not subtract background emission, but rather modeled all sources of background directly in the analysis and added a model for the diffuse emission on top of it. The method we used has been described extensively for *XMM-Newton* in Maggi et al. (2016). Even though we included MOS2 data from a second *XMM-Newton* observation (Table 3) not available in the first analysis of Filipović et al. (2008), the analysis is still hampered by a relatively short exposure time and off-axis location of the source.

The spectrum of the diffuse emission, shown in Fig. 5, is obviously thermal, typical for shock-heated plasma in SNRs. We fit the spectrum with a non-equilibrium ionisation shock model with variable abundances (`vpshock` in XSPEC), finding a temperature $kT = 0.65^{+0.09}_{-0.12}$ keV and ionisation age $n_{\text{et}} = 2.2^{(+1.3)}_{-0.9} \times 10^{11} \text{ s cm}^{-3}$. When left free, the abundances of the main elements (O, Ne, Mg, Fe, and Si) do not depart significantly from the SMC ISM abundance pattern (Russell & Dopita 1992). With an observed flux in the 0.5–8 keV band of $(7.6 \pm 0.5) \times 10^{-14} \text{ erg cm}^{-2} \text{ s}^{-1}$ absorption-corrected flux of $(1.01^{+0.40}_{-0.15}) \times 10^{-13} \text{ erg cm}^{-2} \text{ s}^{-1}$, DEMS5 is in the faint end of the SMC SNR population (e.g. Maggi et al. 2016). The best-fit absorption column (on top of the Galactic one) is relatively low ($N_H = 1.1 \times 10^{21} \text{ cm}^{-2}$) and at the 3σ level consistent with 0, as for the PWN candidate. Therefore, from the point of view of absorption, both the hard X-ray source and the diffuse emission are consistent within one another.

Naively, the shape and location of this emission would suggest that it is thermal emission from the supernova ejecta which was shocked and heated by the reverse shock. However, this is not sustained by the data, which are fully consistent with SMC abundances, suggesting instead a shocked ISM origin. It remains possible that shock-heated ejecta contribute to the diffuse emission, at a level low enough not to be significantly detected in the available *XMM-Newton* data.

2.3 Optical and Infrared observations

The Magellanic Cloud Emission Line Survey (MCELS) was carried out at the 0.6-m University of Michigan/CTIO Curtis Schmidt telescope, equipped with a SITE 2048 \times 2048 CCD, which gave a field of 1.35×1.35 deg at a scale of 2.4×2.4 arcsec pixel $^{-1}$ (Smith et al. 2000; Pellegrini et al. 2012). The SMC was mapped in narrow bands corresponding to $H\alpha$, [O III] ($\lambda = 5007 \text{ \AA}$), and [S II] ($\lambda = 6716, 6731 \text{ \AA}$), plus matched red and green continuum bands. All the data have been continuum subtracted, flux-calibrated and assembled into mosaic images. A cutout around the area of DEMS5 can be seen in Fig. 6.

We also make use of SMC observations from *Spitzer* SAGE (Surveying the Agents of a Galaxy’s Evolution, Gordon et al. 2011). Specifically, we used 4 IRAC bands: band-1 ($3.6 \mu\text{m}$), band-2 ($4.5 \mu\text{m}$), band-3 ($5.8 \mu\text{m}$), and band-4 ($8.0 \mu\text{m}$), as well as MIPS at $24 \mu\text{m}$.

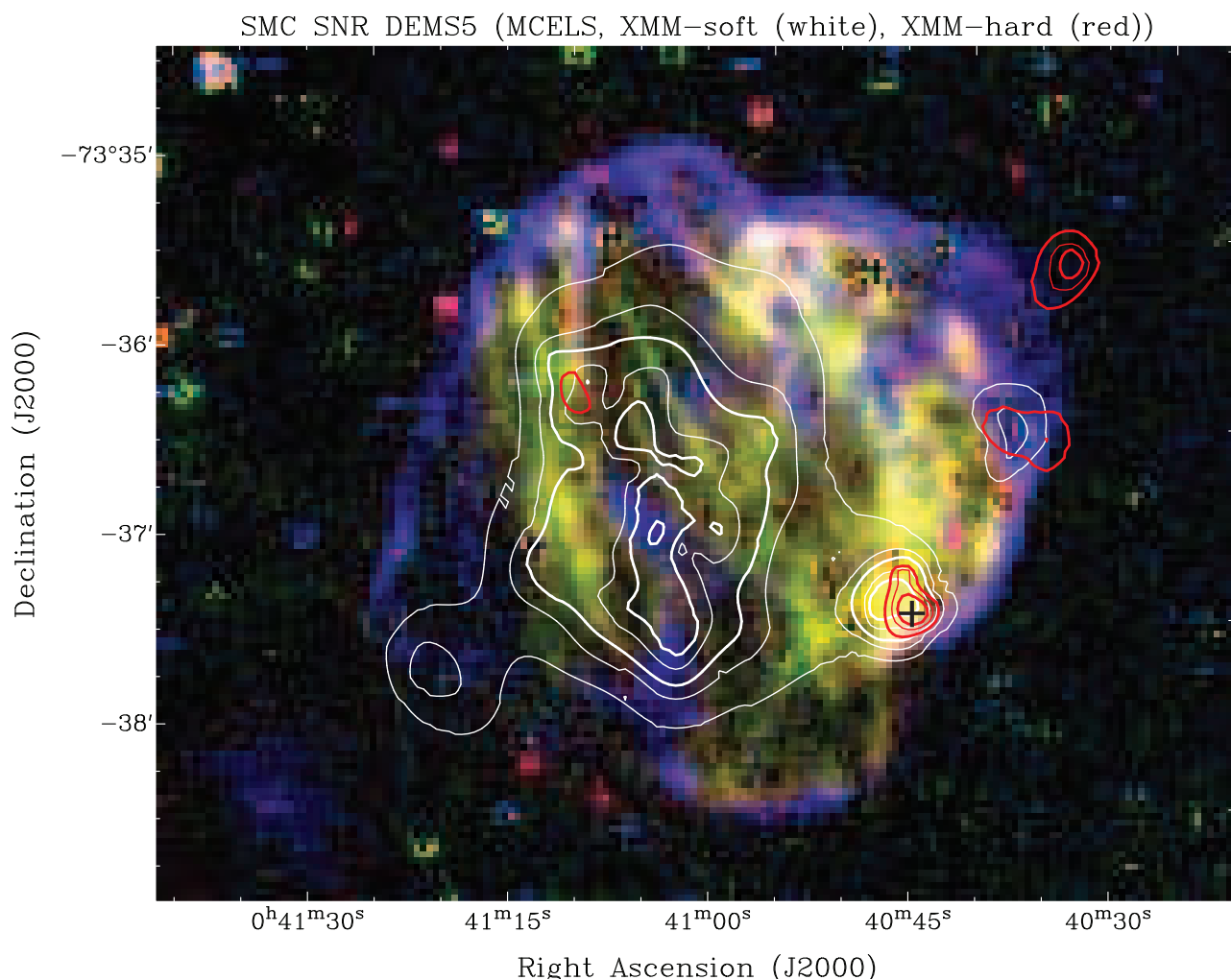


Figure 6. MCELS composite image of DEMS5 (RGB= $H\alpha$, [S II], [O III]) overlaid with *XMM-Newton* EPIC contours, soft (0.2–1 keV) in white (levels are 0.5, 0.75, 1, 1.5, and 2×10^{-5} cts s^{-1} pixel $^{-1}$) and hard (2–4.5 keV) in red (levels are 0.5, 0.75, and 1×10^{-5} cts s^{-1} pixel $^{-1}$). The position of the suggested pulsar is marked with a black plus sign.

Table 1. Summary of ATCA observations for DEM S5.

Date	Project code	Array configuration	Integrated time (minutes)	Flux density calibration	Phase calibration	Channels	Frequency (MHz)	Bandwidth (MHz)
2014-12-30	CX310	6A	29.3	1934–638	0230–790	2049	5500, 9000	2048
2014-12-31	CX310	6A	153	1934–638	0230–790	2049	2100	2048
2015-01-04	CX310	6A	37.3	1934–638	0230–790	2049	5500, 9000	2048
2017-12-22	CX403	6C	377.3	0252–712	0230–790	2049	5500, 9000	2048

2.4 H I observations

Observations of H I have previously been carried out over the whole SMC (20 deg^2) by [Stanimirovic et al. \(1999\)](#) using the ATCA 375-m configuration and the Parkes telescopes. The angular resolution was 98 arcsec, and velocity resolution was 1.65 km s^{-1} , with a column density sensitivity of $4.2 \times 10^{18} \text{ cm}^{-2}$ in the same velocity interval. The heliocentric reference frame was used to define velocities.

Recent ASKAP data are also available over a simi-

lar field-of-view, but at the higher angular resolution of $27 \times 35 \text{ arcsec}$ and the lower velocity resolution of 3.9 km s^{-1} ([McClure-Griffiths et al. 2018](#)). The column density sensitivity per 3.9 km s^{-1} channel is similar to the ATCA data at $5.2 \times 10^{18} \text{ cm}^{-2}$.

Table 2. Measurements of integrated flux density of DEMS5 PWN and putative pulsar as well as the unrelated background source found within the field of DEMS5. Because of the poor survey resolution and sensitivity we couldn't detect or measure the flux density of the pulsar and background source at MWA frequencies.

ν (MHz)	PWN S_ν (Jy)	Pulsar S_ν (Jy)	Background S_ν (Jy)	Telescope	Reference
88	0.288 ± 0.089			MWA	For et al. (2018)
118	0.256 ± 0.052			MWA	For et al. (2018)
155	0.234 ± 0.040			MWA	For et al. (2018)
200	0.205 ± 0.033			MWA	For et al. (2018)
843	0.150 ± 0.015		0.0044 ± 0.0005	MOST	Maggi et. al. (in prep.)
960	0.138 ± 0.014		0.0038 ± 0.0004	ASKAP	Joseph et. al. (in prep.)
1320	0.130 ± 0.013		0.0028 ± 0.0003	ASKAP	Joseph et. al. (in prep.)
1420	0.128 ± 0.013			ATCA	Maggi et. al. (in prep.)
2100	–	0.003 ± 0.001	0.0017 ± 0.0002	ATCA	This work
2370	0.114 ± 0.011			ATCA	Maggi et. al. (in prep.)
4800	0.085 ± 0.009			ATCA	Maggi et. al. (in prep.)
5500	–	0.00042 ± 0.00003	0.00087 ± 0.00003	ATCA	This work
8640	0.072 ± 0.007			ATCA	Maggi et. al. (in prep.)
9000	–	0.00022 ± 0.00007	0.00065 ± 0.00007	ATCA	This work
$\alpha \pm \Delta\alpha$	-0.29 ± 0.01	-1.8 ± 0.2	-0.81 ± 0.04		

Table 3. *XMM-Newton* observations of the hard X-ray point source inside DEMS5.

Date	ObsID	Exposure PN / MOS2 (ks)	CCD Readout mode PN / MOS2	Off-axis angle PN / MOS2	Telescope vignetting PN / MOS2
yyyy/mm/dd					
2006/06/04	0301170301	15.5 / 21.1	Full Frame / Full Frame	8.4' / 7.4'	0.61 / 0.65
2015/10/16	0764780201	– / 47.9	Small Window / Full Frame	– / 9.7'	– / 0.53

3 RESULTS

3.1 PWN and compact source inside the SNR DEMS5

We detect a point-like source at 5500 MHz, which we consider likely to be a pulsar, at RA(J2000) = $00^h40^m46.49^s$, and DEC(J2000) = $-73^\circ37'5.8''$, with a trail/jet behind it and a nebulosity which is morphologically indicative of a PWN (Fig. 3). This trail is clearly visible only in our 2100 and 1320 MHz images because of the sensitivity and missing short spacings at higher frequencies. One should also consider that this trail might be a so-called ‘relic’ PWN behind the present putative pulsar similar to Galactic SNR/PWN G5.4–1.2 (Kothes 2017). While somewhat unlikely, as the trail is still part of PWN-system (see Fig. 1), only future higher sensitivity and resolution radio continuum observations may reveal true nature of this possibility.

The position of the radio point source is also coincident with the hard X-ray point source. There seems to be a small displacement (< 2 arcsec) between the centremost blue (2–4.5 keV) X-ray contour and the radio point-like source. This is attributed to the fact that the X-ray counterpart of the putative pulsar cannot be separated from the PWN/pulsar composite with the current *XMM-Newton* observations and hence its accurate X-ray position cannot be ascertained. Fig. 3 further shows that the PWN emission close to the pulsar is dominated by hard X-rays. This is due to the fact that the X-ray synchrotron electrons have a much shorter

lifetime than radio ones and the X-ray synchrotron spectrum from the PWN would get steeper when moving further away from the pulsar.

The measured integrated flux density of the point source (putative pulsar) at 5500 and 9000 MHz is 0.42 mJy ($\sim 14\sigma$) and < 0.22 mJy ($\sim 3\sigma$) respectively. At 2100 MHz, we cannot precisely measure flux density, but there is a strong indication of an order of magnitude stronger integrated flux density (around 3 mJy, see Table 2). This would make the SED of this point source (putative pulsar) very steep with a spectral index of $\alpha \sim -1.8$. The SED of most known Galactic pulsars can be described above 100 MHz by a simple power-law with a mean spectral index of ~ -1.8 (Han et al. 2016), with a range from -0.46 to -4.84 . Therefore, we propose that this point source is most likely the compact remnant (pulsar or a fast spinning NS) of the DEMS5 supernova explosion with its associated PWN. Also, ultra steep spectrum and Compact Steep Spectrum (CSS) sources would have such a steep radio spectrum (Collier et al. 2016). However, as we see the nebulosity behind the point source, it is very unlikely to be CSS with jet Active Galactic Nuclei (AGN) like structure.

Figs. 1, 3 and 7 show trail-like emission from PWN with the length of ~ 37 arcsec (~ 10.8 pc). The direction of the trail is pointing towards the geometric centre of the SNR (RA(J2000) = $00^h41^m01.675^s$ and DEC(J2000) = $-73^\circ36'30.38''$). We also note that the putative pulsar (compact source) is ‘leading’ the conically shaped PWN that trail

behind it. This is a strong indication that the putative pulsar is moving away from the SNR explosion site at a supersonic velocity (see Table 5). Morphologically, this would qualify the DEM S5 system (pulsar and PWN) as a ‘rifle bullet’ type (Barkov et al. 2019) where the spin and velocity are aligned. The most likely Galactic bow shock PWN analog would be PSR B1951+32 in SNR CTB 80 (see Safi-Harb et al. 1995; Moon et al. 2004) and ‘mouse’ PWN (J1747–2956) (Gaensler et al. 2004; Klingler et al. 2018) where a similar morphology is detected. However, according to Kargaltsev et al. (2017) PSR B1951+32 doesn’t move supersonically. Fig. 7 clearly shows that the putative pulsar with its PWN is reaching the edge of the optical remnant. The putative pulsar may be even outside of it, if the motion is not entirely perpendicular to the line of sight. Although purely visually, it would be probably just at the edge. The densities outside and inside the SNR should be different, with outside expected to be much higher. Therefore, we expect the PWN to be somewhat narrower with higher ambient density.

In Table 5, we used various SNR ages (from 5 to 50 kyr) to estimate the kick (transverse) velocity of the pulsar. We also varied the distance to DEM S5 as Scowcroft et al. (2016) suggested that at the western end of the SMC might reach up to 67.5 kpc. The observed distance between the radio point-like source (putative pulsar) and the centre of the SNR is measured to be ~ 73 arcsec (or 21.2/23.9 pc at the 60/67.5 kpc distance respectively and assuming motion to be perpendicular to the line of sight).

The kick (transverse) velocities in other similar PWN bow shock systems are estimated to be in range of 60–2000 km s^{-1} (Kargaltsev et al. 2017, see their table 1) for the pulsar through the ambient medium. We take this velocity as a possible upper limit which then indicates a very high DEM S5 pulsar velocity through the ambient medium given that the minimum age would be in order of >10 kyr (see Table 5). Other constraints on the age of DEM S5 come from the IKT 16 PWN/SNR system which has an estimated age of 14.7 kyr and has a somewhat larger SNR diameter of 74.5 pc vs 67.6 pc for DEM S5 indicating that IKT 16 PWN/SNR is expanding at a somewhat lower rate probably because the local environment is denser than in/around DEM S5 ($N_{\text{HI}} \sim 4 \times 10^{21} \text{ cm}^{-2}$ for DEM S5 vs. $N_{\text{HI}} \sim 6 \times 10^{21} \text{ cm}^{-2}$ for IKT 16). However, one should be cautious about the line-of-sight column density, calculated by integrating along several kpc for the SMC because of variations in the local ambient medium density. This would suggest that the age of DEM S5 PWN is between 10 and 15 kyr with kick velocities of ~ 1500 – 2500 km s^{-1} . Also, Reynolds et al. (2017) suggest that the pulsar would eventually leave the SNR at an age of ~ 20 – 200 kyr which further limits our DEM S5 PWN as it is still within the SNR boundaries. Given a lower age limit of ~ 10 kyr, the kick-off velocity of $\sim 2000 \text{ km s}^{-1}$ is derived using its distance from the DEM S5 geometric centre, which is the most likely explosion site in a uniform ISM. If the ISM is inhomogeneous or has a large scale gradient the explosion site would be shifted (~ 4.5 arcsec or 1.3 pc) from the geometrical centre towards the west (at RA(J2000) = $00^{\text{h}}41^{\text{m}}01.53^{\text{s}}$ and DEC(J2000) = $-73^{\circ}36'26.6''$; with ellipse radius of $\sim 34 \times 22$ pc). In any case, a large kick velocity would certainly still need to be accounted for. We emphasize that the age and size of different SNRs might not be appropriate to

compare as they all come with their own unique characteristics.

The fastest known moving pulsars are ‘Morla’ (J0357+3205) (Kargaltsev et al. 2017; Marelli et al. 2013) and ‘Lighthouse’ (Pavan et al. 2014a,b; Kargaltsev et al. 2017) at $\sim 2000 \text{ km s}^{-1}$. We note that our DEM S5 PWN cometary tail has a conical shape with the angle behind the putative pulsar of ~ 75 – 80 deg, which suggests somewhat slower velocity than $\sim 2000 \text{ km s}^{-1}$ that we estimate above; unless our PWN system is not just characterised as ‘rifle bullet’ but also ‘frisbee’ or ‘cart-wheel’ (Barkov et al. 2019). Additionally, Holland-Ashford et al. (2017) and Katsuda et al. (2018) suggested that pulsars move preferentially opposite to the ejecta, which lends support to the interpretation that the diffuse X-ray emission originates from shock heated ejecta.

DEM S5 is a very large SNR in general, which argues for a late stage of evolution. We use Cioffi et al. (1988) for calculations of radiative SNRs. Using their equations for the onset of the pressure driven snowplow or radiative phase, we obtain a minimum ambient density of 0.35 cm^{-3} and a lower limit for the age of 24 kyr, using 22 pc radius (towards the west) and 10^{51} erg for the explosion energy – certainly nothing unusual. For a density of 1 cm^{-3} the age would be about 48 kyr but the age estimate could be even a lot higher. We also need to consider the amount of material that would have been swept up in such a large volume if we have normal densities. For this to still be a Sedov SNR we would need very low densities to make this still applicable. The largest distance between the most likely location of the supernova explosion and the edge of the SNR – as indicated by the [O III] shell – is almost straight to the east. In between, we find the diffuse X-ray emission, which might be including some shock heated ejecta. In this case, the reverse shock must have past this area which stretches all the way to the centre of the SNR. With an assumed ejecta mass of 10 solar masses, a radius of 40 pc and the canonical value for the explosion energy of 10^{51} erg, we require an ambient density of 0.02 cm^{-3} – if the reverse shock just reached the location of the SN (McKee & Truelove 1995, see their equations). This is the typical density in the interior of a stellar wind bubble (e.g. Weaver et al. 1977). With these parameters the age would be 28 kyr and the PWN/Pulsar system kick-off velocity would decrease to a ‘reasonable’ 700–800 km s^{-1} . We note that the ejecta mass is not very critical here. If we insert this into the equations of Cioffi et al. (1988) we get an ambient density of 0.45 cm^{-3} for the right (west) part of the SNR. Therefore, this scenario seems to be at least plausible. This implies that the supernova went off inside a low density bubble close to the edge. Alternatively, if the plasma temperature ($kT = 0.8 \text{ keV}$ represents that of shocked ambient ISM as the limited spectral analysis indicates, a naive Sedov model can be used to set an age $\gtrsim 15$ kyr, or, taking a non detection in X-ray of the outer, radiative shell ($kT \lesssim 0.16 \text{ keV}$), an even larger age limit of $\gtrsim 30$ kyr would be implied.

3.2 Radio Spectral Index

Using the flux density measurements from Table 2, we estimate a spectral index of $\alpha = -0.29 \pm 0.01$ across the remnant (including pulsar and PWN) (Fig. 8). The radio spectral index is estimated from the slope of a linear least squares

Table 4. X-ray spectral parameters of the point-like source in DEMS5. Absorption^b was fixed to $6 \times 10^{20} \text{ cm}^{-2}$. Errors are quoted at 90% confidence.

Parameters	Value
Γ	$1.99^{+0.26}_{-0.28}$
Flux ^a (0.5–8.0 keV)	3.1 ± 0.9
Flux (unabsorbed) ^a (0.3–8.0 keV)	3.6 ± 1.0
X-ray Luminosity at $d_{smc} = 60 \text{ kpc}$ (erg s^{-1})	1.5×10^{34}
X-ray Luminosity at $d_{smc} = 67.5 \text{ kpc}$ (erg s^{-1})	1.9×10^{34}

^a Flux in units of $10^{-14} \text{ erg cm}^{-2} \text{ s}^{-1}$

^b Absorption was fixed equal to the Galactic value along the line of sight of SMC to $N_{Hgal} = 6 \times 10^{20} \text{ cm}^{-2}$

regression, in logarithmic space. From all our radio images it is clear that emission from the putative PWN dominates the radio emission (see section 3.4).

The overall radio continuum spectral index $\alpha = -0.29 \pm 0.01$ of the remnant (Fig. 8) adds further support to our claim of the PWN nature of the emission. This value of α falls below that of a typical SNR of -0.5 (Bozzetto et al. 2017), and is in line with what is expected from a SNR/PWN system (e.g., the spectral index of the SNR and PWN for LMC SNR J0453–6829 is -0.39 ± 0.03 ; Haberl et al. (2012b)). As we were unable to disentangle the PWN emission from the rest of the shell, we were not able to estimate the spectral index of the SNR separately. We also note that the estimated value of $\alpha = -0.29$ could be somewhat flatter as our flux density estimates at lower frequencies includes the emission of the pulsar which might not be negligible but is a minor flux density contributor to the whole DEMS5 system (SNR-PWN-Pulsar). We cannot rule out radio emission from the shell but the present radio images show little evidence of any, so we assume that all the radio emission is coming from the putative pulsar (compact source) and its PWN even though we recognise that some emission must come from the SNR itself.

3.3 Search for the Radio Pulsar at Parkes

On 2018 September 14th we observed the point-like source for 2700 seconds using the Directors Time of the ATNF Parkes radio telescope in NSW, Australia. The central beam of the multibeam receiver was used and data were recorded using the Parkes Digital Filterbank (PDFB) systems. We used a 2-bit sampling and a sampling time of 64 microsecond with 512 frequency channels over 256 MHz bandwidth (centred at 1369 MHz). The pulsar searching software package PRESTO (Ransom 2001) was used to carry out RFI zapping and masking, de-dispersion and searches of periodic signals. We searched for dispersion measures (DMs) of up to $1000 \text{ cm}^{-3} \text{ pc}$, but found no convincing candidates with a S/N greater than 8. For a pulse period of 10 ms and DM of $200 \text{ cm}^{-3} \text{ pc}$ and assuming a pulse duty cycle of 10 percent, our observations provide a flux density limit of 0.24 mJy at 1369 MHz (see e.g., equation 9 of Dai et al. 2017).

Table 5. Derived Pulsar kick velocity for the DEMS5 progenitor: estimated as a function of SNR age ($V_{\text{psr}} = 2 \times d_{\text{smc}} \times \text{TAN}(\theta/2)/\text{age}$) which simplifies to $(\theta \times d_{\text{smc}})/\text{age}$ since $\theta \ll 1$. The angular distance is $\theta = 73 \text{ arcsec}$. The adopted distance of $d_{\text{smc}} = 67.5 \text{ kpc}$ for the western side of the SMC is suggested by Scowcroft et al. (2016).

SNR age (kyr)	$V_{\text{psr at 60 kpc}}$ (km s^{-1})	$V_{\text{psr at 67.5 kpc}}$ (km s^{-1})
5.0	4157	4676
7.5	2771	3117
10.0	2078	2338
12.5	1663	1870
15.0	1386	1559
17.5	1188	1336
20.0	1039	1169
22.5	924	1039
25.0	831	935
30.0	693	779
40.0	520	584
50.0	416	468

3.4 Radio Polarisation

Linear polarisation images of DEMS5 at 5500 MHz were created using the Q and U Stokes parameters as shown in Fig. 2. However, no reliable polarisation images could be created at any other frequency, due to the poor signal-to-noise ratio (9000 MHz) and depolarisation (2100 MHz) and/or missing short spacings. The fractional polarisation at 5500 MHz has been evaluated using the standard MIRIAD task `impol`. The majority of the polarised emission is located at the position of the suggested PWN. Our estimated peak fractional polarisation value is $P = 32 \pm 7$ percent while average polarisation is about 23 percent. Such polarisation that we detected in this area would disfavor extragalactic origin of the object and strongly advocate for the SMC birthplace. Moreover, this is in agreement with our other LMC PWN measurements such as Haberl et al. (2012b).

3.5 Optical Morphology

The outer borders of DEMS5 show that [O III] emission dominates in this part of the remnant (Figs. 6, 7 and 9). The X-rays show no oxygen enhancement and the [O III] emission clearly delineates the outer blast waves (Fig. 9; right panel). This indicates that it is likely caused by radiative shocks, since [O III] is the strongest coolant of gas at a few 10^5 K . Since DEMS5 is probably in a radiative phase it presents very different characteristics than found in much younger SNR like Cas A or G292.0+1.8.

DEMS5 is some 300 pc west of the main body of the SMC where the stellar environment and star formation would favour a Type Ia scenario (Maggi et al. 2016). This is the only known SMC SNR with a lack of recent star formation in the Star Formation History (SFH) map of Harris & Zaritsky (2004). All other SMC SNRs are associated with a recent peak in SFH, although some might be just in projection. However, it is possible that the progenitor of DEMS5 was itself a companion in a binary system that got ejected when the primary exploded (i.e. a runaway star), as the linear distance traveled by a runaway star would be

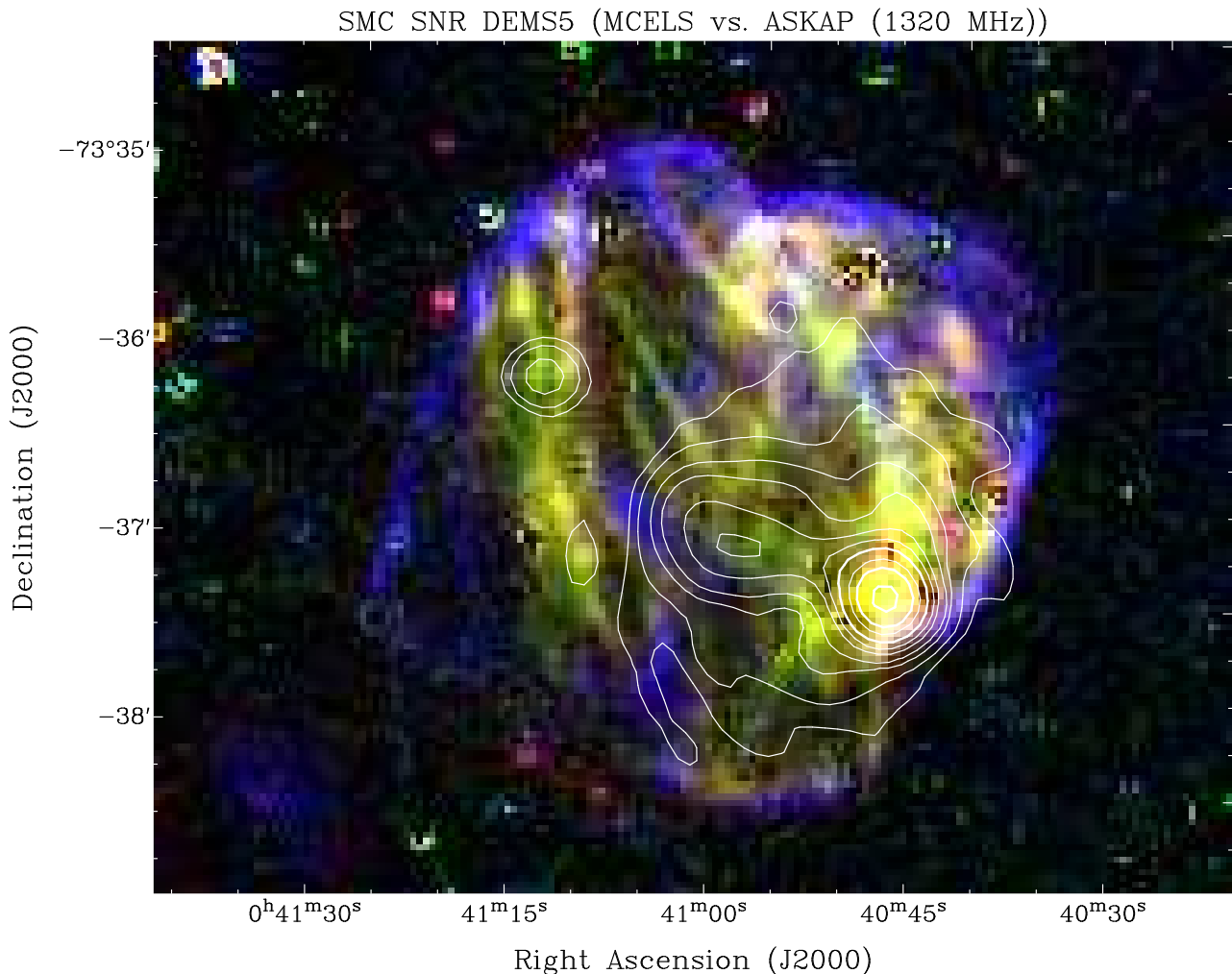


Figure 7. MCELS composite image of DEM S5 [HFPK 530] (RGB= H α , [S II], [O III]) overlaid with ASKAP contours (white solid) at 1320 MHz. The radio image contours are as same as in Fig. 1. An obvious radio continuum tail-like feature is clearly pointing towards the geometric centre of DEMS5. We also note a point source north-east from the remnant centre which we classify as a most likely background galaxy.

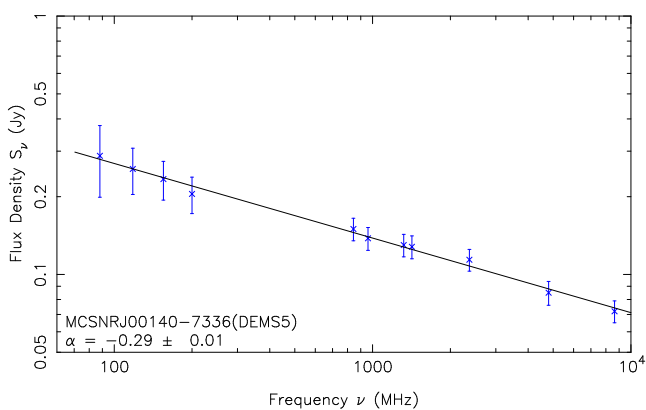


Figure 8. Radio continuum SED of PWN DEM S5.

$\sim 1000 (t/10 \text{ Myr}) (\nu/100 \text{ km s}^{-1}) \text{ pc}$. Therefore, it is possible that if the progenitor of DEM S5 was in a binary system with a much more massive (and thus short-lived) companion, it

had time to reach its current location, devoid of intense recent star-forming activity. Since the orientation of the PWN propagation is also away from the main body of the SMC, we consider the possibility that the motion of DEM S5 PWN could reflect the peculiar velocity of the progenitor star instead of a kick. However, the runaway velocity is unlikely to be that large, so possibly some compounded velocities (progenitor runaway + pulsar kick) are needed.

The central region is dominated by a keV-temperature thermal plasma from the X-rays (Fig. 9) that runs in the north-south direction of DEM S5. Diffuse X-ray emission to the left (east) in the interior is likely thermal emission from either shock-heated ISM or ejecta that was overran by the reverse shock, which now should have dissipated for the whole SNR. Therefore, the SNR is probably in a late stage of evolution and the missing or very weak radio synchrotron emission support that as well as the missing thermal X-ray emission from the shell. The radius differences seem to indicate that the right hand part (west) is further evolved and therefore expanding in a medium of higher density. The

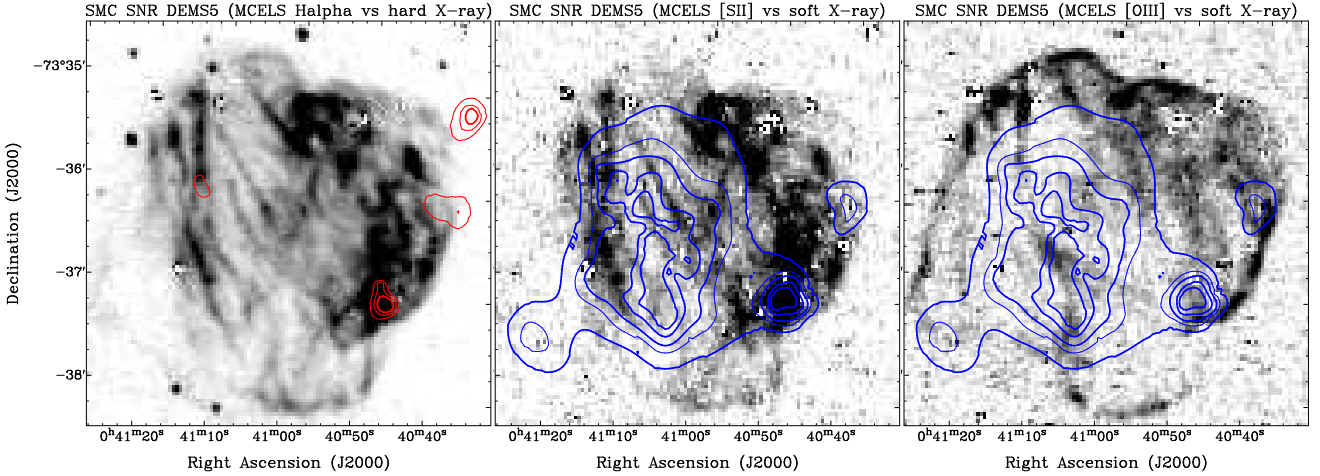


Figure 9. MCELS images of DEM S5 in $H\alpha$ (left; overlaid with the hard X-ray (2–4.5 keV) contours (red)), [S II] and [O III] (middle and right panel; overlaid with the soft band (0.2–1 keV) X-ray contours (blue)). X-ray contour levels are the same as in Fig. 6.

missing or very weak X-ray emission from the ejecta should support that too. We also recognise a somewhat smaller circular shell at the west side of DEM S5 in $H\alpha$ and [S II] bands. This could be because of a density gradient across the entire SNR. If so, the explosion site might not be at the geometric centre but offset to the west which could result in a somewhat lower putative pulsar kick velocity.

3.6 Infrared Morphology

We used the *Spitzer* SAGE survey (Gordon et al. 2011) to search for any extended mid-IR emission in the direction of DEM S5. We found enhanced emission in several bands with $8\ \mu\text{m}$ (IRAC band-4) being the most prominent (see Fig. 10). The IR emission clearly extends towards the north-west of DEM S5 and tightly follows the [S II]/ $H\alpha$ emission in this region just above the radio PWN. Neither the optical nor the IR emission peaks precisely at the putative pulsar position. However, we interpret this displacement as shocked gas trailing the whole PWN DEM S5 system. Alternatively, it could come from the SNR shock itself.

To ascertain the nature of the mid-IR nebulosity, we measure the integrated flux density in the brightest hotspots, and compare across the IRAC colors to discern the dominant emission components. The field is dense with stars, notably in the IRAC-1 band image, and we carefully choose the apertures to avoid stars while also maximizing the diffuse emission captured in the aperture. Three positions are identified, with apertures chosen to be 7.5 arcsec in radius, centered on the equatorial J2000 positions: (#1: 10.203408° , -73.617633°), (#2: 10.198245° , -73.608746°) and (#3: 10.225005° , -73.594583°). These positions correspond to the brightest IRAC-4 band nebulosity near the PWN and along the northern extension; see Figs. 10 and 11.

Emission is detected in all four IRAC bands for the three positions; the integrated flux density measurements (magnitude and mJy units) for the first and brightest position (marked #1 in Fig. 11) are shown in Table 6. We then compute the IRAC colors ratios: $F(4.5)/F(8.0)$ and

$F(3.6)/F(5.8)$, which are used to decode the emission. For the brightest hotspot, the corresponding colors are 0.56 and 0.41, respectively. The other two positions have similar colors: (0.46, 0.37) and (0.44, 0.35) for positions #2 and #3, respectively. The errors of the IRAC colour ratios are small (< few percent). We now consider the nature of the emission based on these colors.

Mid-IR emission arises from atomic, molecular and dust species, excited by star formation and shocks in the ISM. The four broad-bands of IRAC have been effectively used to study SNRs in the Milky Way, including those embedded within dense gas. Reach et al. (2006) modeled the major emission mechanisms and created a set of diagnostics to assess the mid-IR emission associated with SNRs (Reach et al. 2006, see their figs. 1 and 2). They considered thermal (star formation) and shock excitation, with the latter divided between the diffuse and dense gas ($n \sim > 10^2\ \text{cm}^{-3}$) ISM. For example, where ionic line emission dominates, the IRAC-3 and 4 bands tend to be very bright relative to the other bands due to the presence of strong [Ar II] and [Fe II] lines (see their fig. 1). The Galactic SNR RCW103 is a classic example of IRAC colors influenced by ionic-dominated lines. Alternatively, if the blast wave and subsequent shock passes through dense gas, the dominant coolant is molecular hydrogen, and in conjunction with a molecular CO band head in the IRAC-2 band window, the colors conspire to look very different from the ionic case. The other Galactic SNR IC443 is an example of a SNR embedded within a molecular cloud. The color-color diagnostic of Reach et al. (2006) is shown in Fig. 12, where we have plotted the colors of the DEM S5 mid-IR nebulosity.

Based on the IRAC mid-IR emission diagnostic, the DEM S5 nebulosity is consistent with shock-excited molecular hydrogen. It has colors that are similar to the notably (molecular cloud) embedded SNRs, such as in Galactic SNRs IC443, W44, G311.5, and G346.6 (Reach et al. 2006, see fig. 22). The IR emission is spatially coincident with the radio continuum (see Fig. 11), which may indicate synchrotron contribute to the infrared signal at some low level. Nevertheless, the IRAC colors clearly indicate that molecu-

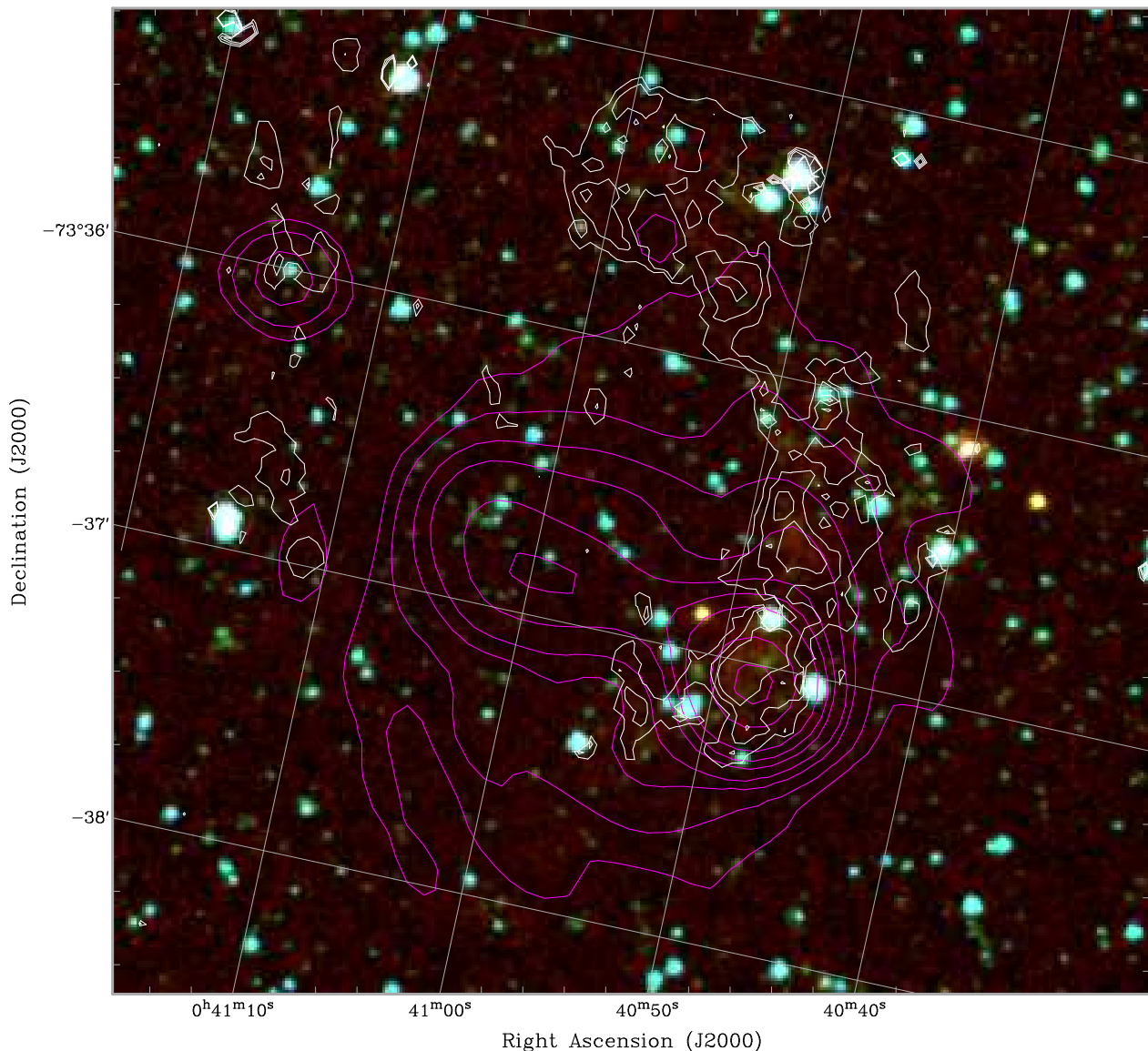


Figure 10. *Spitzer* RGB colour image of DEM S5 overlaid with ASKAP (1320 MHz) contours (magenta) and [S II] in white. Contours are the same as in Fig. 1. RGB images correspond to *Spitzer* IRAC band-4 (R; 8 μm), IRAC band-2 (G; 4.5 μm) and IRAC band-1 (B; 3.6 μm). Mid-IR emission nicely matches [S II] (and H α) indicating the presence of shocked gas.

lar emission is the dominant cooling mechanism of the shock front seen in DEM S5.

While it is not unusual to detect SNRs in the IR bands (see e.g. Reach et al. 2006; Bojčić et al. 2007; Lakićević et al. 2015) this would be the first bow shock supersonic PWN that potentially shows IR emission compared to a population of 28 described by Kargaltsev et al. (2017, see their table 1). However, there are a few cases in our Galaxy and in the LMC of detected IR emission from PWN, e.g. B0540–69.3 (Williams et al. 2008; Brantseg et al. 2014), G54.1+0.3 (Temim et al. 2010), and others. Still, none of these bright IR SNRs have bow-shock PWN that moves supersonically. At the same time, the prominent IR emission from DEM S5 clearly following the [S II] emission which would therefore argue for a more classical SNR shock rather than with the IR emission associated with the outer SNR shock rather than with the PWN/bow shock. Also, DEM S5 is just the second SMC

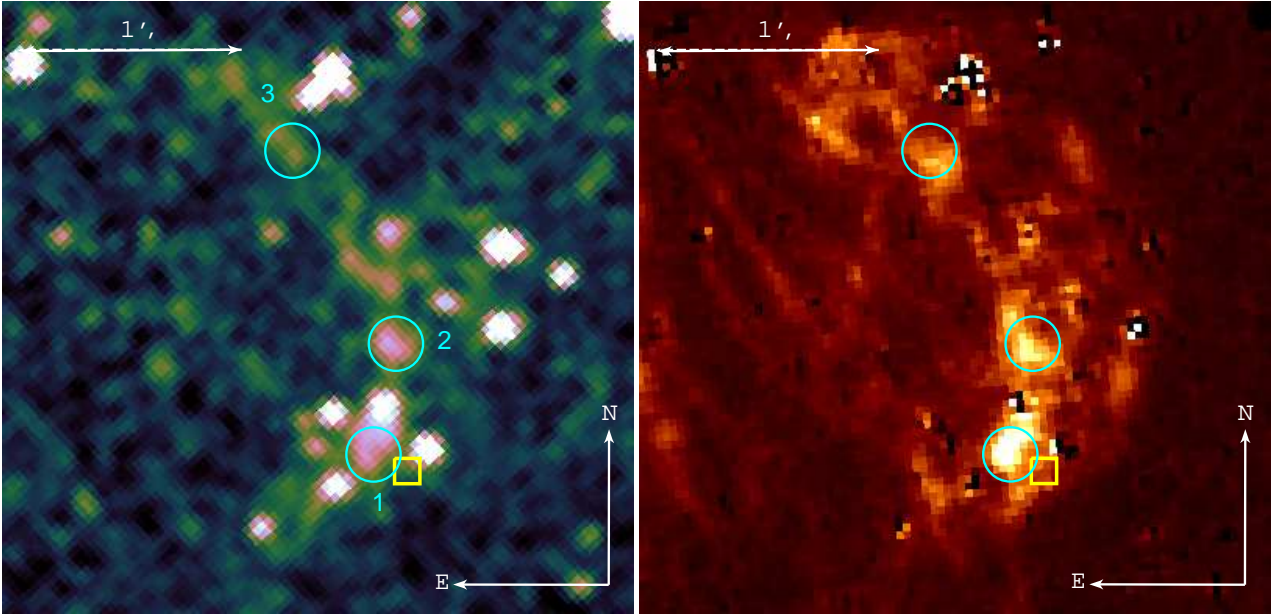
SNR (among a 25 SNR strong population) detected in IR along with SMC SNR J0106–7205 (a.k.a. IKT 25) (Koo et al. 2007) indicating that the SNR appearance in IR frequencies are indeed rare. However, the sensitivity of the present generation of IR telescopes and especially at the distance of the SMC might play an important role in the poor detection rate of IR emission from the SMC SNRs.

3.7 H I Morphology

Fig. 13 shows the velocity channel maps of H I obtained with the ATCA and Parkes telescopes (Stanimirovic et al. 1999). We find two prominent H I peaks at the radial velocities of $\sim 107 \text{ km s}^{-1}$ (hereafter low-velocity cloud) and $\sim 166 \text{ km s}^{-1}$ (hereafter high-velocity cloud). The intensity peak of the high-velocity cloud is $\sim 100 \text{ pc}$ away from the SNR (Fig. 13; bottom middle panel) and unlikely to be associated. For the

Table 6. Integrated flux density (7.5 arcsec radius aperture) of the mid-IR emission for the brightest hotspot (#1 from Fig. 11).

Band	RA(J2000) (degree)	Dec(J2000) (degree)	f (mJy)	mag	dmag	S/N
IRAC-1	10.20294	-73.61740	0.146	15.714	0.396	2.7
IRAC-2	10.20309	-73.61750	0.236	14.704	0.309	3.5
IRAC-3	10.20324	-73.61760	0.357	13.769	0.272	4.0
IRAC-4	10.20380	-73.61760	0.425	12.946	0.236	4.6

**Figure 11.** *Spitzer* western shock front of SNR DEM S5 as viewed in the IRAC-4 band ($8\mu\text{m}$; left panel) and the MCELS [S II] (right panel). Approximate position of the pulsar is marked with the yellow box. Indicated are the three apertures used to measure the mid-IR emission, each is 7.5 arcsec in radius, centered on the bright emission and avoiding field stars. These mid-IR hotspots are also bright in the radio continuum, indicating that at least some (if not most) of the emission arises from synchrotron.

low-velocity cloud the intensity peak shows a good spatial correspondence with the position of the SNR (Fig. 13; top middle panel), and a possible cavity-like structure is seen (top left panel). Recent data taken with the ASKAP telescope of the SMC (McClure-Griffiths et al. 2018) shows this cavity in more detail in Fig. 14. The ASKAP data has three times better spatial resolution (35×27 arcsec) compared to ATCA data and an RMS of 0.7 K per a 3.9 km s^{-1} wide spectral channel. Fig. 14 shows a filament like H I structure that has a cavity corresponding to the location and size of the H α emission of SNR DEM S5. A moment map in this velocity range of $96\text{--}104 \text{ km s}^{-1}$ of the ASKAP data is shown in Fig. 15.

However, the radius of this cavity (~ 70 pc) is over twice as large as the SNR, so may not be directly associated, or may represent the combined energy input from the progenitor and previous generations of nearby stars and SNe. Possible line-splitting is present. If interpreted as shell expansion, the expansion velocity is $\sim 8 \text{ km s}^{-1}$, which leads to a dynamical age of 5 Myr, an average mechanical luminosity of $\sim 400 L_{\odot}$ and a total energy of 2×10^{50} erg, assuming an ambient density of 2 cm^{-3} (Staveley-Smith et al. 1997). These

values indicate that an association with the SNR is plausible, particularly if the SNR has re-accelerated a shell or pre-existing structure created by past events.

4 DISCUSSION

We explore two possible scenarios for the nature of this object. Namely:

(i) A PWN associated with DEM S5: This is supported by (a) the detection of a radio point source coincident with the hard X-ray point source (PWN/pulsar composite), (b) an X-ray spectrum consistent with a power law with photon index typical as seen from PWN/pulsar spectra and the stability of the X-ray flux, (c) the radio spectral indices and (d) shocked IR emission. In the case of PWNe, the extent of the radio emission is generally greater than that in X-rays because of the longer cooling time of radio-emitting electrons. The radio emission may therefore trace the path of the PWN from the centre of the SNR as indicated by the current radio data of DEM S5 at 2100 MHz (Fig. 6). The detection of the cometary morphology in radio indicates a large

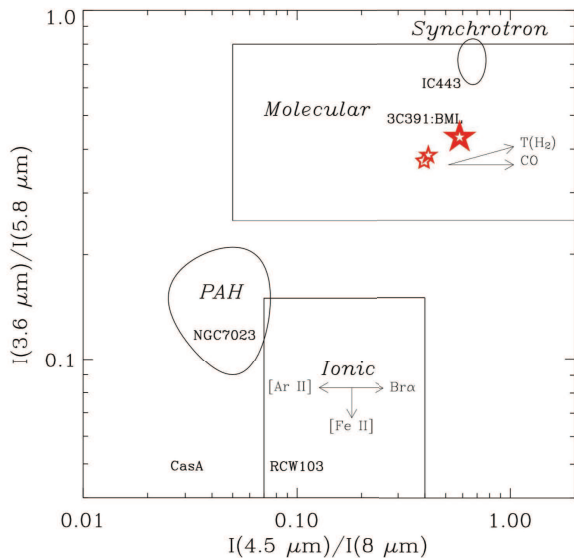


Figure 12. *Spitzer* IRAC color-color diagram, adapted from Reach et al. (2006), shows where the dominant emission mechanism appear in color space. Three basic classes are shown: PAH and H II emission from star formation, ionic shock emission and molecular shock emission. Based on the measurements in the three apertures (Figs. 10 and 11), the mid-IR emission in DEMS5 has colors (indicated by the red stars) that clearly indicate molecular hydrogen emission is dominating the broad-band imaging.

kick velocity of the pulsar at birth. The estimated distance between the point-like source and the centre of the SNR indicates that the transverse velocity of the putative pulsar could be as high as $\sim 2000 \text{ km s}^{-1}$ with an age of 10–15 kyr. The lower and somewhat more realistic limits would put this SNR/PWN system into ~ 28 kyr age and kick-off velocity of $700\text{--}800 \text{ km s}^{-1}$. Determination of the putative pulsar velocity is important to determine the birth kick distribution of the NS which can further constrain supernova explosion models and kick mechanisms (e.g. Ng & Romani 2007). Finding such a source in the SMC is particularly exciting as there might be differences in the pulsar birth, explosion and kick properties in the low-metallicity environment of SMC.

To some extent DEMS5 resembles similar morphological appearance like two well-studied LMC SNRs – MC-SNR J0508–6902 (Bozzetto et al. 2014) and MCSNR J0527–7104 (Kavanagh et al. 2016) as well as, for example, Galactic SNR MSH 11-61A (Filipovic et al. 2005a) or G332.5–5.6 (Stupar et al. 2007). While two LMC SNRs are classified as a likely Type Ia, they all have apparent ‘mixed-morphology’ appearance where SNR looks quite different at different wavebands. Mixed-morphology SNRs have shell-like radio morphologies combined with center-filled X-ray morphologies. The central X-ray morphology is produced by thermal emission rather than a central PWN (Rho & Petre 1998; Pannuti et al. 2017). What makes DEMS5 different from other so called ‘mixed-morphology’ SNRs is its bow-shock PWN.

(ii) An AGN in the background of the SMC: It is possible that the hard X-ray point source is not associated with the SNR but is instead a background AGN coincident with the

SMC. The diffuse radio emission would in this case be due to a radio lobe or jets. A greater absorption component would then be expected to account for the line of sight through the SMC, although this may be sometimes balanced by a soft excess component (Turner & Pounds 1989). As seen in Section 2.2, the absorption at the source position through the depth of the SMC indicates that the source is most likely located in the SMC. We also searched for a possible AGN association of the source using the ALLWISE criterion in the mid-infrared and from the existing quasar catalogs. We did not find any AGN within 3σ of the source position (Maitra et al. 2018).

5 CONCLUSIONS AND FUTURE STUDIES

We have presented results of a newly discovered pulsar-powered nebula associated with SNR DEMS5 in the SMC. The object exhibits a cometary morphology which suggests a pulsar leading the PWN and traveling supersonically through the ambient medium. This is the first detected extragalactic source to exhibit this type of morphology. The distance of this object (~ 21.2 pc) from the centre of DEMS5 SNR would require a kick velocity as high as $\sim 2000 \text{ km s}^{-1}$ and as low as $\sim 700 \text{ km s}^{-1}$ for the pulsar at birth. The SNR/PWN/Pulsar system exhibits a typically flat SED of -0.29 ± 0.01 in line with most other PWNe. We found no convincing DMs candidates (up to 1000 cm^{-3} pc) with a S/N greater than 8. We also detect radio polarisation in the locale of the emission from this object with a peak (fractional) value at 5500 MHz of $P = 32 \pm 7$ percent and average of ~ 23 percent which strongly indicates non-thermal emission. At IR frequencies, we detect associated shock emission that indicates that the DEMS5 SNR is still expanding. Finally, our H I velocity channel maps show possible interaction with the low-velocity cloud at $\sim 107 \text{ km s}^{-1}$.

Future follow-up multi-frequency observations of this object with a high spatial resolution in X-rays will be able to accurately measure the extent of the hard X-ray point source within DEMS5, and resolve the compact object from the diffuse nebula. We will also search for a radio pulsar at this position. Another objective will be to accurately measure the position of the compact object within DEMS5, which will help to better constrain the motion of the pulsar within the SNR and identify its counterpart at other wavelengths.

Finally, the study of PWNe at TeV gamma-ray energies (where the inverse-Compton process provides the gamma-ray photons) allows important constraints on the magnetic field and transport properties of the PWN electrons (e.g. Aharonian et al. 1997). The now well-established X-ray and TeV gamma-ray emission correlation in PWNe (Mattana et al. 2009; Kargaltsev et al. 2013; H. E. S. S. Collaboration et al. 2018) can provide a prediction of the potential TeV flux. For the pulsar spin-down power and characteristic age of DEMS5, the TeV flux could be a factor 5 to 10 times higher than its X-ray flux ($3.6 \times 10^{-14} \text{ erg cm}^{-2} \text{ s}^{-1}$). Such a TeV flux level is within the reach of the forthcoming Čerenkov Telescope Array (CTA) (Martin et al. 2019; Cherenkov Telescope Array Consortium et al. 2019). A similar X-ray to TeV flux scaling may apply to the other PWN in the SMC, IKT 16 (Maitra et al. 2015), bringing it within the reach of the CTA.

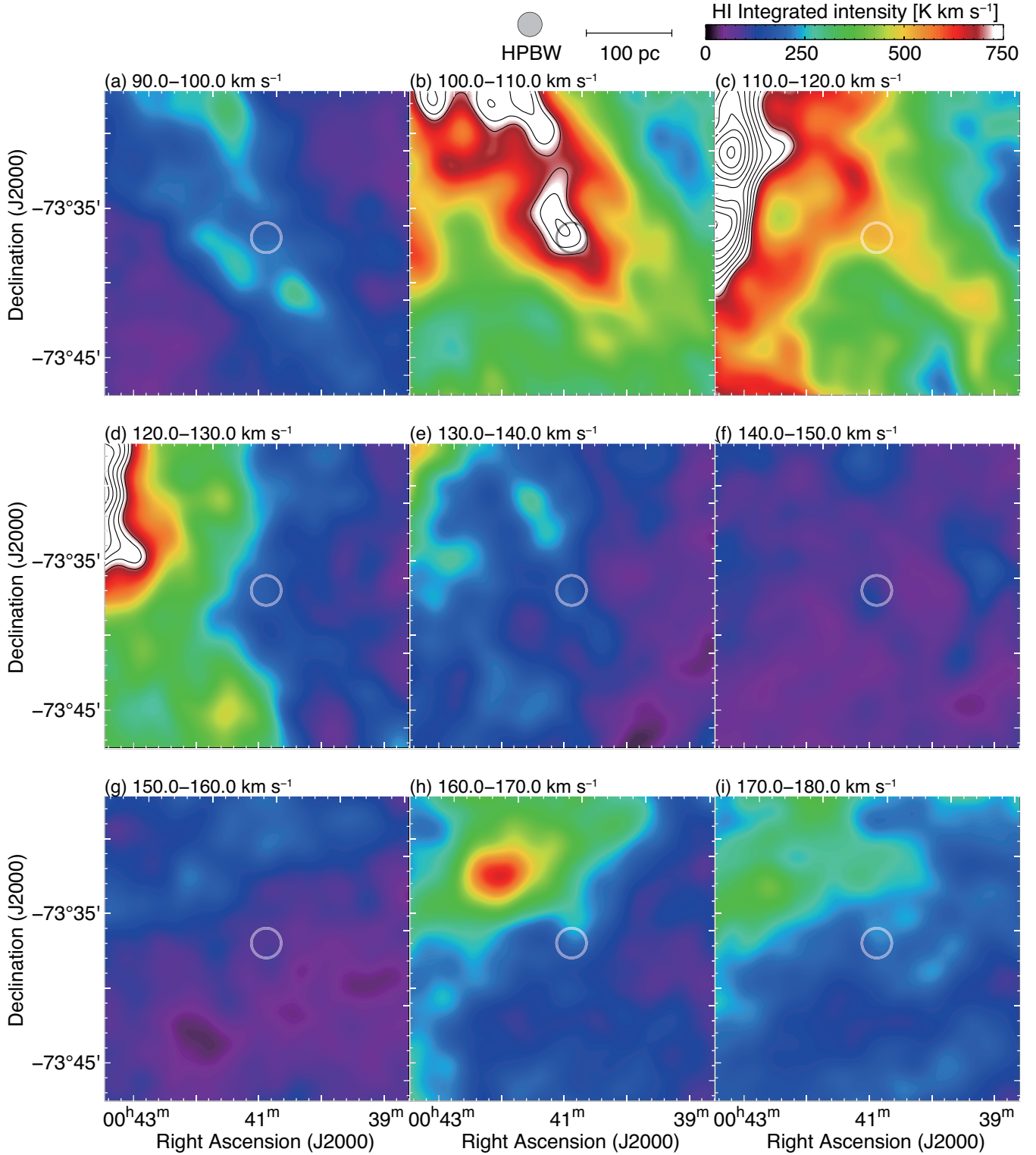


Figure 13. Velocity channel maps of HI toward SNR DEMS5 obtained with the ATCA and Parkes telescopes (Stanimirovic et al. 1999). Each panel shows HI intensity distribution integrated every 10 km s^{-1} in a velocity range from 90 to 180 km s^{-1} . Superposed circles indicate a shell boundary of the SNR. The scale bar and beam size of HI are also shown.

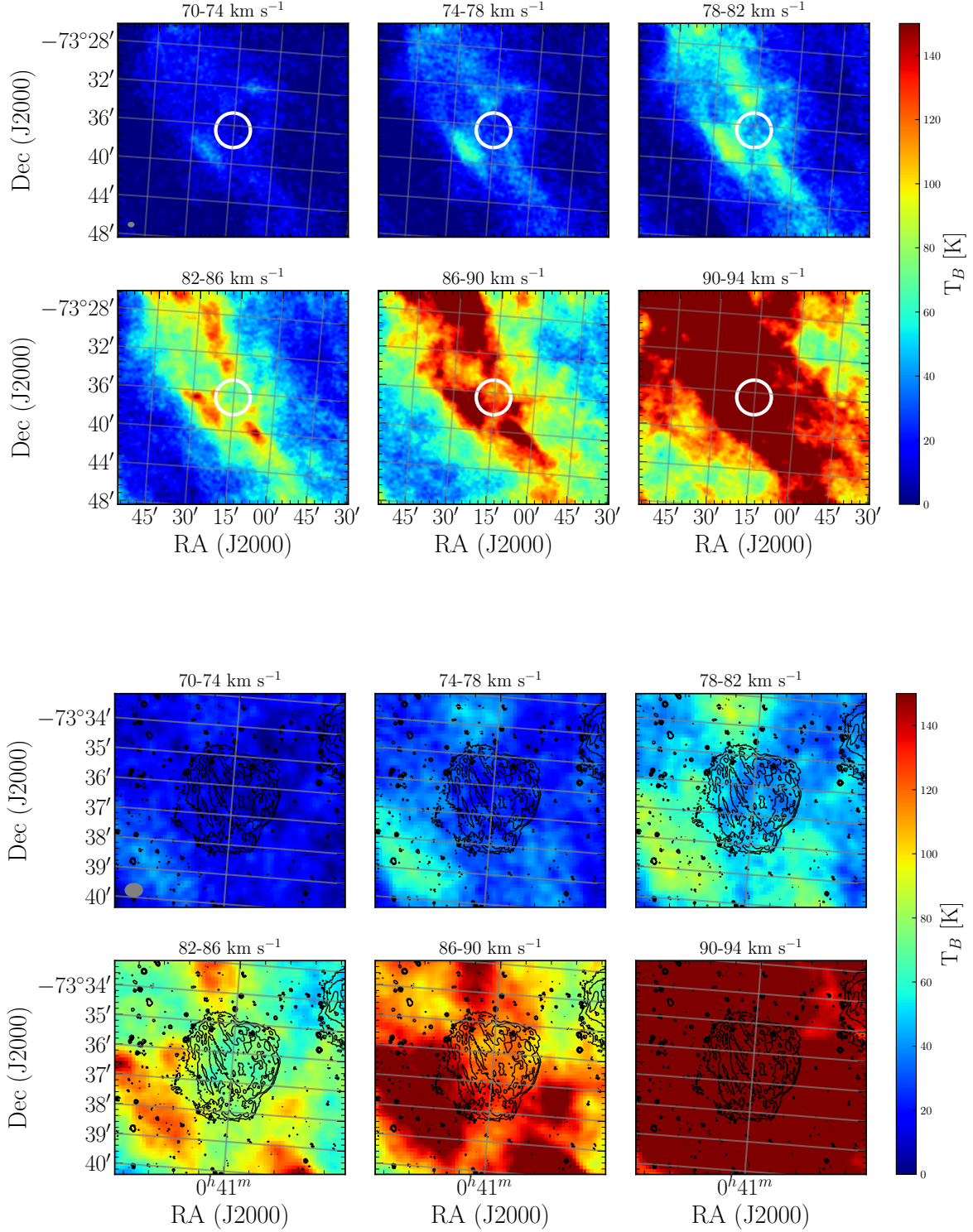


Figure 14. Integrated H I moment maps (70–94 km s⁻¹) toward SNR DEM S5 obtained with the ASKAP and Parkes telescopes (McClure-Griffiths et al. 2018). The maps are integrated over 4 km s⁻¹. A colour bar is shown on the right hand side and the beam size is shown at the bottom left corner of the first images. The top panel shows a 22 arcmin region around SNR DEM S5. The white circle indicates the size and location of the SNR. The bottom panel shows the same region zoomed into the inner 7 arcmin and with the H α contours (25, 50, 100, and 200 $\times 10^{-17}$ ergs cm⁻² s⁻¹) overlaid.

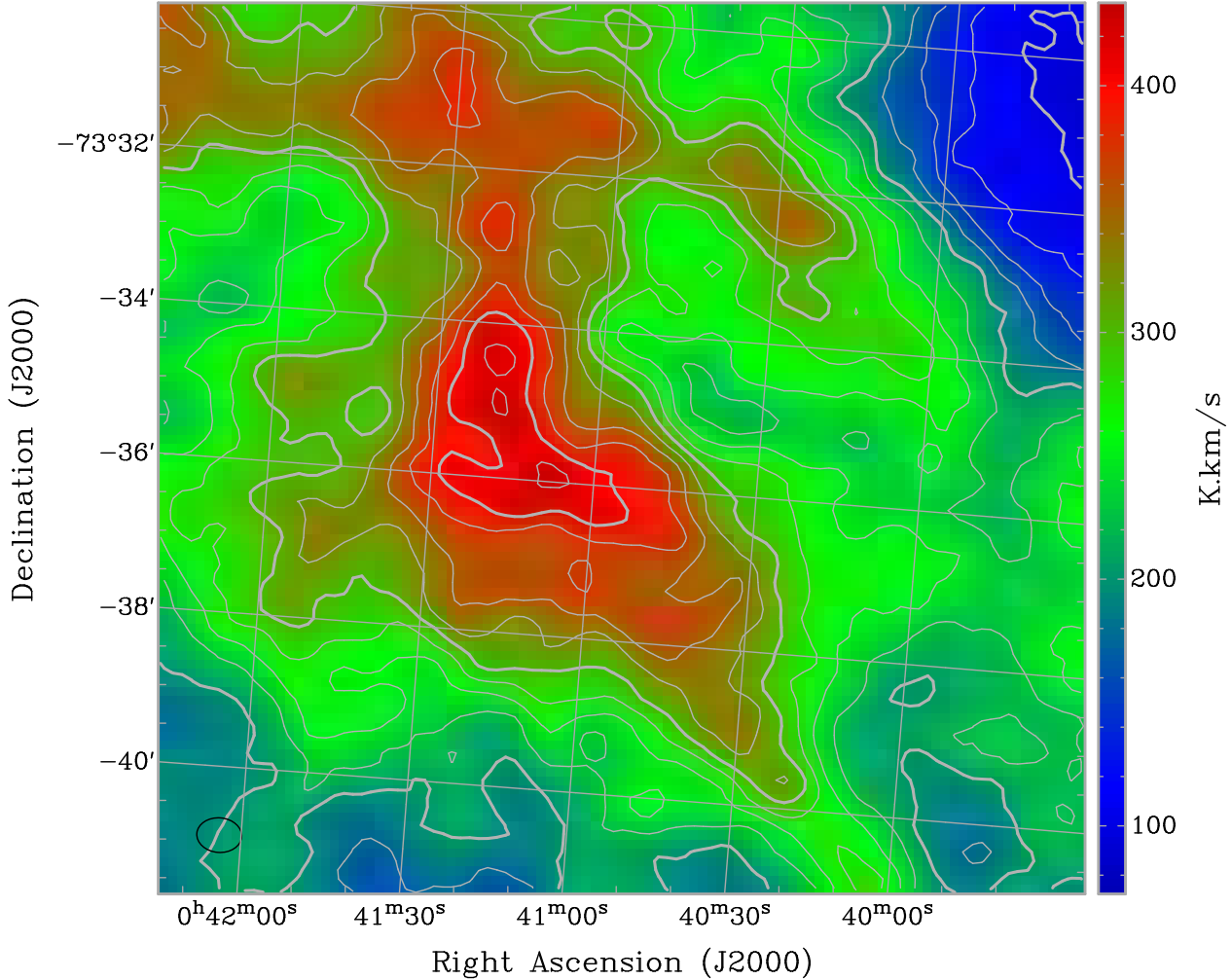


Figure 15. An integrated HI moment map toward SNR DEMS5 obtained with the ASKAP and Parkes telescopes (McClure-Griffiths et al. 2018). The map is integrated over two channels (8 km s^{-1}) centred at a heliocentric velocity of 100 km s^{-1} . The contours are spaced at intervals of 25 K km s^{-1} starting at 75 K km s^{-1} . Bold contours are at intervals of 100 K km s^{-1} starting at 100 K km s^{-1} . A colour bar is shown on the right hand side and the beam size is shown at the bottom left.

ACKNOWLEDGEMENTS

The Australian Compact Array and the Australian SKA Pathfinder (ASKAP) are part of the Australian Telescope which is funded by the Commonwealth of Australia for operation as National Facility managed by CSIRO. This paper includes archived data obtained through the Australia Telescope Online Archive (<http://atoa.atnf.csiro.au>). We used the KARMA and MIRIAD software packages developed by the ATNF. Operation of ASKAP is funded by the Australian Government with support from the National Collaborative Research Infrastructure Strategy. ASKAP uses the resources of the Pawsey Supercomputing Centre. Establishment of ASKAP, the Murchison Radio-astronomy Observatory and the Pawsey Supercomputing Centre are initiatives of the Australian Government, with support from the Government of Western Australia and the Science and Indus-

try Endowment Fund. We acknowledge the Wajarri Yamatji people as the traditional owners of the Observatory site. M.S. acknowledges support by the Deutsche Forschungsgemeinschaft (DFG) through the Heisenberg research grant SA 2131/4-1 and the Heisenberg professor grant SA 2131/5-1. This work is part of project No. 176005, ‘Emission nebulae: structure and evolution’, supported by the Ministry of Education, Science, and Technological Development of the Republic of Serbia. Parts of this research were conducted with support of Australian Research Council Centre of Excellence for All Sky Astrophysics in 3 Dimensions (ASTRO 3D), through project number CE170100013. The authors would like to thank the anonymous referee for a constructive report and useful comments.

REFERENCES

- Aharonian F. A., Atayan A. M., Kifune T., 1997, *MNRAS*, **291**, 162
- Arnaud K. A., 1996, in Jacoby G. H., Barnes J., eds, *Astronomical Society of the Pacific Conference Series Vol. 101, Astronomical Data Analysis Software and Systems V*. p. 17
- Barkov M. V., Lyutikov M., Khangulyan D., 2019, *MNRAS*, **484**, 4760
- Besla G., Kallivayalil N., Hernquist L., Robertson B., Cox T. J., van der Marel R. P., Alcock C., 2007, *ApJ*, **668**, 949
- Bojičić I. S., Filipović M. D., Parker Q. A., Payne J. L., Jones P. A., Reid W., Kawamura A., Fukui Y., 2007, *MNRAS*, **378**, 1237
- Bozzetto L. M., et al., 2012, *MNRAS*, **420**, 2588
- Bozzetto L. M., et al., 2014, *MNRAS*, **439**, 1110
- Bozzetto L. M., et al., 2017, *ApJS*, **230**, 2
- Brantseg T., McEntaffer R. L., Bozzetto L. M., Filipovic M., Grieves N., 2014, *ApJ*, **780**, 50
- Cherenkov Telescope Array Consortium T., et al., 2019, *Science with the Cherenkov Telescope Array*. WORLD SCIENTIFIC (<https://www.worldscientific.com/doi/pdf/10.1142/10986>), [doi:10.1142/10986](https://doi.org/10.1142/10986), <https://www.worldscientific.com/doi/abs/10.1142/10986>
- Cioffi D. F., McKee C. F., Bertschinger E., 1988, *ApJ*, **334**, 252
- Collier J. D., Norris R. P., Filipović M. D., Tohill N. F. H., 2016, *Astronomische Nachrichten*, **337**, 36
- Crawford E. J., Filipovic M. D., de Horta A. Y., Wong G. F., Tohill N. F. H., Draskovic D., Collier J. D., Galvin T. J., 2011, *Serbian Astronomical Journal*, **183**, 95
- Crawford E. J., Filipović M. D., McEntaffer R. L., Brantseg T., Heitritter K., Roper Q., Haberl F., Urošević D., 2014, *AJ*, **148**, 99
- Dai S., Johnston S., Hobbs G., 2017, *MNRAS*, **472**, 1458
- Filipovic M. D., Jones P. A., White G. L., Haynes R. F., Klein U., Wielebinski R., 1997, *A&AS*, **121**, 321
- Filipovic M. D., Haynes R. F., White G. L., Jones P. A., 1998, *A&AS*, **130**, 421
- Filipović M. D., Bohlens T., Reid W., Staveley-Smith L., Jones P. A., Nohejl K., Goldstein G., 2002, *MNRAS*, **335**, 1085
- Filipovic M. D., Payne J. L., Jones P. A., 2005a, *Serbian Astronomical Journal*, **170**, 47
- Filipović M. D., Payne J. L., Reid W., Danforth C. W., Staveley-Smith L., Jones P. A., White G. L., 2005b, *MNRAS*, **364**, 217
- Filipović M. D., et al., 2008, *A&A*, **485**, 63
- For B. Q., et al., 2018, *MNRAS*, **480**, 2743
- Gaensler B. M., van der Swaluw E., Camilo F., Kaspi V. M., Baganoff F. K., Yusef-Zadeh F., Manchester R. N., 2004, *ApJ*, **616**, 383
- Gooch R., 1995, in Shaw R. A., Payne H. E., Hayes J. J. E., eds, *Astronomical Society of the Pacific Conference Series Vol. 77, Astronomical Data Analysis Software and Systems IV*. p. 144
- Gordon K. D., et al., 2011, *AJ*, **142**, 102
- H. E. S. S. Collaboration et al., 2018, *A&A*, **612**, A3
- Haberl F., Sturm R., 2016, *A&A*, **586**, A81
- Haberl F., Sturm R., Filipović M. D., Pietsch W., Crawford E. J., 2012a, *A&A*, **537**, L1
- Haberl F., et al., 2012b, *A&A*, **543**, A154
- Haberl F., et al., 2012c, *A&A*, **545**, A128
- Han J., Wang C., Xu J., Han J.-L., 2016, *Research in Astronomy and Astrophysics*, **16**, 159
- Hancock P. J., Murphy T., Gaensler B. M., Hopkins A., Curran J. R., 2012, *MNRAS*, **422**, 1812
- Hancock P. J., Trott C. M., Hurley-Walker N., 2018, *Publ. Astron. Soc. Australia*, **35**, e011
- Harris J., Zaritsky D., 2004, *AJ*, **127**, 1531
- Holland-Ashford T., Lopez L. A., Auchettl K., Temim T., Ramirez-Ruiz E., 2017, *ApJ*, **844**, 84
- Hurley-Walker N., et al., 2017, *MNRAS*, **464**, 1146
- Kargaltsev O., Pavlov G. G., 2008, in Bassa C., Wang Z., Cumming A., Kaspi V. M., eds, *American Institute of Physics Conference Series Vol. 983, 40 Years of Pulsars: Millisecond Pulsars, Magnetars and More*. pp 171–185 ([arXiv:0801.2602](https://arxiv.org/abs/0801.2602)), [doi:10.1063/1.2900138](https://doi.org/10.1063/1.2900138)
- Kargaltsev O., Rangelov B., Pavlov G. G., 2013, preprint, [p. arXiv:1305.2552 \(arXiv:1305.2552\)](https://arxiv.org/abs/1305.2552)
- Kargaltsev O., Pavlov G. G., Klingler N., Rangelov B., 2017, *Journal of Plasma Physics*, **83**, 635830501
- Katsuda S., et al., 2018, *ApJ*, **856**, 18
- Kavanagh P. J., et al., 2016, *A&A*, **586**, A4
- Klinger R. J., Dickel J. R., Fields B. D., Milne D. K., 2002, *AJ*, **124**, 2135
- Klingler N., Kargaltsev O., Pavlov G. G., Ng C.-Y., Beniamini P., Volkov I., 2018, *ApJ*, **861**, 5
- Koo B.-C., et al., 2007, *PASJ*, **59**, S455
- Kothes R., 2017, *Radio Properties of Pulsar Wind Nebulae*. Springer International Publishing, Cham, pp 1–27, [doi:10.1007/978-3-319-63031-1_1](https://doi.org/10.1007/978-3-319-63031-1_1), https://doi.org/10.1007/978-3-319-63031-1_1
- Lakićević M., et al., 2015, *ApJ*, **799**, 50
- Macri L. M., Stanek K., Bersier D., Greenhill L., Reid M., 2006, *The Astrophysical Journal*, **652**, 1133
- Maggi P., et al., 2016, *A&A*, **585**, A162
- Maitra C., Ballet J., Filipović M. D., Haberl F., Tiengo A., Grieve K., Roper Q., 2015, *A&A*, **584**, A41
- Maitra C., Ballet J., Esposito P., Haberl F., Tiengo A., Filipović M. D., Acero F., 2018, *A&A*, **612**, A87
- Marelli M., et al., 2013, *ApJ*, **765**, 36
- Martin P., Lu C.-C., Voelk H., Renaud M., Filipovic M., 2019, *KSP: Large Magellanic Cloud Survey*. pp 125–141 (<https://www.worldscientific.com/doi/pdf/10.1142/97898132700910007>), [doi:10.1142/97898132700910007](https://doi.org/10.1142/97898132700910007), <https://www.worldscientific.com/doi/abs/10.1142/97898132700910007>
- Mattana F., et al., 2009, *ApJ*, **694**, 12
- McClure-Griffiths N. M., et al., 2018, *Nature Astronomy*, **2**, 901
- McKee C. F., Truelove J. K., 1995, *Phys. Rep.*, **256**, 157
- Moon D. S., et al., 2004, *ApJ*, **610**, L33
- Ng C.-Y., Romani R. W., 2007, *ApJ*, **660**, 1357
- Owen R. A., et al., 2011, *A&A*, **530**, A132
- Pannuti T. G., et al., 2017, *ApJ*, **839**, 59
- Pavan L., et al., 2014a, in *International Journal of Modern Physics Conference Series*. p. 1460172, [doi:10.1142/S2010194514601720](https://doi.org/10.1142/S2010194514601720)
- Pavan L., et al., 2014b, *A&A*, **562**, A122
- Payne J. L., Filipović M. D., Reid W., Jones P. A., Staveley-Smith L., White G. L., 2004, *MNRAS*, **355**, 44
- Payne J. L., White G. L., Filipović M. D., Pannuti T. G., 2007, *MNRAS*, **376**, 1793
- Pellegrini E. W., Oey M. S., Winkler P. F., Points S. D., Smith R. C., Jaskot A. E., Zastrow J., 2012, *ApJ*, **755**, 40
- Ransom S. M., 2001, in *American Astronomical Society Meeting Abstracts*. p. 119.03
- Reach W. T., et al., 2006, *AJ*, **131**, 1479
- Reid W. A., Payne J. L., Filipović M. D., Danforth C. W., Jones P. A., White G. L., Staveley-Smith L., 2006, *MNRAS*, **367**, 1379
- Reynolds S. P., Pavlov G. G., Kargaltsev O., Klingler N., Renaud M., Mereghetti S., 2017, *Space Sci. Rev.*, **207**, 175
- Rho J., Petre R., 1998, *ApJ*, **503**, L167
- Roper Q., McEntaffer R. L., DeRoo C., Filipovic M., Wong G. F., Crawford E. J., 2015, *ApJ*, **803**, 106
- Russell S. C., Dopita M. A., 1992, *ApJ*, **384**, 508
- Safi-Harb S., Ogelman H., Finley J. P., 1995, *ApJ*, **439**, 722
- Sault R. J., Wieringa M. H., 1994, *A&AS*, **108**, 585
- Sault R. J., Teuben P. J., Wright M. C. H., 1995, in Shaw R. A.,

- Payne H. E., Hayes J. J. E., eds, *Astronomical Society of the Pacific Conference Series Vol. 77, Astronomical Data Analysis Software and Systems IV*. p. 433 ([arXiv:astro-ph/0612759](https://arxiv.org/abs/astro-ph/0612759))
- Scowcroft V., Freedman W. L., Madore B. F., Monson A., Persson S. E., Rich J., Seibert M., Rigby J. R., 2016, *The Astrophysical Journal*, 816, 49
- Smith C., Leiton R., Pizarro S., 2000, in Alloin D., Olsen K., Galaz G., eds, *Astronomical Society of the Pacific Conference Series Vol. 221, Stars, Gas and Dust in Galaxies: Exploring the Links*. p. 83
- Stanimirovic S., Staveley-Smith L., Dickey J. M., Sault R. J., Snowden S. L., 1999, *MNRAS*, 302, 417
- Staveley-Smith L., Sault R. J., Hatzidimitriou D., Kesteven M. J., McConnell D., 1997, *MNRAS*, 289, 225
- Strüder L., et al., 2001, *A&A*, 365, L18
- Stupar M., Parker Q. A., Filipović M. D., Frew D. J., Bojčić I., Aschenbach B., 2007, *MNRAS*, 381, 377
- Sturm R., et al., 2013, *A&A*, 558, A3
- Temim T., Slane P., Reynolds S. P., Raymond J. C., Borkowski K. J., 2010, *ApJ*, 710, 309
- Tiengo A., Esposito P., Mereghetti S., 2008, *ApJ*, 680, L133
- Turner T. J., Pounds K. A., 1989, *MNRAS*, 240, 833
- Turner M. J. L., et al., 2001, *A&A*, 365, L27
- Turtle A. J., Ye T., Amy S. W., Nicholls J., 1998, *Publ. Astron. Soc. Australia*, 15, 280
- Weaver R., McCray R., Castor J., Shapiro P., Moore R., 1977, *ApJ*, 218, 377
- Williams B. J., et al., 2008, *ApJ*, 687, 1054
- Wong G. F., Filipovic M. D., Crawford E. J., de Horta A. Y., Galvin T., Draskovic D., Payne J. L., 2011a, *Serbian Astronomical Journal*, 182, 43
- Wong G. F., et al., 2011b, *Serbian Astronomical Journal*, 183, 103
- Wong G. F., et al., 2012a, *Serbian Astronomical Journal*, 184, 93
- Wong G. F., Filipovic M. D., Crawford E. J., Tothill N. F. H., De Horta A. Y., Galvin T. J., 2012b, *Serbian Astronomical Journal*, 185, 53

This paper has been typeset from a $\text{T}_{\text{E}}\text{X}/\text{L}_{\text{A}}\text{T}_{\text{E}}\text{X}$ file prepared by the author.

Appendix D

The ASKAP-EMU Early Science Project: Radio Continuum Survey of the Small Magellanic Cloud

This chapter is a reproduction of: Joseph, T. D., Filipović, M. D., Crawford, E. J., Bojčić, I., *et al.* (2019).
The ASKAP EMU Early Science Project: radio continuum survey of the Small Magellanic Cloud. *MNRAS*,
490(1):1202

The ASKAP-EMU Early Science Project: Radio Continuum Survey of the Small Magellanic Cloud

T. D. Joseph,^{1*} M. D. Filipović,² E. J. Crawford,² I. Bojičić,² E. L. Alexander,¹ G. F. Wong,^{2,3} H. Andernach,⁴ H. Leverenz,² R. P. Norris,^{2,3} R. Z. E. Alsaberi,² C. Anderson,³ L. A. Barnes,² L. M. Bozzetto,² F. Bufano,⁶ J. D. Bunton,⁵ F. Cavallaro,⁶ J. D. Collier,^{2,7} H. Dénes,⁸ Y. Fukui,^{9,10} T. Galvin,^{2,3} F. Haberl,¹¹ A. Ingallinera,⁶ A. D. Kapinska,¹² B. S. Koribalski,³ R. Kothes,¹³ D. Li,^{14,15} P. Maggi,¹⁶ C. Maitra,¹¹ P. Manojlović,^{2,3} J. Marvil,¹² N. I. Maxted,^{2,17} A. N. O'Brien,^{2,3} J. M. Oliveira,¹⁸ C. M. Pennock,¹⁸ S. Riggi,⁶ G. Rowell,¹⁹ L. Rudnick,²⁰ H. Sano,^{9,10} M. Sasaki,²¹ N. Seymour,²² R. Soria,^{15,23} M. Stupar,² N. F. H. Tothill,² C. Trigilio,⁶ K. Tsuge,¹⁰ G. Umana,⁶ D. Urošević,^{24,25} J. Th. van Loon,¹⁸ E. Vardoulaki,²⁶ V. Velović,² M. Yew,² D. Leahy,²⁷ Y.-H. Chu,²⁸ M. J. Michałowski,²⁹ P. J. Kavanagh,³⁰ K. R. Grieve²

¹Department of Physics and Astronomy, University of Manchester, Oxford Road, Manchester, M13 9PL, UK

²Western Sydney University, Locked Bag 1797, Penrith South DC, NSW 2751, Australia

³CSIRO Astronomy and Space Science, PO Box 76, Epping, NSW 1710, Australia

⁴Depto. de Astronomía, DCNE, Universidad de Guanajuato, Apdo. Postal 144, Guanajuato, CP 36000, Gto., Mexico

⁵School of Physics, The University of New South Wales, Sydney, 2052, Australia

⁶INAF Osservatorio Astrofisico di Catania, via Santa Sofia 78, I-95123 Catania

⁷The Inter-University Institute for Data Intensive Astronomy (IDIA), Department of Astronomy, University of Cape Town, Rondebosch, 7701, South Africa

⁸ASTRON - Netherlands Institute for Radio Astronomy, 7991 PD, Dwingeloo, The Netherlands

⁹Institute for Advanced Research, Nagoya University, Furo-cho, Chikusa-ku, Nagoya 464-8601, Japan

¹⁰Department of Physics, Nagoya University, Furo-cho, Chikusa-ku, Nagoya 464-8601, Japan

¹¹Max-Planck-Institut für extraterrestrische Physik, Giessenbachstraße, D-85748 Garching, Germany

¹²National Radio Astronomy Observatory, 1003 Lopezville Rd., Socorro, NM 87801, USA

¹³Dominion Radio Astrophysical Observatory, Herzberg Programs in Astronomy and Astrophysics, National Research Council Canada, PO Box 248, Penticton, BC V2A 6J9, Canada

¹⁴CAS Key Laboratory of FAST, National Astronomical Observatories, Chinese Academy of Sciences, Beijing, 100101, China

¹⁵School of Astronomy and Space Sciences, University of Chinese Academy of Sciences, Beijing 100049, China

¹⁶Observatoire Astronomique de Strasbourg, Université de Strasbourg, CNRS, 11 rue de l'Université, F-67000 Strasbourg, France

¹⁷School of Science, The University of New South Wales, Australian Defence Force Academy, Canberra, 2600, Australia

¹⁸Lennard-Jones Laboratories, Keele University, ST5 5BG, UK

¹⁹School of Physical Sciences, The University of Adelaide, Adelaide 5005, Australia

²⁰School of Physics and Astronomy, University of Minnesota, Minneapolis, MN 55455, USA

²¹Remeis Observatory and ECAP, Universität Erlangen-Nürnberg, Sternwartstr. 7, D-96049 Bamberg, Germany

²²International Centre for Radio Astronomy Research, Curtin University, Bentley, WA 6102, Australia

²³Sydney Institute for Astronomy, School of Physics A28, The University of Sydney, Sydney, NSW 2006, Australia

²⁴Department of Astronomy, Faculty of Mathematics, University of Belgrade, Studentski trg 16, 11000 Belgrade, Serbia

²⁵Isaac Newton Institute of Chile, Yugoslavia Branch

²⁶Argelander-Institut für Astronomie, Auf dem Hügel 71, D-53121 Bonn, Germany

²⁷Department of Physics and Astronomy, University of Calgary, University of Calgary, Calgary, Alberta, T2N 1N4, Canada

²⁸Institute of Astronomy and Astrophysics, Academia Sinica (ASIAA), Taipei 10617, Taiwan

²⁹Astronomical Observatory Institute, Faculty of Physics, Adam Mickiewicz University, ul. Stoleczna 36, PL-60-286 Poznań, Poland

³⁰School of Cosmic Physics, Dublin Institute for Advanced Studies, 31 Fitzwilliam Place, Dublin 2, Ireland

Accepted XXX. Received YYY; in original form ZZZ

ABSTRACT

We present two new radio continuum images from the Australian Square Kilometre Array Pathfinder (ASKAP) survey in the direction of the Small Magellanic Cloud (SMC). These images are part of the Evolutionary Map of the Universe (EMU) Early Science Project (ESP) survey of the Small and Large Magellanic Clouds. The two new source lists produced from these images contain radio continuum sources observed at 960 MHz (4489 sources) and 1320 MHz (5954 sources) with a bandwidth of 192 MHz and beam sizes of $30.0'' \times 30.0''$ and $16.3'' \times 15.1''$, respectively. The median Root Mean Squared (RMS) noise values are $186 \mu\text{Jy beam}^{-1}$ (960 MHz) and $165 \mu\text{Jy beam}^{-1}$ (1320 MHz). To create point source catalogues, we use these two source lists, together with the previously published Molonglo Observatory Synthesis Telescope (MOST) and the Australia Telescope Compact Array (ATCA) point source catalogues to estimate spectral indices for the whole population of radio point sources found in the survey region. Combining our ASKAP catalogues with these radio continuum surveys, we found 7736 point-like sources in common over an area of 30 deg^2 . In addition, we report the detection of two new, low surface brightness supernova remnant candidates in the SMC. The high sensitivity of the new ASKAP ESP survey also enabled us to detect the bright end of the SMC planetary nebula sample, with 22 out of 102 optically known planetary nebulae showing point-like radio continuum emission. Lastly, we present several morphologically interesting background radio galaxies.

Key words: Magellanic Clouds – radio continuum – catalogues – SNRs – YSO – AGNs – PNe

1 INTRODUCTION

This is an exciting time for the study of nearby galaxies. These nearby external galaxies offer an ideal laboratory, since they are close enough to be resolved, yet located at relatively well known distances (see e.g. Pietrzyński et al. 2019). New generations of Magellanic Cloud (MC) surveys across the entire electromagnetic spectrum reflect a major opportunity to study different objects and processes in the elemental enrichment of the Interstellar Medium (ISM). The study of these interactions in different domains, including radio, optical and X-ray, allow a better understanding of objects such as supernova remnants (SNRs), planetary nebulae (PNe), (Super)Bubbles and their environments, young stellar objects (YSOs), symbiotic (accreting compact object) binaries and Wolf-Rayet (WR) wind-wind-collision binaries.

Various new high resolution ($\sim 1''$) and high sensitivity surveys of the Small and Large Magellanic Clouds (MCs), such as *XMM-Newton* and *Chandra* (X-rays; see e.g. Haberl et al. 2012b), *Herschel* (Gordon et al. 2011) and *Spitzer* (IR; Meixner et al. 2006), UM/CTIO Magellanic Cloud Emission Line Survey (MCELS, optical; Winkler et al. 2005) and ATCA/MOST (radio), provide a solid base for detailed multi-wavelength studies of radio objects within and behind the MCs.

Our main area of interest is the radio objects natal to the MCs, particularly SNRs and PNe. To date, some 85 SNRs in the MCs have been identified, with a further 20 candidates awaiting confirmation (Maggi et al. 2016; Bozzetto et al. 2017). Similarly, over 50 PNe (Filipović et al. 2009; Bojčić et al. 2010; Leverenz et al. 2016, 2017) and hundreds of H II regions and YSOs have been identified (see for example Oliveira et al. 2013). Over 8500 radio sources have also been

detected in the region of the Clouds – mainly AGN, radio galaxies and quasars (Wong et al. 2012b; Collier 2016, Grieve et al. in prep.). Additionally, some comprehensive studies of the magnetic fields of the MCs have been undertaken with the present generation of radio continuum surveys (ATCA; Gaensler et al. 2005; Mao et al. 2008, 2012).

In this paper, we focus on the Small Magellanic Cloud (SMC), a dwarf irregular galaxy. Its proximity ($\sim 60 \text{ kpc}$; Hilditch et al. 2005) enables us to conduct detailed radio frequency studies of its gas and stellar content, without the complication of the foreground emission and absorption we encounter when working within our own Galaxy. For these reasons, the SMC has been the subject of many radio studies over several decades.

Starting in the mid 1970s, the SMC has been the subject of both single dish and interferometric radio continuum surveys. These monitoring campaigns have produced over a dozen catalogues of sources towards the SMC (Clarke 1976; McGee et al. 1976; Haynes et al. 1986; Wright & Otrupcek 1990; Filipović et al. 1997; Turtle et al. 1998; Filipović et al. 1998; Filipović et al. 1997, 2002; Payne et al. 2004; Filipović et al. 2005; Reid et al. 2006; Payne et al. 2007; Wong et al. 2011a; Crawford et al. 2011; Wong et al. 2011b, 2012a,b; For et al. 2018) (see also Table 1 in Wong et al. 2011b, for details).

For the reasons mentioned above, the SMC was also selected as a prime target for the Early Science Project (ESP) of the newly built Australian Square Kilometre Array Pathfinder (ASKAP; Johnston et al. 2008). ASKAP is a radio interferometer that allows us to survey the SMC with regularly sampled observations. ASKAP also provides sensitivity down to the μJy range as well as a large field of view of 30 deg^2 (Murphy et al. 2013). The goal of this project is to produce high sensitivity and high resolution continuum images of the MCs as well as to catalogue discrete radio continuum sources.

* E-mail: tana.joseph@manchester.ac.uk (TDJ)

The ASKAP EMU ESP survey will be a good complement to and, in some cases, a significant improvement on previous similar studies of the southern skies. For instance, the Australia Telescope Large Area Survey (ATLAS; Norris et al. 2006; Middelberg et al. 2008) was a 1400 MHz radio survey covering a total of roughly 6 deg^2 on the sky, down to an RMS noise level of $<30 \mu\text{Jy}$, requiring 380 hours of observation time. This survey uncovered over 3000 distinct radio sources out to a redshift of 2. ASKAP’s higher resolution and increased sensitivity will be able to achieve such results on a much shorter time scale (see Fig. 1 in Franzen et al. 2015).

Another obvious advantage of ASKAP is the size of the field of view. For example, the Sydney University Molonglo Sky Survey (SUMSS) would need ~ 16 fields and ~ 192 hours to cover the ASKAP EMU SMC survey area to the required sensitivity (see Mauch et al. 2003); in contrast the ASKAP observations were composed of eight fields of about 12 hours each (a total of 96 hours).

In this paper we present two new catalogues from the ASKAP ESP surveys for different types of radio continuum sources towards the SMC. These catalogues were obtained from images taken at 960 MHz ($\lambda = 32 \text{ cm}$) and 1320 MHz ($\lambda = 23 \text{ cm}$). For the point source catalogue, we combine the ASKAP data with the previously published MOST catalogue (Turtle et al. 1998; Wong et al. 2011b) and the ATCA $\lambda = 20, 13, 6$ and 3 cm catalogues (Wong et al. 2011b, 2012a, and references therein).

The paper is laid out as follows: Section 2 describes the data used to create the source lists. In section 3.1 we describe the source detection methods used, section 3.2 describes the new ASKAP source catalogues and in section 3.3 we compare our work to previous catalogues of point sources towards the SMC. Sections 4 and 5 describe the latest ASKAP SMC populations of SNRs and PNe, respectively. In Section 6, we briefly discuss other sources of interest, including those behind the SMC.

2 DATA, OBSERVING AND PROCESSING

The SMC was observed as part of the ASKAP commissioning and early science verification (DeBoer et al. 2009; Hotan et al. 2014; McConnell et al. 2016). Here, we present observations at 960 MHz taken on 2017 September 3 (Figure 1; using 12 antennas: 2, 3, 4, 6, 12, 14, 16, 17, 19, 27, 28, and 30), and at 1320 MHz on 2017 November 3 - 5 (Figure 2, using 16 antennas: 1, 2, 3, 4, 5, 6, 10, 12, 14, 16, 17, 19, 24, 27, 28, 30). The H I spectral and dynamical analyses of the 1320 MHz data have been presented in McClure-Griffiths et al. (2018) and Di Teodoro et al. (2019) respectively.

We note that the current observations were made with only 33 per cent and 44 per cent (for 960 MHz and 1320 MHz respectively) of the full ASKAP antenna configuration and 66 per cent of the final bandwidth that will be available in the final array. We believe that with the full array, we will be able to achieve a factor of two increase in sensitivity compared to what is currently possible.

A bandwidth of 192 MHz was used and the maximum baseline for these observations was 2.3 km. The observations cover a total field of view of 30 deg^2 , with exposure times of 10 to 11 hours per pointing. To optimise sensitivity and

survey speed, the 36 beams on each antenna were configured in a hexagonal grid on the sky (McConnell 2017). The source 1934-638 was observed and used for the flux density calibration of all images.

The data calibration, processing, and imaging were carried out using the ASKAPsoft pipeline (Cornwell et al. 2011). For both sets of images we processed the data with the multiscale clean algorithm, noting from our previous work (Wong et al. 2011a) that the largest detectable features were $\sim 192''$. Therefore, we selected spacial scales of $192''$, $96''$ and $48''$ as a geometric progression. We also noted features on the scale of $16''$, and so this spatial scale was also selected. The 1320 MHz image was cleaned and then mosaiced. For the 960 MHz image, we set the pixel size to $6''$, and set the restoring beam to $30'' \times 30''$ in order to maximise our resolution and sensitivity and to more easily compare these new results with other SMC surveys referenced in this work.

The properties of the 960 MHz and 1320 MHz images are summarised in Table 1. These two new ASKAP images are shown in Figures 1 and 2, with zoomed in views showing the resolved structure of the emission in Figures. 3 and 4. Figures 5 and 6 show the RMS maps generated by the source finding software, AEGEAN (Hancock et al. 2012, 2018) for the 960 MHz and 1320 MHz images respectively.

We note that our ESP 960 MHz image was made at very early stages of the ASKAP testing and a range of issues, such as positional accuracy and calibration, were discovered. We have made every effort to identify and correct these problems. The 1320 MHz image as made at a later date when these issues were already known and could therefore be avoided, mitigated or corrected as needed.

3 ASKAP ESP SMC SOURCE CATALOGUES

3.1 Source detection

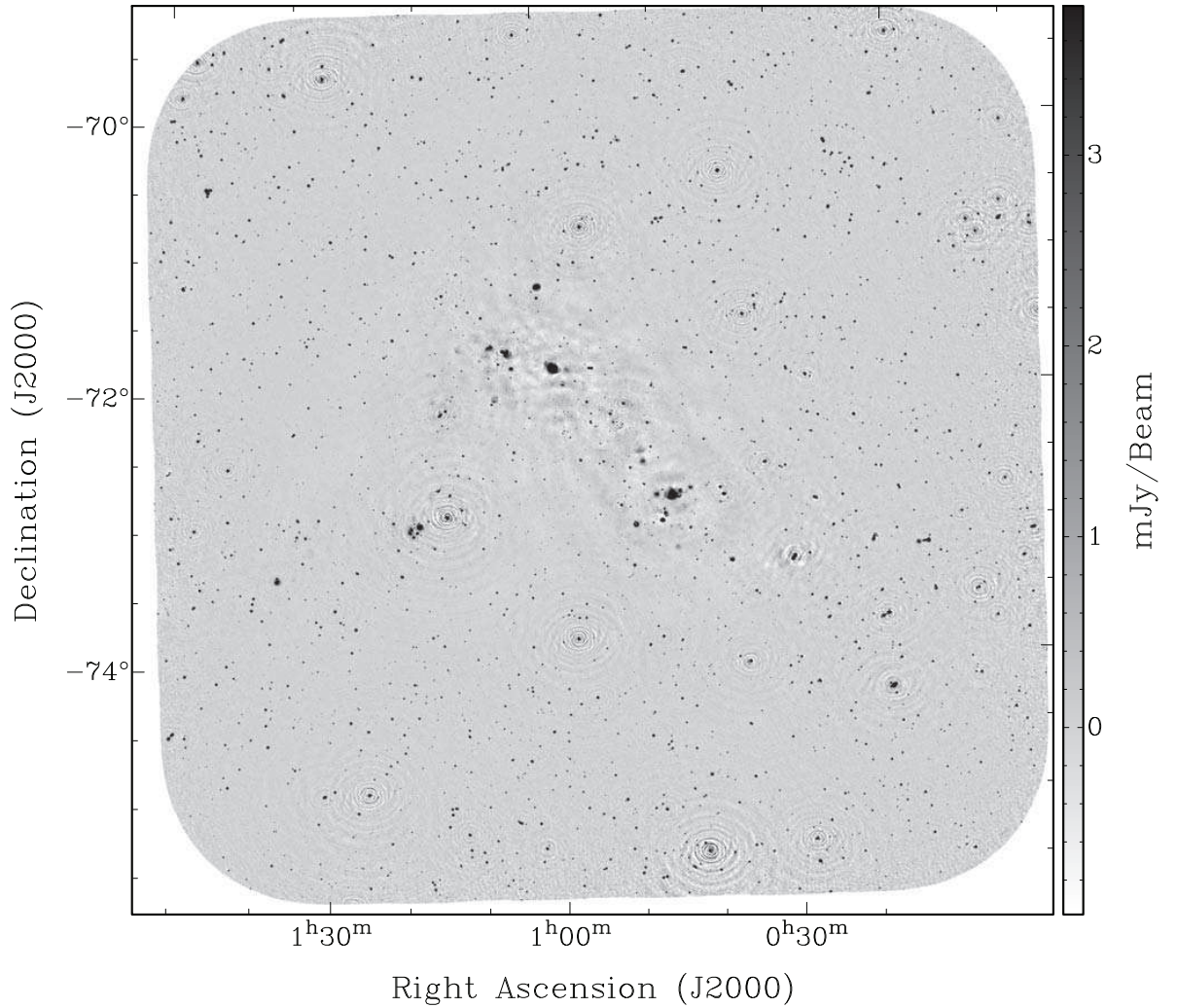
The AEGEAN source finding software was used to create an overall catalogue of sources from the ASKAP images. Due to the combination of the multiple beams and artefacts from bright sources, images from ASKAP have variable noise across the field. This variable noise must be parameterised before source-finding to ensure that accurate source thresholds are determined. To do this, noise (RMS) and background level maps were made using the BANE routine in AEGEAN, with its default parameters. BANE uses a grid algorithm with a sliding box-car and sigma-clipping approach, with the resulting maps being at the same pixel scale as the input images (for further detail, see Hancock et al. 2018). The maps were then used with the default parameters in AEGEAN to create the initial source lists at 5σ level. Visual inspection of the sources was carried out to verify detections from the initial source lists.

3.2 Source Catalogues

In total, we found 4489 and 5954 point sources in our new ASKAP 960 MHz and 1320 MHz images, respectively (see Tables 2 and 3). There are 3536 unique sources that have both ASKAP 960 MHz and 1320 MHz flux densities. This catalogue excludes known SMC SNRs, PNe and H II regions which are listed separately (see Sections 4 and 5).

Table 1. Properties of the 960 MHz and 1320 MHz radio continuum images as well other MOST/ATCA surveys used in this study.

ν (MHz)	λ (cm)	Telescope	Median RMS ($\mu\text{Jy beam}^{-1}$)	Best RMS ($\mu\text{Jy beam}^{-1}$)	Beam Size (arcsec)	Total number of point sources	Reference
1320	23	ASKAP	165	55	16.3×15.1	5954	This work
960	32	ASKAP	186	110	30.0×30.0	4489	This work
843	36	MOST	700	500	40.0×40.0	1689	Wong et al. (2011b)
1400	20	ATCA	700	600	17.8×12.2	1560	Wong et al. (2011b)
2370	13	ATCA	400	300	45.0×45.0	742	Wong et al. (2011b)
4800	6	ATCA	700	500	30.0×30.0	601	Wong et al. (2012a)
8640	3	ATCA	800	700	20.0×20.0	457	Wong et al. (2012a)

**Figure 1.** ASKAP ESP image of the SMC at 960 MHz. The beam size is $30.0'' \times 30.0''$ and the side scale bar represents the image grey scale intensity range.

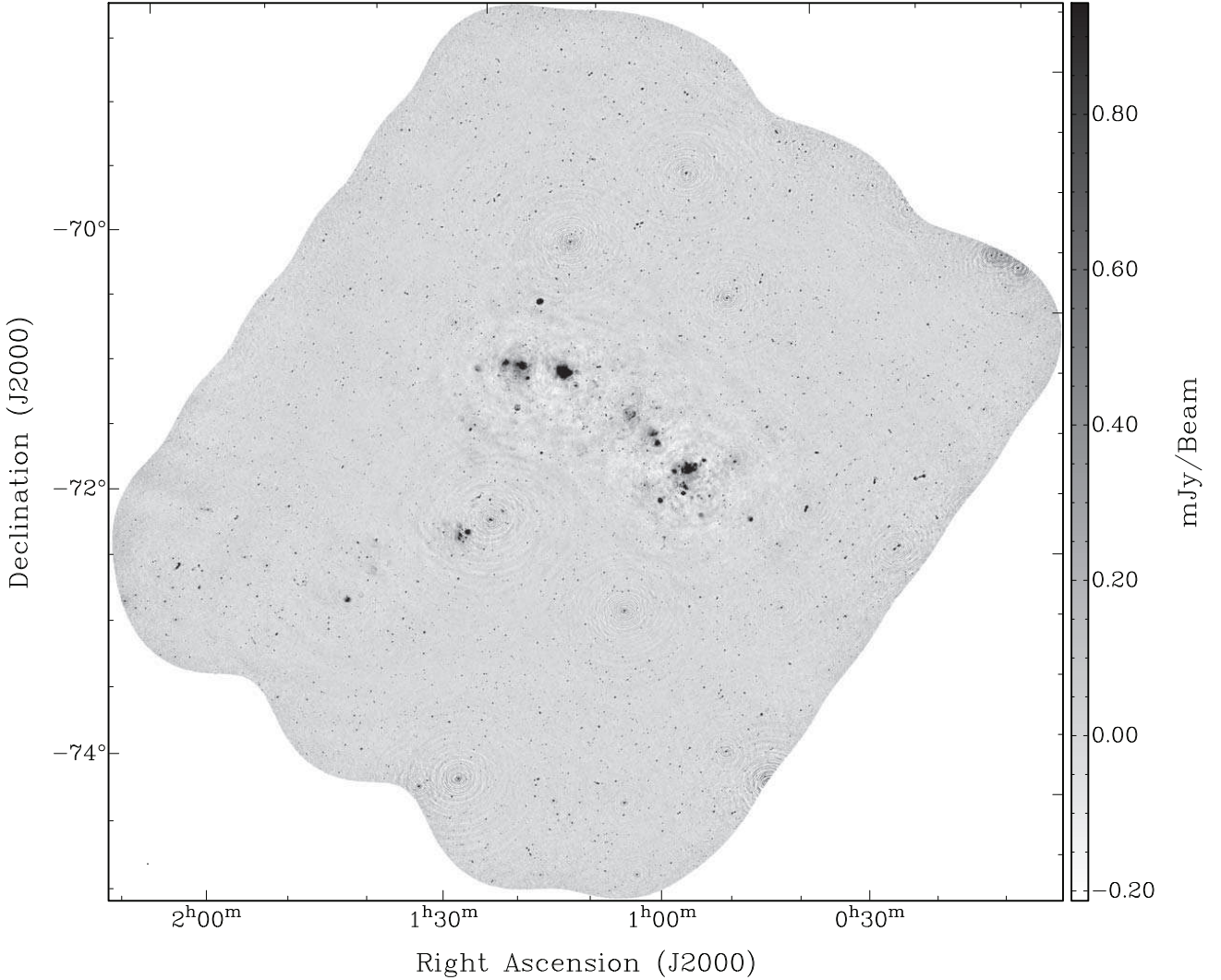


Figure 2. ASKAP ESP image of the SMC at 1320 MHz. The beam size is $16.3'' \times 15.1''$ and the side scale bar represents the image grey scale intensity range.

We combine our two new ASKAP catalogues of point sources with previously published source lists from MOST (at 843 MHz) and ATCA (1400, 2370, 4800 and 8640 MHz). To do this, we used a $10''$ search radius to find common sources and found a total of 7736 discrete sources which we list in Table 4. Out of these 7736 sources, there are 659 sources that do not have any ASKAP flux densities and 112 that do not have MOST/SUMSS flux densities.

Where possible, we also list the estimated spectral index (α)¹ of the source including error (Table 4; Col. 12). We also note that there are 49 (~ 0.5 per cent of the total population) sources in Table 4 with questionable α estimates of $\alpha < -4$ and $\alpha > +2.5$. Where the α values are extreme we flag those sources to emphasis caution. The reasons behind

such unrealistic α for these few sources (< 0.3 per cent out of our 7736 sources) are twofold. One is that the flux density measurements are made between only two nearby frequency bands (such as for example 1400/1320 MHz or 960/843 MHz) where a small change (or error) in size or flux density leads to large changes and unrealistic estimates in α . The second issue is that almost all of such sources lie near the edges of the field where uv coverage and sensitivity are significantly poorer.

Non-point sources, such as blended and extended sources, were flagged and excised to leave only a catalogue of point sources. Although not used in the further analysis, we provide estimates of positions and flux densities for detected non-point sources. We present the results from both catalogues in Tables 5 and 6 where a total of 282 and 641 non-point sources are found at 960 MHz and 1320 MHz surveys, respectively. Because of the different resolution across the various SMC surveys, some of these listed non-point sources

¹ Defined as $S_\nu \propto \nu^\alpha$, where: S_ν is flux density, ν is frequency, and α is spectral index.

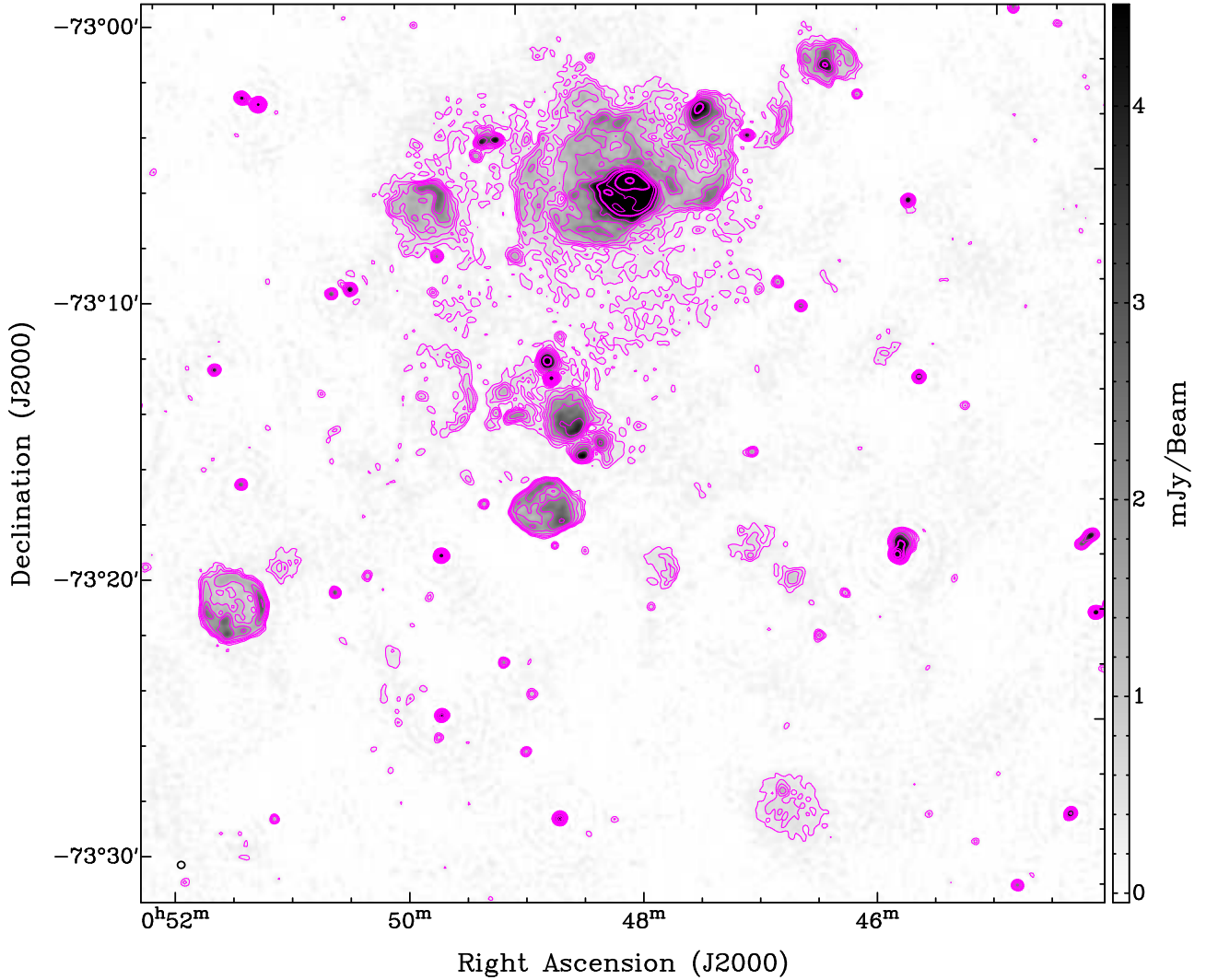


Figure 3. ASKAP ESP image of the SMC N19 region at 1320 MHz (grey scale and contours). Magenta contours are: 0.3, 0.5, 0.7, 1, 1.5, 2, 3, 5, 7, 10 and 15 mJy beam⁻¹. The beam size of 16.3'' × 15.1'' is shown as a small black ellipse in the lower left corner.

Table 2. Point source catalogue derived from our ASKAP 960 MHz image. The catalogue at 960 MHz consists of 4489 point sources. The full table is available in the online version of the article.

Source No.	Name ASKAP	RA (J2000) hh mm ss	Dec (J2000) ° ' "	S _{960MHz} (mJy)
1	J000437-744211	00:04:36.52	-74:42:11.0	4.0±0.5
2	J000506-751559	00:05:05.77	-75:15:58.6	4.0±0.5
3	J000508-745454	00:05:07.97	-74:54:53.6	16.0±0.5
4	J000545-741232	00:05:44.94	-74:12:31.6	16.9±0.6
5	J000550-744806	00:05:49.77	-74:48:05.9	27.7±0.5
6	J000550-742134	00:05:50.46	-74:21:34.4	3.6±0.5
7	J000603-743754	00:06:03.48	-74:37:54.1	10.9±0.5
8	J000608-740148	00:06:08.34	-74:01:47.6	8.2±0.6
9	J000608-740240	00:06:08.50	-74:02:40.2	9.4±0.6
10	J000609-740538	00:06:09.42	-74:05:38.3	2.9±0.6

Table 3. Point source catalogue derived from our ASKAP 1320 MHz image. The catalogue at 1320 MHz consists of 5954 point sources. The full table is available in the online version of the article.

Source No.	Name ASKAP	RA (J2000) hh mm ss	Dec (J2000) ° ' "	S _{1320MHz} (mJy)
1	J000537-715839	00:05:36.81	-71:58:39.2	5.3±0.9
2	J000547-722502	00:05:46.55	-72:25:01.9	3.8±0.5
3	J000646-720801	00:06:45.91	-72:08:01.2	2.1±0.3
4	J000648-722252	00:06:48.25	-72:22:51.8	10.1±0.3
5	J000653-715740	00:06:52.59	-71:57:40.2	36.3±0.4
6	J000654-722034	00:06:54.07	-72:20:34.2	2.1±0.4
7	J000713-714611	00:07:12.94	-71:46:10.6	4.1±0.6
8	J000726-720631	00:07:26.15	-72:06:30.8	3.4±0.2
9	J000732-720732	00:07:31.97	-72:07:32.2	1.4±0.2
10	J000739-721026	00:07:38.64	-72:10:26.1	2.1±0.4

could be resolved in one survey but could appear as a point

source in another and as such they would not be listed in Tables 5 or 6.

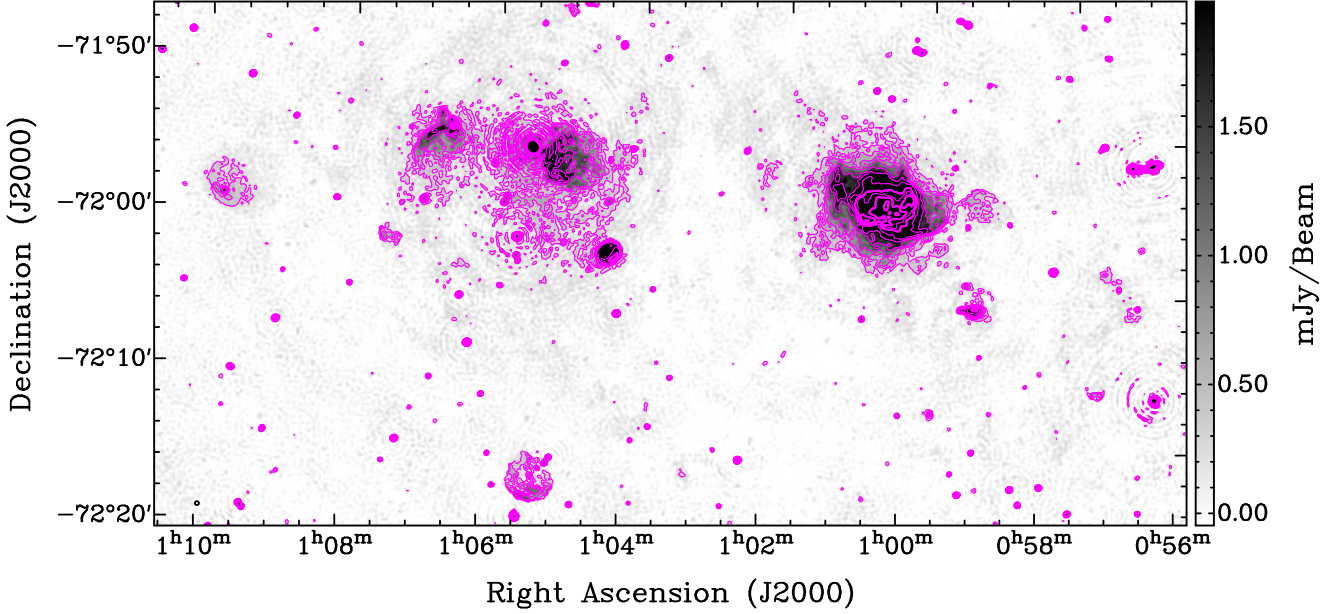


Figure 4. ASKAP ESP image of the SMC N66 and SNR 1E0102-72 region at 1320 MHz (grey scale and contours). Magenta contours are: 0.3, 0.5, 0.7, 1, 1.5, 2, 3, 5, 7, 10 and 15 mJy beam⁻¹. The beam size of 16.3'' × 15.1'' is shown as a small black ellipse in the lower left corner.

Table 4. An excerpt from the combined catalogue of point sources. These sources should be referred to as EMU-ESP-SMC-ffff NNNN. The full table is available in the online version of the article

(1) No	(2) RA (J2000) hh:mm:ss.s	(3) DEC (J2000) dd:mm:ss.s	(4) S _{843MHz} (mJy)	(5) S _{960MHz} (mJy)	(6) S _{1320MHz} (mJy)	(7) S _{1400MHz} (mJy)	(8) S _{2370MHz} (mJy)	(9) S _{4800MHz} (mJy)	(10) S _{8640MHz} (mJy)	(11) No. points	(12) $\alpha \pm \Delta\alpha$	(13) S _{1GHz} (mJy)	(14) Cat. No. 960
3165	00:51:40.16	-72:38:16.5	6.19	5.5	4.1	3	-0.94 ± 0.01	5.3	2021
3166	00:51:41.38	-73:13:36.9	13.96	10.0	...	10.6	19.5	10.0	11.10	6	-0.10 ± 0.10	12.4	2022
3167	00:51:41.65	-70:28:46.3	...	1.1	0.82	2	-0.92	1.1	2025
3168	00:51:41.85	-69:45:10.2	...	3.5	2.7	2	-0.81	3.4	2024
3169	00:51:42.02	-72:55:56.3	71.88	61.3	...	38.42	42.6	21.3	7.26	6	-0.90 ± 0.10	61.7	2023
3170	00:51:42.12	-73:45:04.7	...	3.4	2.72	2	-0.7	3.3	2026
3171	00:51:45.11	-75:22:31.3	0.53	1
3172	00:51:45.98	-69:28:14.6	4.5	1
3173	00:51:46.61	-75:32:16.4	...	4.2	2.7	2	-1.4	4.0	2027
3174	00:51:47.31	-71:03:01.6	0.52	1
3175	00:51:47.84	-73:19:33.4	...	1.1	0.9	2	-0.63	1.1	2028
3176	00:51:47.89	-73:04:54.0	20.24	19.7	12.9	12.68	6.2	2.1	...	6	-1.32 ± 0.06	17.9	2029
3177	00:51:48.39	-72:50:48.3	9.63	8.1	...	8.29	10.3	4	0.1 ± 0.2	8.9	2030
3178	00:51:49.52	-73:38:39.4	0.6	1
3179	00:51:50.04	-74:54:40.4	...	0.9	1.3	2	1.2	0.9	2031
3180	00:51:51.24	-72:55:37.8	4.87	1
3181	00:51:51.24	-74:11:15.2	0.96	1
3182	00:51:51.46	-72:05:53.6	0.51	1
3183	00:51:53.37	-73:31:10.9	0.9	1
3184	00:51:53.67	-73:45:21.6	5.90	5.4	3.96	4.21	4	-0.80 ± 0.10	5.2	2032

3.3 Comparison with previous catalogues

We compare position differences (ΔRA and ΔDEC) between our new ASKAP images and previous catalogues at 843 MHz (see Figure 7) and 1400 MHz (see Figure 8). We did not find any significant shift in position in our 1320 MHz vs. 1400 MHz position comparison. For the 889 sources in common, we found that the $\Delta\text{RA} = -0.58''$ ($\text{SD} = 1.50''$) and $\Delta\text{DEC} = +1.03''$ ($\text{SD} = 1.95''$). Somewhat worse results are

reported for the 843 MHz vs. 960 MHz comparison of 1509 sources with $\Delta\text{RA} = +2.90''$ ($\text{SD} = 2.65''$) and $\Delta\text{DEC} = -1.45''$ ($\text{SD} = 2.92''$). These position differences are only a small fraction of the beamsize at the given frequency.

Positional shifts of $\sim 3''$ in our 960 MHz image are not insignificant, especially if we want to look for multiband counterparts. The reason for the discrepancy lies in the fact that this image comes from the ASKAP testing and early operation period where a number of issues were found and

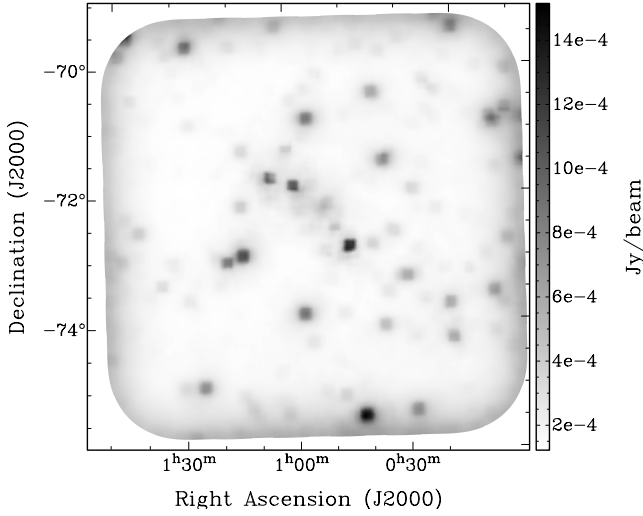


Figure 5. RMS map of the 960 MHz ASKAP observations, produced by BANE with the default parameters. The image is of the same pixel scale as in Figure 1. Higher RMS levels are found at the edge of the field (where only one beam is present) and around the brighter sources.

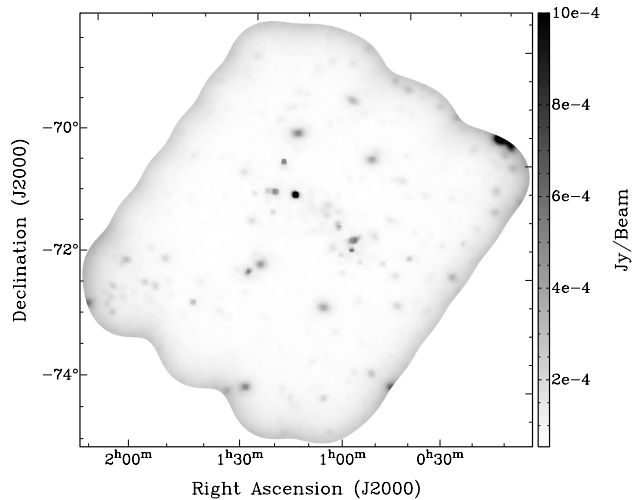


Figure 6. RMS map of the 1320 MHz ASKAP observations, produced by BANE with the default parameters. The image is of the same pixel scale as in Figure 2. Higher RMS levels are found at the edge of the field (where only one beam is present) and around the brighter sources.

acknowledged. Specifically, throughout the paper we use the coordinates from other SMC surveys for the various sources wherever possible. An excerpt of the combined point source catalogue is shown in Table 4.

In order to assess the reliability of our integrated flux values, we compared the values on compact (extended H II regions are excluded) sources to catalogue values from other nearby frequencies. We performed two sets of comparisons: our ASKAP 960 MHz values with the values from MOST at 843 MHz and our ASKAP 1320 MHz values with the ATCA 1400 MHz values. The agreement is excellent, as can be seen in Figures 9 and 10.

As a quick check on flux density scales, we fit $S_{\text{ASKAP}} = k \times S_{\text{other}} + z$, allowing for some small zero level offsets (z).

Table 5. Non-point source catalogue derived from our ASKAP 960 MHz image. The catalogue at 960 MHz consists of 282 non-point sources.

The flags are coded as: 2 partially blended source, 3 fully blended or extended source, 4 source is very likely a part of a larger structure. The full table is available in the online version of the article.

Source number	RA (J2000) hh mm ss	Dec (J2000) ° ' "	$S_{960\text{MHz}}$ (mJy)	Flag
1	00:09:39.65	-73:08:16.6	61.3 ± 6.2	3,4
2	00:09:57.31	-73:08:48.8	74.4 ± 7.5	3,4
3	00:10:12.51	-73:21:23.9	110 ± 11	3
4	00:11:25.26	-74:22:36.1	2.52 ± 0.38	3
5	00:12:15.73	-75:36:56.8	5.97 ± 0.73	3
6	00:14:22.33	-75:18:40.2	3.04 ± 0.38	3
7	00:14:24.67	-72:17:22.5	2.13 ± 0.48	3
8	00:14:29.91	-72:17:21.5	2.13 ± 0.48	3
9	00:14:36.23	-70:53:34.9	119 ± 12	3
10	00:14:47.72	-70:53:25.5	154 ± 15	3

For the $S_{960\text{MHz}}/S_{843\text{MHz}}$ and $S_{1320\text{MHz}}/S_{1400\text{MHz}}$ comparison, we find a slope (k) of 0.89 and 0.99 respectively, which corresponds to an average α of -0.9 and -0.2 respectively. Given that the average α for the majority of sources in our field of view is around -0.8 , we would expect that the integrated flux density at 843 MHz would be ~ 10 per cent higher than at 960 MHz. Similarly, the difference between 1320 MHz and 1400 MHz would cause the average flux density in our ASKAP 1320 MHz image to be higher by about 4.5 per cent. The $S_{960\text{MHz}}/S_{843\text{MHz}}$ value is somewhat steeper than the average α calculated for each source individually across larger frequency ranges. The $S_{1320\text{MHz}}/S_{1400\text{MHz}}$ spectrum suggests a possible flux density scale inconsistency at the 5 per cent level, within the uncertainty expectations. However, the high quality of these data indicate that with the full ASKAP array and final calibration, it may be possible to tie the flux density scales at different frequencies to much higher accuracy than currently possible.

In order to estimate the number of matches between these two new ASKAP catalogues and other combined catalogues which could arise purely by chance, we produced artificial source catalogues with positions shifted from the real position. Positions from the final catalogue were shifted by ± 10 arcmin in RA and DEC (4 different positions) and used as input for AEGEAN's prioritised fitting method (Hancock et al. 2018). Only cross-matches within half the synthesised beam Full Width at Half-Maximum power (FWHM) (for each survey) were considered matches. We found the average number of chance coincidences to be 53 for the 960 MHz image and 60 for the 1320 MHz image (out of total 7736 sources from the point source catalogue Table 4 or ~ 0.7 per cent). This result implies that the large fraction of correlations between two ASKAP catalogues are highly likely to be real.

Finally, we estimate the radio spectral index for all sources in common and show their distribution in Figure 11. There are 4114 sources found at only two frequencies (marked in red; Figure 11) and for those we estimate a mean α of -0.84 . For 1611 sources that are found in three different catalogues (marked in blue; Figure 11) we found a mean α of -0.81 (SD=1.35). We also estimate the average

Table 6. Non-point source catalogue derived from our ASKAP 1320 MHz image. The catalogue at 1320 MHz consists of 641 non-point sources. The flags are coded as in Table 5. The full table is available in the online version of the article.

Source number	RA (J2000) hh mm ss	Dec (J2000) ° ' "	$S_{1320\text{MHz}}$ (mJy)	Flag
1	00:07:36.88	-72:12:00.6	12.4 ± 1.3	3
2	00:09:47.69	-72:44:48.6	20.8 ± 2.1	3
3	00:10:24.52	-72:00:37.6	5.13 ± 0.56	2
4	00:10:28.35	-72:00:23.0	6.23 ± 0.66	2
5	00:11:58.28	-72:00:48.5	22.7 ± 2.3	3
6	00:12:47.55	-73:12:57.6	12.6 ± 1.3	3
7	00:14:25.83	-72:17:20.8	3.06 ± 0.35	3
8	00:14:31.23	-72:09:54.5	4.57 ± 0.48	3
9	00:15:09.85	-72:48:06.5	3.72 ± 0.40	2
10	00:15:24.82	-72:17:43.3	2.74 ± 0.32	2

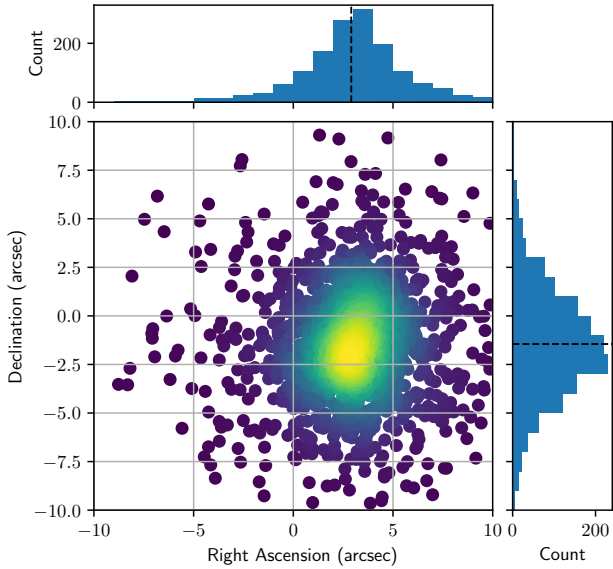


Figure 7. Positional difference (MOST – ASKAP) of 1509 sources found in both the 843 MHz (MOST) and the 960 MHz catalogues. The mean offsets are $\Delta\text{RA} = +2.90''$ (SD=2.65) and $\Delta\text{DEC} = -1.45''$ (SD=2.92).

α for sources that are detected in four (927 sources; purple; Figure 11; $\alpha = -0.71$, SD=0.75), five (569 sources; grey; Figure 11; $\alpha = -0.71$, SD=0.59), six (412 sources; orange; Figure 11; $\alpha = -0.67$, SD=0.72) and seven (172 sources; green; Figure 11; $\alpha = -0.54$, SD=0.51) different frequencies. Given that our sample sizes of SNRs, PNe and H II regions are around 100-150 (see Sections 4 and 5), this distribution is as expected and indicates that the vast majority of our sources from Table 4 are most likely to be background objects (see e.g. Filipović et al. 1998; Collier et al. 2018; Galvin et al. 2018). We note that some sources with flux density measurements at more than two frequencies might exhibit spectral curvature and therefore the fitted value of α would not represent a good estimate.

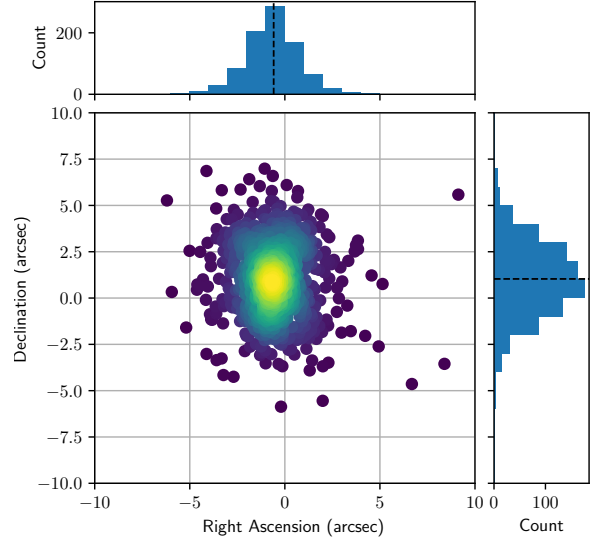


Figure 8. Positional difference (ATCA – ASKAP) of 889 sources found in both the 1320 MHz and the 1400 MHz (ATCA) catalogues. The mean offsets are

$$\Delta\text{RA} = -0.58'' \text{ (SD=1.50) and } \Delta\text{DEC} = +1.03'' \text{ (SD=1.95)}.$$

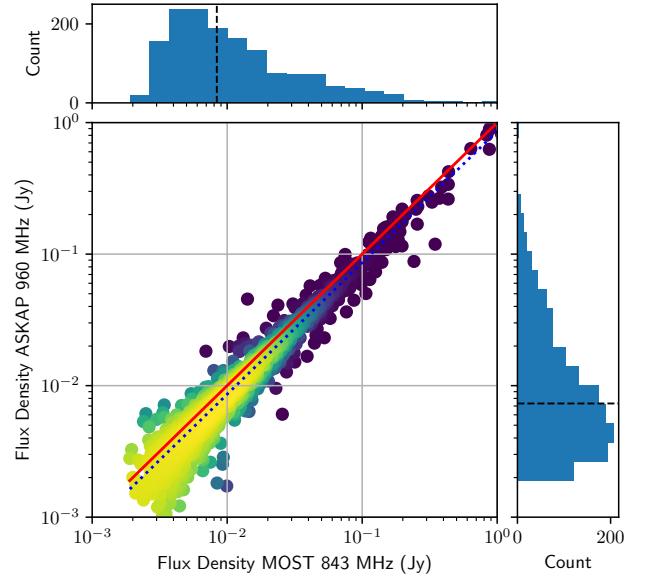


Figure 9. Integrated flux density comparison of sources found in both the 960 MHz and the 843 MHz catalogues. The best fit slope (linear) is 0.89 ± 0.01 (dotted blue) while the red line represent 1-to-1 ratio (see Section 3.3). The points are colour coded to indicate local density, yellow for high density through to purple for low density. The source integrated flux density distributions are shown in the side and top panels, with the black dashed line at the median integrated flux density.

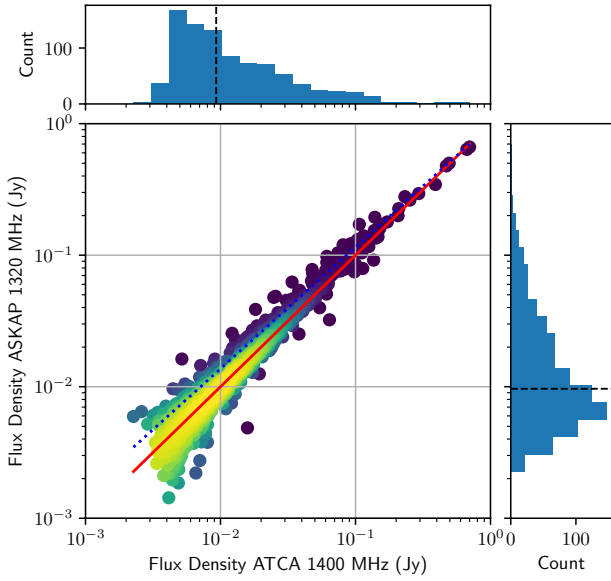


Figure 10. Integrated flux density comparison of sources found in both the 1320 MHz and the 1400 MHz catalogues. The best fit slope (linear) is 0.99 ± 0.01 (dotted blue) while red line represent 1-to-1 ratio (see Section 3.3). The points are colour coded to indicate local density, yellow for high density through to purple for low density. The source integrated flux density distributions are shown in the side and top panels, with the black dashed line at the median integrated flux density.

4 ASKAP SMC SUPERNOVA REMNANT SAMPLE

Because of their proximity and location well away from the Galactic Plane, we are able to study the sources belonging to the MCs, such as the supernova remnant (SNR) population. Together, these galaxies offer the opportunity to produce a complete sample of SNRs suitable for population studies focused on size, evolution, radio spectral index and beyond, as shown by Maggi et al. (2016) and Bozzetto et al. (2017). To that end, one of our prime goals with the next generation of ASKAP surveys is to detect new and predominantly low surface brightness SNRs. Indeed, with its unique coverage and depth, this new ASKAP ESP survey allowed us to search for new SNRs and at the same time, measure the physical properties of the already established SNRs, examples of which are shown in Figures 3 and 4.

Previous studies of SNRs in the SMC (Filipović et al. 2005; Payne et al. 2007; Owen et al. 2011; Haberl et al. 2012b; Crawford et al. 2014; Roper et al. 2015; Alsaberi et al. 2019; Gvaramadze et al. 2019; Sano et al. 2019) have established 19 objects as bona-fide SNRs with two more considered as good candidates. These two SNR candidates are not detected in our radio images and we will discuss them in our subsequent papers.

Here, we present our radio continuum study results which suggest two new sources to be SNR candidates (MCSNR J0057–7211 and MCSNR J0106–7242), bringing our sample of SMC SNRs and SNR candidates to 23. At the same time, we measure integrated flux densities for 18 of the 19 known SMC SNRs (see Table 7) and

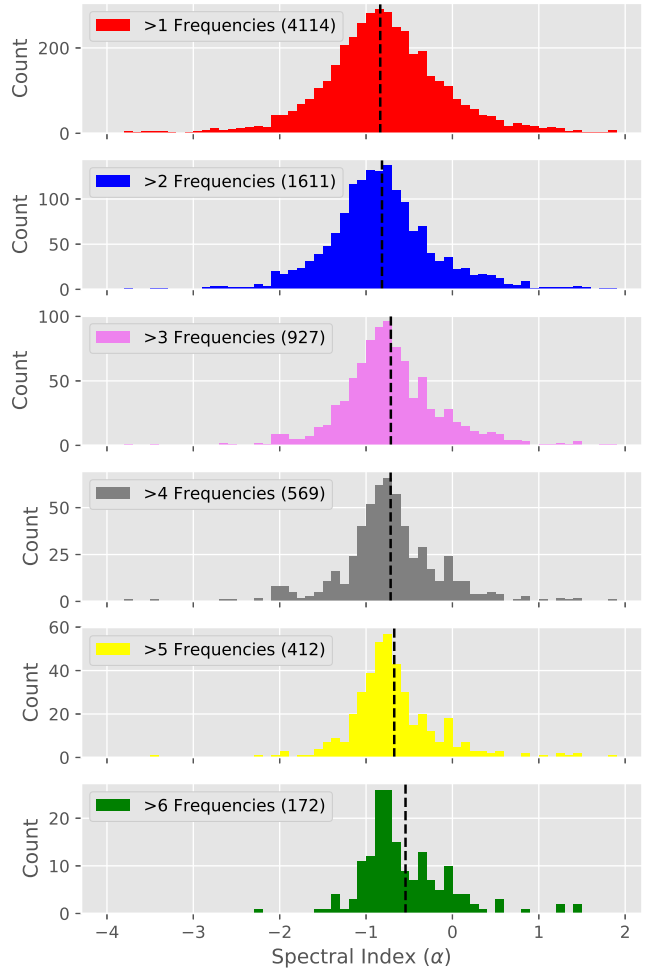


Figure 11. Spectral index distribution of all sources in the field of SMC binned at 0.1. The vertical dashed line represents the mean α of each panel, as discussed in Section 3.3. The uppermost panel includes all the sources of the other panels beneath.

present our integrated flux density estimates for the two new SMC SNR candidates found in our new ASKAP SMC surveys (Table 8). An in-depth study of the SMC SNR population will be presented in Maggi et al. (submitted, <https://arxiv.org/abs/1908.11234>).

These two new SNR candidates were initially selected purely based on their typical morphological appearance (circular shape). As our SMC SNR sample is morphologically diverse, various approaches (and initial parameters) were employed in order to measure the best SNR flux densities. Namely, we used the MIRIAD (Sault et al. 1995) task `imfit` to extract integrated flux density, extensions (diameter/axes) and position angle for each radio detected SNR. For cross checking and consistency, we also used AEGEAN and found no significant difference in integrated flux density estimates.

We used two methods: For SNRs which are known point sources (such as SNR 1E 0102.2–7219, which is not resolved in radio) we use simple Gaussian fitting which produced the best result. The second approach was applied to all resolved SNRs. For those, we measured their local background noise (1σ) and carefully select the exact area of the SNR. We then estimated the sum of all brightnesses above 5σ of each

individual pixel within that area and converted it to SNR integrated flux density following Findlay (1966, eq. 24). We also made corrections for an extended background where applicable i.e. for sources where nearby extended object such as H II region(s) is evident. However, for the most of our SMC SNRs this extended background contribution is minimal.

The two new SNR candidates are shown in Figs. 12 and 13 and their integrated flux density measurements in Table 8. These two new SNR candidates display approximately semi-circular structures consistent with a typical spherical morphology. As expected, they are both of low radio surface brightness, which is the main reason for their previous non-detection. We estimate the spectral index for both objects (Table 8) and they are consistent with typical SNR spectra, as found in, for example, the larger Large Magellanic Cloud (LMC) population (see Fig. 13 in Bozzetto et al. 2017). Therefore, in addition to their typical morphology, their radio spectral index points to a non-thermal origin which further supports that these objects be classified as SNR candidates. Neither of these two SNR candidates are detected at optical or Infrared (IR) wave bands, which is not unusual given that a number of previously known bona-fide SNRs have only been seen at one wavelength (Filipović et al. 2008).

New ASKAP SNR candidate MCSNR J0057-7211 (also see Ye et al. 1991) is located inside the ellipse around XMMU J0057.7-7213 (on the northern side, see Fig. 6 in Haberl et al. 2012b). The nearby point source XMMU J005802.4-721205 is listed as an Active Galactic Nuclei (AGN) candidate (Sturm et al. 2013). Also, there is a moderately bright, point-like X-ray source at 00:58:02.604, -72:12:06.7 with a non-thermal spectrum and $L_X \sim 10^{34}$ erg s $^{-1}$ (Haberl et al. 2012b).

On inspection of present generation *XMM-Newton* mosaic images, we find diffuse emission at the position of the second ASKAP SMC SNR candidate – MCSNR J0106-7242. A more comprehensive study of the whole SMC SNR population will be presented in an upcoming study by Maggi et al. (in prep.).

We also use the equipartition formulae² (Arbutina et al. 2012; Arbutina et al. 2013; Urošević et al. 2018) to estimate the magnetic field strength for these two SNR candidates. While this derivation is purely analytical, we emphasise that it is formulated especially for the estimation of the magnetic field strength in SNRs. The average equipartition field over the whole shell of MCSNR J0057-7211 is ~ 15 μ G while estimates for MCSNR J0106-7242 are around ~ 8 μ G, with an estimated minimum energy³ of $E_{\min}=6 \times 10^{49}$ erg and $E_{\min}=1.5 \times 10^{49}$ erg, respectively. These values are typical of older SNRs at the end of the Sedov phase where the magnetic field is three to four times more compressed than that of middle-age SNRs.

The position of these two SNR candidates on the surface brightness to diameter (Σ - D) diagram ($\Sigma=6.38 \times 10^{-22}$ W m $^{-2}$ Hz $^{-1}$ sr $^{-1}$ and 5.38×10^{-22} W m $^{-2}$ Hz $^{-1}$ sr $^{-1}$, $D=47$ pc and 44.9 pc, respectively) by Pavlović et al. (2018), suggests that these

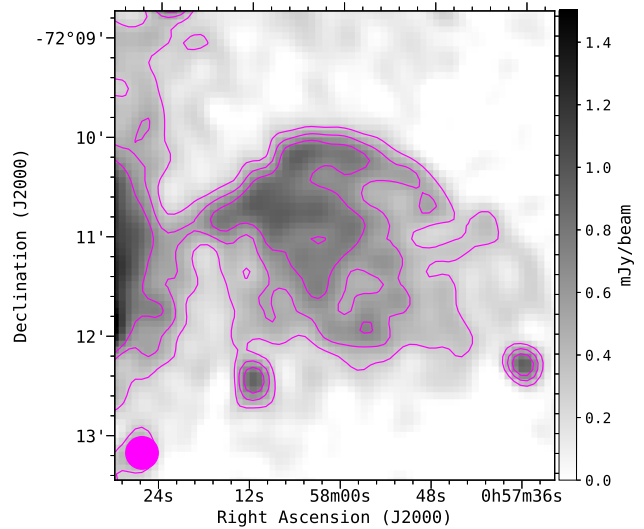


Figure 12. ASKAP ESP image of the new SMC SNR candidate MCSNR J0057-7211 at 1320 MHz (grey scale and contours) smoothed to a resolution of $20'' \times 20''$. Magenta contours are: 0.3, 0.5, and 0.7 mJy beam $^{-1}$. The smoothed beam is shown as a filled magenta circle in the lower left corner. Two point-like sources in the lower right and left corner are unrelated background sources. The local RMS noise is 0.1 mJy beam $^{-1}$.

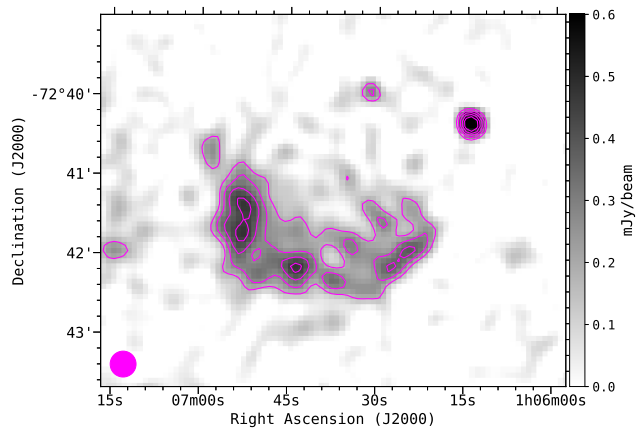


Figure 13. ASKAP ESP image of the new low surface brightness SMC SNR candidate MCSNR J0106-7242 at 1320 MHz (grey scale and contours) smoothed to a resolution of $20'' \times 20''$. Magenta contours are: 0.18, 0.27, 0.36, 0.45 and 0.54 mJy beam $^{-1}$. The smoothed beam is shown as a filled magenta circle in the lower left corner. The point-like source in the upper right corner is an unrelated background source. The local RMS noise is 0.06 mJy beam $^{-1}$.

² <http://poincare.matf.bg.ac.rs/~arbo/eqp/>

³ We use the following values: $\theta=1.37'$ and $1.29'$; $\kappa = 0$; $S_{1\text{GHz}}=0.0307$ Jy and 0.02363 Jy; and $f=0.25$.

remnants are in the late Sedov phase, with an explosion energy of $1-2 \times 10^{51}$ erg, which evolves in an environment with a density of $0.02-0.2$ cm $^{-3}$.

Table 7. 19 SNRs in the SMC. Only MCSNRJ0103–7201 is not detected in our ASKAP ESP images. The integrated flux density errors are <10 per cent. Column 2 (Other Name) abbreviations are: DEMS: Davies et al. (1976), [HFP2000]: Haberl et al. (2000), IKT: Inoue et al. (1983), SXP: Haberl et al. (2012a).

MCSNR Name	Other Name	RA (J2000)	DEC (J2000)	$S_{960\text{MHz}}$ (Jy)	$S_{1320\text{MHz}}$ (Jy)
J0041–7336	DEMS5	00 41 01.7	–73 36 30.4	0.138	0.130
J0046–7308	[HFP2000] 414	00 46 40.6	–73 08 14.9	0.111	0.110
J0047–7308	IKT 2	00 47 16.6	–73 08 36.5	0.441	0.381
J0047–7309		00 47 36.5	–73 09 20.0	0.201	0.185
J0048–7319	IKT 4	00 48 19.6	–73 19 39.6	0.121	0.092
J0049–7314	IKT 5	00 49 07.7	–73 14 45.0	0.068	0.060
J0051–7321	IKT 6	00 51 06.7	–73 21 26.4	0.085	0.096
J0052–7236	DEMS68	00 52 59.9	–72 36 47.0	0.091	0.081
J0058–7217	IKT 16	00 58 22.4	–72 17 52.0	0.079	0.070
J0059–7210	IKT 18	00 59 27.7	–72 10 09.8	0.559	0.502
J0100–7133	DEMS108	01 00 23.9	–71 33 41.1	0.161	0.146
J0103–7209	IKT 21	01 03 17.0	–72 09 42.5	0.100	0.085
J0103–7247	[HFP2000] 334	01 03 29.1	–72 47 32.6	0.0288	0.025
J0103–7201		01 03 36.6	–72 01 35.1	–	–
J0104–7201	1E0102.2-7219	01 04 01.2	–72 01 52.3	0.402	0.272
J0105–7223	IKT 23	01 05 04.2	–72 23 10.5	0.102	0.095
J0105–7210	DEMS128	01 05 30.5	–72 10 40.4	–	0.050
J0106–7205	IKT 25	01 06 17.5	–72 05 34.5	0.0095	0.0090
J0127–7333	SXP 1062	01 27 44.1	–73 33 01.6	0.0072	0.0068

Table 8. Details of two new ASKAP SNRs candidates in the SMC. The integrated flux density errors are <10 per cent. NS abbreviation stands as at Henize (1956)

MCSNR Name	Other Name	RA (J2000)	DEC (J2000)	$S_{960\text{MHz}}$ (Jy)	$S_{1320\text{MHz}}$ (Jy)	$\alpha \pm \Delta\alpha$
J0057–7211	NS66D	00 57 49.9	–72 11 47.1	0.030	0.0244	–0.75±0.04
J0106–7242		01 06 32.1	–72 42 17.0	0.024	0.020	–0.55±0.02

5 ASKAP SMC PLANETARY NEBULA SAMPLE

The location and proximity of the SMC also provides an opportunity to create a complete sample of radio continuum detected planetary nebulae (PNe) in that nearby galaxy. PNe are important for studies of the chemical, atomic, molecular and solid-state galactic ISM enrichment (Kwok 2005, 2015). The next generation ASKAP surveys aim to provide detection of lower surface brightness planetary nebula (PN) to help complete the SMC PN sample.

Previous searches for radio PNe in the SMC (Payne et al. 2008; Filipović et al. 2009; Bojčić et al. 2010; Levens et al. 2016) yielded 16 bona-fide PN detections. Our ASKAP ESP survey has revealed 6 new PN radio detections (see Table 9) reported here for the first time (Figure 14), bringing the total number of known SMC PNe detected in radio to 22. Our new data contribute 18 new accurate radio continuum flux density measurements from ASKAP on this sample (excluding dubious detections and upper flux limits), of which 7 are at 960 MHz and 11 at 1320 MHz.

All finding charts created here have been visually inspected for a possible detection. Of 102 true, likely and possible SMC PNe in our base catalogue we have matched 17

radio counterparts with peak emission over three times the local noise in the 1320 MHz map and 8 in the 960 MHz map. The flux densities were measured using the Gaussian fitting method `imfit` from `CASA`⁴ (McMullin et al. 2007). Since none of the SMC PNe are expected to be resolved based on their known optical size, the Gaussian fitting was constrained to the beam size, effectively measuring the peak of the emission. Calculations of uncertainties for this method are based on Condon (1997) and have been adopted directly from `imfit`'s output. We visually inspected all possible detections with a peak brightness over $F \geq 3\sigma$ using a comparison between the original and the residual maps.

The results are presented in Table 9 and Figure 14. Out of 17 detections at 1320 MHz, we measured accurate flux densities for 11 PNe with peak brightness over 5σ . Likewise, in the 960 MHz band we accurately measured 7 out of 8 detected PNe. We flagged PNe with the peak brightness below 5σ in Table 9 with a value in parentheses. The flux

⁴ We also used `AEGEAN`, `MIRIAD` and `SELAVY` software packages to check for consistency and we found no noticeable discrepancy between various source finders.

density estimates for these PNe can be considered only as upper limits.

We modelled 5 GHz flux densities for all detected PNe in order to construct a radio continuum spectrum distribution of radio-detected SMC PNe. The flux modelling was performed as follows: *a*) if more than 2 data points were available we apply free-free emission spectral energy modelling (Spectral Energy Distribution (SED); see further text), *b*) if only one or two data points were measured, we estimated the 5 GHz integrated flux density from the measurements at the frequency or frequencies available by applying a simple power law approximation i.e. $S_{5\text{GHz}} = S_\nu \cdot (5/\nu[\text{GHz}])^{-0.1}$.

For SED modelling we used a spherical shell model with a constant electron density in the shell (n_e), outer radius (R_{out}) and inner radius (R_{in}). The model can now be applied to measured data points with:

$$S_\nu = \frac{4\pi k T_e \nu^2}{c^2 D^2} R_{\text{out}}^2 \int_0^\infty x(1 - e^{-\tau_\nu \cdot g_1(x)}) dx \quad (1)$$

where τ_ν is the optical thickness through the centre of the nebula at frequency ν which, for an assumption of $n_e = \text{const}$ and a pure hydrogen isothermal plasma, can be approximated with $\tau_\nu \approx 8.235 \cdot 10^{-2} T_e^{-1.35} \nu^{-2.1} n_e^2 \cdot 2(R_{\text{out}} - R_{\text{in}})$. Finally, the function $g(x)$ describes the geometry of the nebula (see Olson 1975, for more details). For this model $g(x)$ has a form:

$$\begin{aligned} g_1(x) &= \sqrt{1-x^2} - \sqrt{\mu^2-x^2} && \text{for } x < \mu, \\ &= \sqrt{1-x^2} && \text{for } \mu \leq x < 1 \text{ and} \\ &= 0 && \text{for } x \geq 1, \end{aligned} \quad (2)$$

where $\mu = R_{\text{in}}/R_{\text{out}}$ i.e. inner to outer radii ratio. We fixed the electron temperature to its canonical value ($T_e = 10^4$ K) and $\mu = 0.4$ as this is found to be the expected average value for majority of Galactic PNe (Schönberner et al. 2007; Marigo et al. 2001). With an assumed distance to the SMC of 60 kpc we fit the two free parameters, R_{out} and the emission measure (EM), through the centre of the nebula. Finally, the model shown here has been used to estimate the integrated flux density at 5 GHz.

In Fig. 15 we show graphical results of the SED fitting. From the six PNe with an adequate number of data points to apply our spherical shell model, only four converged to acceptable values of R_{out} and EM . For two PNe (SMP S14 and SMP S22) the model failed to converge and the data were fitted with the simple power law $S_\nu \sim \nu^\alpha$. The spectral indices (α) obtained are -0.09 and -0.1 for SMP S14 and SMP S22, respectively.

We present the modelled 5 GHz total flux densities in Table 9 (Column 11). The distribution of the modelled 5 GHz total flux densities for the detected sample is presented in Fig. 16. It can be seen that the number of PNe drops down below 0.6 mJy which is approximately the detection limit for ASKAP ESP data. Objects detected below this limit are either upper limits or detections originating from high sensitivity ATCA observations (Wong et al. 2011b). Therefore, we believe that our sample of radio detected SMC PNe is now complete down to ~ 0.6 mJy. We have used this distribution to roughly estimate the number

of SMC PNe which will be detectable in future ASKAP observations of the SMC.

With the approximation that PNe are fully ionised spherical shells of constant mass, expanding with constant velocity and ionised by a non-evolving central star (Henize & Westerlund 1963) the optically thin radio continuum flux would behave as $F \propto R(t)^{-3} \propto t^{-3}$. Although simplistic, this approximation has proven to be quite effective in describing changes in flux from Balmer lines during the expansion phase in a large number of observationally constructed PN luminosity functions (Reid & Parker 2010; Ciardullo 2010).

Using a sample of radio catalogued Galactic PNe, Bojčić (2010) showed that the theoretical shape of the PNLf (Ciardullo et al. 1989) effectively describes the distribution of radio flux densities of PNe at a known distance. Using our assumption that the SMC PN radio sample is now complete down to 0.6 mJy, we have used the theoretical shape of the PNLf to estimate the distribution of 5 GHz integrated flux densities below the ASKAP ESP detection limit (more details in Bojčić et al. 2019, in prep.). We fit the truncated exponential function (Ciardullo et al. 1989) to the obtained distribution of $\log_{10}(S_{5\text{GHz}})$ fluxes (in mJy). The data is binned to 0.2 dex in log flux density and we have used only bins containing PNe with $S_{5\text{GHz}} > 0.6$ mJy for the fit. The estimated rough model is over-plotted on the resulting histogram (Figure 16; dashed line). Finally, we anticipate that increasing the sensitivity by an order of magnitude would allow detection of another 20 SMC PNe, while reaching a $10 \mu\text{Jy beam}^{-1}$ (Norris et al. 2011) will allow us to increase the number of detections to ≈ 120 PNe i.e. over 50 per cent of the expected SMC PNe population (Jacoby & De Marco 2002).

6 OTHER INTERESTING SOURCES

In Sections 4 and 5 we investigated SNRs and PN populations within the SMC. Large SMC H II region complexes N 19 and N 66 are shown in Figures 3 and 4. Together with other SMC H II regions and YSOs, they will be further investigated in our subsequent papers.

We would also like to highlight some sources of interest behind the SMC that are worth following up. Due to their complex radio structure they are probes of galaxy interactions or interaction with the environment. These are presented in Figures 17, 18, 19, 20 and 21 and would fall into the category of extended radio AGN.

One of the most interesting sources behind the SMC revealed by our ASKAP observations is the radio AGN shown in Figure 17. This object displays a set of radio lobes associated to the an infrared IRAC source (background of Figure 17). Also associated with the same source seems to be a radio jet with direction pointing towards the observer. Over the past year there has been a multi-wavelength effort to reveal of the true nature behind this peculiar radio structure, which might be linked to a binary supermassive black hole. Still we cannot rule out chance coincidence. Scheduled follow-up observations, with ATCA (PI: Vardoulaki) and SALT (PI: van Loon), will help shed light to the nature of this interesting radio source.

Other sources also show complex AGN structures with various morphological types (Figures 19 and 20) (see also

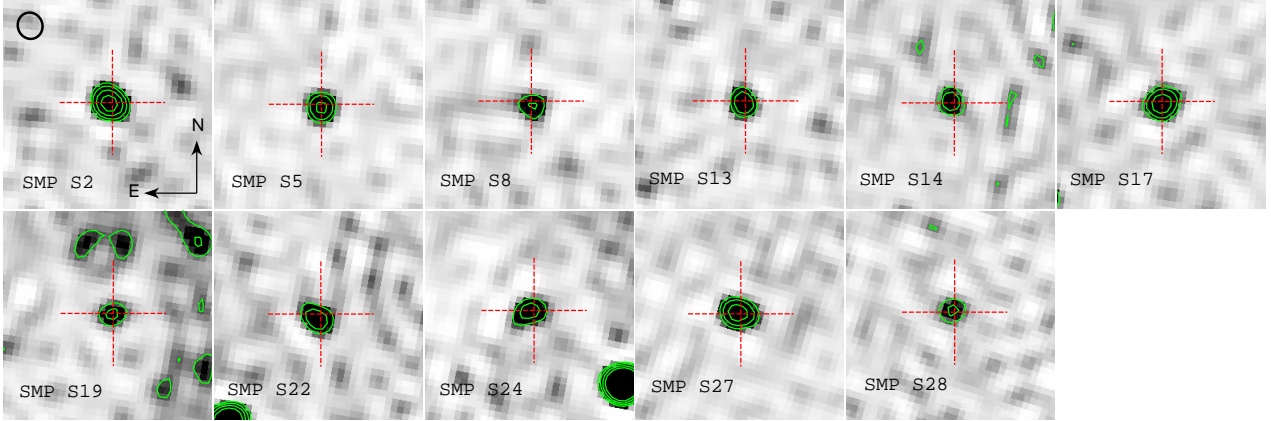


Figure 14. Finding charts of 11 SMC PNe with positive detection at 1320 MHz. Each field is 2 arcmin in size and the grey-scale uses the same *sinh* stretching. The approximate shape of the synthesized beam and orientation of each chart is displayed in the upper left corner. Red cross represents the catalogued position of a PN and green contours are radio continuum intensity at 3, 5, 8 and $12\times$ RMS noise measured in the vicinity of the object. Here, we present only objects with 5σ detections for which we measured accurate flux densities. N is up and E is left in each panel.

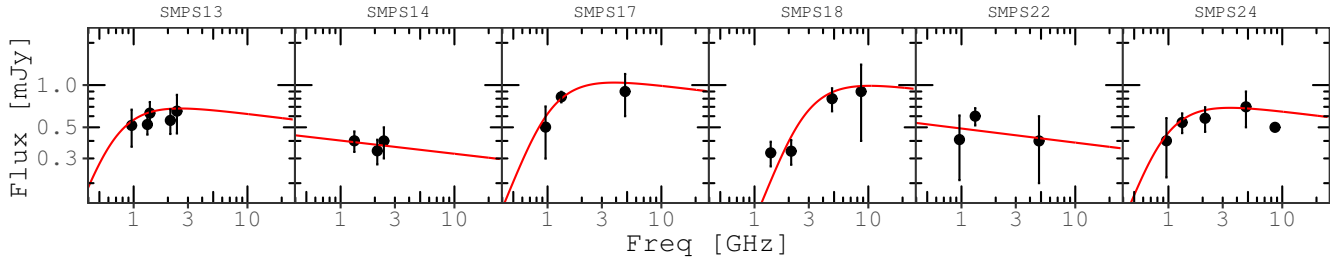


Figure 15. Best fit model SEDs to the observed flux densities for 6 SMC PNe with three or more available and good data points.

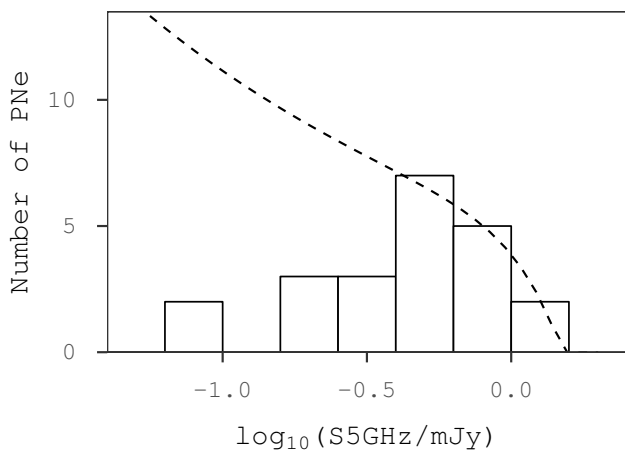


Figure 16. Planetary nebulae luminosity function (PNLF) for the SMC. The dashed line represents the theoretical PNLf estimated assuming the sample is complete down to 0.6 mJy.

O'Brien et al. 2018) and sizes, including a bent source in a possible galaxy cluster (Figure 18). Such morphology of the extended radio emission, is expected from binary driven

jets. A similar configuration is also seen toward other Super Massive Black Hole (SMBH)s, such as OJ 287 (Kushwaha et al. 2019). The object in Figure 21 is a slightly bent FR-I type radio galaxy, possibly the central part of a Wide-Angle Tail (WAT) in a cluster of galaxies.

We also examined seven Flat Spectrum Radio Quasars (FSRQs) and BL Lacertae (BL-Lac) candidates from Żywucka et al. (2018) in our radio catalogues. We found that objects J0111–7302 (proposed BL-Lac⁵; Figure 23) and possibly J0120–7334 (proposed FSRQs; Figure 22) exhibit typical FR-I morphology with complex but steep spectral indices which would argue for their AGN nature. The other five sources listed in Żywucka et al. (2018) are point-like radio sources in our catalogues: J0039–7356 (BL-Lac; $\alpha = -1.1$), J0054–7248 (FSRQs; detected only at 1320 MHz), J0114–7320 and J0122–7152 (both proposed FSRQs but we detect as a complex AGN with jets) and J0123–7236 (BL-Lac; $\alpha = -0.7$). In addition, we found four radio sources in our catalogue that correspond to the Visual and Infrared

⁵ We note that BL-Lac's with large extents are assumed to be compact which is in contrast to this object. We also note that, for example, Hernández-García et al. (2017) show several known extended (even giant) BL-Lac

Table 9. Radio continuum population of PNe in the SMC. The new ASKAP radio continuum detection and integrated flux density measurements of the SMC PNe are indicated with †. Uncertain detections and upper and lower limits in flux estimates are indicated in flux columns with :, < and >, respectively. The integrated flux density errors are <10 per cent unless otherwise stated.

Other Name	RA (J2000)	DEC (J2000)	ATCA $S_{3\text{cm}}$ 8640 MHz (mJy)	ATCA $S_{6\text{cm}}$ 4800 MHz (mJy)	ATCA $S_{13\text{cm}}$ 2400 MHz (mJy)	ATCA-CABB $S_{2.1\text{GHz}}$ 2100 MHz (mJy)	ATCA $S_{20\text{cm}}$ 1388 MHz (mJy)	ASKAP $S_{23\text{cm}}$ 1320 MHz (mJy)	ASKAP $S_{32\text{cm}}$ 960 MHz (mJy)	model $S_{6\text{cm}}$ 5000 MHz (mJy)
(1)	(2)	(3)	(4)	(5)	(6)	(7)	(8)	(9)	(10)	(11)
SMP S2†	00:32:39	-71:41:59.5	(2)	1.25±0.08	1.1±0.2	1.1
SMP S3†	00:34:22	-73:13:21.5	(0.3)	(0.4)	0.3
SMP S5†	00:41:22	-72:45:16.8	0.67±0.08	0.3±0.2	0.6
SMP S6	00:41:28	-73:47:06.4	1.1±0.5	1.3±0.1	>0.2	1.2
SMP S8†	00:43:25	-72:38:18.8	0.43±0.08	...	0.4
SMP S9	00:45:21	-73:24:10.0	0.15	0.1
SMP S10†	00:47:00	-72:49:16.6	(0.3)	(0.4)	...	0.2
SMP S13†	00:49:52	-73:44:21.7	0.7±0.2	0.56	...	0.52±0.08	0.52±0.15	0.6
SMP S14†	00:50:35	-73:42:57.9	0.4±0.1	0.34	...	0.40±0.06	...	0.4
SMP S16†	00:51:27	-72:26:11.7	...	0.6±0.1	<0.4	...	0.6
J18	00:51:43	-73:00:54.5	0.24	0.2
SMP S17†	00:51:56	-71:24:44.2	...	0.9±0.3	0.82±0.07	0.5±0.2	0.9
SMP S18†	00:51:58	-73:20:31.9	0.9±0.5	0.8±0.15	...	0.34	0.3	(0.3)	...	0.8
SMP S19†	00:53:11	-72:45:07.6	0.6±0.2	0.36±0.08	...	0.6
MA891	00:55:59	-72:14:00.3	0.92	0.8
LIN 302†	00:56:19	-72:06:58.5	0.11	...	(0.3)	...	0.1
SMP S21	00:56:31	-72:27:02.0	0.21	0.2
SMP S22†	00:58:37	-71:35:48.8	...	0.4±0.2	0.60±0.08	0.4±0.2	0.4
SMP S23†	00:58:42	-72:56:59.9	(0.4)	...	0.3
SMP S24†	00:59:16	-72:01:59.8	0.5	0.7±0.2	...	0.58	...	0.54±0.09	0.4±0.2	0.7
SMP S27†	01:21:11	-73:14:34.8	0.88±0.08	0.68±0.10	0.8
SMP S28†	01:24:12	-74:02:32.3	0.32±0.07	...	0.3

Survey Telescope for Astronomy (VISTA; Emerson et al. 2006), survey of the MCs (VMC; Cioni et al. 2011) and spectroscopically confirmed quasars (Ivanov et al. 2016). They are J0027-7223 ($S_{1320\text{MHz}}=0.265\text{ mJy}$), J0029-7146 ($\alpha = -1.0$), J0035-7201 ($\alpha = -0.5$) and J0119-7348 ($\alpha = -0.8$). While small, this sample exhibits steep spectral indices typical of the majority of background radio objects.

Finally, we note a radio detection of an ultra-bright submillimeter galaxy MM J01071-7302 (Takekoshi et al. 2013) and found a steep spectrum with $\alpha = -0.9$.

In total, we found 7736 point radio sources with fluxes over 5 times the local noise, the vast majority of which are likely to be in the background of the SMC. Through absorption measurements, all these sources can provide excellent probes for the study of cold gas in both SMC and the Galaxy (e.g. Li et al. 2018; McClure-Griffiths et al. 2015; Dickey et al. 2013). A more detailed analysis of these background sources will be presented in Pennock et al. (in prep.).

7 CONCLUSIONS

In this paper we present the ASKAP EMU ESP radio continuum survey of the SMC taken at 960 MHz and 1320 MHz. Our findings can be summarised as follows:

- This new ASKAP survey is a significant improvement (factor of ~4 in the median RMS) compared to previous ATCA/MOST surveys of the SMC.
- We identify 4489 and 5954 point sources at 960 MHz and 1320 MHz, respectively (Tables 2 and 3), with the majority of these sources detected above the 5σ threshold in their respective bands. We also list non-point sources at both ASKAP frequencies in Tables 5 and 6 (282 and 641, respectively).

- Combining our two new ASKAP catalogues with other radio continuum surveys, we found 7736 point-like sources in common which we list in Table 4, together with spectral indices we determined from all available survey data.

- Two new low surface brightness SNR candidates were discovered, bringing the total number of SNRs and SNR candidates in the SMC to 23.

- Radio counterparts to 22 optically known PNe were detected. This sample of PNe is complete down to 0.6 mJy.

ACKNOWLEDGEMENTS

The Australian SKA Pathfinder (ASKAP) are part of the Australian Telescope which is funded by the Commonwealth of Australia for operation as National Facility managed by CSIRO. We used the KARMA and MIRIAD software packages developed by the Australia Telescope National Facility (ATNF). Operation of ASKAP is funded by the Australian Government with support from the National Collaborative Research Infrastructure Strategy. ASKAP uses the resources of the Pawsey Supercomputing Centre. Establishment of ASKAP, the Murchison Radio-astronomy Observatory and the Pawsey Supercomputing Centre are initiatives of the Australian Government, with support from the Government of Western Australia and the Science and Industry Endowment Fund. We acknowledge the Wajarri Yamatji people as the traditional owners of the Observatory site. T.D.J. acknowledges support for this research from a Royal Society Newton International Fellowship, NF171032. M.J.M. acknowledges the support of the National Science Centre, Poland, through the SONATA BIS grant 2018/30/E/ST9/00208. The National Radio Astronomy Observatory is a facility of the National Science Found-

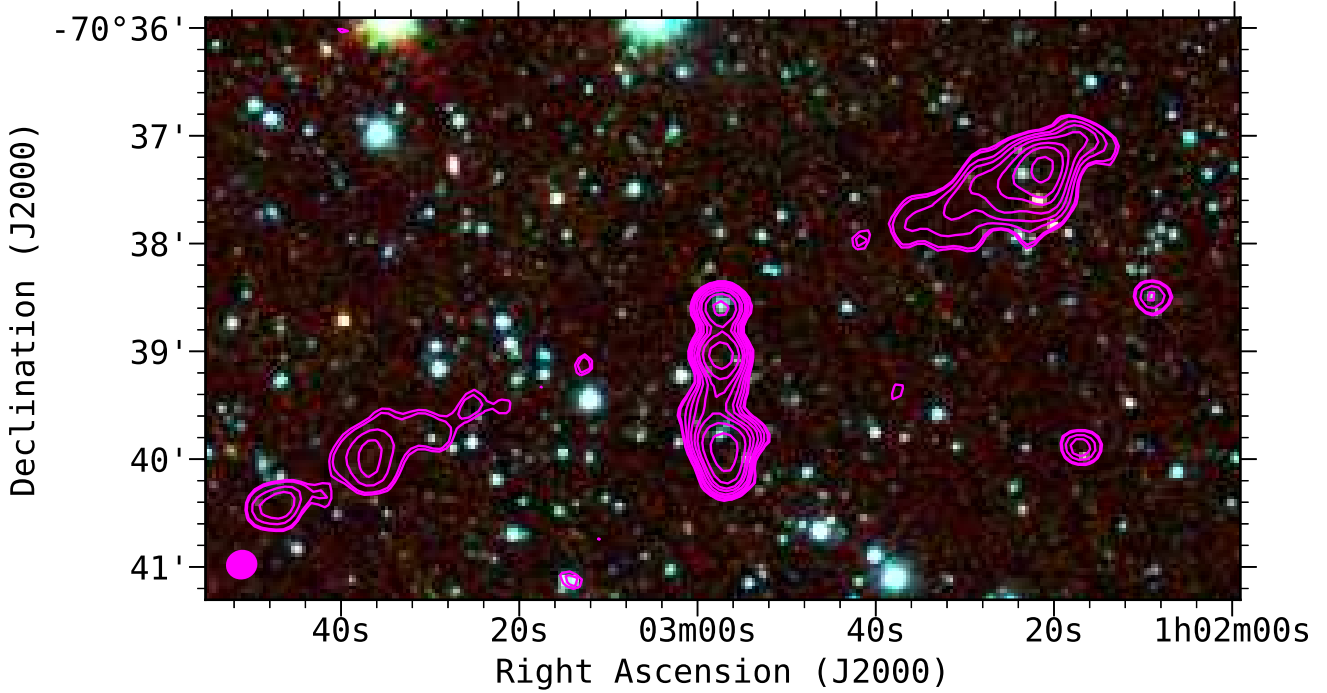


Figure 17. ASKAP ESP image (contours) of the possible double black hole AGN. The background image is a three-colour IRAC composite with 8.0, 4.5 and 3.6 μm represented as red, green and blue, respectively. The magenta radio contours are from our 1320 MHz survey drawn at 0.25, 0.3, 0.5, 0.7, 1, 1.5, 2, 3 and 5 mJy beam^{-1} . The 1320 MHz radio beam size of $16.3'' \times 15.1''$ is shown as a filled magenta ellipse in the lower left corner.

dation operated under cooperative agreement by Associated Universities, Inc. Partial support for L.R. comes from U.S. National Science Foundation grant AST1714205 to the University of Minnesota. Project/paper is partially supported by NSFC No. 11690024, CAS International Partnership No. 114A11KYSB20160008. This work is part of the project 176005 “Emission nebulae: structure and evolution” supported by the Ministry of Education, Science, and Technological Development of the Republic of Serbia. H.A. benefited from project CIIC 218/2019 of University of Guanajuato. The authors would like to thank the anonymous referee for a constructive report and useful comments.

REFERENCES

- Alsaberi R. Z. E., et al., 2019, *MNRAS*, 486, 2507
 Arbutina B., Urošević D., Andjelić M. M., Pavlović M. Z., Vukotić B., 2012, *The Astrophysical Journal*, 746, 79
 Arbutina B., Urošević D., Vučetić M. M., Pavlović M. Z., Vukotić B., 2013, *ApJ*, 777, 31
 Bojičić I., 2010, PhD thesis, Macquarie University
 Bojičić I. S., Filipović M. D., Crawford E. J., 2010, *Serbian Astronomical Journal*, 181, 63
 Bozzetto L. M., et al., 2017, *ApJS*, 230, 2
 Ciardullo R., 2010, *Publ. Astron. Soc. Australia*, 27, 149
 Ciardullo R., Jacoby G. H., Ford H. C., Neill J. D., 1989, *ApJ*, 339, 53
 Cioni M.-R. L., et al., 2011, *A&A*, 527, A116
 Clarke J. N., 1976, *MNRAS*, 174, 393
 Collier J., 2016, PhD thesis, Western Sydney University (Australia)
 Collier J. D., et al., 2018, *MNRAS*, 477, 578
 Condon J. J., 1997, *PASP*, 109, 166
 Cornwell T. J., Humphreys B., Lenc E., Voronkov M., Whiting M. T., 2011, Technical Report 028, Askap-sw-0020: ASKAP science processing
 Crawford E. J., Filipović M. D., de Horta A. Y., Wong G. F., Tothill N. F. H., Draskovic D., Collier J. D., Galvin T. J., 2011, *Serbian Astronomical Journal*, 183, 95
 Crawford E. J., Filipović M. D., McEntaffer R. L., Brantseg T., Heitritter K., Roper Q., Haberl F., Urošević D., 2014, *AJ*, 148, 99
 Davies R. D., Elliott K. H., Meaburn J., 1976, *Mem. RAS*, 81, 89
 DeBoer D. R., et al., 2009, *IEEE Proceedings*, 97, 1507
 Di Teodoro E. M., et al., 2019, *MNRAS*, 483, 392
 Dickey J. M., et al., 2013, *Publ. Astron. Soc. Australia*, 30, e003
 Emerson J., McPherson A., Sutherland W., 2006, *The Messenger*, 126, 41
 Filipović M. D., Jones P. A., White G. L., Haynes R. F., Klein U., Wielebinski R., 1997, *A&AS*, 121, 321
 Filipović M. D., Haynes R. F., White G. L., Jones P. A., 1998, *A&AS*, 130, 421
 Filipović M. D., Bohlson T., Reid W., Staveley-Smith L., Jones P. A., Nohejl K., Goldstein G., 2002, *MNRAS*, 335, 1085
 Filipović M. D., Payne J. L., Reid W., Danforth C. W., Staveley-Smith L., Jones P. A., White G. L., 2005, *MNRAS*, 364, 217

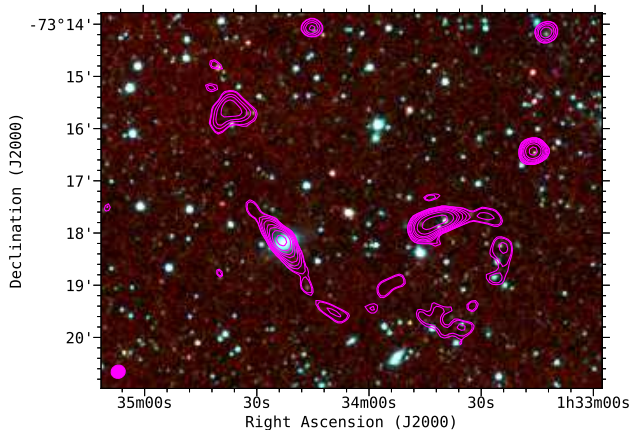


Figure 18. ASKAP ESP image (contours) shows a long, twisted structure that appears to be a highly distorted tailed radio galaxy associated with 2MASX J01342297–7318113, a bright galaxy ($V=15.9$ mag) without spectroscopic redshift. Although the multiple bends might suggest that there is actually more than one radio source, there is no obvious second optical/IR host. The bright compact object near the centre of the radio source elongated E-W and ~ 3 arcmin W of 2MASX J01342297–7318113, is 2MASS J01334172–7317527, but GaiaDR2 (Gaia Collaboration et al. 2018) shows it to be a star with significant parallax and proper motion. The background image is a three-colour IRAC composite with 8.0, 4.5 and 3.6 μm represented as red, green and blue, respectively. The magenta radio contours are from our 1320 MHz survey drawn at 0.25, 0.3, 0.5, 0.7, 1, 1.5, 2, 3 and 5 mJy beam^{-1} . The 1320 MHz beam size of $16.3'' \times 15.1''$ is shown as a filled magenta ellipse in the lower left corner.

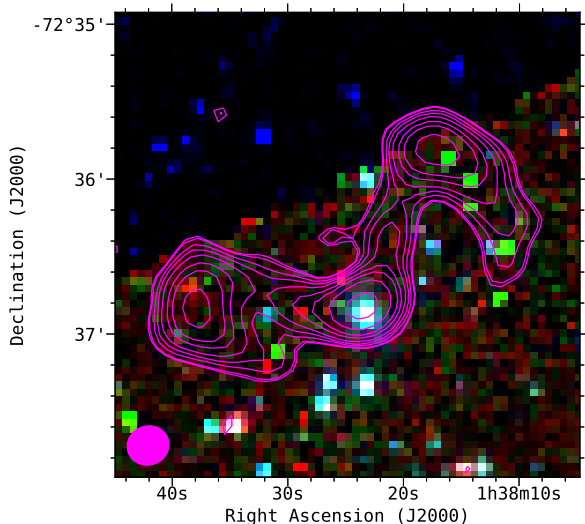


Figure 19. ASKAP ESP image of the “duck” AGN complex or possible bent-tail radio galaxy. The background image is a three-colour IRAC composite with 8.0, 4.5 and 3.6 μm represented as red, green and blue, respectively. The magenta radio contours are from our 1320 MHz survey drawn at 0.25, 0.3, 0.5, 0.7, 1, 1.5, 2, 3 and 5 mJy beam^{-1} . The 1320 MHz beam size of $16.3'' \times 15.1''$ is shown as a filled magenta ellipse in the lower left corner.

- Filipović M. D., et al., 2008, *A&A*, 485, 63
 Filipović M. D., et al., 2009, *MNRAS*, 399, 769
 Findlay J. W., 1966, *ARA&A*, 4, 77
 For B.-Q., et al., 2018, *MNRAS*, 480, 2743
 Franzen T. M. O., et al., 2015, *MNRAS*, 453, 4020
 Gaensler B. M., Haverkorn M., Staveley-Smith L., Dickey J. M., McClure-Griffiths N. M., Dickel J. R., Wolleben M., 2005, *Science*, 307, 1610
 Gaia Collaboration et al., 2018, *A&A*, 616, A1
 Galvin T. J., et al., 2018, *MNRAS*, 474, 779
 Gordon K. D., et al., 2011, *AJ*, 142, 102
 Gvaramadze V. V., Kniazev A. Y., Oskinova L. M., 2019, *MNRAS*, 485, L6
 Haberl F., Filipović M. D., Pietsch W., Kahabka P., 2000, *A&AS*, 142, 41
 Haberl F., Sturm R., Filipović M. D., Pietsch W., Crawford E. J., 2012a, *A&A*, 537, L1
 Haberl F., et al., 2012b, *A&A*, 545, A128
 Hancock P. J., Murphy T., Gaensler B. M., Hopkins A., Curran J. R., 2012, *Agean: Compact source finding in radio images*, Astrophysics Source Code Library (ascl:1212.009)
 Hancock P. J., Trott C. M., Hurley-Walker N., 2018, *Publ. Astron. Soc. Australia*, 35, e011
 Haynes R. F., Klein U., Wielebinski R., Murray J. D., 1986, *A&A*, 159, 22
 Henize K. G., 1956, *ApJS*, 2, 315
 Henize K. G., Westerlund B. E., 1963, *ApJ*, 137, 747
 Hernández-García L., et al., 2017, *A&A*, 603, A131
 Hilditch R. W., Howarth I. D., Harries T. J., 2005, *MNRAS*, 357, 304
 Hotan A. W., et al., 2014, *Publ. Astron. Soc. Australia*, 31, e041
 Inoue H., Koyama K., Tanaka Y., 1983, in Danziger J., Gorenstein P., eds, *IAU Symposium Vol. 101, Supernova Remnants and their X-ray Emission*. pp 535–540
 Ivanov V. D., et al., 2016, *A&A*, 588, A93
 Jacoby G. H., De Marco O., 2002, *AJ*, 123, 269
 Johnston S., et al., 2008, *Experimental Astronomy*, 22, 151
 Kushwaha P., de Gouveia Dal Pino E. M., Gupta A. C., Wiita P. J., 2019, *arXiv e-prints*,
 Kwok S., 2005, *Journal of Korean Astronomical Society*, 38, 271
 Kwok S., 2015, *Highlights of Astronomy*, 16, 623
 Leverenz H., Filipović M. D., Bojčić I. S., Crawford E. J., Collier J. D., Grieve K., Drašković D., Reid W. A., 2016, *Ap&SS*, 361, 108
 Leverenz H., Filipović M. D., Vukotić B., Urošević D., Grieve K., 2017, *MNRAS*, 468, 1794
 Li D., et al., 2018, *ApJS*, 235, 1
 Maggi P., et al., 2016, *A&A*, 585, A162
 Mao S. A., Gaensler B. M., Stanimirović S., Haverkorn M., McClure-Griffiths N. M., Staveley-Smith L., Dickey J. M., 2008, *ApJ*, 688, 1029
 Mao S. A., et al., 2012, *ApJ*, 759, 25
 Marigo P., Girardi L., Groenewegen M. A. T., Weiss A., 2001, *A&A*, 378, 958
 Mauch T., Murphy T., Buttery H. J., Curran J., Hunstead R. W., Pietsch W., Robertson J. G., Sadler E. M., 2003, *MNRAS*, 342, 1117
 McClure-Griffiths N. M., et al., 2015, *Advancing Astrophysics with the Square Kilometre Array (AASKA14)*, p. 130
 McClure-Griffiths N. M., et al., 2018, *Nature Astronomy*, 2, 901
 McConnell D., 2017, *Technical report, ACES memo 15: Observing with ASKAP: Optimisation for survey speed*. CSIRO Australia Telescope National Facility
 McConnell D., et al., 2016, *Publ. Astron. Soc. Australia*, 33, e042
 McGee R. X., Newton L. M., Butler P. W., 1976, *Australian Journal of Physics*, 29, 329
 McMullin J. P., Waters B., Schiebel D., Young W., Golap K.,

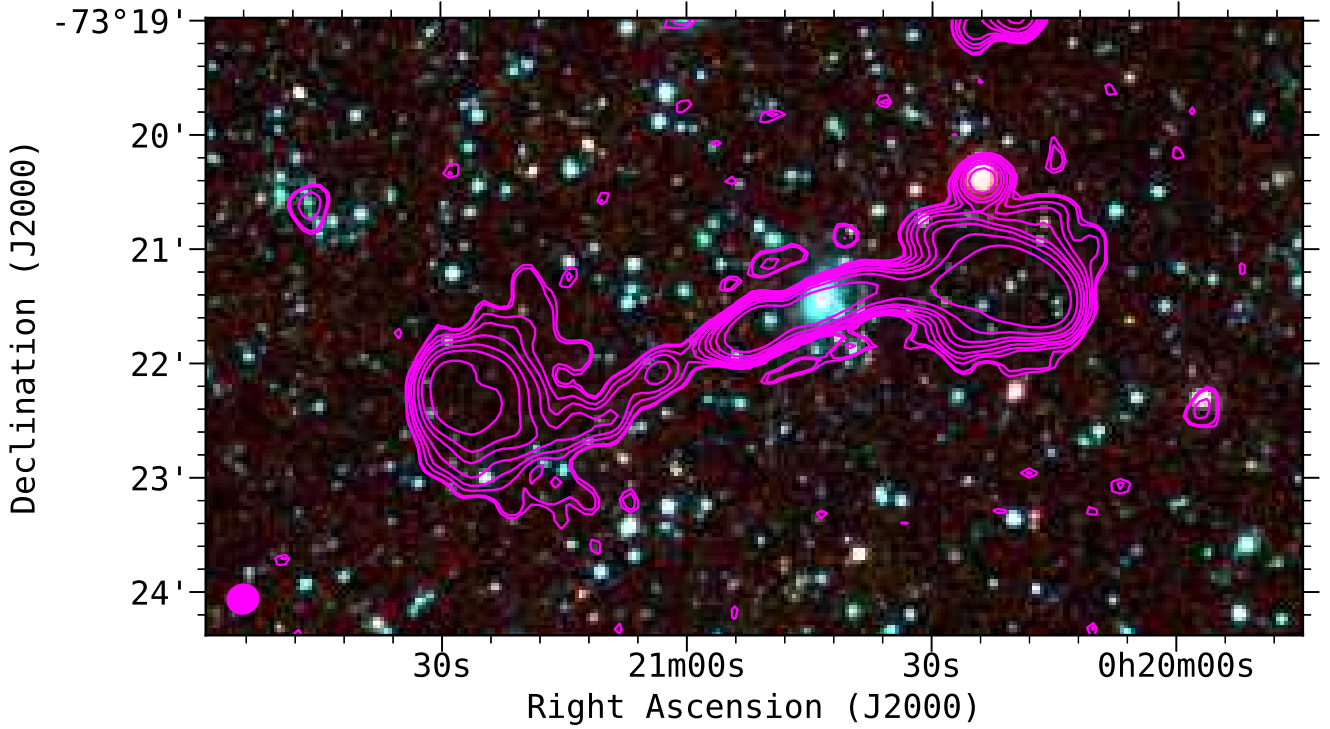


Figure 20. ASKAP ESP image of the FR-II AGN. The background image is a three-colour IRAC composite with 8.0, 4.5 and 3.6 μm represented as red, green and blue, respectively. The magenta radio contours are from our 1320 MHz survey drawn at 0.25, 0.3, 0.5, 0.7, 1, 1.5, 2, 3 and 5 mJy beam^{-1} . The 1320 MHz beam size of $16.3'' \times 15.1''$ is shown as a filled magenta ellipse in the lower left corner.

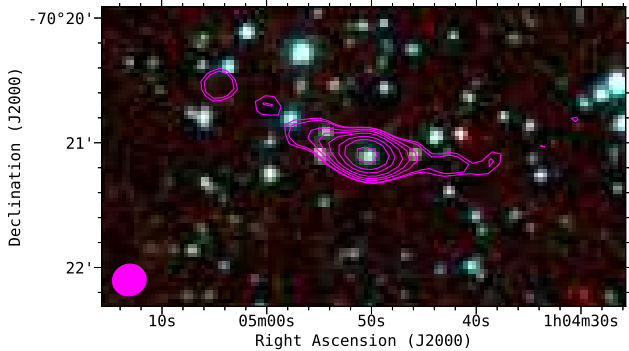


Figure 21. ASKAP ESP image of the FR-I AGN. The background image is a three-colour IRAC composite with 8.0, 4.5 and 3.6 μm represented as red, green and blue, respectively. The magenta radio contours are from our 1320 MHz survey drawn at 0.25, 0.3, 0.5, 0.7, 1, 1.5, 2, 3 and 5 mJy beam^{-1} . The 1320 MHz beam size of $16.3'' \times 15.1''$ is shown as a filled magenta ellipse in the lower left corner.

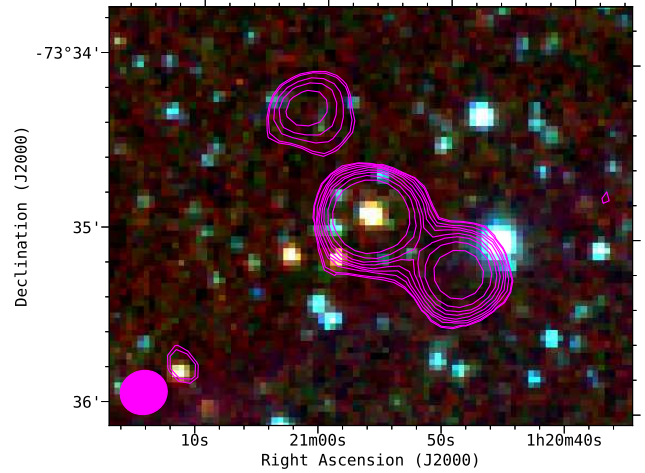


Figure 22. ASKAP ESP image of the possible AGN J0120-7334. The background image is a three-colour IRAC composite with 8.0, 4.5 and 3.6 μm represented as red, green and blue, respectively. The yellow radio contours are from our 1320 MHz survey drawn at 0.25, 0.3, 0.5, 1, 2, 3, 5, 10, 20 and 30 mJy beam^{-1} . The 1320 MHz beam size of $16.3'' \times 15.1''$ is shown as a filled magenta ellipse in the lower left corner.

2007, in *Astronomical data analysis software and systems XVI*, p. 127
 Meixner M., et al., 2006, *AJ*, 132, 2268
 Middelberg E., et al., 2008, *AJ*, 135, 1276
 Murphy T., et al., 2013, *Publ. Astron. Soc. Australia*, 30, e006
 Norris R. P., et al., 2006, *AJ*, 132, 2409
 Norris R. P., et al., 2011, *Publ. Astron. Soc. Australia*, 28, 215
 O'Brien A. N., Norris R. P., Tothill N. F. H., Filipović M. D., 2018, *MNRAS*, 481, 5247

Oliveira J. M., et al., 2013, *MNRAS*, 428, 3001
 Olton F. M., 1975, *A&A*, 39, 217
 Owen R. A., et al., 2011, *A&A*, 530, A132
 Pavlović M. Z., Urošević D., Arbutina B., Orlando S., Maxted N.,

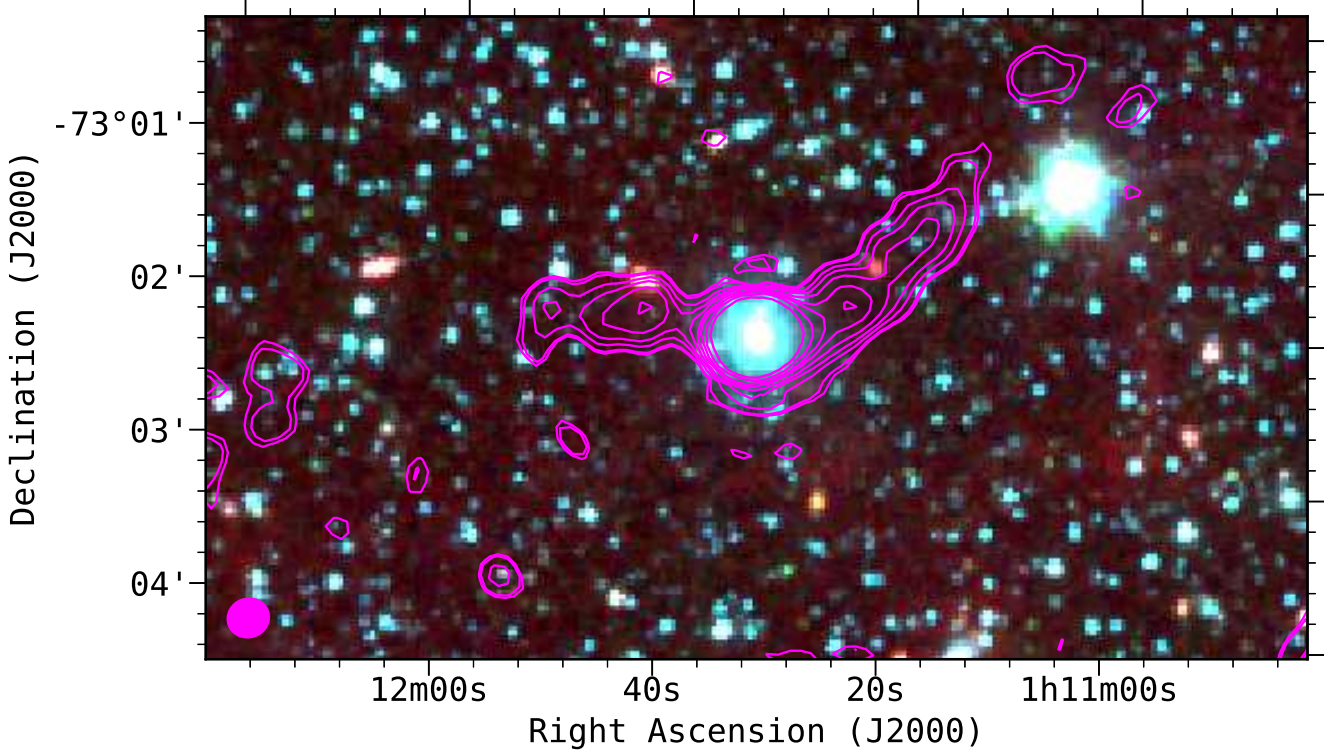


Figure 23. ASKAP ESP image of the AGN complex J0111–7302. The background image is a three-colour IRAC composite with 8.0, 4.5 and 3.6 μm represented as red, green and blue, respectively. The yellow radio contours are from our 1320 MHz survey drawn at 0.25, 0.3, 0.5, 1, 2, 3, 5, 10, 20, 30 and 50 mJy beam^{-1} . The 1320 MHz beam size of $16.3'' \times 15.1''$ is shown as a filled magenta ellipse in the lower left corner.

Filipović M. D., 2018, *ApJ*, 852, 84
 Payne J. L., Filipović M. D., Reid W., Jones P. A., Staveley-Smith L., White G. L., 2004, *MNRAS*, 355, 44
 Payne J. L., White G. L., Filipović M. D., Pannuti T. G., 2007, *MNRAS*, 376, 1793
 Payne J. L., Filipović M. D., Crawford E. J., de Horta A. Y., White G. L., Stootman F. H., 2008, *Serbian Astronomical Journal*, 176, 65
 Pietrzyński G., et al., 2019, *Nature*, 567, 200
 Reid W. A., Parker Q. A., 2010, *MNRAS*, 405, 1349
 Reid W. A., Payne J. L., Filipović M. D., Danforth C. W., Jones P. A., White G. L., Staveley-Smith L., 2006, *MNRAS*, 367, 1379
 Roper Q., McEntaffer R. L., DeRoo C., Filipović M., Wong G. F., Crawford E. J., 2015, *ApJ*, 803, 106
 Sano H., et al., 2019, *arXiv e-prints*,
 Sault R. J., Teuben P. J., Wright M. C. H., 1995, in Shaw R. A., Payne H. E., Hayes J. J. E., eds, *Astronomical Society of the Pacific Conference Series Vol. 77, Astronomical Data Analysis Software and Systems IV*. p. 433 ([arXiv:astro-ph/0612759](https://arxiv.org/abs/astro-ph/0612759))
 Schönberner D., Jacob R., Steffen M., Sandin C., 2007, *A&A*, 473, 467
 Sturm R., et al., 2013, *A&A*, 558, A3
 Takekoshi T., et al., 2013, *ApJ*, 774, L30
 Turtle A. J., Ye T., Amy S. W., Nicholls J., 1998, *Publ. Astron. Soc. Australia*, 15, 280
 Urošević D., Pavlović M. Z., Arbutina B., 2018, *The Astrophysical Journal*, 855, 59
 Winkler P. F., et al., 2005, in *American Astronomical Society Meeting Abstracts*. p. 1380
 Wong G. F., Filipović M. D., Crawford E. J., de Horta A. Y., Galvin T., Draskovic D., Payne J. L., 2011a, *Serbian Astronomical Journal*, 182, 43
 Wong G. F., et al., 2011b, *Serbian Astronomical Journal*, 183, 103
 Wong G. F., et al., 2012a, *Serbian Astronomical Journal*, 184, 93
 Wong G. F., Filipović M. D., Crawford E. J., Tothill N. F. H., De Horta A. Y., Galvin T. J., 2012b, *Serbian Astronomical Journal*, 185, 53
 Wright A., Otrupcek R., 1990, in *PKS Catalog (1990)*.
 Ye T., Turtle A. J., Kennicutt R. C. J., 1991, *MNRAS*, 249, 722
 Żywucka N., Goyal A., Jamrozy M., Stawarz L., Ostrowski M., Kozłowski S., Udalski A., 2018, *ApJ*, 867, 131

This paper has been typeset from a $\text{T}_{\text{E}}\text{X}/\text{L}_{\text{A}}\text{T}_{\text{E}}\text{X}$ file prepared by the author.